Using human tissue models to illuminate the biology of fibrosis and to unlock new drug targets

Rachel Ann Burgoyne

Doctor of Philosophy

Newcastle University

Biosciences institute

April 2024

Abstract

Organ fibrosis is a common endpoint for a broad spectrum of chronic diseases and represents a major cause of morbidity and mortality worldwide. Metabolic dysfunction-associated steatohepatitis (MASH), the fastest growing cause of liver fibrosis and idiopathic pulmonary fibrosis (IPF), the most common and severe interstitial lung disease, are prominent fibrotic diseases which pose an increasing socioeconomic burden. At present, therapeutic approaches are extremely limited and there is an urgent need to better understand mechanisms driving fibrosis to support development of new anti-fibrotics.

There is spatial and temporal heterogeneity of pathological changes within human liver and lung tissue during fibrogenesis, which may correlate to changes in pathophysiological mediators of disease and clinical progression. In this project, we utilised cutting edge single nuclei RNA sequencing (snRNAseq) and 'omics technology to comprehensively characterise human liver and lung tissue at different stages of disease progression to identify key cellular phenotypes and molecular pathways driving fibrosis in MASH and IPF. Specifically, snRNAseq was performed on patient samples selected to represent the spectrum of MASH from F1–F4 fibrosis stage and cirrhosis, resulting in the identification of 9 targets of interest which were almost exclusively upregulated in disease-associated, high collagen type 1 expressing mesenchymal cell subpopulations. Concurrently, 'omics approaches were employed to dissect the molecular landscape of IPF by comparing macroscopically distinct regions of tissue from within the same IPF lung. Interrogation of protein heterogeneity identified novel proteins/pathways that are significantly upregulated in actively remodelling tissue for further investigation. To validate the translational relevance of these targets to human disease, precision-cut slices were generated from human liver and IPF lungs and challenged with candidate inhibitors targeting these proteins/pathways to assess anti-fibrotic and anti-inflammatory efficacy.

Overall, our findings shed light on the complex cellular and molecular mechanisms underlying fibrosis progression and highlight promising targets for further development as novel anti-fibrotic therapies.

Acknowledgements

I would like to express my sincere gratitude to all of my supervisors for their continued support, mentorship and guidance throughout my project. Particularly, I would like to thank Dr Lee Borthwick for being the best supervisor and boss I could ask for over these last 6 years. I gratefully acknowledge and thank the many collaborators who have made important contributions to this work at both Edinburgh University and Pfizer, including Dr Sebastian Wallace, Prof Neil Henderson, Dr Kevin Hart and Dr Stephen Christensen who have been continually supportive and willing to share their expertise and guidance throughout my project. I would also like to express my gratitude to Dr Laura Sabater and Dr Sandra Murphy for the help given and time taken for the acquisition and generation of the 'omics datasets.

Special thanks must be given to Ben Barksby, who has been a great colleague and even better friend, for making all those endless slicing sessions bearable (even at 1AM). Likewise, thanks must also be given to the other members of Team Borthwick, Hannah Paish and Luke Patterson, who have made my time working on this project so enjoyable. Thanks also to the members of Newcastle Fibrosis Research Group, past and present, whom I have worked with over the course of this PhD.

This work would not be possible without the expertise of Prof Andrew Fisher who, alongside Lucy Bates, transplant coordinators, surgeons, nurses and other staff from the Newcastle upon Tyne Hospitals NHS Foundation Trust, have kindly donated their time to help in the acquisition of patient and unused donor tissue. Thanks also to Dr Joaquim Majo for his assistance procuring tissue and informing tissue pathology. Importantly, I am forever grateful to the patients and family members of donors who kindly donated their organs, which were so integral to this project.

Finally, I would like to thank my parents Carl and Julie and my sister Sarah for their unwavering support, encouragement and understanding throughout my entire PhD journey, especially over these final few months.

The work completed during this PhD was funded by a joint research grant awarded to Dr Lee Borthwick and Prof Neil Henderson from Pfizer.

Table of Contents

Abbreviations

AAV	Adeno-associated virus
AEC1	Type I alveolar epithelial cells
AEC2	Type II alveolar epithelial cells
AGO2	Argonaute 2
ALK5	Activin-like kinase 5
AM	Alveolar macrophages
AST	Aspartate Aminotransferase
ATP	Adenosine triphosphate binding
BALF	Bronchoalveolar lavage fluid
BCA	bicinchoninic acid
BDL	Bile duct ligation
BMI	Body mass index
BPI	Bactericidal permeability-increasing protein
CAH	Carbonic anhydrase
CATG	Cathepsin G
CC	Chemokine (C-C motif)
CCl_4	Carbon tetrachloride
CDH11	Cadherin 11
cDNA	Complementary DNA
CLD	Chronic liver disease
COL	collagen
COPD	Chronic obstructive pulmonary disorder
CTGF	Connective tissue growth factor
CXC	Chemokine (C-X-C motif)
DAMP	Damage-associated molecular pattern
DCLK1	Doublecortin Like Kinase 1
DDR	DNA-damage response
DEF	Defensin
dTTP	deoxythymidine triphosphate

dUTP	deoxyuridine triphosphate
ECM	Extracellular matrix
EGFR	Epidermal growth factor receptor
ELISA	Enzyme Linked ImmunoSorbant Assay
EMA	European Medical Association
EMT	Epithelial-mesenchymal transition
EnMT	Endothelial-mesenchymal transition
ER	Endoplasmic reticulum
FC	Fold change
FF	Fibroblastic foci
FGFR	Fibroblast growth factor receptor
FVC	Forced vital capacity
GCKR	Glucokinase regulator
G-CSF	Granulocyte colony-stimulating factor
GM-CSF	Granulocyte-macrophage colony-stimulating factor
GSTP	Glutathione-S-transferase π
H&E	Haematoxylin & Eosin
HAS2	Hyaluronan Synthase 2
HCC	Hepatocellular carcinoma
HMGB1	High-mobility group box 1
HRCT	High-resolution computed tomography
HSC	Hepatic stellate cell
HSD17B13	Hydroxysteroid 17β- dehydrogenase
IL	Interleukin
αR1	Interleukin 1 receptor type 1
ILD	Interstitial lung disease
IM	Interstitial macrophages
IPA	Ingenuity Pathway Analysis
IPF	Idiopathic pulmonary fibrosis
ITB6	Integrin β6
K1C18	Keratin 18

KC	Kupffer cell
LAP	Latency–associated peptide
LC-MS	Liquid chromatography-mass spectrometry
LDH	Lactate Dehydrogenase
LFQ	Label-free quantification
LNP	Lipid nanoparticle
LTBP2	Latent TFG-β2 binding protein
MASH	Metabolic dysfunction-associated steatohepatitis
MASLD	Metabolic dysfunction-associated steatotic liver disease
MBOAT7	Membrane bound O-acyltransferase domain-containing 7
miRNA	micro-RNA
MMP	Metalloprotease
MoMF	Monocyte-derived macrophages
MPO	Myeloperoxidase
MRC2	Mannose receptor C type 2
MRI	Magnetic resonance imaging
MUC5B	Mucin 5B
NAFLD	Non-alcoholic fatty liver disease
NAS	NAFLD Activity Score
NE	Neutrophil elastase
NET	Neutrophil extracellular trap
PBC	Primary biliary cholangitis
PCLS	Precision cut liver slice
PCLuS	Precision cut lung slice
PCR	polymerase chain reaction
PCS	Precision cut slice
PDGF	Platelet-derived growth factor
PDGFR	Platelet-derived growth factor receptor
PF	Portal fibroblast
PFT	Pulmonary function tests
PI3K	Phosphatidylinositol 3-kinase

PNPLA3	Patatin-like phospholipase domain–containing protein 3
PORCN	Porcupine
PRR	Pattern recognition receptor
PSC	Primary sclerosing cholangitis
PSR	Picrosirius Red
QC	Quality control
qHSC	Quiescent HSC
RAGE	Receptor for advanced glycation end products
RISC	RNA-induced silencing complex
RNAseq	RNA sequencing
ROS	Reactive oxygen species
RPBX	RNA purification beads
RTEL1	Regulator of telomere elongation helicase
SAHF	Senescence-associated heterochromatin foci
SAM	Scar-associated macrophage
SASP	Senescent associated secretory phenotype
SA-β-gal	Senescence-associated β-galactosidase activity
scRNAseq	Single cell RNA sequencing
SEM	Standard error of the mean
SEP11	Septin 11
SERPH	Serpin H1
SFTPA2	Surfactant protein A2
SFTPC	Surfactant protein C
snRNAseq	Single nuclei RNA sequencing
SPARC	Secreted Protein, Acidic and Rich in Cysteine
SPP1	Osteopontin
ST	Salt-Tris
T2DM	Type 2 diabetes mellitus
TEAB	Triethylammonium bicarbonate
TERC	Telomerase RNA component
TERT	Telomerase reverse transcriptase

TGF	Transforming growth factor
THBS2	Thrombospondin 2
TIMP	Tissue inhibitors of metalloproteinase
TKI	Tyrosine kinase inhibitor
TM6SF2	Transmembrane 6 superfamily 2
TNFRSF12A	TNF Receptor Superfamily Member 12A
TNFα	Tumour necrosis factor-α
TNKS	Tankyrase
TRFL	lactotransferrin
TST	Tween with salts and Tris
UD	Unused donor
UIP	Usual interstitial pneumonia
UNC5B	Unc-5 Netrin Receptor B
VCAN	Versican
VEGFR	Vascular endothelial growth factor receptor
WNT4	Wnt Family Member 4
WNT9A	Wnt Family Member 9A
αSMA	α-smooth muscle actin

List of Figures

List of Tables

1 Introduction

1.1 Physiological wound healing

Wound healing and timely resolution of injury is understood to be one of the most complex and tightly regulated biological processes in the human body, involving synchronisation of multiple distinct cell types to restore tissue integrity and homeostasis [1]. Following injury, initiation of an acute inflammatory response results in the recruitment of neutrophils, eosinophils and basophils to begin neutralising invading pathogens and aid clearance of cell debris by phagocytosis [2]. This is followed by recruitment of monocytes which later mature to macrophages and other adaptive immune cells to further support elimination of debris as well as coordinating tissue repair [3]. Upon cessation of the inflammatory response, the second stage of wound repair shifts towards generation of new tissue and is characterised by cellular proliferation, migration of cells and angiogenesis. Here, activation and differentiation of fibroblasts to myofibroblasts is followed by the deposition of extracellular matrix (ECM) and secretion of pro-fibrogenic factors to promote edge contractility and facilitate wound closure [4]. Under normal wound healing conditions, this is then followed by the final remodelling phase where apoptosis of endothelial cells, macrophages and myofibroblasts occurs as well as the degradation of excess ECM components, including collagen, by matrix metalloproteases (MMPs) and resolution of injury [1].

1.2 Pathological wound healing - Organ fibrosis

Fibrosis occurs when the physiological wound healing process becomes deregulated either as a result of defective regenerative mechanisms or in response to severe and/or persistent injury, leading to continued proliferation and migration of myofibroblasts, deposition of ECM and release of pro-inflammatory and pro-fibrotic markers with detrimental effects [5]. Fibrosis is a common pathological feature found in a broad spectrum of chronic diseases and is characterised by the replacement of functional tissue architecture with excessive deposition of ECM, resulting in eventual loss of organ function and ultimately death if unresolved [5]. Collectively, fibrotic diseases are considered a major cause of morbidity and mortality worldwide and present an increasing clinical burden, particularly in the Western world [6,7]. While fibrosis is the common endpoint for a wide range of diseases, the underlying aetiologies and mechanisms can be either core or organ specific. Effective therapies to tackle fibrosis are

for that reason, a priority to help reduce the anticipated socioeconomic burden. However, despite considerable research, the precise mechanisms underpinning fibrosis remains relatively unclear [8]. Further investigation is therefore needed to elucidate the underlying molecular drivers of fibrosis which in turn will unveil potential targets for future therapeutic strategies.

1.3 Liver fibrosis

1.3.1 Chronic liver disease

Chronic liver disease (CLD) presents a major global healthcare problem, affecting an estimated 1.5 billion people worldwide [9], with approximately 2 million deaths per year [10]. Typical causes of CLD include, but are not limited to, viral infections (such as hepatitis B and hepatitis C), alcohol and drug consumption, metabolic diseases such as metabolic dysfunction-associated steatotic liver disease (MASLD) and autoimmune diseases such as primary biliary cholangitis (PBC). Until recently, viral hepatitis was considered the main underlying aetiology driving CLD and liver fibrosis, though recent improvements in prevention strategies and treatments options have caused a shift in trends [11]. Within the last few decades, MASLD has rapidly become the most common cause of liver dysfunction in the Western world owing to its strong association with obesity, dyslipidaemia, insulin resistance and type 2 diabetes mellitus (T2DM) [12]. Importantly, in the case of MASLD, the degree of liver fibrosis is associated with adverse patient outcomes, including development of cirrhosis, hepatocellular carcinoma (HCC) and increased mortality [13]. Fibrosis is the final common pathway of various CLDs, and effective anti-fibrotic therapies are therefore crucial to help limit disease progression and improve patient morbidity and mortality.

1.3.2 Metabolic dysfunction-associated steatotic liver disease (MASLD)

MASLD, formerly known as non-alcoholic fatty liver disease (NAFLD), is a chronic condition which encompasses a spectrum of progressive liver diseases, previously characterised by abnormal cytoplasmic retention of triglycerides by hepatocytes in the absence of excessive alcoholic intake (usually set at a threshold of <20g for women and <30g for men per day). Estimated prevalence of MASLD ranges from 24% to 38% in the general population, which substantially rises in patients with known metabolic risk factors [14,15]. Historically, NAFLD was considered as the hepatic manifestation of metabolic syndrome, with risk factors such as advancing age, high body mass index (BMI), T2DM and hypertension associated with a higher risk of progressive disease [16,17]. Accordingly, in June 2023 changes in the nomenclature were

proposed to incorporate cardiometabolic risk factors (including BMI, fasting serum glucose, blood pressure, plasma triglycerides and plasma HDL-cholesterol measurements) into patient diagnosis. Reflecting the increasing prevalence of these conditions due to changes in dietary patterns and increasingly sedentary lifestyles, MASLD is set to continually rise and is predicted to become the leading cause for liver transplantation and the main underlying aetiology for the development of liver cancer in the future [14].

1.3.2.1 Risk factors of MASLD

MASLD spans a wide range of clinical and histopathological features, from simple steatosis (defined by fat accumulation in at least 5% of hepatocytes), through to steatohepatitis (MASH; fat uptake, inflammation and hepatocellular ballooning), with potential to progress to fibrosis, cirrhosis and even HCC (Figure 1). However, not everyone with the above-mentioned risk factors will go on to develop MASLD or progress through the spectrum. Consequently, MASLD is considered a complex disease which occurs as a result of the interaction between environmental risk factors acting against a susceptible polygenic background. It is widely accepted that environmental and genetic factors play important roles in regulating and modifying disease progression in MASLD patients, with heritability in humans estimated between 20-70% [18,19]. To date, at least 5 genetic modifiers have been identified and robustly associated with increased susceptibility to, and progression of MASLD. These include patatin-like phospholipase domain–containing protein 3 (PNPLA3), transmembrane 6 superfamily 2 (TM6SF2), glucokinase regulator (GCKR), membrane bound O-acyltransferase domain-containing 7 (MBOAT7) and hydroxysteroid 17β- dehydrogenase (HSD17B13) [20]. For example, carriage of the PNPLA3 genetic variant I148M (rs738409) has been associated with severity of steatohepatitis, increased fibrosis, cirrhosis and development of HCC [21-23]. Furthermore, the TM6SF2 genetic variant E167K (rs58542926) has been associated with steatosis and advanced hepatic fibrosis [24,25]. Identification and characterisation of these gene variants may prove an important diagnostic tool for patient stratification in the future, facilitating personalised treatment strategies and improving clinical outcomes.

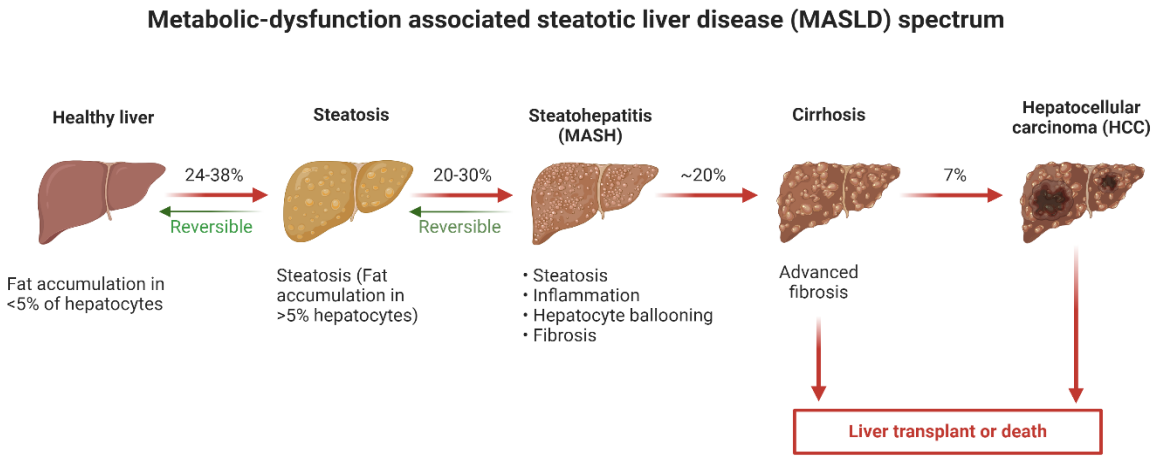

Figure 1: Spectrum of MASLD disease Approximately 24-38% of the population develop steatosis, 20-30% of individuals with steatosis progress to MASH as the tissue microenvironment becomes increasingly inflammatory and fibrotic. ~20% of MASH cases evolve into cirrhosis with severe scarring and poor liver function, before malignant transformation occurs in 7% of cirrhotic livers, resulting in HCC. HCC also develops in a number of patients with MASH in the absence of cirrhosis. Created with BioRender.com

1.3.2.2 Histological features of MASLD

At present, clinical diagnosis of MASLD is ultimately confirmed by histological assessment of tissue following liver biopsy and remains the gold standard in disease classification, allowing direct assessment of fat accumulation, hepatocyte injury, inflammation and fibrosis [26]. However, due to the invasive nature and considerable tissue heterogeneity, biopsies remain an impractical diagnostic tool and research is currently underway to identify alternative, non-invasive methods for widespread use. Over the last decade, several approaches have been investigated, primarily including advanced imaging techniques such as ultrasound, transient elastography (e.g., FibroScan) and magnetic resonance imaging (MRI/MRE) and biomarker panels such as NAFLD fibrosis score, fibrosis index-4 and enhanced liver fibrosis test [27]. However, there are a number of limitations currently associated with these methods which result in difficulties distinguishing disease stages, activity and progression [26,28-30]. The distinct phases of disease, including histological features, are outlined below.

1.3.2.3 Steatosis

Hepatic steatosis is the histological hallmark of MASLD, defined by the accumulation of triglycerides in more than 5% of hepatocytes in the liver, which may be either micro- or macro-vesicular. In macrovesicular steatosis, large lipid droplets occupy the cytoplasm of hepatocytes and displace the nucleus to the periphery whereas microvesicular steatosis refers

to the accumulation of multiple smaller lipid droplets which occupy the cytoplasm without displacing the nucleus [31]. Typically, MASLD patients will present with a mixed steatosis, consisting of both micro- and macro- vesicular lipid droplets, with the degree of steatosis determined using a semi-quantitative scoring system (Table 1) following a pathologist's examination of liver biopsy tissue [32].

1.3.2.4 Steatohepatitis

Although the majority of MASLD patients present solely with simple steatosis and are generally considered to have a benign disease course, approximately 20-30% will progress to metabolic dysfunction-associated steatohepatitis (MASH) [33]. MASH is a complex, multifactorial disease which is characterised by inflammation and hepatocellular injury, alongside steatosis [34]. Hepatocyte ballooning is a key histological feature of MASH, defined by cellular enlargement of hepatocytes with a rarefied cytoplasm [35]. Lobular inflammation observed in MASH consists of a mixed inflammatory cell infiltrate, primarily CD4+ and CD8+ lymphocytes, whereas portal infiltrates are typically CD8+ T cells and macrophages [36]. Histological features are typically assessed using the NAFLD Activity Score (NAS) system, which is calculated by summing the scores for steatosis (0-3), hepatocellular ballooning (0-2) and lobular inflammation (0-3), resulting in a total score ranging from 0 to 8 [32,36].

Table 1: NAFLD activity score (NAS) grading system (adapted from Burt *et al* [32])

Histological Feature	Grading	Criteria
Steatosis Grade	**0**	< 5%
	1	5-33%
	2	34-66%
	3	> 66%
Hepatocyte ballooning	**0**	None
	1	Few
	2	Many
Lobular inflammation	**0**	None
	1	1-2 foci per 20x field
	2	2-4 foci per 20x field
	3	>4 foci per 20x field

1.3.2.5 Fibrosis and cirrhosis

Approximately 25–40% of patients with MASH will develop progressive liver fibrosis, of which ~20% will further progress to end-stage cirrhosis [37-39]. MASH fibrosis is typically categorised into 5 stages ranging from F0 to F4, reflecting increasing disease severity (Table 2). At the early stages (F0-F1), fibrosis is minimal and localised to portal tracts or the space of Disse. However,

as disease progresses to F2 and above, fibrosis becomes more prominent extending beyond portal areas and sinusoids, affecting both perisinusoidal and periportal regions [40,41]. Further progression to F3 is associated with an increase in fibrous septa, which then bridge adjacent portal areas or extend from portal to central areas of the liver lobule in a pattern known as bridging fibrosis, resulting in architectural distortion. Finally, the most advanced stage of liver fibrosis (F4), termed cirrhosis, is characterised by extensive fibrous septa formation and regenerative nodules [42]. Here, the continued replacement of hepatic parenchyma with non-functional scar tissue causes significant distortion of the vascular architecture and impaired liver function (Figure 2). Once established, cirrhosis becomes irreversible and promotes further degeneration, portal hypertension and hepatocellular necrosis. Cirrhosis has also been associated with increased risk of liver cancer, with approximately 7% of patients with liver cirrhosis developing HCC (global incidence 0.5–2.6% per year) [43].

Importantly, fibrosis has been proven to be a key histological feature in predicting MASLD patient outcomes as highlighted by several studies, with advancing fibrosis stages associated with increased risk of future liver-related morbidity and mortality [13,44-46]. Additionally, fibrosis regression is linked with improved clinical outcomes [47]. However, due to the heterogeneity of clinical presentations, varying rates of progression (and regression) and complex histological features, the underlying mechanisms driving fibrosis progression in MASH remains incompletely understood. Consequently, further work is required to elucidate the cellular mediators and mechanistic pathways driving fibrogenesis to help identify novel therapeutic targets, inform patient diagnosis and improve treatment options.

Table 2: METAVIR fibrosis scoring system

Fibrosis stage	Description
F0	No significant fibrosis
F1	1a) Mild zone 3 perisinusoidal fibrosis (PSF) 1b) moderate zone 3 PSF 1c) portal fibrosis only
F2	Zone 3 PSF with periportal fibrosis
F3	Bridging fibrosis
F4	Cirrhosis

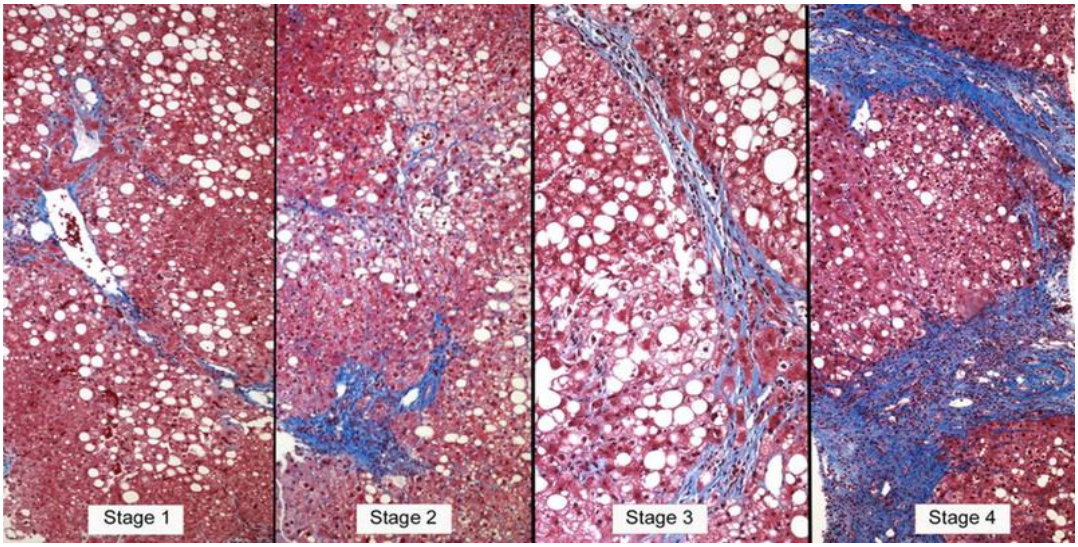

Figure 2: Fibrosis progression in MASH. (Left to right) Stage 1: Centrilobular perisinusoidal fibrosis. Stage 2: Centrilobular perisinusoidal fibrosis and periportal fibrosis. Delicate collagen fibres are deposited around the sinusoids, while denser collagen expands the portal tract. Stage 3: A vascularised septum of fibrous tissue cut across the hepatic parenchyma in a pattern termed bridging fibrosis. Stage 4: Cirrhosis. Nodules of hepatocytes surrounded by fibrous septa of variable sizes. Image from Younossi *et al* [41]. Image available with Creative Commons Attribution License (CC BY).

1.3.3 Pathogenesis of liver fibrosis

In response to acute injury, hepatocytes and biliary cells will self-renew to replace the lost parenchyma coinciding with a tightly organised inflammatory response and minimal ECM deposition [48]. In this instance, regeneration plays a crucial role in maintaining tissue homeostasis and hepatic function. However, in the case of persistent hepatic injury, this response can become impaired, as evidenced in CLD. Here, chronic loss of hepatocytes and cholangiocytes arising from repetitive injury results in the mechanisms of hepatocellular regeneration eventually becoming exhausted, whereby the number of parenchymal cells capable of self-renewal becomes insufficient to effectively restore tissue function, resulting in substitution of hepatocytes with ECM (particularly type I and III collagens) [49-51].

In response to chronic hepatic injury, the reciprocal activation of immune cells and myofibroblasts forms a crucial axis driving fibrogenesis. Persistent hepatocellular damage promotes the continued infiltration of immune cells into the liver microenvironment which, alongside tissue-resident cells, release a wide range of pro-inflammatory and pro-fibrotic mediators. These cytokines, chemokines and growth factors stimulate the activation and proliferation of myofibroblasts, which are widely accepted as key effector cells driving ECM deposition and fibrogenesis [52,53]. Moreover, myofibroblasts secrete a range of pro-fibrotic and pro-inflammatory factors, which further recruit immune cells and activate myofibroblasts,

perpetuating the fibrotic and inflammatory milieu within the liver. This bidirectional crosstalk between immune cells and myofibroblasts establishes a reinforcing loop that sustains and enhances fibrogenesis, ultimately leading to the progressive accumulation of scar tissue and the development of liver fibrosis. Dysregulation of matrix MMPs and tissue inhibitors of metalloproteinases (TIMPs) further exacerbates fibrosis progression by disrupting the balance between matrix synthesis and degradation, causing increased accumulation of ECM in the liver [54]. If unresolved, this results in progressive fibrosis, disrupted hepatic architecture and aberrant regeneration, which are defining features of cirrhosis [49].

1.3.4 Cellular mediators of liver fibrosis

Liver fibrogenesis is a highly dynamic, integrated process involving synchronisation of multiple cell types to drive excess accumulation of ECM and its components in the liver. These cellular mediators interact *via* complex signalling pathways, orchestrating the deposition and remodelling of ECM. Some of the key cellular mediators involved in liver fibrosis are detailed below:

1.3.4.1 Hepatocytes

Hepatocytes are the main parenchymal cells of the liver (accounting for approximately 60% of total cell numbers and about 80% of total liver volume), which are responsible for a variety of cellular functions required to maintain tissue homeostasis including nutrient metabolism, detoxification and immune cell activation [55,56]. The development of MASH has been strongly associated with a range of metabolic injuries to hepatocytes including lipotoxicity, oxidative stress, mitochondrial dysfunction, endoplasmic reticulum (ER) stress and dyslipidaemia which, in turn, stimulate liver regeneration and fibrogenesis [57]. Importantly, damaged and dying hepatocytes actively secrete a range of pro-fibrotic mediators, including transforming growth factor (TGF)-β, platelet-derived growth factor (PDGF), connective tissue growth factor (CTGF) and interleukin (IL)-6, to stimulate inflammation and fibrogenesis. Additionally, soluble mediators that can act as damage-associated molecular patterns (DAMPs) (e.g., high-mobility group box 1 [HMGB1], heat shock proteins, IL33 and adenosine triphosphate binding [ATP]) are released by stressed hepatocytes into the tissue microenvironment where they are recognised by a range of cell types through pattern recognition receptors (PRRs) [58]. DAMPs are crucial danger signals or 'alarmins' which alert the immune system to tissue injury and elicit an inflammatory response [59]. Upon release, hepatocyte-derived DAMPs can stimulate

fibrogenesis through recognition of PRRs on immune cells which, in turn, stimulate release of pro-fibrotic mediators. Additionally, DAMPs can further stimulate fibrogenesis *via* PRR-independent pathways. For example, release of IL-33 from stressed hepatocytes has been shown to trigger the recruitment of group 2 innate lymphoid cells *in vivo*, which then activate hepatic stellate cells (HSCs) through the production of IL-13 [60]. Several studies have also highlighted a direct role of hepatocellular DAMPs in myofibroblast activation and proliferation. Mederacke *et al* recently reported that dying hepatocytes release DAMPs including $P2Y_{14}$ ligands, which bind to their cognate receptors on HSCs, resulting in direct activation in mouse and human HSCs [61]. Similarly, release of HMGB1 from damaged hepatocytes has been shown to directly activate HSCs *in vitro* [62], with genetic ablation of HMGB1 in hepatocytes and myeloid cells *in vivo* preventing development of fibrosis in carbon tetrachloride (CCl_4)-induced liver injury models [63].

1.3.4.2 Hepatic immune cells

Upon injury, damaged hepatocytes rapidly produce pro-inflammatory mediators (primarily chemokines and cytokines) to recruit leukocytes to the site of damage. Among the first circulating immune cells to arrive are neutrophils, which act as first responders to clear apoptotic hepatocytes and entrap harmful bacteria *via* neutrophil extracellular traps (NETs) [64]. The role of neutrophils during liver fibrosis remains controversial, with both pro- and anti-fibrotic affects described in the literature. For example, neutrophil-derived IL-17 is a common signature of advanced liver fibrosis and has been shown to exert a range of pro-fibrogenic functions including recruitment of pro-inflammatory monocytes, increased TGF-β production and enhanced TGF-β responses in HSCs [65-67]. Moreover, pharmacological inhibition of IL-17 and ablation of neutrophils and/or neutrophil chemoattractants (including IL-17) attenuates development of fibrosis in several liver injury models [68,69]. Similarily, production of reactive oxygen species (ROS) and myeloperoxidase by neutrophils have also been found to activate HSCs and drive fibrogenesis *in vivo* [70,71]. Conversely, evidence from several studies suggest an important role for neutrophils in the resolution phase of liver inflammation by inducing a functional switch in macrophages from pro-inflammatory to a restorative phenotype and secretion of MMPs which promote collagen degradation in experimental models of MASH [72,73].

Hepatic macrophages, comprised of tissue-resident Kupffer cells (KCs) and monocyte-derived macrophages (MoMFs), are the most abundant immune cells in the liver and have been extensively implicated in inflammation, injury and fibrogenesis [74,75]. KCs are the self-renewing, resident phagocytes found in the sinusoids of the liver, which act as sentinel cells by sensing hepatocyte stress and changes in tissue integrity [76]. Widely considered the "gatekeepers" in the initiation or suppression of immune responses, KCs play important roles in liver homeostasis by scavenging bacterial/microbial products and secreting inflammatory mediators to further shape the inflammatory response. In response to injury, the pool of hepatic macrophages is rapidly expanded due to the infiltration of monocytes to the site of damage, where they differentiate into MoMFs. Recruitment of MoMFs is facilitated by a range of cell types including activated KCs, HSCs, and liver sinusoidal endothelial cells *via* chemokine C-C motif (CC)L2/CCR2, CCL1/CCR8 and CCL25/CCR9 signalling pathways [77]. These MoMFs are functionally and phenotypically distinct from KCs, though multiple studies have reported high levels of plasticity between lineages [78,79]. As potent producers of TGFβ, MoMFs are thought to be the main macrophage lineage driving fibrogenesis through activation of HSCs. This is supported by *in vivo* mechanistic studies whereby genetic and/or pharmacological inhibition of these cells, or their associated chemokines, resulted in attenuation of liver fibrosis [74,80,81]. Interestingly, recent advances in single-cell sequencing technologies have unveiled novel insights into hepatic myeloid cell heterogeneity, resulting in the identification of MoMFs with a 'scar-associated macrophage' (SAM) phenotype in human MASLD cirrhotic liver tissue [82-85]. Expansion of pro-fibrotic TREM2+, CD9+ macrophage subpopulations in fibrotic/cirrhotic livers have been observed in several studies, with histological analysis revealing that these pro-fibrotic macrophages are spatially localised to regions of collagen-dense scar tissue, providing a direct link between MoMFs and the fibrotic niche [82-85]. Importantly, SAMs have been found to exhibit increased expression of a range of fibrogenic genes, including osteopontin (SPP1), which can regulate myofibroblast function and promote deposition of fibrillar collagen [86].

1.3.4.3 Myofibroblasts

Myofibroblasts, which are not present in the normal liver, are significantly upregulated in response to liver injury where they act as the primary source of ECM (primarily type I and III collagen) during fibrogenesis. Hepatic myofibroblasts are a heterogeneous population of cells characterised by a spindle-like morphology, the expression of fibrogenic intracellular proteins

(e.g., α-smooth muscle actin (αSMA) and vimentin) and secretion of pro-inflammatory and pro-fibrotic soluble mediators [87]. Upon activation, myofibroblasts exhibit a highly contractile phenotype and migrate to areas of active fibrogenesis to facilitate wound contraction, deposition of ECM and further recruitment of immune cells. Though the origins of myofibroblasts have been intensively studied *in vitro* and *in vivo*, this remains challenging in the context of clinical liver disease due to considerable cellular heterogeneity, phenotypic plasticity and temporal and spatial dynamics of CLDs. To date, several sources of myofibroblasts have been identified including HSCs, portal fibroblasts, fibrocytes, epithelial-to-mesenchymal transition and endothelial-to-mesenchymal transition [88,89]. According to cell fate mapping and deep phenotyping of cell populations in experimental models of liver fibrosis, activated HSCs and portal fibroblasts comprise more than 90% of the collagen producing cells during injury, suggesting that these cells are the major sources of myofibroblasts [90].

1.3.4.4 Hepatic stellate cells (HSCs)

Under homeostatic conditions, HSCs reside in the space of Disse where they exhibit a non-proliferative, quiescent phenotype. A defining feature of quiescent HSCs (qHSCs) is the presence of retinoid lipid droplets, which serve as a major storage site of vitamin A. Following injury, HSCs become activated, lose their vitamin A and transdifferentiate into α-SMA positive, collagen type I-producing myofibroblasts [91]. Currently, evidence within the literature suggests that activated HSCs are central drivers of fibrosis. Several soluble mediators released by damaged hepatocytes and/or activated immune cells can directly stimulate the phenotypic switch of HSCs to myofibroblasts including PDGF, TGFβ, ROS and CCL2. Of these, TGF-β is the most potent pro-fibrogenic cytokine which promotes HSC activation in a SMAD2- or SMAD3-dependent manner [92]. Importantly, HSCs have been found to be responsible for as much as 80% of total collagen I in different mouse models of fibrosis, including MASH [93]. Moreover, HSC apoptosis, senescence and reversion to the quiescent state have all been associated with resolution of fibrosis in liver injury models [94,95]. Recent findings from single-cell RNA sequencing have further provided novel insights into HSC and myofibroblast heterogeneity *in vivo*, identifying several distinct populations of activated HSCs in wild type mice subject to CCl_4-liver injury [96] as well as experimental modes of MASH (*foz/foz* mice) on a Western diet [97]. These studies suggest an interplay of functionally diverse myofibroblast phenotypes contribute to liver fibrogenesis.

1.3.4.5 Portal fibroblasts (PFs)

Portal fibroblasts (PFs) are the resident fibroblasts of the portal tracts, which are situated in the mesenchyme surrounding the bile ducts. Under physiological conditions, PFs provide structural support and primarily function to maintain the physical integrity of the portal tract. Although PFs have been identified as potential contributors to liver fibrosis, challenges in isolating and tracking PFs *in vivo* have hindered the comprehensive understanding of their contribution to fibrosis progression [98]. Nonetheless, emerging evidence suggests that PFs undergo activation and transdifferentiation into myofibroblasts, particularly in response to cholestatic injury such as PBC and primary sclerosing cholangitis (PSC). For example, in genetic models of PSC (multidrug resistance gene 2 knockout ($Mdr2^{-/-}$) mice) activated PFs were found to comprise over 50% of the myofibroblasts population during development of cholestatic liver fibrosis [99]. Similarly, activated PFs comprised >70% of myofibroblasts 5 days post bile duct ligation (BDL), though the percentage contribution decreased with progressive injury as HSCs gradually became more activated (14- and 20-days post BDL) [90]. However, the contribution of activated PFs to liver fibrosis arising from aetiologies such as toxin-induced liver injury is less well understood. Further research into the role of PFs in liver fibrosis is required to gain a more comprehensive understanding of the diverse origins and functions of myofibroblasts and may provide new insights into potential therapeutic targets for liver fibrosis.

1.3.5 Current treatment options

Despite the increasing socioeconomic burden of CLDs, there are no specific licensed pharmacological therapies used to treat liver fibrosis, with therapy instead focused on treatment of the underlying aetiology, which may in turn lead to the regression of fibrosis. For instance, recent advances in antiviral therapies have delivered promising results in the treatment of viral hepatitis resulting in the regression of cirrhosis [100]. In the case of metabolic-associated disease, therapy instead focuses on lifestyle and dietary modification and treatment of co-existing features of metabolic syndrome [101]. Indeed, bariatric surgery or weight reduction has been shown to effectively suppress insulin resistance, metabolic syndrome and cause regression of liver fibrosis in some patients with MASH [63]. Nonetheless, a large cohort of patients will be subject to continuing liver insults preventing resolution of injury and enhancing disease progression. Due to the absence of appropriate therapeutic agents, liver transplantation is now a standard therapy for many end-stage CLDs. However,

patient demand for transplantation is vastly exceeding current organ supply and those who do receive transplantation may experience side effects associated with immunosuppression and organ rejection. Given that fibrosis progression and regression determines prognosis in MASH, attenuation of fibrosis represents a major therapeutic goal [102]. Consequently, further investigation is needed to elucidate underlying disease mechanisms and cellular mediators driving fibrogenesis to aid development of anti-fibrotic compounds to limit and/or reverse disease progression.

1.4 Pulmonary fibrosis

1.4.1 Interstitial lung disease

Interstitial lung disease (ILD) is an umbrella term encompassing a broad spectrum of pulmonary disorders characterised by inflammation and fibrosis within the interstitial space of the lung parenchyma [103]. The pulmonary interstitium is comprised of an intricate network of connective tissue located between the alveolar epithelium, capillary endothelium and airways and plays a key role in maintaining lung structure and function. In healthy individuals, the thickness of the pulmonary interstitium ranges from ~0.1-0.2µm which is crucial for enabling efficient gas exchange between the alveoli and capillaries. In the case of ILDs, inflammation and fibrosis cause pathological alterations in the normal architecture of the interstitium including alveolar wall thickening, reduced surface area, altered capillary perfusion and thickening/stiffening of lung tissue, all resulting in a diminished capacity for gas diffusion [104,105].

The classification of ILDs is complex and continually changing as our understanding of these conditions continue to evolve. At present, there are over 200 different ILDs, each with distinct aetiological drivers, underlying mechanisms and disease trajectories, resulting in a wide range of clinical presentations and outcomes. As of 2022, a common classification system broadly categorised ILDs into 6 main categories: idiopathic, exposure-related, autoimmune-related, ILD with cysts/airspace filling, sarcoidosis or rare orphan diseases [106]. Within these categories, disease states can range from acute to chronic with variable rates of progression and, in some conditions, spontaneous reversion or stabilisation can occur. For example, in the case of exposure related ILDs, removal of harmful substances (e.g., asbestos or silica) from the patients' environment can slow or prevent disease progression and may lead to stabilisation [107]. Likewise, drug induced ILDs may regress or improve through discontinuation of the

causative drug [108]. Other ILDs, particularly those characterised by inflammation, such as non-fibrotic hypersensitivity pneumonitis and many forms of sarcoidosis, have generally good outcomes and respond well to therapy [109-112]. Conversely, ILDs defined by progressive pulmonary fibrosis are considered some of the most debilitating lung diseases and have been strongly linked with increased morbidity and mortality [106,107]. Despite advances in treatment of fibrotic ILDs in the last decade, there are significant challenges in effectively managing these disorders due to their complex heterogeneity and pathophysiology. Therefore, elucidating the underlying mechanisms driving pulmonary fibrosis is required to identify novel therapeutic targets which can achieve stabilisation and/or regression of the progressive fibrotic phenotype and improve patient outcomes.

1.4.2 Idiopathic pulmonary fibrosis (IPF)

Idiopathic Pulmonary Fibrosis (IPF) is the most common and lethal ILD, with a median survival rate of 3-5 years after diagnosis, a prognosis worse than many cancers [113]. IPF is a chronic fibrosing disease characterised by the aberrant deposition of scar tissue in multifocal regions of the lung parenchyma resulting in destruction of lung architecture, decreased lung compliance, impaired gas exchange and ultimately respiratory failure [114]. Currently, the number of IPF patients is estimated at between 2.8-9.3 cases per 100 000, with average onset occurring around 65 years and predominantly affecting older males [115]. However, patient numbers are steadily rising in line with an ageing population, particularly in developed countries, posing a significant socioeconomic burden [116].

1.4.2.1 IPF risk factors

Though the underlying aetiology of disease remains to be fully elucidated, current evidence suggests that IPF is the result of several complex factors including age, genetic predisposition, disease comorbidities and environmental exposure. For instance, meta-analysis of observational studies examining environmental and occupational risk factors of IPF performed by Taskar *et al* found that cigarette smoking/exposure, agriculture and livestock, wood/metal dust and stone/sand were all significantly associated with IPF [117]. Similarly, the importance of comorbidities is being increasingly recognised, with a recent study of 272 IPF patients showing 88% of patients presenting with at least one comorbidity [118]. Moreover, a comprehensive systematic literature review by Raghu *et al* found that gastro-oesophageal reflux disorder, pulmonary hypertension, chronic obstructive pulmonary disorder

(COPD)/emphysema, lung cancer and obstructive sleep apnoea were all frequently associated with IPF and, in some cases, linked to increased mortality [119].

Recently, several large genome-wide association studies have also identified a number of genetic variants which appear to contribute to IPF. The most strongly associated variant is a gain-of-function mutation (rs35705950) in the mucin 5B gene, resulting in increased mucin in airway mucus, which has been linked to a greater decline in forced vital capacity (FVC) and increased risk of death [120-122]. This common variant has been reported across multiple cohorts and is believed to account for approximately 30% of the risk of developing IPF in some estimates [123]. Other less frequent mutations have also been reported, primarily relating to surfactant processing (e.g. surfactant protein C (SFTPC) and surfactant protein A2 (SFTPA2)) and telomere biology (e.g. telomerase reverse transcriptase (TERT), telomerase RNA component (TERC), regulator of telomere elongation helicase (RTEL1)) [124].

Ageing is widely considered to be one of the primary risk factors for IPF, as incidence and prevalence of disease increases substantially with age, emphasising the critical role in disease pathogenesis [125]. Ageing is a complex multifactorial process characterised by a progressive loss of physiological integrity and cellular repair mechanisms as well as increased oxidative stress and a higher prevalence of genetic mutations [126]. Importantly, several hallmarks of ageing have been linked to IPF, including genetic instability, telomere attrition, epigenetic alterations, loss of proteostasis, mitochondrial dysfunction, cellular senescence and stem cell exhaustion [127,128]. Current evidence indicates that many of the main hallmarks of ageing occur prematurely in IPF and contribute to the dysfunction of alveolar epithelial cells and fibroblast activation [129]. Age-related, chronic low-grade inflammation, also known as inflammaging, is also thought to contribute to the development and progression of IPF through persistent activation of inflammatory pathways and impaired regulatory mechanisms [130]. Consequently, IPF is considered a highly heterogeneous disease caused by a combination of factors. Despite this, substantial strides in our understanding of IPF aetiology are yet to be made and the contribution of known risk factors to underlying pathomechanisms remain largely unclear.

1.4.2.2 Histological features of IPF

The diagnosis and management of IPF presents several challenges due to the complexity of disease, heterogeneity of clinical presentations and disease trajectories and absence of

definitive diagnostic markers. Current diagnostic approaches include a combination of clinical evaluation, pulmonary function tests (PFTs), radiological imaging (particularly high-resolution computed tomography (HRCT)) and, if required, histopathological examination [131,132]. Typically, when HRCT findings are unclear or inconsistent with usual interstitial pneumonia (UIP), surgical lung biopsies are considered the gold standard for IPF diagnosis [131]. Histologically, IPF is characterised by the distinctive morphology of UIP, defined by the presence of extensive temporal and spatial heterogeneity. Here, subpleural patches of dense established fibrosis can be observed adjacent to regions of lung with seemingly normal tissue architecture, indicating different stages of disease progression and ongoing injury and repair (Figure 3) [114,132]. Fibroblastic foci (FF) are one of the defining features of UIP, representing the leading edge of fibrotic destruction in the lung. These focal aggregations of proliferating fibroblasts and myofibroblasts are found at the interface of fibrotic and seemingly unaffected areas of the lung, often parallel to the alveolar surface [132]. As the primary site of collagen biosynthesis in IPF, FF are key indicators of active fibrosis and tissue remodelling in the lung, with increased FF activity associated with a poorer patient prognosis [133,134]. Alongside this, IPF often shows alveolar epithelial cell abnormalities, including hyperplasia and metaplasia of type II alveolar epithelial cells. In advanced stages of IPF, evidence of cystic spaces lined by bronchiolar epithelium (termed honeycombing) typically appear in subpleural regions of the lung and are associated with extensive loss of functional alveoli and irreversible fibrotic remodelling [131]. This complex spatial and temporal heterogeneity poses a significant challenge in the development of suitable anti-fibrotic compounds as IPF can present in various forms and progress at different rates, underscoring the need for a comprehensive approach to understand disease progression. Further research is therefore essential to elucidate the underlying mechanisms driving these histological features to support development of targeted therapeutic approaches.

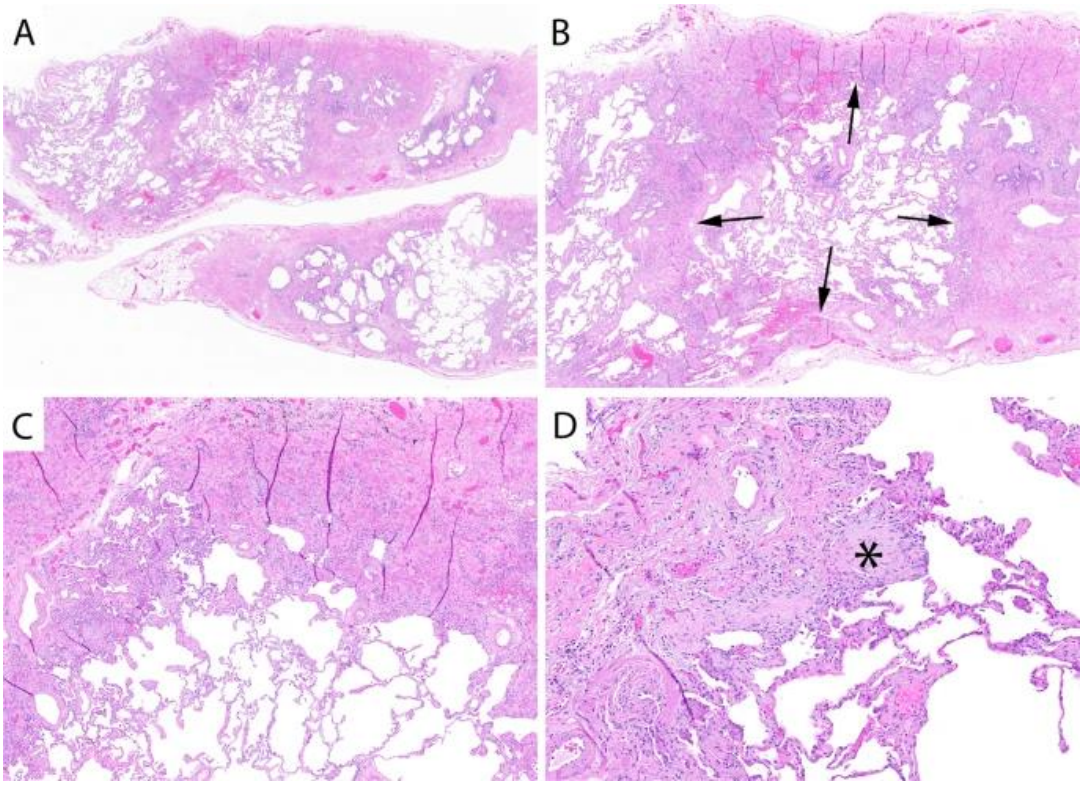

Figure 3: Histological features of IPF Representative images of A) advanced fibrosis with architectural distortion. B) Fibrosis at the periphery of the lung lobule (arrows) with unaffected centrilobular regions. C) Advanced fibrosis adjacent to the normal appearing alveolar space. D) Fibroblastic foci (indicated by *). Figure from Smith *et al* [132]. Image available with Creative Commons Attribution License (CC BY).

1.4.3 Pathogenesis of IPF

Though IPF was first thought to be an inflammatory-driven disease, strong experimental data and the failure of anti-inflammatory and immunosuppressive drugs in clinic have since challenged this theory [114]. The current paradigm now suggests that IPF is an epithelial-driven disease whereby repeated and persistent epithelial injury is a key initiating event driving fibrogenesis [135]. Though the precise aetiology remains unclear, it is believed that continued epithelial micro-injury drives aberrant epithelial repair and dysregulated epithelial-fibroblast crosstalk, resulting in the sustained activation and recruitment of myofibroblasts, distortion of the alveolar structure and irreversible loss of lung function [136].

Under normal conditions, maintenance of the alveolar epithelium is achieved through the proliferation and differentiation of type II alveolar epithelial cells (AEC2s) to type I alveolar epithelial cells (AEC1s) to restore alveolar integrity and cover the exposed basement membrane [137]. However, extensive evidence shows that this process is defective in IPF

patients, resulting in aberrant wound healing responses such as increased apoptosis, premature senescence, increased ER stress and mitochondrial dysfunction [138]. The subsequent loss of effective reepithelialisation results in pronounced areas of denundation (depletion of AECs) in fibrotic regions of tissue and a reduction in surface area available for gas exchange. Concurrently, sustained activation and proliferation of myofibroblasts exacerbates epithelial damage, enhancing basement membrane disruption and alveolar epithelial cell apoptosis, further limiting the proliferation and differentiation of alveolar epithelial cells and reepithelialisation. In response to epithelial injury and myofibroblast activation, both tissue-resident and infiltrating immune cells establish a milieu of injury-related cytokines, chemokines, DAMPs and growth factors which further recruits and activates myofibroblasts, resulting in a positive feedback loop supporting fibrogenesis and impeding tissue repair [139,140]. Enhanced immune cell function can also drive excessive epithelial death, highlighting the dynamic interplay between multiple cell types and their microenvironment, acting in concert to sustain the fibrotic response [141]. Interestingly, changes to the composition of the ECM and increasing mechanical tension and/or lung stiffness have also been shown to promote progression of fibrosis, suggesting that at a certain point, fibrosis can become self-perpetuating irrespective of the initial triggers [106,142].

1.4.4 Cellular mediators of pulmonary inflammation and fibrosis

Pulmonary fibrogenesis involves complex crosstalk between multiple cell types including alveolar epithelial cells, fibroblasts, immune cells and endothelial cells. Some of the key cellular mediators involved in IPF pathophysiology are detailed below:

1.4.4.1 Epithelial cells

The respiratory epithelium differs considerably depending on the location and ranges from simple ciliated cuboidal cells to layer of pseudostratified ciliated, columnar cells based on a fibrous membrane [143]. It is comprised of 6 distinct cell types (Figure 4) dispersed throughout the epithelium, with abundance depending on region [143]. Epithelial cells can be broadly divided into 3 main categories: nasal, bronchial and alveolar epithelial cells. Alveolar epithelial cells can then be further classified into type I or type II pneumoctyes (or AECs) and display distinct physiologic roles [144]. AEC1s make up approximately 90-95% of the alveolar surface with their uniquely thin squamous morphology facilitating gas-exchange to allow passive

diffusion of oxygen into the blood stream [145]. AEC2s, comprising the remaining 5-10% of alveolar epithelial cells, primarily function to produce and secrete pulmonary surfactant which is required to reduce surface tension and aid pulmonary compliance [146].

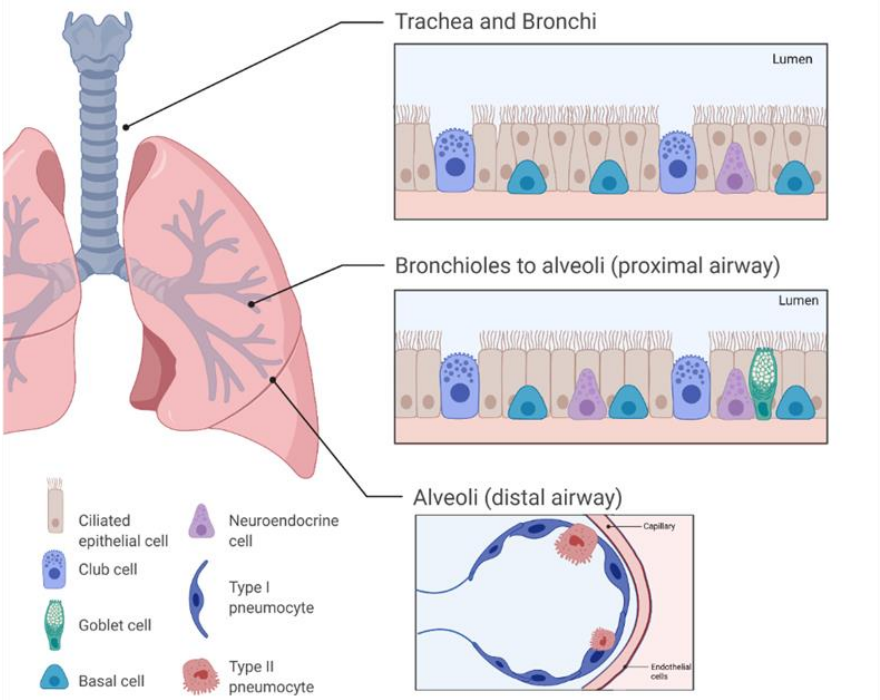

Figure 4: Schematic of the respiratory epithelium. The respiratory epithelium can be broadly classified into 3 regions, each with distinct cellular heterogeneity with abundance of different cell types changing depending on the region as outlined above. Created using Biorender.com.

In the lung, epithelial cells are situated at the interface between the internal and external environment and exert many important functions to maintain tissue integrity by acting as the first line of defence against a broad range of insults [147]. Due to their location, pulmonary epithelial cells are uniquely susceptible to injury and face substantial challenges to tissue integrity. Epithelial cells are routinely exposed to a range of harmful molecules including, but not limited to, bacterial and viral insult, cigarette smoke, asbestos and airborne pollutants [2]. Epithelial damage may also arise in response to oxidative stress, triggering DNA damage and ATP depletion [148]. Various forms of epithelial damage have been reported in IPF, including dysregulation of cellular processes such as apoptosis, necrosis, cell senescence and ER stress [149].

Cellular senescence is a complex, multifaceted process resulting in permanent loss of the proliferative ability of cells, which can be triggered in response to different stimuli, including telomere shortening/damage, oxidative stress and engagement of the DNA-damage response (DDR) [150,151]. Unlike apoptotic and necrotic cells, senescent cells remain metabolically active and can affect activity of themselves and neighbouring cells *via* secretion of a multitude of chemokines, cytokines, proteases, and growth factors known as the senescent associated secretory phenotype (SASP) [152]. Senescent epithelial cells exert diverse roles in the lung due to the heterogeneity of SASP factors, including activation of fibroblasts and immune cells to drive fibrosis and inflammation, respectively (Figure 5). Importantly, senescent epithelial cells can also induce senescence in neighbouring cells, reinforcing growth arrest, impairing epithelial regeneration and efficient lung function [153,154].

Emerging evidence suggests that senescence may be a key contributing factor to IPF pathophysiology with numerous senescence biomarkers, including senescence-associated β-galactosidase activity (SA-β-gal), p16 and p21, identified in fibroblasts and epithelial cells of IPF patients [155,156]. Several studies have confirmed that senescent cells in IPF patient samples are predominantly epithelial cells which are spatially located proximal to fibroblastic foci, suggesting an active involvement in fibrogenesis [157-160]. Consistent with this, data from a recent pilot study found that depletion of senescent cells in IPF patients using the senolytic compound Dasatinib conferred significant clinical benefit and alleviated physical dysfunction [161]. Furthermore, *in vivo* studies have demonstrated that genetic and pharmacological ablation of senescent epithelial cells can successfully attenuate fibrosis and restore tissue

function in experimental models of pulmonary fibrosis [162,163]. Interestingly, single-cell RNA sequencing studies examining transcriptomic differences between IPF-derived and healthy control AEC2s predicted Wnt/β-catenin to be one of the main transcriptional factors driving aberrant changes in fibrotic AEC2s [164]. In keeping with these results, subsequent studies have confirmed that the Wnt/β-catenin signalling pathway induces AEC2 senescence in several pre-clinical models including *in vivo* mouse models, 3D organoids and precision-cut lung slices [165]. More recently, the crosstalk between senescent epithelial cells and fibroblasts has begun to be explored with one study showing that co-culture of pulmonary fibroblasts with senescent epithelial cells resulted in increased activation of fibroblasts and expressed increased levels of α-SMA, collagen I and vimentin [159]. These data suggest that senescent epithelial cells can induce activation of fibroblasts downstream to drive fibrogenesis. Indeed, inhibition of epithelial senescence with rapamycin (mTOR inhibitor) effectively suppressed fibroblast activation and limited development of fibrosis *in vivo* [159]. TGF-β1-induced senescent epithelial cells have also been reported to trigger differentiation of fibroblasts into myofibroblasts *via* secretion of IL-1β [157].

In addition to epithelial senescence, aberrant activation of programmed cell death pathways, such as apoptosis, has been shown to play a major role in the pathogenesis of IPF. For instance, early studies investigating human IPF lung biopsies found increased expression of pro-apoptotic markers in alveolar and bronchial epithelial cells, including p53, p21, and caspase-3 [166]. Additionally, work by Anathy *et al* demonstrated that FAS, a pro-apoptotic member of the TNF receptor superfamily, is a key regulator of pathogenesis of fibrosis *in vivo* [167]. Furthermore, GSTP (glutathione-S-transferase π), which critically interacts with FAS during epithelial cell apoptosis, was shown to be upregulated in AEC2s in human IPF lungs, particularly in areas of active fibrosis [168]. Consistent with these results, global knockdown or inhibition of GSTP resulted in protection from bleomycin-induced and adenovirus-driven TGF-β overexpression models of pulmonary fibrosis [169]. Taken together, these studies highlight a key role for epithelial apoptosis in IPF disease progression.

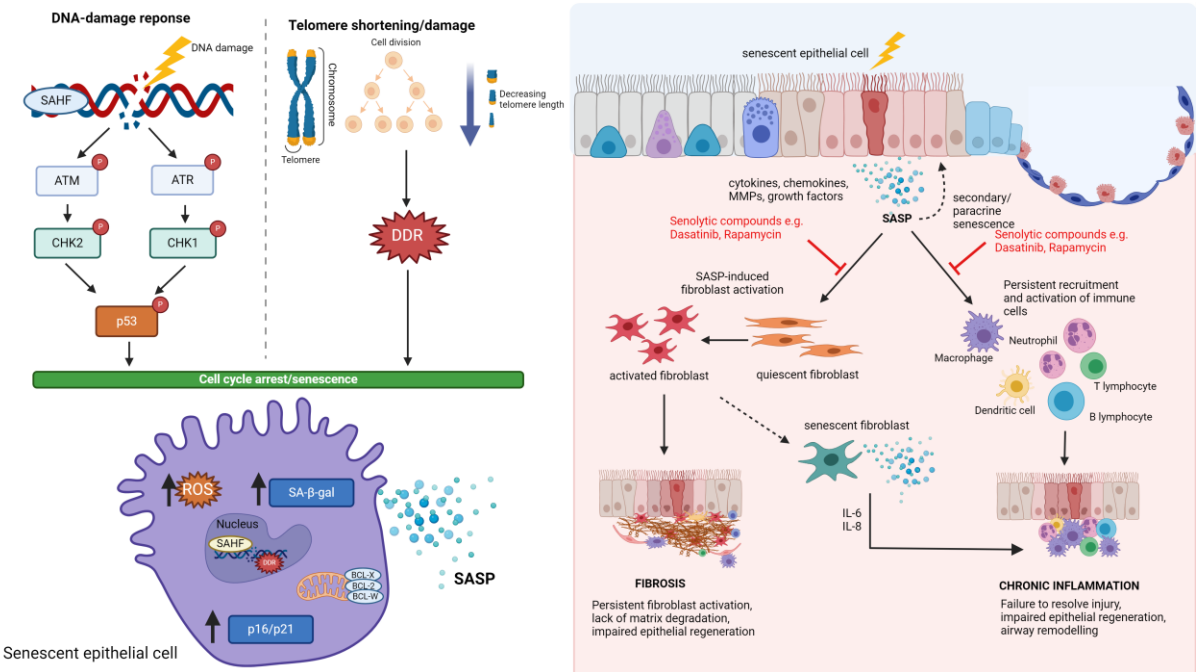

Figure 5: Schematic diagram of epithelial senescence in the lung. Cellular senescence can be triggered in response to different stimuli, including telomere shortening/damage and engagement of the DNA-damage response (DDR). Senescent cells upregulate expression of senescence-associated heterochromatin foci (SAHF), senescence-associated β-galactosidase activity (SA-β-gal), p16 and p21 and secrete a multitude of chemokines, cytokines, proteases, and growth factors known as the senescent-associated secretory phenotype (SASP). Senescent epithelial cells exert diverse roles in the lung due to the heterogeneity of SASP factors, including activation of fibroblasts and immune cells to drive fibrosis and inflammation, respectively. Senescent epithelial cells can also induce senescence in neighbouring cells, reinforcing growth arrest, impairing epithelial regeneration and efficient lung function. Senescent fibroblasts further impair lung function and repair of epithelial cells, suggesting bi-directionality and positive feedback mechanisms driving epithelial damage and fibroblast activation. Senolytic compounds including Dasatinib and Rapamycin can successfully attenuate fibroblast activation and immune cell recruitment in the lung, making modulation of senescence an attractive therapeutic target for several chronic diseases. Image from Burgoyne *et al* [149]. Image available with Creative Commons Attribution License (CC BY).

Other cell death pathways, such as unprogrammed necrosis, have been implicated in IPF due to their ability to release DAMPs into the tissue microenvironment. Although DAMPs primarily function to stimulate the immune response, several studies have highlighted a direct role in fibrogenesis in multiple organs [170,171]. In the context of the lung, DAMPs including HMGB1, S100 proteins, uric acid and extracellular ATP are all significantly increased in BAL fluid of IPF patients compared with healthy controls [172-176]. Though information on the cellular origin of these DAMPs in humans is limited, histological assessment of IPF samples found that HMGB1 was predominantly expressed in the nuclei of infiltrating inflammatory cells and epithelial cells in fibrotic IPF lesions. Likewise, HMGB1 was found to be upregulated primarily in bronchiolar and alveolar epithelial cells in bleomycin-induced fibrotic mouse models [177].

Several studies have now demonstrated a potentially key role for epithelial-derived DAMPs in the pathogenesis of pulmonary fibrosis, with release of alarmins from epithelial cells enhancing the fibrotic response in multiple systems (Figure 6). For instance, extracellular ATP has been found to cause upregulation of TGF-β1, collagen and fibronectin in pulmonary fibroblasts [178]. Interestingly, depletion of HMGB1 using neutralising antibodies [177] and ethyl pyruvate (a HMGB1 inhibitor) [179] in bleomycin-challenged mice successfully attenuated the fibrotic response, suggesting a key role in fibrogenesis. Though the involvement of HMGB1 in fibrosis is incompletely understood, some studies suggest that activation of fibroblasts and production of IL-1β are key drivers in disease progression. Indeed, it has been shown that HMGB1 released from damaged epithelial cells *in vitro* causes upregulation of IL-1β, which in turn activates TGF-β1 to facilitate alveolar epithelial cell repair [180]. Li *et al* provided the first evidence that HMGB1 can mediate epithelial-to-mesenchymal transition in both human and rat airway epithelial cells through activation of TGF-β1/Smad2/3 signalling pathways [181]. Wang *et al* subsequently showed that HMGB1-induced TGF-β1 release precedes the upregulation of α-smooth muscle actin (SMA) and collagen I in pulmonary fibroblasts, indicating that TGF-β1 is required for the differentiation of human lung fibroblasts to myofibroblasts in response to HMGB1 [182]. Collectively, these studies provide novel evidence that HMGB1 released from damaged epithelial cells might contribute to the development of fibrosis through persistent upregulation of TGF-β1, causing fibroblast activation, differentiation and deposition of ECM.

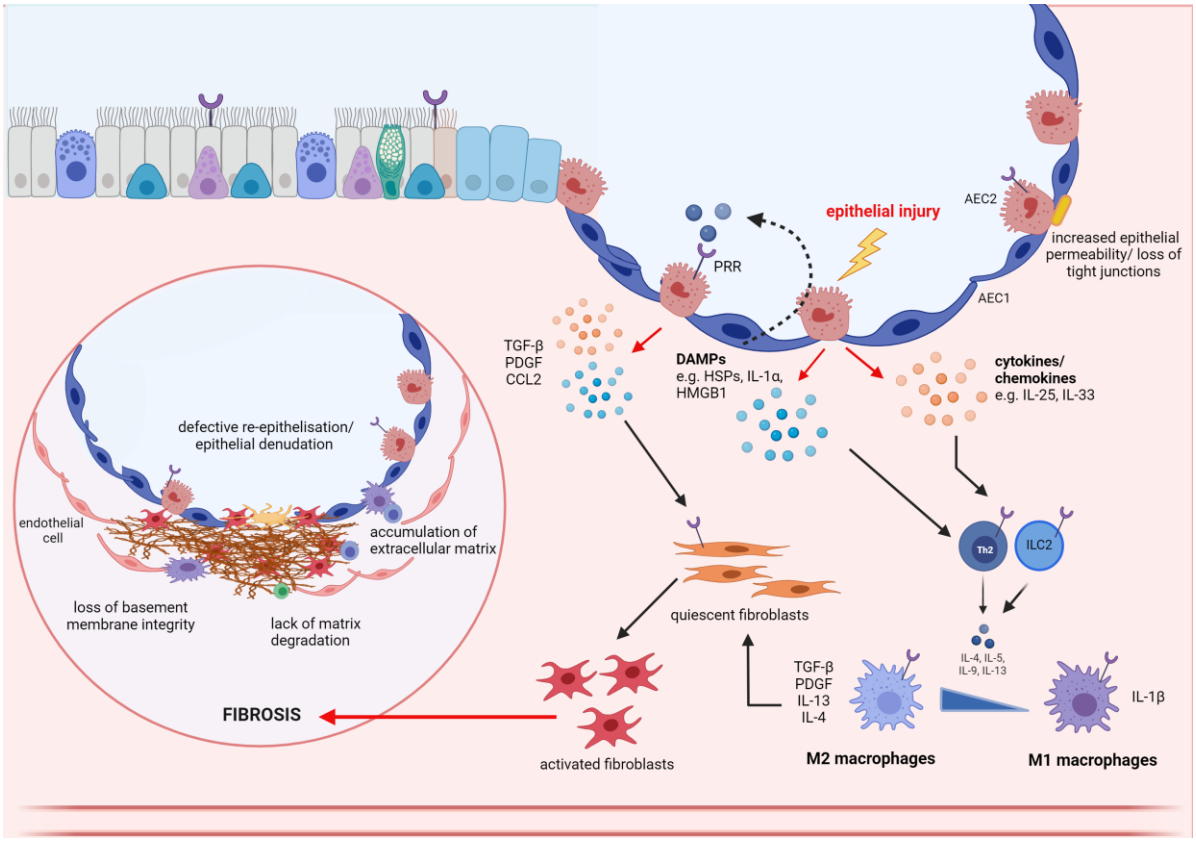

Figure 6: **Schematic diagram of downstream effects of epithelial damage in IPF.** Upon injury, epithelial cells release chemokine/cytokines and DAMPs (e.g., high-mobility group box-1 (HMGB1), heat shock proteins (HSPs) and interleukin (IL)-1α) into the extracellular space. DAMPs can activate pattern recognition receptors (PRRs) on neighbouring epithelial cells and immune cells, directly stimulating the release of profibrotic cytokines including tumour growth factor (TGF)-β, PDGF and CCL2, which are involved in the activation of fibroblasts. Epithelial cells also secrete proinflammatory cytokines which recruit and activate innate immune cells (e.g., neutrophils, macrophages and dendritic cells), as well as adaptive immune cells (e.g., T lymphocytes and B lymphocytes), which further secrete pro fibrotic factors including IL-33, IL-4, IL-5, IL-13. For example, IL-33 promotes the differentiation of macrophages towards to a pro-fibrotic M2 phenotype, causing upregulation of pro-fibrotic cytokines including CCL2, IL-6 and TGF-β. Once activated, fibroblasts begin secretion of extracellular matrix (ECM) and pro-fibrotic factors to promote edge contractility and facilitate wound closure. Fibrosis is thought to occur in response to persistent epithelial damage leading to continued proliferation and migration of myofibroblasts, deposition of extracellular matrix (ECM) and recruitment of pro-inflammatory and pro-fibrotic markers with detrimental effects. Image from Burgoyne *et al* [149]. Image available with Creative Commons Attribution License (CC BY).

1.4.4.2 Pulmonary immune cells

Interactions between epithelial cells and immune cells are essential to maintain tissue homeostasis, mount an effective immune response and promote resolution of epithelial injury. Acute inflammation is considered an integral component of a normal wound healing response to epithelial damage [183,184]. This is a highly synchronised and carefully regulated process involving the secretion of multiple cytokines and chemokines to stimulate recruitment and activation of inflammatory cells to the site of injury [185]. However, in many chronic lung diseases this process becomes dysregulated resulting in a persistent inflammatory response and establishment of a pro-fibrotic milieu which, in turn, drives pathological wound repair and loss of functional tissue architecture [186]. Though inflammation is no longer thought to be a key determinant of pulmonary fibrosis, multiple immune cell types are reported to have altered signalling in IPF. This is achieved through multiple mechanisms both directly and indirectly, including epithelial- and fibroblast-immune cell cross talk, resulting in modulation of the fibrotic response.

Following tissue damage, neutrophils quickly migrate to the site of injury in response to several chemoattractants, including chemokine C-X-C motif (CXC)L8 (also known as IL-8). As previously mentioned, neutrophils exert diverse roles in the tissue microenvironment such as phagocytosis, degranulation and release of pro-inflammatory cytokines, ROS and NETs, shaping the ensuing immune response [187]. Furthermore, neutrophils also play an important role in ECM turnover, primarily due to production of neutrophil elastase (NE). Interestingly, inhibition of NE *in vivo* has been reported to reduce bleomycin-induced pulmonary fibrosis [188] and NE is increased in the bronchoalveolar lavage fluid (BALF) of IPF patients [189]. Consistent with these findings, elevated levels of IL-8 and granulocyte colony-stimulating factor (G-CSF) are also observed in the BALF and sputum of patients, suggesting increased levels of neutrophil attraction and activation. Though this was previously reported to have no effect of survival rates of IPF patients [190], subsequent studies have challenged these findings. In two separate IPF cohorts, neutrophilia was associated with a decline in forced vital capacity and/or all-cause mortality [191,192]. However, whether neutrophils contribute directly to fibrosis progression or are upregulated in an attempt to restore homeostasis remains to be elucidated.

Pulmonary macrophages are a heterogeneous population of cells comprised of alveolar macrophages (AMs), interstitial macrophages (IMs) and monocyte-derived macrophages (MoMFs), which play crucial roles in maintaining tissue homeostasis in the lung [193]. However, macrophages have also been widely implicated in aberrant tissue repair and pulmonary fibrosis [194-196]. Recent characterisation of immune cell populations during bleomycin-induced pulmonary fibrosis revealed that macrophage-related interactions were consistently highest and most dynamic, with AM and MoMF populations exhibiting the greatest heterogeneity and expression of pro-fibrotic genes during disease progression [197]. Similarily, lineage-tracing and single-cell RNA sequencing analysis of experimental models of fibrosis identified expansion of pro-fibrotic MoMFs during fibrogenesis, which were subsequently shown to localise to areas of fibrosis [198,199]. Moreover, targeted deletion of these pro-fibrotic MoMFs was sufficient to protect mice from bleomycin-induced fibrosis, suggesting that they play a pivotal role in disease [200]. Consistent with these findings, CCL2 (a key monocyte chemokine) is elevated in human IPF patients and associated with increased risk of disease progression and mortality [201]. Taken together, these data suggest that MoMFs adopt a pro-fibrotic phenotype in IPF, causing an imbalance between pro-repair and pro-fibrotic macrophage states, hindering effective epithelial restoration.

Functionally, macrophages can be further subdivided into two distinct populations: classically activated M1 macrophages and alternatively activated M2 macrophages. In this context, M1 macrophages are generally considered to be pro-inflammatory/anti-fibrotic whereas M2 macrophages are typically anti-inflammatory/pro-fibrotic. M2 macrophages are activated by a range of soluble factors including IL-4, IL-10, granulocyte-macrophage colony-stimulating factor (GM-CSF), and IL-13 [202]. Importantly, M2 macrophages release pro-fibrotic mediators including TGF-β1, CCL18, galectin, CTGF and MMPs, all of which promote fibroblast migration, proliferation and transdifferentiation to myofibroblasts [202]. In IPF, increased polarisation of macrophages towards an M2-like phenotype has been reported in multiple systems, with CCL18 upregulation in the BALF and sputum of IPF patients correlated with a poorer prognosis and mortality [203,204]. More recently, advances in next generation sequencing have allowed further characterisation of macrophage populations in IPF, resulting in identification of pro-fibrotic, secreted phosphoprotein-1 (SPP1) high macrophages, which localise to fibroblastic foci and interact with myofibroblasts [205-208].

1.4.4.3 Mesenchymal cells

Fibroblasts are the most abundant cell type found in connective tissue throughout the body [209]. Under homeostatic conditions, fibroblasts remain quiescent and are predominantly involved in the routine production of ECM required to maintain tissue function. However, during wound repair, fibroblasts are quickly upregulated and differentiated to activated myofibroblasts [210] before beginning secretion of ECM and pro-fibrotic factors to promote edge contractility and facilitate wound closure [211]. The origins of myofibroblasts in pulmonary fibrosis has long been debated and remains incompletely understood. However, developments in *in vivo* lineage-tracing models has enabled more accurate interrogation of potential precursor cells [212] and it is now thought that myofibroblasts may be derived from a range of cell types (Figure 7), with TGF-β1 being regarded as a key mediator driving myofibroblast differentiation and the fibrotic response [213,214]. In addition to tissue resident fibroblasts, both fibrocytes and pericytes have been implicated in fibrogenesis in the lung [215,216], kidney [217,218] and liver [87,219] where they have been reported to migrate to the site of injury and adopt a myofibroblastic phenotype [220]. *In vitro* work has confirmed their ability to differentiate to myofibroblasts and begin producing collagen, fibronectin and TGF-β to promote ECM deposition [221-223]. Moreover, the process of epithelial-mesenchymal transition (EMT) has been postulated as a contributing factor of the fibrotic response in a number of chronic diseases [224]. In this process, epithelial cells lose contact adhesion, alter their morphology and acquire phenotypic properties of mesenchymal cells, migrating to the interstitium and producing ECM [225]. Accumulating evidence now suggests EMT may play a functional role in the pathophysiology of a number of fibrotic lung disease including COPD [226], bronchiolitis obliterans syndrome [227] and IPF [228], though there are conflicting reports in the literature surrounding the extent of EMT involvement [225,228]. More recently, endothelial-mesenchymal transition (EnMT) has emerged as another possible source of myofibroblast accumulation which can be induced by TGF-β1 [229]. Similar to EMT, endothelial cells are seen to lose their distinctive markers, acquire a myofibroblastic phenotype and begin production of α-SMA and type I collagen and has been described in the pathogenesis of pulmonary [230] and renal fibrosis [231].

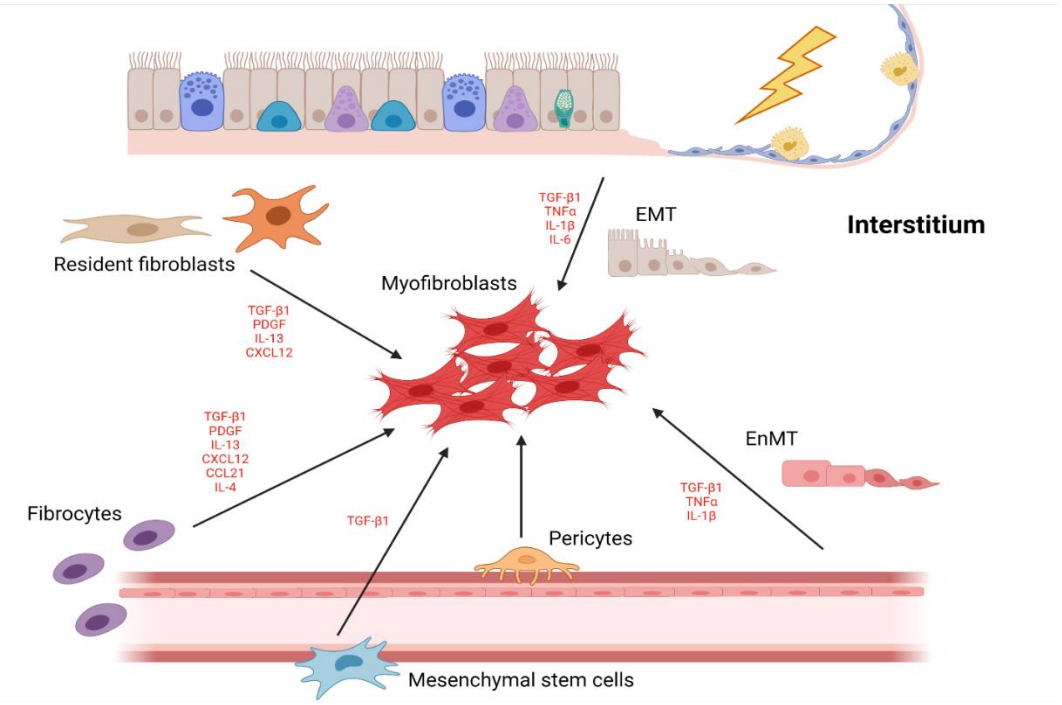

Figure 7: Proposed origins of myofibroblasts and relevant signals In addition to tissue resident fibroblasts, myofibroblasts have also been suggested to arise from a range of other cell types including pericytes, fibrocytes, mesenchymal stem cells, epithelial-mesenchymal transition (EMT), and endothelial-mesenchymal transition (EnMT). Created using Biorender.com

In the context of normal wound healing, after initiation of reepithelialisation, myofibroblasts are no longer required and subsequently undergo apoptosis to clear them from the site of injury [232]. However, in fibrotic disease, apoptotic resistance occurs early on in disease pathogenesis whereby myofibroblasts can become resistant to Fas-Ligand mediated apoptosis and continue to proliferate causing the progressive accumulation of ECM [233,234]. Recent studies have shown that apoptotic resistance precedes progressive tissue scarring in mouse models of pulmonary fibrosis, highlighting the importance of regulated apoptotic cell death in maintaining normal tissue function. Furthermore, HMGB-1 release (an indicator of necrotic cell death) coincided with onset of fibroblast apoptotic resistanance after radiation-induced epithelial damage [234]. This suggests the inability of damaged cells to undergo apoptosis, coupled with initation of the necrotic pathway could directly contribute to stimulation of the fibrotic response, though the pathways involved remain ill-defined. Additionally, presence of senescent fibroblasts enhances apoptotic resistance and senescent fibroblasts have been found to accumulate in the lungs of IPF patients [235,236]. Interestingly, co-culture of alveolar epithelial cells with senescent fibroblasts was found to impair function and repair of epithelial cells, suggesting bi-directionality and positive feedback mechanisms driving epithelial damage and fibroblast activation [237]. Notably, Orjalo *et al* demonstrated that pulmonary fibroblasts

increase production and secretion of IL-1α in response to senescence-inducing stimuli. Moreover, they showed that IL-1α was an essential positive regulator of IL-6 and IL-8 secretion and that senescent fibroblasts could act in an autocrine manner to drive inflammation and reinforce senescent growth arrest in themselves and neighbouring fibroblasts [238].

Fibroblasts have long been considered as cells whose function was limited chiefly to restoration of tissue architecture. However, it is becoming increasingly apparent that fibroblasts play other critical roles in wound healing and that interactions between the pulmonary epithelium and fibroblasts play a major role in tissue homeostasis, as well as in the initiation and progression of several chronic lung diseases [239]. For example, fibroblasts have been identified as having a critical role in regulating the switch from acute to chronic inflammation through modulation of immune cell function [240]. Indeed, evidence suggests that dysfunctional fibroblasts can induce a persistent inflammatory state in the cellular microenvironment through secretion of proinflammatory cytokines, driving accumulation of immune cells and impeding wound repair [148]. Suwara *et al* successfully demonstrated that pulmonary fibroblasts challenged with conditioned media from damaged/dying epithelial cells undergo a phenotypic switch to a proinflammatory state, characterised by the secretion of chemokines involved in the recruitment of neutrophils, monocytes and T cells. This phenotypic switch was driven exclusively *via* IL1α released from damaged epithelial cells engaging interleukin 1 receptor type 1 (IL-1R1) on fibroblasts, and this effect could be attenuated using an IL1α neutralising antibody or IL-1R1 antagonist, suggesting that IL1α is a key epithelial-derived factor driving a proinflammatory phenotype in human fibroblasts [148]. Taken together, these data suggest that epithelial damage and release of intracellular alarmins can initiate aberrant crosstalk between epithelial cells and fibroblasts to drive inflammation and alter wound repair signalling. Single-cell sequencing of mouse and human lungs have further identified subpopulations of pulmonary fibroblasts unique to fibrotic lungs that can adopt a pro-fibrotic phenotype [241]. Functionally, these cells exhibit enhanced migratory functions and localise to regions of fibrotic tissue, suggesting an important role in driving pulmonary fibrosis.

1.4.5 Current treatment options

At present there is no cure for IPF, treatment options are scarce with lung transplantation remaining the only viable intervention to increase life expectancy. However, due to limited availability of donor organs and stringent suitability criteria, only a small minority of IPF patients will be eligible to undergo transplantation [242]. Treatment strategies are therefore primarily focused on slowing disease progression and alleviating patient discomfort. Currently, there are only 2 clinically available anti-fibrotic drugs which are licensed exclusively for the treatment of mild-moderate IPF [243,244]. Pirfenidone (a modified pyridine small molecule inhibitor) was the first pharmacological therapy approved by the European Medical Association (EMA) in 2011 for the treatment of IPF, with proven anti-fibrotic and anti-inflammatory affects. Pirfenidone has been evaluated in 3 multicentre phase 3 trials, including the CAPACITY and ASCEND trials [245-247] which confirmed clinically meaningful reductions in disease progression (measured by decline in FVC, lung volume, exercise tolerance and progression-free survival) and favourable benefit-risk profiles representing an appropriate treatment option for IPF patients [245,247]. Though the exact mechanism of action remains unclear, it is thought to exert pleiotropic effects through modulation of multiple cellular pathways, including the inhibition of TGF-β1 across numerous cell types [248-251]. Nintedanib was subsequently approved by the EMA in 2015 after clinical evidence arising from the INPULSIS -1 and -2 [252] and the TOMORROW [253] trials reported a significant decrease in the rate of FVC deterioration and fewer exacerbations in IPF patients, although the death rate remained unchanged. Nintedanib's mechanism of action is somewhat more defined, as an intracellular tyrosine kinase inhibitor it is thought to exert its anti-fibrotic affects *via* binding to ATP sites, supressing signalling pathways linked to vascular endothelial growth factor receptor (VEGFR), fibroblast growth factor receptor (FGFR) 1-3 and platelet-derived growth factor receptor (PDGFR) α and β [254-256].

Despite the proven ability to slow FVC deterioration in patients, neither Pirfenidone nor Nintedanib are good first line therapies for IPF treatment due to heterogeneous treatment responses and wide-ranging side effect profiles [257-260]. While these adverse effects are generally well tolerated and can often be managed with medication (skin rash, weight loss, nausea, vomiting and fatigue [261]), there have been reported cases of drug-induced liver injury and hepatotoxicity [243,262-264] and approximately 29% of IPF patients prematurely discontinue their treatment as a direct result of adverse side effects [265]. Additionally, not

every patient is eligible for anti-fibrotic treatment due to current suitability criteria. It is currently estimated that only 54% of patients with an IPF diagnosis in Europe receive anti-fibrotic treatment with an approved drug [266]. Consequently, there is an urgent unmet need to better understand the underlying mechanisms driving pulmonary fibrosis to support development of new anti-fibrotic agents to improve the quality of life and life expectancy of patients.

1.5 Current methods to investigate fibrosis and disease

Current research into fibrosis, including understanding the initiating triggers and the underlying mechanisms, relies heavily upon *in vitro* cell culture of human and rodent cells and *in vivo* mouse models. Though these techniques have yielded significant insight into our understanding of basic disease mechanisms, they have often failed to translate to clinical benefit. Despite considerable investments into drug discovery and development, the probability of a drug progressing from Phase I trial to full approval currently stands at less than 10% [267,268]. One possible explanation for this phenomenon is sub-optimal and/or inconsistent preclinical research, in which animal models and other non-physiologically relevant cell culture systems are used to bridge the gap from bench to bedside [269]. Consequently, it is important to consider the substantial limitations of both cell culture and mouse models and their failure to recapitulate the incredibly complex pathophysiology observed in human disease (Figure 8). Additionally, reproducibility between studies and laboratories remains a critical issue when translating findings from academia to pharmaceutical drug development. Differences in experimental design, methodologies, biological variability and quality control measures have all been identified as key variables, with minor differences potentially resulting in significant outcome discrepancies [270]. Enhancing collaboration and communication between these sectors is therefore essential to improve reproducibility between models and ensure that promising academic findings can be reliably translated into effective therapies. An overview of commonly used model systems of fibrosis are outlined below:

1.5.1 In vitro: 2D cell culture and 3D models

1.5.1.1 2D cell culture

2D mono- and co-culture systems provide cheap, reproducible models which are fundamental research tools in many settings, particularly large-scale rapid drug screening [271]. However, the conventional methodology of culturing cells in a 2D monolayer is known to restrict contact between cells and prevent the formation of multi-dimensional structures seen in tissue [272]. Moreover, cells exist within the complex ECM scaffold i*n situ*, providing structural support and facilitating signalling between multiple cell types. These interactions are required for a number of vital functions including cell differentiation, proliferation and response to stimuli, all of which are impeded in 2D culture systems [273]. Additionally, cells cultured in a submerged monolayer are exposed to supra-physiological levels of stiffness which has been shown to impair function of cells *in vitro*, altering phenotype and reducing viability [274]. For example, when cultured in a 2D system, normally quiescent fibroblasts are found to rapidly differentiate to activated myofibroblasts [275,276].

1.5.1.2 3D models

To overcome some of the inherent limitations associated with 2D monoculture, single or multicellular spheroids may be used. Spheroids are 3D cell aggregates grown using a scaffold-free system such as hanging droplets or ultra-low attachment plates [277]. Like 2D cell cultures, spheroids are cheap, reproducible models for studying disease biology and high-throughput drug screening. Formation of spheroids into a 3D structure effectively reduces the supra-physiological levels of stiffness observed in classical monoculture systems, enabling cells to maintain more physiologically relevant phenotypes in culture as well as facilitating cell-cell interactions [278]. Despite this, cell types are still limited to broad clusters of cells (e.g., hepatocytes or pulmonary epithelial cells) lacking matrix and tissue structure. Furthermore, spheroids are unable to regenerate and are often susceptible to central necrosis [269,279].

More recently, research has progressed to incorporate the use of more advanced 3D models (e.g., organoids, airway liquid interface (ALI) and organ-on-a-chip) to alleviate the limitations outlined above. These models display structures and functions more consistent with tissue *in vivo* and can interact with neighbouring cells enabling better interrogation of cellular crosstalk [269]. For example, organoids (often termed 'mini organs') are stem cell-derived 3D structures resembling the organ they are fated towards with the capacity to regenerate [280]. Unlike spheroids, organoids rely on artificial ECM scaffolds to facilitate self-organisation into

structures that mimic the architecture of a whole organ and recapitulate some aspects of the cellular microenvironment [281]. Though there has been considerable progress in the development of 3D models for use in research, 3D systems are still limited to include few cell types and fail to address the complex cellular heterogeneity and cell-cell interactions present in the lung and liver [282].

1.5.2 In vivo mouse models

Animal models are widely used in the study of fibrotic diseases and can overcome several of the issues seen *in vitro*, allowing multiple cell-to-cell interactions and providing a tissue microenvironment to study basic physiology. Mouse models remain one of the most commonly used *in vivo* models owing to their short gestational period, extensive genome characterisation and ease of genetic manipulation. Numerous models have been developed for the study of both liver [283] and lung [284] fibrosis, with recent advances leading to improved models of targeted epithelial injury, fibroblast-selective genetic manipulations and epithelial–mesenchymal crosstalk. For instance, Sisson *et al* recently described a model of pulmonary fibrosis utilising a transgenic mouse expressing the human diphtheria toxin receptor (DTR) on AEC2 cells. Repetitive delivery of diphtheria toxin was then delivered daily for 14 days to induce hyperplastic proliferation in an AEC2-selective manner, resulting in a model of interstitial thickening similar to IPF [285]. In the case of liver fibrosis, there are several experimental models available reflecting the variety of pathogenic factors leading to pathological wound healing. Fibrogenesis can be induced *via* exogenous chemical challenge, surgical intervention, dietary modification or transgenic manipulation, each with their own advantages and limitations [283]. Although these models still fail to recapitulate the full spectrum of disease pathogenesis, they allow for specific analyses of signalling pathways and interactions among different cell types. However, there remains significant challenge in translating *in vivo* findings to human patients based on the biological differences between species [286]. Additionally, many established rodent models rely on accelerated disease progression in young mice (8-12 weeks old), often using non-physiologically relevant stimuli (e.g. CCl_4) [284]. Given that fibrosis develops over the course of decades, and in the case of IPF

in response to unknown stimuli, it can be concluded that these models will be incapable of accurately replicating the complex pathophysiology seen in humans.

1.6 Emerging translational pre-clinical models and research tools

1.6.1 Ex vivo precision-cut slices (PCS)

Precision cut slice (PCS) technology provides an exciting alternative to currently available models and has been utilised successfully in a range of organs including lung, liver, kidney, and heart [287-289]. Critically, PCS preserves tissue architecture, matrix scaffolds and cellular heterogeneity of native tissue, offering a physiologically and structurally relevant system in which to test potential therapeutics and interrogate underlying mechanisms of disease [269,287]. PCS technology has been used extensively to investigate drug metabolism and toxicity [290] and is becoming an increasingly common tool for fibrosis research, from modelling early onset to end-stage disease in both murine and human tissue. To investigate changes associated with early-stage fibrosis in the lung, *ex vivo* models have been established by challenging PCS derived from excess human donor lungs with a pro-fibrogenic cocktail (TGF-β, tumour necrosis factor-α (TNFα), PDGF-AB, and lysophosphatidic acid) to promote induction of fibrosis, alveolar thickening and increased secretion of ECM proteins, whilst maintaining tissue viability [291]. Similarily, PCS generated from human liver tissue can be

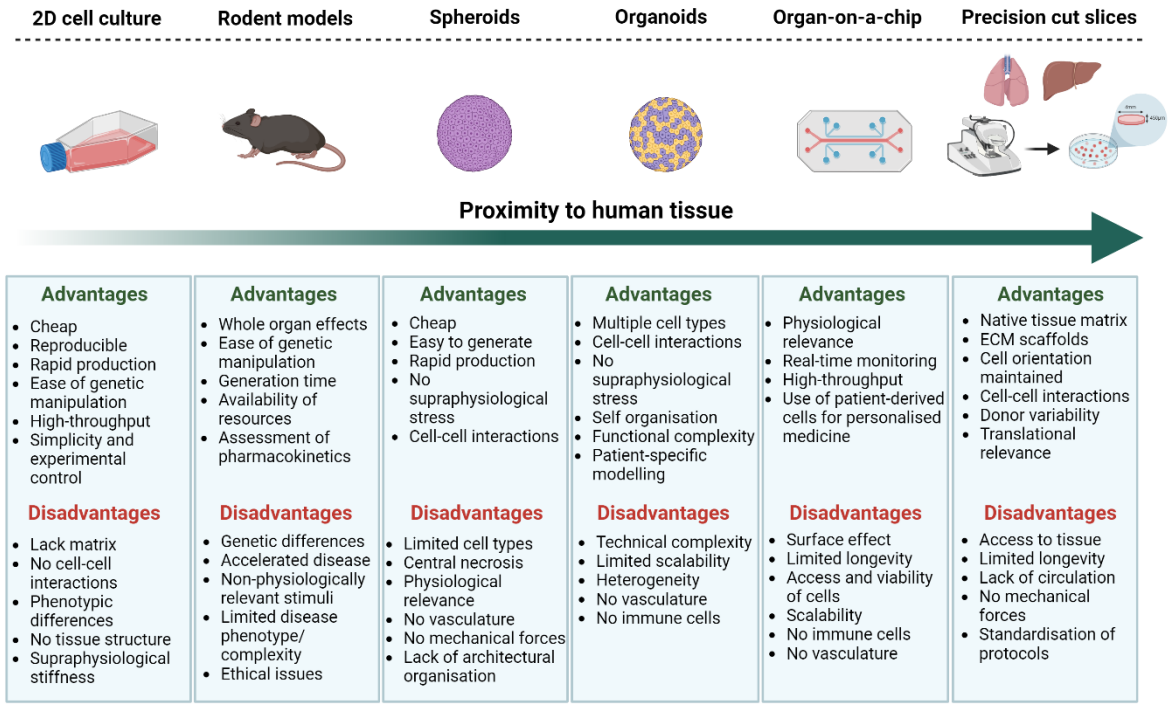

Figure 8: Pre-clinical models for fibrosis disease modelling. Summary of pre-clinical systems currently used to model fibrotic disease, along with the main advantages and disadvantages of each method. Created with BioRender.com.

stimulated with exogenous compounds such as ethanol, bile acids and pro-fibrogenic recombinant proteins to induce fibrogenesis and validate efficacy of anti-fibrotic therapies [287,292,293]. PCS have also been generated from patients with established disease pathology such as IPF [294], COPD [295] and severe liver fibrosis and/or cirrhosis [296] to interrogate pathomechanisms successfully. For example, Mercer *et al* utilised IPF-derived PCS to demonstrate that PI3K/mTOR pathway activation plays a role in disease remodelling and further showed that inhibition of this pathway resulted in decreased secretion of pro-fibrogenic markers suggesting a direct link between PI3K/mTOR signalling and ECM formation in IPF [294].

Although PCS technology has significant advantages compared to other available models, it is not without its limitations. Access to tissue remains one of the central issues, with many researchers unable to establish the required ethical approval and networks between hospitals and laboratories to receive human tissue. The absence of infiltrating immune cells is also a fundamental caveat in the system as, in patients, infiltrating immune cells play key roles in modulating disease. Limited tissue longevity and maintenance of tissue-resident cells is also a prominent obstacle due to non-uniform culturing protocols, with some groups only capable of culturing tissue for 24-48 hours. Our laboratory has significant expertise in the generation and culture of PCS in multiple organs, including resected liver tissue [287], healthy unused donor lung tissue and explant diseased lung tissue which can be maintained for up to 14 days whilst remaining viable and metabolically active. Treatment of PCS prepared from explanted lung tissue with Pirfenidone and Nintedanib have effectively shown that the PCS system can be used to test therapeutic compounds in diseased human lung tissue including IPF, COPD and obliterative bronchiolitis and subsequently can be used to investigate other inflammatory and/or fibrotic mechanisms. Additionally, we have shown the ability to stimulate (and blunt) inflammatory and fibrotic responses in normal unused donor lungs and resected liver tissue, using IL1α and TGF-β1/PDGFββ challenge, respectively. Both systems therefore provide attractive models to interrogate underlying disease mechanisms and validate targets of interest.

1.6.2 'Omics Technology

Over the past few decades there has been considerable progress made in understanding the molecular mechanisms of organ fibrosis in experimental animal models of disease. However,

insights into pathomechanisms underlying the initiation and progression of fibrosis in humans are only just beginning to emerge [297]. This is due, in part, to the technological advancements of high-throughput 'omics data generation including genomics, transcriptomics, proteomics, metabolomics and single-cell sequencing. Unbiased 'omics technologies, particularly when coupled with physiologically relevant pre-clinical models, offer powerful tools to investigate the molecular networks driving fibrosis, providing comprehensive molecular profiles of control and diseased tissues.

1.6.2.1 Transcriptomics

Transcriptomics, which involves the high-throughput profiling of gene expression, has become a cornerstone in fibrosis research, providing novel insights into dysregulated gene expression signatures associated with fibrosis progression in multiple organs. For example, before the routine use of next-generation sequencing technologies, development of IPF pathogenesis was thought to be caused by higher expression of TIMPs and reduced activity of MMPs [298]. However, microarray profiling of human lungs subsequently challenged this theory, reporting increased gene expression of several MMPs in IPF lungs [299]. These findings have since been validated in several transcriptomic studies and it is now well accepted that MMPs are upregulated during disease, affecting multiple signalling pathways to contribute to fibrogenesis [297,300,301]. More recently, integrative analysis combining transcriptomic data with clinical outcomes have identified potential diagnostic and prognostic biomarkers of disease. Interestingly, work by Herazo-Maya *et al* identified a 52-gene expression profile in the peripheral blood of IPF patients which was predictive of patient survival across numerous cohorts [302,303]. However, while transcriptomics provides valuable insights into gene expression patterns, it has one major caveat in that RNA expression does not necessarily correlate with protein abundance due to post-transcriptional regulatory mechanisms such as alternative splicing, mRNA stability and translational control [304]. Consequently, we are unable to discern the rate at which RNA is translated into protein, or if the protein is active in the cell. Moreover, in cases where upregulation of genes in one cell type is offset by downregulation in another (or vice versa), the net change in overall expression may be negligible, leading to false negatives in differential expression analysis. RNA sequencing (RNAseq) results could therefore be misleading and may obscure functional insights into cellular activity and disease mechanisms.

1.6.2.2 Proteomics

Proteomics, the large-scale profiling of protein expression and function, offers complementary insights into fibrosis pathogenesis by characterising the total protein content of cells and/or tissue. Rapid advances in proteomic technologies, particularly liquid chromatography-mass spectrometry (LC-MS), have facilitated the identification and quantification of proteins in normal and fibrotic tissues and patient serum in multiple organs and disease states. Furthermore, proteomic profiling has uncovered novel protein biomarkers associated with disease severity, progression and response to anti-fibrotic therapy [305,306]. More recently, proteogenomic approaches integrating transcriptomic and proteomic data have enhanced our understanding of gene expression regulation and protein dynamics in fibrosis. For example, multi-omic profiling of IPF blood samples performed by Ruan *et al* identified two novel endotypes of IPF associated with distinct clinical characteristics [307]. However, challenges such as sample complexity due to different chemical and physical properties, dynamic range limitations, and sensitivity to low-abundance proteins and data integration remain key considerations in proteomic studies. Furthermore, despite intensive efforts, the total coverage of the cell proteome remains incomplete, with an estimated 11% of the expected proteome still unaccounted for [308].

1.6.2.3 Single cell RNA sequencing

Since its inception in the mid-late 2000s, bulk RNAseq has become one of the most valuable and routinely used tools in research, enabling in-depth interrogation of entire transcriptomes [309]. However, over time it became increasingly clear that potentially biologically relevant differences between cells and/or rare cell populations could be obscured by this method as bulk RNA-seq data represents an average of gene expression profile across thousands/millions of cell types [310]. This biological challenge served as a catalyst to the advent of single-cell RNA sequencing (scRNAseq) technology as a next generation sequencing approach to overcome this problem. scRNAseq is a rapidly evolving methodology which has become more readily available over the past decade and is transforming our understanding of disease pathogenesis, enabling the unbiased interrogation of individual cell populations at an extraordinary resolution [311]. By isolating single cells, capturing their transcripts and mapping gene expression, scRNAseq enables detailed analysis of the biological properties of diverse cell populations in different disease states and biological systems [312].

Multiple studies utilising these cutting-edge single-cell approaches have already begun to unpick the complex, multicellular interplay driving both liver and lung fibrosis resulting in novel insights into disease pathomechanisms. For example, Ramachandran *et al* recently described a previously unreported subpopulation of scar-associated macrophages which expand in liver fibrosis and adopt a pro-fibrogenic phenotype [82]. Similarily, investigation of explant IPF tissue using scRNAseq identified a distinct population of aberrant basaloid cells spatially located at the edge of fibroblast foci [205]. As this exciting field continues to evolve, it is now possible to assess multiple 'omic readouts (transcriptome, genome, epigenome) from the same single cell as well as spatially profiling cells to understand cell-to-cell interactions *in situ* [311,313]. Integration of these single-cell technologies are providing even more comprehensive assessments of cell phenotypes and function in human disease, enabling unprecedented interrogation of underlying cellular and molecular mechanisms driving fibrosis. Biological insights gained from these single-cell approaches should therefore help drive the identification of potential therapeutic targets for a broad range of fibrotic diseases.

1.7 Aims and objectives

1.7.1 Study rationale

Fibrosis is a common pathological feature underpinning a broad spectrum of chronic diseases and is characterised by the replacement of functional tissue architecture with excessive deposition of ECM, resulting in eventual loss of organ function and ultimately death if unresolved. Collectively, fibrotic diseases are considered a major cause of morbidity and mortality worldwide and present an increasing clinical burden, particularly in the Western world. To date, therapeutic approaches have been extremely disappointing and there is an urgent need to better understand mechanisms that drive fibrosis to support the development of new anti-fibrotic agents. Access to human tissue is one of the main factors impeding development of suitable anti-fibrotic compounds. Consequently, much of the research carried out in the field relies heavily on the use of 2D/3D cell culture systems and *in vivo* mouse models which poorly translate to patients. In this project, we will utilise cutting edge methodologies in both whole human tissue and PCS generated from different disease-states/organs to identify and interrogate potential therapeutic targets with the goal of illuminating novel targets to dampen the inflammatory and fibrotic response.

1.7.2 Hypothesis/research question

I hypothesise that investigation of diseased organs with a broad 'omics/single-cell sequencing approach will identify novel therapeutic targets/pathways driving fibrogenesis with direct relevance to lung and liver fibrosis. Through the application of novel therapeutics in our human precision-cut slice models I will be able to develop a greater understanding of the mechanisms driving hepatic and pulmonary inflammation and fibrosis to generate hypotheses for further exploration.

1.7.3 Aims

1. Utilise single nuclei RNA sequencing in human MASLD/cirrhosis samples to identify novel fibrotic targets (Edinburgh University) and validation of targets of interest in human precision-cut slices.

2. Utilise an unbiased 'omics approach to identify potential therapeutic targets in regional IPF samples.

3. Development of a 96-well medium-throughput PCS methodology using IPF explant tissue to test novel candidate compounds for anti-fibrotic and anti-inflammatory effects.

2 General materials & methods

2.1 Human liver acquisition and ethical approval

All work derived from human liver tissue was performed with approval of the Newcastle and North Tyneside Ethics Committee (12/NE/0395) and informed consent was obtained from patients prior to involvement in the study. Human liver tissue was acquired from resection margins surrounding colorectal metastasis from patients who undergoing surgery at the Freeman Hospital, Newcastle-upon-Tyne.

2.2 Precision-cut liver slices (PCLS)

Resected liver tissue was collected from the Freeman hospital, Newcastle in 4°C Krebs buffer comprised of molecular grade water (693520, Sigma) supplemented with krebs ringer powder (SLC07890, Sigma), 1.26g/L sodium bicarbonate (S-6014, Sigma), and 1.80g/L D-glucose powder (G8769, Sigma). To minimise ischaemic time and preserve hepatocyte viability, PCLS were generated no longer than 2 hours post-resection [287].

2.2.1 12-well methodology

To generate 8mm PCLS, liver tissue was cored using an 8mm biopsy punch (BI3000, Stiefel) before being transferred vertically to a metal mould, submerged in 3% low gelling temperature agarose (A9414, Sigma) and placed on ice to set. Agarose-embedded cores were superglued to the vibratome mounting stage, loaded into the media chamber containing 4°C Krebs buffer, and cut using a Leica VT1200S vibrating blade microtome (Leica Biosystems) at a speed of 0.3 mm/sec, amplitude 2 mm and thickness of 250µm. PCLS were then transferred into 8µm pore transwell inserts (66563, Greiner bio-one) in custom made 12 well cell culture plates containing paired wells (BioR plates) and placed on bioreactor platforms (patent PCT/GB2016/053310) to rock plates at a flow rate of 18.136 µL/sec (Figure 9). PCLS were cultured in 1.5ml/well (500µl inside transwell and 1ml outside) of Williams medium E (W4128, Sigma), supplemented with 1% penicillin/streptomycin (100U/ml and 100µg/ml; P0781, Sigma), 1× insulin transferrin-selenium X (1g/L, 0.55g/L and 0.00067g/L; 51500056, Gibco), 1x glutamine (200mM; G7513, Sigma)/pyruvate (100mM; 58636, Sigma), 2% foetal bovine serum (10500-064, Gibco) and 100nM of dexamethasone (D-085, Cerilliant). PCLS were incubated at 37°C, supplemented with 5% CO_2. Media was refreshed at 24-hour intervals with collected media snap frozen for downstream analysis.

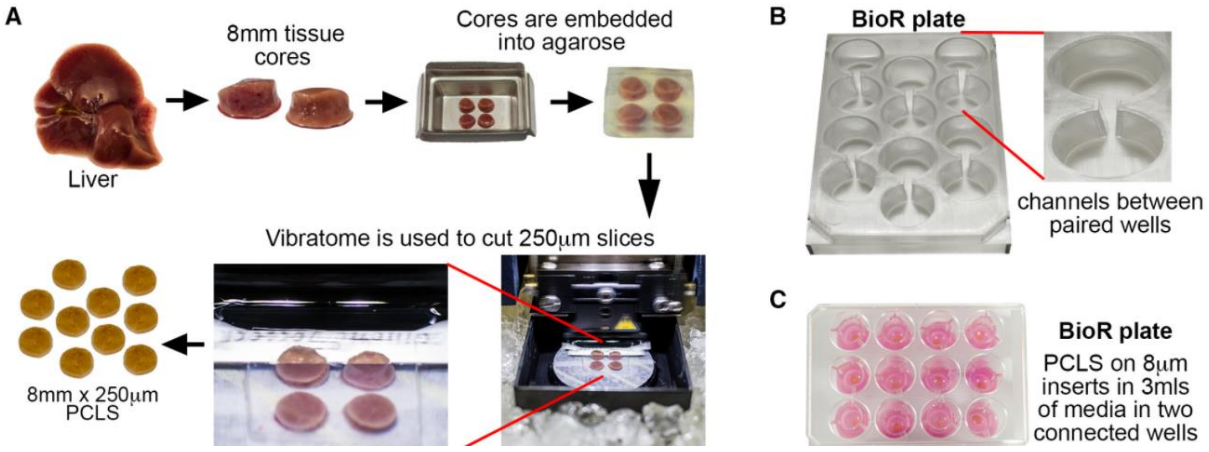

Figure 9: **Workflow to generate precision cut liver slices (PCLS) from resected liver tissue** A) Workflow to generate 8mm x 250µM PCLS. Briefly, tissue was cored using 8mm biopsy punch, embedded in low-gelling agarose and glued to vibratome mounting stage. 250µM-thick PCLS were generated using Leica VT1200S vibrating blade microtome. B) Custom made BioR plate containing paired wells. C) PCLSs cultured on 8µm Transwell inserts in the Bioreactor (BioR) plate. Image from Paish et al [287].

2.2.2 96-well methodology

To generate 3mm PCLS for 96-well transwells, liver tissue was cut to 1.5cm^3 before being transferred to a metal mould, submerged in 3% low gelling temperature agarose (A9414, Sigma) and placed on ice to set. Agarose-embedded tissue blocks were superglued to the vibratome mounting stage, loaded into the media chamber containing 4°C Krebs buffer, and cut using a Leica VT1200S vibrating blade microtome (Leica Biosystems) at a speed of 0.3 mm/sec, amplitude 2 mm and thickness of 250µm to generate tissue sheets. Sheets of 250µm-thick tissue were then cored using 3mm biopsy punches (BP30F, Kai medical) before being transferred into 8µm pore transwell inserts (3384, Corning) in custom made 96 well cell culture plates containing paired wells (BioR plates) and placed on bioreactor platforms (patent PCT/GB2016/053310) to rock plates at a flow rate of 18.136 µL/sec. PCLS were cultured in 250µl/well (100µl inside transwell and 150µl outside) of Williams medium E (W4128, Sigma), supplemented with 1% penicillin/streptomycin (100U/ml and 100µg/ml; P0781, Sigma), 1× insulin transferrin-selenium X (1g/L, 0.55g/L and 0.00067g/L; 51500056, Gibco), 1x glutamine (200mM; G7513, Sigma)/pyruvate 100mM; 58636, Sigma), 2% foetal bovine serum (10500-064, Gibco) and 100nM of dexamethasone (D-085, Cerilliant). PCLS were incubated at 37°C, supplemented with 5% CO_2. Media was refreshed at 24-hour intervals with collected media snap frozen for downstream analysis.

2.3 Human lung acquisition and ethical approval

All human explant lung experiments were carried out with approval by the Newcastle and North Tyneside Local Regional Ethics Committee (lung: 11/NE/0291) and informed written consent was obtained from patients prior to their involvement in the study. Human lung tissue was collected at the Freeman Hospital, Newcastle upon Tyne from patients who underwent either single or bi-lateral lung transplants. Normal unused donor lungs were acquired through Blood and Transport Research Unit (lung: 11/NE/0352).

2.4 Precision-cut lung slices (PCLuS)

Explanted lung tissue was collected in 4°C Hank's Balanced Salt Solution (HBSS; 14170, Gibco) and transported from the Freeman Hospital, Newcastle to the Royal Victoria Infirmary Pathology department for processing by a pathologist to determine if the samples were suitable for research and to advise on areas for sampling. Tissue was then dissected into 6cm x 6cm x 3cm regions and warmed to 37^{o}C for 60mins in HBSS prior to processing. Tissue was inflated with ~20ml of 3% low gelling agarose (A9414, Sigma) using a 19g Luer needle (AN*1938R1, Terumo) and 25ml syringe before being left to set on ice at 4°C.

2.4.1 24-well methodology

To generate PCLuS for 24 well transwells, tissue was cored using an 8mm biopsy punch (BI3000, Stiefel) before cores were transferred vertically to a metal mould, submerged in 3% low gelling agarose and set on ice for 15mins at 4^{o}C. Tissue blocks were superglued to the vibratome mounting stage, loaded into the media chamber and submersed in 4°C HBSS. Slicing was performed using a Leica VT1200S vibrating blade microtome at a speed of 0.3 mm/sec, amplitude 2mm and a thickness of 450µm (Figure 10). PCLuS were transferred to 8µm pore transwell inserts in 24 well cell culture plates (662638, Greiner bio-one) and cultured in 500µl/well (200µl inside transwell and 300µl outside) of Small Airway Epithelial Cell media (C-21270, Promo Cell) supplemented with a supplement pack (bovine pituitary extract [0.004ml/ml], recombinant human L-epidermal growth factor recombinant human [10ng/ml], recombinant human Insulin [5µg/ml], hydrocortisone [0.5µg/ml], epinephrine [0.5µg/ml], triiodo-L-thyronine [6.7ng/ml], recombinant human transferrin [10µg/ml], retinoic acid [0.1ng/ml] and bovine serum albumin-fatty acid free [2.5mg/ml]; C-39170, Promo Cell) and 1% penicillin/streptomycin (100U/ml and 100µg/ml; P0781, Sigma). PCLuS were incubated at

37°C, supplemented with 5% CO_2. Media was refreshed at 24-hour intervals with collected media snap frozen for downstream analysis.

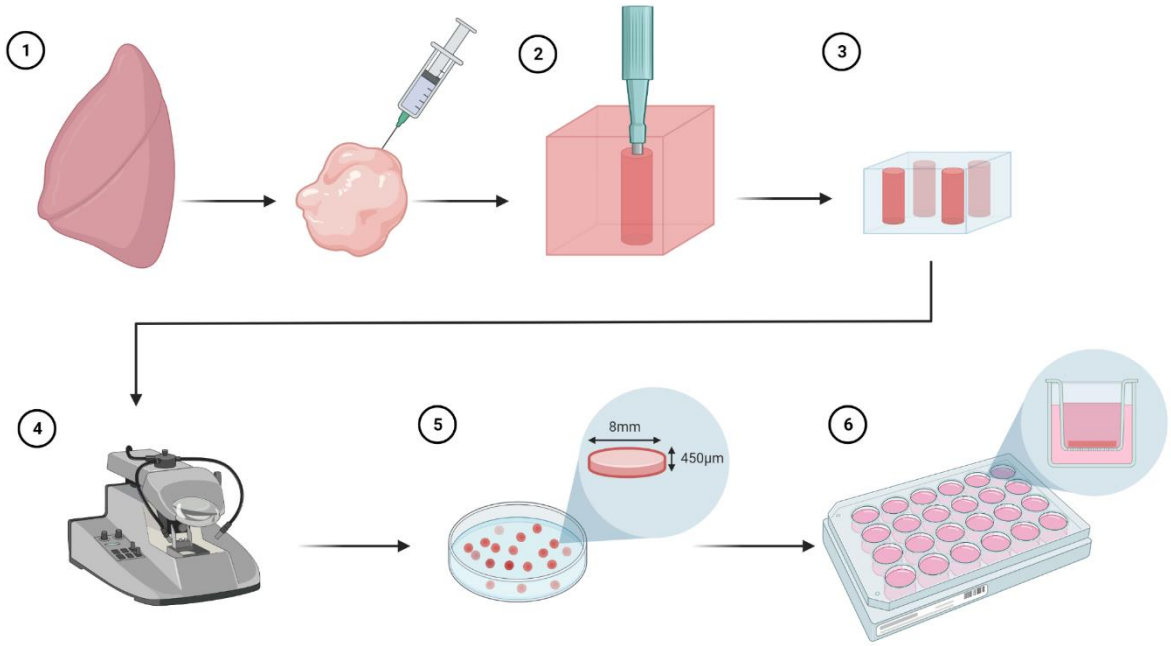

Figure 10: Workflow to generate precision cut lung slices (PCLuS) from explant lung tissue 1) Explant IPF tissue acquired, cut into smaller sections, inflated using 3% low gelling agarose and allowed to set on ice 2) Tissue cored using an 8mm biopsy punch and 3) cores were transferred to metal mould and submerged in 3% low gelling agarose and allowed to set on ice 4) Agarose-embedded cores glued to Leica VT1200S vibratome stage and set to generate 5) 450µm-thick 8mm diameter PCLuS. 6) PCLuS transferred to 8µm pore transwell inserts in 24 well cell culture plate.

2.4.2 96-well methodology

To generate 3m or 4mm PCLuS, after inflation, tissue was cut to smaller 1.5cm^3 sections before being transferred to a metal mould, submerged in 3% low gelling agarose and set on ice for 15mins at 4ºC. Tissue blocks were superglued to the vibratome mounting stage, loaded into the media chamber and submersed in 4°C HBSS. Slicing was performed using a Leica VT1200S vibrating blade microtome at a speed of 0.3 mm/sec, amplitude 2mm and thickness of 450µm to produce sheets of tissue which were then transferred to a 10cm petri dish containing culture media and cored using a 3mm or 4mm biopsy punch (BP-30F and BP-40F, Kai medical) (Figure 11). Slices were transferred to 8µm pore transwell inserts in 96 well cell culture plates (3384, Corning) and cultured in 200µl/well (50µl inside transwell and 150µl outside) of Small Airway Epithelial Cell media (C-21270, Promo Cell) supplemented with a supplement pack (see above; C-39170, Promo Cell) and 1% penicillin/streptomycin (100U/ml and 100µg/ml); P0781, Sigma). PCLuS were incubated at 37°C, supplemented with 5% CO_2. Media was refreshed at 24-hour intervals with collected media snap frozen for downstream analysis.

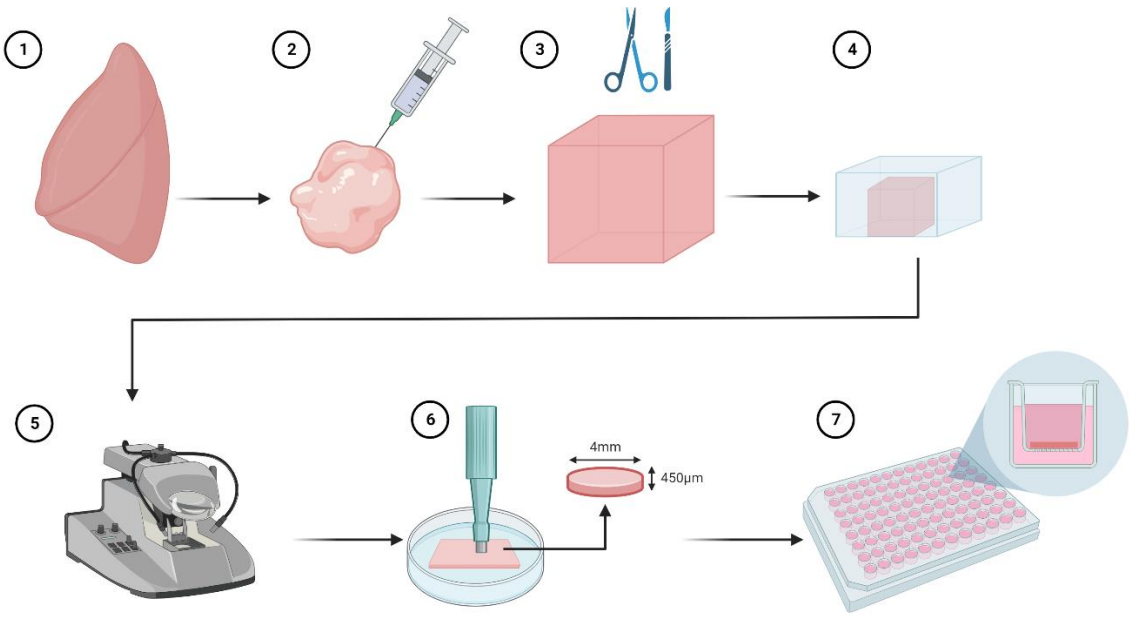

Figure 11: Workflow to generate precision cut lung slices (PCLuS) from explant lung tissue 1) Explant IPF tissue acquired and cut into smaller sections 2) Smaller tissue sections inflated using 3% low gelling agarose and allowed to set on ice 3) Set tissue blocks cut to approx. 1.5cm^3 and any uninflated tissue discarded 4) Tissue blocks transferred to metal mould and submerged in 3% low melting point agarose and allowed to set on ice 5) Tissue blocks glued to Leica VT1200S vibratome stage and set to generate 450µm-thick sheets of tissue 6) Tissue sheets collected into SAEC culture media in a 10cm dish and 3/4mm cored using 3/4mm biopsy punch to generate PCLuS 7) PCLuS transferred to 8µm pore transwell inserts in 96 well cell culture plate.

2.5 Enzyme Linked Immunosorbent Assay (ELISA)

Sandwich ELISA was performed using DuoSet ELISA Kits (unless otherwise mentioned) on conditioned culture media and tissue homogenates to measure fibrotic and inflammatory markers including Collagen 1α1 (DY6220-05, R&D), TIMP-1 (DY970, R&D), IL-6 (DY206, R&D) and IL-8 (DY208, R&D) according to manufacturer's guidelines. Briefly, capture antibodies were diluted in PBS and used to coat 96 well half area plates (3365, Corning) before overnight incubation on a rocking platform. Plates were washed 3 times with wash buffer (PBS + 0.05% Tween) before non-specific binding was blocked by incubation with reagent diluent (1% BSA + PBS) for 1hr at room temperature (RT). Next, plates were washed, and relevant samples/standards were added before incubation at RT for 2hrs on a rocking platform. Following this, samples were removed and plates washed 3 times before incubation with biotinylated detection antibodies diluted in PBS for 2hrs at RT, with rocking. Streptavidin-horseradish protein (HRP) was added after washing and plates were incubated in the dark for 20mins. Plates were washed for the final time before incubation with substrate solution

(DY999, R&D). Colour change was stopped when the standard curve was clearly defined by adding stop solution (1M sulfuric acid). Optical density was measured at 450nm and 570nm using Tecan Infinite Pro 2000 with sample concentrations calculated using the 7-point standard curve.

2.6 Lactate Dehydrogenase (LDH) Assay

Lactate dehydrogenase (LDH) is a cytosolic enzyme present in cells that is released into culture medium upon damage to the plasma membrane and can be used to determine cellular cytotoxicity. To measure extracellular LDH in conditioned media, Pierce LDH cytotoxicity Assay Kit (C20300, Thermo Scientific) was used following manufacturer's guidelines. Briefly, reaction mixture was made by adding Substrate Mix to ultrapure water and dissolved by gentle mixing before addition of Assay Buffer. A tissue positive control was prepared by the addition of a tissue slice to 20% Triton X in culture media at RT before being added in duplicate to a 96 well plate (3365, Corning). Samples and a negative media control were added in duplicate to the plate before being incubated for 30mins in the dark. Finally, the reaction was stopped using Stop solution and plates were read using Tecan Infinite Pro 2000 with optical density measured at 490nm and 680nm.

2.7 Resazurin assay

To assess the metabolic activity of PCS, 4.5mM resazurin stock solution (ab145513, Abcam) was diluted into relevant culture media to produce a 450µM resazurin working solution. For tissue, 8mm PCS were incubated in 100µl of the working solution and 3/4mm PCLS and PCLuS were incubated in 50µl of working solution in 96 well tissue culture plates for 1hr at 37°C supplemented with 5% CO_2. For cells, culture media was removed and wells were washed x2 with PBS before incubation with of 50µl of the working solution at 37°C supplemented with 5% CO_2. A media blank (containing media and working stock resazurin but no tissue/cells) for each media type was cultured alongside tissue/cells. After incubation, resazurin working solution was transferred to a white 96 well plate (Greiner) and fluorescence was measured at excitation 535nm and emission 595nm using a Max Filter 5 plate reader. Media blank fluorescent values were subtracted from each tissue/cell values, and fluorescence was normalised to control unstimulated tissue/cells for each donor/cell line (presented as % change from baseline).

2.8 RNA isolation and quantification

2.8.1 RNA isolation from whole tissue

Total RNA was isolated from snap frozen whole tissue using RNeasy mini kits (74104, Qiagen) according to manufacturer's guidelines. Briefly, samples were homogenised in 350µl of RLT lysis buffer containing β-mercaptoethanol (444203, Sigma) in Precellys® Ceramic hard tissue tubes (432-3752, VWR) using a Precellys bead homogeniser at 0°C. Lysate was transferred to a Qiashredder column (79656, Qiagen) and spun at 8,000 x g for 2mins to further homogenise samples. Following this, an equal volume of 70% ethanol was added to each sample and mixed by pipetting. Next, samples were transferred to RNeasy spin columns and spun at 8,000 x g for 15secs, discarding flow through. Spin columns were washed with Buffer RW1 followed by Buffer RPE, each time spinning samples at 8,000 x g for 15 secs and discarding flow through. Samples were washed a second time with RPE buffer at 8,000 x g for 2mins to eliminate residual ethanol contamination before 30µl of RNase-free water (129112, Qiagen) was added to each spin column and spun at 8,000 x g for 1min to elute samples. RNA was collected into a fresh collection tube and quantified before long-term storage at -80°C.

2.8.2 RNA isolation from PCS

Total RNA was isolated from individual PCS by homogenising tissue samples in 500µl QIAzol lysis reagent (79306, Qiagen) using a Tissue Lyser II bead homogeniser (Leica) before incubation for 5mins at RT. Tissue lysate was transferred to a Qiashredder column and spun at 8,000 x g for 2mins to further homogenise tissue and reduce viscosity. Next, 140µl chloroform (437581, Sigma) was added to each sample, vortexed briefly for 15secs and incubated for 2-3mins at RT. Samples were spun at 12,000 x g for 15mins at 4°C and the clear upper aqueous layer was collected into a new tube before an equal volume of 70% ethanol was added and vortexed. Samples were transferred to RNeasy spin columns and spun at 8,000 x g for 15secs, discarding flow through. Following this, spin columns were washed with Buffer RW1 followed by Buffer RPE, each time spinning samples at 8,000 x g for 15 secs and discarding flow through. Samples were washed a second time with RPE buffer at 8,000 x g for 2mins to eliminate residual ethanol contamination before 30µl of RNase-free water was added to each spin column and spun at 8,000 x g for 1min to elute samples. RNA was collected into a fresh collection tube and quantified before long-term storage at -80°C.

2.8.3 RNA quantification

RNA quality was ascertained by measuring absorbance at wavelengths of 260nm and 280nm *via* Nanodrop 2000 spectrophotometer. After a blank measurement (RNase free water), 1µl of sample was loaded onto the lower optical pedestal and measured. RNA concentration and purity were then calculated with absorbance A260/A280 ratios of >1.8 indicating acceptable sample purity.

2.9 cDNA synthesis

RNA stock (1µg per sample) was diluted in RNase free water to a total volume of 8µl before incubation at 37°C for 30mins with DNase (M6101 and M610A, Promega) to remove genomic contaminants. After incubation, 1µl of DNase Stop solution (M199A, Promega) was added to each sample before 0.5µl of random hexamers/primers (C1181, Promega) was added at RT and incubated at 70°C for 5mins. Following this, samples were immediately placed on ice for 5mins prior to addition of reverse transcriptase mix (comprised of 0.5µl RNAsin, 1µl M-MLV RT, 1µl 10mM dNTPs oligonucleotides and 4µl 5X M-MLV RT buffer; N2515, M1705, C1141; Promega) to each sample and incubation at 42^{o}C for 1hr. cDNA was then stored at -80°C.

2.10 Reverse transcription polymerase chain reaction (RT-PCR)

RT-PCR was used to investigate gene transcription levels in samples using a 7500 fast System (Applied Biosciences). For each gene of interest, a master mix was prepared consisting of 10µl 2x TaqMan™ Fast Advanced Master Mix (4444556, Sigma), 1µl 20x PCR Probe mix (Sigma) and 7µl nuclease free water and added to a 96-well PCR plate. 2µl of cDNA (at 20ng/µl) was added to each well containing 18µl of master mix before the plate was sealed and spun at 200*g* for 3mins. Reactions were run on 7500 fast PCR System (Applied Biosciences) in quadruplicate. All samples were subject to 40 cycles of denaturing (at 95°C for 15secs), annealing (at 60°C for 30secs) and elongation (at 72°C for 30secs) before a dissociation curve was produced by a final cycle of 95°C for 15secs, 60°C for 60secs and 95°C for 30secs to confirm specificity of the PCR amplification by distinguishing the desired product from primer-dimers and/or non-specific products based on their melting temperatures (where a single sharp peak typically indicates amplification specificity). Results were normalised to β-actin housekeeping gene (Hs01060665_g1, Sigma) and presented as relative levels of transcriptional difference (RLTD) in which the experimental data is displayed relative to a control sample (set at 100%) according to the delta-delta Ct method. Briefly, cycle threshold (Ct) values (defined as the

cycle at which the fluorescence of a sample rises above the background fluorescence indicating detectable gene expression) were obtained for each reaction using the QuantStudio design & analysis software v1.4.1 (ThermoFisher) and normalised to a reference gene (e.g. β-actin), which is assumed to be consistently expressed across all samples (ΔCt value= $Ct_{target\ gene} - Ct_{reference\ gene}$). The average ΔCt value for experimental controls was calculated, giving a calibrator value and this was then subtracted from all ΔCt values (ΔΔCt value= $\Delta Ct_{sample\ of\ interest} - \Delta Ct_{calibrator\ sample}$).

2.11 Histology

2.11.1 Haematoxylin & Eosin

5µM- thick formalin-fixed, paraffin-embedded tissue sections were dewaxed for 2x 5mins in clearene (3803600E, Leica) and rehydrated in 100% ethanol and 70% ethanol (each for 5mins) before being washed in running tap water. Samples were then incubated with Mayer's haematoxylin for 2mins, washed in running tap water and incubated with Eosin (PRC/66/1, PRC) for 40 secs before being dehydrated through graded alcohols of 50%, 75% and 100% (x2) ethanol for 20 secs. Slides were transferred to clearene for 10mins before being mounted with coverslips using Pertex (SEA-0100-00A, Cell Path).

2.11.2 Picrosirius Red (PSR)

5µM- thick formalin-fixed, paraffin-embedded tissue sections were dewaxed in clearene and rehydrated in graded alcohols before being washed in deionised water and incubated with 0.2% phosphomolybdic acid (79560, Sigma) for 5mins. Next, sections were washed in deionised water and incubated in 0.1% Picro Sirius Red (365548, Sigma) for 2hrs. After incubation, sections were washed twice in 0.01M HCl (258148, Sigma) and dehydrated through graded alcohols of 70%, 90%, 100% ethanol for 20 seconds each before 2mins in 100% ethanol and transfer to clearene for 10mins prior to mounting in pertex.

2.12 Immunohistochemistry

Tissue sections were deparaffinised and rehydrated before blocking endogenous peroxidase activity using 0.6% hydrogen peroxide/methanol solution. Antigen retrieval was performed using antigen unmasking solution (H-3300, Vector laboratories), 20 µg/ml proteinase K (P2308, Sigma) or Tris-EDTA. Endogenous avidin and biotin were blocked for 20mins respectively using Avidin/Biotin Blocking Kit (SP-2001, Vector laboratories). Non-specific binding was blocked with 20% swine serum (C15SB, Bio-Rad) or 10% goat serum (S-1000-20,

Vector Laboratories) dependant on the secondary antibody for 45mins before incubation with the primary antibody at 4°C overnight. Slides were washed and incubated with secondary antibody (goat anti-fluorescein [BA-0601, Vector Laboratories] 1/300 dilution, swine anti-rabbit [E0353, Dako] 1/200 dilution or goat anti-mouse [BA-9200, Vector Laboratories] 1/300 dilution) for 1hr, followed by incubation with Vectastain R.T.U Elite ABC HRP Reagent (PK-7100, Vector Laboratories) for 45mins. Visualisation was carried out using DAB peroxidase substrate kit (SK-4100, Vector Laboratories) prior to counterstaining with Mayer's haematoxylin. Slides were then dehydrated and mounted using Pertex to allow histological assessment. Nikon Eclipse Upright DS-U3 microscope and NIS-Elements BR programme was used to analyse tissue sections.

2.13 Statistical analysis

Statistical analysis was performed using GraphPad Prism 9.5.0. Results are presented as mean ± standard error of the mean (SEM). Data were considered statistically significant with $p<0.05$ *, $p<0.01$ **, $p<0.001$ *** and $p<0.0001$ ****. Specific statistical analysis is detailed within each results chapter.

3 Identification and validation of novel fibrotic disease targets using human precision-cut slices

Statement of contribution

- snRNAseq of human liver samples, including processing of tissue and downstream bioinformatics analysis, was performed by Dr Sebastian Wallace and Professor Neil Henderson (Edinburgh University) to identify targets of interest for exploration in this project (Figures 12-14 provided by Dr Sebastian Wallace).
- Experiments carried out to generate pre-existing transcriptomic datasets in PCLS (Figure 15 and Figure 16) and pulmonary fibroblasts (Figure 37 and Figure 38) prior to the start of this project were performed by equal contribution between myself and Dr William Reilly. Downstream bioinformatics analysis of these datasets was performed by Dr Laura Sabater.
- Investigation of targets of interest in a pre-existing scRNAseq datasets generated from 6 integrated single cell lung atlases was performed by Dr Stephen Christensen (Figure 35 and Figure 36).
- All other work in this chapter was performed solely by the author.

3.1 Introduction

Organ fibrosis represents a major cause of morbidity and mortality worldwide. As a common endpoint for a wide range of diseases, the underlying causes and mechanisms of fibrosis can be either core or organ specific, and in the majority of cases remain poorly defined [314]. To date, there are only two approved anti-fibrotic therapies (Pirfenidone and Nintedanib) and their usage is restricted exclusively to the treatment of patients with mild-moderate Idiopathic Pulmonary Fibrosis (IPF) [315]. Meanwhile, the escalating global prevalence of metabolic dysfunction-associated steatohepatitis (MASH) in conjunction with the mounting rates of obesity, type 2 diabetes and cardiometabolic syndrome, has become a leading cause of liver fibrosis [16,17]. Similarily, as the most common and severe fibrosing interstitial lung disease, IPF continues to rise in line with an ageing population [316]. This growing health challenge emphasises the urgent unmet need for the development of novel anti-fibrotic therapies to address the increasing socioeconomic burden of MASH and other fibrotic diseases.

The process of drug discovery is widely considered an inefficient and expensive process, characterised by high costs, lengthy timelines and high rates of attrition at various stages [317,318]. Consequently, despite significant efforts to unpick the underlying molecular mechanisms of fibrosis, the translation of promising pre-clinical findings into effective anti-fibrotic therapies remains extremely limited. These inefficiencies can be, in part, attributed to our limited understanding of disease heterogeneity and pathomechanisms driving fibrosis, impeding the identification of actionable therapeutic targets. This critical gap from bench to bedside is further exacerbated by the frequent use of reductionist pre-clinical models, which fail to recapitulate the intricate pathophysiology and cellular heterogeneity of human disease. For example, the conventional methodology of culturing cells in a 2D monolayer is known to restrict contact between cells and their ability to form the multi-dimensional structures seen in tissue [272]. Additionally, the 2D system exposes cells to supra-physiological levels of stiffness and has been shown to impair function of fibroblasts *in vitro*, altering phenotype and reducing viability [274]. More recently, research has advanced to incorporate the use of 3D models such as organoids to alleviate the limitations outlined above. These models display structures and functions more consistent with tissue *in vivo* and can interact with neighbouring cells enabling better interrogation of cellular crosstalk [269]. However, 3D systems are still limited to include few cell types and fail to address the complex cellular

heterogeneity present in disease [282]. Animal models can overcome several of the issues seen *in vitro*, allowing multiple cell-to-cell interactions, and providing a microenvironment to study basic physiology. However, there remains significant challenge in translating *in vivo* findings to human patients based on the biological differences between species [286]. Additionally, many established rodent models rely on accelerated disease progression in young mice (8-12 weeks old), using non-physiologically relevant stimuli (e.g., CCl_4 and Bleomycin) [284]. Given that fibrosis develops over the course of decades, and in many cases in response to unknown stimuli, it can be concluded that these models will be incapable of accurately replicating the disease state seen in humans.

Addressing these limitations requires innovative technologies that provide a more nuanced and accurate representation of the cellular landscape observed during fibrosis development. In this context, the integration of single-nuclei sequencing (snRNAseq) and precision cut slice (PCS) technology emerges as a cutting-edge approach to enable identification of common and distinct mechanisms driving fibrosis toward end-stage disease. Importantly, snRNAseq enables the unbiased interrogation of cellular heterogeneity at an unprecedented resolution, unravelling the complex interplay of various cell types within the fibrotic microenvironment [311]. Having already yielded new discoveries in the field [82,205,319,320], snRNAseq methodologies provide previously unattainable insights into the diverse cell populations, phenotypes and signalling pathways in health and disease, laying the groundwork for the identification of key fibrogenic cell types, interactions and novel therapeutic targets. Furthermore, PCS technology provides an exciting alternative to currently available pre-clinical models and has been utilised successfully from a range of organs [287-289]. Critically, PCS preserves tissue architecture and cellular heterogeneity of human tissue and offers a physiologically and structurally relevant system in which to test potential therapeutics and interrogate underlying mechanisms of disease [269,287].

Here, we combined our extensive knowledge in the generation and culture of PCS with the expertise of Prof Neil Henderson's group in single-cell technologies to identify and validate novel fibrotic and disease targets.

3.2 Materials and methods

3.2.1 Target identification using single nuclei RNA sequencing

The identification of targets of interest *via* snRNAseq of human liver samples was performed by Dr Sebastian Wallace and Professor Neil Henderson, Edinburgh University. Specifically, Dr Sebastian Wallace performed single nuclei isolation, processing of human samples and downstream bioinformatics analysis under the supervision of Prof Neil Henderson as outlined below.

3.2.1.1 Sample ethics and acquisition

Non-cirrhotic liver tissue was acquired from patients undergoing partial liver resections at the Royal Infirmary of Edinburgh, with tissue obtained from normal resection margins surrounding solid tumour metastases or hepatic adenomas. Cirrhotic explant liver tissue was acquired by identifying patients on the Scottish Liver Transplant Unit waiting list through BIOBANK Study (EC:15/ES/0094). MASH biopsies were obtained from NHS Lothian and NHS Grampian as excess tissue during routine clinical biopsies/trials as part of the Liver Cell Atlas (LiCA) study (approved by the Northwest Ethics committee in February 2020, EC: 20/NW/0075, Submitted by Sebastian Wallace, PI Prakash Ramachandran). All subjects provided written, informed consent prior to their involvement in the study.

3.2.1.2 Single nuclei isolation

Nuclei isolation was performed from snap frozen liver samples using the Tween with salts and Tris (TST) method described by Slyper *et al* [321]. Briefly, 40-60ug of frozen tissue was placed in a 6-well plate on ice with 1ml of 1% TST buffer (2ml 2x Salt-Tris (ST) buffer (Table 3) plus TWEEN-20 (Bioshop) and 20% BSA (Sigma Aldrich)) before being chopped for 10mins with Noyes Spring scissors (FST). Tissue lysate was then filtered using a 35µm Falcon™ cell strainer before being washed with 1ml TST. Next, 3ml 1x ST buffer was added to tissue lysate before transferring to 15ml conical tube and centrifuging at 4°C for 5 minutes at 500*g*. Finally, the pellet was resuspended in 1ml 1x ST buffer and nuclei quality was assessed by Hoecsht staining. Nuclei were then loaded onto the BioRad nuclei counter and the concentration was adjusted for the 10x protocol. For MASH biopsies, the volume of TST and ST buffer was diluted 10-fold in ultrapure water.

Table 3: 2x ST buffer components diluted in ultrapure water

Compound	Concentration	Supplier	Code
NaCl	292mM	Thermo Fisher Scientific	AM9759
Tris-HCl pH 7.5	20mM	Thermo Fisher Scientific	15567027
CaCl2	2mM	VWR International Ltd	97062-820
MgCl2	42mM	Sigma Aldrich	M1028

3.2.1.3 10X sample processing, cDNA library preparation and sequencing

Single nuclei samples were processed through the 10X Genomics Chromium Platform using the Chromium Single Cell 3' Library and Gel Bead Kit v3 (10X Genomics, PN-1000075) and the Chromium Single Cell B Chip Kit (10X Genomics, PN-1000074) as per the manufacturer's guidelines. In brief, single nuclei suspensions were diluted to a targeted capture of 5000 single-nuclei libraries per sample, loaded onto the single cell B chip and partitioned into Gel Beads in Emulsion (GEM) using the Chromium instrument. Next, reverse transcription of RNA occurred, followed by amplification, fragmentation and 5' adaptor and sample index attachment. Samples were sequenced on NovaSeq 6000 by Genewiz ™.

3.2.1.4 Computational analysis

In total, 317,428 nuclei from healthy (n=14), MASH (n=25) and cirrhotic (n=14) liver samples were isolated from liver donors outlined in

Table 4 with snRNAseq sample readouts detailed in Table 6. The total spectrum of MASH fibrosis was represented by F0 (n=1), F1 (n=4), F2 (n=6), F3 (n=10) and F4 (n=4) outlined in Table 7. A summary table of liver donor demographics is provided in Table 5, where all continuous variables are reported as mean ± SD. Statistical analysis was performed using Kruskal-Wallis test with *post hoc* Dunn's multiple comparisons test to infer homogeneity or heterogeneity between patient ages between cohorts. Results confirmed no statistical differences between cohorts (see Appendix A; Table 1). Chi-square test was performed to assess sex distribution between the cohorts where chi-square statistic=12.94, degrees of freedom=6 and p value=0.0441, indicating that the observed differences are unlikely due to random chance.

Table 4: Liver snRNAseq donor demographics

Tissue	Age	Sex	Biopsies	Age	Sex
Healthy 1	39	M	MASH BIOPSY 1	40	M
Healthy 2	70	M	MASH BIOPSY 2	50	F
Healthy 3	80	M	MASH BIOPSY 3	58	F
Healthy 4	71	F	MASH BIOPSY 4	56	F
Healthy 5	62	F	MASH BIOPSY 5	64	M
Healthy 6	70	M	MASH BIOPSY 6	58	F
Healthy 7	59	M	MASH BIOPSY 7	55	M
Healthy 8	72	M	MASH BIOPSY 8	61	M
Healthy 9	62	F	MASH BIOPSY 9	66	M
Healthy 10	59	M	MASH BIOPSY 10	29	F
Healthy 11	66	M	MASH BIOPSY 11	47	F
Healthy 12	64	M	MASH BIOPSY 12	66	M
Healthy 13	60	F	MASH BIOPSY 13	58	F
Healthy 14	71	M	MASH BIOPSY 14	44	M
Cirrhotic 1	60	F	MASH BIOPSY 15	59	M
Cirrhotic 2	70	M	MASH BIOPSY 16	36	M
Cirrhotic 3	59	M	MASH BIOPSY 17	68	M
Cirrhotic 4	56	M	MASH BIOPSY 18	63	M
Cirrhotic 5	64	F	MASH BIOPSY 19	60	M
Cirrhotic 6	58	M	MASH BIOPSY 20	45	M
Cirrhotic 7	60	F	MASH BIOPSY 21	56	F
Cirrhotic 8	64	M	MASH BIOPSY 22	45	M
Cirrhotic 9	70	M	MASH BIOPSY 23	65	F
Cirrhotic 10	56	F	MASH BIOPSY 24	42	M
Cirrhotic 11	60	F	MASH BIOPSY 25	65	M
Cirrhotic 12	59	M			
Cirrhotic 13	56	M			
Cirrhotic 14	70	M			

Table 5: Liver snRNAseq summary donor demographics

Variable		Healthy	MASH F0	MASH F1	MASH F2	MASH F3	MASH F4	Cirrhotic
N (number)		14	1	4	6	10	4	14
Sex	*Female*	4	0	0	2	6	0	9
	Male	10	1	4	4	3	4	5
Age (years)		64.6 ± 9.56	56	51.75 ± 11	55.7 ± 10.71	52.3 ± 12.17	59 ± 9.7	61.6 ± 5.2

Table 6: snRNAseq sample readouts

Tissue	nCells	nGenes	nUMI	Biopsies	nCells	nGenes	nUMI
Healthy 1	4910	98,091	3115	MASH BIOPSY 1	6117	2464	5402
Healthy 2	7730	61,734	816	MASH BIOPSY 2	638	1332	2014
Healthy 3	7469	64,707	1282	MASH BIOPSY 3	573	2459	4788
Healthy 4	1223	1048	1860	MASH BIOPSY 4	676	1224	1964
Healthy 5	7883	1265	2102	MASH BIOPSY 5	808	109	161
Healthy 6	3958	1156	1816	MASH BIOPSY 6	2127	12	48
Healthy 7	6535	2750	7898	MASH BIOPSY 7	4678	884	1146
Healthy 8	4469	1777	3224	MASH BIOPSY 8	4165	972	1228
Healthy 9	4721	1199	1999	MASH BIOPSY 9	1464	834	1058
Healthy 10	3712	1455	2467	MASH BIOPSY 10	1583	931	1166
Healthy 11	7087	2844	8423	MASH BIOPSY 11	25551	861	1099
Healthy 12	3865	1281	2162	MASH BIOPSY 12	12323	843	1022
Healthy 13	1855	1269	1919	MASH BIOPSY 13	3753	1342	1868
Healthy 14	7477	2043	4355	MASH BIOPSY 14	16785	1173	1577
Cirrhotic 1	7717	2180	5109	MASH BIOPSY 15	15559	246	307
Cirrhotic 2	1223	1048	1860	MASH BIOPSY 16	5278	551	718
Cirrhotic 3	1265	1577	4995	MASH BIOPSY 17	7223	644	850
Cirrhotic 4	3316	2182	5099	MASH BIOPSY 18	4041	782	978
Cirrhotic 5	2588	2018	4310	MASH BIOPSY 19	10370	560	991
Cirrhotic 6	1146	1326	3818	MASH BIOPSY 20	13627	705	918
Cirrhotic 7	7633	1641	2988	MASH BIOPSY 21	12701	845	1155
Cirrhotic 8	3310	2333	5270	MASH BIOPSY 22	14105	1259	1936
Cirrhotic 9	4581	2267	5181	MASH BIOPSY 23	22187	2323	4420
Cirrhotic 10	1650	2868	6276	MASH BIOPSY 24	8671	983	1286
Cirrhotic 11	3752	2046	4912	MASH BIOPSY 25	3149	680	778
Cirrhotic 12	5525	1298	2091				
Cirrhotic 13	1026	770	1096				
Cirrhotic 14	1650	2868	6276				

nCells= number of cells, nGenes= average number of genes per cell and nUMI= number of unique cells per gene

Table 7: Fibrosis grading of MASH biopsies in snRNAseq dataset

Biopsy	Fibrosis Stage	Steatosis	Ballooning	Inflammation
MASH BIOPSY 4	0	1	0	0
MASH BIOPSY 18	1a	2	0	1
MASH BIOPSY 20	1a	1	0	1
MASH BIOPSY 1	1c	2	1	1
MASH BIOPSY 15	1c	2	1	1
MASH BIOPSY 7	2	1	0	1
MASH BIOPSY 8	2	2	1	1
MASH BIOPSY 13	2	3	2	2
MASH BIOPSY 16	2	2	1	2
MASH BIOPSY 17	2	2	1	1
MASH BIOPSY 21	2	2	1	2
MASH BIOPSY 2	3	2	2	1
MASH BIOPSY 3	3	3	1	1
MASH BIOPSY 5	3	1	2	1
MASH BIOPSY 6	3	2	2	2
MASH BIOPSY 9	3	2	2	2
MASH BIOPSY 10	3	3	2	2
MASH BIOPSY 11	3	0	0	0
MASH BIOPSY 14	3	2	2	1
MASH BIOPSY 23	3	2	2	2
MASH BIOPSY 24	3	2	1	1
MASH BIOPSY 12	4	1	2	1
MASH BIOPSY 19	4	1	1	1
MASH BIOPSY 22	4	2	2	1
MASH BIOPSY 25	4	2	1	1

3.2.1.5 Processing snRNAseq datasets and QC

To generate feature-barcoded matrices of genes mapped to their single cell for downstream analysis, sequencing reads were aligned to GRCh38 reference genomes (modified to allow intronic feature alignment) and nuclei-containing partitions and unique molecular identifiers (UMIs) were estimated using the CellRanger v3.1.0 Single-Cell Software Suite (10X Genomics). Poor quality nuclei and empty droplets were excluded by removing droplets containing <200 UMIs and >10% mitochondrial genes of the total UMI count.

Data quality control was performed using the SeuratPipe R package v3.1.2. Scrublet python module v0.2.3 [322] was used to identify potential doublets and the SoupX R package v1.5.2 [323] was used to analyse and correct background mRNA contamination. Samples were normalised by dividing the UMI count per gene by the total UMI count in the corresponding nucleus and log-transforming using the Seurat 'ScaleData' function. Sample transcriptomes were concatenated using mergeData function, re-normalised and re-scaled before the top 200 genes exhibiting high cell-to-cell variation were identified and 'subsetted' for downstream principal component analysis (PCA) using the 'vst' method. Merged sample datasets were then integrated using the Harmony® v0.1.0 package to correct for sample bias on PC embedding and linear dimensional reduction was performed using PCA (Seurat RunPCA) on the variable features. Next, cells were clustered using the 'FindNeighbours' and 'FindClusters' function before being clustered with variable PC dimensions and resolution depending on the size and variability of each dataset or subset. The mesenchyme clusters were subsetted using the subset () function and pre-processed with the SCTransform package [324] replacing the NormalizeData(), ScaleData(), and FindVariableFeatures() functions. This was developed to improve downstream analytical tasks such as variable gene selection and dimensional reduction. UMAP non-linear dimensional reduction function was run with the Louvain algorithm to visualise PC clustering. Clusters were characterised by heat maps, feature plots and violin plots.

3.2.2 PCLS liver patient demographics

PCLS were generated from the donors outlined in Table 8 with ethical approval (outlined in Chapter 2).

Table 8: Liver PCS donor patient demographics

12-well PCLS					96-well PCLS				
Donor	**Sex**	**Age**	**Fibrosis**	**Steatosis**	**Donor**	**Sex**	**Age**	**Fibrosis**	**Steatosis**
Liver Donor 1	**M**	**53**	**1**	**0**	**Liver Donor 6**	**F**	**70**	**3**	**0**
Liver Donor 2	**M**	**65**	**1**	**0**	**Liver Donor 7**	**M**	**84**	**1+**	**1**
Liver Donor 3	**F**	**56**	**2**	**1**	**Liver Donor 8**	**F**	**60**	**1**	**1**
Liver Donor 4	**F**	**45**	**1**	**0**	**Liver Donor 9**	**M**	**87**	**1**	**1**
Liver Donor 5	**F**	**59**	**1**	**0**	**Liver Donor 10**	**M**	**81**	**1**	**0**

3.2.3 Treatment of PCLS for target validation

For initial target validation, 8mm PCLS were generated (as outlined in Chapter 2) and cultured in a 12-well Bioreactor plate (n=5 donors [liver donors 1-5 in Table 8]). Once generated, PCLS were rested for 24 hours to allow the post-slicing stress period to elapse before challenge with either control media, a combination treatment of recombinant human TGF-β1(3ng/ml)/PDGFββ(50ng/ml) to stimulate fibrogenesis or TGF-β1/PDGFββ + activin-like kinase 5 (ALK5) inhibitor SB525334 (10μM) to blunt the fibrotic response (n=6 PCS per condition) according to established protocols based on previous dose-optimisation experiments [287]. Media, including all treatments, was refreshed at 24-hour intervals with conditioned media snap frozen for downstream analysis. At the terminal 96-hour time point, PCLS were harvested and snap frozen for downstream analysis (see Figure 17C).

3.2.4 Aspartate Aminotransferase (AST) Assay

AST is a pyridoxal phosphate-dependent enzyme that catalyses the conversion of aspartate and α-keto-glutarate to oxaloacetate and glutamate and can be used as a measure of liver function. To measure AST in conditioned culture media, AST Activity Assay Kit (Sigma, MAK055) was used by incubating samples and Glutamate standards with Reaction Mix according to manufacturer's guidelines in a 96 well flat-bottom plate. After addition of the Reaction Mix, sampled were briefly mixed using an orbital shaker before being incubated at 37°C (protected from light). After 2-3mins, ($T_{initial}$) timepoint absorbance was measured at 450nm (A_{450}) using Tecan Infinite Pro 2000. Plates were returned to incubate at 37°C (protected from light) taking (A_{450}) every 5mins until the value of the most active sample was greater than the highest glutamate standard (10nmole/well). The final measurement ([A450]

final) for calculating enzyme activity was the penultimate reading before samples exceeded the linear range of the standard curve. Samples were corrected for background and AST activity was measured using the following equation: AST activity= (B x Sample dilution factor)/ ([Reaction time] x V) where Glutamate amount (B), reaction time ($T_{final} – T_{initial}$ [minutes]) and volume (V).

3.2.5 Testing of candidate compounds in PCLS

To test candidate compounds at multiple doses, 3mm PCLS were generated for culture in a 96-well CMR plate (outlined in Chapter 2) before being subject to the following treatment course.

3.2.5.1 Candidate compounds in combination with inflammatory stimuli

PCLS were generated from resected liver tissue (n=3 donors) and rested for 48 hours, with media being refreshed after 24 hours, before being challenged with control media, human recombinant IL1α (1ng/ml) alone to stimulate inflammation or in combination with IKK2 (10μM) to blunt the inflammatory response (n=6 PCLS per condition, n=3 donors, n=18 PCLS total). Alongside this, PCLS were challenged with IL1α in combination with 3 (or 5 in the case of HAS2) escalating doses of each inhibitor (outlined in Table 9) to assess ability to blunt inflammation (see Figure 22B). Conditioned media was snap frozen for analysis and PCLS were harvested for resazurin assay at T72 to measure metabolic activity as an indicator of tissue viability (outlined in chapter 2). The following experiments were performed using liver donors 7 and 9 for HAS2i compound screening and liver donors 7-9 for all other inhibitors (see Table 8).

Table 9: Details of candidate compounds for testing in 96-well PCS

Compound	Target	Supplier	Code	Vehicle	Reported *in vitro* IC50*
IKK2 Inhibitor VI	IKK2	Cayman chemical	17276	DMSO	13nM (cell-free assay)
SB-525334	ALK5i	Sigma	S8822	DMSO	14.3nM (cell-free assay)
4-Methylumbelliferone (4-MU)	HAS2	Apexbio	B6001	DMSO	400μM
DCLK1-in 1	DCLK1/2	Tocris	7285	DMSO	279nM
E-7386	β-catenin	MedChemExpress	HY-111386	DMSO	48.4nM
LGK974	Porcupine (PORCN)	Selleckchem	S7143	DMSO	0.05-2.4nM (cell-free assay)
NVP-TNKS656	Tankyrase (TNKS)	Selleckchem	S7238	DMSO	6nM (cell-free assay)

**Reported IC50 values are generated from 2D cell culture assays (unless otherwise indicated) which can vary depending on cell lines used for validation.*

3.2.5.2 Candidate compounds in combination with fibrogenic stimuli

Once generated, PCLS (n=4 donors) were rested for 24 hours to allow the post-slicing stress period to elapse before challenge with either control media, a combination treatment of recombinant human TGF-β1(3ng/ml)/PDGFββ(50ng/ml) to stimulate fibrogenesis or TGF-β1/PDGFββ + ALK5i (10μM) to blunt the fibrotic response (n=6 PCLS per condition, n=4 donors, n=24 PCLS total). Alongside this, PCLS were also challenged with TGF-β1/PDGFββ in combination with 3 (or 5 in the case of HAS2) escalating doses of each inhibitor (outlined in Table 4) to assess the ability to blunt fibrogenesis. Media, including all treatments, was refreshed at 24-hour intervals with conditioned media snap frozen for downstream analysis (see Figure 28A). At the terminal 96-hour timepoint, PCLS were harvested for resazurin assay to measure metabolic activity. The following experiments were performed using liver donors 6-8 and 10 for HAS2i compound screening and liver donors 7-10 for all other inhibitors.

3.2.6 ELISA

ELISA was performed on conditioned culture media and tissue homogenates (as outlined in Chapter 2) for the following markers in Table 10:

Table 10: ELISA kits used to quantify target protein expression

Marker	Supplier	Reference Number
Albumin	R&D Systems	DY1455
Col1a1	R&D Systems	DY6220
TIMP-1	R&D Systems	DY970
IL-8	R&D Systems	DY208
IL-6	R&D Systems	DY206
UNC5B	LS bio	LS-F55900-1
WNT4	LS bio	LS-F8794-1
THBS2	R&D	DY1635
DCLK1	Abbexa	abx151261
CDH11	R&D	DY1790-05
TNFRSF12A	Aviva systems	OKEH01840
HAS2	LS bio	LS-F7247
WNT9A	ThermoFisher	EH486RB
VCAN	Novus biological	NBP2-75354

3.2.7 RT-PCR

To analyse expression of target genes in PCLS (n=2 pooled PCLS per condition, n=5 donors) RT-PCR was performed (as detailed in Chapter 2) with the following Taqman probes

(Thermofisher, 4331182) with a FAM-MGB dye: UNC5B (Hs00900710_m1), WNT4 (Hs01573505_m1), THBS2 (Hs01568063_m1), DCLK1 (Hs00178027_m1), CDH11 (Hs00901479_m1), TNFRSF12A (Hs00171993_m1), HAS2 (Hs00193435_m1), WNNT9A (Hs01573829_m1), VCAN (Hs00171642_m1) and ACTB (Hs01060665_g1).

3.2.8 Histology

H&E and PSR was carried out as previously described in Chapter 2. Immunohistochemistry was performed for the following markers (Table 11) according to the general methodology previously described in Chapter 2. When performing immunohistochemical staining of targets of interest, negative controls were included for each of the antibodies. Control slides were ran in parallel with test slides as previously outlined for relevant markers, but were not incubated with primary antibodies (available in Appendix A; Figure 2).

Table 11: Details of primary antibodies and antigen retrieval for immunohistochemistry

Antigen	Supplier	Code	Host species	Dilution	Antigen retrieval
HAS2	Invitrogen	MA5-17087	Mouse	1/1000	Tris-EDTA
WNT4	Proteintech	14371-1-AP	Rabbit	1/100	Citrate
WNT9A	Abcam	ab125957	Rabbit	1/100	Proteinase K

3.2.9 Lung patient demographics

PCLuS were generated from unused donor lung tissue and explant IPF tissue outlined in Table 12 with ethical approval (see Chapter 2).

Table 12: Patient demographics from IPF explant and unused donor lungs

Donor ID	Sex	Age	FEV1, L	FVC, L	TLC, L	TLCO, mmol CO/min/kPa	KCO, mmol CO/min/kPa	Smoking history
Unused donor PCLuS 1	Female	70	N/A	N/A	N/A	N/A	N/A	Never Smoked
Unused donor PCLuS 2	Male	48	N/A	N/A	N/A	N/A	N/A	Never Smoked
Unused donor PCLuS 3	Female	57	N/A	N/A	N/A	N/A	N/A	Never Smoked
IPF PCLuS donor 1	Female	47	1.20(47%)	1.25(42%)	N/A	N/A	N/A	Never Smoked
IPF PCLuS donor 2	Female	61	2.23(42%)	2.66(44%)	4.84(51%)	N/A	N/A	Never Smoked
IPF PCLuS donor 3	Male	64	1.78	1.98	N/A	3.41	N/A	Never Smoked

FEV1= forced expiratory volume in 1 second, FVC= forced vital capacity, TLC= total lung capacity, TLCO= carbon monoxide transfer factor, KCO=carbon monoxide transfer coefficient and N/A= not available Percentages of predicted values are in parentheses.

3.2.10 Generation and treatment of PCLuS

To test candidate compounds at multiple doses, 4mm PCLuS were generated for culture in a 96-well cell culture plate (outlined in Chapter 2) before being subject to the following treatment courses.

3.2.10.1 Testing of candidate compounds in combination with inflammatory stimuli in unused donor PCLuS

PCLuS were generated from unused donor lung tissue (n=3 donors) and rested for 48 hours, with media being refreshed after 24 hours, before being challenged with control media, human recombinant IL1α (1ng/ml) alone to stimulate inflammation or in combination with IKK2 (10μM) to blunt the inflammatory response (n=5 PCLuS per condition, n=3 donors, n=15 PCLuS total). Alongside this, PCLuS were challenged with IL1α in combination with the highest dose of each inhibitor (outlined in Table 9) to assess ability to blunt inflammation. Conditioned media was snap frozen for analysis and PCLuS were harvested for resazurin assay at T72 to measure metabolic activity as an indicator of tissue viability.

3.2.10.2 Testing of candidate compounds in combination with inflammatory stimuli in unused donor PCLuS

Once generated, PCLuS (n=3 donors) generated from unused donor lung tissue was rested for 48 hours, with media being refreshed after 24 hours, to allow the post-slicing stress period to elapse. Next, PCLuS were challenged with either control media, a combination treatment of recombinant human TGF-β1(10ng/ml)/PDGFββ(50ng/ml) to stimulate fibrogenesis or TGF-β1/PDGFββ + ALK5i (10μM) to blunt the fibrotic response (n=5 PCLuS per condition, n=3 donors, n=15 PCLuS total). Alongside this, PCLuS were challenged with TGF-β1/PDGFββ in combination with the highest dose of each inhibitor (outlined in Table 4) to assess the ability to blunt fibrogenesis. Media, including all treatments, was refreshed at 24-hour intervals with conditioned media snap frozen for downstream analysis. At the terminal 144-hour timepoint, PCLuS were harvested for resazurin assay to measure metabolic activity.

3.2.10.3 Testing of candidate compounds in IPF-derived PCLuS

PCLuS generated from explant IPF tissue (n=3 donors) was rested for 48 hours, with media being refreshed after 24 hours, to allow the post-slicing stress period to elapse. Next, PCLuS were challenged with either control media, standard of care compounds Pirfenidone (2.5mM) and Nintedanib (2.5μM) or ALK5i (10μM) to blunt fibrosis (n=10 PCLuS per condition, n=3 donors, n=30 PCLuS total) with doses selected based on previous dose-response optimisation

experiments carried out prior to this project. Concurrently, PCLuS were challenged with 3 escalating doses of each candidate compound to assess the ability to reduce pre-existing fibrosis. Media, including all treatments, was refreshed at 24-hour intervals with conditioned media snap frozen for downstream analysis. At the terminal 144-hour timepoint, PCLuS were harvested for resazurin assay to measure metabolic activity.

3.2.11 Statistical analysis

Statistical analysis was performed using GraphPad Prism 9.5.0. All results are presented as mean ± SEM. Statistical significance of markers from PCS was determined using ANOVA with post-hoc Dunnett's test where *p<0.05, **p<0.01, ***p<0.001, ****p<0.0001, unless otherwise indicated. Statistical analysis was performed on graphs in this chapter which show results as percentage change from baseline (with baseline specified in the associated figure legends), unless otherwise indicated. This normalisation accounts for the differences in the secretion of pro-inflammatory and pro-fibrogenic markers between PCS, primarily driven by differences in cellular composition and tissue density. For PCLS, this also accounts for differences in fibrosis staging between donor tissue and, in the case of IPF-derived PCLuS, presence/absence/numbers of fibroblastic foci thereby providing a uniform approach to determine changes in the secretion of markers over the duration of culture in multiple donors. Therefore, the "percentage change from baseline" are the data that should be considered when observing the effects of any given treatment. Briefly, the mean of the baseline treatment group (or control tissue in the case if IPF) of PCS was calculated for each PCS donor, which was subsequently subtracted from each experimental sample of the same donor (including individual baseline PCS samples) to provide a % change from baseline value for each individual PCS.

Assumption of Normal Distribution in PCS for parametric statistical tests: PCS data is assumed to follow a normal distribution, where approximately 95% of the data points fall within 2 standard deviations of the mean. Samples that fall outside this range are relatively rare and are considered outliers, potentially distorting the overall data representation.

Minimisation of Outlier Impact: Outliers can significantly skew the mean, consequently impacting the reliability of conclusions drawn from the data in the summary tables included in the report. Consequently, all samples from a particular PCS were excluded if values (% change from baseline) were greater than 2 standard deviations from the mean of the other PCS in the group.

3.3 Results

3.3.1 Identification of targets of interest using single nuclei RNA sequencing

As part of our collaboration with Pfizer and Edinburgh University, we aimed to identify novel molecular targets of fibrosis in human MASH/Cirrhosis. To achieve this, single nuclei were isolated from 14 healthy, 26 MASH biopsy and 14 cirrhotic human tissue samples (selected to represent the transitions of MASH from F1–F4 fibrosis stage and cirrhosis) and snRNAseq was performed by Dr Sebastian Wallace (Edinburgh University) using the 10X chromium system (Figure 12A). The combined snRNAseq dataset (317,428 nuclei) was annotated using signatures of known lineage markers, resulting in the identification of 39 distinct cell populations, including a large hepatocyte cluster and a smaller mesenchyme compartment, in keeping with the expected liver cell lineage proportions (Figure 12B-C). Interrogation of the mesenchyme compartment identified classic hepatic stellate cell (HSC) signature genes (HGF, RELN, PTHR1, PDGFRA) and myofibroblast (MFB) signature genes (C7, COL1A1, COL1A2, LUM) corresponding to the 7th and 8th Clusters (Figure 12D).

As mesenchymal cells are widely regarded as major contributors to the development and progression of liver fibrosis, cells of mesenchymal lineage were re-clustered to permit further interrogation of cell heterogeneity, with vascular smooth muscle cells (VSMCs) removed to enable higher-resolution clustering. In total, 5,339 nuclei from the mesenchyme compartment were isolated from liver tissue across the spectrum of healthy, MASH and cirrhotic (Figure 13A) samples. Further clustering of mesenchymal cells identified 8 subpopulations (Figure 13B-C), of which clusters 3 and 5 were found to be disease-associated, high collagen type 1 producers. Following this, analysis of the top 100 differentially expressed genes within these groups identified 9 genes of interest which were almost exclusively upregulated in myofibroblast lineages (cluster 3 and 5). Clusters were prioritised on specificity and not included if there was detectable expression in other lineages of the pan-lineage dataset. This collagen I high subpopulation expressed the following markers which were largely mesenchyme-restricted and selected for further interrogation: Unc-5 Netrin Receptor B (UNC5B, a netrin receptor involved in axon guidance), Wnt Family Member 4 (WNT4, a ligand of frizzled receptors), Thrombospondin 2 (THBS2, a glycoprotein that mediates cell-to-cell and cell-to-matrix interactions), Doublecortin Like Kinase 1 (DCLK1, a kinase involved in calcium-signalling pathways), Cadherin 11 (CDH11, a cell adhesion molecule), TNF Receptor

Superfamily Member 12A (TNFRSF12A, a TNF receptor which may modulate cell adhesion to matrix proteins), Hyaluronan Synthase 2 (HAS2, a key regulator of hyaluronan synthesis), Wnt Family Member 9A (WNT9A, a ligand of frizzled receptors) and Versican (VCAN, a proteoglycan involved in ECM organisation) (Figure 14; Table 13).

A)

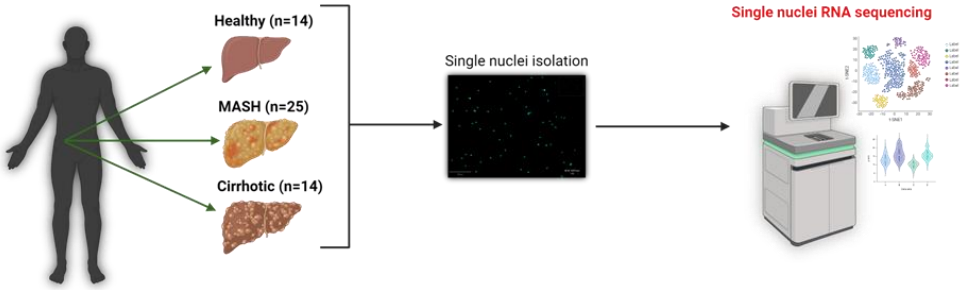

B)

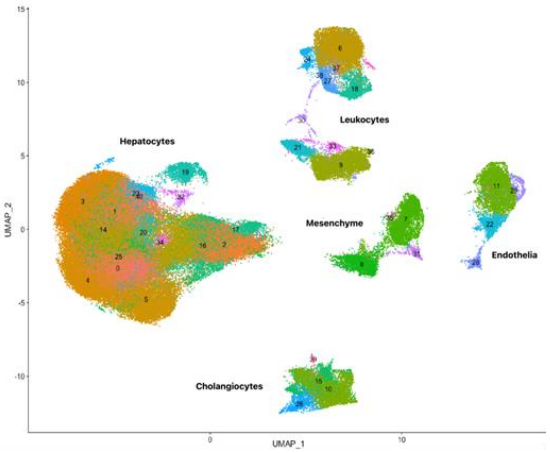

Lineage	Clusters	Cell type
Hepatocytes	0,1,2,3,4,5,12,14,16,17, 19,20,23,25,32,34,40	Hepatocytes*
Mesenchyme	5	Hepatic stellate cells
	7	Fibroblasts
	31	VSMC
	35	Activated Myofibroblasts
Leukocytes	6,18,24,27,38	Monocytes/macrophages
	9,36	T Lymphocytes
	30,33	B Lymphocytes
	21	Plasma cells
Endothelia	11,29	LSECs
	22	Venous endothelia
	28	Arterial endothelia
Cholangiocytes	10,15,26,39	Cholangiocytes*

C)

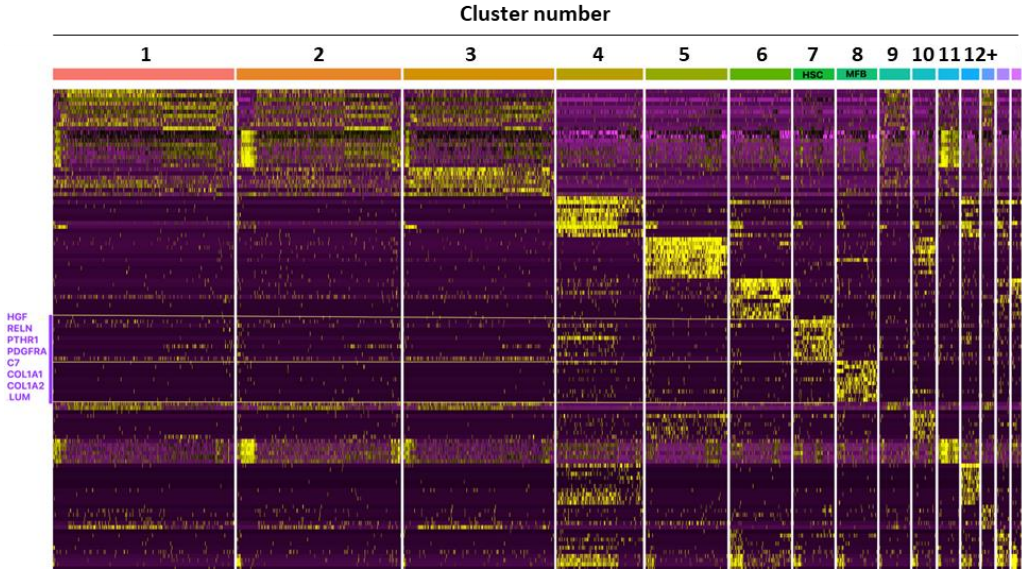

Figure 12: **Single nuclei RNA sequencing (snRNAseq) of human MASLD patient samples** A) Single nuclei were isolated from 14 healthy, 26 MASH biopsy and 14 cirrhotic liver samples acquired at Edinburgh University and processed for snRNAseq. The total spectrum of MASH fibrosis was represented by F0 (n=1), F1 (n=4), F2 (n=7), F3 (n=10) and F4 (n=4). B) Clustering datasets (labelled by lineage) featured a large hepatocyte cluster and a smaller mesenchyme compartment, in keeping with the expected liver cell lineage proportions (enlarged image provided in Appendix A). C) Identified cell lineages labelled 1-39 (* indicates cell lineages whose sub-groups were not further characterised). D) Labelled heat map (Cropped), showing a Human HSC signature genes (HGF, RELN, PTHR1, PDGFRA) and MFB signature genes (C7, COL1A1, COL1A2, LUM) corresponding to the 7th and 8th Clusters. (Figures B-D provided by Dr Sebastian Wallace).

A)

Fibrosis grade	n cells
Healthy	1852
MASH F0	628
MASH F1	560
MASH F2	528
MASH F3	224
MASH F4	974
Cirrhotic	573
Total	**5339**

C)

Cluster	Annotation
0	Quiescent HSC(1)
1	Portal fibroblasts
2	Activated HSC
3	Myofibroblasts 1
4	RBFOX+ mesenchyme
5	Myofibroblasts 2
6	Quiescent HSC (2)
7	ALB/APO hepatocyte high mes

B)

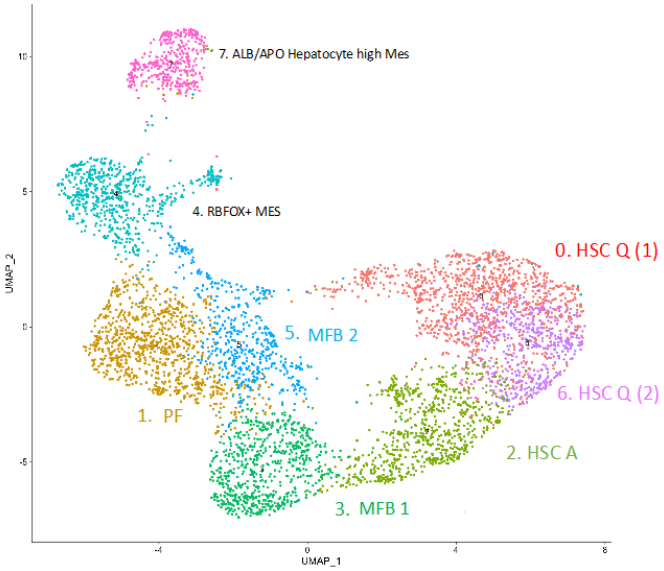

Figure 13: Mesenchyme subset of snRNAseq dataset A) 5,339 cells of mesenchyme lineage identified from the 14 healthy, 25 MASH biopsy and 14 cirrhotic liver samples acquired at Edinburgh University. B) UMAP of mesenchyme sub clustering generated from snRNAseq dataset, with vascular smooth muscle cells (VSMCs) removed to enable higher-resolution clustering. C) Clusters are annotated as Cluster 0: Quiescent HSCs, Cluster 1: Portal fibroblasts, Cluster 2: Activated HSCs, Cluster 3: Myofibroblasts 1, cluster 4: RBFOX+ Mesenchyme, Cluster 5: Myofibroblasts 2, cluster 6: Quiescent HSCs 2. (Hepatic stellate cell (HSC)_Q = Quiescent HSC, HSC_A = activated HSC) (Figure provided by Dr Sebastian Wallace).

Table 13: Targets of interest identified from snRNAseq

Target Name	Target ID	Target Function	References
Cadherin 11	CDH11	Cell adhesion molecule. Involved in tissue morphogenesis, osteogenesis and fibroblast function	[325,326]
Doublecortin Like Kinase 1	DCLK1	Associated with cancer stem cell properties. Role in promoting cancer-associated fibroblasts in other tissue e.g., gastrointestinal cancers	[327,328]
Hyaluronan Synthase 2	HAS2	Involved in the synthesis of hyaluronic acid, a component of the ECM. Changes in expression may contribute to fibrogenesis	[329,330]
Thrombospondin 2	THBS2	Matricellular glycoprotein involved in ECM modulation. May influence ECM remodelling, cell-matrix interactions and cell responses in liver fibrosis.	[331,332]
TNF Receptor Superfamily Member 12A	TNFRSF12A	Member of TNF receptor superfamily involved in immune response, apoptosis and angiogenesis. Limited information of role in fibrosis.	[333]
Unc-5 Netrin Receptor B	UNC5B	Netrin receptor involved in axon guidance during development. Implicated in non-neuronal tissue but involvement in liver fibrosis unclear.	[334]
Versican	VCAN	Large chondroitin sulfate proteoglycan. Contributes to ECM organisation.	[335,336]
Wnt Family Member 4	WNT4	Member of Wnt signalling pathway. Implicated in cellular responses in fibrosis	[337-339]
Wnt Family Member 9A	WNT9A	Member of Wnt signalling pathway. Dysregulation of Wnt signalling associated with liver fibrosis	[339]

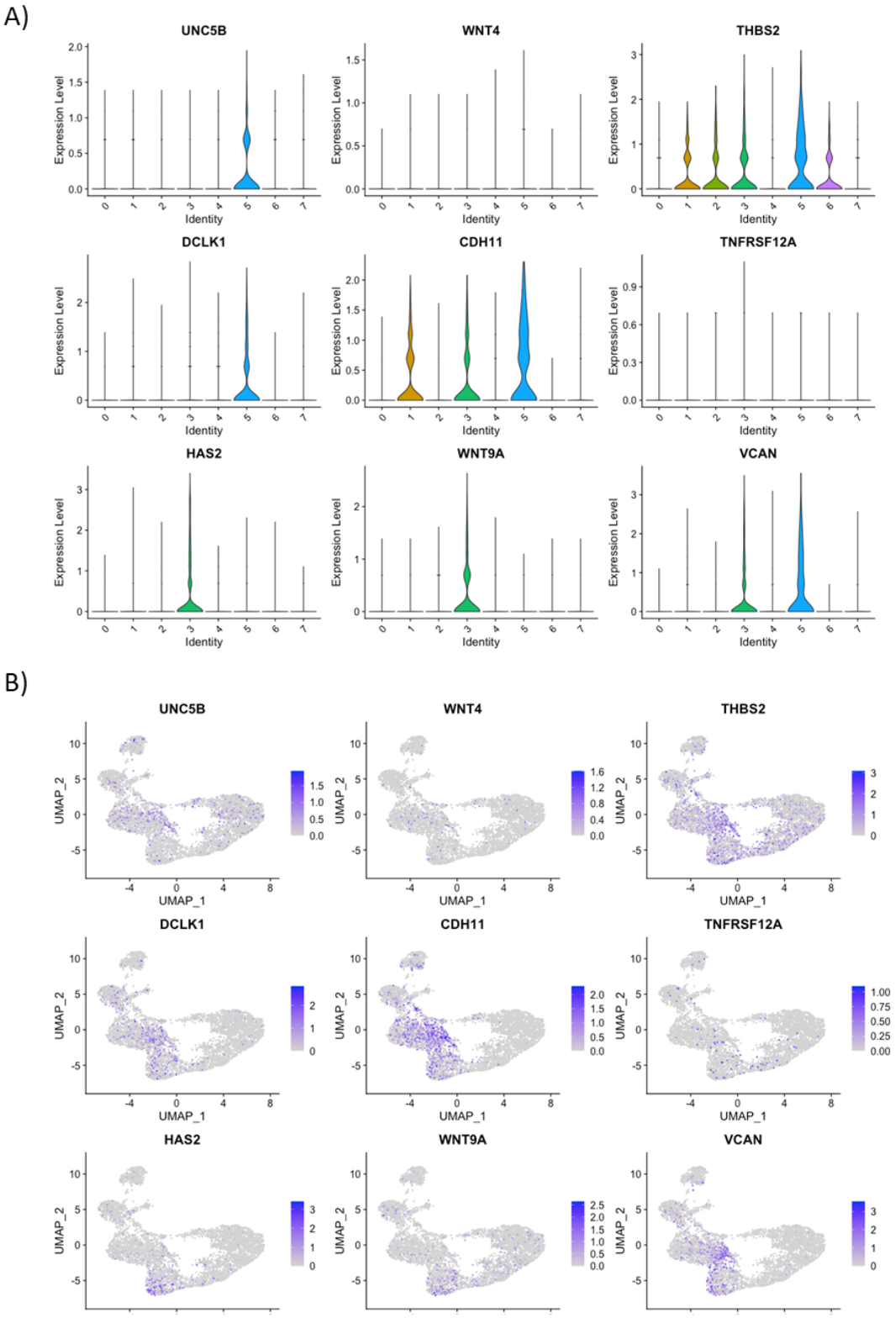

Figure 14: Target identification from snRNAseq mesenchyme datasets Interrogation of mesenchyme datasets identified 9 genes of interest which were disease-associated, collagen I high producing cells which were primarily in myofibroblast lineages (cluster 3 and 5). Clusters were prioritised on specificity and not included if there was detectable expression in other lineages of the pan-lineage dataset. A) Violin plots of 9 target genes showing higher expression in cluster 3 and 5 MFBs. B) UMAPs of 9 target genes showing higher expression in cluster 3 and 5 MFBs**.** (Figures provided by Dr Sebastian Wallace).

3.3.2 Interrogation of targets in precision-cut liver slices

3.3.2.1 Investigation of targets in pre-existing datasets

To begin investigating the targets of interest in our PCLS system, we first interrogated pre-existing transcriptomic datasets generated in collaboration with Dr William Reilly. Initial datasets were generated from PCLS prepared from resected liver tissue (n=7 donors), with slices (n=6 PCLS per condition) being rested for 24 hours before challenge with either control media, TGF-β1 to induce fibrogenesis or IL1α to stimulate an inflammatory response. After 24 hours challenge, PCLS were snap frozen and processed for bulk RNAseq (see Appendix B). Results showed that all 9 targets of interest were present in the transcriptomic dataset, though the abundance varied considerably between targets (Figure 15A). Further analysis confirmed that, though target gene expression remained unchanged in response to acute inflammatory challenge, there was a significant increase in expression of *CDH11, HAS2, WNT4* and *WNT9A* in TGF-β1-challenged PCLS ($p<0.05$; Figure 15B-J).

To ascertain if target gene expression could be further increased in response to repeated fibrogenic stimuli, we next looked at datasets generated from PCLS prepared from resected liver tissue, with slices (n=6 PCLS per condition) being rested for 24hrs before challenge with either control media (n=6 donors), a combination treatment of pro-fibrotic TGF-β1/PDGFββ alone (n=6 donors) or co-treated with ALK5i (TGFβ receptor I inhibitor) to blunt the fibrotic response (n=4 donors) for 72hrs. Media, including all treatments, was refreshed at 24-hour intervals before PCLS were harvested and snap frozen at 96hrs for RNAseq (see Appendix C). Like previous results, we found that all 9 targets were present in varied abundance in each PCLS donor (Figure 16A). Further investigation revealed that many of the targets followed the same trend whereby gene expression was significantly upregulated compared to control slices in response to fibrotic stimuli and modulated back to near control levels with the addition of ALK5i (Figure 16B-E, G-J), with the exception of *TNFRSF12A* which appeared to show no change in response to treatment (Figure 16F). Notably, results established that repeated stimulation over a 72hr period with TGF-β1/PDGFββ was able to increase target gene expression in liver tissue significantly more than a single dose of TGF-β1 alone. Taken together, these data demonstrated that target genes were present in our PCLS system and could be modulated using pro-fibrogenic stimuli (TGF-β1/PDGFββ) and anti-fibrotic compounds.

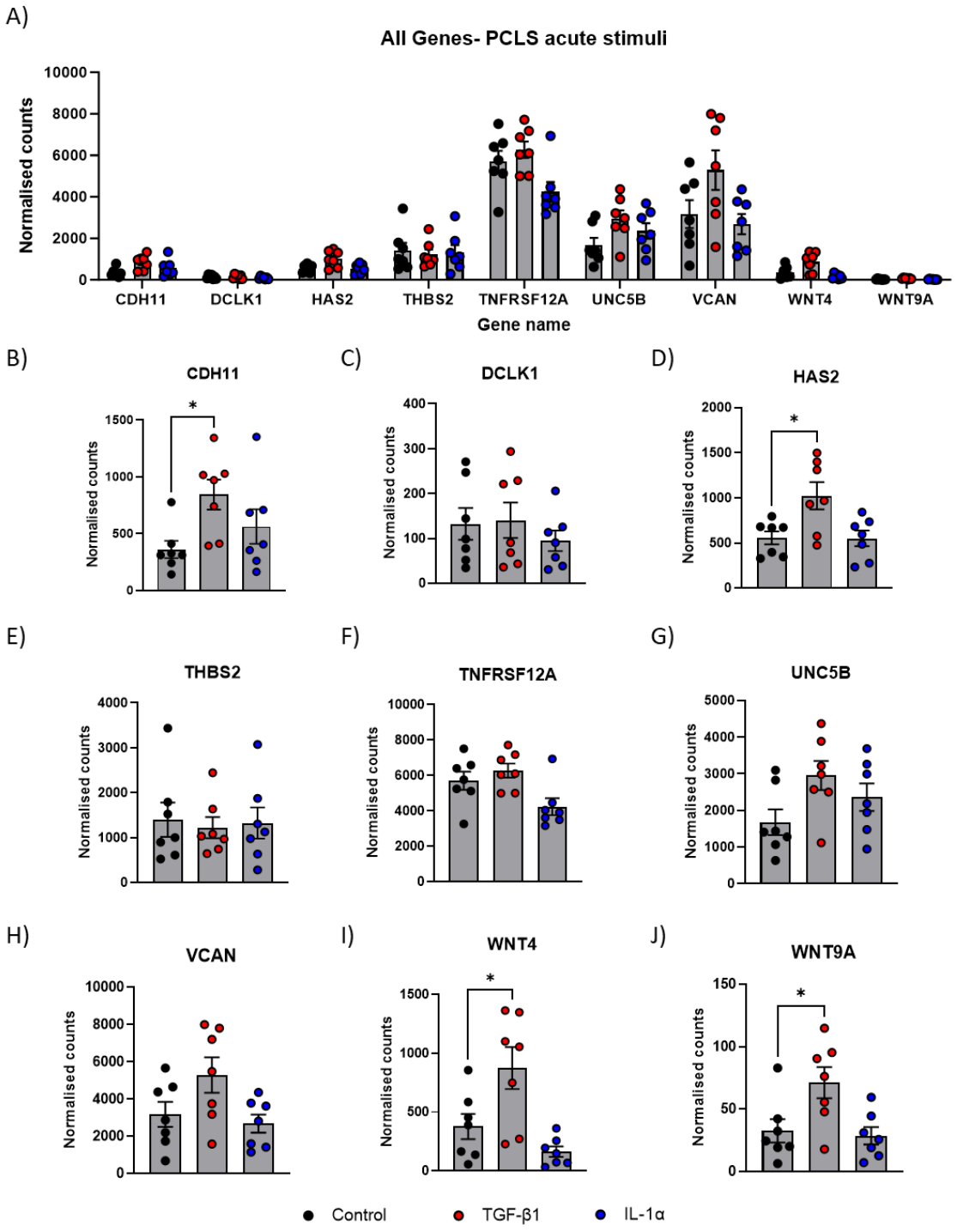

Figure 15: Interrogation of pre-existing transcriptomic PCLS datasets for targets of interest Investigation of transcriptomic datasets generated from PCLS prepared from resected liver tissue (n=7 donors), with slices (n=6 PCLS per condition) being rested for 24 hours before 24-hour challenge with either control media, TGF-β1 (3ng/ml) to stimulate fibrogenesis or IL1α (1ng/ml) to stimulate inflammation. A) Normalised counts of all target genes and individual graphs of B) CDH11 C) DCLK1 D) HAS2 E) THBS2 F) TNFRSF12A G) UNC5B H) VCAN I) WNT4 and J) WNT9A were generated. All data are mean ± SEM. Statistical significance was determined using ANOVA with post-hoc Tukey HSD Test (*p<0.05, **p<0.01, ***p<0.001 and ****p<0.0001).

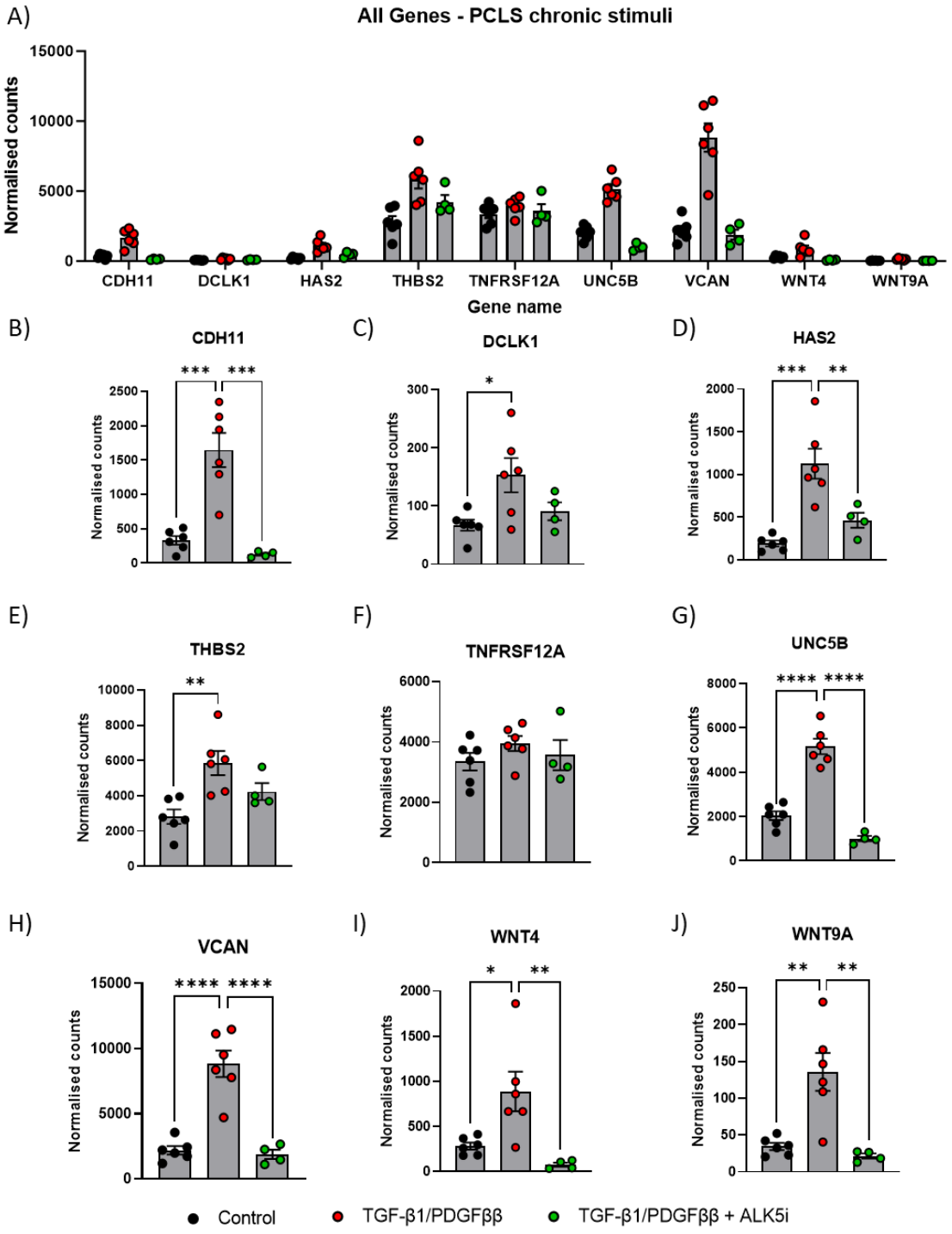

Figure 16: Interrogation of pre-existing transcriptomic PCLS datasets for targets of interest Investigation of transcriptomic datasets generated from PCLS prepared from resected liver tissue, with slices (n=6 PCLS pooled per condition) being rested for 24 hours before challenge with either control media (n=6 donors), a combination treatment of TGF-β1(3ng/ml)/PDGFββ(50ng/ml) to stimulate fibrogenesis (n=6 donors) or TGF-β1/PDGFββ + ALK5i (10μM) to blunt the fibrotic response (n=4 donors) for 72hrs. A) Normalised counts of all target genes and individual graphs of B) CDH11 C) DCLK1 D) HAS2 E) THBS2 F) TNFRSF12A G) UNC5B H) VCAN I) WNT4 and J) WNT9A were generated. All data are mean ± SEM. Statistical significance was determined using ANOVA with post-hoc Tukey HSD Test (*p<0.05, **p<0.01, *** p<0.001 and ****p<0.0001).

3.3.2.2 Investigation of targets of interest in additional PCLS

To confirm the transcriptomic results and investigate target protein expression, we acquired additional PCLS donors (n=5 donors) with similar fibrosis and steatosis grades (Figure 17A-B) to further validate these findings *via* RT-PCR and ELISA. PCLS were challenged with repeated TGF-β1/PDGFββ-challenge (alone and in combination with ALK5i) as previously described (Figure 17C). Media, including all treatments, was refreshed at 24-hour intervals with conditioned media snap frozen for downstream analysis before PCLS were snap frozen at 96hrs for RT-PCR or ELISA.

Prior to target evaluation, we first validated suitability of each individual donor tissue for further assessment. PCLS viability was confirmed by measurement of soluble markers of cell death (LDH), liver damage (AST) and hepatocellular health and function (albumin) in conditioned culture media at each time point. Results showed that after an initial post-slicing spike in LDH and AST in the first 24 hours, the level of damage is reduced, and hepatocyte function is maintained throughout culture (Donor 1 presented as an example; Figure 17D-F). Notably, there was a slight reduction of albumin in the slices challenged with fibrotic stimuli in Donor 1, likely due to dedifferentiation of hepatocytes. Next, we evaluated response to fibrotic challenge through quantification of secreted collagen 1α1, TIMP-1 and IL-6 at each time point. Results confirmed that TGF-β1/PDGFββ stimulation effectively increased collagen 1α1, TIMP-1 and IL-6 secretion compared to control unstimulated PCLS, and this was attenuated by co-treatment with ALK5i (Donor 1 presented as an example; Figure 17G-I).

Following individual assessment of each donor for viability and response to stimuli, quantification of the above markers was normalised to % change from control PCLS for each donor to allow for integration. Results showed that although LDH and AST was significantly increased, and hepatocyte function (as measured by albumin) significantly reduced in response to TGF-β1/PDGFββ treatment, this could be modulated back to near control levels with ALK5i therapy (Figure 18A-C). Importantly, donors were responsive to fibrotic stimuli as collagen 1α1, TIMP-1 and IL-6 secretion was significantly increased in all donors compared to control PCLS, and this was significantly attenuated by ALK5i co-treatment. (Figure 18D-F). Consequently, the 5 PCLS donors were deemed suitable for further analysis and processed to look at gene and protein expression of targets of interest.

A)

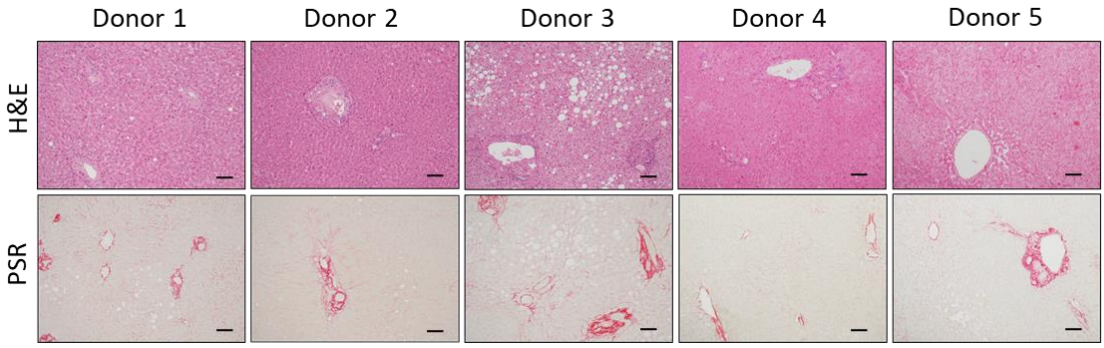

B)

	Donor 1	Donor 2	Donor 3	Donor 4	Donor 5
Fibrosis score	F1	F1	F2	F1	F1
Steatosis score	S0	S0	S2	S0	S0

C)

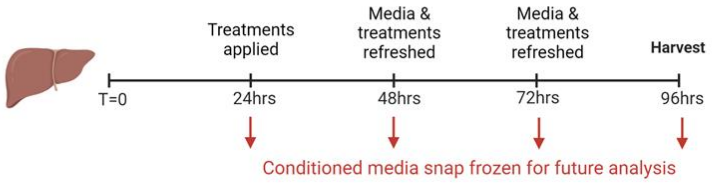

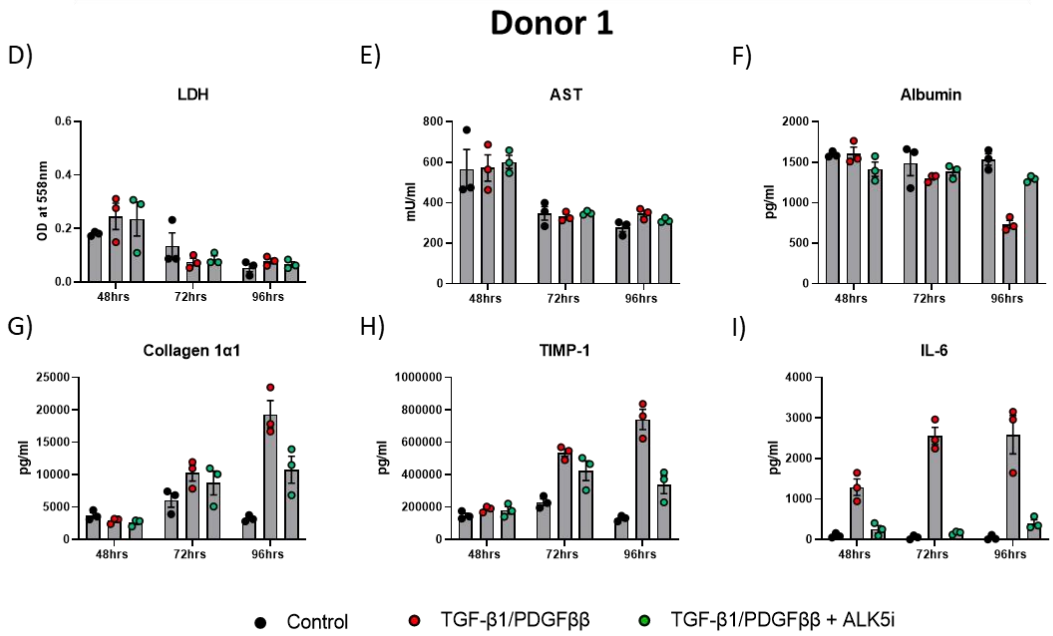

Figure 17: Validation of viability and response to stimuli in additional PCLS donors A) Histological assessment of T0 explant tissue was performed *via* H&E and PSR (scale bar=100µM) to confirm B) fibrosis and steatosis scores of PCLS donors. C) PCLS were generated from resected liver tissue with slices (n=6 PCLS per condition) being rested for 24 hours before challenge with either control media, a combination treatment of TGF-β1(3ng/ml)/PDGFββ(50ng/ml) or TGF-β1/PDGFββ + ALK5i (10µM). Media, including all treatments, was refreshed at 24-hour intervals with conditioned media snap frozen for downstream analysis before PCLS were harvested and snap frozen at 96hrs for downstream analysis. PCLS viability was determined in each donor (e.g., Donor 1 shown) by quantification of soluble D) LDH E) AST and F) Albumin in conditioned media samples (n=3 per condition). Response to stimuli was assessed by quantification of soluble G) collagen 1α1 H) TIMP-1 and I) IL-6 conditioned media samples (n=3 per condition) at each time point.

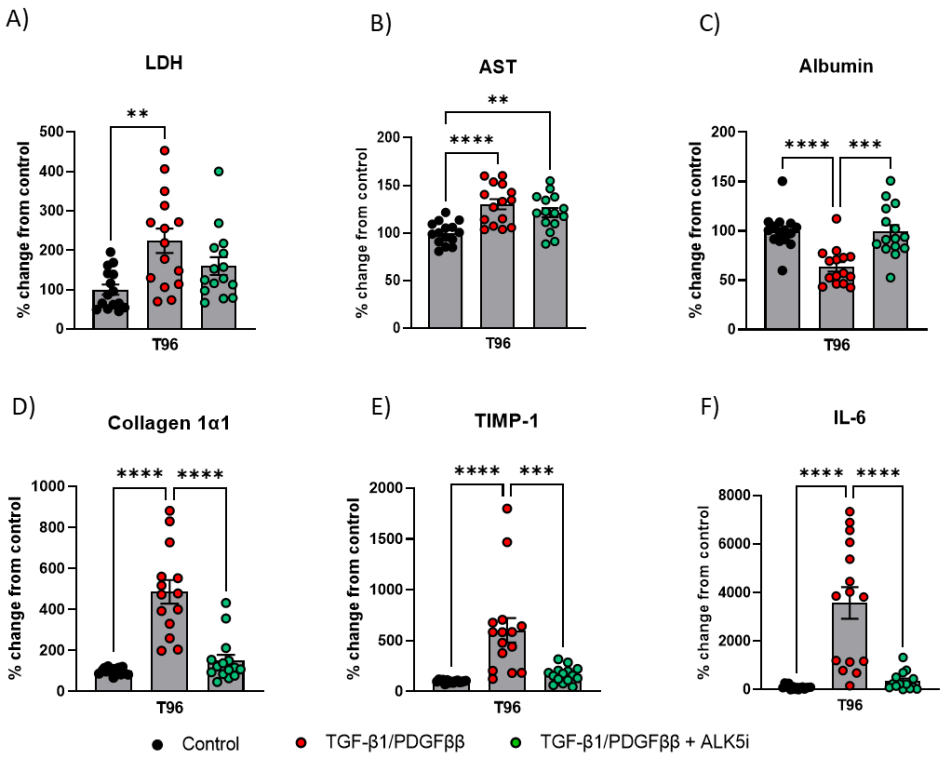

Figure 18: Validation of viability and response to stimuli in additional PCLS donors (n=5) PCLS viability was determined in all donors (n=3 conditioned media per condition, n=5 donors, n=15 pooled media total) by quantification of soluble A) LDH B) AST and C) Albumin presented as a % change from control PCLS at the final timepoint (T96). Response to stimuli was assessed by quantification of soluble D) collagen 1α1 E) TIMP-1 and F) IL-6 presented as a % change from control PCLS at the final timepoint (T96). All data are mean ± SEM. Statistical significance was determined using ANOVA with post-hoc Tukey HSD Test (*p<0.05, **p<0.01, ***p<0.001 and ****p<0.0001).

Having confirmed that the donors were suitable for downstream analysis, we next quantified gene expression of each target in the 5 additional donors *via* RT-PCR, using RNA isolated from n=2 individual slices per treatment in each donor. Results showed that *CDH11, HAS2, THBS2, TNFRSF12A, UNC5B, VCAN* and *WNT4* were detected in all 5 donors (Figure 19A, C-H), whereas *DCLK1* was detected in 2 donors (Donor 4 and Donor 5; Figure 19B) and *WNT9A* in one donor (Donor 4; Figure 19I). Consistent with data from pre-existing PCLS transcriptomic datasets, we found that target gene expression was significantly upregulated compared to control slices in response to challenge with TGF-β1/PDGFββ and modulated back to near control levels with the addition of ALK5i (Figure 19A, C, F-I), except for *THBS2* (Figure 19D) and *TNFRSF12A* (Figure 19E) which showed no change in response to treatment.

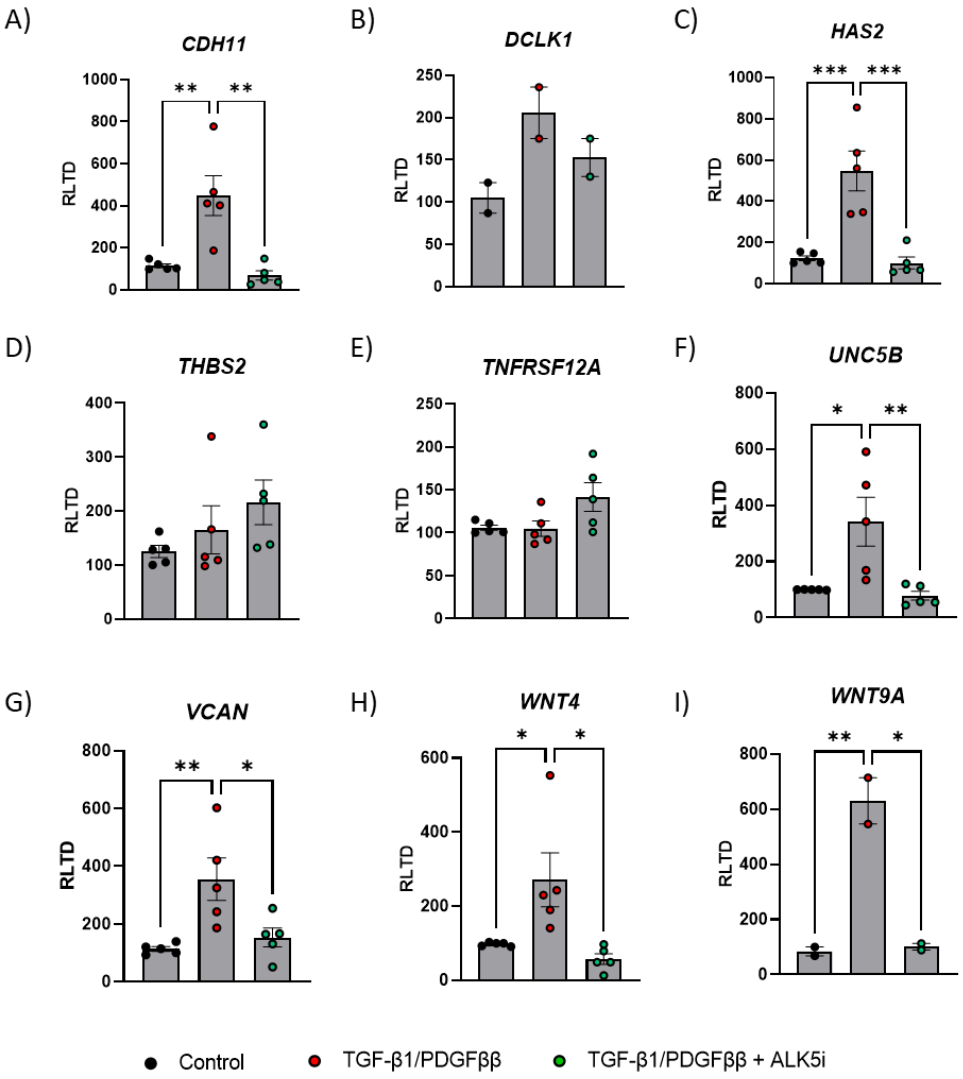

Figure 19: Validation of target gene expression in additional PCLS donors Quantification of target gene expression was performed *via* RT-PCR (n=2 slices per condition) and the mean relative level of transcriptional difference (RLTD) of each donor (n=5) was graphed for A) *CDH11* B) *DCLK1* C) *HAS2* D) *THBS2* E) *TNFRSF12A* F) *UNC5B* G) *VCAN* H) *WNT4* and I) *WNT9A.* All data are mean ± SEM. Statistical significance was determined using ANOVA with post-hoc Tukey HSD Test (*p<0.05, **p<0.01, ***p<0.001).

Alongside gene expression, we also sought to quantify protein expression of targets in response to challenge. To achieve this, n=4 slices per treatment were individually homogenised from all 5 PCLS donors and normalised to a concentration of 0.5mg/ml (determined by BCA assay) before measuring target protein expression *via* ELISA. Target proteins were detected in all 5 donors (Figure 20A-F, H), except for WNT4 which was detected in only one donor (Donor 4, Figure 20G). However, unlike gene expression, there were no clear changes in protein expression in response to treatment with TGF-β1/PDGFββ or TGF-β1/PDGFββ + ALK5i (Figure 20) and target protein expression remained similar to unstimulated PCLS regardless of treatment.

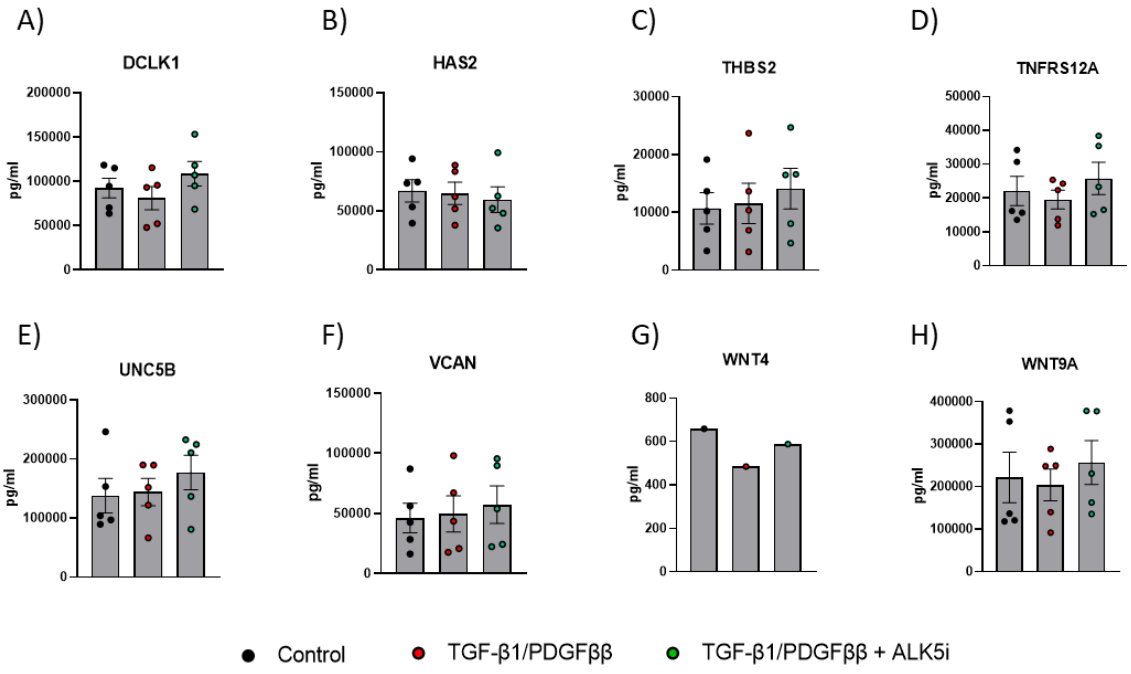

Figure 20: Validation of target protein expression in additional PCLS donors Quantification of target protein expression (pg/ml) was performed *via* ELISA in protein homogenates generated from n=4 individual slices per condition (normalised to 0.5mg/ml after BCA assay) and the mean protein expression per treatment of each donor was graphed for A) DCLK1 B) HAS2 C) THBS2 D) TNFRSF12A E) UNC5B F) VCAN G) WNT4 and H) WNT9A. All data are mean ± SEM. Statistical significance was determined using ANOVA with post-hoc Tukey HSD Test (*p<0.05, **p<0.01, ***p<0.001 and ****p<0.0001).

Next, we performed an initial screening on conditioned media samples for possible secretion of target proteins. Results showed that DCLK1, HAS2, THBS2, TNFRSF12A, UNC5B and VCAN could all be detected in the culture media (Figure 21). Following this, quantification of secreted target proteins in all donors found that HAS2 (Figure 21B) and THBS2 (Figure 21C) were the most abundantly secreted proteins, followed by DCLK1 (Figure 21A) and TNFRSF12A (Figure 21D). UNC5B (Figure 21E) and VCAN (Figure 21F) were also present in the conditioned media but to a lesser extent. Consistent with results seen in protein homogenates, assessment of secreted proteins at the final point of culture showed no effect of TGF-β1/PDGFββ challenge (alone or in combination with ALK5i) on target protein expression which remained similar to unstimulated PCLS.

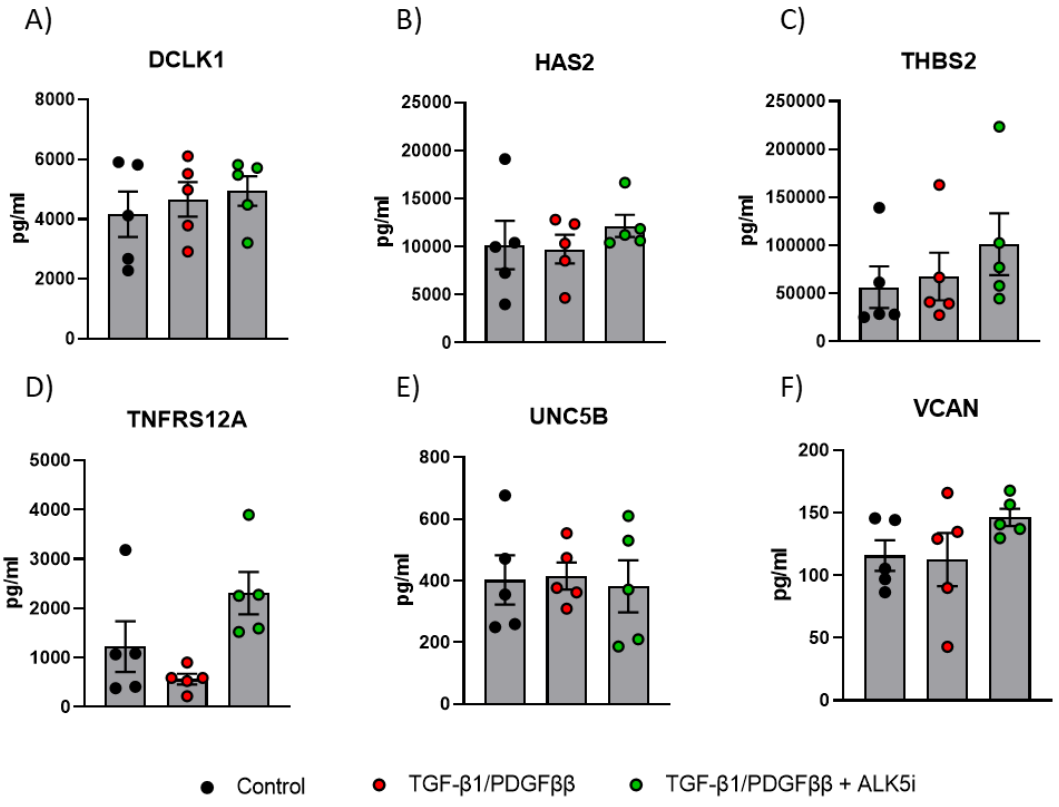

Figure 21: **Validation of secreted target protein expression in additional PCLS donors** Quantification of target protein expression (pg/ml) was performed *via* ELISA on conditioned culture media (n=3 media samples from n=6 PCLS per condition) collected at T96 from additional PCLS (n=5 donors). Mean protein expression per treatment of each donor was graphed for A) DCLK1 B) HAS2 C) THBS2 D) TNFRSF12A E) UNC5B and F) VCAN. All data are mean ± SEM. Statistical significance was determined using ANOVA with post-hoc Tukey HSD Test (*p<0.05, **p<0.01, ***p<0.001 and ****p<0.0001).

3.3.3 Validation of candidate inhibitory compounds in PCLS

3.3.3.1 Candidate compounds anti-inflammatory properties in PCLS

Having confirmed target gene and protein expression in response to fibrogenic stimuli, we next sought to investigate whether inhibition of these targets in combination with IL1α or TGF-β1/PDGFββ treatment could effectively blunt inflammation and fibrogenesis, respectively. Work carried out at Pfizer identified 5 candidate compounds targeting HAS2 (HAS2i; 4-MU), DCLK1 (DCLK1-in-1) and different components of the WNT signalling pathway for further investigation: E-7386 (a β-catenin inhibitor), LGK974 (a porcupine [PORCN] inhibitor) and TNKS6565 (a tankyrase [TNKS] inhibitor) (Figure 22A).

First, to evaluate potential anti-inflammatory properties of candidate compounds, we utilised recombinant IL1α, a pro-inflammatory cytokine which is widely known to be a key regulator of the immune response. PCLS were generated from resected liver tissue (n=3 donors) and rested for 48 hours, with media being refreshed after 24 hours, before being challenged with control media, IL1α alone or in combination with IKK-2 inhibitor VII (IKK2), or three (or 5 in the case of HAS2) escalating doses of each inhibitor (Figure 22B). PCLS were harvested for resazurin at T72, and results were normalised to % of control PCLS for each donor to allow comparison. An arbitrary 70% threshold was applied where compounds/doses which resulted in <70% metabolic activity compared to unstimulated tissue was considered to have negatively impacted PCLS function (Figure 22C). Results demonstrated that all 5 compounds were generally well tolerated and did not affect metabolic activity of tissue after 24-hour challenge, except for the two highest doses of HAS2 inhibitor (500µM and 1000µM) in Donor 1 (Figure 22C). As this compound was only tested in 2 donors, evaluation in additional PCLS donors would help clarify whether these doses consistently reduced metabolic activity or if this effect was specific to Donor 1. Additionally, more specific/sensitive measurements of tissue viability (e.g. Cell titer glo assay [Promega] which generates a luminescent signal proportional to the amount of ATP present in tissue) and/or measurements of cytostatic and cytotoxic effects (e.g. Green Cytotoxicity and Caspase 3/7 [Promega] which measures DNA and caspases, respectively) should be considered to more accurately determine tissue viability throughout culture and in response to different exogenous stimuli and compounds.

To determine effective induction of an acute pro-inflammatory response in donor tissue, we quantified soluble markers of inflammation in the conditioned media at the end of culture.

Results confirmed that IL1α stimulation significantly increased secretion of IL-8 ($p<0.0001$) and IL-6 ($p<0.0001$), and co-treatment with IKK2 could attenuate this response back to control levels ($p<0.0001$; Figure 22G, H). This panel of secreted markers was further used to evaluate anti-inflammatory properties of each candidate compound at multiple doses. Results found that DCLK1 (Figure 23) and TNKS656 (Figure 24) had no effect on IL-8 and IL-6 secretion irrespective of dose. Similarily, LGK974 (Figure 25) and HAS2 (Figure 27) had no effect on IL-8 secretion but were able to significantly reduce IL-6 secretion at the highest dose, (LGK974 10μM and HAS2 1000μM ($p<0.05$). Notably, PCLS challenged with E-7386 showed a significant reduction in IL-8 at 1μM ($p<0.001$) and 10μM ($p<0.01$) doses, and a substantial dose-dependent reduction of IL-6 ($p<0.0001$) suggesting that inhibition of β-catenin signalling could reduce IL1α-driven inflammation (Figure 26).

A)

Compound	Compound Target	Target of interest
HAS2	HAS2	HAS2
DCLK1-IN-1	DCLK1/2	DCLK1
E-7386	β-Catenin	WNT4/WNT9A
LGK974	PORCN	
NVP-TNKS656	TNKS	

B)

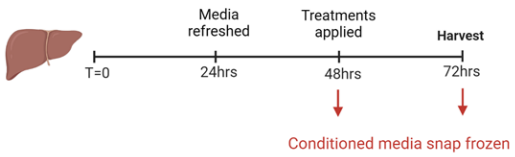

C)

	HAS2					DCLK1			E-7386			LGK974			TNKS656		
% of ctrl	30μM	100μM	300μM	500μM	1000μM	0.1μM	1μM	10μM	0.1μM	1μM	10μM	0.1μM	1μM	10μM	0.1μM	1μM	10μM
Donor 7	71	88	70	51	55	85	101	88	73	67	80	67	75	78	72	71	86
Donor 8	95	87	94	94	80	87	91	87	97	82	95	98	99	111	109	111	111
Donor 9						102	97	106	87	88	90	88	84	86	87	95	82

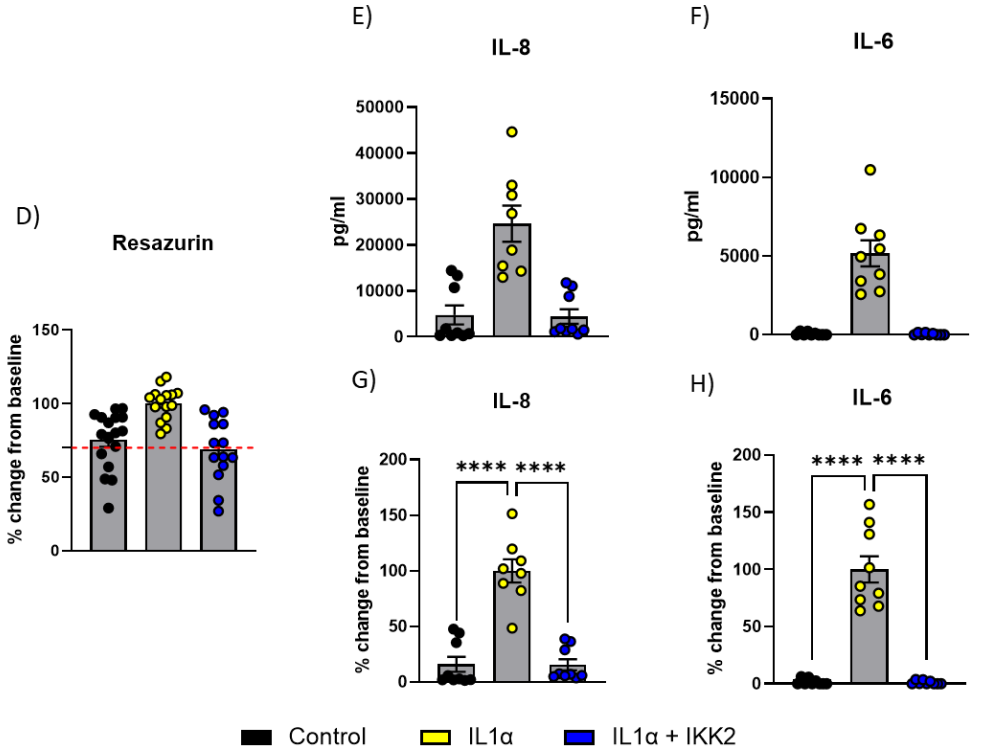

Figure 22: **Validation of IL1α-challenged PCLS** A) 5 candidate compounds were identified based on their ability to inhibit targets of interest either directly or indirectly. B) PCLS were generated from resected liver tissue (n=3 donors) and rested for 48 hours, with media being refreshed after 24 hours, before being challenged (n=6 slices per condition) with control media, IL1α alone or in combination with IKK2. PCLS were also challenged with IL1α in combination with escalating doses of each of the candidate compounds for 24 hours (n=6 PCLS per condition, n=3 donors, n=9 pooled media total). Conditioned media was snap frozen for analysis and PCLS were harvested for resazurin assay at T72 as an indicator of tissue viability. C) Resazurin values were normalised for each donor and presented as a % of control PCLS (green values indicate resazurin values ≥70% of control, yellow/orange 50-69% of control and red <50% of control). Quantification of D) Resazurin (where red dashed line represents arbitrary 70% viability threshold), IL-8 and IL-6 was performed and plotted as E-F) absolute pg/ml and G-H) % change from baseline (IL1α-challenged PCLS). for all PCLS donors (n=3 conditioned media per donor, n=3 donors, n= 9 samples total) All data are mean ± SEM. Statistical significance was determined on graphs G and H using ANOVA with post-hoc Dunnett's test where IL1α-challenged PCLS was set as the control group (*p<0.05, **p<0.01, ***p<0.001 and ****p<0.0001).

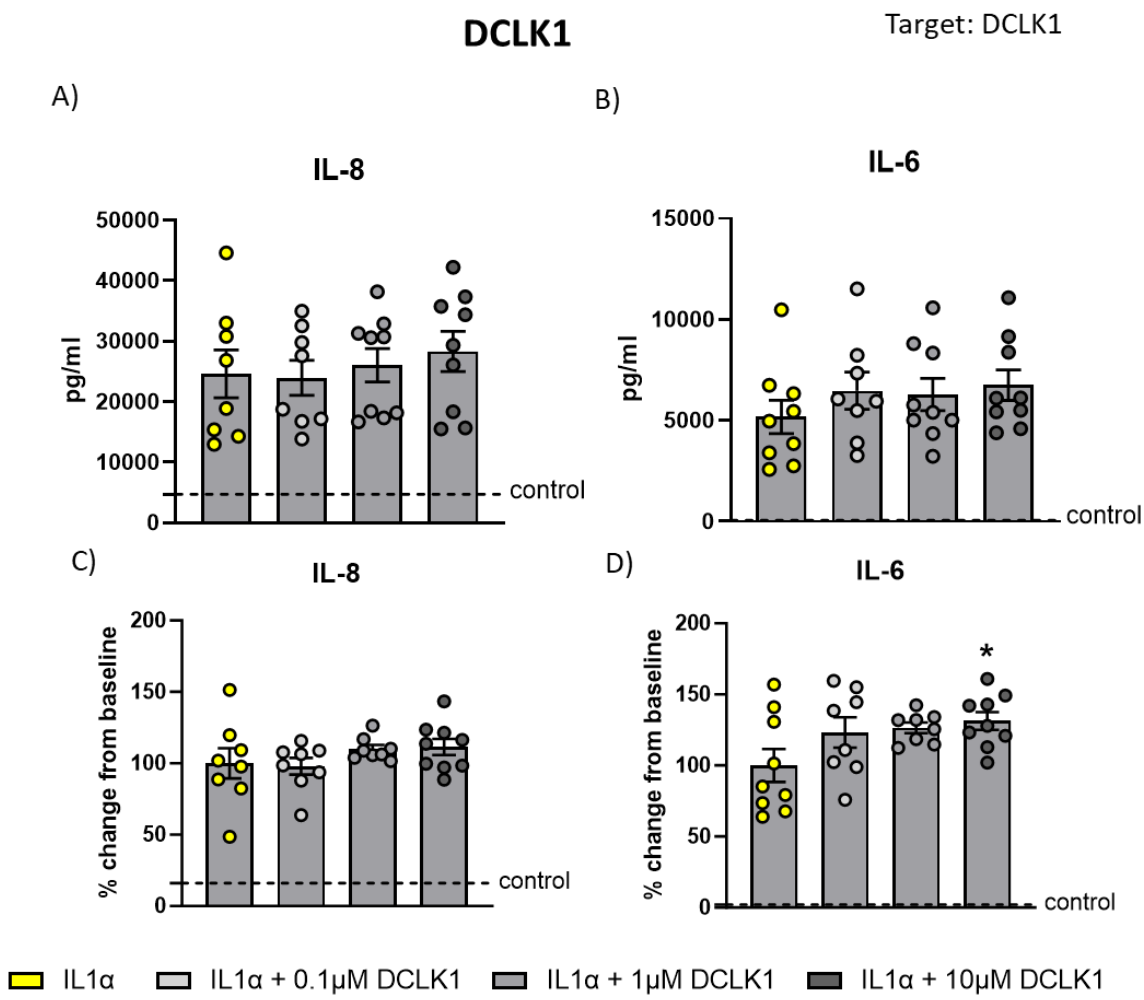

Figure 23: Validation of DCLK1 compound in IL1α-challenged PCLS P PCLS were generated from resected liver tissue (n=3 donors) and rested for 48 hours, with media being refreshed after 24 hours, before being challenged (n=6 slices per condition) with control media, IL1α alone, in combination with IKK2 or 3 escalating doses of DCLK1 inhibitor for 24 hours (n=6 PCLS per condition, n=3 donors, n=9 pooled media total). Conditioned media was collected at T72 and protein secretion of inflammatory markers) IL-8 and IL-6 were measured *via* ELISA and plotted as A-B) absolute pg/ml and C-D) average % change from baseline (IL1α-challenged PCLS) for all donors (n=3 conditioned media, n=3 donors, n=9 samples total).Black dashed line denotes unstimulated control PCLS A-B) pg/ml and C-D) % expression compared to IL1α-treated tissue. All data are mean ± SEM. Statistical significance was determined on graphs C and D using ANOVA with post-hoc Dunnett's test where IL1α-challenged PCLS was set as the control group (*p<0.05, **p<0.01, ***p<0.001 and ****p<0.0001).

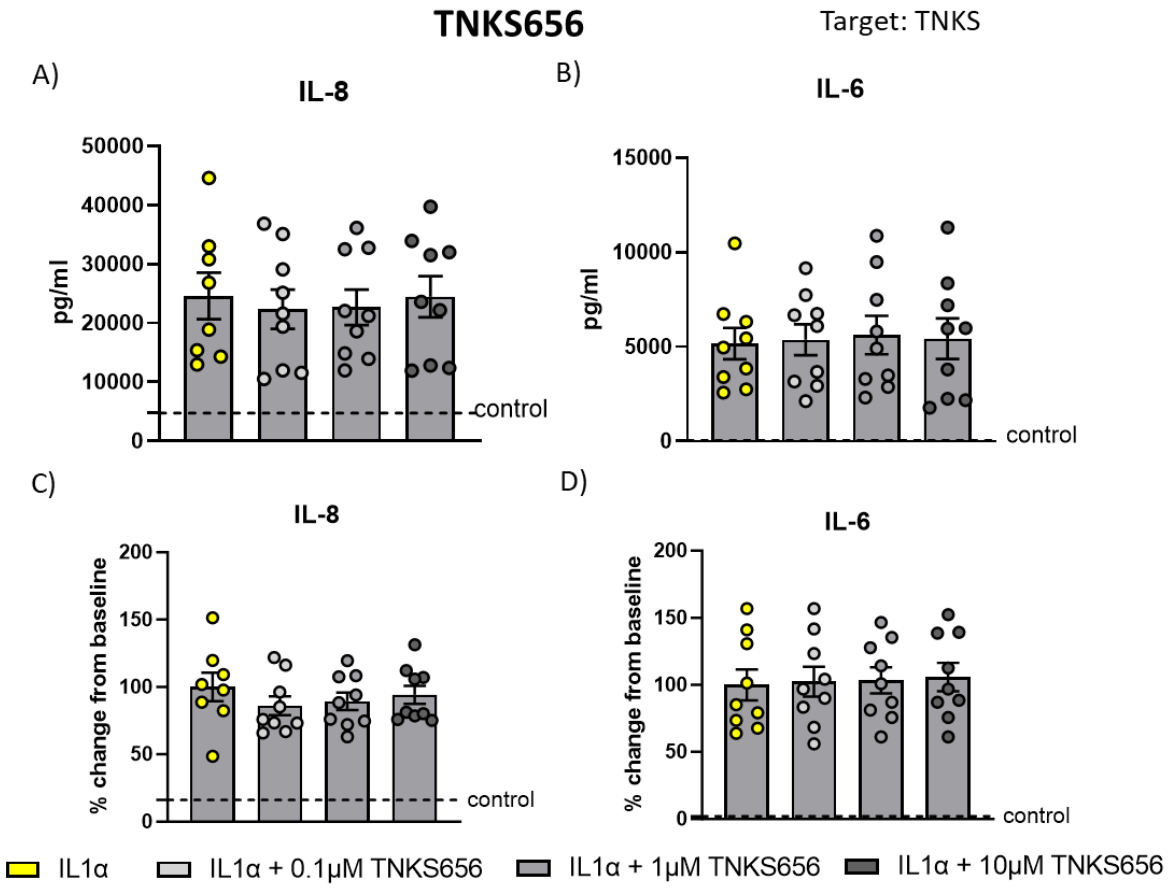

Figure 24: Validation of TNKS656 compound in IL1α-challenged PCLS PCLS were generated from resected liver tissue (n=3 donors) and rested for 48 hours, with media being refreshed after 24 hours, before being challenged (n=6 slices per condition) with control media, IL1α alone, in combination with IKK2 or 3 escalating doses of TNKS656 inhibitor for 24 hours (n=6 PCLS per condition, n=3 donors, n=9 pooled media total). Conditioned media was collected at T72 and protein secretion of inflammatory markers IL-8 andIL-6 were measured *via* ELISA and plotted as A-B) absolute pg/ml and C-D) average % change from baseline (IL1α-challenged PCLS) for all donors (n=3 conditioned media, n=3 donors, n=9 samples total).Black dashed line denotes unstimulated control PCLS A-B) pg/ml and C-D) % expression compared to IL1α-treated tissue. All data are mean ± SEM. Statistical significance was determined on graphs C and D using ANOVA with post-hoc Dunnett's test where IL1α-challenged PCLS was set as the control group (*p<0.05, **p<0.01, ***p<0.001 and ****p<0.0001).

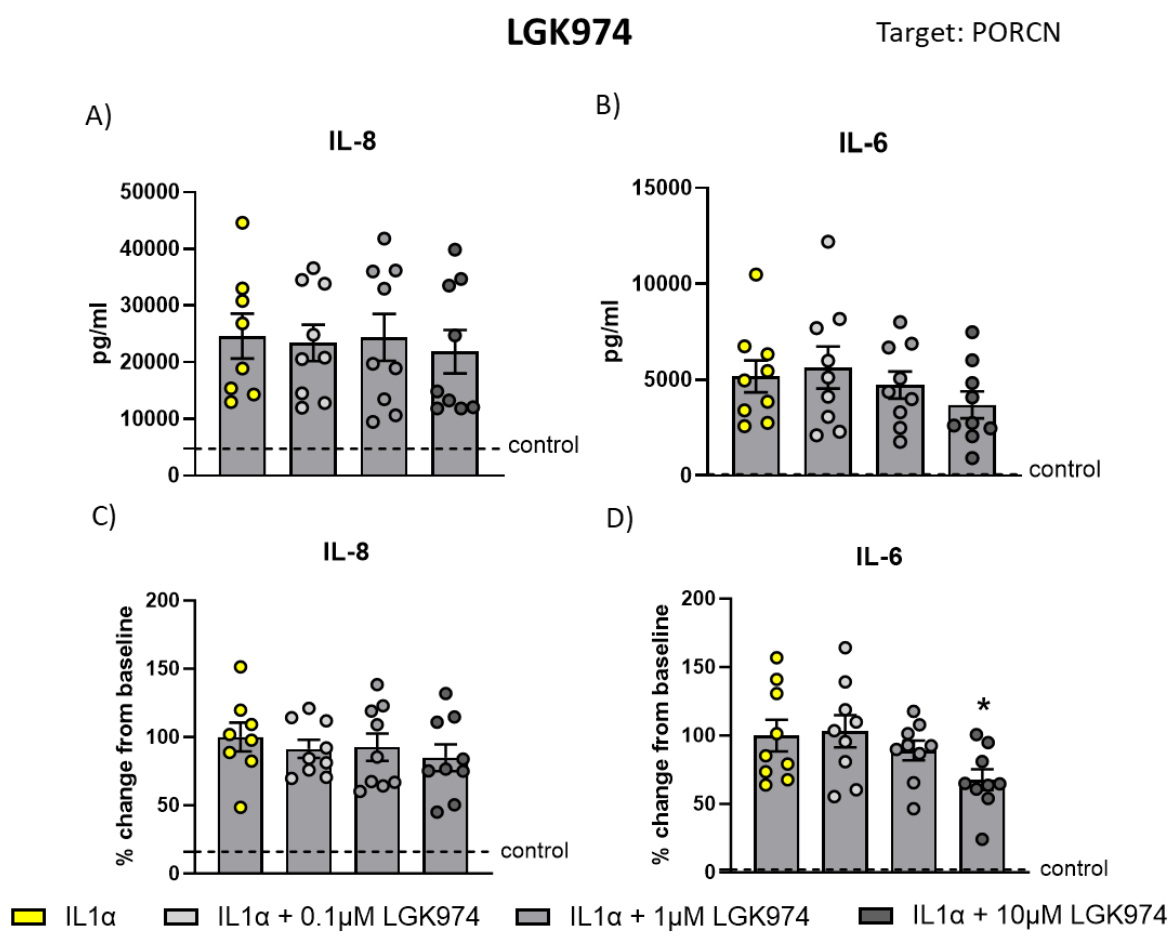

Figure 25: Validation of LGK974 compound in IL1α-challenged PCLS PCLS were generated from resected liver tissue (n=3 donors) and rested for 48 hours, with media being refreshed after 24 hours, before being challenged (n=6 slices per condition) with control media, IL1α alone, in combination with IKK2 or 3 escalating doses of LGK974 inhibitor for 24 hours (n=6 PCLS per condition, n=3 donors, n=9 pooled media total). Conditioned media was collected at T72 and protein secretion of inflammatory markers IL-8 and IL-6 were measured *via* ELISA and plotted as A-B) absolute pg/ml and C-D) average % change from baseline (IL1α-challenged PCLS) for all donors (n=3 conditioned media, n=3 donors, n=9 samples total).Black dashed line denotes unstimulated control PCLS A-B) pg/ml and C-D) % expression compared to IL1α-treated tissue. All data are mean ± SEM. Statistical significance was determined on graphs C and D using ANOVA with post-hoc Dunnett's test where IL1α-challenged PCLS was set as the control group (*p<0.05, **p<0.01, ***p<0.001 and ****p<0.0001).

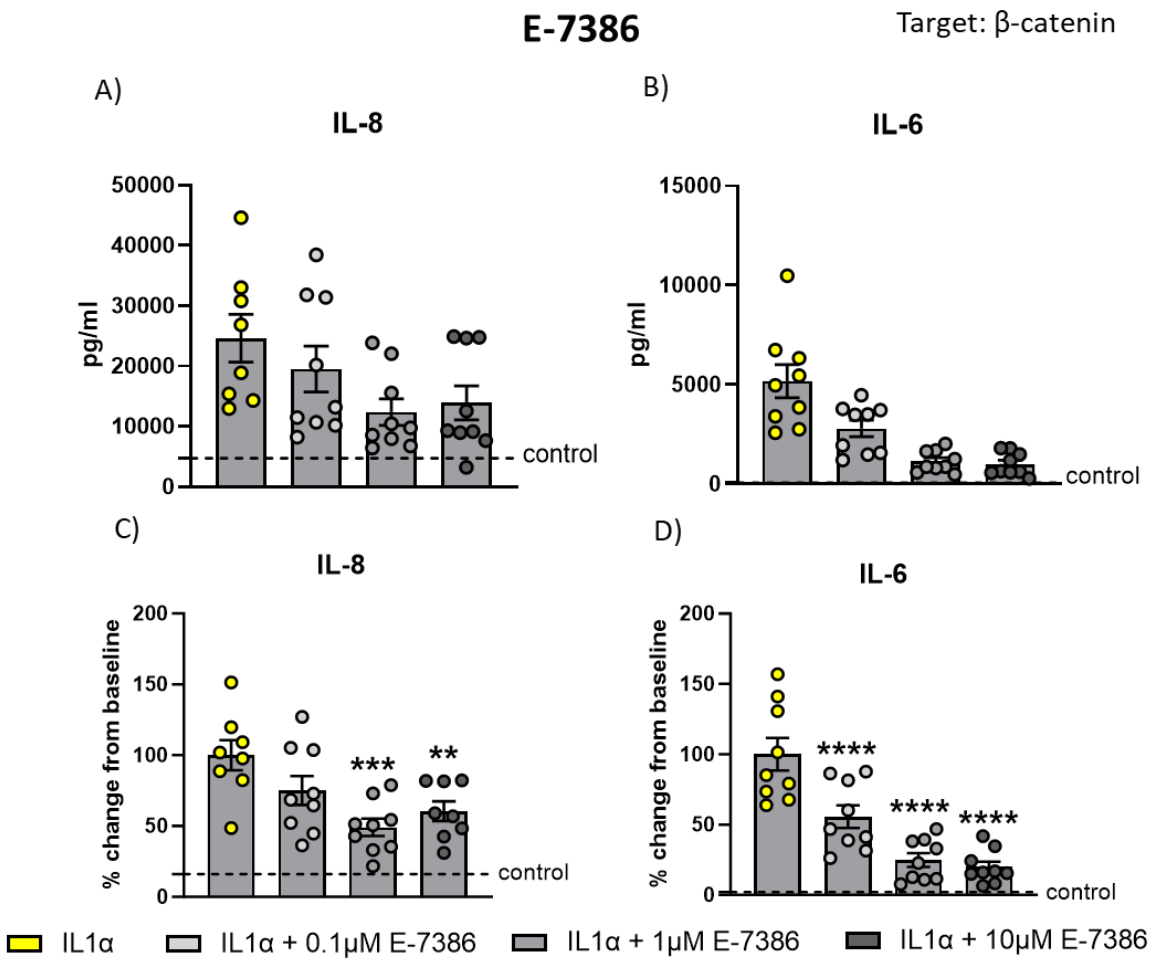

Figure 26: Validation of E-7386 compound in IL1α-challenged PCLS PCLS were generated from resected liver tissue (n=3 donors) and rested for 48 hours, with media being refreshed after 24 hours, before being challenged (n=6 slices per condition) with control media, IL1α alone, in combination with IKK2 or 3 escalating doses of E-7386 inhibitor for 24 hours (n=6 PCLS per condition, n=3 donors, n=9 pooled media total). Conditioned media was collected at T72 and protein secretion of inflammatory markers IL-8 and IL-6 were measured *via* ELISA and plotted as A-B) absolute pg/ml and C-D) average % change from baseline (IL1α-challenged PCLS) for all donors (n=3 conditioned media, n=3 donors, n=9 samples total).Black dashed line denotes unstimulated control PCLS A-B) pg/ml and C-D) % expression compared to IL1α-treated tissue. All data are mean ± SEM. Statistical significance was determined on graphs C and D using ANOVA with post-hoc Dunnett's test where IL1α-challenged PCLS was set as the control group (*p<0.05, **p<0.01, ***p<0.001 and ****p<0.0001).

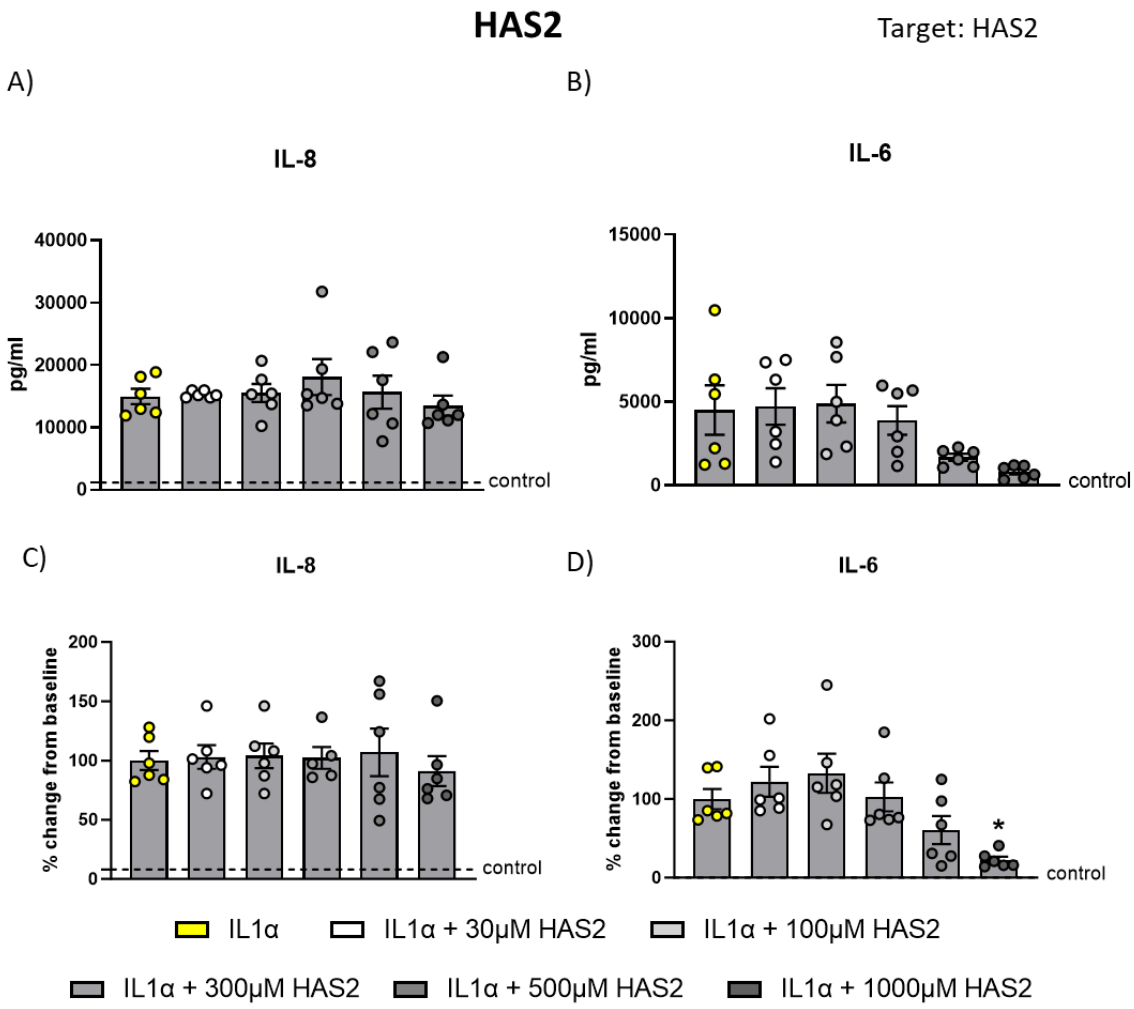

Figure 27: Validation of HAS2 compound in IL1α-challenged PCLS PCLS were generated from resected liver tissue (n=2 donors) and rested for 48 hours, with media being refreshed after 24 hours, before being challenged (n=6 slices per condition) with control media, IL1α alone, in combination with IKK2 or 5 escalating doses of HAS2 inhibitor for 24 hours (n=6 PCLS per condition, n=2 donors, n=6 pooled media total). Conditioned media was collected at T72 and protein secretion of inflammatory markers IL-8 and IL-6 were measured *via* ELISA and plotted as A-B) absolute pg/ml and C-D) average % change from baseline (IL1α-challenged PCLS) for all donors (n=3 conditioned media, n=3 donors, n=9 samples total).Black dashed line denotes unstimulated control PCLS A-B) pg/ml and C-D) % expression compared to IL1α-treated tissue. All data are mean ± SEM. Statistical significance was determined on graphs C and D using ANOVA with post-hoc Dunnett's test where IL1α-challenged PCLS was set as the control group (*p<0.05, **p<0.01, ***p<0.001 and ****p<0.0001).

3.3.3.2 Candidate compounds anti-fibrotic properties in PCLS

Having determined the anti-inflammatory effects of candidate compounds in response to IL1α-induced inflammation, we next sought to assess the ability to blunt fibrogenesis in response to TGF-β1/PDGFββ-challenge. To achieve this, PCLS were generated from resected liver tissue (n=4 donors) as previously described and challenged with either control media, TGF-β1/PDGFββ alone or in combination with ALK5i or escalating doses of each of the candidate compounds (Figure 28A). Media, including all treatments, was refreshed at 24-hour intervals with conditioned media snap frozen for downstream analysis. PCLS were harvested for resazurin assay at 96hrs and results were normalised to % of control PCLS. This determined that several compounds reduced metabolic activity below the viability threshold at multiple doses. Though DCLK1 and LGK974 appeared to have no effect on tissue viability, we found that PCLS from two or more donors challenged with the highest dose of HAS2 inhibitor (1000μM) and TNKS inhibitor (10μM) fell below 70% metabolic activity compared to control slices. Furthermore, treatment with E-7386 resulted in a considerable reduction in PCLS viability at both the 1μM and 10μM dose (Figure 28B). However, further viability assessment will be required to confirm these findings with confidence.

Histological assessment of targets showed that HAS2 was highly expressed in all donor tissue and appeared to localise to areas of perisinusoidal/periportal and bridging fibrosis (Figure 29). However, we were unable to validate expression of other protein targets in tissue samples due to suboptimal antibody performance making it difficult to interpret the results of these targets with confidence (data not shown).

To validate effective stimulation of fibrogenesis in PCLS donors and assess potential anti-fibrotic effects of candidate compounds, we quantified a panel of pro-fibrotic markers at the final time-point of culture. Resulted confirmed that, in response to TGF-β1/PDGFββ-challenge there was a significant increase in soluble collagen 1α1, TIMP-1 and IL-6 ($p<0.0001$). Additionally, we demonstrated the ability to blunt this response *via* co-treatment with ALK5i back to control levels ($p<0.0001$; Figure 28G-I). Further analysis revealed that DCLK1 (Figure 30) and TNKS656 (Figure 31) had no beneficial anti-fibrotic effects and were unable to reduce any of the quantified pro-fibrotic markers. Similarily, PCLS co-challenged with 0.1μM and 1μM LGK974 showed no reduction in our panel. However, PCLS challenged with the higher 10μM dose of LGK974 significantly reduced collagen 1α1 ($p<0.01$), TIMP-1 ($p<0.001$) and IL-6 (p

<0.0001) (Figure 32). Despite the 1µM and 10µM doses of E-7386 impacting tissue viability (Figure 28B), we found that 0.1µM E-7386 treated PCLS were able to reduce collagen 1α1 secretion by 90% compared to TGF-β1/PDGFββ-stimulated tissue (p<0.0001), resulting in less soluble collagen 1α1 than unstimulated control tissue (63% reduction compared to TGF-β1/PDGFββ-stimulated tissue; Figure 33D). Likewise, we observed a 79% reduction in TIMP-1 secretion (p<0.0001), back to below- control levels (69% reduction compared to TGF-β1/PDGFββ-stimulated tissue; Figure 33E). Finally, quantification of IL-6 demonstrated that co-treatment with 0.1µM E-7386 resulted in a 72% reduction of IL-6 compared to TGF-β1/PDGFββ-stimulated tissue (Figure 33F). Evaluation of PCLS challenged with TGF-β1/PDGFββ and HAS2 revealed a strong dose-dependent reduction in all pro-fibrotic markers in correlation with escalating doses (Figure 34). Though 1000µM HAS2 reduced metabolic activity <70% of control tissue (Figure 28B), the remaining 4 doses resulted in a significant reduction in collagen 1α1 (p<0.0001). Furthermore, TIMP-1 secretion was significantly reduced at all doses (30µM [p<0.001] and 100µM, 300µM and 500µM [p<0.0001]) and IL-6 at all doses except for the lowest 30µM dose (100µM [p<0.0.1], 300µM and 500µM [p<0.001]; Figure 34).

A)

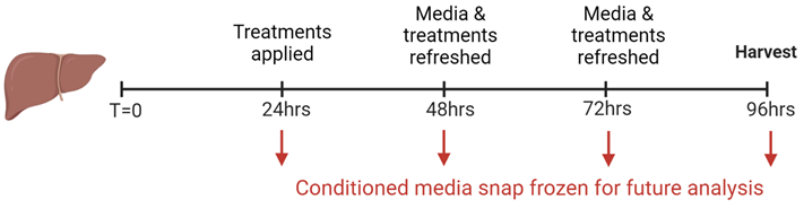

B)

	HAS2					DCLK1			E-7386			LGK974			TNKS656		
% of ctrl	30μM	100μM	300μM	500μM	1000μM	0.1μM	1μM	10μM	0.1μM	1μM	10μM	0.1μM	1μM	10μM	0.1μM	1μM	10μM
Donor 6	60	74	70	70	48	86	105	94	70	56	52	89	82	75	87	70	76
Donor 7	97	103	88	75	81	72	81	86	52	43	41	84	88	73	78	83	65
Donor 8	71	69	65	57	57	86	84	78	76	60	38	69	71	67	53	69	61
Donor 10	73	71	87	80	53	73	89	82	98	76	74	99	98	93	76	55	75

C)

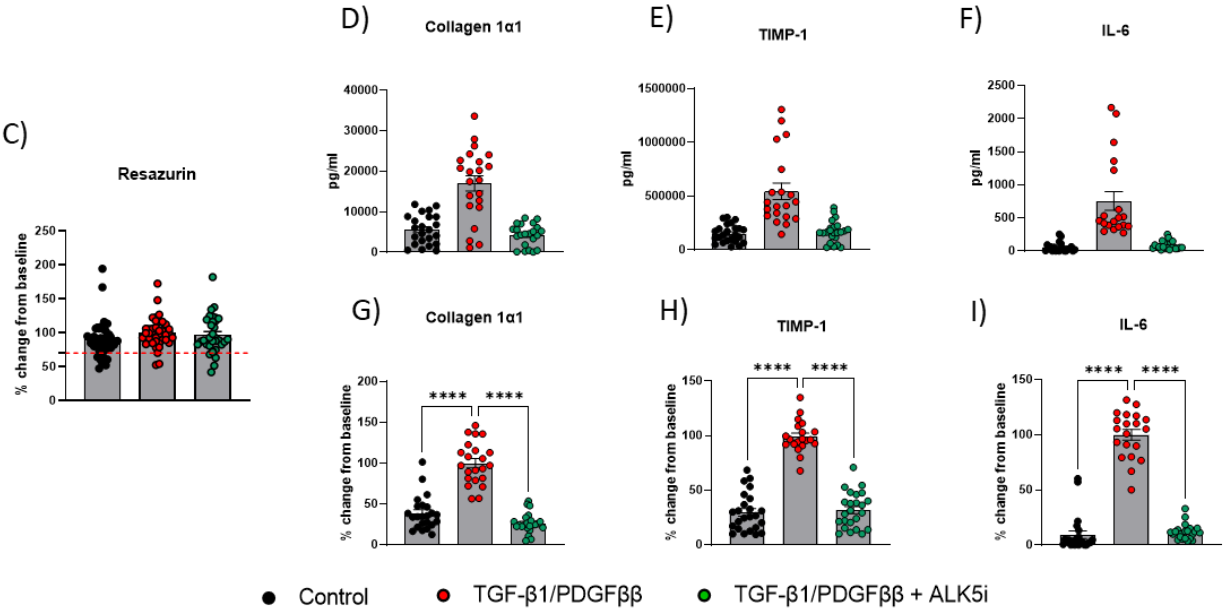

Figure 28: **Validation of TGF-β1/PDGFββ-challenged liver PCLS** A) PCLS were generated from resected liver tissue (n=4 donors) with slices (n=6 or n=10 PCLS per condition) being rested for 24 hours before challenge with either control media, a combination treatment of TGF-β1/PDGFββ or TGF-β1/PDGFββ + ALK5i. PCLS were also challenged with TGF-β1/PDGFββ in combination with escalating doses of each of the candidate compounds. Media, including all treatments, was refreshed at 24-hour intervals with conditioned media snap frozen for downstream analysis before PCLS were harvested for resazurin assay as an indicator of tissue viability. B) Resazurin assay performed at T96 presented as the average % of control (for n=6 or n=10 slices per treatment) for each donor (green values indicate resazurin values ≥70% of control, yellow/orange 50-69% of control and red <50% of control). Quantification of C) Resazurin (where red dashed line represents arbitrary 70% viability threshold) Collagen 1α1, TIMP-1 and IL-6 was performed on T96 media and plotted as D-F) absolute pg/ml and G-I) average % change from baseline (TGF-β1/PDGFββ-challenged PCLS)to confirm tissue could be effectively modulated. All data are mean ± SEM. Statistical significance was determined on graphs G-I using ANOVA with post-hoc Dunnett's test where TGF-β1/PDGFββ-challenged PCLS was set as the control group (*p<0.05, **p<0.01, ***p<0.001, ****p<0.0001).

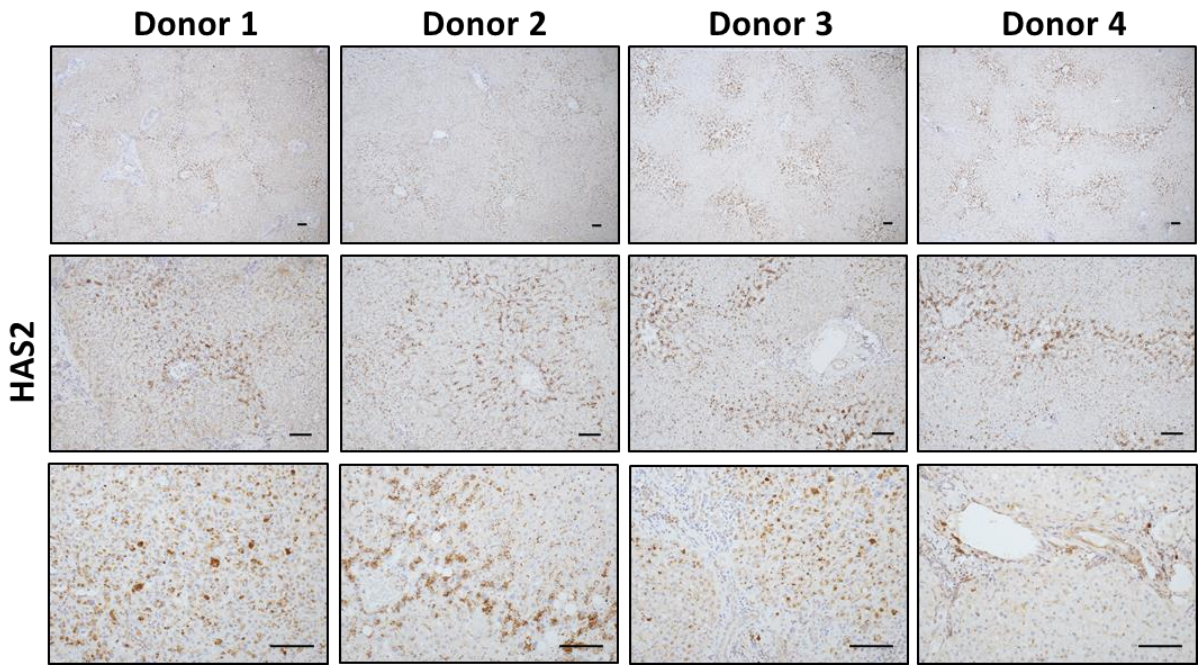

Figure 29: Histological validation of target proteins in PCLS donor livers Representative images of HAS2+ cells in PCS liver donor tissue (scale bar= 100µm). Primary antibody was applied at 1/100 dilution.

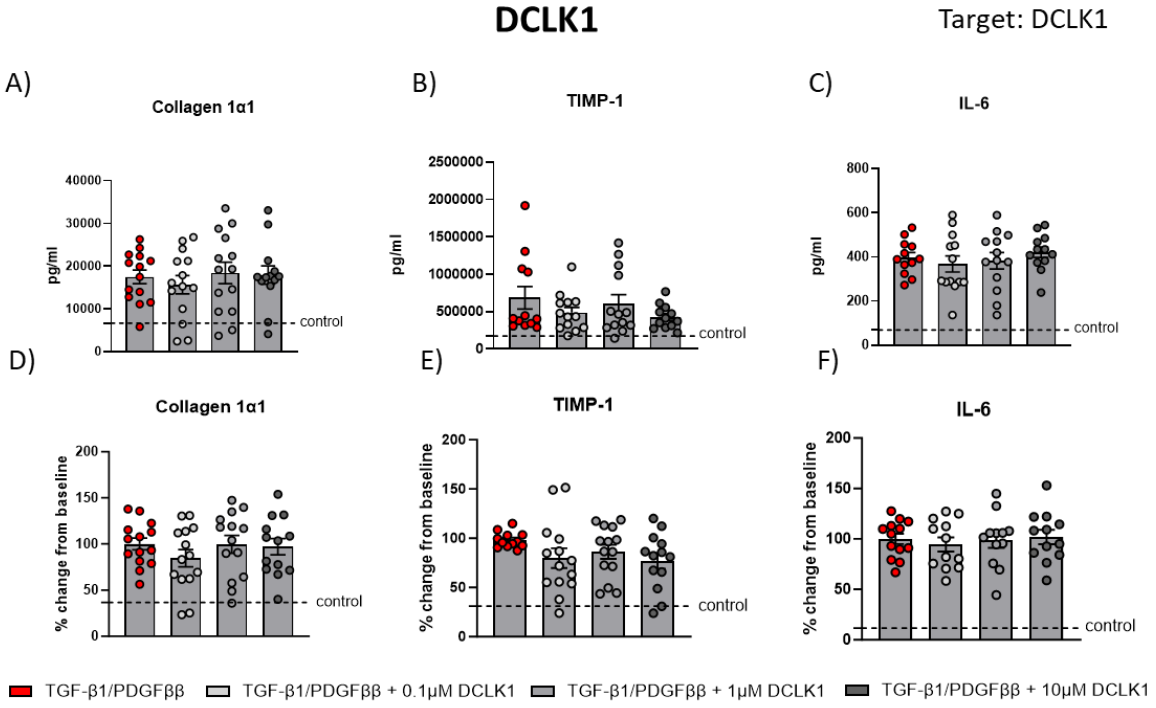

Figure 30: Validation of DCLK1 compound in TGF-β1/PDGFββ-challenged liver PCLS PCLS were generated from resected liver tissue (n=4 donors) with slices (n=6 PCLS per condition) being rested for 24 hours before challenge with either control media, a combination treatment of TGF-β1/PDGFββ alone or in combination with 3 escalating doses of DCLK1 (n=6 PCLS per condition, n=4 donors, n=12 pooled media total). Media, including all treatments, was refreshed at 24-hour intervals with conditioned media snap frozen for downstream analysis before PCLS were harvested for resazurin assay at 96hrs. Quantification of soluble Collagen 1α1, TIMP-1 and IL-6 was measured in T96 media *via* ELISA and plotted as A-C) absolute pg/ml and D-F) average % change from baseline (TGF-β1/PDGFββ-challenged PCLS) for all donors (n=3 conditioned media, n=4 donors, n=12 samples total).. Black dashed line denotes unstimulated control PCLS A-C) pg/ml and D-F) % expression compared to TGF-β1/PDGFββ-treated tissue. All data are mean ± SEM. Statistical significance was determined on graphs D, E and F using ANOVA with post-hoc Dunnett's test where TGF-β1/PDGFββ-challenged PCLS was set as the control group (*p<0.05, **p<0.01, ***p<0.001, ****p<0.0001).

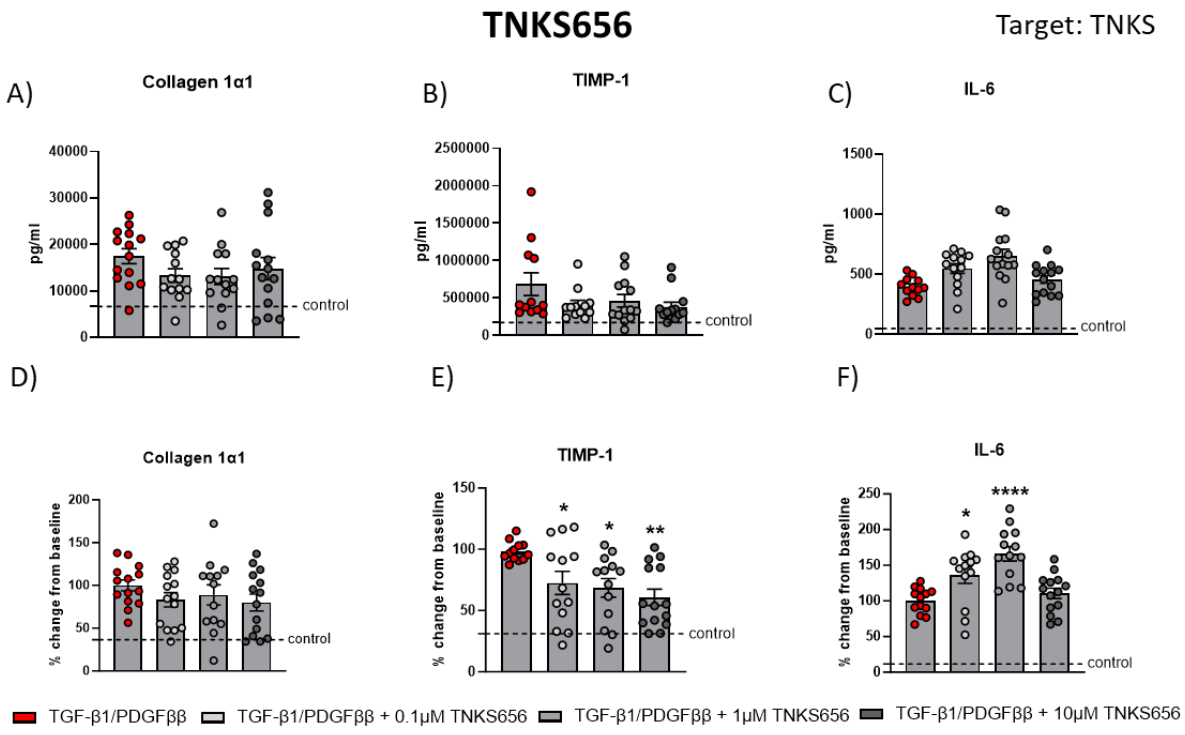

Figure 31: Validation of TNKS656 compound in TGF-β1/PDGFββ-challenged liver PCLS PCLS were generated from resected liver tissue (n=4 donors) with slices (n=6 PCLS per condition) being rested for 24 hours before challenge with either control media, a combination treatment of TGF-β1/PDGFββ alone or in combination with 3 escalating doses of TNKS656 (n=6 PCLS per condition, n=4 donors, n=12 pooled media total). Media, including all treatments, was refreshed at 24-hour intervals with conditioned media snap frozen for downstream analysis before PCLS were harvested for resazurin assay at 96hrs. Quantification of soluble Collagen 1α1, TIMP-1 and IL-6 was measured in T96 media *via* ELISA and plotted as A-C) absolute pg/ml and D-F) average % change from baseline (TGF-β1/PDGFββ-challenged PCLS) for all donors (n=3 conditioned media, n=4 donors, n=12 samples total). Black dashed line denotes unstimulated control PCLS A-C) pg/ml and D-F) % expression compared to TGF-β1/PDGFββ-treated tissue. All data are mean ± SEM. Statistical significance was determined on graphs D, E and F using ANOVA with post-hoc Dunnett's test where TGF-β1/PDGFββ-challenged PCLS was set as the control group (*p<0.05, **p<0.01, ***p<0.001, ****p<0.0001).

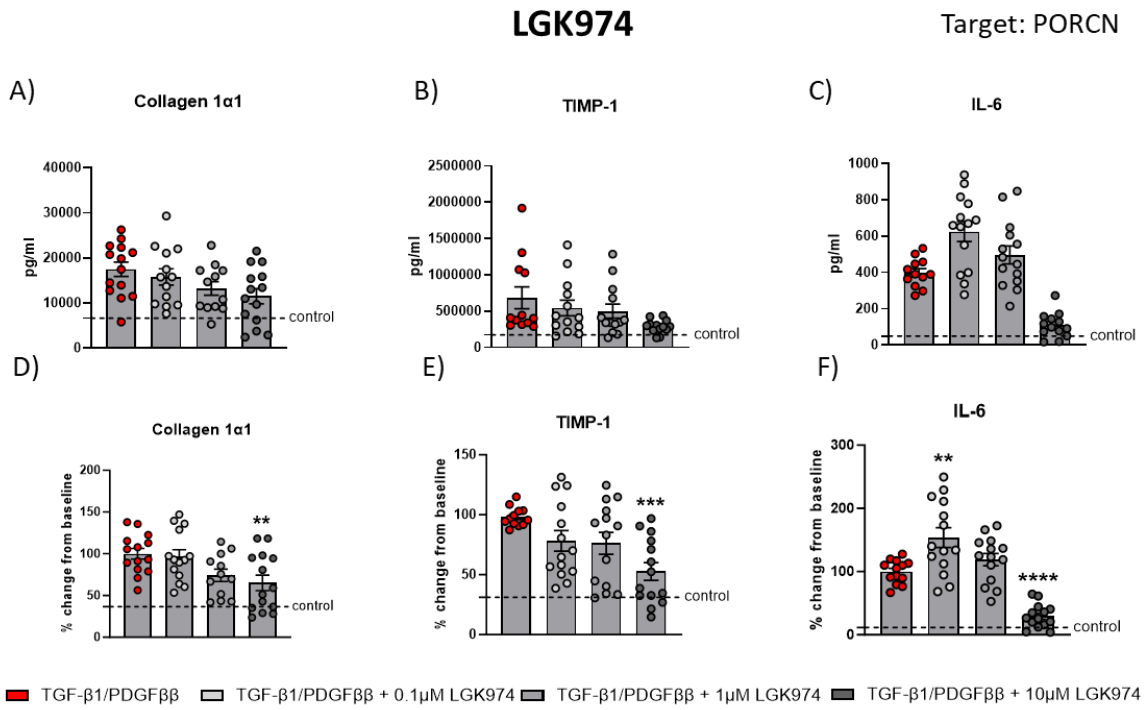

Figure 32: Validation of LGK974 compound in TGF-β1/PDGFββ-challenged liver PCLS PCLS were generated from resected liver tissue (n=4 donors) with slices (n=6 PCLS per condition) being rested for 24 hours before challenge with either control media, a combination treatment of TGF-β1/PDGFββ alone or in combination with 3 escalating doses of LGK974 (n=6 PCLS per condition, n=4 donors, n=12 pooled media total). Media, including all treatments, was refreshed at 24-hour intervals with conditioned media snap frozen for downstream analysis before PCLS were harvested for resazurin assay at 96hrs. Quantification of soluble Collagen 1α1, TIMP-1 and IL-6 was measured in T96 media *via* ELISA and plotted as A-C) absolute pg/ml and D-F) average % change from baseline (TGF-β1/PDGFββ-challenged PCLS) for all donors (n=3 conditioned media, n=4 donors, n=12 samples total).. Black dashed line denotes unstimulated control PCLS A-C) pg/ml and D-F) % expression compared to TGF-β1/PDGFββ-treated tissue. All data are mean ± SEM. Statistical significance was determined on graphs D, E and F using ANOVA with post-hoc Dunnett's test where TGF-β1/PDGFββ-challenged PCLS was set as the control group (*p<0.05, **p<0.01, ***p<0.001, ****p<0.0001).

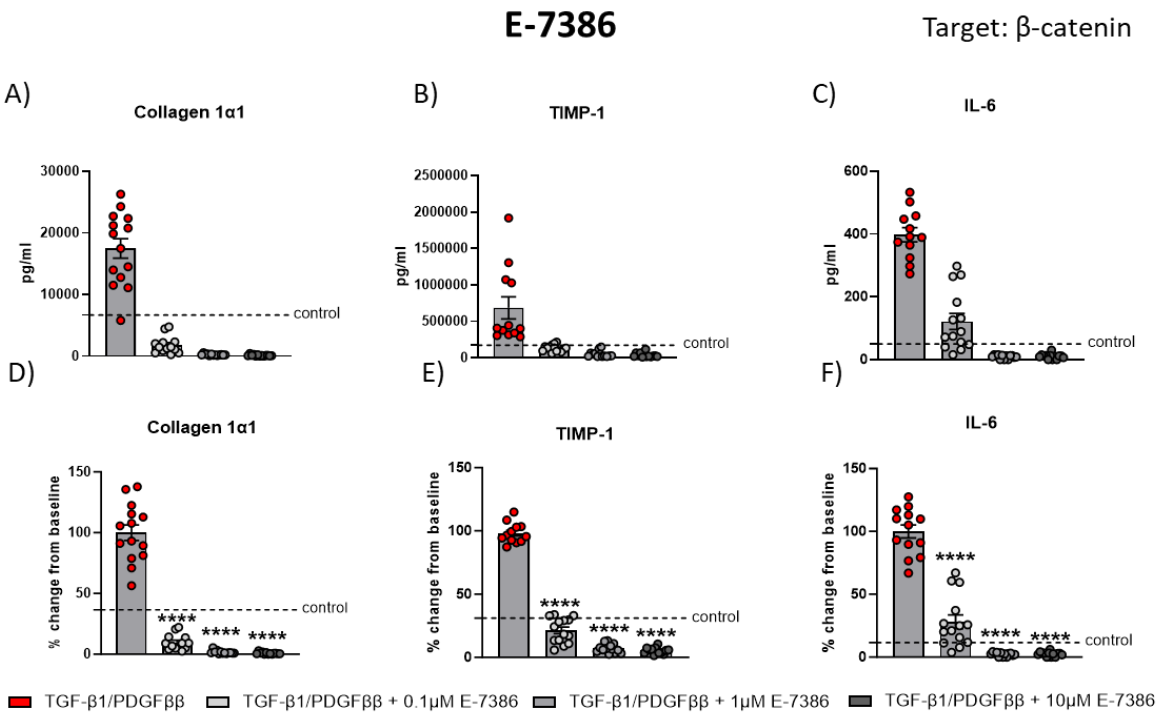

Figure 33: **Validation of E-7386 compound in TGF-β1/PDGFββ-challenged liver PCLS** PCLS were generated from resected liver tissue (n=4 donors) with slices (n=6 PCLS per condition) being rested for 24 hours before challenge with either control media, a combination treatment of TGF-β1/PDGFββ alone or in combination with 3 escalating doses of E-7386 (n=6 PCLS per condition, n=4 donors, n=12 pooled media total). Media, including all treatments, was refreshed at 24-hour intervals with conditioned media snap frozen for downstream analysis before PCLS were harvested for resazurin assay at 96hrs. Quantification of soluble Collagen 1α1, TIMP-1 and IL-6 was measured in T96 media *via* ELISA and plotted as A-C) absolute pg/ml and D-F) average % change from baseline (TGF-β1/PDGFββ-challenged PCLS) for all donors (n=3 conditioned media, n=4 donors, n=12 samples total).. Black dashed line denotes unstimulated control PCLS A-C) pg/ml and D-F) % expression compared to TGF-β1/PDGFββ-treated tissue. All data are mean ± SEM. Statistical significance was determined on graphs D, E and F using ANOVA with post-hoc Dunnett's test where TGF-β1/PDGFββ-challenged PCLS was set as the control group (*p<0.05, **p<0.01, ***p<0.001, ****p<0.0001).

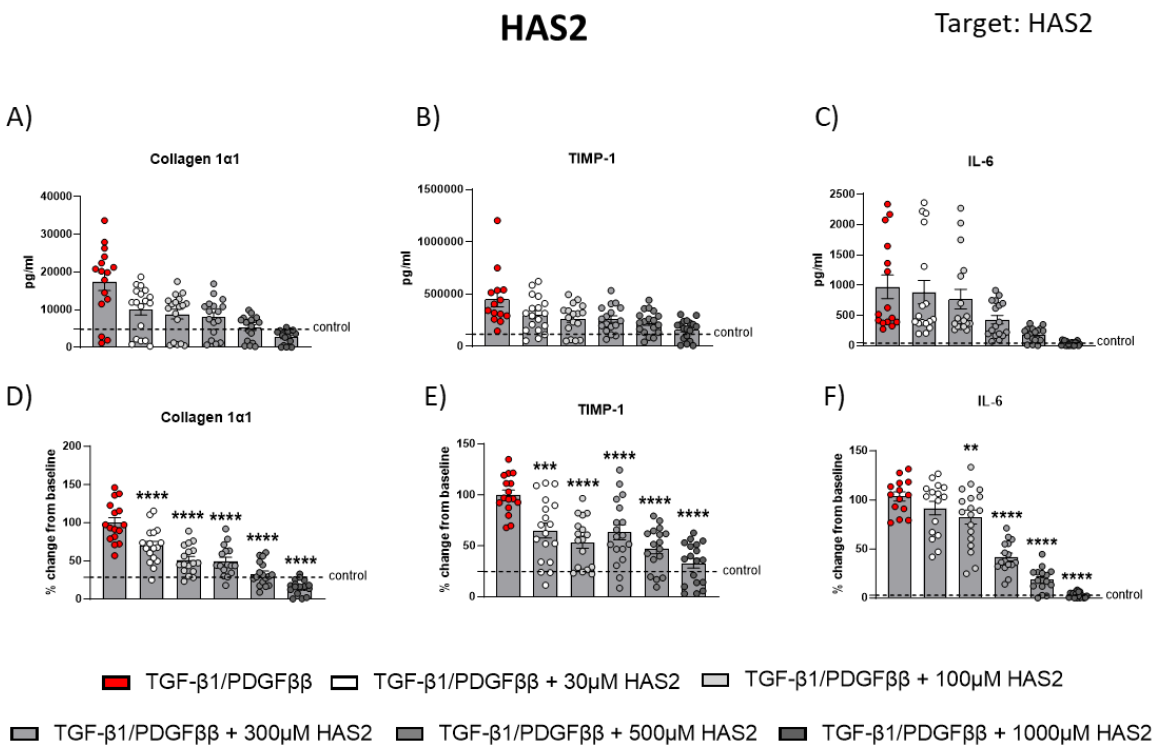

Figure 34: Validation of HAS2 compound in TGF-β1/PDGFββ-challenged liver PCLS PCLS were generated from resected liver tissue (n=4 donors) with slices (n=6 or n=10 PCLS per condition) being rested for 24 hours before challenge with either control media, a combination treatment of TGF-β1/PDGFββ alone or in combination with 5 escalating doses of HAS2 (n=6 or n=10 PCLS per condition, n=4 donors, n=18 pooled media total). Media, including all treatments, was refreshed at 24-hour intervals with conditioned media snap frozen for downstream analysis before PCLS were harvested for resazurin assay at 96hrs. Quantification of soluble Collagen 1α1, TIMP-1 and IL-6 was measured in T96 media via ELISA and plotted as A-C) absolute pg/ml and D-F) average % change from baseline (TGF-β1/PDGFββ-challenged PCLS) for all donors (n=3 conditioned media, n=4 donors, n=12 samples total).. Black dashed line denotes unstimulated control PCLS A-C) pg/ml and D-F) % expression compared to TGF-β1/PDGFββ-treated tissue. All data are mean ± SEM. Statistical significance was determined on graphs D, E and F using ANOVA with post-hoc Dunnett's test where TGF-β1/PDGFββ-challenged PCLS was set as the control group (*p<0.05, **p<0.01, ***p<0.001, ****p<0.0001).

3.3.4 Investigation of targets of interest in lung fibrosis

3.3.4.1 Target exploration in lung scRNAseq datasets

To determine whether the targets identified from liver snRNAseq were common to other fibrotic diseases or organ specific, gene expression was explored in lung-derived single cell RNAseq datasets by Dr Stephen Christensen, Pfizer. To achieve this, six publicly available scRNAseq studies were integrated, comprising 616,918 cells (51 healthy and 66 fibrotic patients [n=10 systemic sclerosis interstitial lung disease and n=56 IPF]; available online athttps://singlecell.broadinstitute.org/single_cell/study/SCP2155/). Preliminary analysis of the lung atlas revealed gene expression of 6 of the 9 targets of interest were increased in fibrotic lung disease, particularly in fibroblast populations (Figure 35; Appendix E Figures 1-3). Further interrogation of stromal cell populations within this dataset confirmed that target gene expression was upregulated predominantly in inflammatory and ECM-producing fibroblasts (Figure 36; Appendix E Figures 4-6).

Next, we proceeded to look at target expression in pre-existing transcriptomic datasets generated in collaboration with Dr William Reilly. Here, primary lung fibroblasts isolated from unused donor (n=6 donors) and IPF explant tissue (n=6 donors) were exposed to IL1α or TGF-β1 for 24 hours to stimulate inflammation and fibrogenesis, respectively (see appendix D). Results showed that there were no significant differences in target gene expression between unused donor and IPF-derived fibroblasts in the absence of exogenous stimuli. However, in response to IL1α challenge, TNFRSF12A was significantly upregulated only in fibroblasts isolated from IPF tissue ($p<0.05$; Figure 37E). Conversely, unused donor lung fibroblasts decreased expression of WNT9A ($p<0.05$; Figure 37I). Finally, exposure to pro-fibrotic TGF-β1 resulted in increased expression of TNFRSF12A, UNC5B and VCAN in fibroblasts from both healthy and diseased lungs, whereas THBS2 was significantly upregulated in IPF-derived, but not unused donor fibroblasts ($p<0.05$; Figure 38).

Taken together, these data confirmed that several previously identified targets in the liver demonstrated increased gene expression in fibrotic lung disease. Furthermore, we found that a number of these targets could be significantly upregulated in pulmonary fibroblasts via pro-fibrotic TGF-β1 stimulation, therefore warranting further investigation.

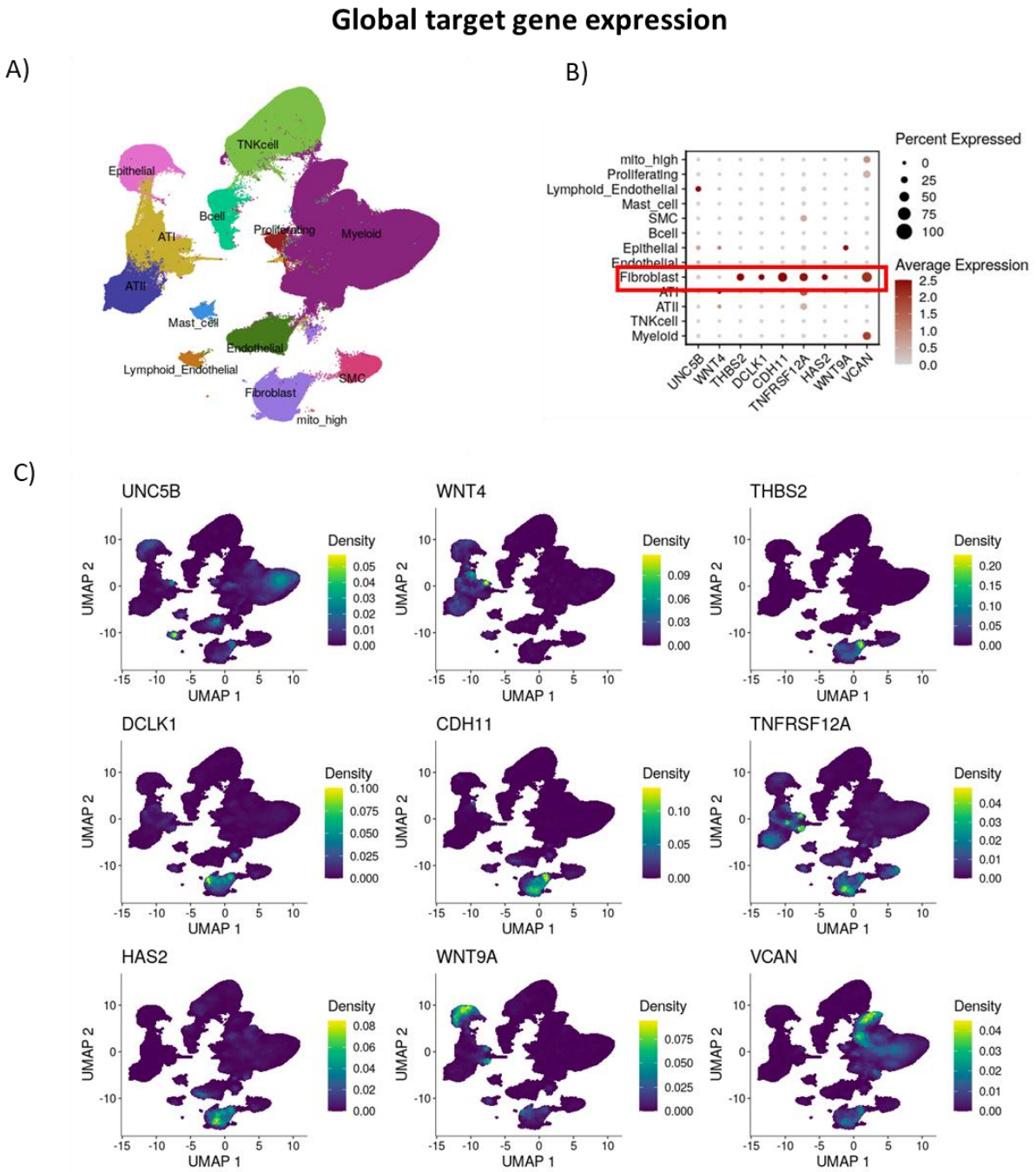

Figure 35: Investigation of target gene expression in lung scRNAseq datasets Target gene expression was investigated in scRNAseq datasets generated from 6 integrated single cell lung atlases (https://singlecell.broadinstitute.org/single_cell/study/SCP2155/) created by Dr Stephen Christensen, Pfizer. A) In total, 616,918 cells were included from multiple different fibrotic lung diseases, comprising 13 different cell lineages. B) Dot plots showed increased average gene expression of multiple targets in fibroblast populations which was further interrogated by generation of C) individual UMAPs of target density (Figures provided by Dr Stephen Christensen, Pfizer).

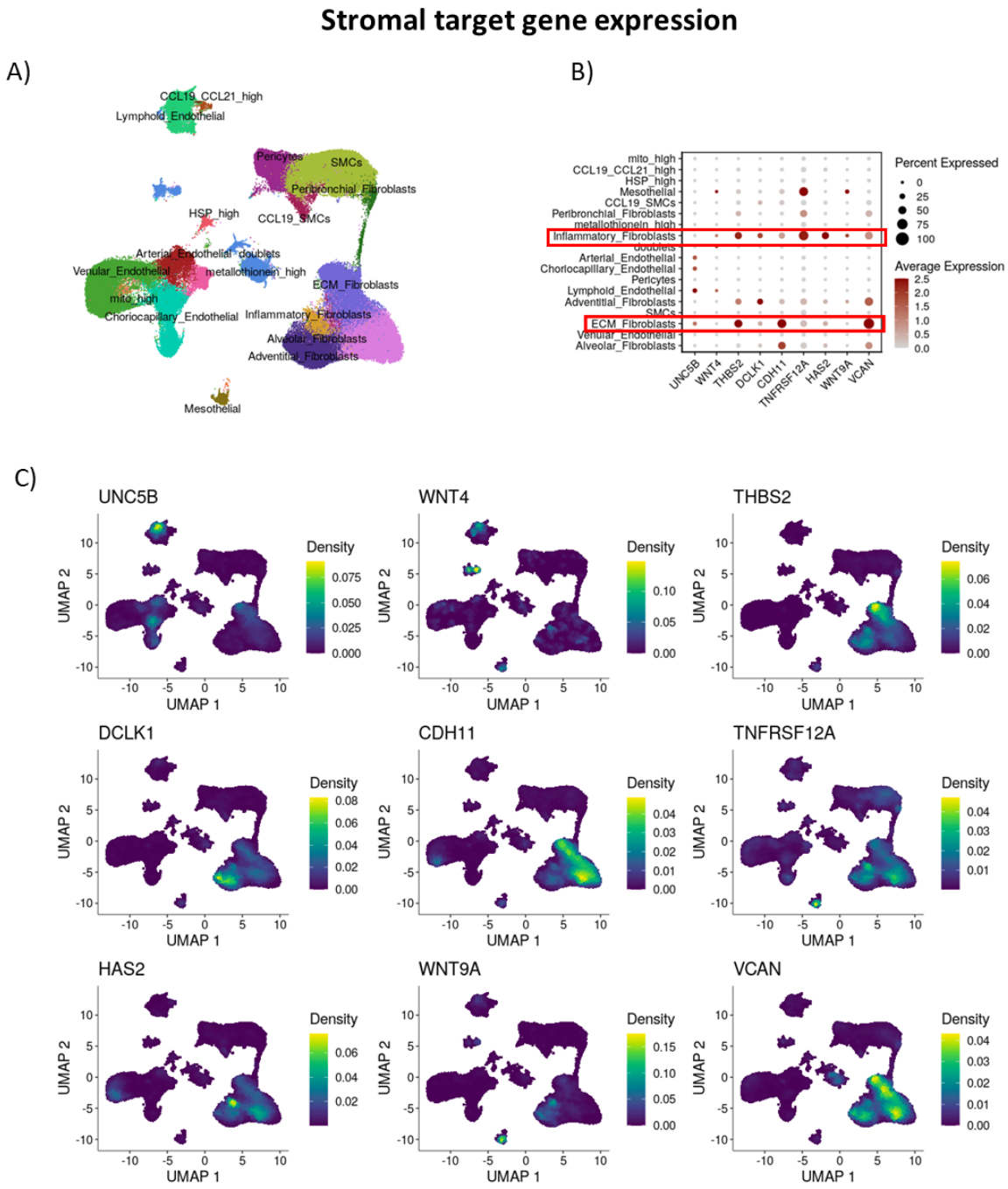

Figure 36: Investigation of target gene expression in stromal subset of lung scRNAseq datasets Target gene expression was investigated in the stromal cell subset of scRNAseq datasets generated from 6 integrated single cell lung atlases (https://singlecell.broadinstitute.org/single_cell/study/SCP2155/) created by Dr Stephen Christensen, Pfizer. A) Cells were included from multiple different fibrotic lung diseases, comprising 18 different stromal cell lineages. B) Dot plots showed increased average gene expression of multiple targets in inflammatory and ECM fibroblast populations which was further interrogated by generation of C) individual UMAPs of target density in stromal compartment (Figures provided by Dr Stephen Christensen, Pfizer).

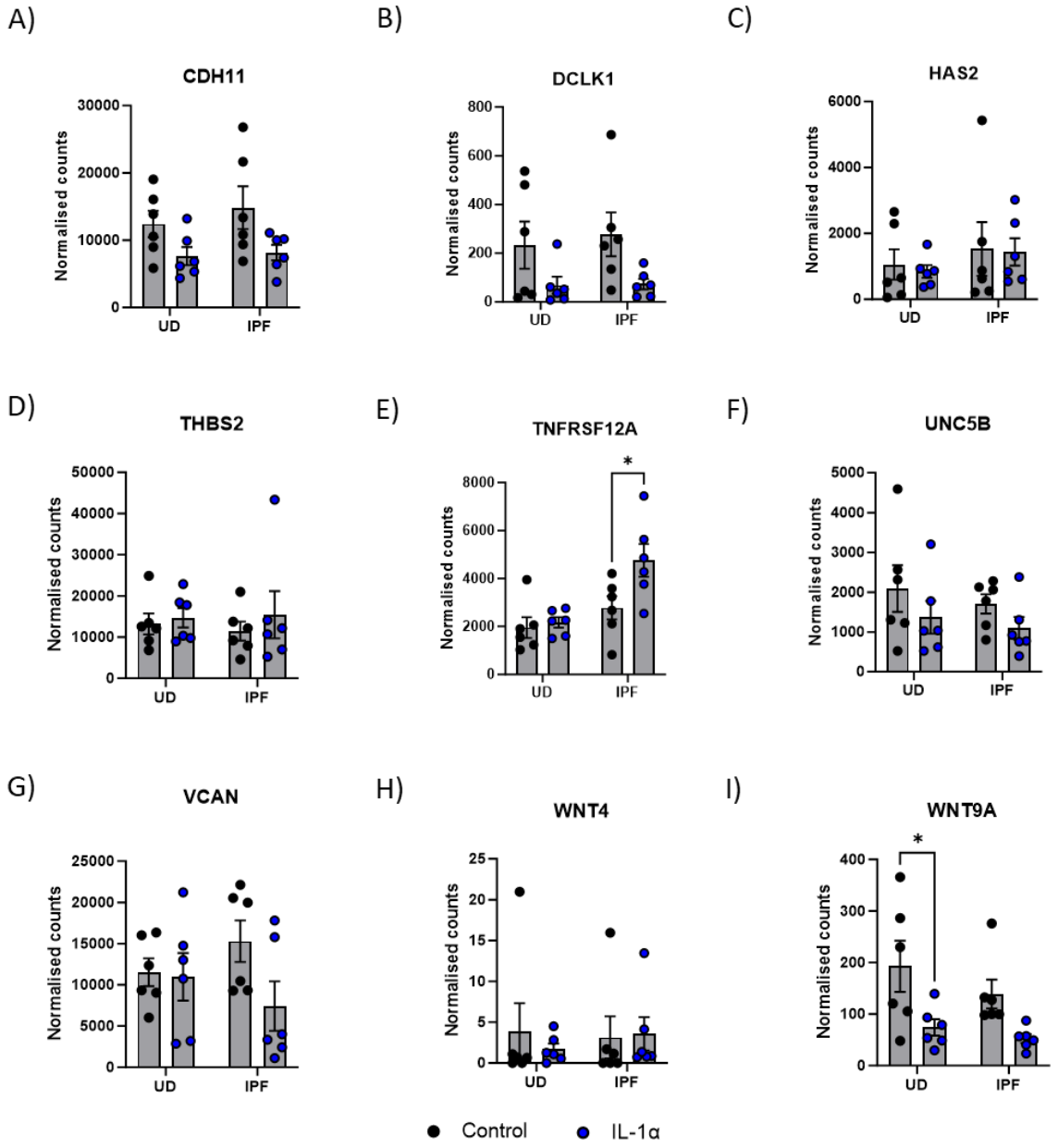

Figure 37: Investigation of target gene expression in IL1α-challenged pulmonary fibroblasts Target gene expression was investigated in transcriptomic datasets previously generated from primary parenchymal fibroblasts isolated from unused donor lungs (n=6 donors) and IPF explant tissue (n=6 donors). Fibroblasts were seeded into T75 flasks and (once 70% confluent) serum starved for 24-hours prior to 24-hour challenge with control media or IL1α (1ng/ml) before being harvested and processed for bulk RNAseq. Normalised counts of A) CDH11, B) DCLK1, C) HAS2, D) THBS2, E) TNFRSF12A, F) UNC5B, G) VCAN H) WNT4 and I) WNT9A were plotted. All data are mean ± SEM. Statistical significance was determined using two-way ANOVA with Šidák's multiple comparisons test where the mean of each treatment was compared with the mean of every other treatment (*p<0.05, **p<0.01, ***p<0.001 and ****p<0.0001).

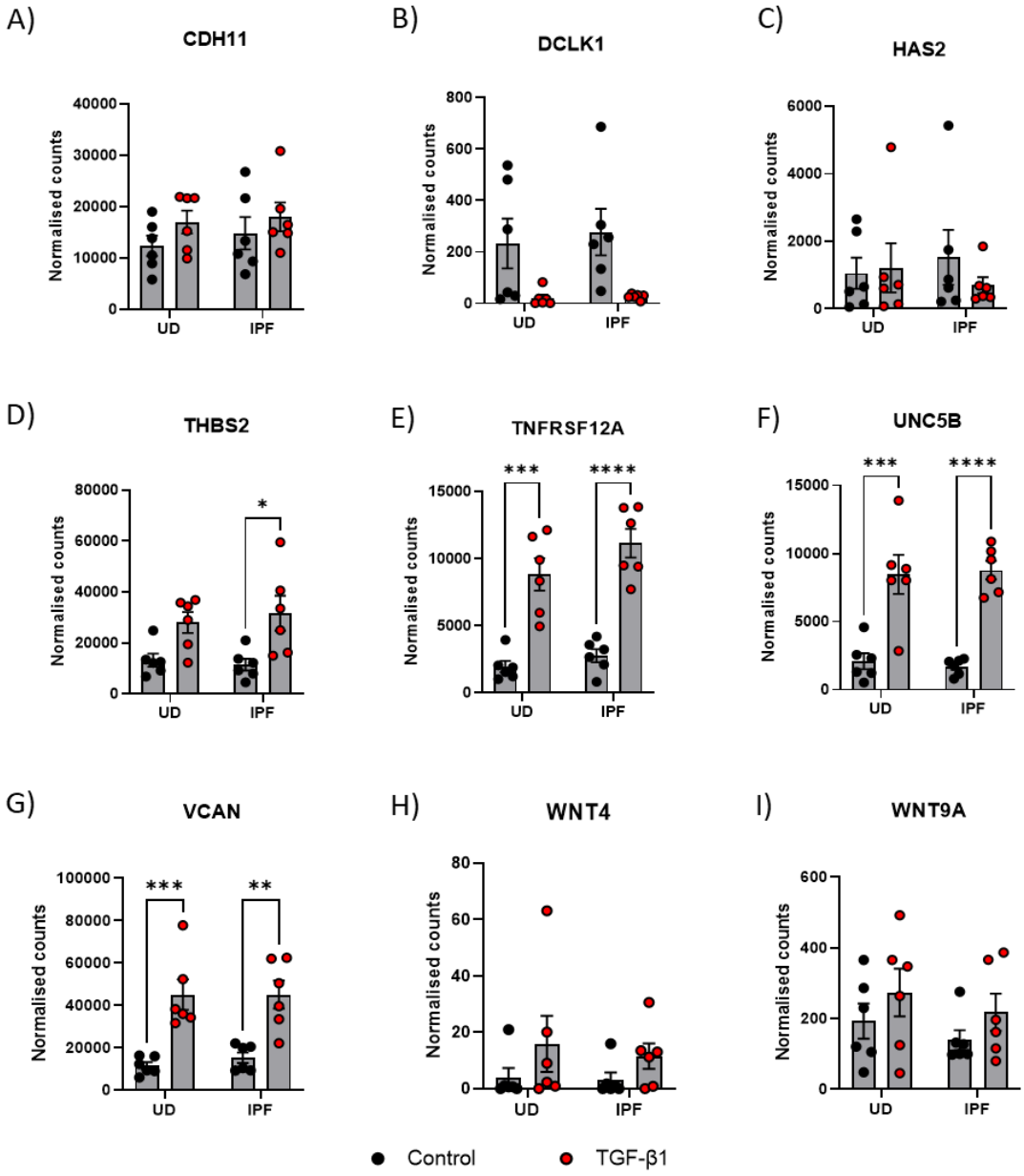

Figure 38: Investigation of target gene expression in TGF-β1-challenged pulmonary fibroblasts Target gene expression was investigated in transcriptomic datasets previously generated from primary parenchymal fibroblasts isolated from unused donor lungs (n=6 donors) and IPF explant tissue (n=6 donors). Fibroblasts were seeded into T75 flasks and (once 70% confluent) serum starved for 24 hours prior to 24-hour challenge with control media or TGF-β1 (5ng/ml) before being harvested and processed for bulk RNAseq. Normalised counts of A) CDH11, B) DCLK1, C) HAS2, D) THBS2, E) TNFRSF12A, F) UNC5B, G) VCAN H) WNT4 and I) WNT9A were plotted. All data are mean ± SEM. Statistical significance was determined using two-way ANOVA with Šidák*'s* multiple comparisons test where the mean of each treatment was compared with the mean of every other treatment (*p<0.05, **p<0.01, ***p<0.001 and ****p<0.0001).

3.3.4.2 Interrogation of candidate compounds in unused donor PCLuS

To begin investigating the candidate compounds in the context of lung fibrosis, we first sought to replicate the experimental design previously used in the liver. Here, PCLuS were generated from unused donor lung tissue (n=3) and rested for 48 hours, with media being refreshed after 24 hours, before being challenged with control media, IL1α alone, in combination with IKK2, or the highest dose of each inhibitor (Figure 39A). PCLuS were harvested for resazurin assay at T72 after 24-hour treatment, and results were normalised to % of control PCLuS for each donor. Assessment of metabolic activity revealed that all inhibitory compounds were well tolerated in Donor 1 and 3, though HAS2 and LGK974 –challenged PCLuS from Donor 2 fell below the 70% threshold (Figure 39B). Consistent with previous results from the liver, we confirmed that IL1α stimulation significantly increased secretion of IL-8 ($p<0.0001$) and IL-6 ($p<0.0001$) in unused donor PCLuS, and co-treatment with IKK2 could attenuate this response back to control levels ($p<0.0001$) (Figure 39F-G). However, quantification of these pro-inflammatory markers in PCLuS co-challenged with each of the candidate compounds showed no change in soluble IL-8 or IL-6, suggesting none were able to blunt IL1α-induced inflammation in the lung (Figure 40).

A)

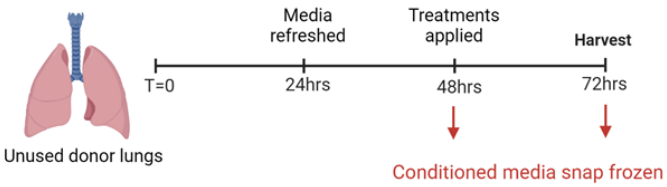

B)

% of ctrl	1000µM HAS2	10µM DCLK1	10µM E-7386	10µM LGK974	10µM TNKS656
Unused Donor 1	91	120	76	172	81
Unused Donor 2	45	71	92	40	70
Unused Donor 3	108	92	88	92	120

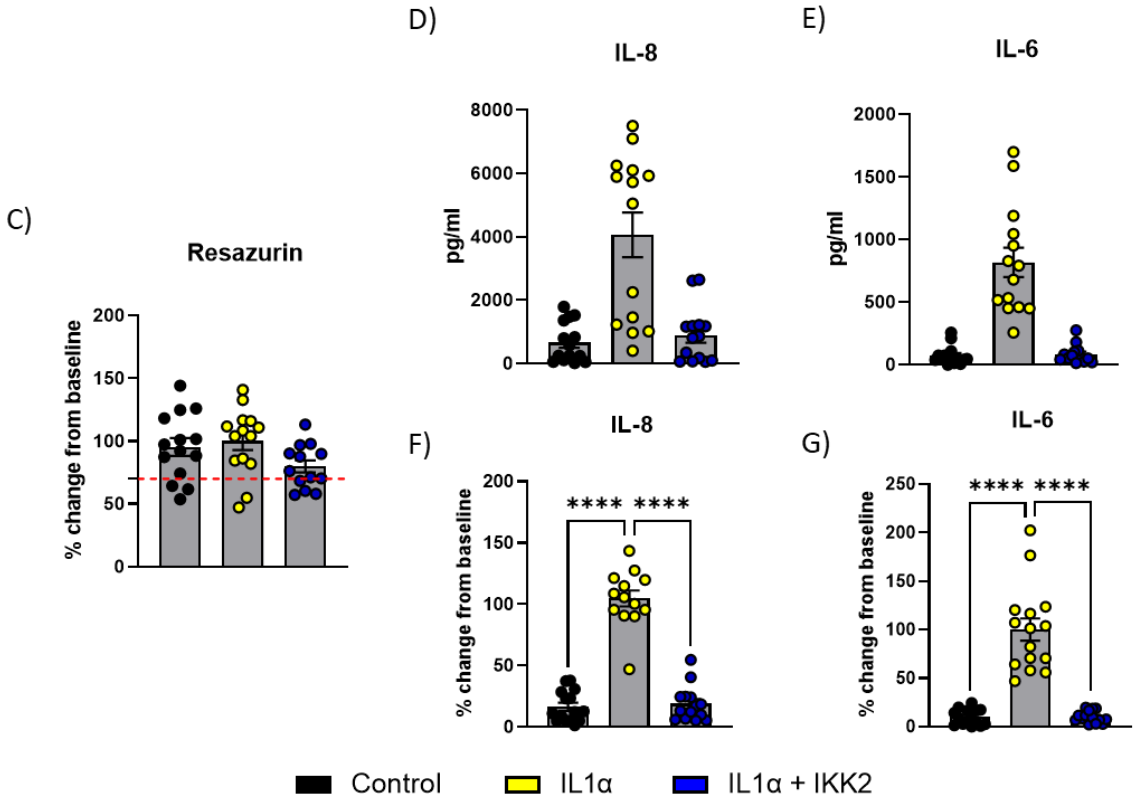

Figure 39: **Validation of IL1α-challenged unused donor PCLuS** A) PCLuS were generated from unused lung donor tissue (n=3 donors) and rested for 48 hours, with media being refreshed after 24 hours, before being challenged (n=5 slices per condition) with control media, IL1α alone or in combination with IKK2 (n=5 PCLuS per condition, n=3 donors, n=15 PCLuS total). PCLuS were also challenged with IL1α in combination with the highest dose of each of the candidate compounds for 24 hours. Conditioned media was snap frozen for analysis and PCLuS were harvested for resazurin assay at T72 as an indicator of tissue viability. B) Resazurin presented as the average % of control for n=5 slices per treatment for each donor (green values indicate resazurin values ≥70% of control, yellow/orange 50-69% of control and red <50% of control). Quantification of C) Resazurin (where red dashed line represents arbitrary 70% viability threshold) IL-8 and IL-6 was performed and plotted as D-E) absolute pg/ml and F-G) % change from baseline (IL1α-challenged PCLuS) for all donors (n=5 conditioned media, n=3 donors, n=15 samples total) to confirm tissue could be effectively modulated. All data are mean ± SEM. Statistical significance was determined on graphs F and G using ANOVA with post-hoc Dunnett's test where IL1α-challenged PCLuS was set as the control group (*p<0.05, **p<0.01, ***p<0.001 and ****p<0.0001).

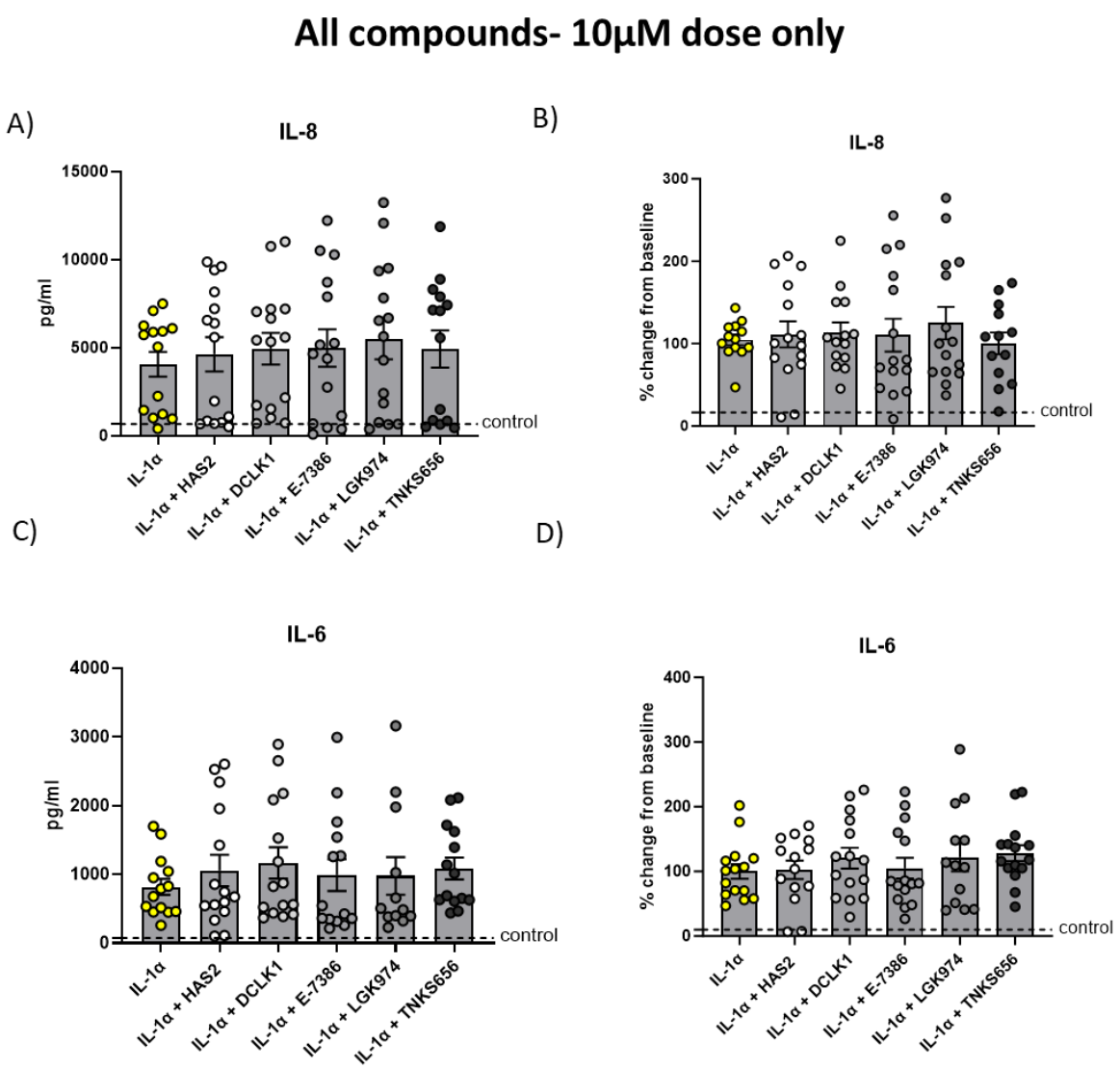

Figure 40: Validation of candidate compounds in IL1α-challenged unused donor PCLuS PCLuS were generated from unused lung donor tissue (n=3 donors) and rested for 48 hours, with media being refreshed after 24 hours, before being challenged (n=5 slices per condition) with control media, IL1α alone or in combination with the highest dose of each of the candidate compounds for 24 hours (n=5 PCLuS per condition, n=3 donors, n=15 PCLuS total). Conditioned media was collected at T72 and protein secretion of inflammatory markers IL-8 and IL-6 were measured *via* ELISA and plotted as A-B) absolute pg/ml and C-D) % change from baseline (IL1α- challenged PCLuS) for all donors n=5 conditioned media, n=3 donors, n=15 samples total). Black dashed line denotes unstimulated control PCLuS A-B) pg/ml and C-D) % expression compared to IL1α-treated tissue. All data are mean ± SEM. Statistical significance was determined on graphs C and D using ANOVA with post-hoc Dunnett's test where IL1α-challenged PCLuS was set as the control group (*$p < 0.05$, **$p < 0.01$, ***$p < 0.001$ and ****$p < 0.0001$).

Alongside this, we also investigated potential anti-fibrotic effects of the 5 candidate compounds in response to TGF-β1/PDGFββ-driven fibrogenesis. To achieve this, PCLuS (n=3 donors) were rested for 48 hours before challenge with either control media, a combination treatment of TGF-β1/PDGFββ alone or in combination with ALK5i, or with the highest dose of each of the candidate compounds. Media, including all treatments, was refreshed at 24-hour intervals with conditioned media snap frozen for downstream analysis before PCLuS were harvested for resazurin at T144 (Figure 41A). After normalisation, assessment of metabolic activity found that all tissue remained viable after challenge, except for E-7386-challenged PCLuS in Donor 1 and TNKS656- challenged PCLuS in Donor 2 (Figure 41B).

To assess target expression prior to culture and/or challenge with exogenous stimuli, histological assessment of HAS2, Wnt4 and Wnt9a was performed in all donor tissue and confirmed that all targets were either lowly abundant or not present in non-diseased lungs prior to culture (Figure 42). Following this, quantification of pro-fibrotic markers was used to confirm effective modulation of fibrosis as previously described (Figure 41G-I). Results found that PCLuS treated with TGF-β1/PDGFββ + 10μM LGK974 had no effect on secretion of collagen 1α1, TIMP-1 or IL-6 (Figure 43). This was also true for PCLuS co-treated with 10μM TNKS656, where secretion remained comparable to TGF-β1/PDGFββ (Figure 43). Investigation of DCLK1-treated PCLuS revealed a modest reduction of collagen 1α1 ($p<0.05$), but no effect on TIMP-1 or IL-6 (Figure 43). Conversely, both HAS2 and E-7386 inhibitors showed a considerable reduction in collagen 1α1 secretion, with an 86% and 88% reduction from baseline (TGF-β1/PDGFββ), respectively ($p<0.0001$; Figure 43). Likewise, HAS2 ($p<0.05$) and E-7386 ($p<0.01$) showed a significant reduction in secretion of TIMP-1 and IL-6 when treated alongside fibrogenic stimuli (Figure 43). These results were in keeping with findings from the liver which demonstrated that HAS2 (Figure 34) and E-7386 (Figure 33) were able to blunt TGF-β1/PDGFββ-induced fibrogenesis. However, unlike PCLS, it appeared that both compounds were better tolerated at the highest dose in the unused donor lung tissue, generally maintaining >70% of metabolic activity compared to control PCLuS at the end of culture.

A)

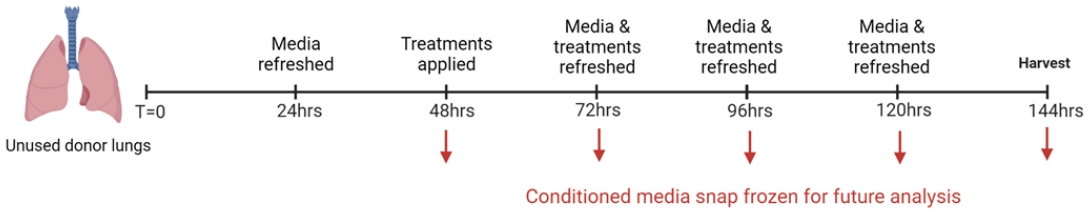

B)

% of ctrl	1000µM HAS2	10µM DCLK1	10µM E-7386	10µM LGK974	10µM TNKS656
Unused Donor 1	72	81	45	85	112
Unused Donor 2	80	72	93	81	64
Unused Donor 3	106	71	109	97	72

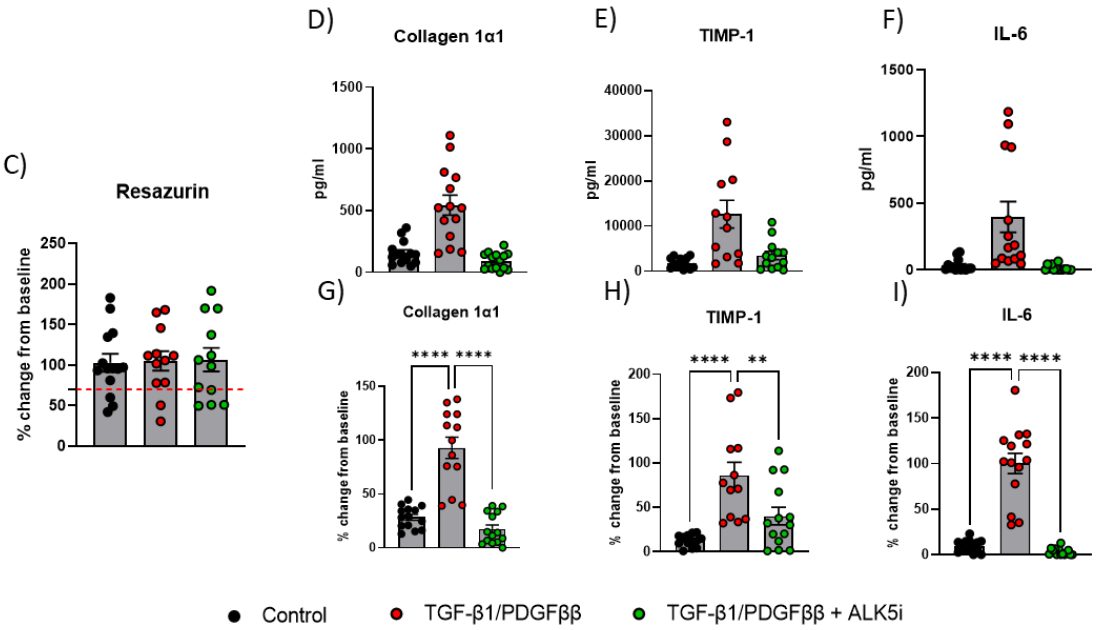

Figure 41: Validation of TGF-β1/PDGFββ-challenged unused donor PCLuS A) PCLuS were generated from unused lung donor tissue (n=3 donors) with slices (n=5 per condition) being rested for 48 hours before challenge with either control media, a combination treatment of TGF-β1/PDGFββ or TGF-β1/PDGFββ + ALK5i. PCLuS were also challenged with TGF-β1/PDGFββ in combination with the highest dose of each of the candidate compounds (n=5 PCLuS per condition, n=3 donors, n=15 PCLuS total). Media, including all treatments, was refreshed at 24-hour intervals with conditioned media snap frozen for downstream analysis before PCLuS were harvested at 144hrs for resazurin assay to quantify metabolic activity. B) Resazurin presented as the average % of control for n=6 slices per treatment for each donor (green values indicate resazurin values ≥70% of control, yellow/orange 50-69% of control and red <50% of control). Quantification of C) Resazurin (where red dashed line represents arbitrary 70% threshold),Collagen 1α1, TIMP-1 and IL-6 was performed on T144 media and plotted as D-F) absolute pg/ml and G-I) % change from baseline (TGF-β1/PDGFββ-challenged PCLuS) for all donors (n=5 conditioned media, n=3 donors, n=15 samples total)to confirm tissue could be effectively modulated. All data are mean ± SEM. Statistical significance was determined on graphs G, H and I using ANOVA with post-hoc Dunnett's test where TGF-β1/PDGFββ-challenged PCLuS was set as the control group (*p<0.05, **p<0.01, ***p<0.001, ****p<0.0001).

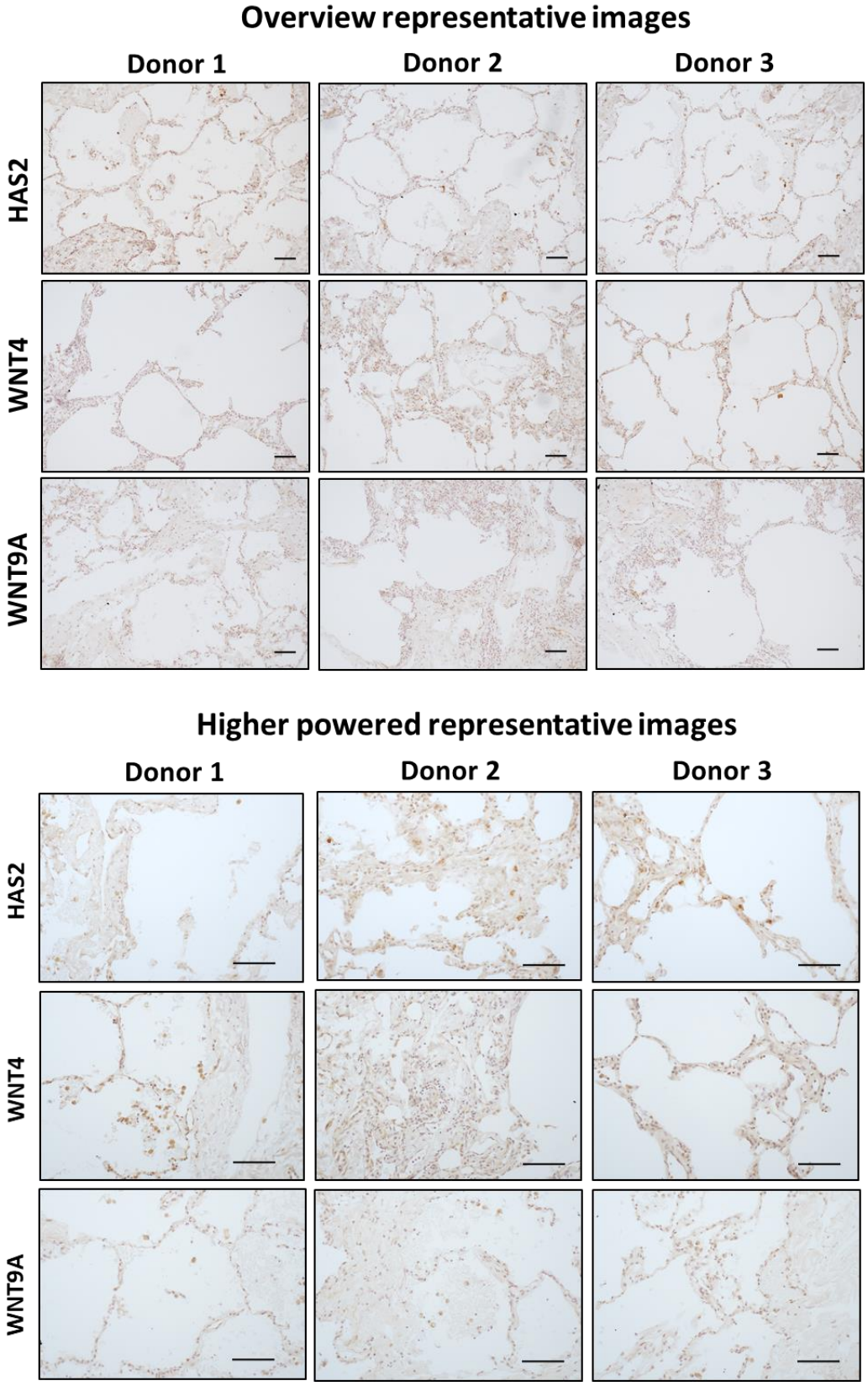

Figure 42: Histological validation of target proteins in PCLuS donor lungs Representative images of HAS2+, WNT4+ and WNT9+ cells in unused donor lung tissue used to generate PCLuS (scale bar= 100µm). Primary antibodies were used at the following dilutions: HAS2; 1/1000, WNT; 1/100 and WNT9A; 1/100.

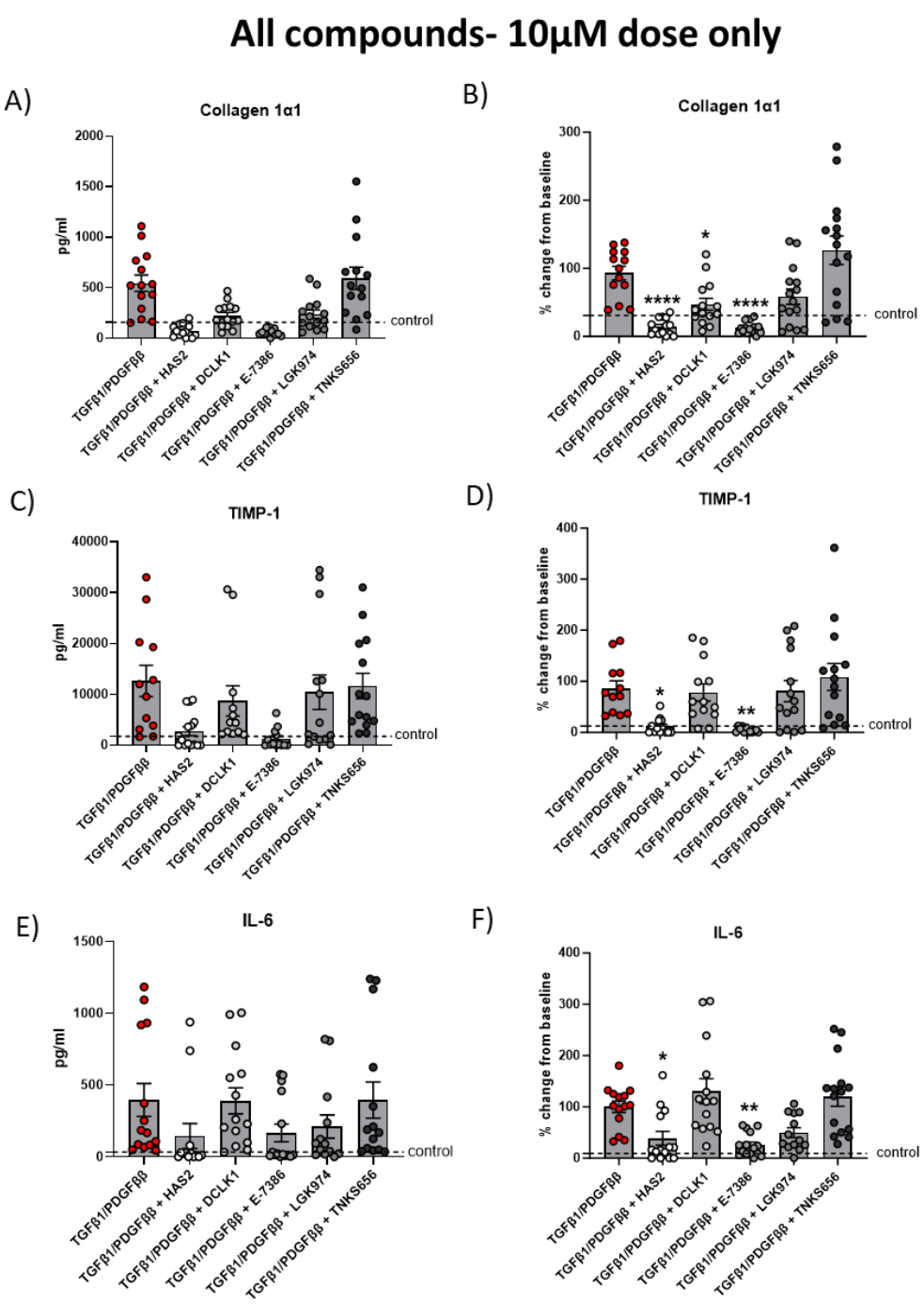

Figure 43: **Validation of candidate compounds in TGF-β1/PDGFββ-challenged unused donor PCLuS** PCLuS were generated from unused lung donor tissue (n=3 donors) with slices (n=5 per condition) being rested for 48 hours before challenge with either control media, a combination treatment of TGF-β1/PDGF-ββ alone or in combination with the highest dose of each of the candidate compounds (n=5 PCLuS per condition, n=3 donors, n=15 PCLuS total). Media, including all treatments, was refreshed at 24-hour intervals with conditioned media snap frozen for downstream analysis. Quantification of Collagen 1α1, TIMP-1 and IL-6 was performed on T144 media and plotted as A,C and E) absolute pg/ml and B,D and F)% change from baseline (TGF-β1/PDGFββ-challenged PCLuS) for all donors(n=5 conditioned media, n=3 donors, n=15 samples total). All data are mean ± SEM. Statistical significance was determined on graphs B, D and F using ANOVA with post-hoc Dunnett's test where TGF-β1/PDGFββ-challenged PCLuS was set as the control group (*p<0.05, **p<0.01, ***p<0.001, ****p<0.0001).

3.3.4.3 Interrogation of candidate compounds in IPF-derived PCLuS

To further interrogate these targets in pulmonary fibrosis, candidate compounds were assessed in PCLuS generated from IPF explant tissue (n=3 donors). One significant benefit of this system is the ability to test therapeutic agents in the presence of established fibrosis accumulated over a prolonged time period in human donors (typically 60+ yrs old). Once generated, post-rest PCLuS were challenged with either control media, standard of care compounds (Pirfenidone and Nintedanib) or ALK5i to confirm ability to modulate fibrosis in donor IPF tissue. Concurrently, PCLuS were challenged with 3 escalating doses of each candidate compound to assess the ability to modulate pre-existing fibrosis (Figure 44A). Media, including all treatments, was refreshed at 24-hour intervals with conditioned media snap frozen for downstream analysis before PCLuS were harvested for resazurin assay at 144hrs. Results showed that DCLK1, LGK974 and TNKS656 had no effect on tissue viability after 96hours challenge. HAS2-challenged PCLuS remained above the 70% threshold at all doses in Donor 2 and 3, but below 70% compared to control PCLuS in Donor 1. Similar to results from liver PCS, E-7386 appeared to impact tissue viability at the 1µm and 10µM dose in IPF tissue, but 0.1µM E-7386- challenged PCLuS maintained >70% metabolic activity in 2 of the 3 donors (Figure 44B).

Histological assessment of targets showed that HAS2, WNT4 and to a lesser extent WNT9A were present in all donor tissue prior to culture and appeared to localise to the epithelium and areas of dense inflammatory infiltrates (Figure 46). Next, quantification of soluble collagen 1α1, TIMP-1, IL-6 and IL-8 at the final timepoint of culture was performed to evaluate individual compound effect on fibrosis and inflammation. Using this panel of secreted markers, we established that Pirfenidone, Nintedanib and ALK5i all demonstrated strong anti-inflammatory and anti-fibrotic effects, providing a benchmark for candidate compounds (Figure 45). As expected, DCLK1 had no beneficial effect on IPF-derived PCLuS (Figure 47). Equally, TNKS656-challenged tissue showed no reduction in fibrotic markers, significantly increasing collagen 1α1, TIMP-1 and IL-6 at various doses, though IL-8 secretion showed a modest reduction at the 10µM dose ($p<0.05$; Figure 48). Conversely, inhibition of PORCN *via* 10µM LGK974 resulted in decreased expression of collagen 1α1 ($p<0.001$), TIMP-1 ($p<0.05$), IL-6 ($p<0.0001$) and IL-8 ($p<0.001$), though lower doses (1µM and 0.1µM) had no effect (Figure 49). Interestingly, E-7386-treated PCLuS showed a significant reduction in all markers at all doses. However, as the higher 1µM and 10µM doses were shown to negatively impact

metabolic activity, the reduction in soluble markers was likely due to decreased tissue viability (Figure 44B). Despite this, PCLuS challenged with 0.1µM E-7386 were highly efficacious, reducing secretion of collagen 1α1 ($p<0.0001$), TIMP-1 ($p<0.0001$), IL-6 ($p<0.0001$) and IL-8 ($p<0.05$) (Figure 50), whilst maintaining >70% metabolic activity in two of the three donors (Fig 44B). Finally, we found that HAS2 was able to significantly reduce collagen 1α1 ($p<0.0001$) and IL-8 (300µM [$p<0.001$], 500µM and 1000µM [$p<0.0001$]) at all doses, whilst also strongly reducing TIMP-1 and IL-6 at the highest dose ($p<0.0001$) (Figure 51).

These data confirmed that 1000µM HAS2 (87% reduction compared to control PCLuS) and 0.1µM E-7386 (86% reduction compared to control PCLuS) were able to significantly reduce the amount of collagen 1α1 secretion more than clinically available standard of care compounds Pirfenidone (71% reduction compared to control PCLuS) and Nintedanib (52% reduction compared to control PCLuS) in IPF-derived PCLuS, though further work is required to determine dose-response curves. Similarly, 1000µM HAS2 (56% reduction compared to control PCLuS) and 0.1µM E-7386 (73% reduction compared to control PCLuS)- challenged PCLuS reduced TIMP-1 secretion more than Pirfenidone (32% reduction compared to control PCLuS) and Nintedanib (55% reduction compared to control PCLuS) -challenged PCLuS. Evaluation of pro-inflammatory markers further showed that 1000µM HAS2 (75% reduction IL-6 and 79% reduction IL-8), 0.1µM E-7386 (73% reduction IL-6 and 36% reduction IL-8) and 10µM LGK974 (70% reduction IL-6 and 56% reduction IL-8), demonstrated considerable anti-inflammatory properties, though failed to surpass the efficacy of Pirfenidone (75% reduction IL-6 and 83% reduction IL-8), which has clinically proven anti-inflammatory effects in IPF patients.

A)

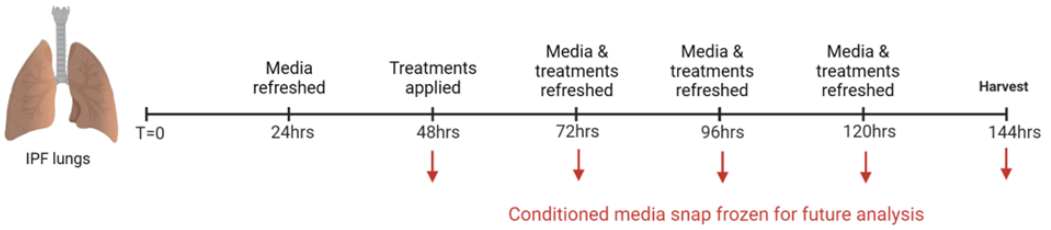

B)

	HAS2			DCLK1			E-7386			LGK974			TNKS656		
% of ctrl	300µM	500µM	1000µM	0.1µM	1µM	10µM	0.1µM	1µM	10µM	0.1µM	1µM	10µM	0.1µM	1µM	10µM
IPF Donor 1	61	63	63	106	103	92	75	68	62	93	77	77	73	80	82
IPF Donor 2	94	94	73	111	91	104	78	60	61	110	95	93	110	95	93
IPF Donor 3	70	79	83	143	147	159	65	62	56	125	118	108	126	126	155

Figure 44: Validation of IPF-derived PCLuS A) PCLuS were generated from explant IPF tissue (n=3 donors) with slices (n=10 per condition) being rested for 48 hours before challenge with either control media, standard of care compounds Pirfenidone (2.5mM) and Nintedanib (2.5µM) or ALK5i (10µM) to blunt fibrosis (n=10 PCLuS per condition). Concurrently, PCLuS were challenged with 3 escalating doses of each candidate compound to assess the ability to reduce pre-existing fibrosis (n=10 PCLuS per condition, n=3 donors, n=30 PCLuS total). Media, including all treatments, was refreshed at 24-hour intervals with conditioned media snap frozen for downstream analysis before PCLuS were harvested at 144hrs for resazurin assay to quantify metabolic activity. B) Resazurin assay performed at T144 presented as the average % of control for n=10 slices per treatment for each donor (green values indicate resazurin values ≥70% of control, yellow/orange 50-69% of control and red <50% of control).

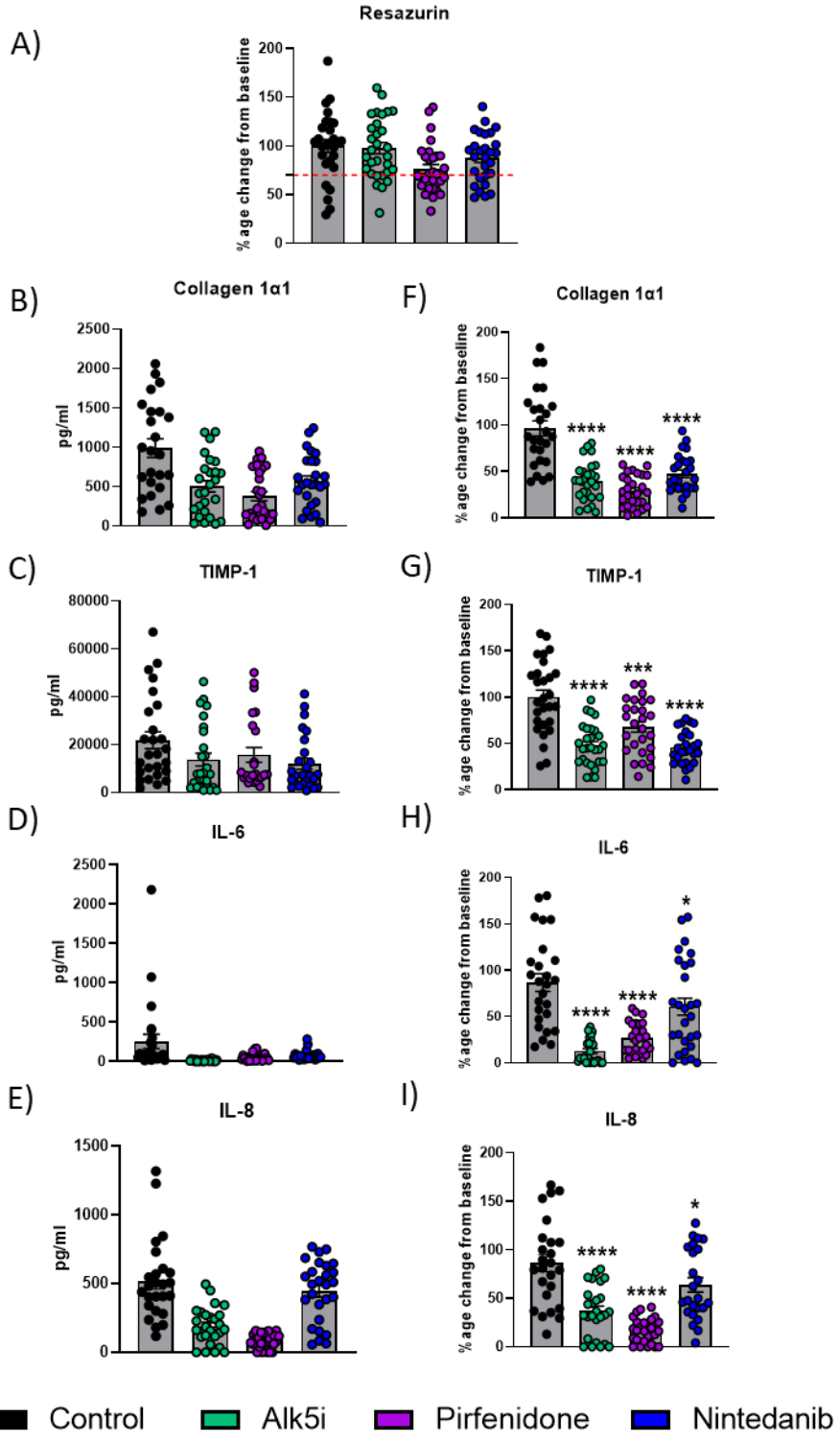

Figure 45: Validation of IPF-derived PCLuS Quantification of A) Resazurin (where red dashed line represents arbitrary 70% viability threshold) Collagen 1α1, TIMP-1, IL-6 and IL-8 was performed on T144 media and plotted as B-E) absolute pg/ml and F-I) % change from baseline (control PCLuS) for all donors (n=10 conditioned media, n=3 donors, n=30 samples total) to confirm tissue could be effectively modulated. All data are mean ± SEM. Statistical significance was determined on graphs F-I using ANOVA with post-hoc Dunnett's test where unchallenged PCLuS was set as the control group (*p<0.05, **p<0.01, ***p<0.001, ****p<0.0001).

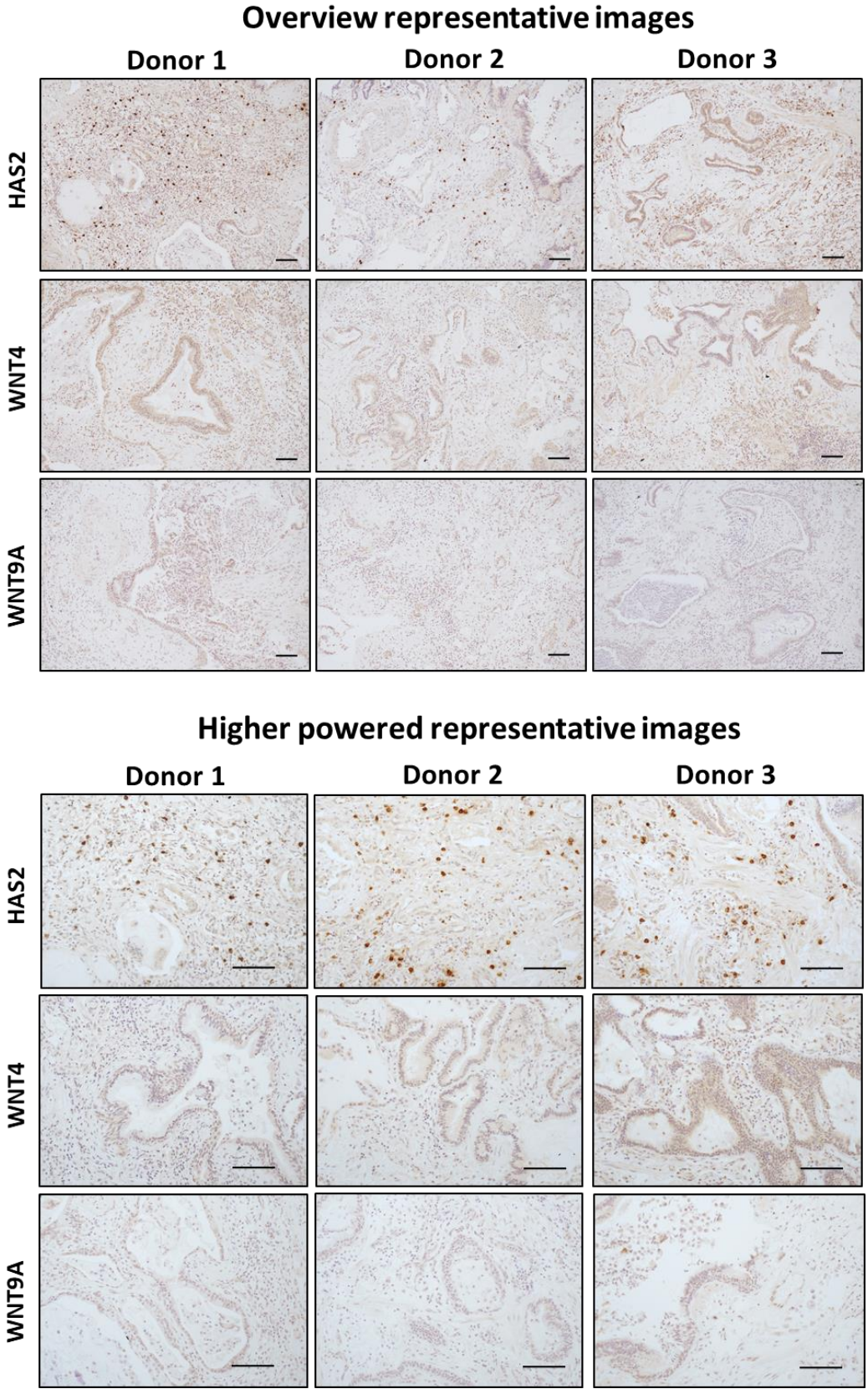

Figure 46: Histological validation of target proteins in PCLuS IPF lungs Representative images of HAS2+, WNT4+ and WNT9+ cells in IPF explant tissue used to generate PCLuS (scale bar= 100µm). Primary antibodies were used at the following dilutions: HAS2; 1/1000, WNT; 1/100 and WNT9A; 1/100.

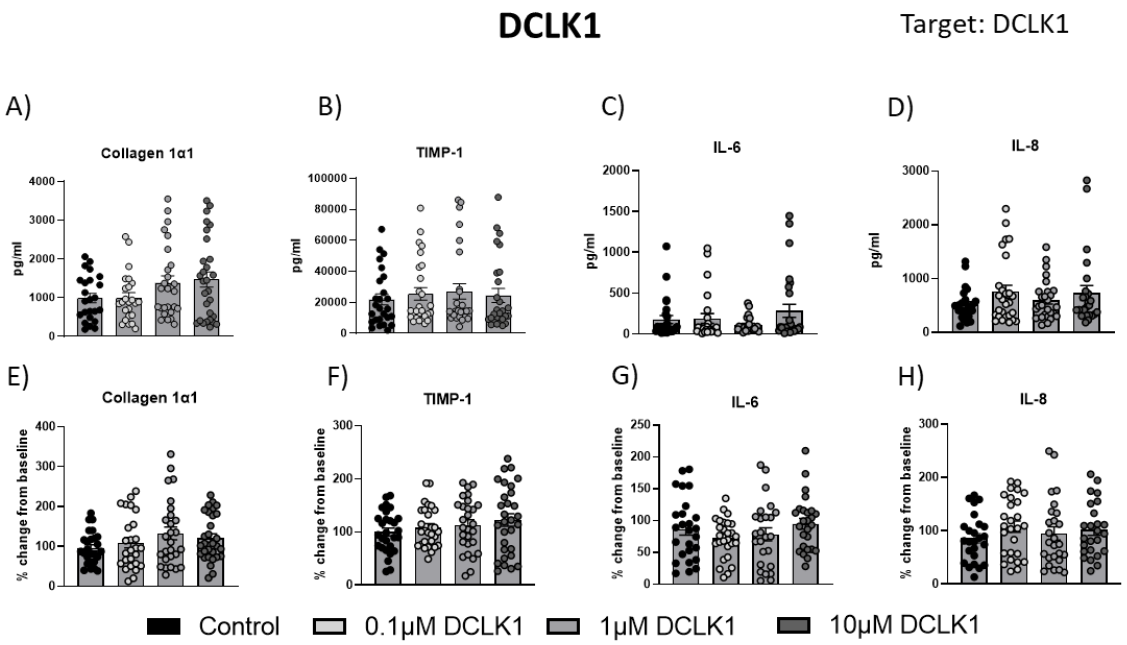

Figure 47: Validation of DCLK1 compound in IPF-derived PCLuS PCLuS were generated from explant IPF tissue (n=3 donors) with slices (n=10 per condition) being rested for 48 hours before challenge with either control media, or 3 escalating doses of DCLK1 compound to assess the ability to reduce pre-existing fibrosis (n=10 PCLuS per condition, n=3 donors, n=30 PCLuS total). Media, including all treatments, was refreshed at 24-hour intervals with conditioned media snap frozen for downstream. Quantification of Collagen 1α1, TIMP-1, IL-6 and IL-8 was performed on T144 media and plotted as A-D) absolute pg/ml and E-H) % change from baseline (control PCLuS) for all donors (n=10 conditioned media, n=3 donors, n=30 samples total). All data are mean ± SEM. Statistical significance was determined on graphs E-H using ANOVA with post-hoc Dunnett's test where unchallenged PCLuS was set as the control group (*p<0.05, **p<0.01, ***p<0.001, ****p<0.0001).

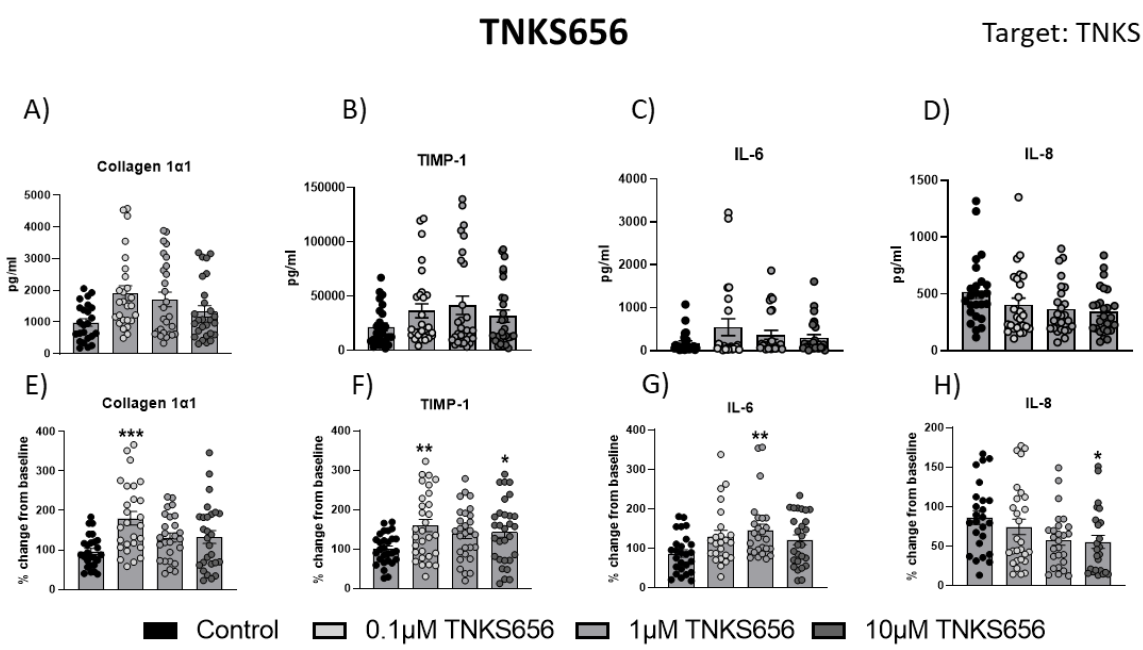

Figure 48: Validation of TNKS656 compound in IPF-derived PCLuS PCLuS were generated from explant IPF tissue (n=3 donors) with slices (n=10 per condition) being rested for 48 hours before challenge with either control media, or 3 escalating doses of TNKS656 compound to assess the ability to reduce pre-existing fibrosis (n=10 PCLuS per condition, n=3 donors, n=30 PCLuS total). Media, including all treatments, was refreshed at 24-hour intervals with conditioned media snap frozen for downstream analysis. Quantification of Collagen 1α1, TIMP-1, IL-6 and IL-8 was performed on T144 media and plotted as A-D) absolute pg/ml and E-H) % change from baseline (control PCLuS) for all donors (n=10 conditioned media, n=3 donors, n=30 samples total). All data are mean ± SEM. Statistical significance was determined on graphs E-H using ANOVA with post-hoc Dunnett's test where unchallenged PCLuS was set as the control group (*p<0.05, **p<0.01, ***p<0.001, ****p<0.0001).

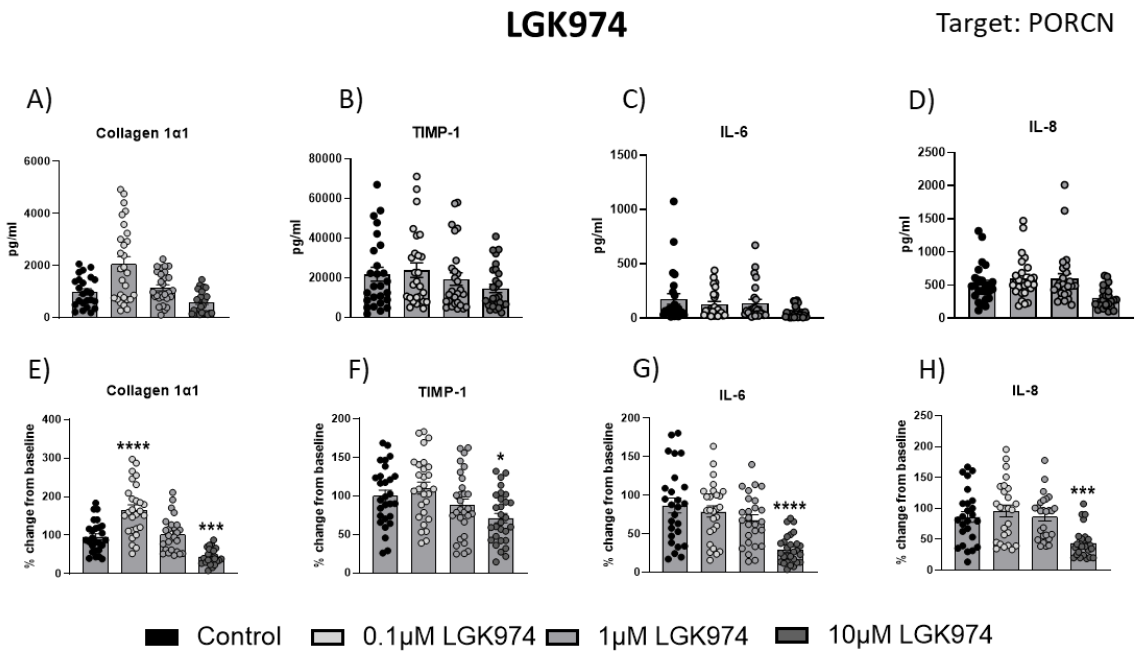

Figure 49: Validation of LGK974 compound in IPF-derived PCLuS PCLuS were generated from explant IPF tissue (n=3 donors) with slices (n=10 per condition) being rested for 48 hours before challenge with either control media, or 3 escalating doses of LGK974 compound to assess the ability to reduce pre-existing fibrosis (n=10 PCLuS per condition, n=3 donors, n=30 PCLuS total). Media, including all treatments, was refreshed at 24-hour intervals with conditioned media snap frozen for downstream. Quantification of Collagen 1α1, TIMP-1, IL-6 and IL-8 was performed on T144 media and plotted as A-D) absolute pg/ml and E-H) % change from baseline (control PCLuS) for all donors (n=10 conditioned media, n=3 donors, n=30 samples total). All data are mean ± SEM. Statistical significance was determined on graphs E-H using ANOVA with post-hoc Dunnett's test where unchallenged PCLuS was set as the control group (*p<0.05, **p<0.01, ***p<0.001, ****p<0.0001).

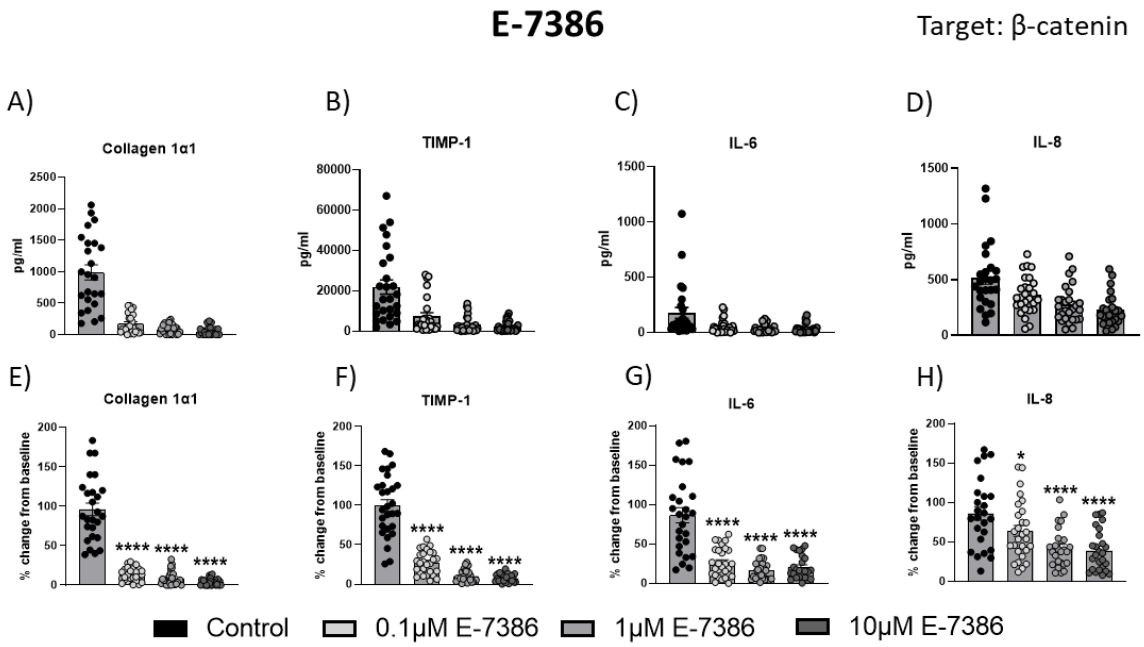

Figure 50: Validation of E-7386 compound in IPF-derived PCLuS PCLuS were generated from explant IPF tissue (n=3 donors) with slices (n=10 per condition) being rested for 48 hours before challenge with either control media, or 3 escalating doses of E-7386 compound to assess the ability to reduce pre-existing fibrosis (n=10 PCLuS per condition, n=3 donors, n=30 PCLuS total). Media, including all treatments, was refreshed at 24-hour intervals with conditioned media snap frozen for downstream. Quantification of Collagen 1α1, TIMP-1, IL-6 and IL-8 was performed on T144 media and plotted as A-D) absolute pg/ml and E-H) % change from baseline (control PCLuS) for all donors (n=10 conditioned media, n=3 donors, n=30 samples total). All data are mean ± SEM. Statistical significance was determined on graphs E-H using ANOVA with post-hoc Dunnett's test where unchallenged PCLuS was set as the control group (*p<0.05, **p<0.01, ***p<0.001, ****p<0.0001).

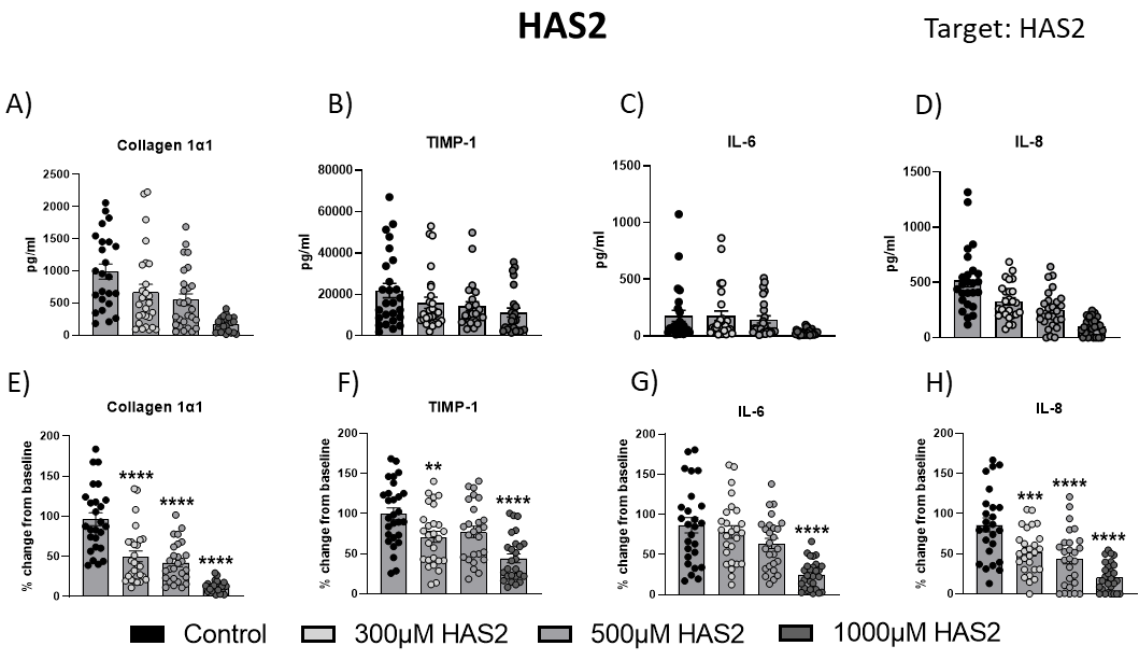

Figure 51: Validation of HAS2 compound in IPF-derived PCLuS PCLuS were generated from explant IPF tissue (n=3 donors) with slices (n=10 per condition) being rested for 48 hours before challenge with either control media, or 3 escalating doses of HAS2 compound to assess the ability to reduce pre-existing fibrosis (n=10 PCLuS per condition, n=3 donors, n=30 PCLuS total). Media, including all treatments, was refreshed at 24-hour intervals with conditioned media snap frozen for downstream analysis. Quantification of Collagen 1α1, TIMP-1, IL-6 and IL-8 was performed on T144 media and plotted as A-D) absolute pg/ml and E-H) % change from baseline (control PCLuS) for all donors (n=10 conditioned media, n=3 donors, n=30 samples total). All data are mean ± SEM. Statistical significance was determined on graphs E-H using ANOVA with post-hoc Dunnett's test where unchallenged PCLuS was set as the control group (*p<0.05, **p<0.01, ***p<0.001, ****p<0.0001).

3.4 Discussion

The rising prevalence of fibrosis represents a growing healthcare challenge on a global scale [340,341]. Consequently, discovery of key therapeutic targets with relevance to human fibrotic disease and development of effective anti-fibrotic therapies directed against these targets continues to be a priority. However, complex disease heterogeneity and cellular diversity remains a significant obstacle to understanding disease pathomechanisms. Conventional 2D cell culture assays and widely used mouse models often fail to recapitulate these features, impeding translatability of findings to clinical application [273]. To overcome these challenges, we leveraged the expertise of Neil Henderson's group in single-nuclei sequencing, with our own experience in the generation of precision cut slices from human tissue. These cutting-edge tools offered a more comprehensive exploration of fibrosis in the context of human disease, overcoming many of the limitations of traditional methodologies.

To examine the intricate cellular landscape during liver fibrosis, colleagues at Edinburgh University generated snRNAseq datasets from human liver samples, selected to represent the transitions of healthy liver tissue to MASH (F1–F4 fibrosis stage) through to end-stage cirrhosis, using the 10× Genomics Chromium platform. Given the pivotal role of mesenchymal cells in orchestrating the fibrotic response [342], we prioritised the sub clustering of mesenchymal cells for further interrogation. This approach identified a distinct population of disease-associated, collagen I high producing myofibroblasts with specific molecular signatures. From this, 9 targets of interest were selected for validation in our precision-cut slice system.

Firstly, we utilised established protocols of fibrogenic induction *via* combination treatment of TGFβ-β1/PDGFββ to evaluate gene and protein expression of targets during fibrogenesis [292,343]. Results confirmed that six of the identified target genes were significantly upregulated in response to fibrogenic stimuli and could be attenuated by co-treatment with ALK5i, suggesting they may be upregulated during fibrogenesis. However, no changes in target protein expression were observed in either tissue homogenates or conditioned media after pro-fibrotic challenge. This could be explained by the limited culture period, as PCLS were challenged with fibrotic stimuli for 72 hours, it is possible that a longer culture time would be needed for the proteins to accumulate and exert its function. Similarily, post translational modifications arising from TGF-β1/PDGFββ treatment may impact protein turnover rate.

When evaluating target protein expression, it is also important to consider the abundance of target cell populations present in the liver tissue. As mesenchymal cells (excluding VSMCs) made up <2% of the snRNAseq datasets, it is expected that disease-associated myofibroblasts would similarly make up a small percentage of PCLS cellular composition. Consequently, if target protein upregulation was limited to this small cellular subpopulation, it could explain no effect being observed overall in whole tissue. To investigate this further, future work could employ flow cytometry or multi-plex imaging to determine target protein expression in distinct cell types. Additionally, single-cell technologies could be used to confirm cellular composition of PCLS donor tissue before and after culture.

Having confirmed that targets could be detected and modulated in our PCLS system, we next evaluated anti-fibrotic and anti-inflammatory properties of 5 candidate inhibitory compounds targeting DCLK1, HAS2 and different components of the WNT signalling pathway (β-catenin, porcupine and tankyrase). Furthermore, as several of these targets were also upregulated in fibroblasts populations of fibrotic lung disease, we utilised our ability to generate PCS from unused donor lung and IPF explant tissue to determine whether these targets were common to other fibrotic diseases or organ specific.

Wnt signalling is a conserved pathway critical during development and tissue homeostasis, aiding regulation of cell proliferation, differentiation, and apoptosis [344]. The family of Wnt ligands, consisting of 19 distinct secreted glycoproteins, exhibits diverse specificities for various receptors and co-receptors resulting in activation of canonical (β-catenin-dependent) or non-canonical (β-catenin-independent) Wnt signalling pathways [345]. In order to exert their signalling effects, Wnt ligands are required to undergo extensive post translational modifications due to their hydrophobic nature [346]. Consequently, lipid modification termed palmitoylation (the addition of palmitic acid) is mediated by porcupine (a multipass transmembrane protein) in the endoplasmic reticulum, before transport to the cell surface and binding to cognate receptors [347,348]. Assessment of compounds targeting the Wnt signalling pathway confirmed that inhibition of β-catenin (*via* E-7386) and porcupine (*via* LGK974) caused a significant reduction in pro-fibrotic and pro-inflammatory markers in both liver and lung-derived PCS at various doses. These findings were consistent with a growing body of evidence which has highlighted aberrant Wnt signalling as a key driver of fibrosis in multiple organs, including kidney, skin, heart, liver and lungs [339,349-351]. To date, studies

have primarily focused on β-catenin activity, identifying increased expression in several diseases including pulmonary and liver fibrosis [352-354]. Here, sustained activation of Wnt/β-catenin signalling is associated with increased production of ECM components, including collagen, and fibroblast-myofibroblast differentiation [355,356]. Consistent with our findings, modulation of Wnt signalling has been shown to be extremely effective in attenuating fibrosis in mouse models of lung, kidney and liver fibrosis [356-358]. For example, targeted inhibition of Wnt/β-catenin signalling *via* ICG-001 (a peptidomimetic small molecule inhibitor), resulted in reduced mesenchymal-myofibroblast transition, matrix gene expression and cell apoptosis after bleomycin treatment [355]. Similarily, Akcora *et al* showed that inhibition of Wnt/β-catenin signalling *via* ICG-001 significantly attenuated collagen accumulation and HSC activation in CCl_4-induced acute liver injury models [356].

However, given that β-catenin activity can be influenced by several factors [359], it remains unclear whether increased Wnt signalling observed in fibrosis is driven by specific Wnt ligands. Our work suggests that Wnt4 and Wnt9a may be involved in stimulating fibrogenesis in the liver. Though these ligands have not been studied extensively in the context of fibrosis, there is some evidence that they may regulate β-catenin activity. For example, work by Yin *et al* outlined a clear link between Wnt4, β-catenin/NF-κB activation, and pro-fibrotic signalling in both *in vitro* and *in vivo* models of cardiac fibrosis [360]. Utilising both genetic and pharmacological manipulation, work showed that elevated levels of Wnt4 resulted in increased β-catenin/NF-kB activation and pro-fibrotic markers, and that targeted inhibition of Wnt4 could negate these effects. Similarily, work by Surendran *et al* found that in a mouse model of renal fibrosis, Wnt4 expression increased primarily in collagen 1α1, αSMA producing myofibroblasts, and was reported to induce stabilisation of cytosolic β-catenin [361]. As we were unable to inhibit Wnt4 and Wnt9a directly in this study, future work should aim to evaluate the specific contribution of these ligands to fibrosis initiation and progression.

At present, the number of clinical trials investigating the therapeutic potential of targeting the Wnt signalling pathway to treat fibrotic diseases remains limited. In the liver, a recent phase 1/2a open-label, non-randomised, multi-centre clinical trial (study no: NCT03620474) found that intravenous administration of the CBP/β-catenin inhibitor PRI-724 in patients with hepatitis C and B virus-induced liver cirrhosis was well tolerated and resulted in statistically significant reduction in liver stiffness, Model for End-stage Liver Disease (MELD) score and

serum albumin level after 12 weeks of treatment. However, evaluation of patient biopsies obtained at screening and within 2 weeks of final treatment showed no significant reduction in fibrosis in response to PRI-724 as assessed by ordinal scoring systems (e.g. Ishak-modified histology activity index [362]) and further evaluation of anti-fibrotic effects in patients with cirrhosis is therefore warranted [363]. Though limited in regards to fibrotic disease, several clinical trials are currently underway to investigate the effect on Wnt signalling pathway inhibition for the treatment of a range of cancers [364]. For example, E-7386 (which was screened for anti-fibrotic efficacy during this project) is currently being evaluated in phase 1 clinical trials in patients with advanced solid tumours (study no: NCT03833700) and in advanced neoplasms (study no: NCT03264664) with initial dose-escalation studies reporting preliminary safety and tolerability of 120mg twice daily oral administration [365]. Similarily, a recent dose-escalation phase 1 study of LGK974 in patients with advanced solid tumours (study no: NCT01351103) found that LGK974 treatment was generally well tolerated, with preliminary biomarker analyses also suggesting a potential effect on immune cell recruitment to tumours, though further validation in a larger cohort would be required [366]. Interestingly, results from work carried out in this project found that co-treatment of IL1α-challenged PCLS with LGK974 was able to significantly reduce IL-6 secretion at the highest dose. Additionally, LGK974-challenge to IPF-derived PCLuS was able to effectively blunt pro-inflammatory IL-6 and IL-8 secretion at the highest dose, suggesting that LGK974 may be involved in modulating immune cells. These results are in keeping with previous reports in the literature which have shown that LGK974 is able to suppress inflammatory responses in several pre-clinical models. For example, Jang *et al* recently showed that pre-treatment with LGK974 was able to blunt an lipopolysaccharide (LPS)-induced inflammatory response in bronchial epithelial cells [367] as well as an LPS-induced endotoxaemia in a mouse model of sepsis [368]. Here, LGK974 was found to suppress LPS-induced cytokine production by reducing the crosstalk between Wnt/β-catenin and NF-κB pathways during endotoxaemia. Taken together, these results suggest that, providing the candidate compounds meet the required safety and tolerability endpoints during clinical trials, that these drugs may be repurposed for treatment of fibrotic diseases in the future to investigate potential anti-fibrotic effects.

Hyaluronan synthase 2 (HAS2) plays a central role in the production of hyaluronan (HA), a component of the ECM, which has been implicated in the development fibrosis [369]. Though

the role of HAS2 in diseases such as cancer and fibrosis has been well studied, it often relies heavily on the use of *in vitro* an *in vivo* mouse models, with little data generated from human tissue [370-373]. In this study, we provided evidence that HAS2 was transcriptionally upregulated in disease-associated myofibroblasts and in human liver-derived PCLS in response to TGF-β1/PDGFββ stimulation. Additionally, we showed that modulation of HAS2 had significant anti-fibrotic and anti-inflammatory effects in early-fibrosis models in the liver and lung, as well as in established fibrotic pulmonary disease. These results were in line with previous reports that inhibition of hyaluronan synthesis (*via* 4-MU) prevents liver fibrosis progression in mouse models of liver injury [369,370]. Consistent with this, work by Halimani *et al* recently showed that in addition to pharmacological inhibition of HAS2 *via* 4-MU, genetic knockdown of HAS2 utilising targeted siRNA was able to significantly blunt collagen and HA deposition in mouse models of CCl_4-induced liver injury, as well as significantly reducing biochemical markers of hepatic damage [374]. Furthermore, transcriptomic analysis revealed that siRNA-mediated HAS2 knockdown was associated with attenuation of ECM-associated pathways, suggesting that HAS2 inhibition may be an important therapeutic target for the treatment of hepatic fibrosis. Though previous work has identified a key role for HAS2 promoting HSC activation [370,375], investigation into HAS2 in other mesenchymal cell populations is limited. In contrast to these findings, we report that HAS2 was upregulated specifically in myofibroblast populations, but not HSCs. Interestingly, a recent study by Vollman *et al* similarly reported that HAS2 was overexpressed in myofibroblasts during CCl_4-induced liver fibrosis. In this study, unbiased siRNA-formulated lipid nanoparticles (LNP) screening identified HAS2 as one of five pro-fibrotic genes present in myofibroblasts that were responsible for modulating fibrogenesis and collagen accumulation during CCl_4-induced liver injury [376].

In the context of the lung, reduction of pro-fibrotic and inflammatory markers in response to treatment with our HAS2 inhibitor in PCLuS was consistent with previous mechanistic studies by Li *et al* [4]. Here, results showed that HAS2 overexpression in myofibroblasts was associated with an aggressive, invasive fibroblast phenotype leading to severe lung fibrosis and death in bleomycin-induced injury models. Conversely, conditional knockdown of HAS2 in mesenchymal cells attenuated myofibroblast invasiveness and accumulation and prevented the development of pulmonary fibrosis [4]. In a follow up study, Li *et al* further showed that

deletion of HAS2 in mesenchymal cells increased cellular senescence of fibroblasts, suggesting that HAS2 may be a critical regulator of pulmonary fibrosis [377]. These data suggest that HAS2 overexpression in myofibroblasts plays a key role in fibrosis progression in both the liver and the lung. At present, there are no clinically approved drugs which specifically target HA for the treatment of fibrotic disease. However, Hymecromone (also known as 4-methylumbelliferone [4-MU]), is an oral drug (which inhibits HA production by decreasing HAS2/HAS3 expression) currently approved for use in Europe and Asia exclusively for the treatment of biliary spasm [378]. Though this drug has not currently been trialled in patients with fibrotic disease, a recent open-label, single-centre, dose-response study of Hymecromone in healthy adults (study no: NCT02780752) found that treatment was well tolerated and also resulted in a significant reduction in sputum HA levels after 4 days, suggesting that this drug could potentially be repurposed for the treatment of other diseases [379]. Interestingly, HAS2 has also been found to be upregulated in the lungs during acute respiratory distress syndrome [380] and in patients with severe COVID-19 [381], where HA exudates were predominantly found obstructing alveoli and in thickened perialveolar interstitium [382]. These findings were supported by Yang *et al* who similarly reported that HA was increased in patients with pulmonary lesions and significantly correlated to the clinical parameters used to predict COVID-19 severity, including lymphocytes, C-reactive protein and fibrinogen [383]. Moreover, treatment with Hymecromone was shown the promote recovery of lymphopenia, decrease CRP and fibrinogen elevation and accelerate pulmonary lesion abruption in COVID-19 patients (study no: NCT05386420). Taken together, these results suggest that targeted inhibition of HAS2 *via* 4-MU or other therapeutic interventions may be beneficial for the treatment of fibrotic diseases having demonstrated preliminary safety and tolerability in clinical trials and the treatment of other conditions, therefore warranting further investigation.

Despite Wnt signalling and HAS2 having been previously implicated in fibrosis, there is limited information available on how these two targets relate to each other in disease. In models of cutaneous wound repair, Wnt ligands have been shown to upregulate HAS2 in embryonic fibroblasts [384]. Likewise, there is evidence in FGF9-deficient mouse models that FGF9 promotes HAS2 expression *via* the Wnt/β-catenin signalling pathway [385]. While these studies suggest a potential link between Wnt signalling and increased HAS2 expression, further work is required to elucidate the precise molecular mechanisms and the extent of their involvement

during fibrogenesis. It is also possible that Wnt signalling may act indirectly on HAS2 through interactions with other signalling pathways involved in fibrosis, such as TGF-β1 [386].

By utilising small molecule inhibitors in our PCS system, we were able to modulate target expression across various tissues. Additionally, we were able to explore dose-dependent effects in response to different stimuli and validate efficacy. However, there are several constraints to consider when interpreting experimental outcomes. For example, small molecule inhibitors may lack specificity, affecting not only the target protein but also other structurally similar proteins, potentially resulting in off-target effects [387]. Likewise, incomplete target inhibition, driven by factors such as drug half-life, metabolism and tissue distribution, can pose challenges in sustaining the desired effect over extended periods [388]. Some inhibitors may also have limited penetration into certain tissues/organs or may struggle to permeate cell membranes, limiting their effectiveness in reaching intracellular targets. One of the main limitations of this work was the inability to selectively inhibit the targets of interest in myofibroblast populations in PCS. Consequently, future work should consider the use of RNA interference or gene editing tools in combination with viral vectors (such as adeno-associated virus (AAV)s or lentivirus), neutralising antibodies or lipid nanoparticle (LNP) technology to achieve targeted inhibition and reduce off-target effects.

When interpreting experimental results involving small molecule inhibitors, it is important to consider the half maximal inhibitory concentration (IC50) of each compound screened in this project due to potential off-target effects and/or toxicity (as detailed in Table 9). Low IC50 value indicate that the drug is potent at low concentrations and will therefore be less likely to cause systemic toxicity when administered to patients [389]. Several of the compounds used to inhibit targets of interest in this work are reported to have low IC50 values. For example, E-7386 is reported to have an IC50 value of 48.4nM in HEK293 cells [390]. Similarily, DCLK1-in-1 has been shown to potently inhibit DCLK1 and DCLK2 kinases at low treatment doses in binding assays (IC50: DCLK1=9.5nM and DCLK2=31nM), kinase assays (IC50: DCLK1=57.2nM and DCLK2=103nM) and cellular assays (IC50: DCLK1=279nM in HCT116 cells) [391]. LGK974 has been reported to have an IC50 value of 1nM in radioligand binding assays and showed no major cytotoxicity in cells up to 20μM. Furthermore, LGK974 demonstrated comparable inhibitory activities against different Wnt ligands (Wnt1, -2, -3, -3A, -6, -7A, and -9A) in Wnt-dependent reporter assays, with IC50 values ranging from 0.05-2.4nM [392]. Finally, NVP-

TNKS656 has an IC50 value of 6nM in cell-free assays [393]. Taking these reported IC50 values into consideration in the context of this study, it would be reasonable to assume that the doses used in this study (0.1µM, 1µM and 10µM), particularly the highest 10µM dose, could potentially results in off-target inhibition and increased risk of higher systemic exposure in patients, if complete on-taget inhibition is achieved at much lower drug concentrations. However, traditional experiments to determine the IC50 curves for drugs are typically performed in 2D monolayer cell cultures and/or cell-free assays. Additionally, IC50 values can vary considerably dependent on the cell line and/or model system used [394], with values provided by suppliers typically generated from 2D cell culture models utilising various cell lines. For example, ALK5i (or SB525334) which was treated at 10µM in PCS in this study, is reported to have nanomolar potency with an IC50 value of 14.3nM in a cell-free kinase assay [395]. Consequently, treatment at the 10µM dose could potentially result off-target effects on other kinases such as ALK4 which is reported to also be inhibited by SB25334 with an IC50 value of 58.5nM in kinase assays (SB25334 inhibited ALK2, ALK3 and ALK6 with >1000-fold less selectivity over ALK5, requiring >10µM dose to achieve 50% inhibition) [395], rather than the specific inhibition of the intended fibrotic pathways. However, utilising cell-based assays, Mercer *et al* reported an IC50 value of 200.5nM for inhibition of TGF-β1- induced collagen deposition with the same drug in primary lung fibroblasts and similarly used 10µM SB525334 as a positive control in IPF–derived PCLuS [294]. Likewise, 10µM SB525334 has previously been used by Paish *et al* in liver-derived PCS as a positive control in early fibrogenesis models [292]. Conversely, the HAS2i used in this study (4-MU) is a substrate analogue for HAS2 which outcompetes the natural substrate but requires a high concentration to achieve inhibition, with a reported IC50 of 400µM, resulting in treatment doses of 30µM, 100µM, 300µM, 500µM and 1000µM.

Importantly, there are a number of discrepancies between 2D *in vitro* cell cultures and more complex 3D models to consider when extrapolating reported *in vitro* IC50s from monolayer cell culture systems. It has been widely reported that, with respect to drug efficacy and sensitivity, many drugs display enhanced potency in 2D cell culture systems when directly compared with 3D models [396,397] suggesting that predicted clinical efficacy in patients is often overestimated [398]. For example, a recent study by Nowacka *et al* investigating cytotoxic drug resistance of the same cell lines in 2D and 3D cell culture models found a nearly

ten-fold difference in IC50 values, with spheroids requiring a higher concentration of Cisplatin and Paclitaxel to achieve the same level of inhibition in 3D than 2D [399]. Similarily, cytotoxic therapies for the treatment of pancreatic ductal adenocarcinoma (such as Gemcitabine and Oxaliplatin) were found to require 200-fold greater doses to achieve the same IC50 value in spheroids compared to monolayer cultures [400]. These differences could be explained by differences in cell density, proliferation rate, ECM proteins as well as the ability of small molecule inhibitors to penetrate and diffuse into the spheroid and drug mechanisms of action [389]. Given that PCS models are considerably more complex than spheroids, with multiple cell types and established ECM scaffolds and that PCS can retain enzymatic activity that metabolises drugs [401], possibly reducing its effective concentration and leading to a higher IC50, it can be reasonably concluded that the IC50 of a drug will differ significantly between PCS and *in vitro* cell cultures. Consequently, additional screening of candidate compounds at lower doses and additional titrations is advised to obtain a more accurate measurement of IC50 values in *ex vivo* PCS directly rather than estimates from 2D models.

Taken together, our findings provide potential therapeutic targets for the treatment of MASH and further our understanding of the molecular mechanisms underpinning liver fibrosis onset and progression. Furthermore, evaluation of targets in lung tissue confirmed multi-organ efficacy, suggesting these may be common fibrogenic regulators. Future work will aim to investigate the precise contribution of this disease-associated myofibroblast population to disease progression, as well as optimisation of gene editing and delivery tools to investigate these targets selectively in PCS.

4 Utilising an unbiased ‘omics approach to identify therapeutic targets in regional IPF samples

Statement of contribution

- Tissue processing and RNA isolation was performed by the author before sample processing, cDNA library preparation and sequencing was performed at Newcastle University’s Genomics Core facility.
- Dr Laura Sabater performed downstream bioinformatics processing of transcriptomic datasets, generation of transcriptomic PCA plots and IPA analysis.
- Dr Sandra Murphy performed mass spectrometry and downstream bioinformatics analysis, including generation of PCA plots.
- Investigation of targets of interest in a pre-existing scRNAseq datasets generated from 6 integrated single cell lung atlases was performed by Dr Stephen Christensen (Figure 104).
- All other work in this chapter, including histological validation, multi-plex ELISA, further processing of datasets to identify targets of interest, generation of bar charts, Venny diagrams, all volcano plots and heat maps was performed solely by the author.

4.1 Introduction

Idiopathic Pulmonary Fibrosis (IPF) is a devastating progressive lung disease characterised by the excessive accumulation of scar tissue within the lungs, resulting in impaired pulmonary function and eventual respiratory failure [402,403]. IPF is the most common and lethal interstitial lung disease, with a median survival rate of 3-5 years after diagnosis, a prognosis worse than many cancers [113]. Currently, the number of IPF patients is estimated at between 2.8-9.3 cases per 100 000, with average onset occurring around 65 years and predominantly affecting older males [115]. Globally, patient numbers are steadily rising in line with an ageing population, particularly in developed countries, posing a significant socioeconomic burden [116]. Despite this, substantial strides in our understanding of IPF are yet to be made and the underlying aetiology of disease remains to be fully elucidated.

At present there is no cure for IPF, treatment options are scarce with lung transplantation remaining the only viable intervention to increase life expectancy. However, due to limited availability of donor organs and stringent suitability criteria, only a small minority of IPF patients will be eligible to undergo transplantation [404]. Treatment strategies are therefore primarily focused on slowing disease progression and alleviating patient discomfort. Pirfenidone and Nintedanib, both approved first-line therapies for IPF, have demonstrated the ability to reduce the rate of decline in FVC and improve progression-free survival in some patients [405,406]. Despite this, both anti-fibrotics have considerable limitations with approximately 50% of patients deemed unsuitable for treatment [407]. In those which do receive treatment, efficacy is highly varied and impact on long-term survival is negligible. Moreover, a significant portion of patients experience adverse effects, such as gastrointestinal symptoms, which leads to treatment discontinuation in up to a third of cases [406,408,409]. The limited efficacy of Pirfenidone and Nintedanib underscores the complex heterogeneity of IPF, both in terms of clinical presentation and disease pathomechanisms, posing a significant challenge for therapeutic interventions and the identification of suitable drug targets. Consequently, there is an urgent unmet need to better understand the underlying molecular events driving pulmonary fibrosis to support development of new anti-fibrotics which can effectively halt or reverse disease progression.

As research technologies continue to advance, human tissue samples remain invaluable resources for understanding mechanisms of disease and developing targeted therapies. To

date, most of the research carried out involving human IPF samples has centred on inter-patient studies comparing healthy and diseased tissue. Though this approach has undoubtedly aided our understanding of disease it nonetheless fails to consider the incredibly complex spatial heterogeneity of pathological changes in IPF. Small tissue samples, such as biopsies, are therefore unable to capture the full breadth of this heterogeneity, potentially leading to the identification of therapeutic targets that are not universally applicable to all patients and may also fail to identify crucial drivers of fibrosis dependant on the region of lung sampled. Furthermore, as IPF is a dynamic disease that evolves over time, single timepoint comparisons may not adequately reflect the temporal changes associated with disease progression. However, obtaining repeat tissue samples from patients over a sustained period is challenging due to the invasiveness of the procedure and limited availability. To this end, alternative strategies must be adopted to overcome these limitations and allow identification of common and distinct mechanisms driving fibrosis toward end-stage disease.

Here, we utilised a two-pronged approach to investigate disease progression by comparing macroscopically distinct regions of tissue from within the same IPF lung. We then performed RNA sequencing and proteomic profiling of the differentially affected IPF regions, alone and alongside non-diseased age-matched unused donor lungs as a control, to determine gene and protein expression at these different stages of disease. Following this, interrogation of gene and protein heterogeneity was performed to identify novel therapeutic targets for further investigation.

4.1 Materials and methods

4.1.1 Patient demographics

IPF explant tissue and unused donor lung tissue was acquired with ethical consent as detailed in Chapter 2. Measures of FEV_1, FVC, TLC, TL_{CO} and K_{CO} were retrospectively extracted from pulmonary function test (PFT) data from each participant's medical records at the date closest to lung transplantation (Table 14). Data are presented as absolute values and as a percent of a predicted value (%) for patient pulmonary function tests where available. A summary table of patient demographics is provided where all continuous variables are reported as mean ± SD (Table 15). Statistical analysis was performed using independent samples t-tests to infer homogeneity or heterogeneity between unused donor and IPF patient cohorts for age ($p=0.18$), Fisher's exact test was performed to assess sex distribution ($p=0.29$) and Chi-square test of independence was performed to assess smoking history ($p=0.219$) between the 2 cohorts, where a $p<0.05$ was considered significant. IPF patient pre-transplant white blood cell counts (Table 16) and and-fibrotic medications (Table 17) were also retrospectively obtained from each participant's medical records where available.

Table 14: IPF and unused donor patient demographics for regional sampling

Patient Number	Sex	Age	FEV1, L	FVC, L	TLC, L	TLCO, mmol CO/min/kPa	KCO, mmol CO/min/kPa	Smoking history
IPF donor 1	M	53	0.57 (18%)	2.00 (51%)	5.39 (87%)	1.72 (19%)	1.72 (38%)	Non-smoker
IPF donor 2	M	64	2.32 (72%)	2.66 (65%)	4.26 (62%)	1.75 (19%)	1.60(65%)	Ex-smoker stopped (30 pack year)
IPF donor 3	M	61	2.1 (64%)	2.32(56%)	3.32(48%)	1.76(19%)	0.58(42%)	Ex-smoker (15 pack year)
IPF donor 4	F	50	1.33(46%)	1.51(45%)	2.21(41%)	2.21(25%)	1.20(75%)	Ex-smoker
IPF donor 5	M	63	1.55(68%)	1.85(68%)	3.00(60%)	1.05(14%)	0.46(30%)	Unknown if previous smoker
IPF donor 6	M	63	1.53(59%)	1.79(54%)	3.00(52%)	1.48(19%)	0.69(52%)	Ex-smoker
IPF donor 7	M	50	1.17(56%)	1.40(55%)	N/A	0.56(23%)	N/A	Smoking history unknown
IPF donor 8	M	49	1.30(35%)	1.43(31%)	2.16(32%)	3.00(32%)	1.00(66%)	Non-smoker
Unused donor 1	M	52	N/A	N/A	N/A	N/A	N/A	Non-smoker
Unused donor 2	M	40	N/A	N/A	N/A	N/A	N/A	Ex-smoker
Unused donor 3	F	52	N/A	N/A	N/A	N/A	N/A	Smoker
Unused donor 4	F	52	N/A	N/A	N/A	N/A	N/A	Non-smoker
Unused donor 5	M	59	N/A	N/A	N/A	N/A	N/A	N/A
Unused donor 6	M	64	N/A	N/A	N/A	N/A	N/A	N/A
Unused donor 7	F	43	N/A	N/A	N/A	N/A	N/A	N/A
Unused donor 8	M	42	N/A	N/A	N/A	N/A	N/A	Smoker 20 cigarettes per day for 31yrs
Unused donor 9	F	59	N/A	N/A	N/A	N/A	N/A	N/A

FEV1= forced expiratory volume in 1 second, FVC= forced vital capacity, TLC= total lung capacity, TLCO= carbon monoxide transfer factor, KCO=carbon monoxide transfer coefficient and N/A= not available. Percentages of predicted values are in parentheses.

Table 15: Summary demographics of IPF patient and unused donor cohorts

Variable		Unused donor	IPF
N (number)		9	8
Sex	*Female*	4	1
	Male	5	7
Age (years)		51.4 ± 6.69	56.7 ± 8.4
FEV1, L		N/A	1.48 ± 0.54
FVC, L		N/A	1.88 ± 0.48
TLC, L		N/A	3.39 ± 1.25
TLCO, mmol CO/min/kPa		N/A	1.72 ± 0.78
KCO, mmol CO/min/kPa		N/A	1.09 ± 0.52
Smoking history	*Smoker*	2	0
	Ex-smoker	1	4
	Non-Smoker	2	2
	Unknown	4	2

FEV1= forced expiratory volume in 1 second, FVC= forced vital capacity, TLC= total lung capacity, TLCO= carbon monoxide transfer factor, KCO=carbon monoxide transfer coefficient and N/A=not available. Percentages of predicted values are in parentheses.

Table 16: IPF donor white blood cell counts pre-transplant

Patient Number	Total WBC (10^9/L)	Neutrophil (10^9/L)	Eosinophil (10^9/L)	Lymphocyte (10^9/L)	Monocyte (10^9/L)	Basophil (10^9/L)
IPF donor 1	8.81	7.56	0.02	0.58	0.6	0.05
IPF donor 2	8.08	5.5	0.13	1.77	0.62	0.06
IPF donor 3	6.98	4.62	0.12	1.66	0.54	0.04
IPF donor 4	16.35	14.03	0.03	1.33	0.94	0.02
IPF donor 5	10.56	8.26	0.32	1.34	0.57	0.07
IPF donor 6	7.97	6.06	0.08	1.17	0.64	0.02
IPF donor 7	44.2	42.8	0.02	0.21	1.09	0.08
IPF donor 8	8.37	7.17	0.03	0.62	0.52	0.03

Table 17: IPF donor pre-transplant anti-fibrotic medication

Patient Number	Pre-transplant medication
IPF donor 1	Unknown
IPF donor 2	Nintedanib
IPF donor 3	Pirfenidone then switched to Nintedanib
IPF donor 4	Pirfenidone
IPF donor 5	Mycophenolate mofetil, no anti-fibrotics
IPF donor 6	Nintedanib
IPF donor 7	Prednisolone 40mg
IPF donor 8	Nintedanib

4.1.2 Histology and immunohistochemistry

H&E was carried out as previously described in Chapter 2. Masson Trichome staining was carried out at Cell Pathology, RVI Newcastle. Histology was performed for the following markers (Table 18) according to the general methodology previously described in Chapter 2.

Table 18: Primary antibodies and antigen retrieval

Antigen	Supplier	Code	Host species	Dilution	Antigen retrieval
αSMA	Sigma-Aldrich	F3777	Mouse monoclonal	1/1000	Citrate pH 6
CD68	Aviva systems	OABB00472	Rabbit polyclonal	1/200	Citrate pH 6
Cathepsin G	Abcam	Ab282105	Rabbit monoclonal	1/100	Citrate pH 6
Lactoferrin	Santa Cruz	Sc-53498	Mouse monoclonal	1/100	Tris EDTA pH 9
Myeloperoxidase	R&D systems	MAB3174	Mouse monoclonal	1/100	Tris EDTA pH 9
Mannose receptor 2	Abcam	Ab64693	Rabbit polyclonal	1/1000	Citrate pH 6
Integrin β6	R&D systems	AF4155	Sheep polyclonal	1/40	Proteinase K
Cytokeratin 18	Abcam	Ab181597	Rabbit polyclonal	1/800	Tris EDTA pH 9

4.1.3 RNA sequencing

Bulk RNA sequencing was performed on whole tissue samples as detailed below:

4.1.3.1 RNA isolation

1µg total RNA was isolated from snap frozen whole tissue as previously detailed in chapter 2, treated with DNase and sent for transcriptomic analysis at Newcastle University's Genomics Core facility.

4.1.3.2 Sample processing, cDNA library preparation and sequencing

RNA samples were quality assessed by performing RNA Screentape analysis (50567, Aligent) in combination with a 4200 TapeStation (Aligent). mRNA sequencing libraries were prepared using the Illumina Stranded mRNA Prep kit (20040534, Illumina) following manufacturer's guidelines. Briefly, total RNA was diluted in nuclease-free water to a final volume of 25µl before mRNA was purified and captured using RNA purification beads (RPBX). Purified mRNA was eluted, fragmented and copied into first strand complimentary DNA (cDNA) using reverse transcriptase and random primers. Following this, a second strand cDNA synthesis step was performed to replace deoxythymidine triphosphate (dTTP) with deoxyuridine triphosphate (dUTP) to achieve strand specificity and generate blunt-ended, double-stranded cDNA fragments. Adenine and thymine nucleotide bases were added to 3' ends of the blunt fragments to prevent them ligating to each other and provide a complementary overhang for ligating the adapter to the fragment, respectively. Pre-index anchors were ligated to the ends

of cDNA fragments to prepare them for dual indexing before subsequent PCR amplification to add index adapter sequences. Adapter-ligated cDNA fragment were purified using AMPure XD beads and selectively amplified using PCR to generate a dual-indexed library (a DNA fragment with adapters at each end). Dual-indexed libraries were further purified using AMPure XP beads before quality assessment (fragment size and concentration) using a 4200 TapeStation and D1000 Screentape (5067-5582, Aligent) and Qubit 4 Fluorometer (16223001, Invitrogen). Finally, libraries were normalised to 10nM and sequenced on a NovaSeq 6000 (Illumina) following the NovaSeq 6000 Sequencing System Guide at >30 million 100 bp single reads per sample.

4.1.3.3 Computational analysis, processing datasets and quality control (QC)

Downstream processing of transcriptomic datasets was performed by Dr Laura Sabater. Quality control (QC) analysis of fastq files was performed using fastQC (Available online at: http://www.bioinformatics.babraham.ac.uk/projects/fastqc/). All fastq files from samples had an average >Q30 across more than 90% of the bases and therefore passed the QC check. Sequences were trimmed using trimmomatic software (version 0.39). TruSeq3_adaptor sequences from trimmomatic software were used as adaptors, allowing 1 mismatch, simple clip threshold >10, minimum length of the remaining fragment after trimming >30 and quality average after trimming >36. Trimmed sequences were further QC analysed to ensure quality for further analysis. Mapping and quantification of sequences was performed using salmon software (version 1.9.0). First, transcript index was created using Human genome assembly release 31 (gencode.v31.pc_transcripts.fa). Then, pseudo-mapping and quantification of the mRNA sequences was performed using the transcript index previously created as a reference. A gene map for Human genome assembly release 31 (gencode.v31.annotation.gff3) was created in order to annotate the mRNA found during pseudo-mapping process using 'GenomicFeatures' and 'tximportData' R packages (version 1.54.4 and 1.24.0, respectively) before Salmon quantification values were uploaded into R Studio for differential expression (DE) analysis. DE analysis was performed using R studio (version 4.2.0). mRNA counts were imported into R using 'tximport' R package, and counts matrix was created using DESeq2 R package. The estimation of the dispersion, normalisation and PCA were performed using DESeq2 R package (version 1.36.0). A negative binomial GLM was applied to model RNA count data using DESeq2 R package and mRNA were classified as significantly different when log2 fold change >2 and p-value (adjusted) <0.05.

4.1.4 Mass spectrometry

Proteomic assessment of whole tissue samples was performed by Dr Sandra Murphy as detailed below:

4.1.4.1 Protein preparation

Snap frozen whole tissue was homogenised in 200µl of SDS lysis buffer (5% SDS, 50mM triethylammonium bicarbonate (TEAB) pH 7.5) in Precellys® Ceramic hard tissue tubes (432-3752, VWR) using a Precellys bead homogeniser at 0°C. Protein concentration was determined by the bicinchoninic acid (BCA) assay. A total of 20µg protein was reduced by incubation with 5mM tris(2-carboxyethyl)phosphine (TCEP) for 20min at 37°C, and subsequently alkylated with 20mM iodoacetamide for 30mins at RT in the dark. Protein digestion was performed using the suspension trapping (S-Trap™) sample preparation method using the manufacturer's guidelines (ProtiFi™, Huntington NY). Briefly, 2.5µl of 12% phosphoric acid was added to each sample, followed by the addition of 165µl S-Trap binding buffer (90% methanol in 100mM TEAB, pH 7.1). This was added to the S-Trap Micro spin column. The samples were centrifuged at 4,000 x g for 2mins until all the solution passed through the filter. Each S-Trap Mini-spin column was washed with 150 µl S-trap binding buffer by centrifugation at 4,000 x g for 1min. This process was repeated for a total of four washes. 25µl of 50mM TEAB, pH 8.0 containing trypsin (1:20 ratio of trypsin to protein) was added to each sample, followed by proteolytic digestion for 4hrs at 47°C using a thermomixer (Eppendorf) without shaking. Peptides were eluted with 50mM TEAB pH 8.0 and centrifugation at 4,000 x g for 2 mins. Elution steps were repeated using 0.2% formic acid and 0.2% formic acid in 50% acetonitrile, respectively. The three eluates from each sample were combined and dried using a speed-vac before storage at -80°C.

4.1.4.2 Mass spectrometry (MS)

Peptides were resuspended in 5% formic acid and each digested sample was analysed on an Orbitrap Fusion Lumos Tribrid mass spectrometer (Thermo Fisher Scientific), connected to an UltiMate 3000 RSLCnano System (Thermo Fisher Scientific). Peptides were injected on an Acclaim PepMap 100 C18 LC trap column (300µm ID × 5mm, 5µm, 100Å) followed by separation on an EASY-Spray nanoLC C18 column (75 IDµm × 500mm, 2µm, 100Å) at a flow rate of 250nl min^{-1}. Solvent A was water containing 0.1% formic acid, and solvent B was 80% acetonitrile containing 0.1% formic acid. The gradient used was as follows: solvent B was maintained at 2% for 5mins, followed by an increase from 2 to 35% B in 120mins, 35-90% B in

0.5mins, maintained at 90% B for 4mins, followed by a decrease to 2% in 0.5mins and equilibration at 2% for 10mins. The Orbitrap Fusion Tribrid mass spectrometer was operated in data dependent, positive ion mode. Full scan spectra were acquired in a range from 400 m/z to 1600 m/z, at a resolution of 120,000, with automated gain control (AGC) set to standard and a maximum injection time of 50ms. Precursor ions were isolated with a quadrupole mass filter width of 1.6 m/z and HCD fragmentation was performed in one-step collision energy of 30%. Detection of MS/MS fragments was acquired in the linear ion trap in rapid mode using a Top 3s method, with AGC target set to standard and a dynamic maximum injection time. The dynamic exclusion of previously acquired precursors was enabled for 35secs with a tolerance of +/-10 ppm.

4.1.4.3 MS Data analysis

All spectra were analysed using MaxQuant version 2.4.13.0 using the SwissProt *Homo sapiens* fasta file and a contaminant sequence set provided by MaxQuant. Peak list generation was performed within MaxQuant and searches were performed using default parameters and the built-in Andromeda search engine. The following search parameters were used: first search peptide tolerance of 20ppm and second search peptide tolerance 4.5ppm. Cysteine carbamidomethylation was set as a fixed modification and oxidation of methionine was set as variable modification. A maximum of two missed cleavage sites were allowed. False Discovery Rates (FDR) were set to 1% for both peptides and proteins. Label-free quantification (LFQ) intensities were calculated using the MaxLFQ algorithm from razor and unique peptides with a minimum ratio count of two peptides across samples. Match between runs was enabled. Statistical analysis was performed using R (version 4.2.0). The data was first filtered to remove proteins that matched to a contaminant or a reverse database, or which were only identified by site. Only proteins identified by a minimum of 2 unique peptides were retained. LFQ intensity values were log2 transformed. For the analysis of regional IPF lung tissue the data was filtered to contain at least 4 valid values in all 3 groups (IPF normal, IPF intermediate and IPF fibrotic). For the analysis of unused donor (UD) versus regional IPF lung tissue the data was filtered to contain at least 4 valid values in each two groups of the comparison being tested (UD vs IPF normal, UD vs IPF inter and UD vs IPF fibrotic). LIMMA was used for statistical analysis (paired t-tests) where proteins with a p-value <0.05 were considered as statistically significant. For the analysis of regional IPF lung tissue, the effect of patient was included in the linear model.

4.1.5 MesoScaleDiscovery U-Plex Assay

To detect additional immune markers typically not present in proteomic datasets, 111 Immuno-oncology (K153424-1, MSD), biomarker (K15067L-1, K151A9H-1, K151AGL-1 , MSD), metabolic (K151ACL-1, MSD) and TGF-β (K15241K-1, MSD) assays were performed on samples using U-Plex Multi-Spot Assay System (MesoScale Discovery™) as per manufacturer's instructions. Briefly, U-plex plates were coated with the relevant linker-coupled capture antibodies, sealed and incubated for 1hr at RT, with shaking. Plates were washed 3 times using 1X MSD wash buffer (PBS + 0.05% Tween20) before adding samples and calibrators and incubating at RT with shaking for 1hr. Plates were washed before biotinylated detection antibodies were added to each well and incubated for 1hr at RT, with shaking. Plates were washed prior to Read Buffer Gold being added to each well and the plate read using MesoScale DiscoveryTM Sector imager 2400 plate reader. Analysis of results was performed using the MSD Discovery Workbench 4.0 analysis software.

4.1.6 Ingenuity pathway analysis (IPA)

Significant data from all proteomic comparisons were uploaded in IPA (QIAGEN, version 111725566) and core expression analysis was performed using log2FC differences for z-score and prediction calculations. Proteins from the ingenuity knowledge base were used as reference and all direct and indirect relations, tissues, node types and data sources from experimentally observed data were considered.

4.1.7 Statistical analysis

Volcano plots, heatmaps and bar charts (represented as ± SEM) were created using GraphPad prism (version 9.5.0). To generate heat maps from transcriptomic and proteomic datasets, normalised counts and LFQ intensities were z-score normalised using Perseus (version 2.0.11.0) software. Genes/proteins common to multiple conditions were calculated using Venny version 2.1.0 (available from www.bioinfogp.es/tools/venny.html).

4.2 Results

4.2.1 Acquisition and histological characterisation of regional IPF samples

Over the past few decades much of the research into the pathogenesis of IPF has relied heavily on the use of 2D/3D cell culture systems and *in vivo* mouse models, which poorly translate to patients. More recently, advances in next generation sequencing and unbiased 'omics technologies has enabled novel insights into pathomechanisms underlying the initiation and progression of fibrosis in human tissue. In the context of IPF, most of the research involving human tissue samples revolves around studies comparing tissue collected from healthy patients (often from the margins of cancer resections) versus tissue collected from diseased lungs (interpatient studies). Due to the considerable spatial and temporal heterogeneity within IPF lungs, it is likely that these studies may not accurately capture the full spectrum of pathological changes associated with disease. Hence, we sought to interrogate regional areas of IPF tissue from the same donor in a more physiologically relevant, intrapatient approach to assess differences between early-stage, actively diseased regions ('normal' and 'intermediate') of tissue and end-stage burned out fibrotic regions.

To achieve this, macroscopically 'normal', 'intermediate' and end-stage 'fibrotic' tissue was sampled under pathology guidance from the upper left lobe of IPF lungs (n=8 donors) collected from patients undergoing lung transplantation (Figure 52A, B). During tissue sampling, 3 separate samples (from different areas of the lung) were acquired for each stage of disease (n=3 normal, n=3 intermediate and n=3 fibrotic per donor) and snap frozen for downstream processing, with an additional 3 samples per region acquired to generate formalin-fixed paraffin embedded tissue (n=3 normal, n=3 intermediate and n=3 fibrotic per donor). Next, smaller sections of snap frozen tissue from each of the 3 samples per region were pooled together to generate a normal, intermediate and fibrotic sample for each IPF donor (n=3 samples per donor, n=8 donors, n=34 samples total for RNA sequencing and n=3 samples per donor, n=8 donors, n=34 samples total for proteomics). Following this, samples were processed to generate RNA and tissue homogenates, which were then analysed by transcriptomic analysis and mass-based spectrometry, respectively (Figure 52C). Alongside this, samples from the upper left lobe of age-matched, non-diseased unused donor (UD) lungs (n=9 donors) were similarly processed and sent for 'omics sequencing as an additional control.

Before processing tissue for downstream analysis, histological assessment of unused donor control lungs and IPF regions was performed to confirm correct selection of regions (Figure 53). Results showed that UD lungs generally displayed normal lung histology, with no sign of usual interstitial pneumonia or fibrosis upon microscopic examination. However, evaluation of macroscopically unaffected or 'normal' regions of IPF tissue showed clear microscopic differences to non-diseased lungs and early signs of fibrogenesis, with αSMA+ cells (a marker of myofibroblasts) localised primarily to the epithelium and mild alveolar wall thickening, indicating aberrant tissue repair mechanisms. Intermediate regions of IPF tissue showed a considerable increase in ECM deposition, collagen-rich scar tissue and αSMA+ cells, often adjacent to regions of lung with seemingly normal tissue architecture. Furthermore, there was evidence of fibroblastic foci and a further reduction in alveolar space compared to IPF normal regions, coupled with dense patches of inflammatory clusters. Finally, macroscopically fibrotic regions of IPF tissue demonstrated several hallmarks of advanced pulmonary fibrosis including dense regions of tissue scarring and ECM deposition, extensive loss of alveolar space, patchy inflammatory cell infiltration, epithelial denudation and hyperepithelialisation. Importantly, all lung sections displayed temporal and spatial heterogeneity of fibrotic and inflammatory features (including collagen abundance, inflammatory infiltrates, fibroblastic foci and expansion of the lung interstitium) across all three regions. These observations were subsequently validated by a pathologist, confirming that the regions of IPF tissue became progressively more fibrotic the further along the disease spectrum the sample were, confirming correct selection of macroscopic tissue regions.

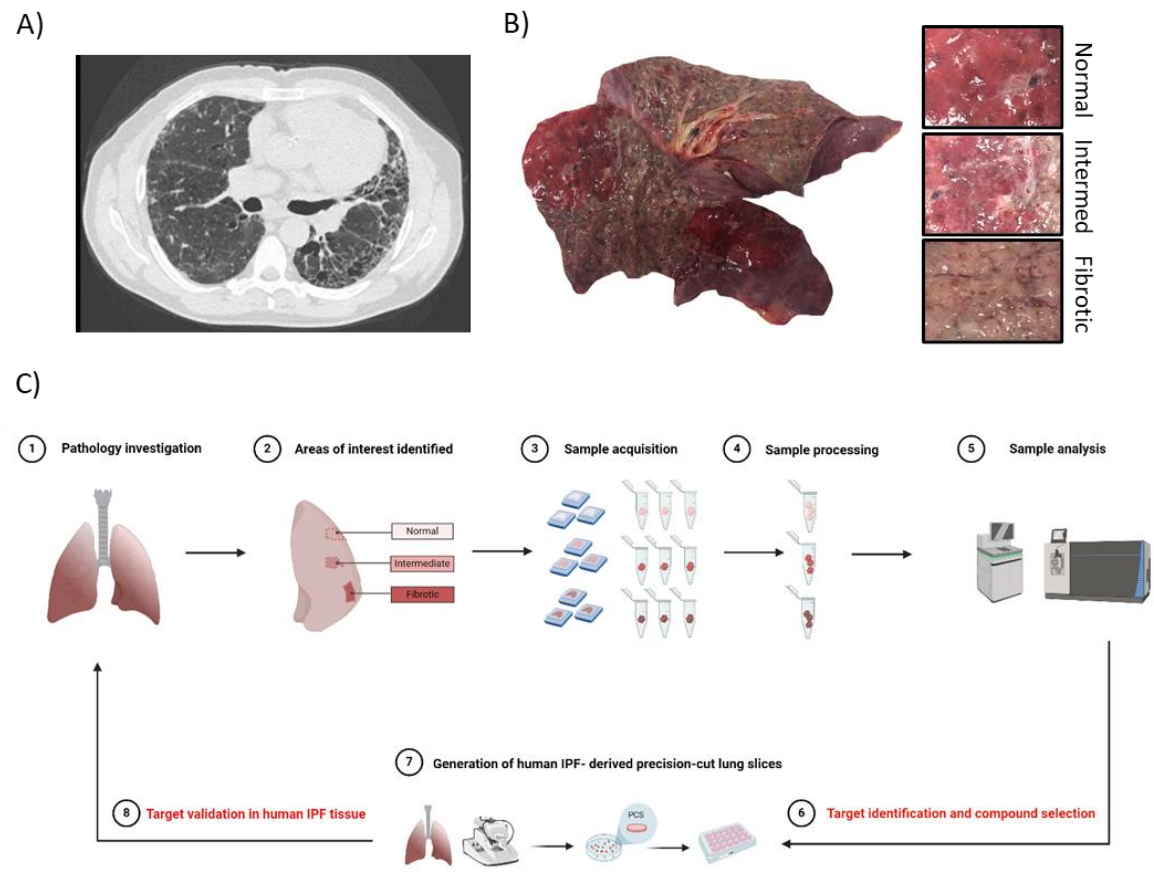

Figure 52: **Regional IPF explant sampling and workflow** A) Representative HRCT image of IPF donor prior to explantation B) Macroscopic image of upper lobe of IPF tissue and areas of regional sampling**.** C) Schematic workflow of regional IPF tissue sampling and downstream processing. 1. Isolation of upper-left lobe of IPF explant lung post-transplantation and pathology assessment 2. Three separate regions of macroscopically normal, intermediate and fibrotic tissue identified from upper left lobe 3. Samples isolated from 9 selected regions and harvested for FFPE or snap frozen for later processing 4. Smaller sections of each sample pooled per region for each IPF donor 5. 3 samples per IPF donor prepared for bulk RNA sequencing and mass-based spectrometry 6. Target identification and compound selection 7. Generation of precision-cut lung slices (PCLuS) from human IPF tissue. 8. Screening of candidate compounds identified through 'omics in IPF-derived PCLuS

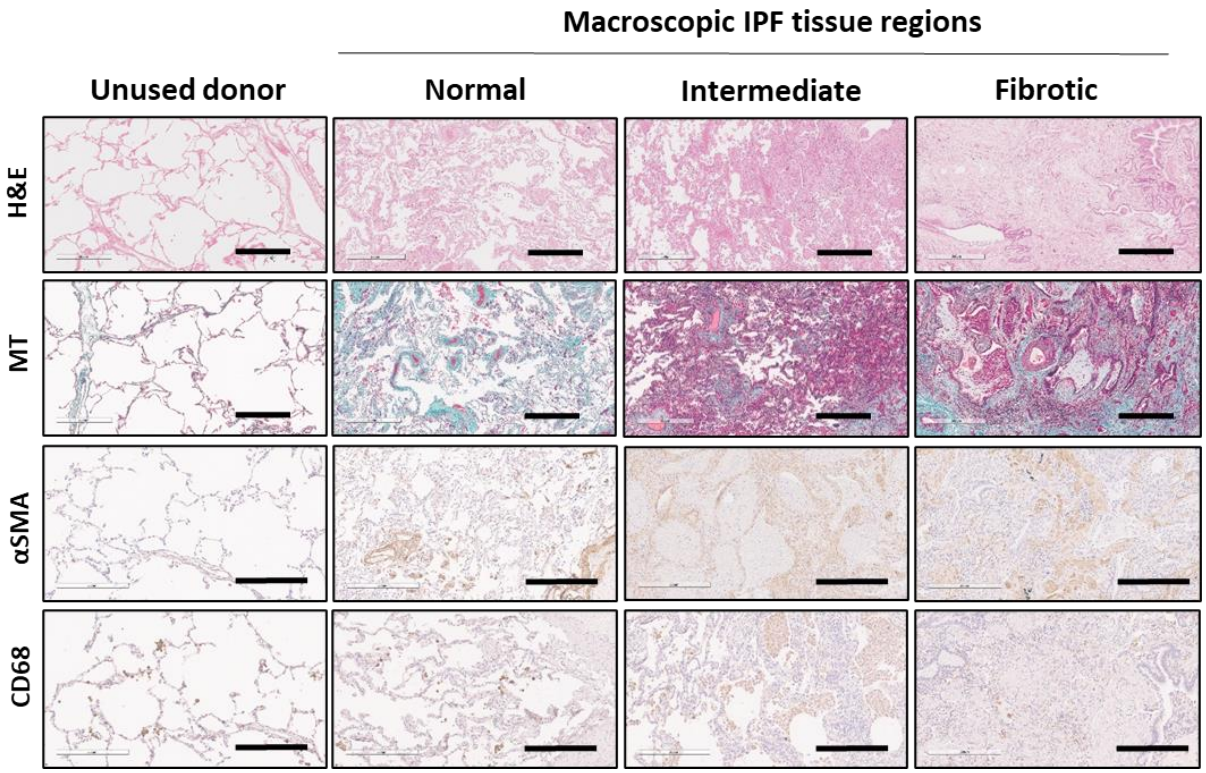

Figure 53: Histological characterisation of UD and regional IPF samples Representative images of unused donor samples and IPF regional tissue (staged normal, intermediate and fibrotic upon macroscopic examination) to assess tissue architecture (H&E, scale bar= 500µm), collagen deposition (Masson Trichrome [MT], scale bar= 500µm), myofibroblasts (αSMA+ cells, scale bar= 300µm) and macrophages (CD68+ cells, scale bar= 300µm). Primary antibodies were used at the following dilutions: αSMA; 1/1000 and CD68; 1/200.

4.2.2 Interpatient comparison

4.2.2.1 Interpatient RNAseq

To begin investigation of our regional IPF tissue, we first sought to replicate previous interpatient studies, to confirm differences between 'healthy' UD control lungs and macroscopically distinct regions of diseased IPF tissue. To achieve this, PCA plots were generated to compare UD samples to each IPF region to visualise the variation in patient tissue based on degree of fibrosis (Figure 54A, Figure 57A, Figure 60A). Evaluation of non-diseased UD lungs (n=9 donors) and IPF normal regions (n=7 donors) revealed that 4 of the 9 UD lungs (UD 2, UD 6, UD 7 and UD 8) appeared to be more similar to IPF normal regions than the other 5 UD controls (Fig 54). One possible explanation for this is that, in some cases, there is evidence of prior damage or reduced lung function of UD tissue which precludes them from being viable for transplantation. Consequently, some UD lungs may have altered gene expression to typically 'healthy' tissue. Alternatively, this could be attributed to normal age-related changes in the unused donor lungs as many of the hallmarks of ageing have also been shown to be present in IPF patients. However, all IPF intermediate and fibrotic regions, with the exception of IPF 7 fibrotic tissue sample, appeared to cluster based on disease state, with IPF samples becoming less similar to controls in line with increasing severity of fibrosis (Figure 57, Figure 60A).

Of the 57,449 genes identified, 1,043 genes were significantly different between normal regions of IPF tissue (n=7 donors) compared to UD lungs (n=9 donors) (Figure 54) with 538 upregulated (Figure 55) and 505 downregulated (Figure 56) genes in normal IPF tissue. GO enrichment analysis (performed using https://geneontology.org and https://pantherdb.org/) revealed a number of upregulated genes in IPF normal regions vs UD controls were related to extracellular matrix organisation (GO:0030198, n=29 genes, fold enrichment (FE)=4.57 and padj=1.04E-08) and extracellular structure organisation (GO:0043062, n=29 genes, FE=4.65 and padj=1.04E-08). Additionally, upregulated genes were enriched for collagen fibril organisation (GO:0030199, n=11 genes, FE=8.72 and padj=3.8E-05), collagen catabolic processes (GO:0030574, n=8 genes, FE=9.3 and padj=0.0011) and collagen metabolic processes (GO:0032963, n=11 genes, FE=5.38 and padj=0.0031) in IPF normal tissue compared to UD controls (see Appendix F; Table 1 and Figure 1A), suggesting that there is an early shift towards matrix remodelling in macroscopically unaffected regions of IPF lungs. Conversely, a number of significantly downregulated genes were enriched for processes in the innate

immune response and antimicrobial genes, such as leukocyte chemotaxis (GO:0030595, n=25 genes, FE=6.94 and padj=2.2E-11) and migration (GO:0050900, n=28 genes, FE=4.65 and padj=4.51E-09), myeloid leukocyte migration (GO:0097529, n=25 genes, FE=6.88 and padj=2.18E-11), granulocyte chemotaxis (GO:0071621, n=18 genes, FE=9.25 and padj=3.94E-10) and granulocyte migration (GO:0097529, n=19 genes, FE=8.12 and padj=9.0E-10). Additionally, downregulated genes in IPF normal were associated with neutrophil chemotaxis (GO:0030593, n=16 genes, FE=9.84 and padj=2.32E-09) and neutrophil migration (GO:1990266, n=17 genes, FE=8.67 and padj=3.75E-09) versus UD controls (see Appendix F; Table 2 and Figure 1B), suggesting that immune function is altered early on in IPF pathogenesis.

1,326 genes were significantly different between intermediate regions of IPF tissue (n=7 donors) and UD controls (n=9 donors) (Figure 57), with 806 upregulated (Figure 58) and 520 downregulated (Figure 59) genes in IPF intermediate tissue. As expected, upregulated genes in intermediate regions of IPF were enriched for extracellular matrix organisation (GO:0030198, n= 33 genes, FE= 3.41 and padj=3.4E-07), extracellular structure organisation (GO:0043062, n=33 genes, FE=3.4 and padj=3.4E-07), collagen fibril organisation (GO:0030199, n=13 genes, FE=6.76 and padj=1.3E-05), collagen catabolic processes (GO:0030574, n=9 genes, FE=6.87 and padj=0.0009) and collagen metabolic processes (GO:0032963, n=12 genes, FE=3.85 and padj=0.01) versus UD controls. However, unlike IPF normal tissue, IPF intermediate regions showed strong gene set enrichment for pathways involved in the adaptive immune response including lymphocyte-mediated immunity (GO:0002449, n=62 genes, FE=5.72 and padj=1.2E-26), immunoglobulin production (GO:0002377, n=58 genes, FE=10.27 and padj=6.6E-39), B cell –mediated immunity (GO:0019724, n=57 genes, FE=9.23 and padj=8.0E-36) and B cell receptor signalling pathways (GO:0050853, n=19 genes, FE=8.37 and padj=3.0E-10), suggesting that the adaptive immune response is exacerbated and/or deregulated in intermediate regions of IPF tissue (see Appendix F; Table 3 and Figure 2A). Interestingly, of the downregulated genes in IPF intermediate regions vs UD controls, genes were similarly enriched for innate-immunity associated genes (previously identified in IPF normal regions) as well as cellular response to IL-1 (GO:0071347, n=16 genes, FE=10.14 and padj=5.3E-09) and antimicrobial responses such as response to lipopolysaccharide (GO:0032496, n=27 genes, FE=5.41 and padj=4.0E-09),

response to molecule of bacterial origin (GO:0002237, n=27 genes, FE=5.1 and padj=5.3E-09) and antimicrobial response (GO:0019730, n=14 genes, FE=7.39 and padj=1.4E-06), indicating persistent downregulation of innate immune signalling during early and ongoing fibrogenesis (see Appendix F; Table 4 and Figure 2B).

Finally, 2,473 significantly different genes were identified in end-stage fibrotic regions of tissue (n=7 donors) compared to UD controls (n=9 donors) (Figure 60), of which 1764 genes were significantly upregulated (Figure 61) and 709 genes were significantly downregulated (Figure 62). Analysis of gene set enrichment revealed that upregulated genes in IPF fibrotic regions of IPF tissue vs UD controls were predominantly involved in cilium-related GO terms (see Appendix F; Table 5 and Figure 3A), whereas collagen and ECM-related pathways were less prominent than in normal and intermediate regions of fibrosis. These results were consistent with previous reports in the literature, which similarly identified upregulation of cilium-associated genes in line with more extensive honeycombing in IPF patient tissue [410,411]. Moreover, Yang *et al* reported that elevated expression of cilium-related genes was also associated with higher expression of MUC5B and MMP7 [411], a gene recently implicated in attenuation of ciliated cell differentiation during wound repair [412], both of which were significantly upregulated in IPF fibrotic vs UD lungs (MUC5B: log2FC=4.41 and padj=0.00078, MMP7: log2FC=4.27 and padj= 2.21E-08). Additionally, downregulated genes in IPF fibrotic regions were associated with antimicrobial responses also downregulated in IPF normal and intermediate regions (see Appendix F; Table 6 and Figure 3B), as well as regulation of the humoral immune response (GO:0006959, n=27 genes, FE=5.39 and padj= 9.9E-10) and the inflammatory response (GO:0050727, n=30 genes, FE=3.63 and padj= 5.2E-07 and GO:0050729, n=17 genes, FE=5.72, and padj= 2.7E-06), suggesting that modulation of the normal immune response occurs early in fibrogenesis and persists through to end-stage fibrosis.

Of the significantly upregulated genes, 307 (14.9%) were common to all regions of IPF tissue and included several metalloproteases (ADAMTS14, ADAMTS18, MMP7, MMP11, and MMP16), collagens (COL1A1, COL3A1, COL5A1, COL9A1, COL10A1, COL11A1, COL15A1, COL17A1, COL1A2 and COMP) and other ECM-related genes. 279 (13.5%) genes were upregulated in IPF intermediate and fibrotic regions, 105 (5.1%) were upregulated in IPF normal and intermediate and 48 (2.3%) were upregulated in IPF normal and fibrotic only.

Additionally, a number of genes were exclusively upregulated in each region of normal (78, 3.8%), intermediate (115 genes, 5.6%) and fibrotic (1130 genes, 54.8%) IPF tissue (Figure 63B). Of the significantly downregulated genes, 238 (22.9%) were common to all regions of IPF tissue, 99 (9.5%) were downregulated in IPF intermediate and fibrotic regions, 70 (6.7%) were downregulated in IPF normal and intermediate and 51 (4.9%) were downregulated in IPF normal and fibrotic only. Additionally, a number of genes were exclusively downregulated in each region of normal (146, 14.1%), intermediate (113 genes, 10.9%) and fibrotic (321 genes, 30.9%) IPF tissue (Figure 63C).

Taken together, these data confirmed an expected dysregulation of genes, including known pro-fibrogenic markers, in each region of IPF tissue compared to 'healthy' unused donor controls. Furthermore, consistent with previous studies, we demonstrated that even before fibrosis is macroscopically evident, there are a large number of genes which are significantly different to non-diseased lungs, suggesting that seemingly unaffected regions of IPF lungs are primed for injury and represents the first step on the spectrum of disease. Interrogation of these differential genes, particularly at early stages of disease, could therefore aid identification of novel targets for early therapeutic intervention.

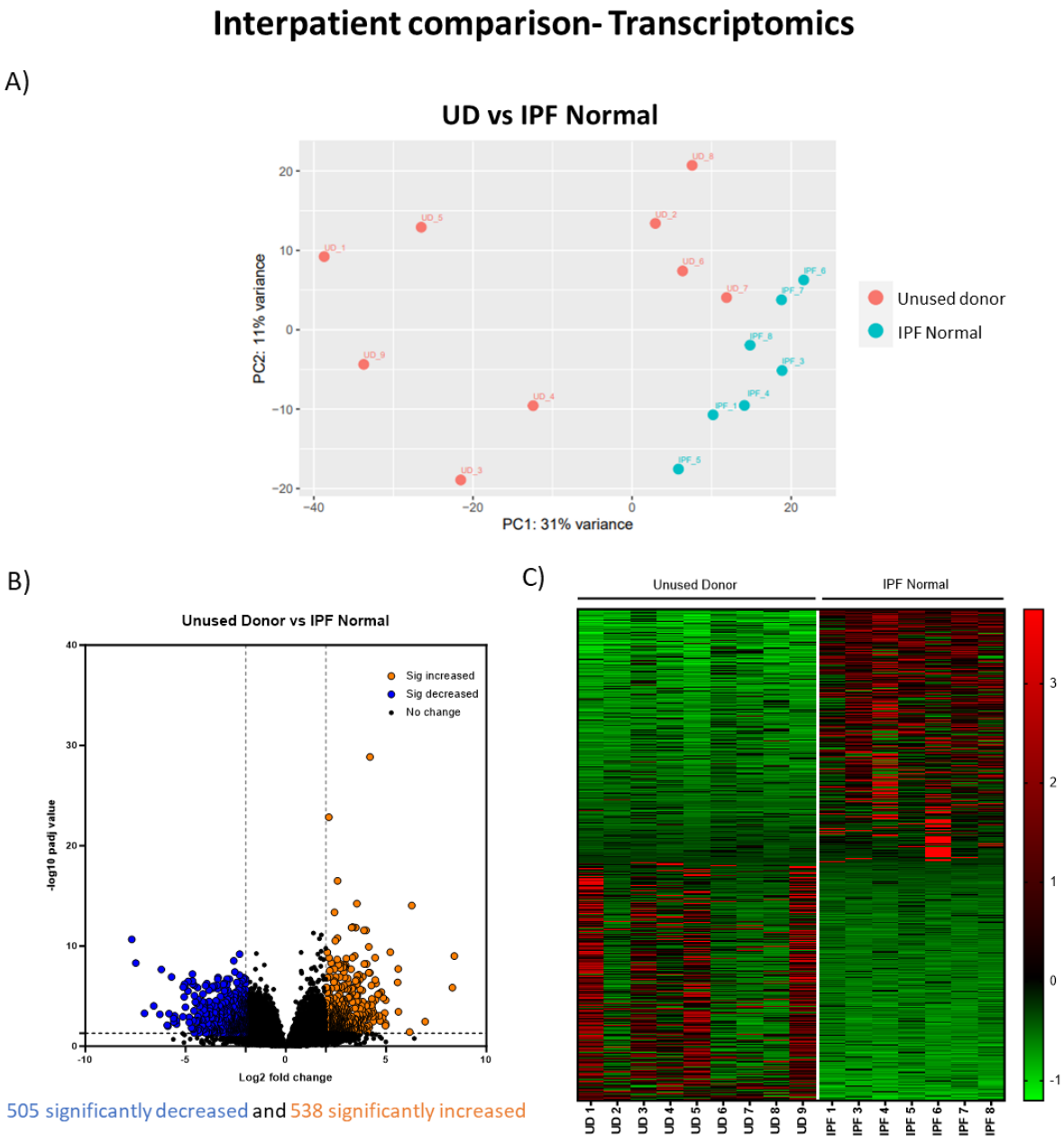

Figure 54: Transcriptomic analysis of interpatient unused donor vs IPF normal comparison A) Principal component analysis (PCA) plot of unused donor (n=9 donors) and IPF normal (n=7 donors) samples. Significantly different genes were graphed as B) volcano plot (downregulated genes in blue and upregulated genes in orange) where horizontal dashed line represents p adjusted (padj) <0.05 and vertical dashed lines represent Log 2-Fold Change (FC) ±2 threshold criteria applied for significance C) heat map (downregulated genes in green and upregulated genes in red) for significantly different genes (padj<0.05 and Log2FC ±2).

A)

UD vs IPF Normal- Top significantly upregulated genes

Ensembl ID	Gene ID	Description	logFC	P Adj Value
ENSG00000167656	LY6D	lymphocyte antigen 6 family member D	8.41	9.90E-10
ENSG00000275896	PRSS2	serine protease 2	8.31	1.40E-06
ENSG00000181092	ADIPOQ	adiponectin, C1Q and collagen domain containing	6.95	3.40E-03
ENSG00000123500	COL10A1	collagen type X alpha 1 chain	6.28	9.19E-15
ENSG00000178363	CALML3	calmodulin like 3	5.62	4.00E-04
ENSG00000165376	CLDN2	claudin 2	5.60	1.91E-08
ENSG00000144583	MARCHF4	membrane associated ring-CH-type finger 4	5.21	4.15E-10
ENSG00000140557	ST8SIA2	ST8 alpha-N-acetyl-neuraminide alpha-2,8-sialyltransferase 2	4.98	2.49E-05
ENSG00000205076	LGALS7	galectin 7	4.97	5.20E-03
ENSG00000204983	PRSS1	serine protease 1	4.96	8.70E-03
ENSG00000170373	CST1	cystatin SN	4.93	5.00E-04
ENSG00000134757	DSG3	desmoglein 3	4.86	1.50E-05
ENSG00000264717	NPY4R2	neuropeptide Y receptor Y4-2	4.83	1.50E-03
ENSG00000169676	DRD5	dopamine receptor D5	4.77	3.90E-06
ENSG00000163599	CTLA4	cytotoxic T-lymphocyte associated protein 4	4.70	2.80E-03
ENSG00000086570	FAT2	FAT atypical cadherin 2	4.66	9.00E-04
ENSG00000145681	HAPLN1	hyaluronan and proteoglycan link protein 1	4.65	5.63E-06
ENSG00000268297	CLEC4GP1	C-type lectin domain family 4 member G pseudogene 1	4.50	5.30E-07
ENSG00000151952	TMEM132D	transmembrane protein 132D	4.47	2.45E-05
ENSG00000183715	OPCML	opioid binding protein/cell adhesion molecule like	4.46	1.10E-03

B)

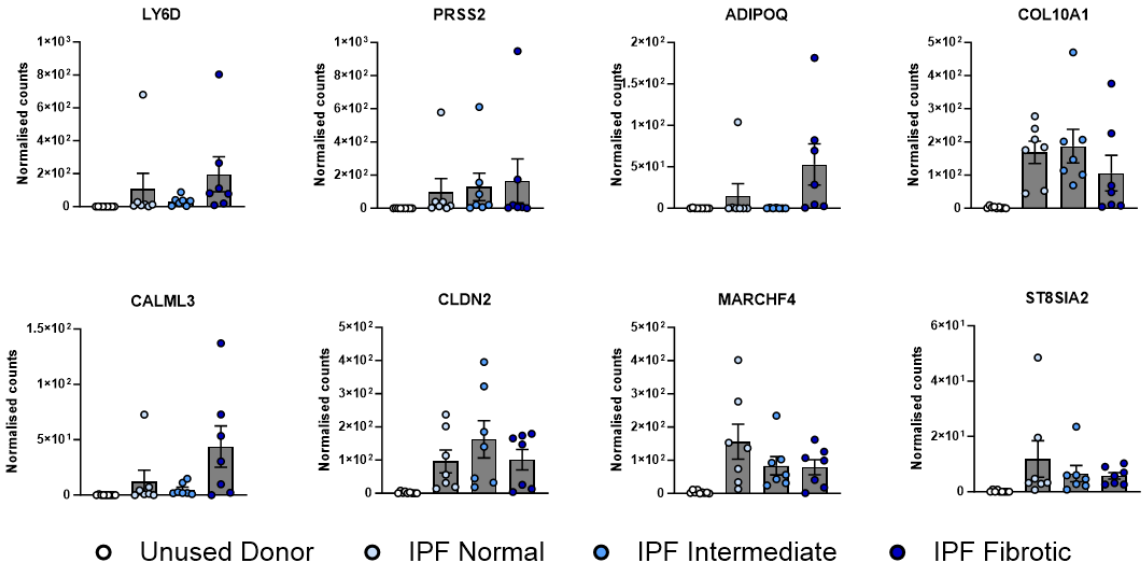

Figure 55: Top significantly upregulated genes in unused donor vs IPF normal comparison A) Table of significantly upregulated genes (padj<0.05 and Log2FC±2) beginning with highest log2FC B) Graphs of top 8 upregulated genes in all IPF regions and unused donor controls. All data are presented as mean ± SEM.

A)

UD vs IPF Normal- Top significantly downregulated genes

Ensembl ID	Gene ID	Description	logFC	P Adj Value
ENSG00000187094	CCK	cholecystokinin	-7.68	2.2E-11
ENSG00000108342	CSF3	colony stimulating factor 3	-7.49	5.0E-09
ENSG00000212901	KRTAP3-1	keratin associated protein 3-1	-7.05	5.0E-04
ENSG00000170423	KRT78	keratin 78	-6.59	1.0E-04
ENSG00000219163	HMGB1P20	high mobility group box 1 pseudogene 20	-6.28	6.0E-04
ENSG00000171711	DEFB4A	defensin beta 4A	-5.92	7.9E-03
ENSG00000177257	DEFB4B	defensin beta 4B	-5.88	9.8E-03
ENSG00000114349	GNAT1	G protein subunit alpha transducin 1	-5.83	6.0E-04
ENSG00000115009	CCL20	C-C motif chemokine ligand 20	-5.70	1.2E-07
ENSG00000186466	AQP7P1	aquaporin 7 pseudogene 1	-5.60	1.6E-03
ENSG00000009724	MASP2	MBL associated serine protease 2	-5.59	3.7E-03
ENSG00000240023	RPLP0P3	ribosomal protein, large, P0 (RPLP0) pseudogene	-5.54	9.0E-04
ENSG00000232656	IDI2-AS1	IDI2 antisense RNA 1	-5.46	2.7E-03
ENSG00000236581	STARD13-AS	STARD13 antisense RNA	-5.45	6.1E-03
ENSG00000140465	CYP1A1	cytochrome P450 family 1 subfamily A member 1	-5.13	1.1E-03
ENSG00000197632	SERPINB2	serpin family B member 2	-5.11	1.3E-06
ENSG00000163661	PTX3	pentraxin 3	-5.05	6.5E-07
ENSG00000205362	MT1A	metallothionein 1A	-5.04	1.0E-06
ENSG00000213386	LINC00478	family with sequence similarity 58, member A (FAM58A) pseudogene	-5.01	1.0E-04
ENSG00000189410	SH2D5	SH2 domain containing 5	-4.88	3.0E-06

B)

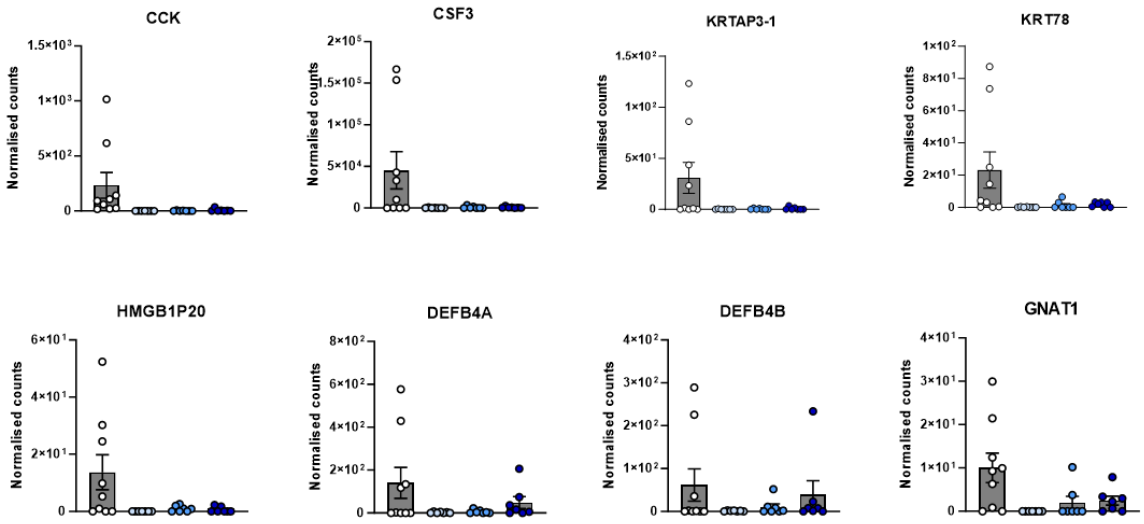

Figure 56: Top significantly downregulated genes in unused donor vs IPF normal comparison A) Table of significantly downregulated (padj<0.05 and Log2FC±2) with smallest log2FC B) Graphs of top 8 downregulated genes in all IPF regions and unused donor controls. All data are presented as mean ± SEM.

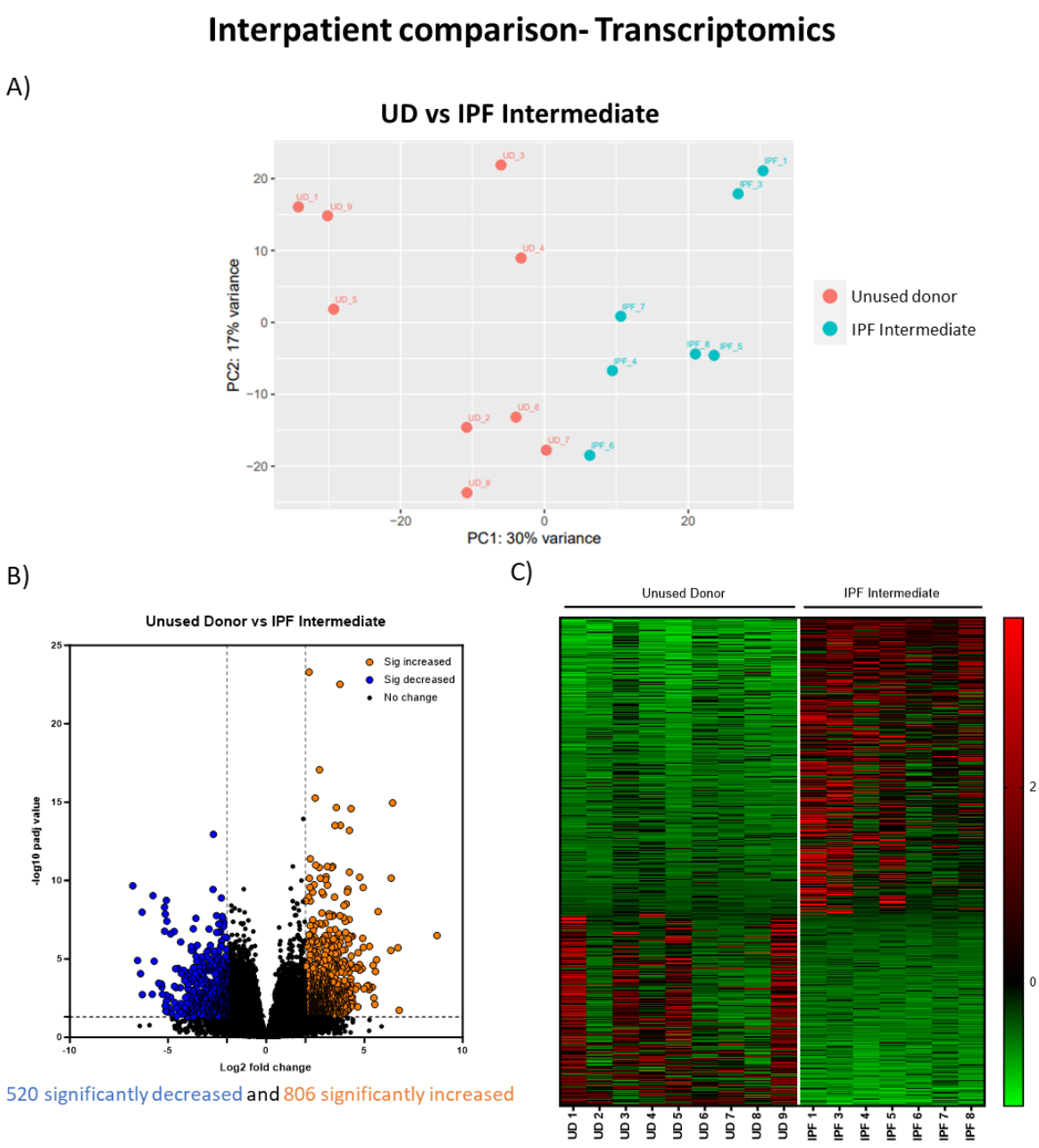

Figure 57: Transcriptomic analysis of interpatient unused donor vs IPF intermediate comparison A) Principal component analysis (PCA) plot of unused donor (n=9 donors) and IPF intermediate (n=7 donors) samples. Significantly different genes were graphed as B) volcano plot (downregulated genes in blue and upregulated genes in orange) where horizontal dashed line represents padj<0.05 and vertical dashed lines represent Log2FC±2 threshold criteria applied for significance C) heat map (downregulated genes in green and upregulated genes in red) for significantly different genes (padj<0.05 and Log2FC ±2).

A)

UD vs IPF Intermediate- Top significantly upregulated genes

Ensembl ID	Gene ID	Description	logFC	P Adj Value
ENSG00000275896	PRSS2	serine protease 2	8.70	3.27E-07
ENSG00000167656	LY6D	lymphocyte antigen 6 family member D	6.71	1.95E-06
ENSG00000123500	COL10A1	collagen type X alpha 1 chain	6.44	1.12E-15
ENSG00000165376	CLDN2	claudin 2	6.36	7.12E-11
ENSG00000170373	CST1	cystatin SN	6.35	2.90E-06
ENSG00000169676	DRD5	dopamine receptor D5	5.69	9.64E-09
ENSG00000166426	CRABP1	cellular retinoic acid binding protein 1	5.62	1.13E-05
ENSG00000211633	IGKV1D-42	immunoglobulin kappa variable 1D-42 (non-functional)	5.56	1.00E-04
ENSG00000066230	SLC9A3	solute carrier family 9 member A3	5.53	8.00E-03
ENSG00000204983	PRSS1	serine protease 1	5.48	3.10E-03
ENSG00000183715	OPCML	opioid binding protein/cell adhesion molecule like	5.44	2.55E-05
ENSG00000204780	IGKV1OR9-1	immunoglobulin kappa variable 1/OR9-1 (pseudogene)	5.40	6.00E-04
ENSG00000241186	TDGF1	teratocarcinoma-derived growth factor 1	5.26	1.59E-06
ENSG00000259303	IGHV2OR16-5	immunoglobulin heavy variable 2/OR16-5 (non-functional)	5.24	9.00E-04
ENSG00000163599	CTLA4	cytotoxic T-lymphocyte associated protein 4	5.24	7.00E-04
ENSG00000170374	SP7	Sp7 transcription factor	5.13	5.00E-04
ENSG00000233705	SLC26A4-AS1	SLC26A4 antisense RNA 1	4.98	8.00E-04
ENSG00000156234	CXCL13	C-X-C motif chemokine ligand 13	4.95	1.85E-06
ENSG00000211893	IGHG2	immunoglobulin heavy constant gamma 2 (G2m marker)	4.93	2.76E-10
ENSG00000234224	TMEM229A	transmembrane protein 229A	4.91	4.86E-07

B)

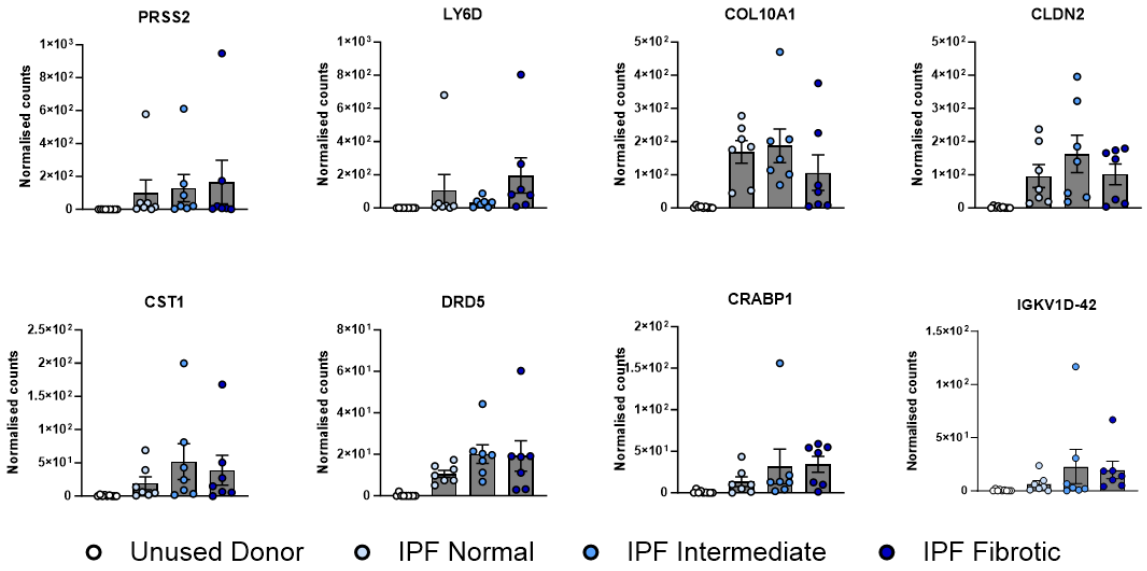

Figure 58: Top significantly upregulated genes in unused donor vs IPF intermediate comparison A) Table of significantly upregulated genes (padj<0.05 and Log2FC±2) beginning with highest log2FC B) Graphs of top 8 upregulated genes in all IPF regions and unused donor controls. All data are presented as mean ± SEM.

A)

UD vs IPF Intermediate- Top significantly downregulated genes

Ensembl ID	Gene ID	Description	logFC	P Adj Value
ENSG00000187094	CCK	cholecystokinin	-6.80	2.17E-10
ENSG00000169836	TACR3	tachykinin receptor 3	-6.55	1.25E-05
ENSG00000240023	RPLP0P3	ribosomal protein, large, P0 (RPLP0) pseudogene	-6.40	1.00E-04
ENSG00000212901	KRTAP3-1	keratin associated protein 3-1	-6.31	1.90E-03
ENSG00000168703	WFDC12	WAP four-disulfide core domain 12	-5.77	9.25E-10
ENSG00000108342	CSF3	colony stimulating factor 3	-5.71	1.41E-05
ENSG00000244215	LINC02016	long intergenic non-protein coding RNA 2016	-5.47	4.00E-04
ENSG00000140465	CYP1A1	cytochrome P450 family 1 subfamily A member 1	-5.32	6.00E-04
ENSG00000260799	KRT8P50	keratin 8 pseudogene 50	-5.29	1.80E-03
ENSG00000110203	FOLR3	folate receptor gamma	-5.18	5.10E-09
ENSG00000189410	SH2D5	SH2 domain containing 5	-5.17	1.72E-07
ENSG00000115602	IL1RL1	interleukin 1 receptor like 1	-5.14	1.40E-08
ENSG00000280924	LINC00628	long intergenic non-protein coding RNA 628	-5.14	9.80E-03
ENSG00000232656	IDI2-AS1	IDI2 antisense RNA 1	-5.09	5.00E-03
ENSG00000163283	ALPP	alkaline phosphatase, placental	-5.08	1.86E-09
ENSG00000138411	HECW2	HECT, C2 and WW domain containing E3 ubiquitin protein ligase 2	-5.07	2.10E-03
ENSG00000115008	IL1A	interleukin 1 alpha	-5.06	3.91E-08
ENSG00000204792	LINC01291	long intergenic non-protein coding RNA 1291	-4.94	1.31E-02
ENSG00000162771	FAM71A	family with sequence similarity 71 member A	-4.87	2.80E-03
ENSG00000110243	APOA5	apolipoprotein A5	-4.83	2.83E-02

B)

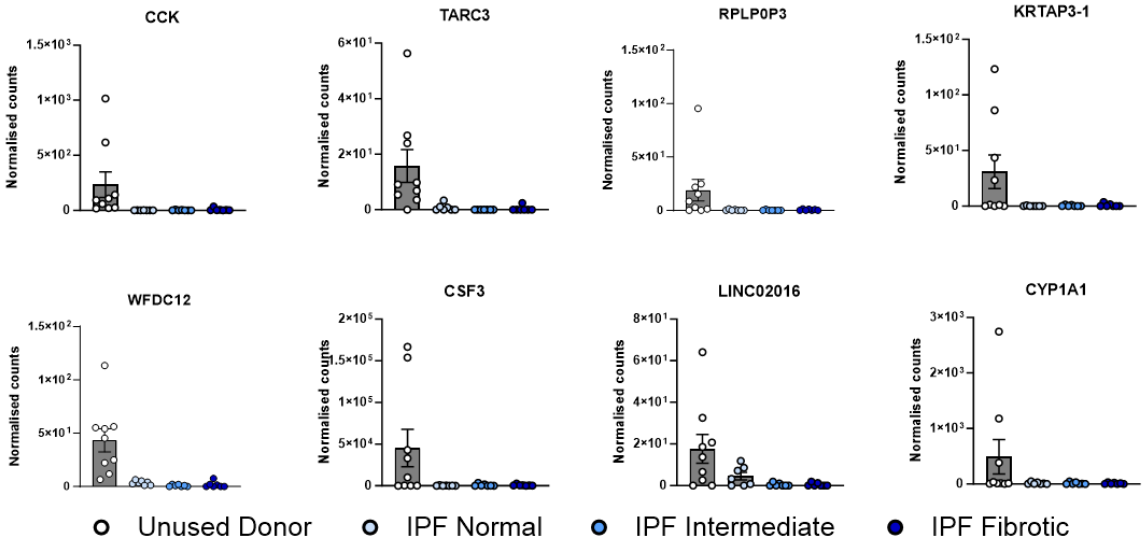

Figure 59: Top significantly downregulated genes in unused donor vs IPF intermediate comparison A) Table of significantly downregulated genes (padj<0.05 and Log2FC±2) beginning with smallest log2FC B) Graphs of top 8 downregulated genes in all IPF regions and unused donor controls. All data are presented as mean ± SEM.

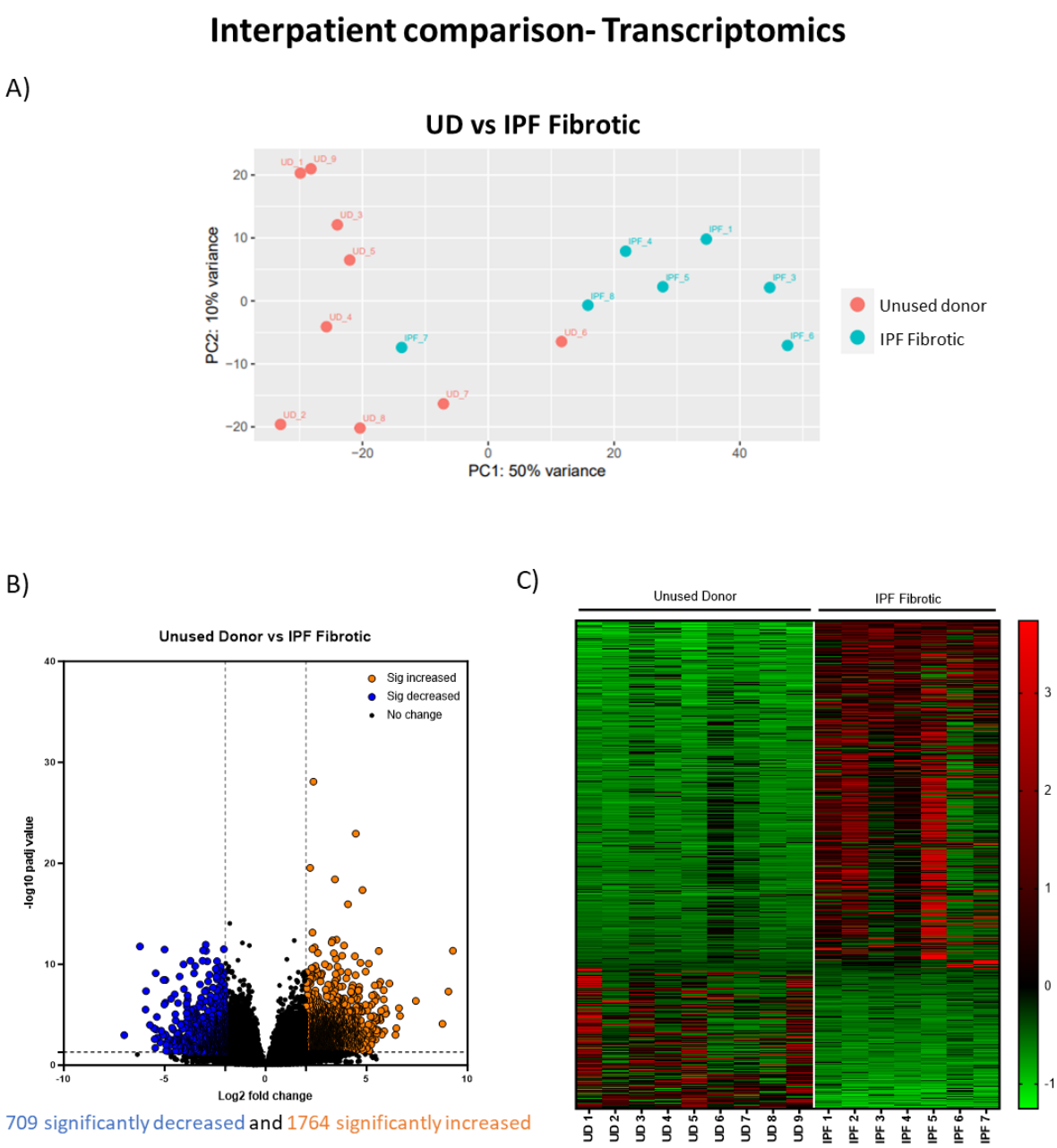

Figure 60: Transcriptomic analysis of interpatient unused donor vs IPF fibrotic comparison A) Principal component analysis (PCA) plot of unused donor (n=9 donors) and IPF fibrotic (n=7 donors) samples. Significantly different genes were graphed as B) volcano plot (downregulated genes in blue and upregulated genes in orange) where horizontal dashed line represents padj<0.05 and vertical dashed lines represent Log2FC±2 threshold criteria applied for significance C) heat map (downregulated genes in green and upregulated genes in red) for significantly different genes (padj<0.05 and Log2FC ±2).

A)

UD vs IPF Fibrotic- Top significantly upregulated genes

Ensembl ID	Gene ID	Description	logFC	P Adj Value
ENSG00000167656	LY6D	lymphocyte antigen 6 family member D	9.28	4.59E-12
ENSG00000275896	PRSS2	serine protease 2	9.06	5.06E-08
ENSG00000181092	ADIPOQ	adiponectin, C1Q and collagen domain containing	8.76	1.00E-04
ENSG00000178363	CALML3	calmodulin like 3	7.44	4.22E-07
ENSG00000170454	KRT75	keratin 75	6.66	1.28E-05
ENSG00000233705	SLC26A4-AS1	SLC26A4 antisense RNA 1	6.60	2.18E-06
ENSG00000204983	PRSS1	serine protease 1	6.47	2.00E-04
ENSG00000066230	SLC9A3	solute carrier family 9 member A3	6.43	1.00E-03
ENSG00000134757	DSG3	desmoglein 3	6.13	8.01E-09
ENSG00000198183	BPIFA1	BPI fold containing family A member 1	5.97	6.41E-06
ENSG00000170373	CST1	cystatin SN	5.94	8.26E-06
ENSG00000180347	ITPRID1	ITPR interacting domain containing 1	5.90	2.43E-06
ENSG00000145642	SHISAL2B	shisa like 2B	5.87	4.00E-04
ENSG00000241186	TDGF1	teratocarcinoma-derived growth factor 1	5.85	3.68E-08
ENSG00000166426	CRABP1	cellular retinoic acid binding protein 1	5.72	4.07E-06
ENSG00000174697	LEP	leptin	5.69	3.35E-05
ENSG00000165376	CLDN2	claudin 2	5.68	5.55E-09
ENSG00000169676	DRD5	dopamine receptor D5	5.61	1.09E-08
ENSG00000123500	COL10A1	collagen type X alpha 1 chain	5.60	4.81E-12
ENSG00000229544	NKX1-2	NK1 homeobox 2	5.58	4.00E-04

B)

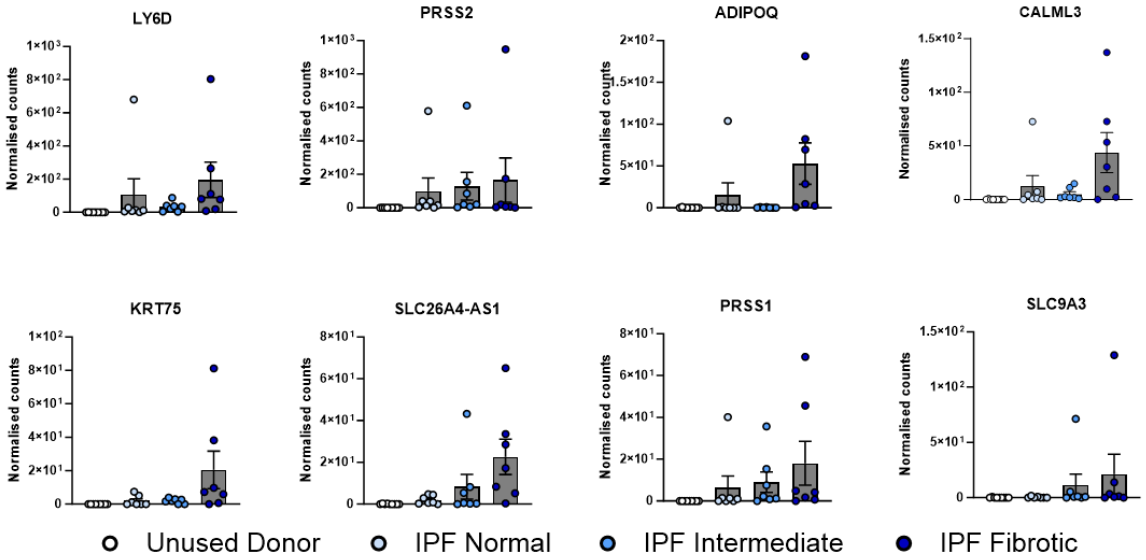

Figure 61: Top significantly upregulated genes in unused donor vs IPF fibrotic comparison A) Table of significantly upregulated genes (padj<0.05 and Log2FC±2) beginning with highest log2FC B) Graphs of top 8 upregulated genes in all IPF regions and unused donor controls. All data are presented as mean ± SEM.

A) **UD vs IPF Fibrotic- Top significantly downregulated genes**

Ensembl ID	Gene ID	Description	logFC	P Adj Value
ENSG00000115602	IL1RL1	interleukin 1 receptor like 1	-6.23	1.71E-12
ENSG00000108342	CSF3	colony stimulating factor 3	-5.95	3.08E-06
ENSG00000244215	LINC02016	long intergenic non-protein coding RNA 2016	-5.74	1.00E-04
ENSG00000140465	CYP1A1	cytochrome P450 family 1 subfamily A member 1	-5.54	2.00E-04
ENSG00000009724	MASP2	MBL associated serine protease 2	-5.50	2.60E-03
ENSG00000228437	LINC02474	long intergenic non-protein coding RNA 2474	-5.47	1.88E-02
ENSG00000110203	FOLR3	folate receptor gamma	-5.45	7.58E-10
ENSG00000187821	HELT	helt bHLH transcription factor	-5.39	1.60E-05
ENSG00000232656	IDI2-AS1	IDI2 antisense RNA 1	-5.37	1.90E-03
ENSG00000212901	KRTAP3-1	keratin associated protein 3-1	-5.23	5.40E-03
ENSG00000169836	TACR3	tachykinin receptor 3	-5.17	4.00E-04
ENSG00000164283	ESM1	endothelial cell specific molecule 1	-5.06	3.57E-09
ENSG00000187094	CCK	cholecystokinin	-5.02	9.72E-07
ENSG00000142748	FCN3	ficolin 3	-5.01	3.43E-12
ENSG00000189410	SH2D5	SH2 domain containing 5	-4.97	6.36E-07
ENSG00000168703	WFDC12	WAP four-disulfide core domain 12	-4.97	3.68E-09
ENSG00000153086	ACMSD	aminocarboxymuconate semialdehyde decarboxylase	-4.96	9.00E-04
ENSG00000240457	RN7SL472P	RNA, 7SL, cytoplasmic 472, pseudogene	-4.93	3.66E-02
ENSG00000199161	MIR126	microRNA 126	-4.93	9.60E-03
ENSG00000189419	SPATA41	spermatogenesis associated 41	-4.84	3.88E-02

B)

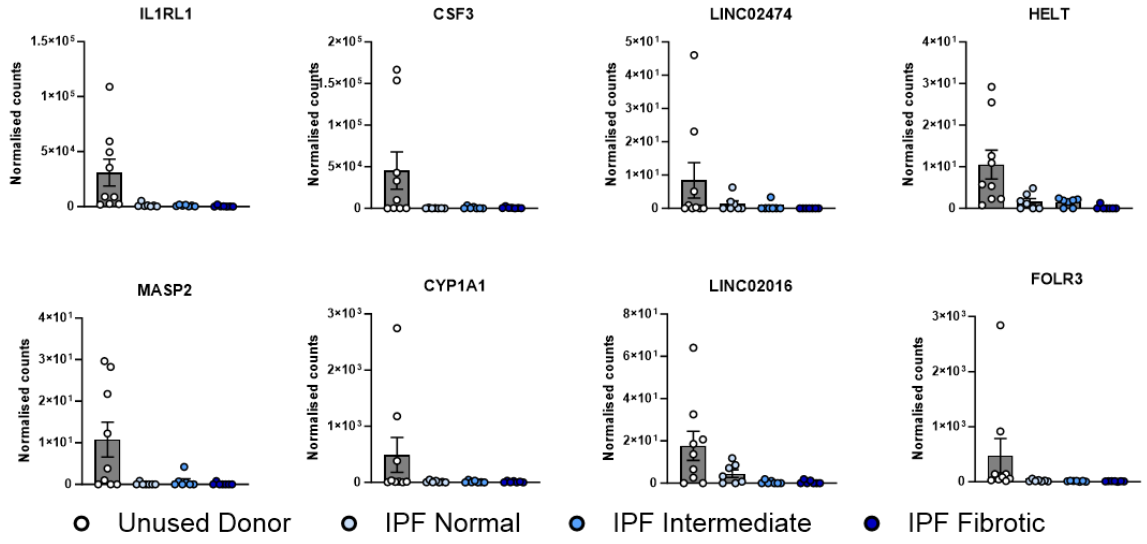

Figure 62: Top significantly downregulated genes in unused donor vs IPF fibrotic comparison A) Table of significantly downregulated genes (padj<0.05 and Log2FC±2) beginning with smallest log2FC B) Graphs of top 8 downregulated genes in all IPF regions and unused donor controls.

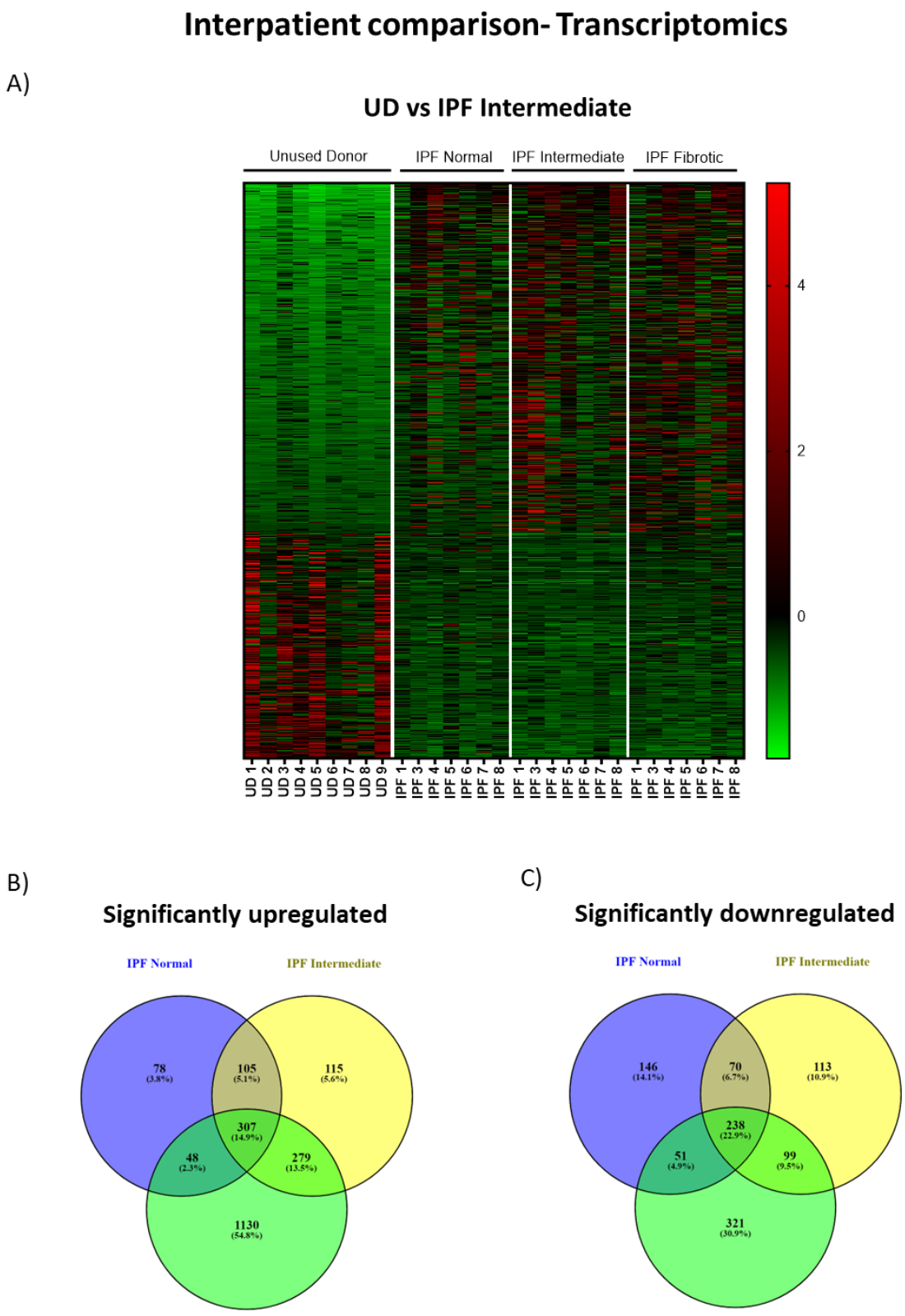

Figure 63: Overview of transcriptomic interpatient analysis A) Heat map of significantly different genes (padj<0.05 and Log2FC±2) identified from unused donor vs IPF intermediate comparison in all samples (downregulated genes in green and upregulated genes in red). Venny diagram of B) significantly upregulated genes in IPF normal, intermediate and fibrotic vs unused donor samples and C) significantly downregulated genes in IPF normal, intermediate and fibrotic vs unused donor samples.

4.2.2.2 Interpatient proteomics

While RNA sequencing provides valuable insights into gene expression patterns, the presence and abundance of a transcript does not necessarily correlate with the levels of the corresponding protein. Consequently, proteomic profiling of unused donor lungs and regional IPF tissue was performed to provide a more direct measurement of protein abundance and gain insights into functional changes that may not be captured at the transcript level. First, in order to visualise the variation in patient samples, PCA plots were generated for the comparison of UD tissue to each IPF region (Figure 64A, Figure 67A, Figure 70A). Results confirmed distinct clustering based on disease state, with IPF tissue being more similar to each other than to UD samples, with the exception of IPF 1 donor normal and intermediate regions which appeared to be more similar to UD lungs (Figure 64A, Figure 67A). Interestingly, IPF tissue was shown to become less similar to unused donor controls the further along the disease spectrum the samples were, with IPF fibrotic regions of tissue showing the most variation to UD controls (Figure 70A).

Of the 3,886 proteins identified, 2,600 proteins were present in a minimum of 4 replicates of unused donor (n=9 donors) and IPF normal (n=8 donors) samples. Of these 2,600 proteins, 625 proteins (24%) were significantly different between normal IPF tissue and UD control lungs, with 242 upregulated proteins (of which 26 proteins have a fold change (FC)>1.5; Figure 65) and 383 downregulated proteins (of which 29 proteins have FC>1.5; Figure 66) in the macroscopically normal regions compared to UD lungs (Figure 64B,C). 2,643 proteins were present in a minimum of 4 replicates of unused donor (n=9 donors) and IPF intermediate (n=8 donors) samples, with 726 (27%) significantly different proteins identified. Of these, 270 proteins were significantly increased (of which 45 have FC>1.5; Figure 68) and 456 proteins were significantly decreased (of which 33 have FC>1.5; Figure 69) in intermediate regions of IPF tissue compared to UD lungs (Figure 67B, C). Finally, 2,575 proteins were present in a minimum of 4 replicates of unused donor (n=9 donors) and IPF fibrotic (n=8 donors) samples, with 1,007 (39%) significantly differential proteins identified between regions. 342 proteins were significantly increased (of which 75 have FC>1.5; Figure 71) and 665 proteins were significantly decreased (of which 49 have a FC>1.5; Figure 72) in IPF fibrotic tissue compared to UD lungs (Figure 70B, C).

Further interrogation of protein heterogeneity between IPF regions and UD controls revealed that, of the significantly upregulated proteins, 146 (33.3%) were common to all regions of IPF

tissue, suggesting they represented core IPF proteins. Moreover, 78 (17.8%) were upregulated in IPF intermediate and fibrotic regions, 30 (6.8%) were upregulated in IPF normal and intermediate and 15 (3.5%) were upregulated in IPF normal and fibrotic only. Finally, a number of proteins were exclusively upregulated in each region of normal (51 proteins, 11.6%), intermediate (16 proteins, 3.6%) and fibrotic (103 proteins, 23.5%) IPF tissue (Figure 73B). Consistent with histological findings, assessment of COL1A1 found no changes in protein expression in the IPF normal regions compared to UD controls (logFC=0.428, p=0.259), but significantly more COL1A1 in later stage intermediate (logFC=0.902, p=0.01) and end-stage fibrotic (logFC=1.225, p=0.007) regions compared to control tissue. These findings were in contrast to transcriptomic analysis of the same regions, where COL1A1 was significantly upregulated in all regions of IPF tissue, including macroscopically normal regions, suggesting that upregulation of pro-fibrotic genes in normal tissue is a precursor to functional changes in pro-fibrotic protein expression in the later intermediate regions.

Conversely, of the significantly downregulated proteins, 224 (34.3%) were common to all regions of IPF tissue, 114 (13.9%) were downregulated in IPF intermediate and fibrotic regions, 54 (6.6%) were downregulated in IPF normal and intermediate and 25 (3%) were downregulated in IPF normal and fibrotic only. Additionally, 60 proteins (7.3%) were exclusively downregulated in IPF normal regions, 44 proteins (5.3%) were downregulated in IPF intermediate regions alone and 282 proteins (34.3%) were downregulated only in end-stage fibrotic tissue (Figure 73C). One of the most highly downregulated proteins in the actively remodelling (normal and intermediate) regions of IPF tissue was RAGE (UD vs IPF normal; logFC=-1.85, p=0.015 and UD vs IPF intermediate; logFC=-2.688, p=0.0001), which has previously been shown to be decreased in IPF [413]. Notably, downregulated proteins in all IPF regions were enriched with innate-immunity associated proteins and antimicrobial peptides including bactericidal permeability-increasing protein (BPI), myeloperoxidase (MPO), S100A8/9, neutrophil collagenase (MMP8), neutrophil defensin 3 (DEF3), neutrophil cytosol factor 2 and 4 and neutrophil elastase (NE), indicating early changes in innate immune signalling during fibrogenesis.

Taken together, these data show that, similar to transcriptomic findings, there are distinct patterns of protein expression present in each region of IPF tissue compared to 'healthy' unused donor lungs. Moreover, there are a number of proteins which are significantly up- or

down- regulated in all regions of IPF tissue compared to control lungs, which may be considered as core IPF proteins. Interestingly, approximately 24% of proteins detected in macroscopically normal regions of IPF tissue were significantly different to unused donor lungs, suggesting that even at this early stage there are significant changes in the protein landscape of seemingly unaffected regions of tissue. However, though this method of interpatient sampling is able to determine differences between health and disease, it does not specifically address how these differential proteins are modulated throughout disease progression. Consequently, further interrogation of differential proteins between IPF regions could aid identification of novel targets for early therapeutic intervention.

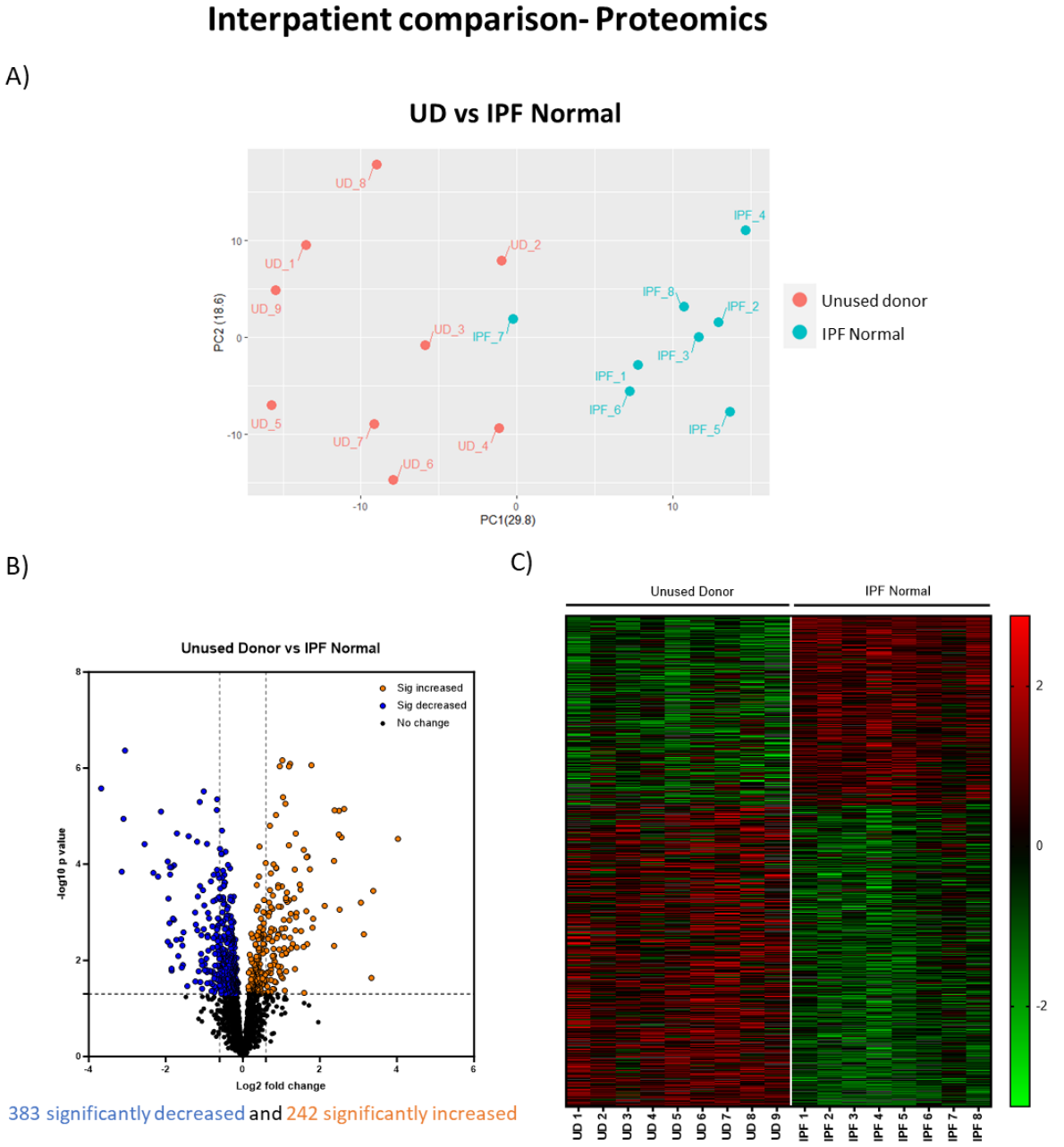

Figure 64: Proteomic analysis of interpatient unused donor vs IPF normal comparison A) Principal component analysis (PCA) plot of unused donor (n=9 donors) and IPF normal (n=8 donors) samples. Significantly different proteins ($p<0.05$) were graphed as B) volcano plot (downregulated proteins in blue and upregulated proteins in orange) and C) heat map (downregulated proteins in green and upregulated proteins in red).

A)

UD vs IPF Normal- Top significantly upregulated proteins

Accession Code	Protein ID	Protein Name	log2FC	P Value
P04114	APOB	Apolipoprotein B-100	4.02	2.97E-05
P11277-2	SPTB1	Isoform 2 of Spectrin beta chain, erythrocytic	3.38	4.00E-04
P01861-1	IGHG4	Isoform 1 of Immunoglobulin heavy constant gamma 4	3.34	2.32E-02
P69891	HBG1	Hemoglobin subunit gamma-1	3.14	2.90E-03
P02549	SPTA1	Spectrin alpha chain, erythrocytic 1	3.06	6.00E-04
P69905	HBA	Hemoglobin subunit alpha	2.63	7.10E-06
P02730	B3AT	Band 3 anion transport protein	2.56	2.77E-05
P16157-14	ANK1	Isoform Er13 of Ankyrin-1	2.51	9.00E-04
P68871	HBB	Hemoglobin subunit beta	2.50	7.73E-06
P00915	CAH1	Carbonic anhydrase 1	2.49	2.42E-05
P02042	HBD	Hemoglobin subunit delta	2.38	7.58E-06
P08263	GSTA1	Glutathione S-transferase A1	2.37	5.00E-03
Q14192	FHL2	Four and a half LIM domains protein 2	2.36	1.00E-04
Q8N2S1-2	LTBP4	Isoform 2 of Latent-transforming growth factor beta-binding protein 4	2.12	7.00E-04
P01031	CO5	Complement C5	1.82	1.40E-03
O15061	SYNEM	Synemin	1.81	2.10E-03
P22570	ADRO	NADPH:adrenodoxin oxidoreductase, mitochondrial	1.78	8.71E-07
Q14767	LTBP2	Latent-transforming growth factor beta-binding protein 2	1.74	1.00E-04
P0DOY3	IGLC3	Immunoglobulin lambda constant 3	1.68	1.00E-04
Q9UMS6-2	SYNP2	Isoform 2 of Synaptopodin-2	1.67	4.60E-03

B)

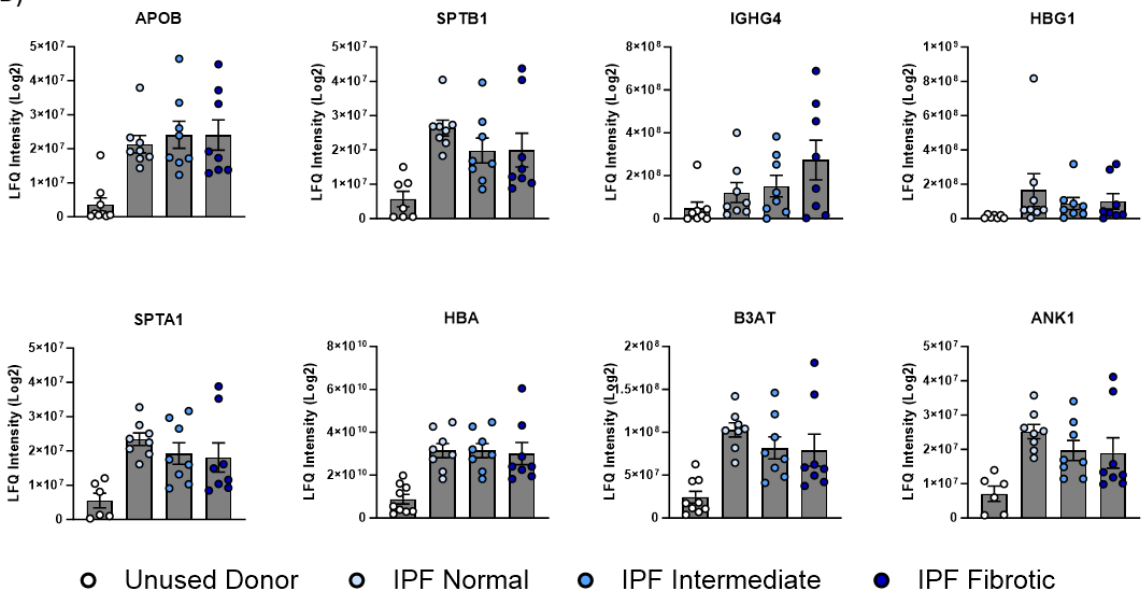

Figure 65: **Top significantly upregulated proteins in unused donor vs IPF normal comparison** A) Table of significantly upregulated proteins ($p<0.05$) beginning with highest log2FC B) Graphs of top 8 upregulated proteins in all IPF regions and unused donor controls. All data are presented as mean ± SEM.

A)

UD vs IPF Normal- Top significantly downregulated proteins

Accession Code	Protein ID	Protein Name	log2FC	P Value
Q9HD89	RETN	Resistin	-3.68	2.66E-06
P17213	BPI	Bactericidal permeability-increasing protein	-3.14	1.00E-04
P22748	CAH4	Carbonic anhydrase 4	-3.10	1.14E-05
P16671	CD36	Platelet glycoprotein 4	-3.06	4.32E-07
P20160	CAP7	Azurocidin	-2.55	3.82E-05
Q9UM07	PADI4	Protein-arginine deiminase type-4	-2.32	2.00E-04
P24158	PRTN3	Myeloblastin	-2.20	2.00E-04
P05164-2	PERM	Isoform H14 of Myeloperoxidase	-2.12	8.05E-06
P08246	ELNE	Neutrophil elastase	-1.95	1.00E-04
P20292	AL5AP	Arachidonate 5-lipoxygenase-activating protein	-1.95	4.10E-03
O75594	PGRP1	Peptidoglycan recognition protein 1	-1.93	5.00E-04
P12821	ACE	Angiotensin-converting enzyme	-1.91	1.70E-03
P59666	DEF3	Neutrophil defensin 3	-1.89	1.00E-04
P02788	TRFL	Lactotransferrin	-1.89	2.00E-04
P53420	CO4A4	Collagen alpha-4(IV) chain	-1.88	4.90E-03
P06702	S10A9	Protein S100-A9	-1.85	1.00E-04
Q15109	RAGE	Advanced glycosylation end product-specific receptor	-1.85	1.50E-02
Q9BXM0	PRAX	Periaxin	-1.85	1.64E-02
P14780	MMP9	Matrix metalloproteinase-9	-1.81	1.40E-03
P22894	MMP8	Neutrophil collagenase	-1.79	1.40E-03

B)

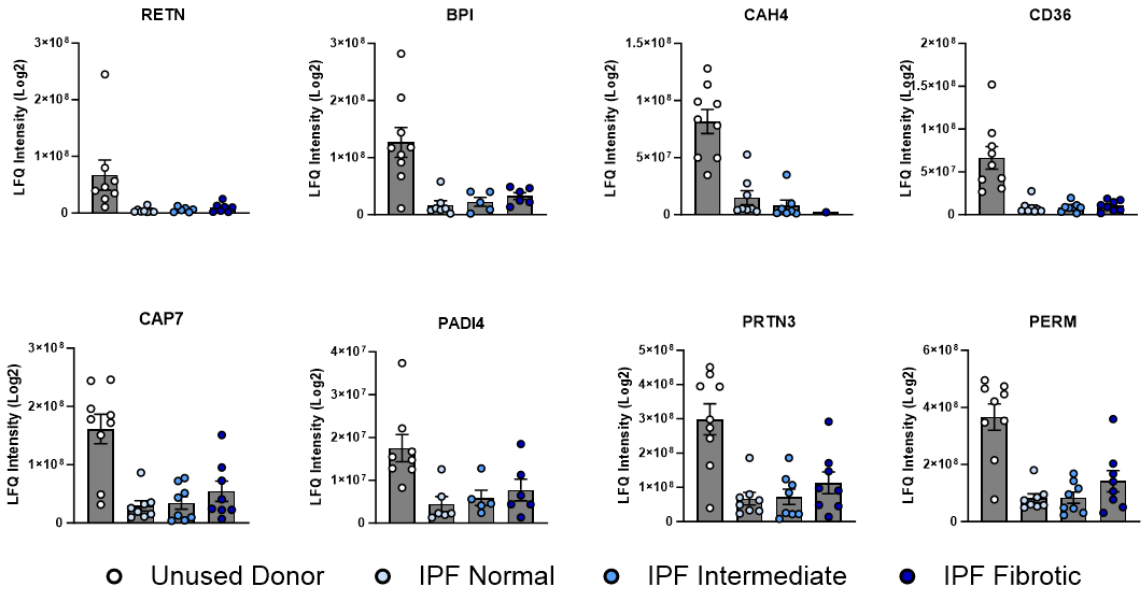

Figure 66: Top significantly downregulated proteins in unused donor vs IPF normal comparison A) Table of significantly downregulated proteins ($p<0.05$) beginning with smallest log2FC B) Graphs of top 8 downregulated proteins in all IPF regions and unused donor controls. All data are presented as mean ± SEM.

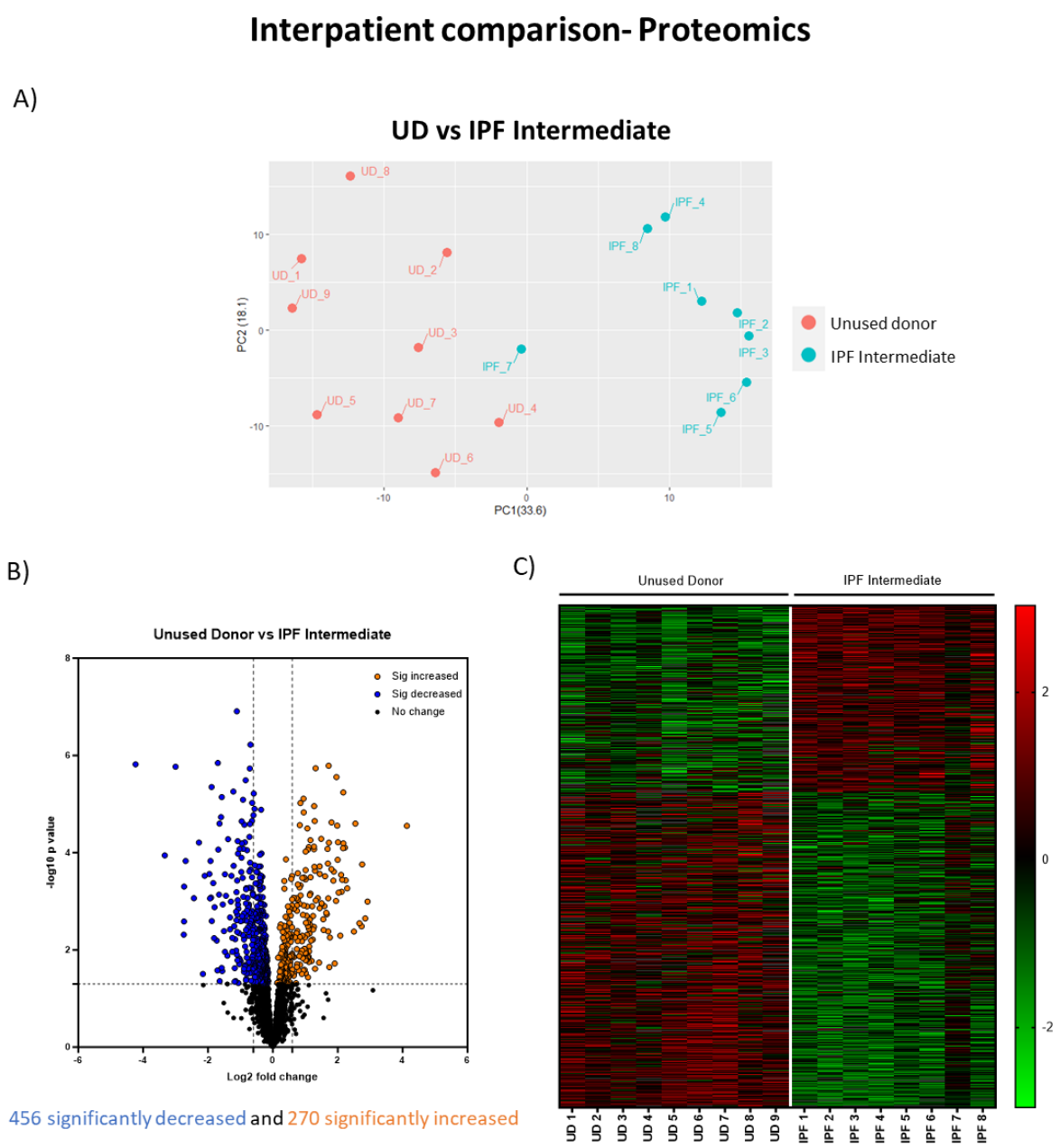

Figure 67: Proteomic analysis of interpatient unused donor vs IPF intermediate comparison A) Principal component analysis (PCA) plot of unused donor (n=9 donors) and IPF intermediate (n=8 donors) samples. Significantly different proteins ($p<0.05$) were graphed as B) volcano plot (downregulated proteins in blue and upregulated proteins in orange) and C) heat map (downregulated proteins in green and upregulated proteins in red).

A)

UD vs IPF Intermediate- Top significantly upregulated proteins

Accession Code	Protein ID	Protein Name	log2FC	P Value
P04114	APOB	Apolipoprotein B-100	4.13	2.81E-05
Q8WU39	MZB1	Marginal zone B- and B1-cell-specific protein	2.92	1.00E-03
P11277-2	SPTB1	Isoform 2 of Spectrin beta chain, erythrocytic	2.85	2.30E-03
O15061	SYNEM	Synemin	2.75	2.00E-04
P69891	HBG1	Hemoglobin subunit gamma-1	2.74	3.30E-03
P02549	SPTA1	Spectrin alpha chain, erythrocytic 1	2.67	2.80E-03
Q14192	FHL2	Four and a half LIM domains protein 2	2.54	2.52E-05
P08263	GSTA1	Glutathione S-transferase A1	2.50	4.20E-03
Q9UMS6-2	SYNP2	Isoform 2 of Synaptopodin-2	2.29	5.00E-04
Q9BY50	SC11C	Signal peptidase complex catalytic subunit SEC11C	2.24	4.00E-04
P69905	HBA	Hemoglobin subunit alpha	2.22	1.00E-04
P17661	DESM	Desmin	2.17	1.00E-04
Q05707	COEA1	Collagen alpha-1(XIV) chain	2.17	5.75E-06
P68871	HBB	Hemoglobin subunit beta	2.17	1.00E-04
P02730	B3AT	Band 3 anion transport protein	2.14	4.00E-04
Q8N2S1-2	LTBP4	Isoform 2 of Latent-transforming growth factor beta-binding protein 4	2.12	6.00E-04
P00915	CAH1	Carbonic anhydrase 1	2.10	3.00E-04
P16157-14	ANK1	Isoform Er13 of Ankyrin-1	2.08	5.10E-03
P01031	CO5	Complement C5	2.03	7.00E-04
P04216	THY1	Thy-1 membrane glycoprotein	2.01	1.00E-04

B)

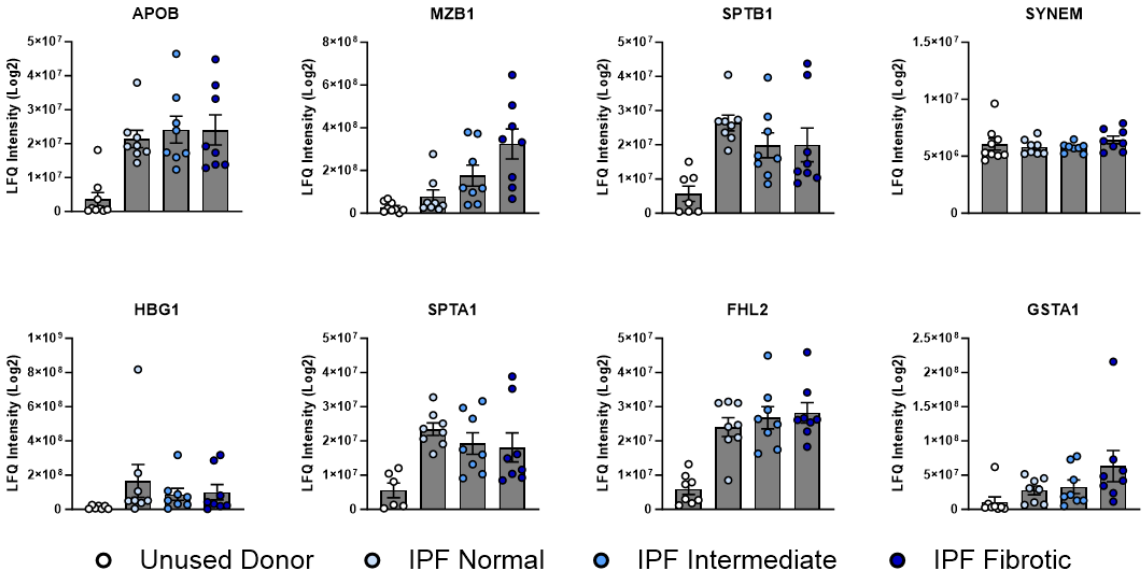

Figure 68: Top significantly upregulated proteins in unused donor vs IPF intermediate comparison A) Table of significantly upregulated proteins ($p<0.05$) beginning with highest log2FC B) Graphs of top 8 upregulated proteins in all IPF regions and unused donor controls. All data are presented as mean ± SEM.

A)

UD vs IPF Intermediate Top significantly downregulated proteins

Accession Code	Protein ID	Protein Name	log2FC	P.Value
P22748	CAH4	Carbonic anhydrase 4	-4.23	1.52E-06
Q9HD89	RETN	Resistin	-3.33	1.14E-04
P16671	CD36	Platelet glycoprotein 4	-3.00	1.71E-06
Q9BXM0	PRAX	Periaxin	-2.75	4.85E-03
P17213	BPI	Bactericidal permeability-increasing protein	-2.74	2.61E-03
P20160	CAP7	Azurocidin	-2.74	4.99E-04
Q15109	RAGE	Advanced glycosylation end product-specific receptor	-2.69	1.48E-04
P24158	PRTN3	Myeloblastin	-2.43	8.66E-04
P05164-2	PERM	Isoform H14 of Myeloperoxidase	-2.28	6.20E-05
Q16787	LAMA3	Laminin subunit alpha-3	-2.16	3.13E-02
P08246	ELNE	Neutrophil elastase	-2.10	3.00E-04
P59666	DEF3	Neutrophil defensin 3	-1.96	2.74E-04
Q9NZN3	EHD3	EH domain-containing protein 3	-1.94	8.73E-04
P05109	S10A8	Protein S100-A8	-1.93	1.48E-04
P02788	TRFL	Lactotransferrin	-1.91	8.38E-04
P61626	LYSC	Lysozyme C	-1.89	4.47E-06
P12821	ACE	Angiotensin-converting enzyme	-1.88	2.55E-03
P06702	S10A9	Protein S100-A9	-1.84	4.21E-04
P14780	MMP9	Matrix metalloproteinase-9	-1.81	5.73E-03
O75594	PGRP1	Peptidoglycan recognition protein 1	-1.80	1.32E-03

B)

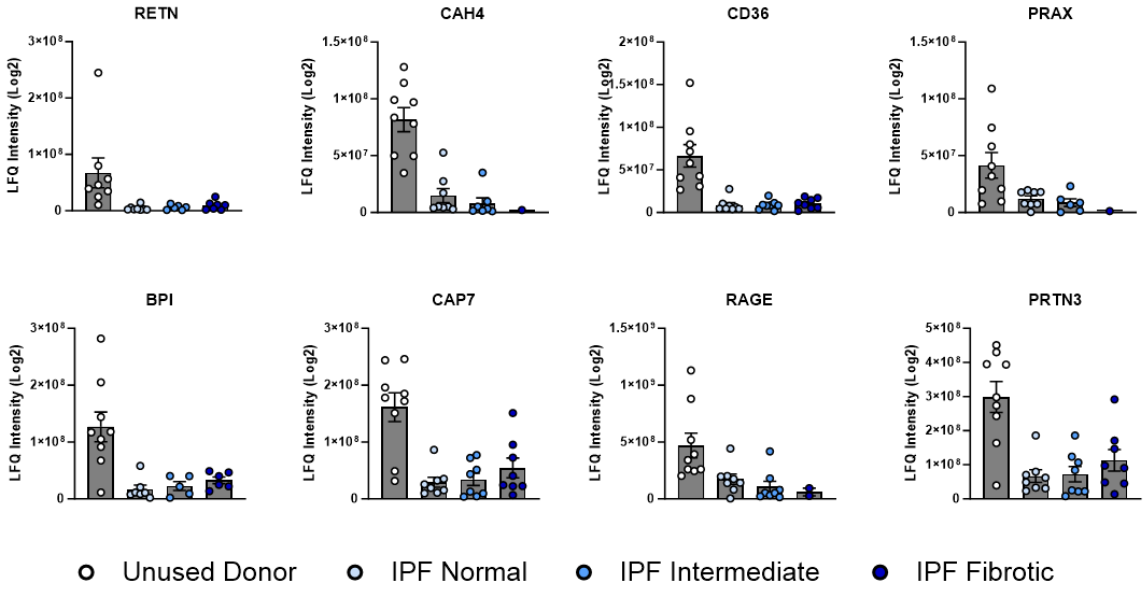

Figure 69: Top significantly downregulated proteins in unused donor vs IPF intermediate comparison
A) Table of significantly downregulated proteins ($p<0.05$) beginning with smallest log2FC B) Graphs of top 8 downregulated proteins in all IPF regions and unused donor controls. All data are presented as mean ± SEM.

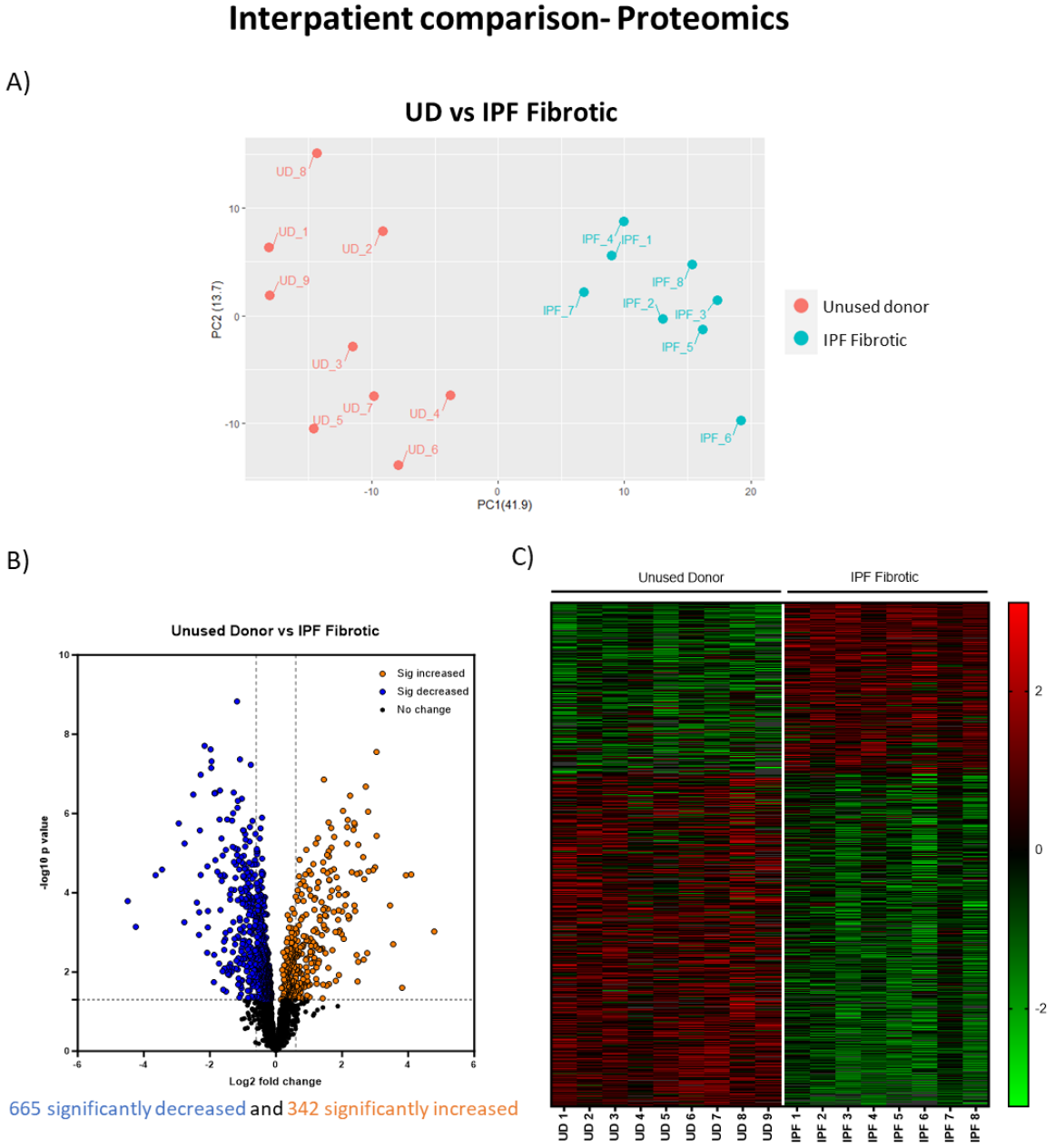

Figure 70: Proteomic analysis of interpatient unused donor vs IPF fibrotic comparison A) Principal component analysis (PCA) plot of unused donor (n=9 donors) and IPF fibrotic (n=8 donors) samples. Significantly different proteins ($p<0.05$) were graphed as B) volcano plot (downregulated proteins in blue and upregulated proteins in orange) and C) heat map (downregulated proteins in green and upregulated proteins in red).

UD vs IPF Fibrotic- Top significantly upregulated proteins

A)

Accession Code	Protein ID	Protein Name	log2FC	P Value
Q8TDL5	BPIB1	BPI fold-containing family B member 1	4.79	1.00E-03
P04114	APOB	Apolipoprotein B-100	4.09	3.46E-05
Q8WU39	MZB1	Marginal zone B- and B1-cell-specific protein	3.93	3.62E-05
P01861-1	IGHG4	Isoform 1 of Immunoglobulin heavy constant gamma 4	3.82	2.50E-02
Q13938-4	CAYP1	Isoform 3 of Calcyphosin	3.54	2.00E-03
P08263	GSTA1	Glutathione S-transferase A1	3.45	2.00E-04
Q9BY50	SC11C	Signal peptidase complex catalytic subunit SEC11C	3.04	3.68E-06
P01876-1	IGHA1	Isoform 1 of Immunoglobulin heavy constant alpha 1	3.04	2.79E-08
Q13683-3	ITA7	Isoform Alpha-7X1B of Integrin alpha-7	3.00	2.27E-05
Q9UMS6-2	SYNP2	Isoform 2 of Synaptopodin-2	2.94	2.69E-05
O15061	SYNEM	Synemin	2.80	2.87E-05
P17661	DESM	Desmin	2.79	8.99E-07
P11277-2	SPTB1	Isoform 2 of Spectrin beta chain, erythrocytic	2.76	3.30E-03
P0DOY3	IGLC3	Immunoglobulin lambda constant 3	2.72	2.09E-07
P0DP08	HVD82	Immunoglobulin heavy variable 4-38-2	2.67	4.56E-05
P11678	PERE	Eosinophil peroxidase	2.66	4.90E-03
Q14192	FHL2	Four and a half LIM domains protein 2	2.64	1.26E-05
P01591	IGJ	Immunoglobulin J chain	2.54	3.16E-05
P0DOX5	IGG1	Immunoglobulin gamma-1 heavy chain	2.49	6.15E-06
P02549	SPTA1	Spectrin alpha chain, erythrocytic 1	2.49	5.50E-03

B)

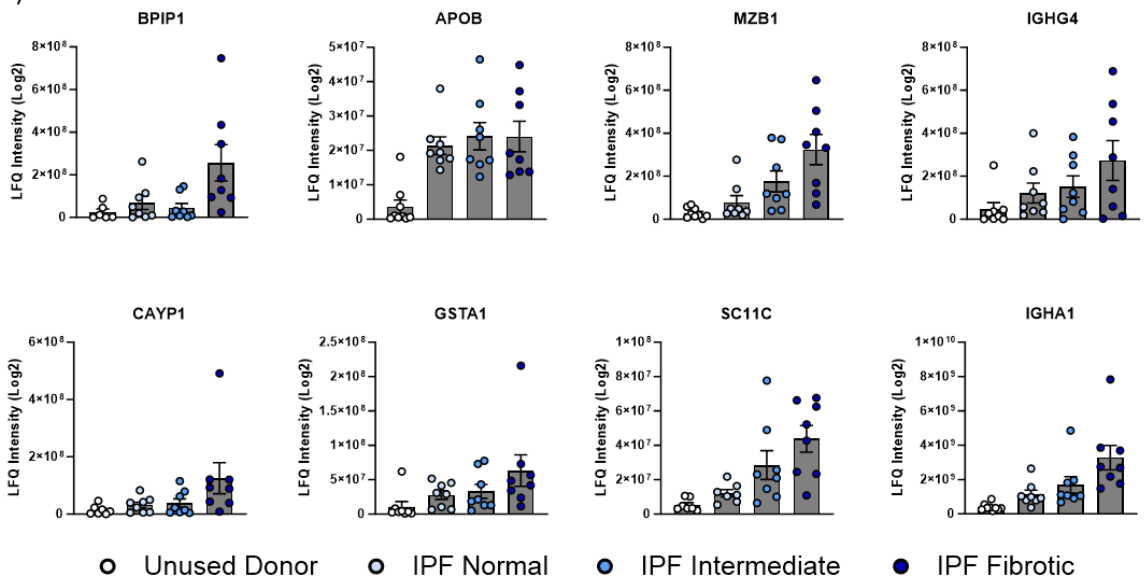

Figure 71: Top significantly upregulated proteins in unused donor vs IPF fibrotic comparison A) Table of significantly upregulated proteins ($p<0.05$) beginning with highest log2FC B) Graphs of top 8 upregulated proteins in all IPF regions and unused donor controls**.** All data are presented as mean ± SEM.

A)

UD vs IPF Fibrotic- Top significantly downregulated proteins

Accession Code	Protein ID	Protein Name	log2FC	P Value
Q16787	LAMA3	Laminin subunit alpha-3	-4.49	2.00E-04
Q13751	LAMB3	Laminin subunit beta-3	-4.24	7.00E-04
Q99758	ABCA3	Phospholipid-transporting ATPase ABCA3	-3.64	3.60E-05
P12821	ACE	Angiotensin-converting enzyme	-3.45	2.61E-05
Q9NZA1-2	CLIC5	Isoform 1 of Chloride intracellular channel protein 5	-2.94	1.78E-06
Q9HD89	RETN	Resistin	-2.78	6.00E-04
P16671	CD36	Platelet glycoprotein 4	-2.77	5.71E-06
Q10589-2	BST2	Isoform 2 of Bone marrow stromal antigen 2	-2.50	3.32E-07
Q9H8L6	MMRN2	Multimerin-2	-2.40	2.00E-04
O96009	NAPSA	Napsin-A	-2.33	1.20E-03
Q9BW04	SARG	Specifically androgen-regulated gene protein	-2.32	3.00E-04
O76041-2	NEBL	Isoform 2 of Nebulette	-2.30	2.68E-06
P12429	ANXA3	Annexin A3	-2.28	1.05E-07
Q9UGT4	SUSD2	Sushi domain-containing protein 2	-2.28	3.56E-05
Q5U651	RAIN	Ras-interacting protein 1	-2.16	1.95E-08
Q92817	EVPL	Envoplakin	-2.08	3.30E-03
P33151	CADH5	Cadherin-5	-2.07	2.15E-05
Q15067-2	ACOX1	Isoform 2 of Peroxisomal acyl-coenzyme A oxidase 1	-2.06	7.00E-04
Q9NZN3	EHD3	EH domain-containing protein 3	-2.06	3.00E-04
Q15599	NHRF2	Na(+)/H(+) exchange regulatory cofactor NHE-RF2	-1.98	2.40E-08

B)

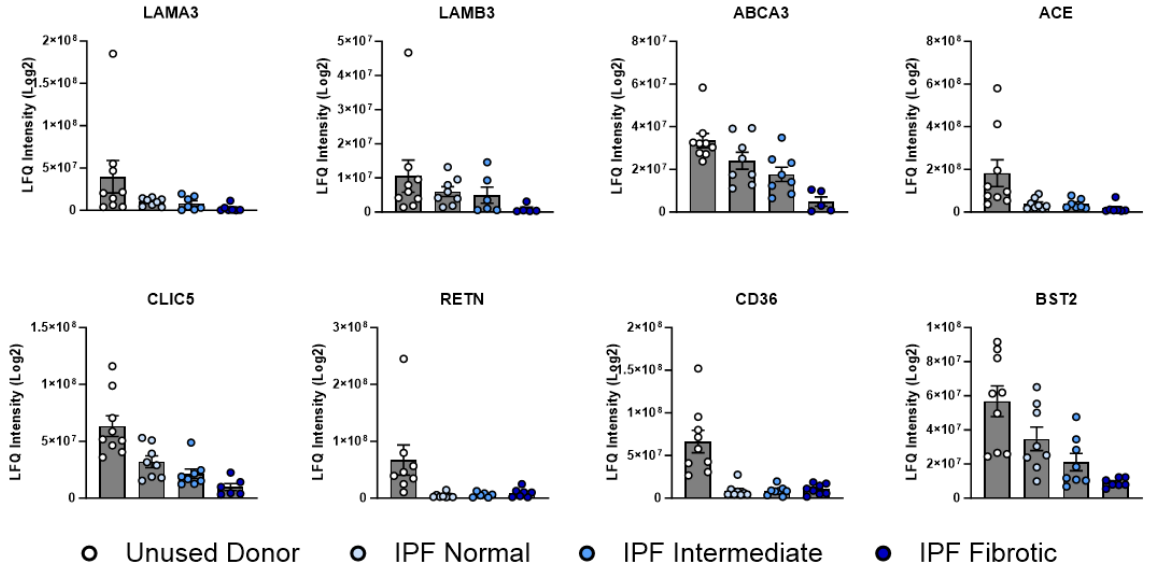

Figure 72: **Top significantly downregulated proteins in unused donor vs IPF fibrotic comparison** A) Table of significantly downregulated proteins ($p<0.05$) beginning with smallest log2FC B) Graphs of top 8 downregulated proteins in all IPF regions and unused donor controls. All data are presented as mean ± SEM.

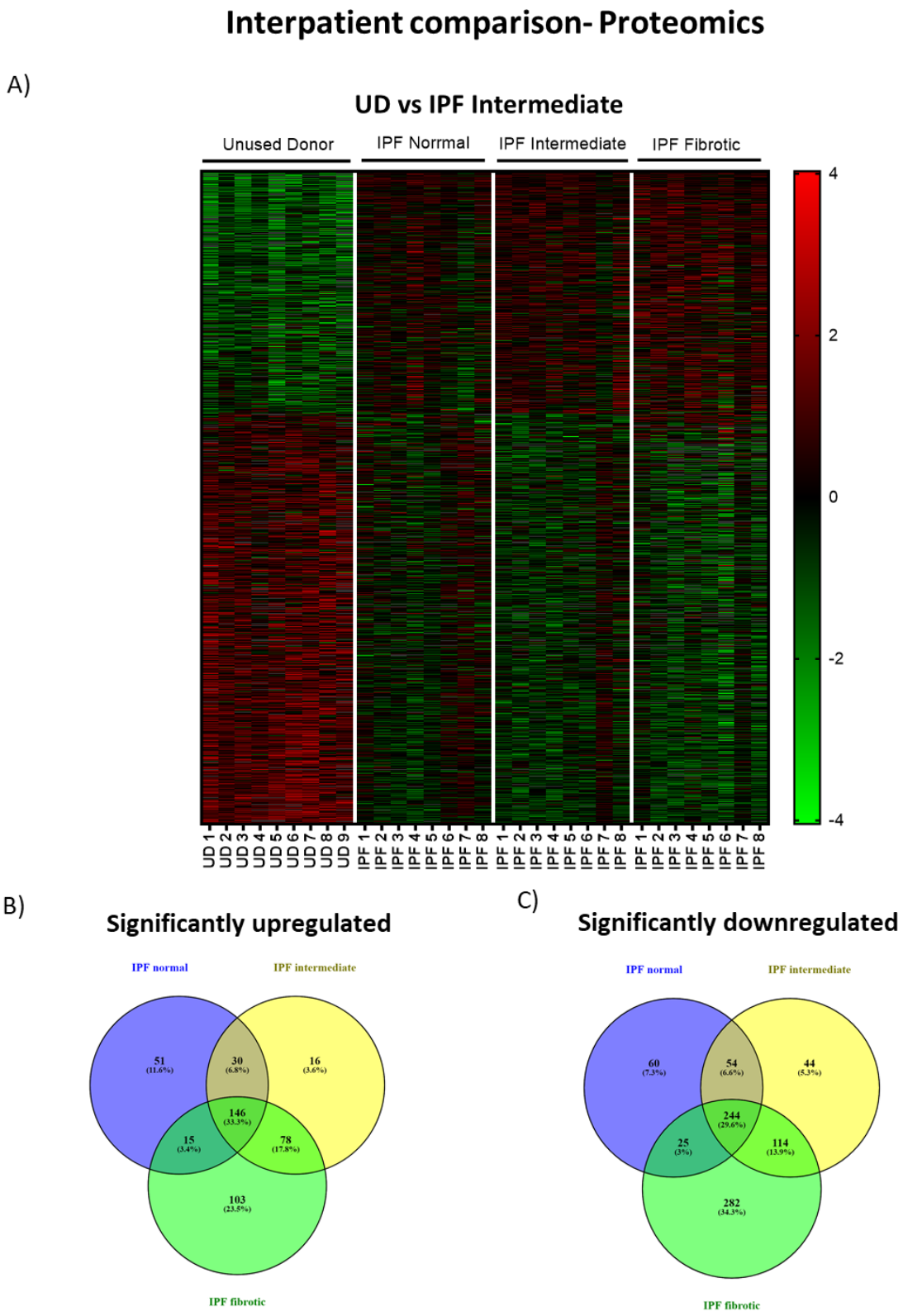

Figure 73: Overview of proteomic interpatient analysis A) Heat map of significantly different proteins ($p<0.05$) identified from unused donor vs IPF intermediate comparison in all samples (downregulated proteins in green and upregulated proteins in red). Venny diagram of B) significantly upregulated proteins in IPF normal, intermediate and fibrotic vs unused donor samples and C) significantly downregulated proteins in IPF normal, intermediate and fibrotic vs unused donor samples.

4.2.3 Intrapatient comparison

4.2.3.1 Intrapatient RNAseq

Having confirmed that all IPF regions were different to 'healthy' UD controls, we next sought to assess whether intrapatient comparisons of the macroscopically distinct IPF regions within the same lung would yield novel insight into the molecular heterogeneity between differentially affected regions of human IPF tissue. Accordingly, IPF samples from all regions (n=7 donors per region) were batch corrected for patient variability and presented as a PCA plot to assess variability of tissue samples. Evaluation of PCA plots revealed that samples tended to cluster based on early (normal and intermediate regions) and late stage (fibrotic regions) disease, with no clear differences between normal and intermediate IPF tissue (Figure 74). However, there were several instances where samples clustered with regions different to their macroscopic classification. For example, IPF 6 normal and IPF 1 and IPF 5 intermediate samples appeared to cluster more closely with fibrotic regions of tissue based on their transcriptomic profiles. Conversely, the fibrotic sample of donor IPF 7 appeared to share closer homogeny with less advanced regions of disease (normal and intermediate), suggesting this sample was less fibrotic than end-stage regions of other IPF donors (Figure 75). Notably, donor IPF 7 was also on a heavy dose of steroids prior to explantation (see Table 17) which was likely due to an acute exacerbation as shown by elevated levels of white blood cells pre-transplant (see Table 16), which may account for the differences observed.

Of the 54,779 genes identified, 17 genes were significantly different between normal and intermediate regions of IPF tissue with 5 genes upregulated in intermediate tissue, and 12 genes downregulated (Figure 76). 874 genes were significantly different between normal and fibrotic regions of IPF tissue (Figure 77) with 731 genes increased (Figure 78) and 143 genes decreased (Figure 79) in fibrotic regions compared to IPF normal. Finally, 214 genes were significantly different between areas of fibrotic and intermediate IPF tissue (Figure 80) with 160 increased (Figure 81) and 54 decreased (Figure 82) in end-stage fibrotic regions compared to intermediate tissue.

While these results did not identify clear distinctions in gene expression between normal and intermediate regions of disease, comparison of earlier regions of IPF tissue (normal and intermediate) with late-stage disease did highlight upregulation of a number of genes that have previously been associated with fibrosis and/or IPF pathogenesis in severe stages.

Among these genes are MUC5AC, MUC5B, SPP1, MMP1, MMP3, AGER, C6, DNAH6, DNAH7, DNAI1, LCN2, NELL1, PCSK1 and RXFP1 [414]. Gene set enrichment analysis of the differentially expressed genes found that several cilium-related pathways were upregulated in IPF fibrotic regions of tissue versus IPF normal (see Appendix F; Table 7 and Figure 4A) and IPF intermediate regions of tissue (see Appendix F; Table 8 and Figure 4B). Interestingly, MUC5B, which has been reported to be preferentially expressed in epithelial cells lining honeycomb cysts and in AEC2s [415], was one of the top most upregulated genes in end-stage fibrotic tissue regions compared to IPF normal (Figure 78B), and has previously been strongly associated with expression of cilium genes in IPF lungs [416,417].

These data, when considered alongside previous interpatient analysis, indicate that though many of the transcriptional changes in IPF are already present in seemingly unaffected regions of the lungs, there are also a number of genes which become dysregulated only in the late stages of disease (IPF fibrotic regions). Notably, evaluation of individual donor transcriptomes (Figure 75C, Figure 77C, Figure 80C) in each comparison confirmed that IPF6 normal regions of tissue exhibited a different gene profile to normal regions of tissue from other IPF donors (n=6). Additionally, intermediate regions of IPF 1 and IPF 5 appeared to have similar gene profiles to fibrotic tissue samples, whereas donors IPF 7 and IPF 8 fibrotic samples were inconsistent with the other 5 tissue samples of the same region. Consequently, it is possible that potentially significant changes in gene expression between regions is obscured by the variability between samples.

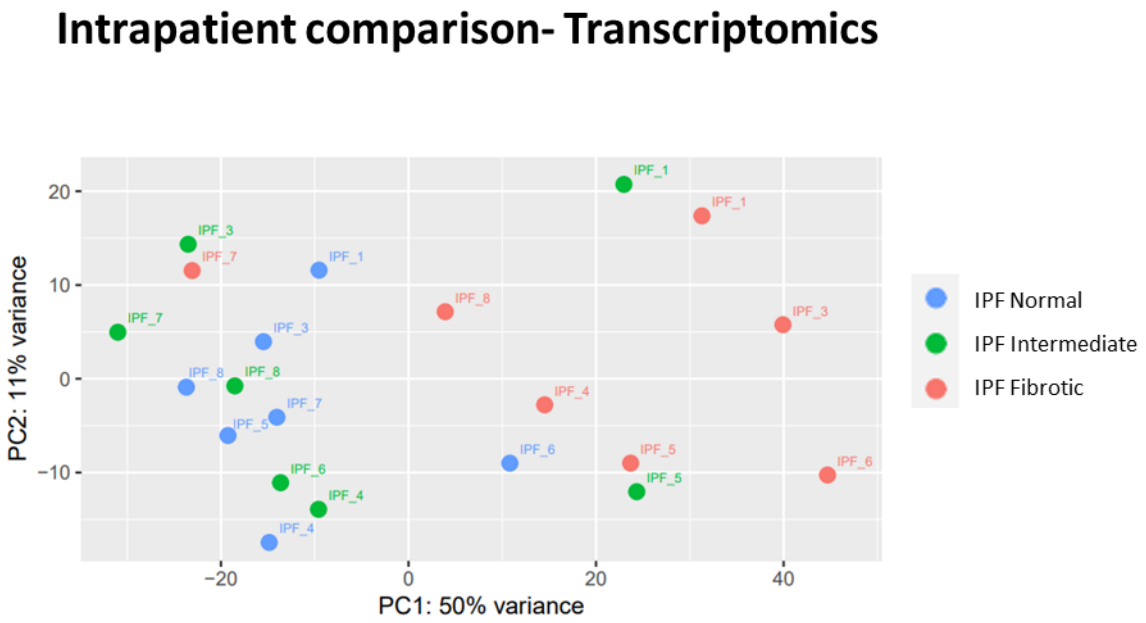

Figure 74: Transcriptomic analysis of intrapatient comparison Principal component analysis (PCA) plot of batch corrected IPF normal (n=7 donors), IPF intermediate (n=7 donors) and IPF fibrotic (n=7) RNA samples.

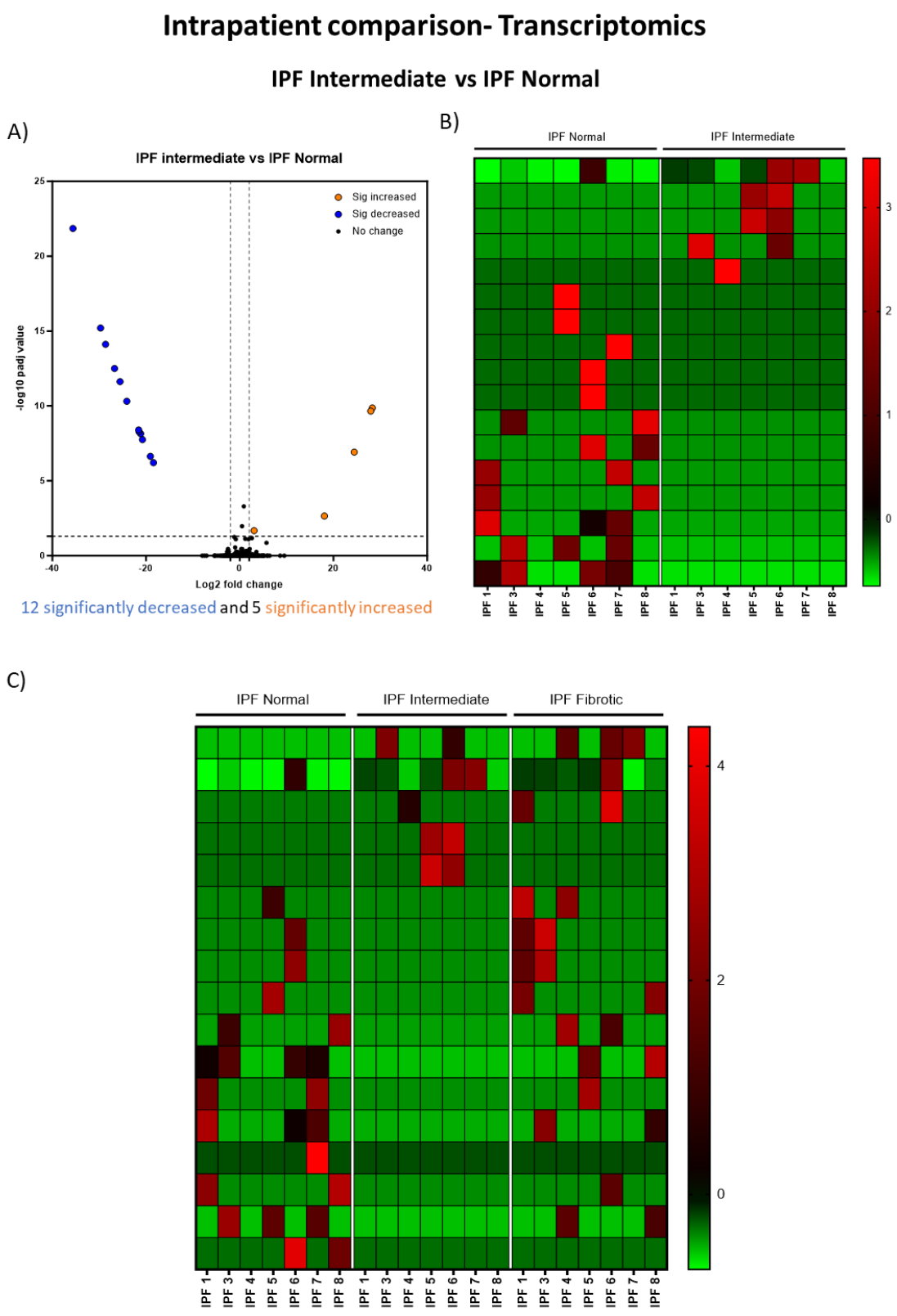

Figure 75: Transcriptomic analysis of intrapatient IPF intermediate vs IPF normal comparison Significantly different genes (padj<0.05 and Log2FC±2) were graphed as A) volcano plot (downregulated genes in blue and upregulated genes in orange) and B) heat map (downregulated genes in green and upregulated genes in red). C) Heat map of significantly different proteins in all 3 IPF regions.

Intrapatient comparison- Transcriptomics

A)

IPF Intermediate vs IPF Normal- Top significantly upregulated genes

Ensembl ID	Gene ID	Description	logFC	P Adj Value
ENSG00000259604		novel transcript	28.30	1.40E-14
ENSG00000275976	SPDYE11	long intergenic non-protein coding RNA 656	27.96	2.88E-14
ENSG00000276612		proline rich protein BstNI subfamily 4	24.43	2.51E-11
ENSG00000267110		novel transcript	18.07	9.95E-07
ENSG00000196092	PAX5	speedy/RINGO cell cycle regulator family member E11	3.04	1.04E-05

B)

IPF Intermediate vs IPF Normal- Top significantly downregulated genes

Ensembl ID	Gene ID	Description	logFC	P Adj Value
ENSG00000263917		paired box 5	-35.62	5.49E-18
ENSG00000233746	LINC00656	novel transcript	-29.71	1.21E-11
ENSG00000230657	PRB4	metaxin 1 pseudogene 1	-28.65	9.88E-11
ENSG00000276919		novel transcript, similar to YY1 associated myogenesis RNA 1 YAM1	-26.73	2.05E-09
ENSG00000176289	IDSP1	NA	-25.55	1.30E-08
ENSG00000205085	FAM71F2	novel pseudogene	-24.12	2.07E-07
ENSG00000273007		dexamethasone-induced transcript (DEXI) pseudogene	-21.58	1.54E-05
ENSG00000256951		novel transcript, antisense to FGF2	-21.53	1.83E-05
ENSG00000231615		family with sequence similarity 71 member F2	-21.15	2.28E-05
ENSG00000276692	NA	novel protein	-20.77	5.29E-05
ENSG00000281383		iduronate 2-sulfatase pseudogene 1	-19.09	5.94E-04
ENSG00000236675	MTX1P1		-18.42	1.48E-03

Figure 76: Top significantly upregulated and downregulated genes in IPF intermediate vs IPF normal comparison Table of significantly A) upregulated genes (padj<0.05 and Log2FC±2) beginning with highest log2FC and B) Table of significantly A) downregulated genes (padj<0.05 and Log2FC±2) beginning with smallest log2FC.

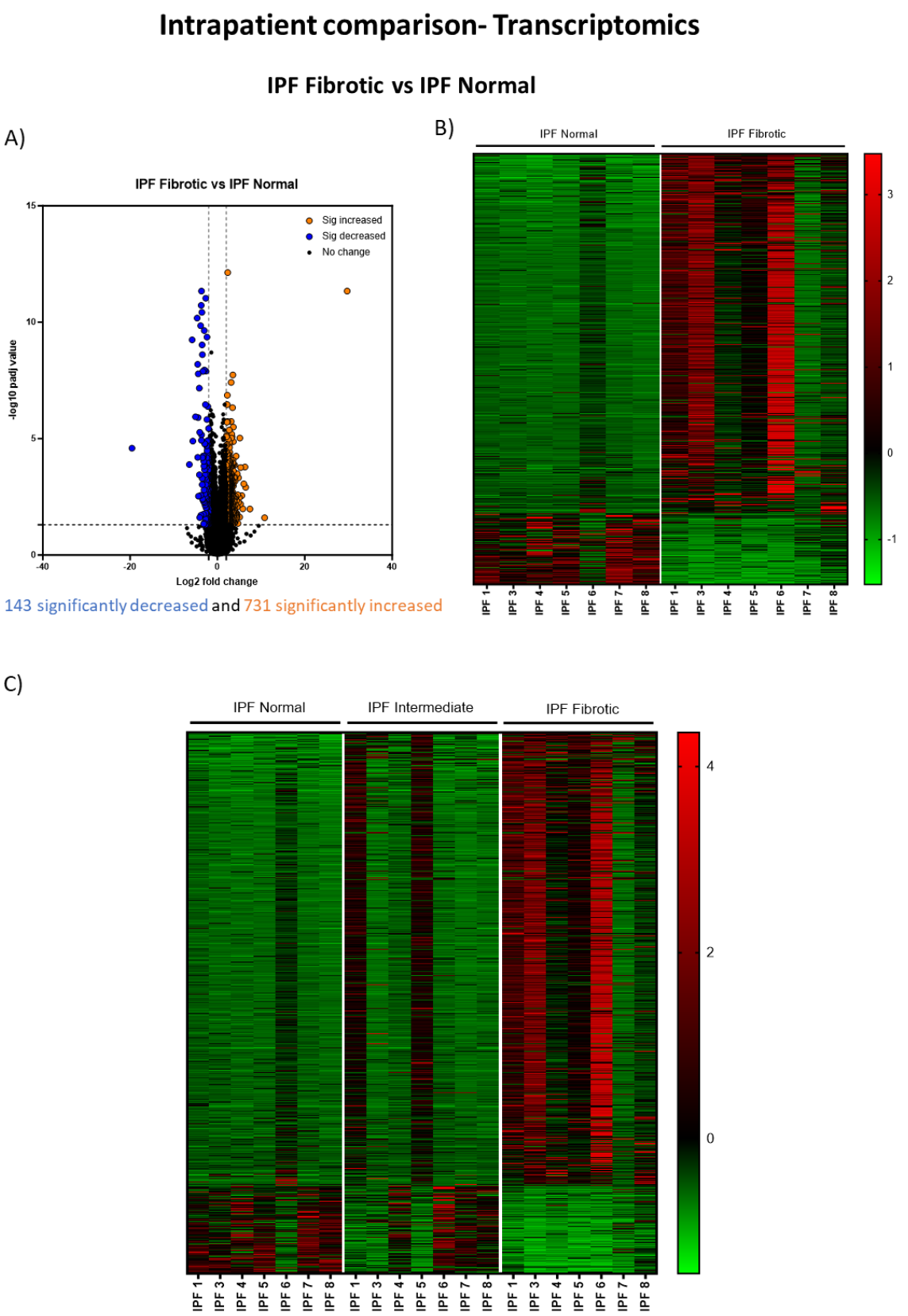

Figure 77: Transcriptomic analysis of intrapatient IPF fibrotic vs IPF normal comparison Significantly different genes (padj<0.05 and Log2FC±2) were graphed as A) volcano plot (downregulated genes in blue and upregulated genes in orange) and B) heat map (downregulated genes in green and upregulated genes in red). C) Heat map of significantly different proteins in all 3 IPF regions.

A) **IPF Fibrotic vs IPF Normal- Top significantly upregulated genes**

Ensembl ID	Gene ID	Description	logFC	P Adj Value
ENSG00000244094	SPRR2F	small proline rich protein 2F	6.47	1.20E-03
ENSG00000184956	MUC6	mucin 6, oligomeric mucus/gel-forming	6.03	9.00E-04
ENSG00000152611	CAPSL	calcyphosine like	5.80	1.02E-02
ENSG00000215182	MUC5AC	mucin 5AC, oligomeric mucus/gel-forming	5.31	2.00E-04
ENSG00000255319	ENPP7P8	ectonucleotide pyrophosphatase/phosphodiesterase 7 pseudogene 8	5.28	6.40E-03
ENSG00000255071	SAA2-SAA4	SAA2-SAA4 readthrough	5.13	0.00E+00
ENSG00000246731	MGC16275	uncharacterized protein MGC16275	5.08	2.34E-02
ENSG00000181092	ADIPOQ	adiponectin, C1Q and collagen domain containing	5.01	3.40E-03
ENSG00000111262	KCNA1	potassium voltage-gated channel subfamily A member 1	4.84	5.40E-03
ENSG00000169562	GJB1	gap junction protein beta 1	4.82	5.00E-04
ENSG00000224843	LINC00240	long intergenic non-protein coding RNA 240	4.51	3.00E-04
ENSG00000102313	ITIH6	inter-alpha-trypsin inhibitor heavy chain family member 6	4.46	1.66E-02
ENSG00000171711	DEFB4A	defensin beta 4A	4.44	2.27E-02
ENSG00000186910	SERPINA11	serpin family A member 11	4.37	4.60E-03
ENSG00000227308	LINC02832	long intergenic non-protein coding RNA 2832	4.26	1.00E-04
ENSG00000280780	JAKMIP2-AS1	JAKMIP2 antisense RNA 1	4.10	1.64E-02
ENSG00000006128	TAC1	tachykinin precursor 1	4.01	3.60E-03
ENSG00000129455	KLK8	kallikrein related peptidase 8	4.00	4.02E-02
ENSG00000145642	SHISAL2B	shisa like 2B	3.99	2.68E-02
ENSG00000066813	ACSM2B	acyl-CoA synthetase medium chain family member 2B	3.94	1.00E-04

B)

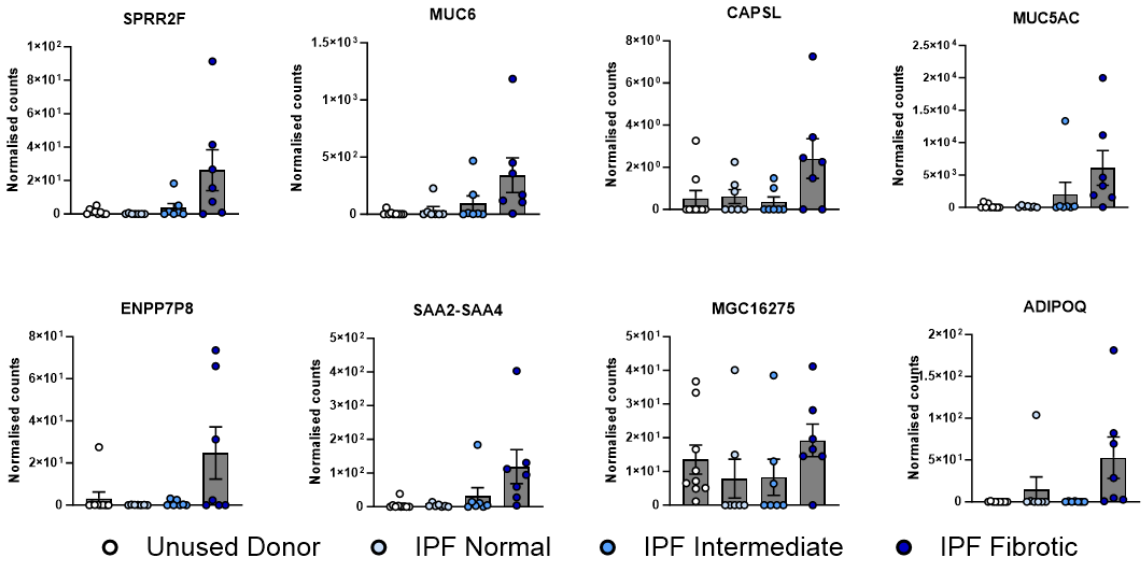

Figure 78: Top significantly upregulated genes in IPF fibrotic vs IPF normal comparison A) Table of significantly upregulated genes (padj<0.05 and Log2FC±2) beginning with highest log2FC B) Graphs of top 8 upregulated genes in all IPF regions and unused donor controls.

A)

IPF Fibrotic vs IPF Normal- Top significantly downregulated genes

Ensembl ID	Gene ID	Description	logFC	P Adj Value
ENSG00000230657	PRB4	proline rich protein BstNI subfamily 4	-19.57	2.55E-05
ENSG00000104938	CLEC4M	C-type lectin domain family 4 member M	-5.81	5.68E-10
ENSG00000108576	SLC6A4	solute carrier family 6 member 4	-5.65	1.27E-05
ENSG00000178084	HTR3C	5-hydroxytryptamine receptor 3C	-5.04	1.16E-06
ENSG00000164283	ESM1	endothelial cell specific molecule 1	-4.64	6.60E-11
ENSG00000171388	APLN	apelin	-4.54	6.37E-09
ENSG00000269186	LINC01082	long intergenic non-protein coding RNA 1082	-4.43	1.25E-06
ENSG00000168539	CHRM1	cholinergic receptor muscarinic 1	-4.40	1.65E-08
ENSG00000184374	COLEC10	collectin subfamily member 10	-4.14	6.77E-08
ENSG00000148677	ANKRD1	ankyrin repeat domain 1	-4.13	4.00E-04
ENSG00000196296	ATP2A1	ATPase sarcoplasmic/endoplasmic reticulum Ca2+ transporting 1	-4.07	5.32E-06
ENSG00000151025	GPR158	G protein-coupled receptor 158	-4.07	2.44E-02
ENSG00000114812	VIPR1	vasoactive intestinal peptide receptor 1	-3.86	1.40E-10
ENSG00000236816	ANKRD20A7P	ankyrin repeat domain 20 family member A7, pseudogene	-3.80	1.95E-02
ENSG00000218358	RAET1K	retinoic acid early transcript 1K pseudogene	-3.78	2.70E-03
ENSG00000142748	FCN3	ficolin 3	-3.72	1.89E-11
ENSG00000267551	GNA15-DT	GNA15 divergent transcript	-3.67	1.18E-05
ENSG00000111981	ULBP1	UL16 binding protein 1	-3.67	4.59E-12
ENSG00000167434	CA4	carbonic anhydrase 4	-3.56	3.77E-11
ENSG00000171243	SOSTDC1	sclerostin domain containing 1	-3.52	9.35E-10

B)

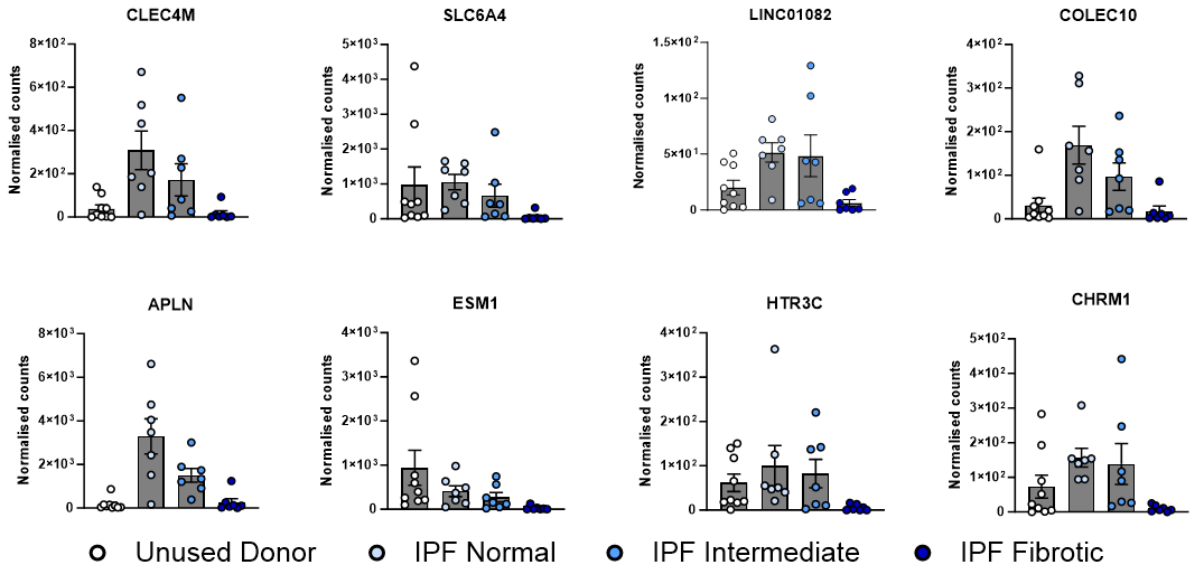

Figure 79: Top significantly downregulated genes in IPF fibrotic vs IPF normal comparison A) Table of significantly downregulated genes (padj<0.05 and Log2FC±2) beginning with smallest log2FC B) Graphs of top 8 downregulated genes in all IPF regions and unused donor controls.

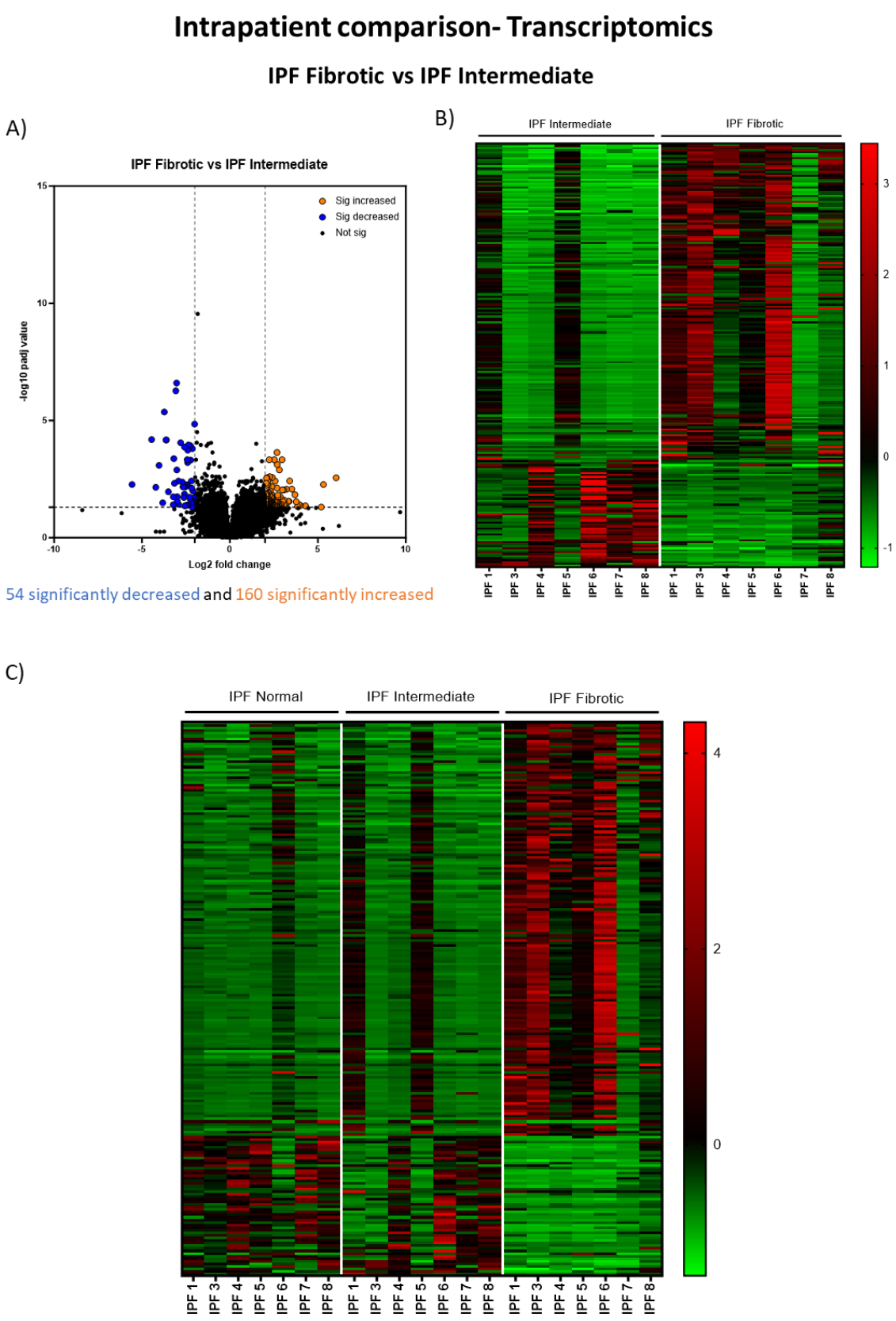

Figure 80: Transcriptomic analysis of intrapatient IPF fibrotic vs IPF normal comparison Significantly different genes (padj<0.05 and logFC>±2) were graphed as A) volcano plot (downregulated genes in blue and upregulated genes in orange) and B) heat map (downregulated genes in green and upregulated genes in red). C) Heat map of significantly different proteins in all 3 IPF regions.

A)

IPF Fibrotic vs IPF Intermediate- Top significantly upregulated genes

Ensembl ID	Gene ID	Description	logFC	P Adj Value
ENSG00000181092	ADIPOQ	adiponectin, C1Q and collagen domain containing	6.04	2.80E-03
ENSG00000152611	CAPSL	calcyphosine like	5.19	4.89E-02
ENSG00000184956	MUC6	mucin 6, oligomeric mucus/gel-forming	4.29	4.34E-02
ENSG00000205076	LGALS7	galectin 7	4.01	4.21E-02
ENSG00000245750	DRAIC	downregulated RNA in cancer, inhibitor of cell invasion and migration	3.93	3.83E-02
ENSG00000078898	BPIFB2	BPI fold containing family B member 2	3.84	4.58E-02
ENSG00000215182	MUC5AC	mucin 5AC, oligomeric mucus/gel-forming	3.77	2.91E-02
ENSG00000186474	KLK12	kallikrein related peptidase 12	3.70	1.46E-02
ENSG00000255071	SAA2-SAA4	SAA2-SAA4 readthrough	3.52	8.40E-03
ENSG00000134339	SAA2	serum amyloid A2	3.40	3.80E-03
ENSG00000206075	SERPINB5	serpin family B member 5	3.36	2.82E-02
ENSG00000016602	CLCA4	chloride channel accessory 4	3.31	2.79E-02
ENSG00000142700	DMRTA2	DMRT like family A2	3.22	8.50E-03
ENSG00000185479	KRT6B	keratin 6B	3.18	4.78E-02
ENSG00000241635	UGT1A1	UDP glucuronosyltransferase family 1 member A1	3.16	3.87E-02
ENSG00000169562	GJB1	gap junction protein beta 1	3.12	4.78E-02
ENSG00000234602	MCIDAS	multiciliate differentiation and DNA synthesis associated cell cycle protein	3.08	2.49E-02
ENSG00000267348	GEMIN7-AS1	GEMIN7 antisense RNA 1	3.07	3.84E-02
ENSG00000166670	MMP10	matrix metallopeptidase 10	3.06	9.20E-03
ENSG00000198807	PAX9	paired box 9	2.98	9.20E-03

B)

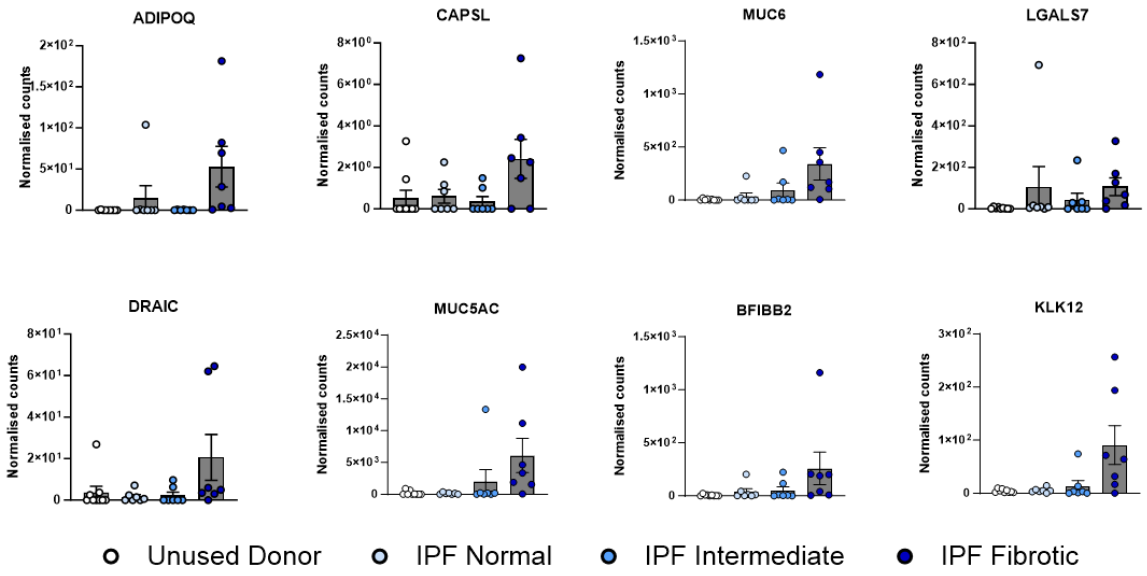

Figure 81: Top significantly upregulated genes in IPF fibrotic vs IPF intermediate comparison A) Table of significantly upregulated genes (padj<0.05 and Log2FC±2) beginning with highest log2FC B) Graphs of top 8 upregulated genes in all IPF regions and unused donor controls.

A)

IPF Fibrotic vs IPF Intermediate- Top significantly downregulated genes

Ensembl ID	Gene ID	Description	logFC	P Adj Value
ENSG00000104938	CLEC4M	C-type lectin domain family 4 member M	-4.45	1.00E-04
ENSG00000108576	SLC6A4	solute carrier family 6 member 4	-4.21	7.00E-03
ENSG00000178084	HTR3C	5-hydroxytryptamine receptor 3C	-4.03	8.00E-04
ENSG00000164283	ESM1	endothelial cell specific molecule 1	-3.73	4.28E-06
ENSG00000171388	APLN	apelin	-3.63	1.00E-04
ENSG00000168539	CHRM1	cholinergic receptor muscarinic 1	-3.61	1.00E-04
ENSG00000204420	MPIG6B	megakaryocyte and platelet inhibitory receptor G6b	-3.22	1.80E-02
ENSG00000184374	COLEC10	collectin subfamily member 10	-3.19	4.00E-04
ENSG00000269186	LINC01082	long intergenic non-protein coding RNA 1082	-3.16	4.70E-03
ENSG00000142748	FCN3	ficolin 3	-3.08	5.41E-07
ENSG00000111981	ULBP1	UL16 binding protein 1	-3.03	2.50E-07
ENSG00000173826	KCNH6	potassium voltage-gated channel subfamily H member 6	-3.02	1.30E-03
ENSG00000167941	SOST	sclerostin	-3.00	1.78E-02
ENSG00000171557	FGG	fibrinogen gamma chain	-2.99	2.79E-02
ENSG00000148677	ANKRD1	ankyrin repeat domain 1	-2.93	3.71E-02
ENSG00000267551	GNA15-DT	GNA15 divergent transcript	-2.92	3.80E-03
ENSG00000114812	VIPR1	vasoactive intestinal peptide receptor 1	-2.80	1.00E-04
ENSG00000116147	TNR	tenascin R	-2.71	4.20E-03
ENSG00000196296	ATP2A1	ATPase sarcoplasmic/endoplasmic reticulum Ca2+ transporting 1	-2.62	1.90E-02
ENSG00000163736	PPBP	pro-platelet basic protein	-2.60	6.40E-03

B)

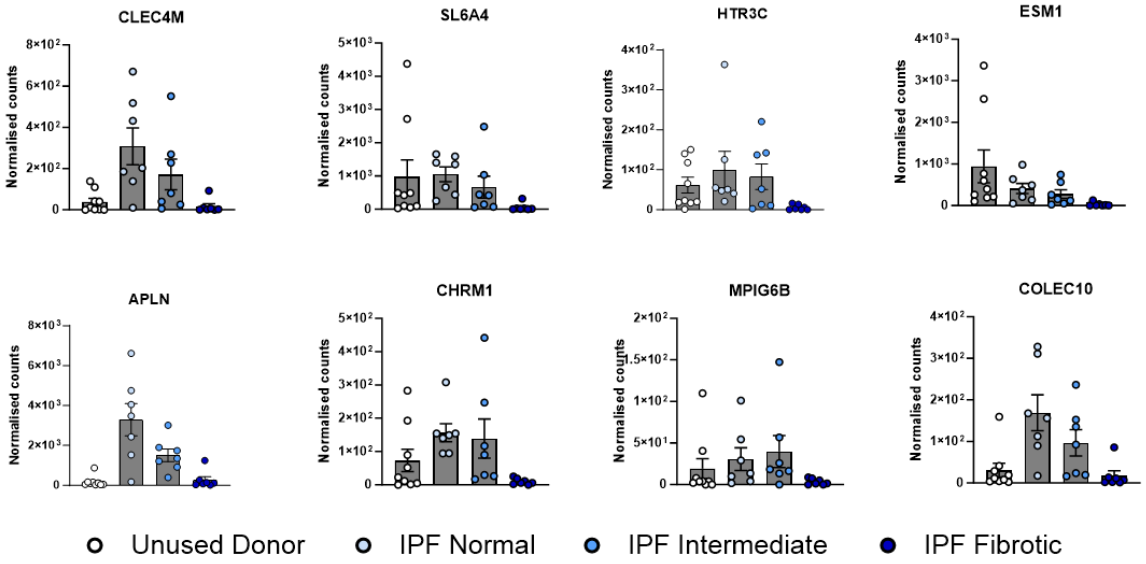

Figure 82: Top significantly downregulated genes in IPF fibrotic vs IPF intermediate comparison A) Table of significantly downregulated genes (padj<0.05 and Log2FC±2) with smallest log2FC B) Graphs of top 8 downregulated genes in all IPF regions and unused donor controls.

4.2.3.2 Intrapatient proteomics

To further interrogate protein heterogeneity between regions of IPF tissue with increasing severity of fibrosis, intrapatient analysis was also performed on proteomic datasets, following batch correction for patient variability. PCA plots were generated as previously described and revealed that, unlike the transcriptomic analysis, there was clearing clustering of tissue samples based on the degree of fibrosis at all stages, with normal and intermediate regions of IPF showing less variation to each other than to end-stage fibrotic regions of the same IPF lung (Figure 83).

Of the 3,886 proteins identified, 2,700 proteins were present in a minimum of 50% of all replicates. Of these, 234 proteins (8.7%) were significantly different between normal and intermediate regions of IPF tissue with 97 proteins upregulated (Figure 85) and 137 proteins downregulated (Figure 86) in intermediate IPF tissue compared to normal regions (Figure 84). 1,037 proteins (38.4%) were significantly different between fibrotic and normal regions of IPF tissue with 384 increased (of which 14 have FC>1.5; Figure 88) and 653 decreased proteins (of which 16 have FC>1.5; Figure 89) in IPF fibrotic tissue compared to IPF normal (Figure 87). Finally, 560 proteins (20.7%) were significantly different between areas of fibrotic and intermediate IPF tissue with 173 increased (of which 6 have FC>1.5; Figure 91) and 387 decreased (of which 9 have a FC>1.5; Figure 92) in fibrotic regions (Figure 90).

Assessment of changes in protein expression at the early stages of disease revealed that 17 of the 97 upregulated proteins in IPF intermediate tissue compared to normal regions were further increased in end-stage fibrotic tissue (compared to intermediate tissue), including ITA7, SYNP2, PRDX and FBLN2. Conversely, 5 proteins (ARL8A, AGFG1, UBP21, TOLIP and PMVK) were significantly downregulated in IPF fibrotic (compared to intermediate regions). The remaining 75 proteins showed no significant changes in fibrotic tissue compared to intermediate regions. Of the 137 significantly downregulated proteins in intermediate regions of IPF tissue (compared to normal regions), 58 were further downregulated in IPF fibrotic tissue (compared to intermediate regions), whereas 4 proteins (SRSF4, PTBP3, H10 and GOT1B) were significantly increased in fibrotic regions (compared to intermediate tissue) and 75 showed no further significant changes from intermediate tissue.

Notably, of the 2,700 proteins assessed, 1,093 proteins (40.5% of detected proteins) in IPF fibrotic regions were significantly different to IPF normal and/or intermediate regions of

tissue. Of these 1,093 proteins, 410 (37.5% of significantly different proteins) were upregulated in fibrotic regions of IPF tissue compared to less advanced normal and intermediate regions of disease (Figure 93A). For example, mucin 5B (MUC5B) which is known to be increased in IPF [416], was one of the most significantly increased proteins in IPF fibrotic tissue compared to intermediate (logFC=3.03, p=0.0012) and normal (logFC=2.39, p=0.0074) regions of the same lung. Conversely, 683 proteins (62.5% of significantly different proteins) were downregulated in IPF fibrotic samples compared to IPF normal and/or intermediate regions of tissue (Figure 93B). As end-stage fibrotic regions of IPF lungs represent late stages of disease in which tissue remodelling is reduced, it is likely that initial pathobiological mechanisms driving IPF pathogenesis have dissipated. Consequently, investigation of proteins which are elevated in earlier stages of disease but downregulated in end-stage fibrotic tissue may allow for the detection of key mechanisms driving disease progression and allow identification of novel targets for early therapeutic intervention.

Taken together, these data confirm that there is significant protein heterogeneity in IPF tissue with distinct proteins present in each region, particular between early (normal and intermediate) and late-stage (fibrotic) disease. All regional comparisons identified many significantly different proteins which were modulated in line with disease severity. Further analysis of these proteins may unveil potentially key proteins involved in the fibrotic response seen in IPF patients, particularly those which are significantly different in the normal and intermediate regions of IPF lungs to end-stage fibrotic.

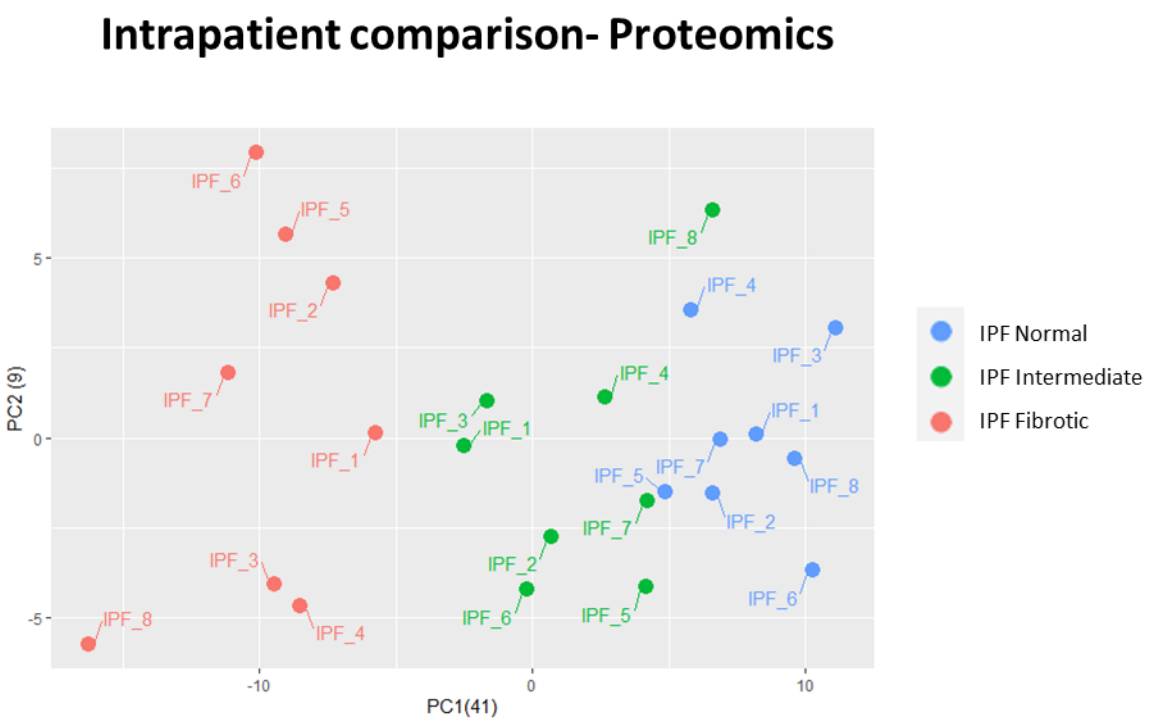

Figure 83: Proteomic analysis of intrapatient comparison Principal component analysis (PCA) plot of batch corrected IPF normal (n=8 donors), IPF intermediate (n=8 donors) and IPF fibrotic (n=8) protein samples.

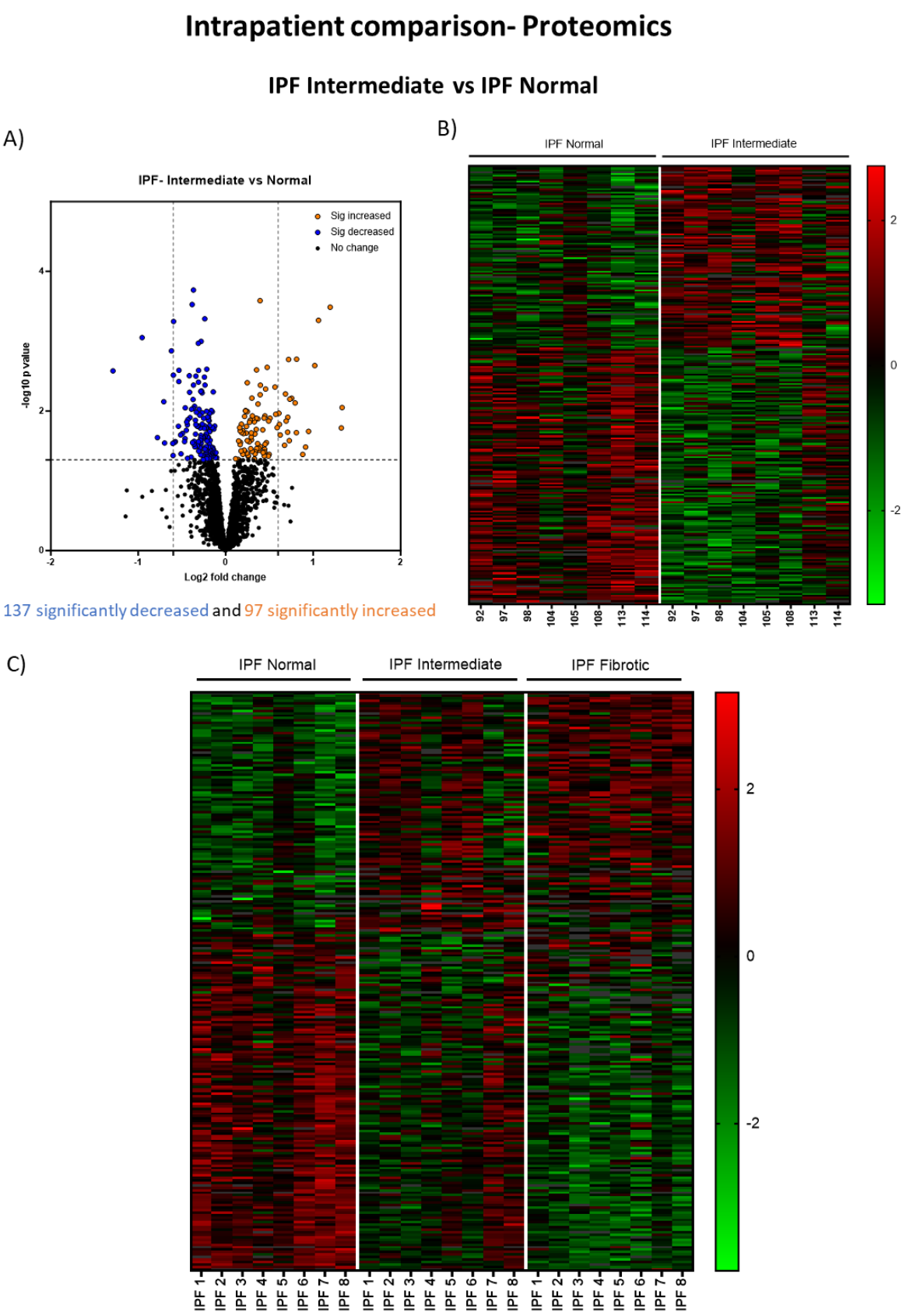

Figure 84: Proteomic analysis of intrapatient IPF intermediate vs IPF normal comparison Significantly different proteins ($p<0.05$) were graphed as A) volcano plot (downregulated proteins in blue and upregulated proteins in orange) and B) heat map (downregulated proteins in green and upregulated proteins in red). C) Heat map of significantly different proteins in all 3 IPF regions.

A)

IPF Intermediate vs Normal- Top significantly upregulated proteins

Accession Code	Protein ID	Protein Name	log2FC	P Value
Q8WU39	MZB1	Marginal zone B- and B1-cell-specific protein	1.33	8.90E-03
P14555	PA2GA	Phospholipase A2, membrane associated	1.32	1.75E-02
P20774	MIME	Mimecan	1.20	3.00E-04
Q05707	COEA1	Collagen alpha-1(XIV) chain	1.06	5.00E-04
P50479	PDLI4	PDZ and LIM domain protein 4	1.02	2.20E-03
O15061	SYNEM	Synemin	0.95	1.96E-02
Q9BY50	SC11C	Signal peptidase complex catalytic subunit SEC11C	0.91	3.28E-02
Q13683-3	ITA7	Isoform Alpha-7X1B of Integrin alpha-7	0.88	4.18E-02
P53708	ITA8	Integrin alpha-8	0.81	1.80E-03
P17661	DESM	Desmin	0.81	2.04E-02
P63267	ACTH	Actin, gamma-enteric smooth muscle	0.79	7.60E-03
P07585	PGS2	Decorin	0.75	6.60E-03
Q06828	FMOD	Fibromodulin	0.73	6.80E-03
Q9UBY9	HSPB7	Heat shock protein beta-7	0.73	2.66E-02
Q16647	PTGIS	Prostacyclin synthase	0.72	1.80E-03
P27658	CO8A1	Collagen alpha-1(VIII) chain	0.71	1.23E-02
P53814-5	SMTN	Isoform B2 of Smoothelin	0.71	2.01E-02
P20292	AL5AP	Arachidonate 5-lipoxygenase-activating protein	0.69	1.39E-02
Q53GG5-2	PDLI3	Isoform 2 of PDZ and LIM domain protein 3	0.68	5.70E-03
Q14BN4-5	SLMAP	Isoform 5 of Sarcolemmal membrane-associated protein	0.67	3.09E-02

B)

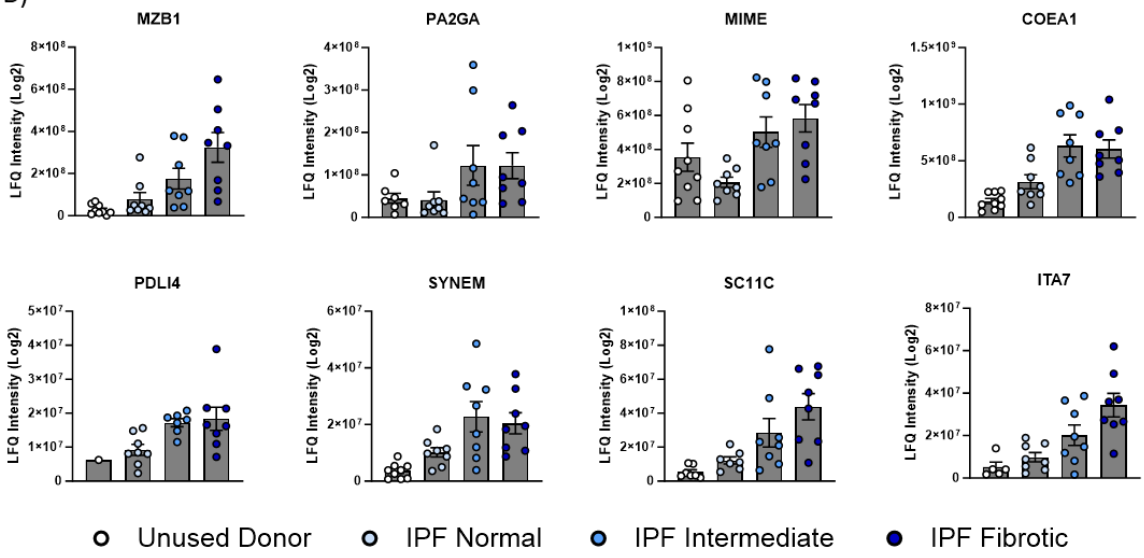

Figure 85: Top significantly upregulated proteins in IPF intermediate vs IPF normal comparison A) Table of significantly upregulated proteins ($p<0.05$) beginning with highest log2FC B) Graphs of top 8 upregulated proteins in all IPF regions and unused donor controls. All data are presented as mean ± SEM.

A)

IPF Intermediate vs Normal- Top significantly downregulated proteins

Accession Code	Protein ID	Protein Name	log2FC	P Value
P15428	PGDH	15-hydroxyprostaglandin dehydrogenase [NAD(+)]	-1.29	2.70E-03
Q5U651	RAIN	Ras-interacting protein 1	-0.96	9.00E-04
Q10589-2	BST2	Isoform 2 of Bone marrow stromal antigen 2	-0.78	2.41E-02
Q68CZ2	TENS3	Tensin-3	-0.71	7.40E-03
P13747	HLAE	HLA class I histocompatibility antigen, alpha chain E	-0.70	2.87E-02
O00423	EMAL1	Echinoderm microtubule-associated protein-like 1	-0.62	1.40E-03
P33151	CADH5	Cadherin-5	-0.60	2.91E-02
Q07075	AMPE	Glutamyl aminopeptidase	-0.60	4.34E-02
Q15599	NHRF2	Na(+)/H(+) exchange regulatory cofactor NHE-RF2	-0.60	3.10E-03
Q03135-2	CAV1	Isoform 2 of Caveolin-1	-0.60	5.00E-04
P15328	FOLR1	Folate receptor alpha	-0.59	2.81E-02
Q9UHA4	LTOR3	Ragulator complex protein LAMT	-0.58	2.74E-02
P30273	FCERG	High affinity immunoglobulin epsilon receptor subunit gamma	-0.54	1.65E-02
Q15165	PON2	Serum paraoxonase/arylesterase 2	-0.54	3.80E-03
O00468-6	AGRIN	Isoform 6 of Agrin	-0.54	2.60E-03
Q96MM6	HS12B	Heat shock 70 kDa protein 12B	-0.52	2.20E-02
P12429	ANXA3	Annexin A3	-0.51	4.11E-02
Q7Z406	MYH14	Myosin-14	-0.49	2.10E-02
O95810	CAVN2	Caveolae-associated protein 2	-0.47	2.75E-02
P50895	BCAM	Basal cell adhesion molecule	-0.46	2.49E-02

B)

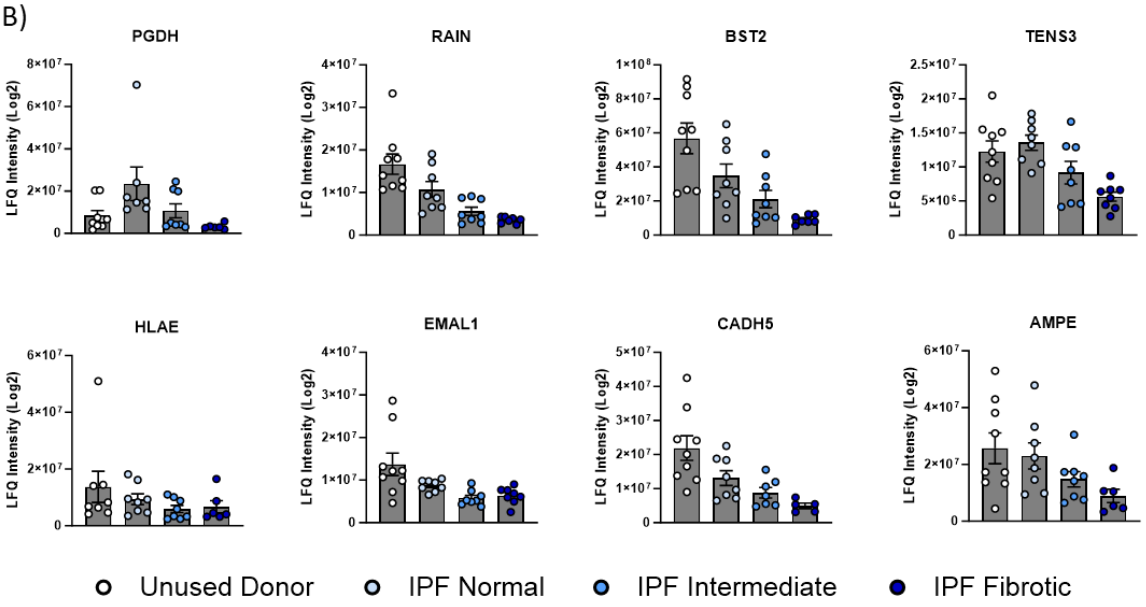

Figure 86: Top significantly downregulated proteins in IPF intermediate vs IPF normal comparison A) Table of significantly downregulated proteins ($p<0.05$) beginning with smallest log2FC B) Graphs of top 8 downregulated proteins in all IPF regions and unused donor controls. All data are presented as mean ± SEM.

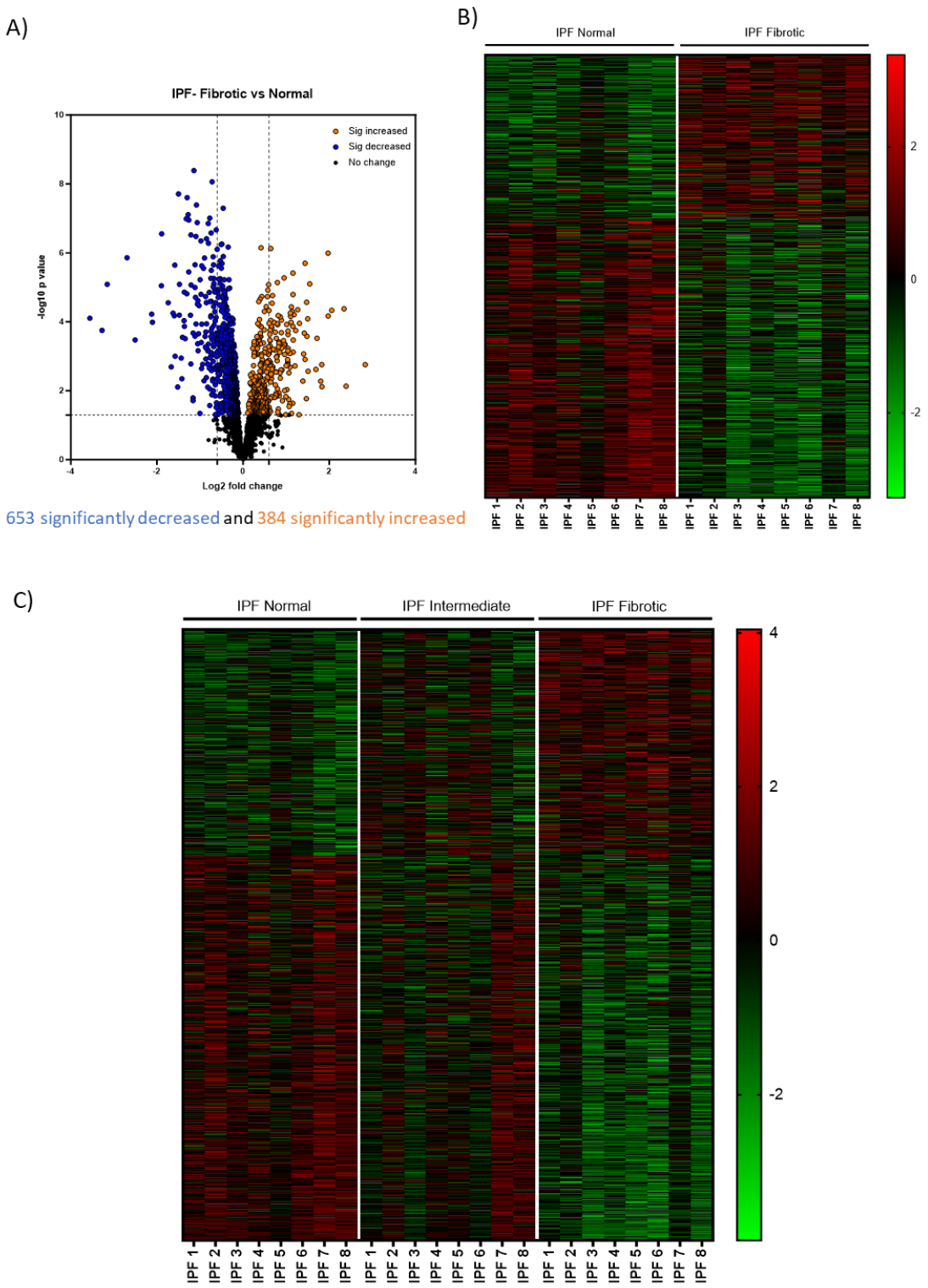

Figure 87: Proteomic analysis of intrapatient IPF fibrotic vs IPF normal comparison Significantly different proteins ($p<0.05$) were graphed as A) volcano plot (downregulated proteins in blue and upregulated proteins in orange) and B) heat map (downregulated proteins in green and upregulated proteins in red). C) Heat map of significantly different proteins in all 3 IPF regions.

A)

IPF Fibrotic vs Normal- Top significantly upregulated proteins

Accession Code	Protein ID	Protein Name	logFC	P Value
Q8TDL5	BPIB1	BPI fold-containing family B member 1	2.83	1.70E-03
Q9HC84	MUC5B	Mucin-5B	2.39	7.40E-03
Q8WU39	MZB1	Marginal zone B- and B1-cell-specific protein	2.34	4.18E-05
P06727	APOA4	Apolipoprotein A-IV	2.06	4.65E-05
Q13683-3	ITA7	Isoform Alpha-7X1B of Integrin alpha-7	1.97	1.00E-04
P01591	IGJ	Immunoglobulin J chain	1.97	1.02E-06
Q13938-4	CAYP1	Isoform 3 of Calcyphosin	1.83	7.60E-03
P14555	PA2GA	Phospholipase A2, membrane associated	1.83	1.70E-03
P15088	CBPA3	Mast cell carboxypeptidase A	1.80	5.20E-03
Q9BY50	SC11C	Signal peptidase complex catalytic subunit SEC11C	1.71	3.00E-04
P01833	PIGR	Polymeric immunoglobulin receptor	1.69	2.40E-03
P01876-1	IGHA1	Isoform 1 of Immunoglobulin heavy constant alpha 1	1.55	7.91E-06
P16050	LOX15	Polyunsaturated fatty acid lipoxygenase AL	1.51	2.70E-03
Q96NY7-2	CLIC6	Isoform A of Chloride intracellular channel protein 6	1.50	1.00E-04
P80748	LV321	Immunoglobulin lambda variable 3-21	1.48	3.00E-04
P20774	MIME	Mimecan	1.48	2.70E-05
P17213	BPI	Bactericidal permeability-increasing protein	1.47	1.70E-02
P0DOX2	IGA2	Immunoglobulin alpha-2 heavy chain	1.44	1.99E-06
P30838	AL3A1	Aldehyde dehydrogenase, dimeric NADP-preferring	1.44	1.20E-03
P17661	DESM	Desmin	1.42	2.00E-04

B)

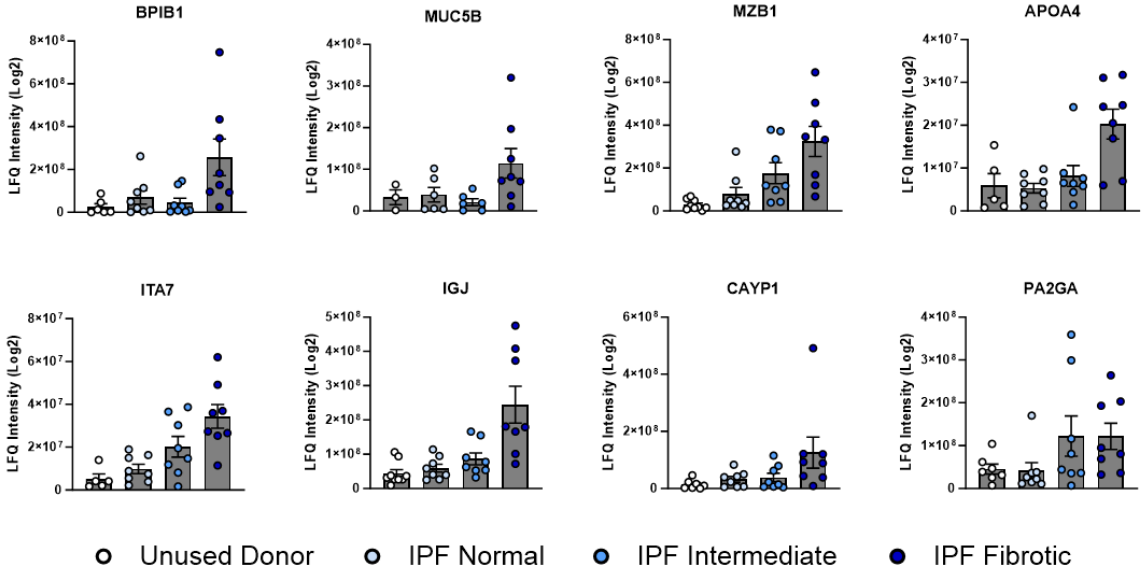

Figure 88: Top significantly upregulated proteins in IPF fibrotic vs IPF normal comparison A) Table of significantly upregulated proteins ($p<0.05$) beginning with highest log2FC B) Graphs of top 8 upregulated proteins in all IPF regions and unused donor controls. All data are presented as mean ± SEM.

A)

IPF Fibrotic vs Normal- Top significantly downregulated proteins

Accession Code	Protein ID	Protein Name	logFC	P.Value
Q16787	LAMA3	Laminin subunit alpha-3	-3.56	1.00E-04
Q13751	LAMB3	Laminin subunit beta-3	-3.27	2.00E-04
Q99758	ABCA3	Phospholipid-transporting ATPase ABCA3	-3.16	8.12E-06
P15428	PGDH	15-hydroxyprostaglandin dehydrogenase [NAD(+)]	-2.69	1.38E-06
P09601	HMOX1	Heme oxygenase 1	-2.51	3.00E-04
Q92817	EVPL	Envoplakin	-2.12	1.00E-04
O96009	NAPSA	Napsin-A	-2.11	1.00E-04
Q9NZA1-2	CLIC5	Isoform 1 of Chloride intracellular channel protein 5	-1.90	8.94E-06
Q8NF37	PCAT1	Lysophosphatidylcholine acyltransferase 1	-1.89	2.79E-07
Q10589-2	BST2	Isoform 2 of Bone marrow stromal antigen 2	-1.74	2.80E-05
P02792	FRIL	Ferritin light chain	-1.67	2.00E-03
Q6UVK1	CSPG4	Chondroitin sulfate proteoglycan 4	-1.63	1.00E-04
O76041-2	NEBL	Isoform 2 of Nebulette	-1.60	1.00E-04
P09668	CATH	Pro-cathepsin H	-1.59	2.25E-06
P12821	ACE	Angiotensin-converting enzyme	-1.58	1.00E-03
Q96RW7	HMCN1	Hemicentin-1	-1.52	7.80E-03
Q15599	NHRF2	Na(+)/H(+) exchange regulatory cofactor NHE-RF2	-1.50	1.94E-08
Q07075	AMPE	Glutamyl aminopeptidase	-1.48	1.00E-04
Q5U651	RAIN	Ras-interacting protein 1	-1.48	8.11E-06
Q02809	PLOD1	Procollagen-lysine,2-oxoglutarate 5-dioxygenase 1	-1.44	1.10E-03

B)

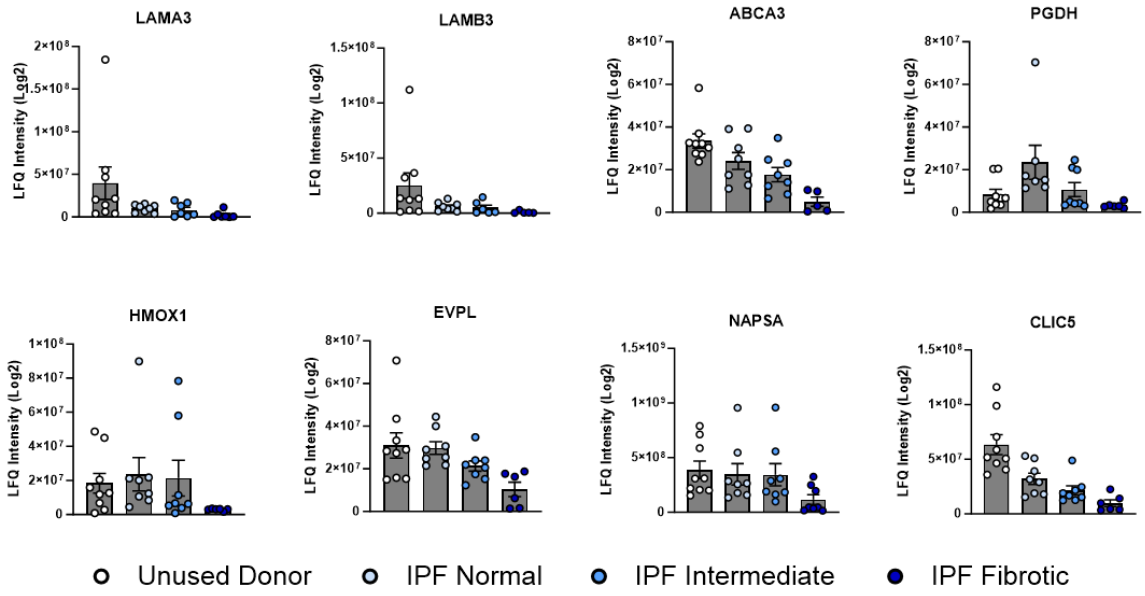

Figure 89: Top significantly downregulated proteins in IPF fibrotic vs IPF normal comparison A) Table of significantly downregulated proteins ($p<0.05$) beginning with smallest log2FC B) Graphs of top 8 downregulated proteins in all IPF regions and unused donor controls. All data are presented as mean ± SEM.

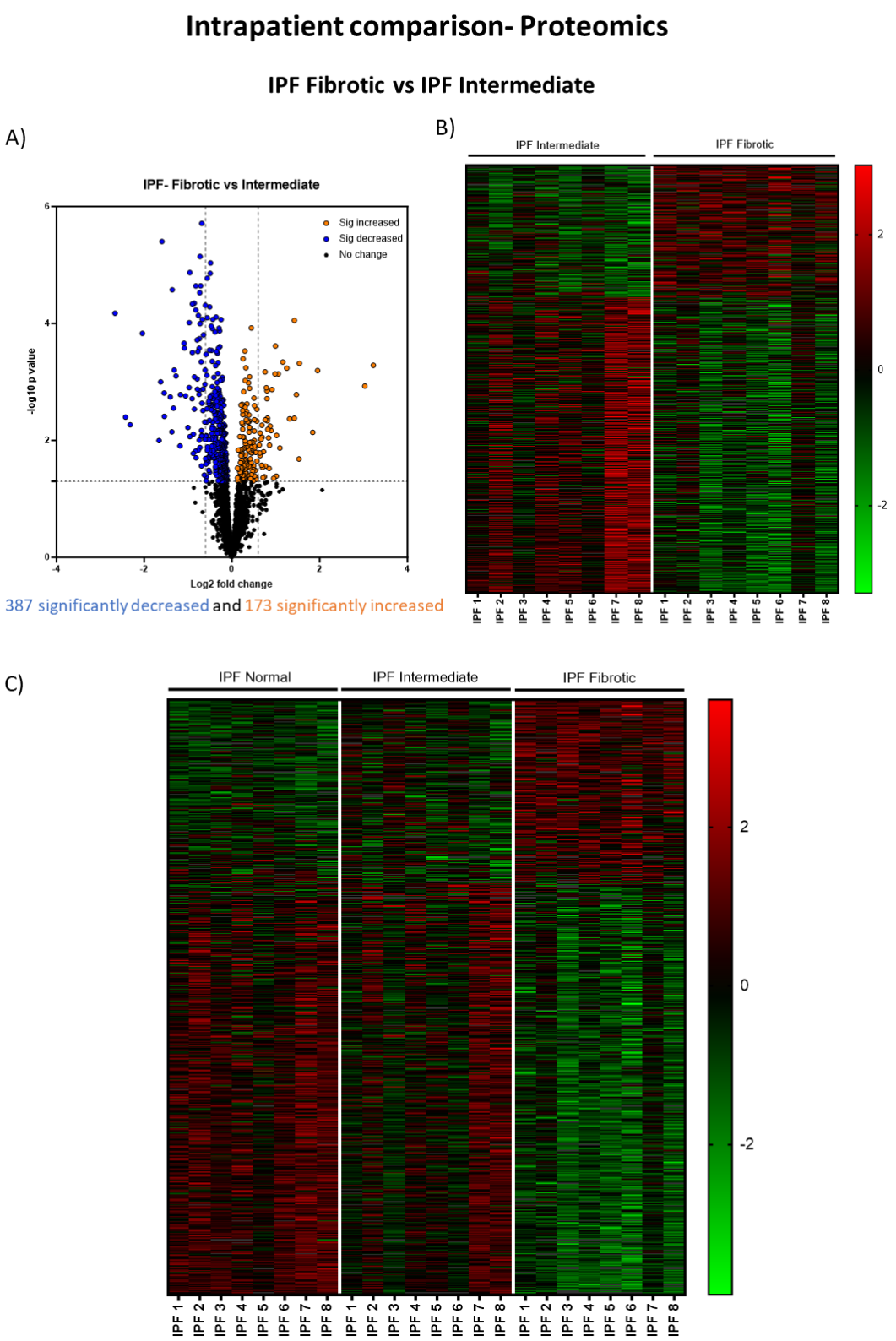

Figure 90: **Proteomic analysis of intrapatient IPF fibrotic vs IPF intermediate comparison** Significantly different proteins ($p<0.05$) were graphed as A) volcano plot (downregulated proteins in blue and upregulated proteins in orange) and B) heat map (downregulated proteins in green and upregulated proteins in red). C) Heat map of significantly different proteins in all 3 IPF regions**.**

A)

IPF Fibrotic vs Intermediate- Top significantly upregulated proteins

Accession Code	Protein ID	Protein Name	logFC	P Value
Q8TDL5	BPIB1	BPI fold-containing family B member 1	3.22	5.00E-04
Q9HC84	MUC5B	Mucin-5B	3.03	1.20E-03
P01833	PIGR	Polymeric immunoglobulin receptor	1.95	6.00E-04
Q13938-4	CAYP1	Isoform 3 of Calcyphosin	1.84	7.30E-03
P30838	AL3A1	Aldehyde dehydrogenase, dimeric NADP-preferring	1.54	5.00E-04
P15924	DESP	Desmoplakin	1.53	2.08E-02
P06727	APOA4	Apolipoprotein A-IV	1.47	1.70E-03
P01591	IGJ	Immunoglobulin J chain	1.43	1.00E-04
P16050	LOX15	Polyunsaturated fatty acid lipoxygenase AL	1.42	4.20E-03
P03973	SLPI	Antileukoproteinase	1.31	4.30E-03
Q96NY7-2	CLIC6	Isoform A of Chloride intracellular channel protein 6	1.25	6.00E-04
P80188	NGAL	Neutrophil gelatinase-associated lipocalin	1.16	5.00E-04
Q13683-3	ITA7	Isoform Alpha-7X1B of Integrin alpha-7	1.09	1.35E-02
P01876-1	IGHA1	Isoform 1 of Immunoglobulin heavy constant alpha 1	1.06	7.00E-04
P80748	LV321	Immunoglobulin lambda variable 3-21	1.02	8.20E-03
Q8WU39	MZB1	Marginal zone B- and B1-cell-specific protein	1.01	4.08E-02
P0DOX2	IGA2	Immunoglobulin alpha-2 heavy chain	0.99	2.00E-04
P12724	ECP	Eosinophil cationic protein	0.98	7.00E-04
P08263	GSTA1	Glutathione S-transferase A1	0.95	4.45E-02
Q9BX97	PLVAP	Plasmalemma vesicle-associated protein	0.91	1.40E-03

B)

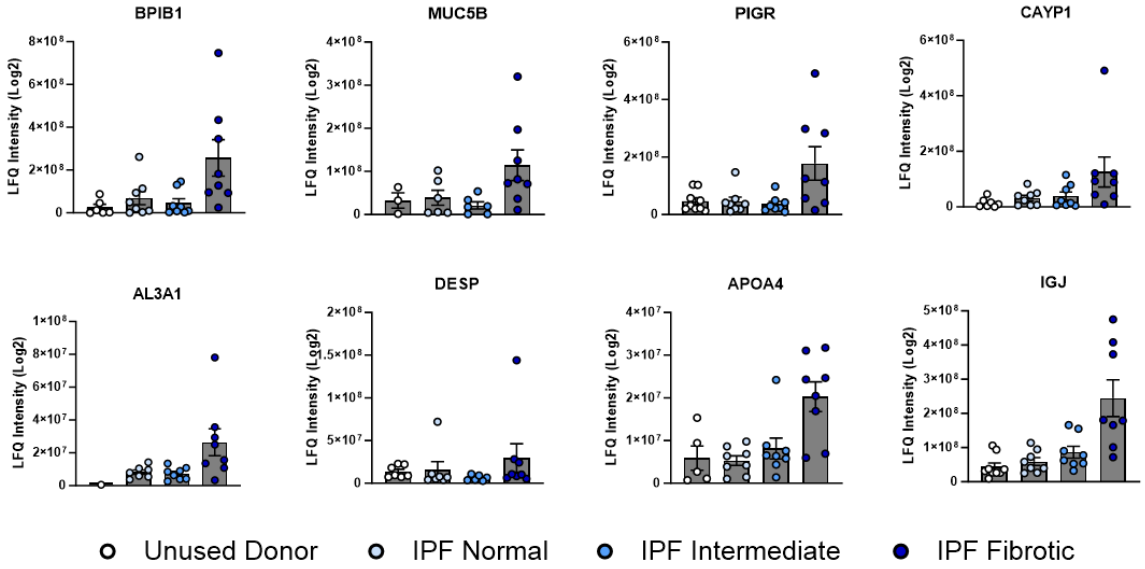

Figure 91: Top significantly upregulated proteins in IPF fibrotic vs IPF intermediate comparison A) Table of significantly upregulated proteins ($p<0.05$) beginning with highest log2FC B) Graphs of top 8 upregulated proteins in all IPF regions and unused donor controls. All data are presented as mean ± SEM.

A)

IPF Fibrotic vs Intermediate- Top significantly downregulated proteins

Accession Code	Protein ID	Protein Name	logFC	P Value
Q99758	ABCA3	Phospholipid-transporting ATPase ABCA3	-2.66	1.00E-04
Q16787	LAMA3	Laminin subunit alpha-3	-2.43	4.00E-03
Q13751	LAMB3	Laminin subunit beta-3	-2.32	5.40E-03
O96009	NAPSA	Napsin-A	-2.04	1.00E-04
P09601	HMOX1	Heme oxygenase 1	-1.66	1.01E-02
Q92817	EVPL	Envoplakin	-1.62	1.00E-03
Q8NF37	PCAT1	Lysophosphatidylcholine acyltransferase 1	-1.59	3.95E-06
P12821	ACE	Angiotensin-converting enzyme	-1.54	1.50E-03
P02792	FRIL	Ferritin light chain	-1.54	3.90E-03
P15428	PGDH	15-hydroxyprostaglandin dehydrogenase [NAD(+)]	-1.40	1.80E-03
Q9BW04	SARG	Specifically androgen-regulated gene protein	-1.37	7.10E-03
P09668	CATH	Pro-cathepsin H	-1.36	2.65E-05
Q02809	PLOD1	Procollagen-lysine,2-oxoglutarate 5-dioxygenase 1	-1.33	2.80E-03
Q9NZA1-2	CLIC5	Isoform 1 of Chloride intracellular channel protein 5	-1.31	6.00E-04
O76041-2	NEBL	Isoform 2 of Nebulette	-1.27	8.00E-04
Q9H8L6	MMRN2	Multimerin-2	-1.18	1.24E-02
Q15067-2	ACOX1	Isoform 2 of Peroxisomal acyl-coenzyme A oxidase 1	-1.17	1.60E-03
O95340	PAPS2	Bifunctional 3-phosphoadenosine 5-phosphosulfate synthase 2	-1.09	2.00E-04
O95436-2	NPT2B	Isoform 2 of Sodium-dependent phosphate transport protein 2B	-1.08	3.00E-04
P09467	F16P1	Fructose-1,6-bisphosphatase 1	-1.06	1.70E-03

B)

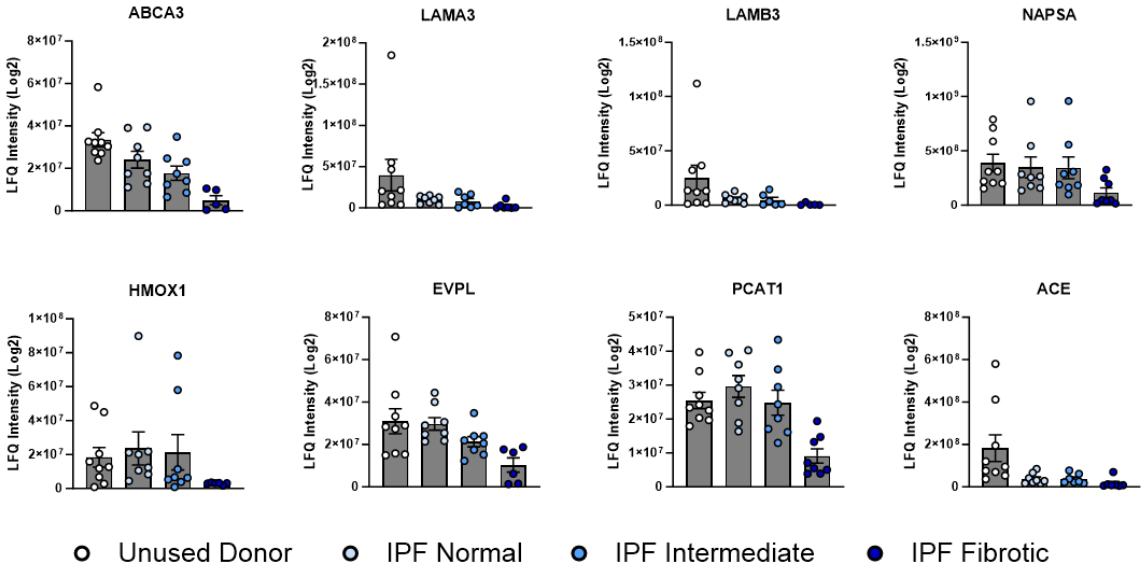

Figure 92: Top significantly downregulated proteins in IPF fibrotic vs IPF intermediate comparison A) Table of significantly downregulated proteins ($p<0.05$) beginning with smallest log2FC B) Graphs of top 8 downregulated proteins in all IPF regions and unused donor controls. All data are presented as mean ± SEM.

A) **Significantly upregulated proteins in IPF fibrotic vs IPF normal and intermediate**

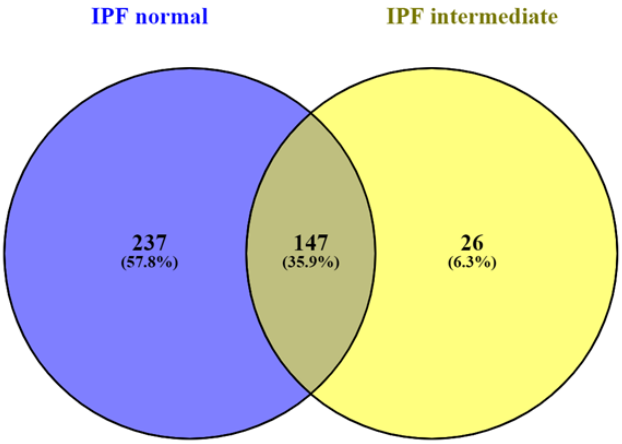

B) **Significantly downregulated proteins in IPF fibrotic vs IPF normal and intermediate**

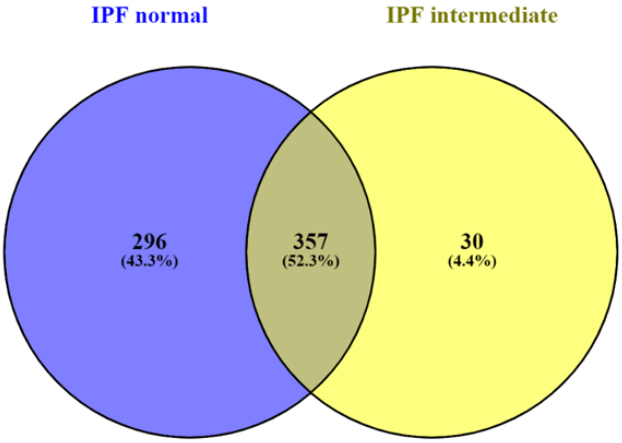

Figure 93: Significantly different proteins in IPF fibrotic regions vs early-stage disease Venny diagram of A) significantly upregulated and B) significantly downregulated proteins in IPF fibrotic regions vs IPF normal and IPF intermediate regions.

4.2.4 Interrogation of additional protein markers

To overcome some of the limitations of mass-based spectrometry, such as the inability to detect lowly abundant or small proteins, we further sought to quantify proteins within regional IPF and UD lung tissue *via* multi-plex ELISA (MesoScaleDiscovery). To achieve this, tissue homogenates were normalised to 0.5mg/ml (as measured by BCA assay) and U-PLEX ELISA was performed to determine the protein concentration of 123 additional markers including interleukins, metabolic markers and cytokines (Figure 94). Quantification of these additional proteins identified a number of markers which were significantly downregulated (Figure 95) and significantly upregulated (Figure 96) in IPF tissue compared to UD controls. Interestingly, of the 9 proteins which were found to be significantly downregulated in IPF tissue compared to UD controls, 7 of these were downregulated exclusively in the IPF normal and/or intermediate region but not end-stage fibrotic tissue (Figure 95A-E,G-H) including IFN-γ (UD vs IPF intermediate, $p<0.05$), IL-4 (UD vs IPF normal and intermediate, $p<0.05$), IL-5 (UD vs IPF normal and intermediate, $p<0.05$), IL-8 (UD vs IPF normal and intermediate, $p<0.05$), IL-10 (UD vs IPF normal and intermediate, $p<0.05$), MCP-1 (UD vs IPF normal, $p<0.05$) and PD-L1 epitope 2 (UD vs IPF normal, $p<0.05$).

Conversely, 18 of the 123 proteins quantified were found to be significantly upregulated in IPF donor samples in comparison to UD controls (Figure 96). These included proteins which were predominantly upregulated in IPF intermediate and fibrotic regions, but not IPF normal (Figure 96A, D, K, O, R) such as BCMA (UD vs IPF intermediate [$p<0.05$] and UD vs IPF fibrotic [$p<0.0.1$]), CD27 (UD vs IPF intermediate and fibrotic [$p<0.01$]), IL-2Rα (UD vs IPF intermediate and fibrotic [$p<0.05$]), TGF-β3 (UD vs IPF intermediate [$p<0.05$] and UD vs IPF fibrotic [$p<0.0.1$]) and TIE2 (UD vs IPF intermediate and fibrotic [$p<0.05$]). Additionally, a number of proteins were exclusively upregulated in IPF normal regions including CD276 ($p<0.05$), CD40 ($p<0.05$), fractalkine ($p<0.05$), granzyme A ($p<0.05$), TGF-β1 ($p<0.05$) and TGF-β2 ($p<0.05$). Of these, CD40 was also significantly downregulated in IPF intermediate ($p<0.05$) and IPF fibrotic regions ($p<0.05$) compared to IPF normal tissue (Figure 96G). Similarily, fractalkine was found to be significantly downregulated in IPF fibrotic regions ($p<0.05$) compared to IPF normal regions (Figure 96I). Finally, several proteins including CD20 ($p<0.01$), CD28 (0.01), FLT3L ($p<0.05$) and MDC ($p<0.05$) were significantly increased in IPF fibrotic regions compared to UD lungs and TNB-β ($p<0.05$) was the only protein to be upregulated in the IPF intermediate region alone (Figure 96Q).

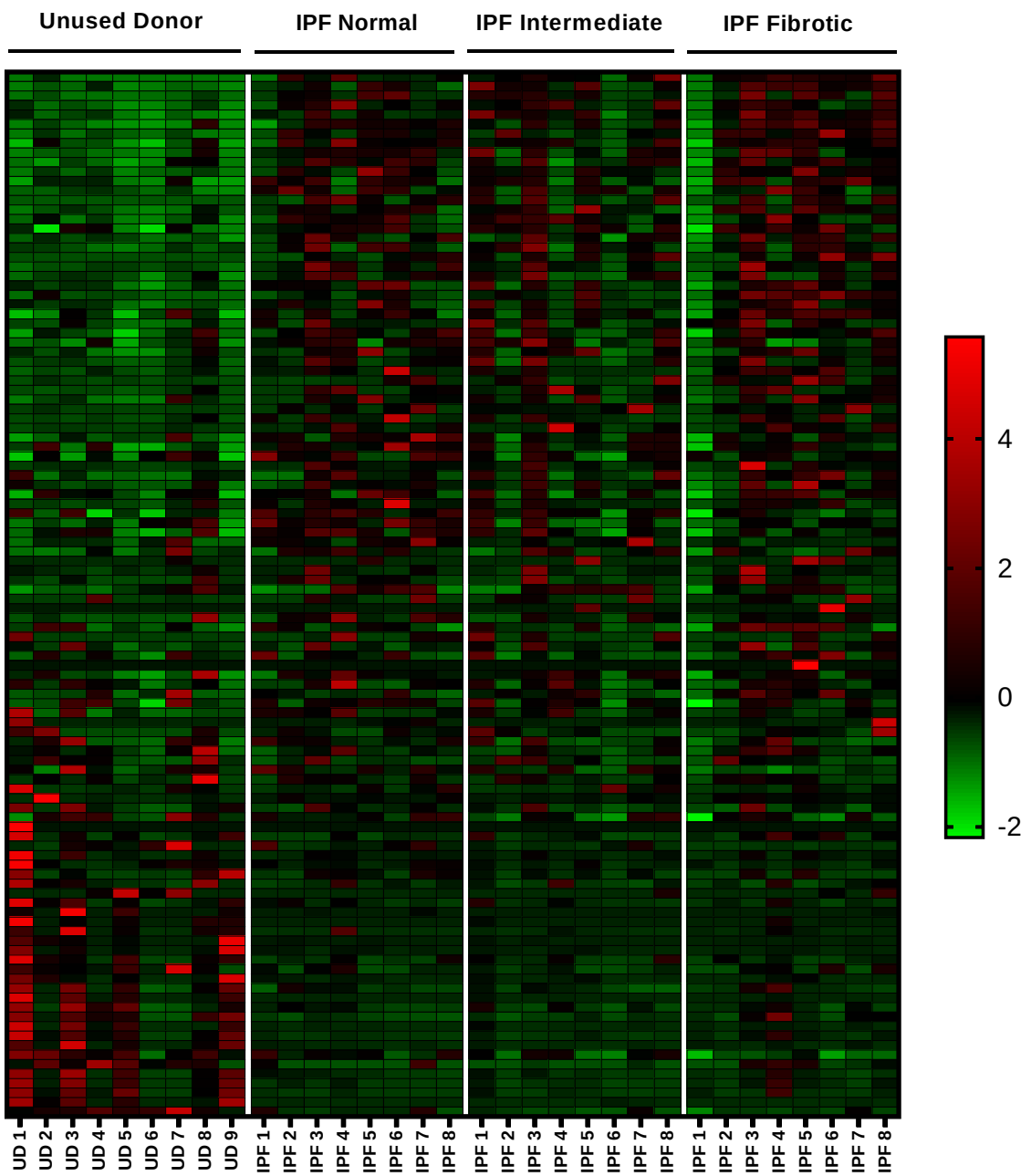

Figure 94: Quantification of additional protein markers Heat map of additional protein marker expression quantified in unused donor controls (n=9), IPF normal (n=8 donors), IPF intermediate (n=8 donors) and IPF fibrotic (n=8 donors) homogenates (normalised to 0.5mg/ml *via* BCA assay) by multi-plex ELISA.

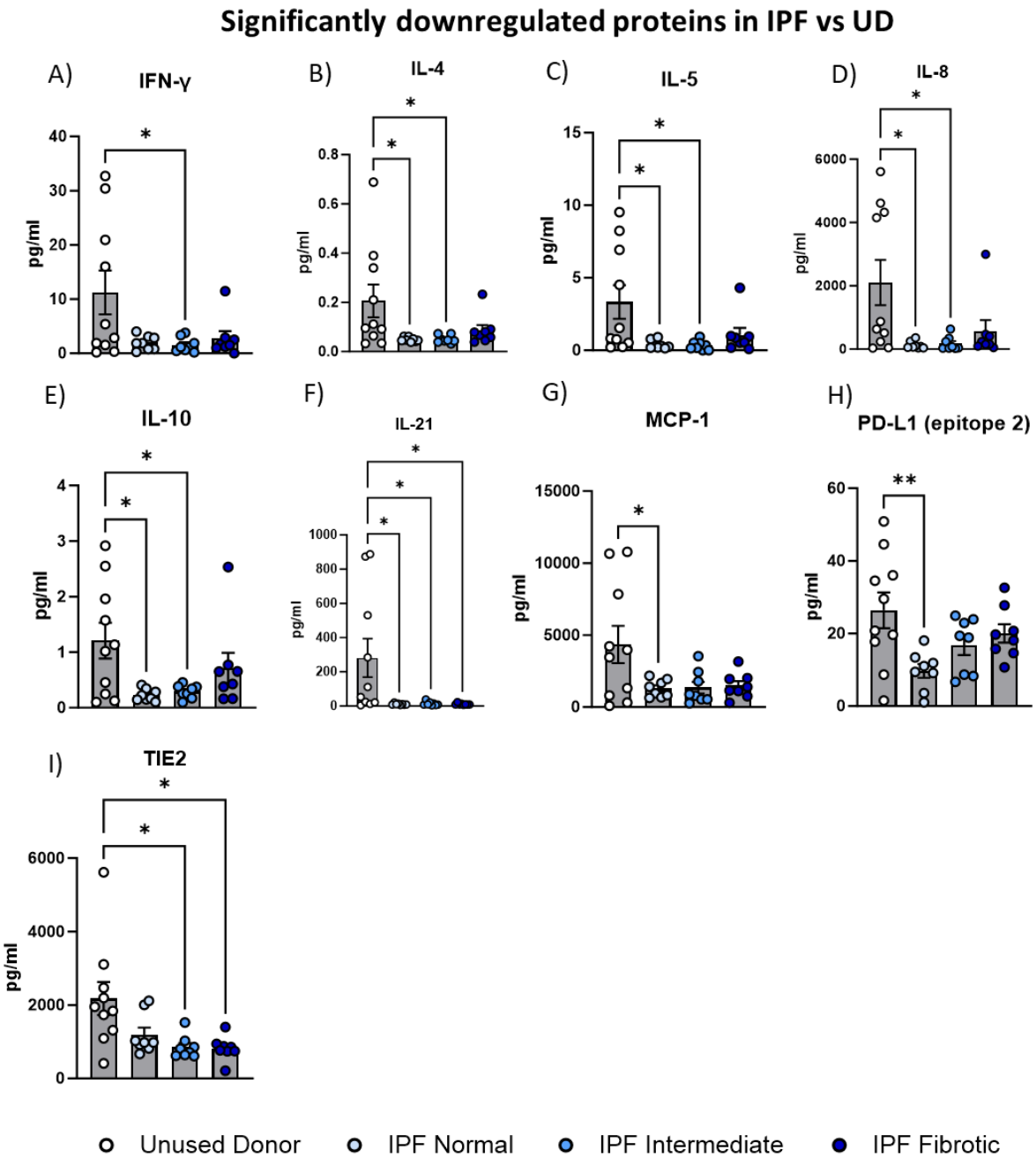

Figure 95: Significantly downregulated additional protein markers in IPF regions vs UD Quantification of additional protein markers was performed for 123 immune and metabolic markers in tissue homogenates (normalised to 0.5mg/ml as measured by BCA assay) generated from unused donor lungs (n=9 donors), IPF normal (n=8 donors), IPF intermediate (n=8 donors) and IPF fibrotic (n=8 donors) *via* MSD. A-I) Proteins which were significantly downregulated in IPF vs UD lungs were graphed. All data are mean ± SEM. Statistical significance was determined using ANOVA with post-hoc Tukey HSD Test (*p<0.05, **p<0.01, ***p<0.001 and ****p<0.0001).

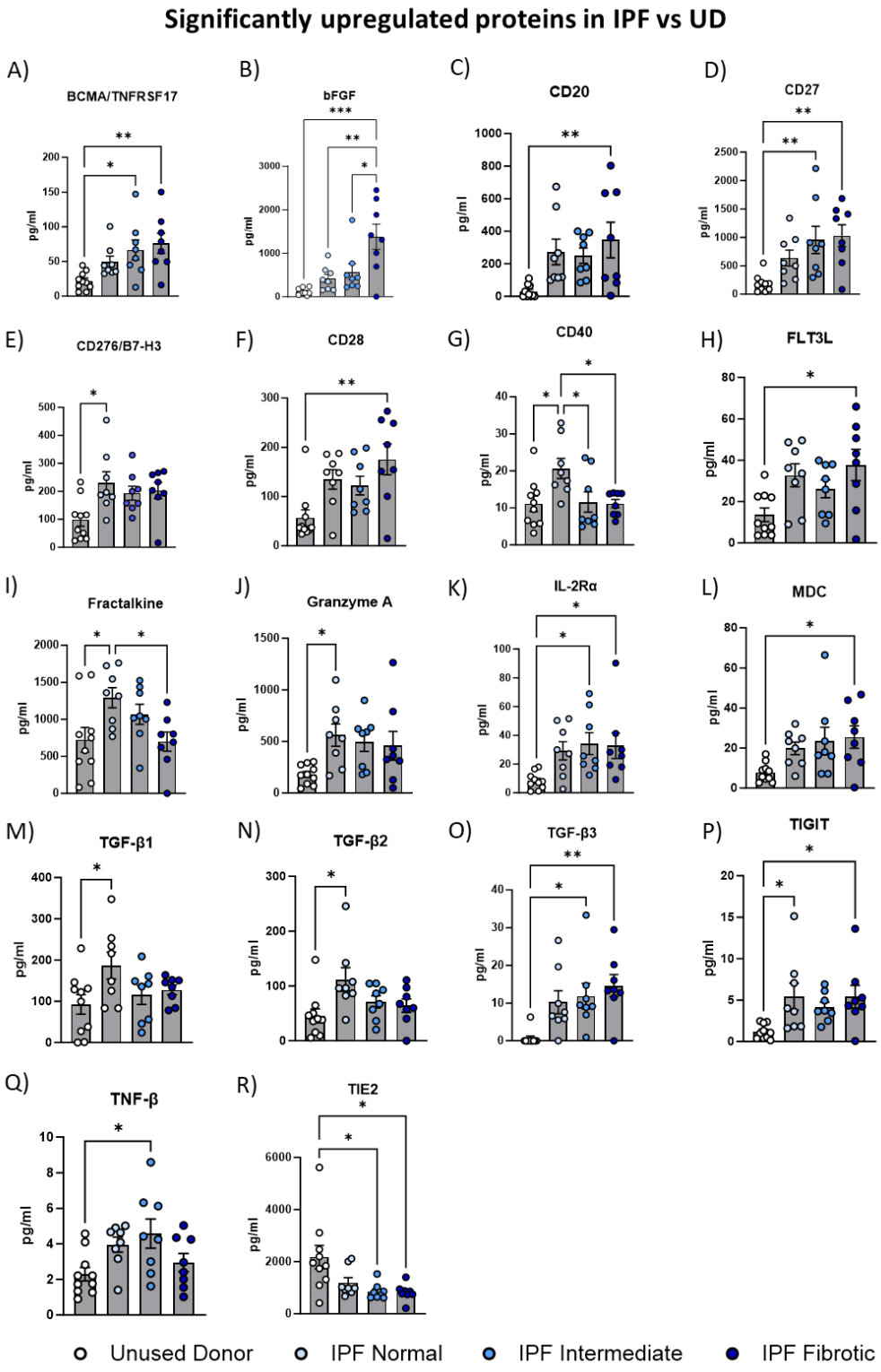

Figure 96: Significantly upregulated additional protein markers in IPF regions vs UD Quantification of additional protein markers was performed for 123 immune and metabolic markers in tissue homogenates (normalised to 0.5mg/ml as measured by BCA assay) generated from unused donor lungs (n=9 donors), IPF normal (n=8 donors), IPF intermediate (n=8 donors) and IPF fibrotic (n=8 donors) *via* MSD. A-R) Proteins which were significantly upregulated in IPF vs UD lungs were graphed. All data are mean ± SEM. Statistical significance was determined using ANOVA with post-hoc Tukey HSD Test (*p<0.05, **p<0.01, ***p<0.001 and ****p<0.0001).

4.2.5 Identification of potential targets of interest

To begin discovering potential targets of interest and given that we found clear differences in functional protein expression in both inter- and intra- patient analysis, we first sought to identify any proteins which were uniquely up- or down- regulated within the regions of IPF tissue thought to be undergoing active remodelling (normal and intermediate). First, to identify proteins which were actively downregulated during fibrogenesis (Figure 98A), results from both inter- and intra-patient comparisons were filtered to contain only proteins which were significantly downregulated ($p<0.05$) in normal and intermediate IPF regions compared to UD samples, but also significantly upregulated ($p<0.05$) in the end-stage fibrotic regions of IPF lungs. Here, UD vs IPF normal and UD vs IPF intermediate interpatient datasets were filtered for significance ($p<0.05$) and ranked smallest to largest based on logFC values. Negative logFC values (downregulated proteins) from both interpatient comparisons were merged, and duplicate proteins removed, to generate a list of 541 proteins which were significantly downregulated in IPF normal and intermediate IPF regions vs UD controls. Alongside this, IPF fibrotic vs IPF normal and IPF fibrotic vs IPF intermediate intrapatient datasets were filtered for significance ($p<0.05$) and ranked largest to smallest based on logFC values. Positive logFC values (upregulated proteins) from both intrapatient comparisons were merged, and duplicate proteins removed, to generate a list of 410 proteins which were significantly upregulated in end-stage fibrotic regions of IPF compared to IPF normal and intermediate regions. Finally, these 2 protein lists were merged together and filtered to select for proteins which appeared in both datasets, resulting in the identification of 54 proteins (Figure 97). Of the 54 proteins identified (Figure 98B), 3 targets were selected for immunohistochemical validation based on their intracellular location and antibody availability: myeloperoxidase (PERM), lactotransferrin (TRFL) and cathepsin G (CATG) (Figure 99A-C). Results confirmed that all 3 targets were present primarily in UD lungs and fibrotic regions of IPF tissue, with few positive cells observed in normal and intermediate regions of IPF donors (Figure 99D). Histologically, positive cells displayed a rounded morphology consistent with neutrophils which primarily localised to the epithelium in UD and IPF fibrotic tissue as well as within dense clusters of immune cells in IPF fibrotic tissue.

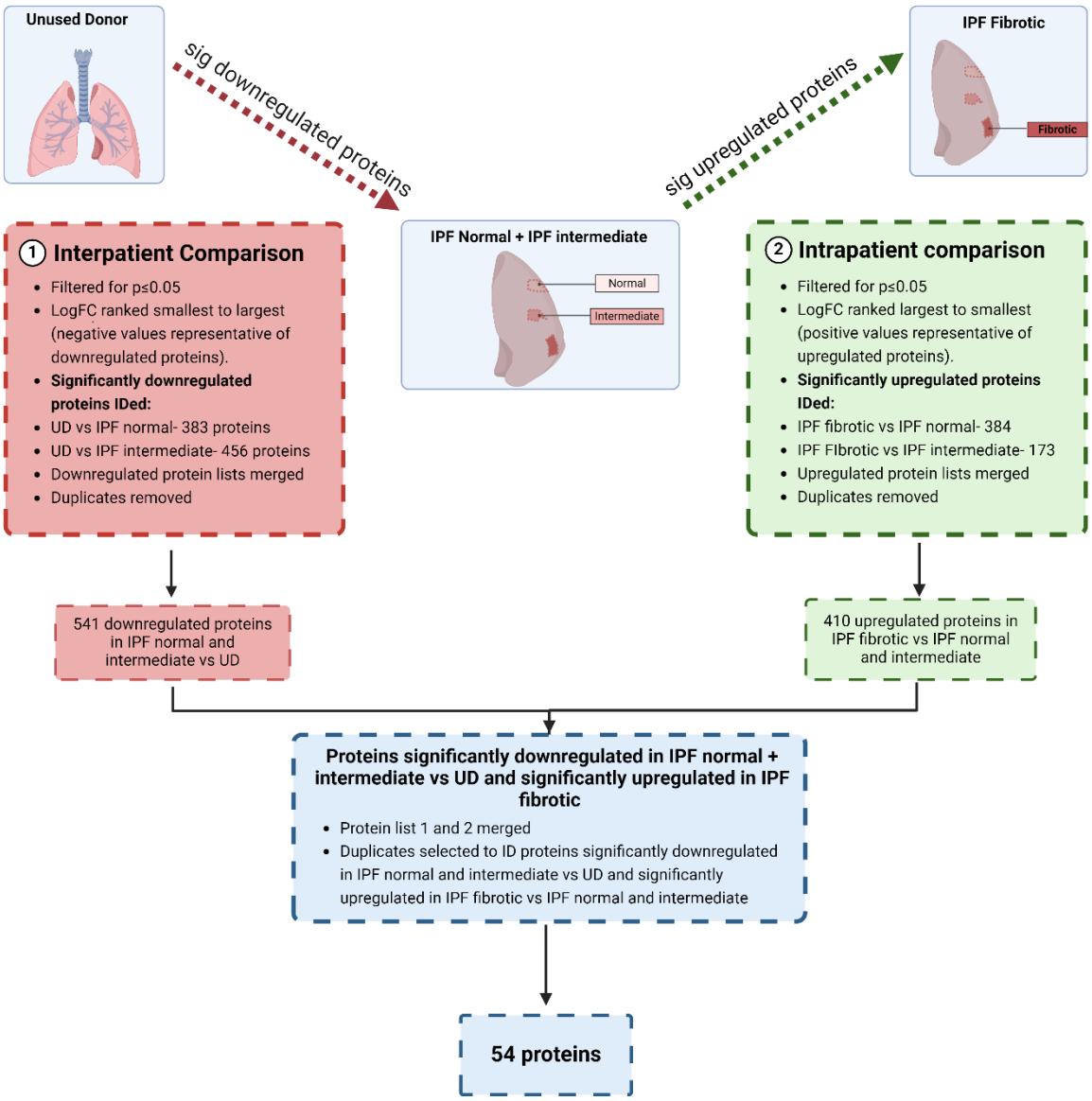

Figure 97: Identification of downregulated proteins of interest in IPF normal and intermediate regions 1. Unused donor vs IPF normal and unused donor vs IPF intermediate interpatient datasets were filtered for significance ($p<0.05$) and ranked smallest to largest based on logFC values. Negative logFC values (downregulated proteins) from both interpatient comparisons were merged, and duplicate proteins removed, to generate a list of 541 proteins which were significantly downregulated in IPF normal and intermediate IPF regions vs unused donor controls. 2. IPF fibrotic vs IPF normal and IPF fibrotic vs IPF intermediate intrapatient datasets were filtered for significance ($p<0.05$) and ranked largest to smallest based on logFC values. Positive logFC values (upregulated proteins) from both intrapatient comparisons were merged, and duplicate proteins removed, to generate a list of 410 proteins which were significantly upregulated in end-stage fibrotic regions of IPF compared to IPF normal and intermediate regions. Protein lists 1 and 2 were merged and filtered to select for proteins which appeared in both datasets, resulting in the identification of 54 proteins.

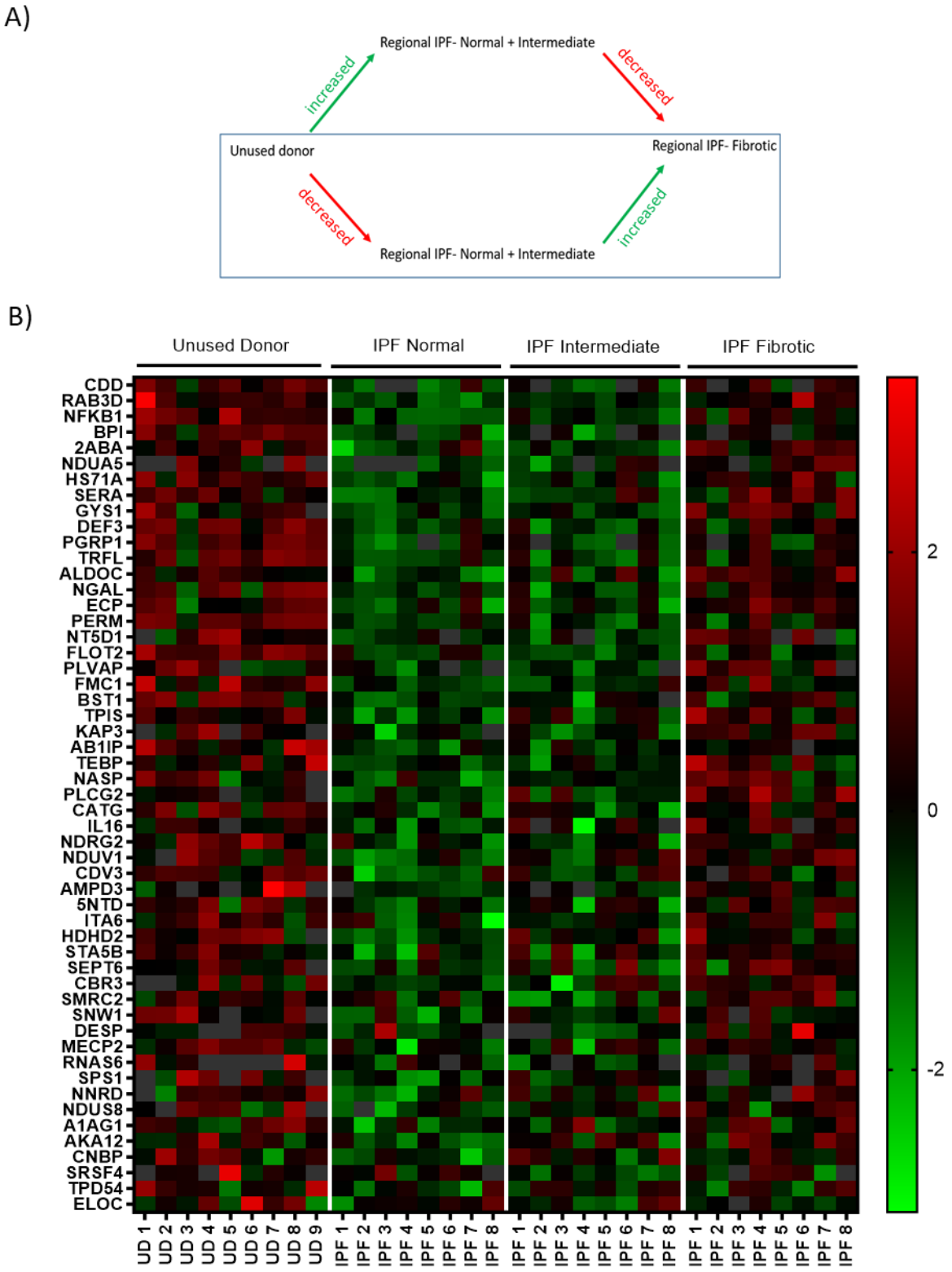

Figure 98: Downregulated protein target identification A) Schematic of identification of proteins of interest which were significantly downregulated ($p<0.05$) in normal and intermediate IPF regions compared to UD samples and significantly upregulated ($p<0.05$) in the end-stage IPF fibrotic regions. B) Heat map of 54 proteins of interest identified in UD and IPF regions.

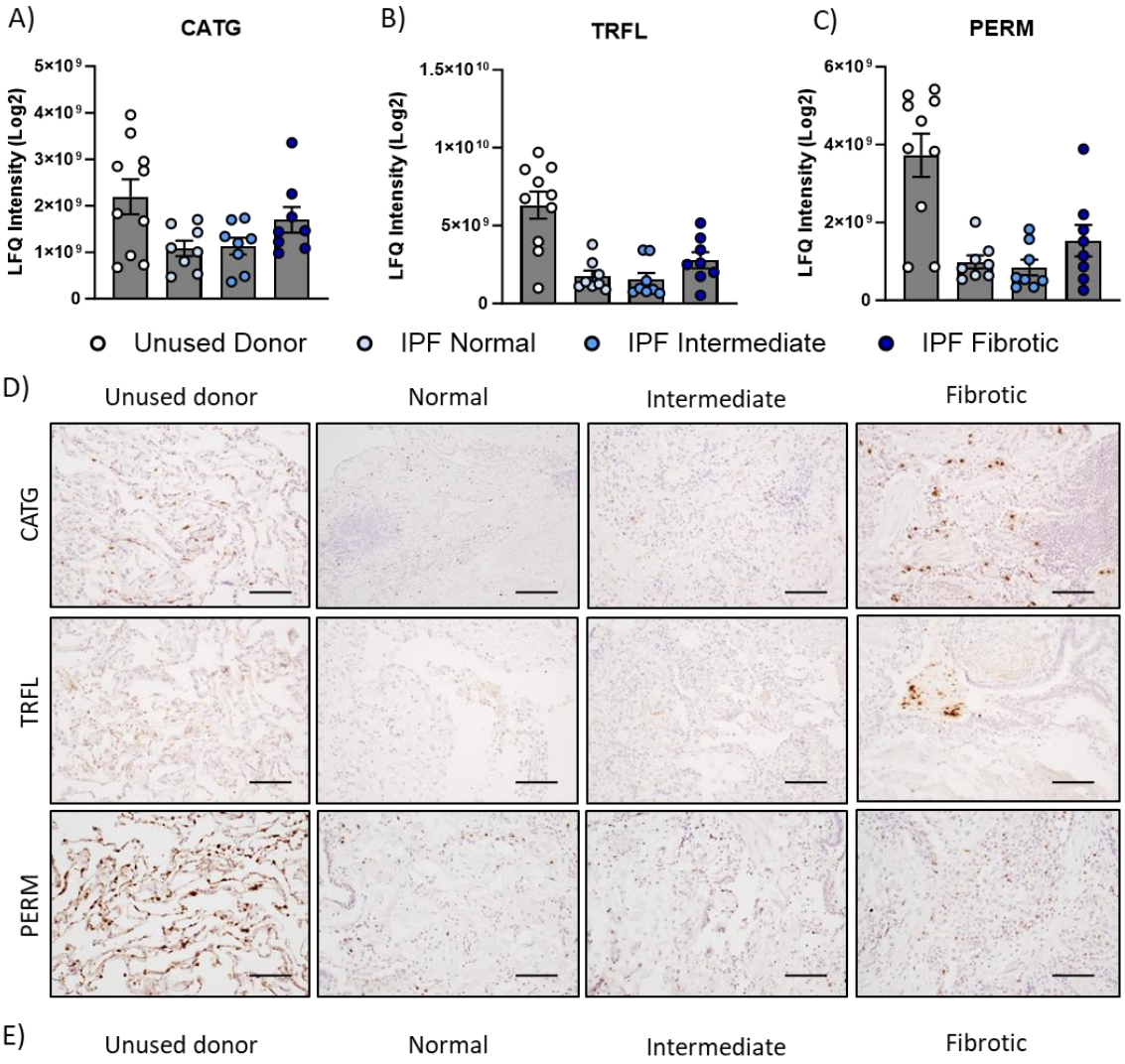

Figure 99: **Downregulated protein target histological validation** LFQ intensity identified through proteomic analysis were Log2 transformed and plotted for A) cathepsin G (CATG), B) lactotransferrin (TRFL) and C) myeloperoxidase (PERM). Histological validation of proteins was performed as shown by D) overview representative images of selected targets in all IPF regions and unused donor controls (scale bar= 100µm). Primary antibodies were used at the following dilutions: cathepsin G; 1/100, lactoferrin; 1/100 and myeloperoxidase; 1/100. All data are mean ± SEM.

Next, datasets were filtered by selecting for proteins which were significantly upregulated ($p<0.05$) in normal and intermediate IPF regions compared to UD samples and significantly downregulated ($p<0.05$) in the end-stage IPF fibrotic regions (Figure 101A). Here, UD vs IPF normal and UD vs IPF intermediate interpatient datasets were filtered for significance ($p<0.05$) and ranked largest to smallest based on logFC values. Positive logFC values (upregulated proteins) from both interpatient comparisons were merged, and duplicate proteins removed, to generate a list of 337 proteins which were significantly upregulated in IPF normal and intermediate IPF regions vs UD controls. Alongside this, IPF fibrotic vs IPF normal and IPF fibrotic vs IPF intermediate intrapatient datasets were filtered for significance ($p<0.05$) and ranked smallest to largest based on logFC values. Negative logFC values (downregulated proteins) from both intrapatient comparisons were merged, and duplicate proteins removed, to generate a list of 683 proteins which were significantly downregulated in end-stage fibrotic regions of IPF compared to IPF normal and intermediate regions. Finally, these 2 protein lists were merged together and filtered to select for proteins which appeared in both datasets, resulting in the identification of 75 proteins (Figure 100). Of the 75 proteins identified (Figure 101B), 3 targets were further selected for immunohistochemical validation based on their intracellular location and antibody availability: mannose receptor C type 2 (MRC2), integrin beta-6 (ITB6) and cytokeratin 18 (K1C18) (Figure 102A-C). Histologically, these proteins were frequently found adjacent to areas of ECM deposition, coupled with dense inflammatory infiltrates. MRC2+ cells typically displayed a rounded immune cell morphology and appeared primarily within clusters of inflammatory cells, whereas K1C18+ and ITB6+ (well defined epithelial markers) cells were predominantly found in the epithelium. Results showed that, consistent with proteomic findings, all 3 protein targets appeared to be upregulated in the normal and intermediate IPF regions compared to the UD controls and end-stage IPF fibrotic regions of the same donor (Figure 102D). Consequently, these targets could be considered for further investigation to understand their potential role in driving fibrogenesis.

For instance, there is strong evidence within the literature that ITB6 may be an attractive therapeutic target as well as a potential biomarker of disease progression in IPF patients [418,419]. The β6 subunit of integrins is known to specifically dimerize with the αv subunit to form the αvβ6 integrin heterodimer. Following dimerization, αvβ6 has been proven to play a key role in the activation of TGF-β, widely considered to be the master regulator of fibrosis,

resulting in pro-fibrotic effects in multiple organs [420-422]. As the αv subunit can also form heterodimers with other integrin β subunits, further investigation of integrins was performed to assess expression throughout the different IPF regions and UD controls. Results confirmed that, like the β6 subunit (Figure 103F), αv integrin was also significantly increased in normal and intermediate regions of IPF tissue compared to UD lungs, before decreasing in end-stage fibrotic regions (Figure 103A). Consistent with this, the β5 integrin subunit was the mostly highly expressed in normal regions of IPF tissue before gradually decreasing in the intermediate and fibrotic regions (Figure 103E). Conversely, β1 (Figure 103B) and β2 (Figure 103C) both demonstrated a trend of decreased expression in IPF tissue in line with disease severity, whereas β3 (Figure 103D) expression was the highest in fibrotic tissue compared to earlier IPF regions and UD controls. These results confirmed that integrin subunits exhibit diverse trajectories throughout the different IPF regions and may therefore warrant further investigation to determine their role in IPF pathogenesis.

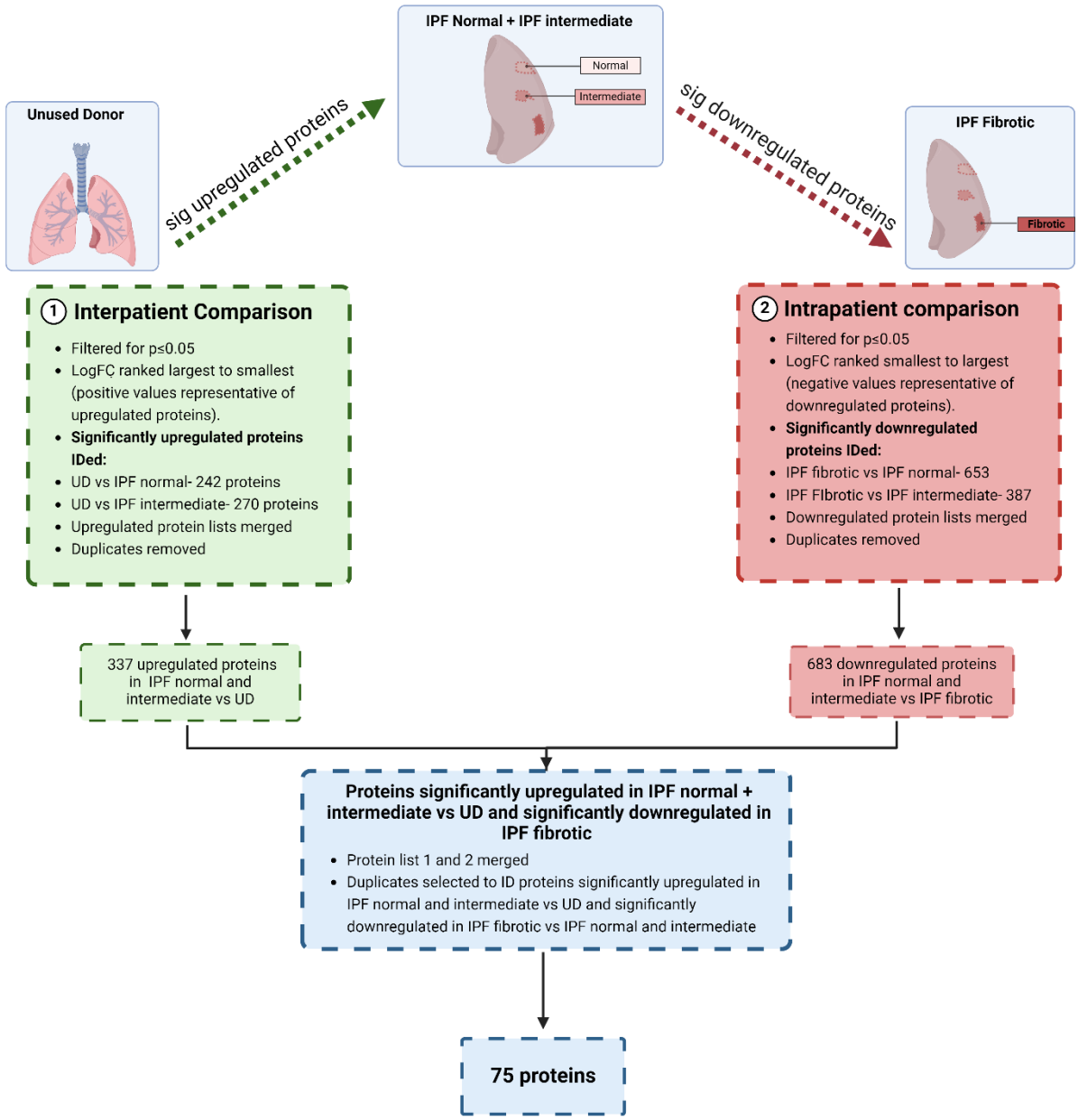

Figure 100: Identification of upregulated proteins of interest in IPF normal and intermediate regions 1. Unused donor vs IPF normal and unused donor vs IPF intermediate interpatient datasets were filtered for significance ($p<0.05$) and ranked largest to smallest based on logFC values. Positive logFC values (upregulated proteins) from both interpatient comparisons were merged, and duplicate proteins removed, to generate a list of 337 proteins which were significantly upregulated in IPF normal and intermediate IPF regions vs unused donor controls. 2. IPF fibrotic vs IPF normal and IPF fibrotic vs IPF intermediate intrapatient datasets were filtered for significance ($p<0.05$) and ranked smallest to largest based on logFC values. Negative logFC values (downregulated proteins) from both intrapatient comparisons were merged, and duplicate proteins removed, to generate a list of 683 proteins which were significantly downregulated in end-stage fibrotic regions of IPF compared to IPF normal and intermediate regions. Finally, these 2 protein lists were merged and filtered to select for proteins which appeared in both datasets, resulting in the identification of 75 proteins.

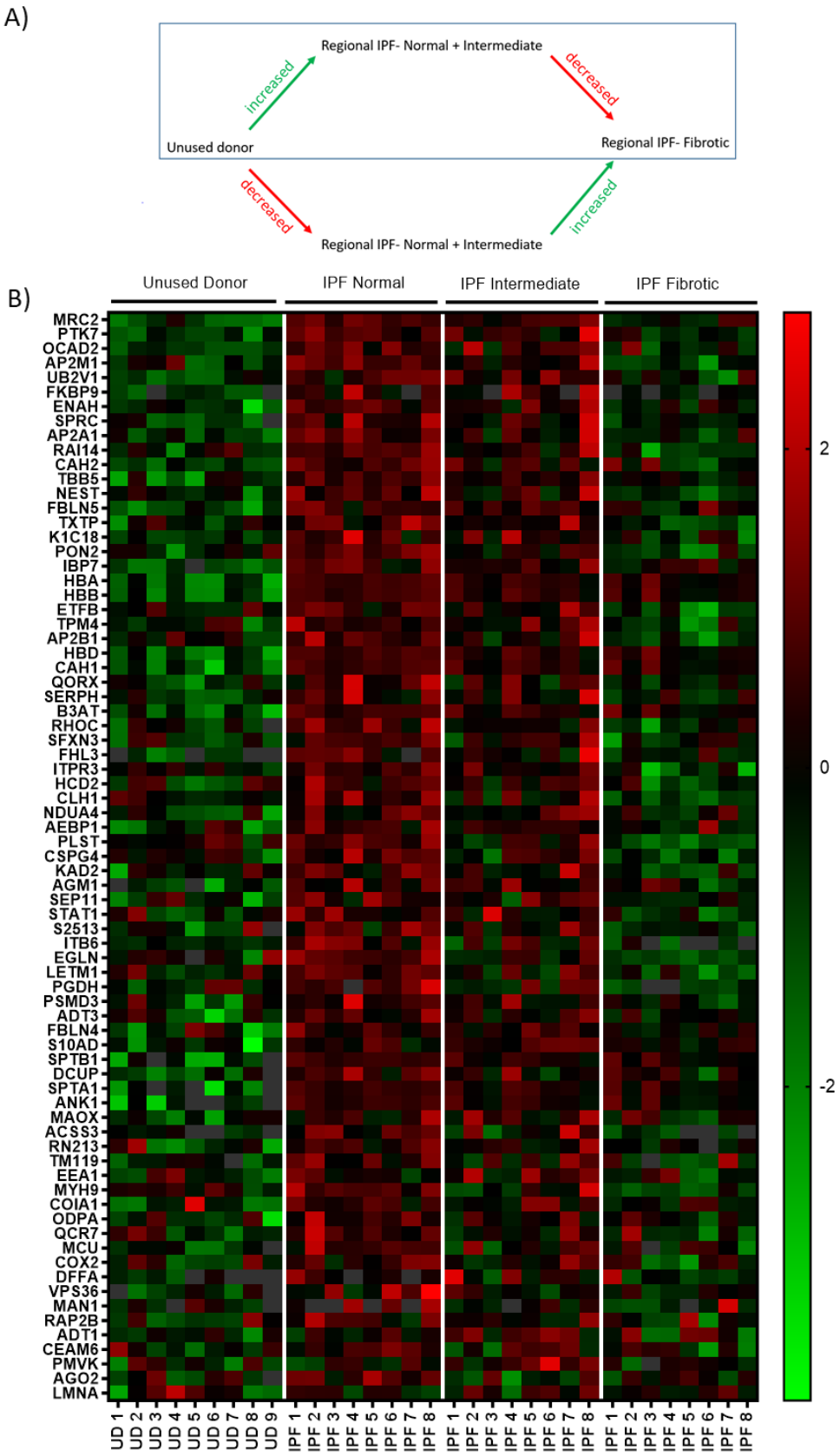

Figure 101: **Upregulated protein target identification** A) Schematic of identification of proteins of interest which were significantly upregulated ($p<0.05$) in normal and intermediate IPF regions compared to UD samples and significantly downregulated ($p<0.05$) in the end-stage IPF fibrotic regions. B) Heat map of 75 proteins of interest identified in UD and IPF regions.

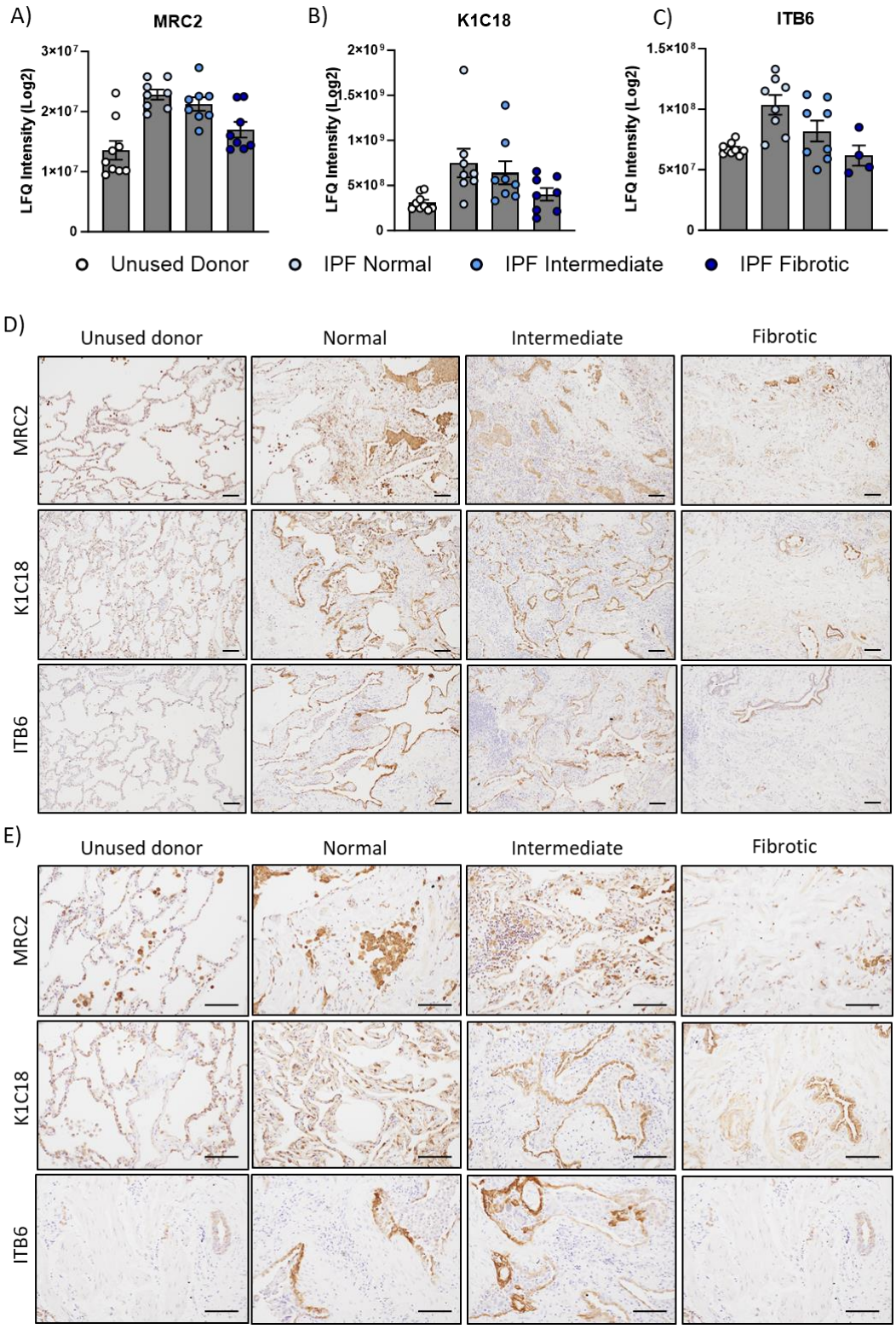

Figure 102: **Upregulated protein target histological validation** LFQ intensity identified through proteomic analysis were Log2 transformed and plotted for A) mannose receptor 2 (MRC2), B) cytokeratin 18 (K1C18) and C) integrin β6 (ITB6). Histological validation of proteins was performed as shown by D) overview representative images and E) higher powered images of selected targets in all IPF regions and unused donor controls (scale bar= 100μm). Primary antibodies were used at the following dilutions: mannose receptor 2; 1/1000, cytokeratin 18; 1/800 and integrin β6; 1/40. All data are mean ± SEM.

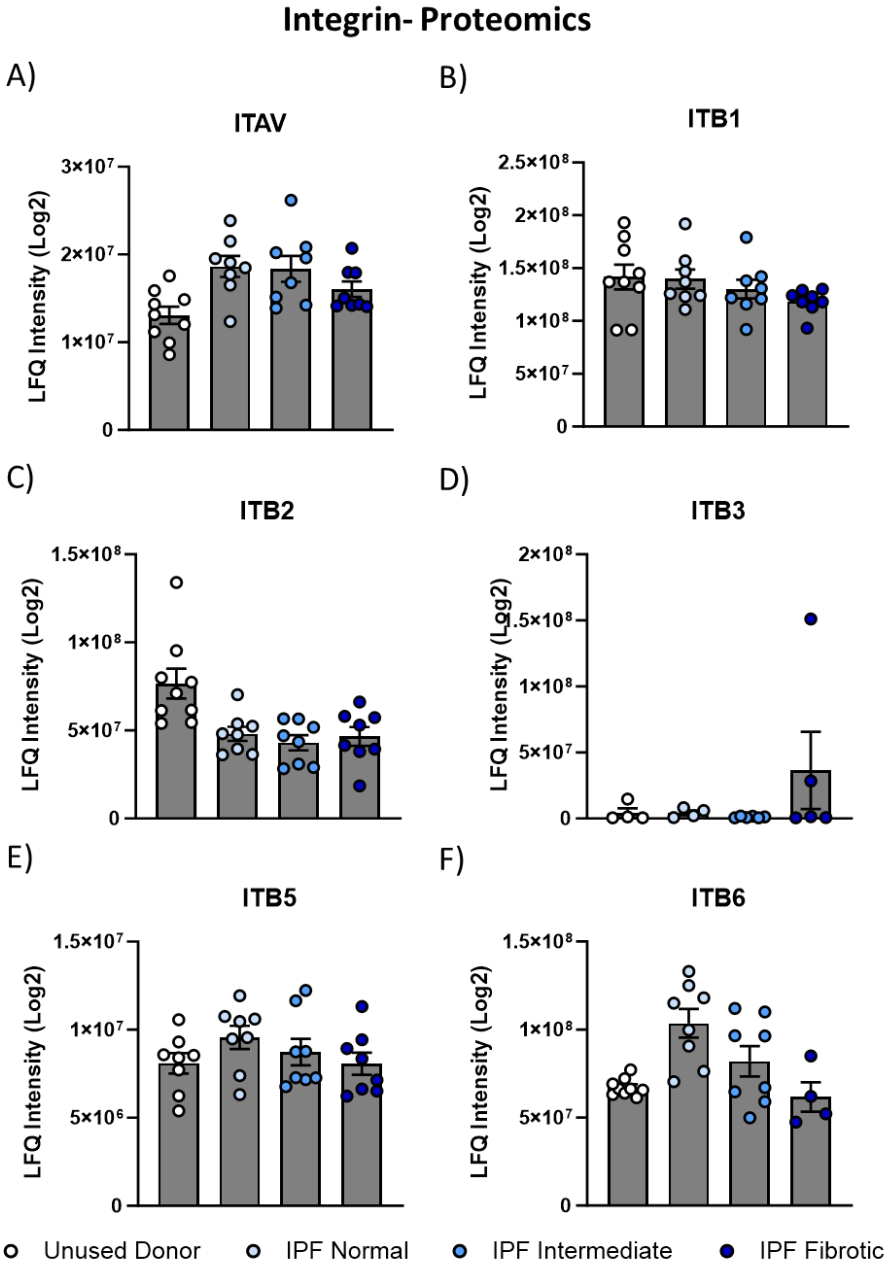

Figure 103: Integrin subunit protein expression LFQ intensity identified through proteomic analysis (n=9 unused donor lungs, n=8 IPF normal regions, n=8 IPF intermediate regions and n=8 IPF fibrotic regions) were Log2 transformed and plotted for A) ITAV B) ITB1 C) ITB2 D) ITB3 E) ITB5 and F) ITB6. All data are mean ± SEM.

As we were unable to directly ascertain the origins of upregulated proteins, we next sought to evaluate the cellular source of targets of interest by using annotated cell types from publicly available single cell RNA datasets derived from human fibrotic lung diseases. To achieve this, six publicly available scRNAseq studies were integrated by Dr Stephen Christensen, comprising 616,918 cells (51 healthy and 66 fibrotic patients [n=10 systemic sclerosis interstitial lung disease and n=56 IPF]; available online at https://singlecell.broadinstitute.org/single_cell/study/SCP2155/) and 20 of the proteins which were significantly upregulated exclusively in the normal and intermediate regions of IPF tissue were explored. Preliminary analysis of global gene expression of these targets revealed that several targets of interest were upregulated in epithelial cell populations (including AT1 and AT2) such as KRT18, OCIAD2, CA2, ITGB6 and S100A13 (Figure 104A). Furthermore, approximately 10 of the 20 proteins were overexpressed primarily in fibroblast cell populations, including SPRC, MOXD1, FBLN5, LTBP2, MRC2, SERPINH1, EFEMP2, AEBP1, TUBB and S100A13 (Figure 104A). Further interrogation of stromal cell populations within this dataset confirmed that target gene expression was upregulated predominantly in ECM-producing fibroblasts and, to a lesser extent, alveolar and inflammatory fibroblasts (Figure 104B). These data confirmed that many of the upregulated proteins of interest in our proteomic dataset were also found to be upregulated in key cell types related to IPF, including AT2 cells and fibroblasts.

With this in mind, the following proteins were selected for further investigation: αv, β3, β5 and β6 integrin subunits, latent TFG-β2 binding protein (LTBP2, a mediator of TGF-β2 function), serpin H1 (SERPH, an ER protein which plays a role in collagen biosynthesis), carbonic anhydrase 1 (CAH1, a zinc-metalloenzyme) and 2 (CAH2, a zinc-metalloenzyme), septin 11 (SEP11, a filament-forming cytoskeletal GTPase), S100A13 (S10AD, a calcium binding protein required for the copper-dependent stress-induced export of IL1α and FGF1) and argonaute 2 (AGO2, a protein involved in post-translational gene silencing and the biogenesis of microRNA) (Figure 105A-I). To interrogate these targets, 12 candidate compounds were selected for investigation in IPF-derived precision-cut slices based on commercial availability and target antagonism (Figure 105J).

Finally, to identify additional candidate compounds for validation in PCS, Ingenuity Pathway Analysis (IPA) was used to highlight upregulated markers/pathways of interest in normal and

intermediate regions of IPF tissue to target therapeutically. To achieve this, significantly upregulated proteins (and associated log2 fold change) in IPF normal and intermediate tissue (compared to UD controls) were used to perform core expression analysis and the upstream regulator function was used to identify potential upstream regulators that may be responsible for observed changes in protein abundance in our proteomic datasets. Identified upstream regulators were filtered according to predicted activation state and the activation z-score, resulting in the identification of 18 candidate compounds to target upstream regulators in IPF-derived PCLuS (Table 19).

In summary, interrogation of protein heterogeneity identified distinct patterns of protein expression that are modulated in line with changes in disease severity. Furthermore, by interrogating proteins/pathways which were significantly upregulated in regions of IPF tissue thought to be undergoing active remodelling (normal and intermediate) we were able to identify 30 candidate inhibitory compounds for validation in PCLuS to assess ability to blunt inflammation and fibrogenesis in human IPF tissue *ex vivo* and investigate potential roles in disease progression.

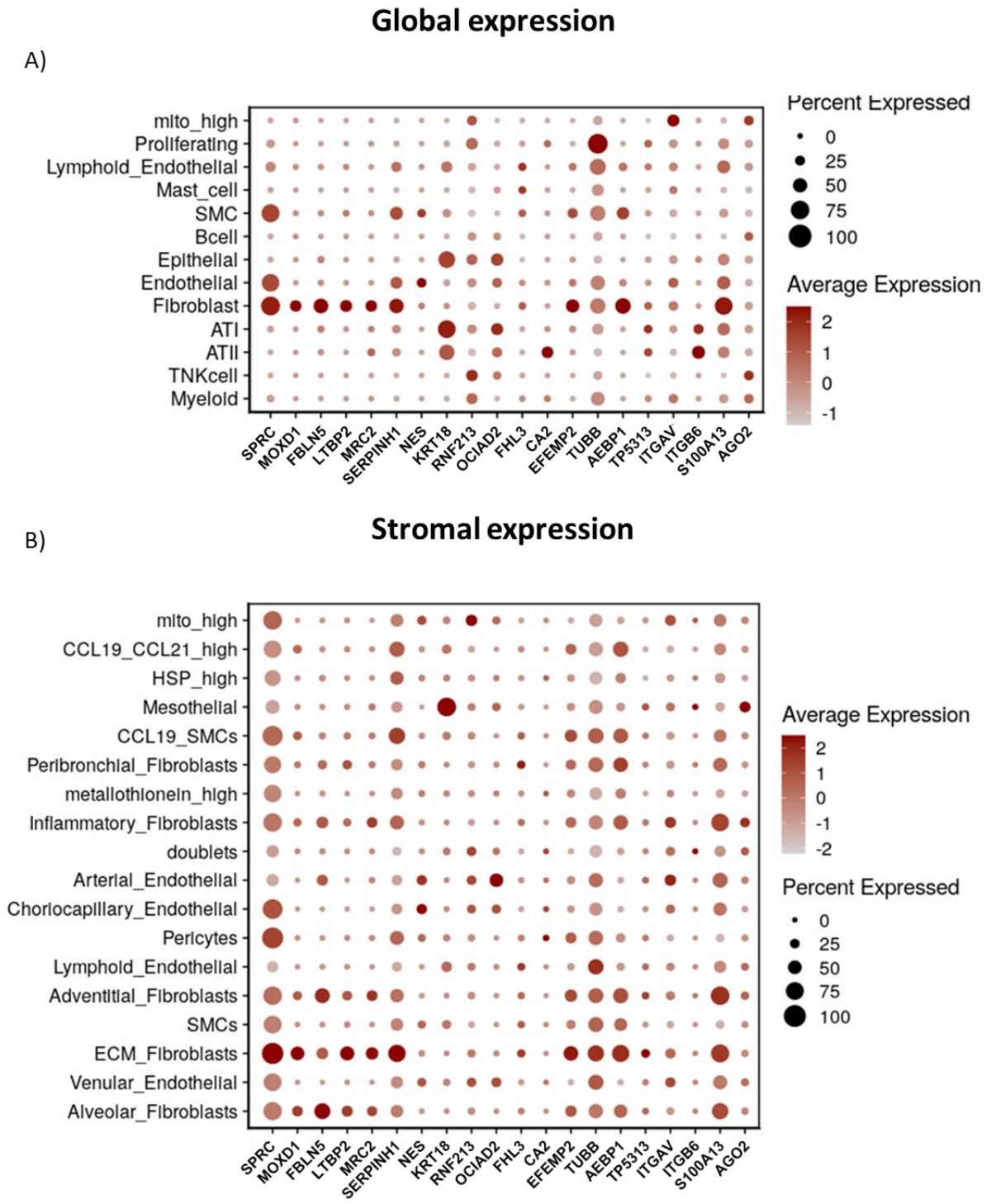

Figure 104: Investigation of targets of interest in lung scRNAseq datasets Target gene expression was investigated in scRNAseq datasets generated from 6 integrated single cell lung atlases (https://singlecell.broadinstitute.org/single_cell/study/SCP2155/) created by Dr Stephen Christensen, Pfizer. In total, 616,918 cells were included from multiple different fibrotic lung diseases, comprising 13 different cell lineages. Dot plots show increased average gene expression of multiple targets in A) global cell populations and B) stromal cell populations. (Figures provided by Dr Stephen Christensen, Pfizer).

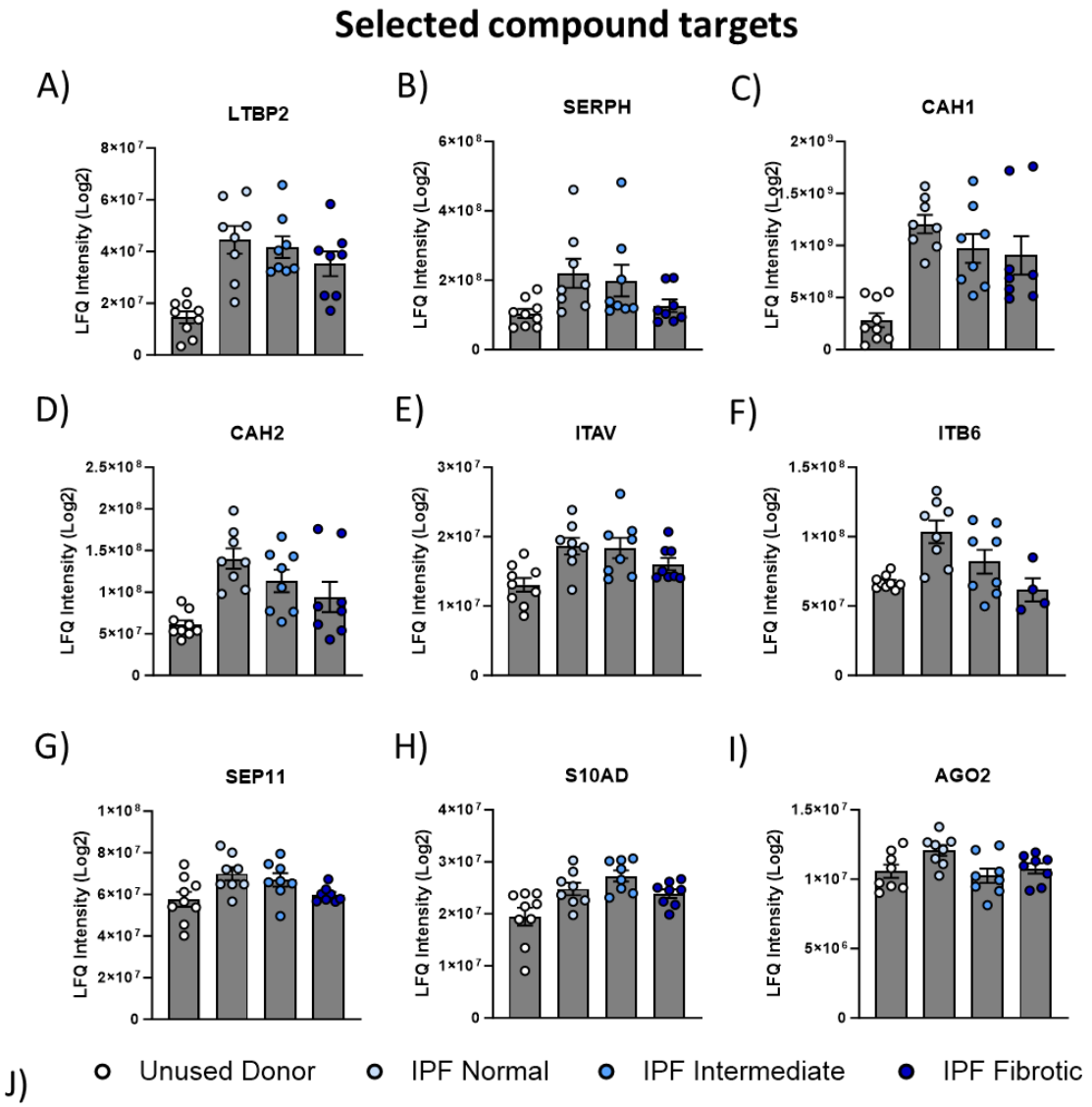

Compound	Target
ITD-1	TGFB2
EMD 527040 hydrochloride	αvβ6
SB273005	αvβ3 receptor and αvβ5 receptor
Cyclo (-RGDfK)	αvβ3 integrin
GLPG-0187	αv integrin
Cilengitide	αvβ3, αvβ5
Amlexanox	S100-A13
BCI-137	Argonaute 2
KT-30	Septin
Acetazolamide	Carbonic anhydrase
Dorzolamide HCL	Carbonic anhydrase II and IV
Brinzolamide	Carbonic anhydrase II

Figure 105: Selected compounds for validation in precision cut lung slices LFQ intensity identified through proteomic analysis (n=9 unused donor lungs, n=8 IPF normal regions, n=8 IPF intermediate regions and n=8 IPF fibrotic regions) were Log2 transformed and plotted for A) LTBP2 B) SERPH C) CAH1 D) CAH2 E) ITAV F) ITB6 G) SEP11 and H) S10AD and I) AGO2. J) 12 candidate compounds were selected based on the ability to target proteins of interest or related proteins. All data are mean ± SEM.

Table 19: IPA compounds selected for validation in precision cut lung slices

Compound	UD vs IPF normal		UD vs IPF intermediate		Inhibitor description
	Activation z-score	p-value of overlap	Activation z-score	p-value of overlap	
Tyrphostin AG490	2,138	5,05E-07	2,219	1,37E-03	Selective inhibitor of epidermal growth factor (EGF) receptor tyrosine kinase
GW9662	N/A	N/A	2,219	7,38E-03	Selective irreversible PPARγ antagonist
T-5224	1,342	3,86E-03	2,000	4,27E-02	Selective inhibitor of transcription factor c-Fos/activator protein (AP)-1
Gefitinib	N/A	8,01E-03	1,922	2,32E-02	Selective inhibitor of EGFR tyrosine kinase
Raloxifene	1,342	2,14E-02	1,890	9,39E-04	Selective oestrogen receptor modulator (SERM)
Wortmannin	1,486	5,03E-03	1,769	5,15E-03	Potent, selective and irreversible PI3K inhibitor
Lactacystin	2,376	8,76E-05	1,715	3,48E-06	Cell-permeable, potent and selective proteasome inhibitor (20S proteasome)
Imatinib	N/A	N/A	1,664	1,76E-02	Potent and selective v-Abl tyrosine kinase inhibitor; also inhibits PDGFR
Bisindolylmaleimide I	1,154	2,32E-02	1,446	1,22E-02	Potent PKC inhibitor
Mifepristone	2,041	6,39E-05	1,411	5,67E-04	Progesterone and glucocorticoid receptor antagonist
PLX5622	1,254	3,74E-04	1,342	2,65E-02	Highly selective CSF-1R inhibitor
Pyrrolidine dithiocarbamate	0,747	2,85E-02	1,133	1,57E-02	Potent nuclear factor-κB (NF-κB) inhibitor
Entinostat	N/A	3,47E-02	1,091	1,29E-02	Class I HDAC inhibitor
Rapamycin	1,268	2,20E-03	1,065	8,40E-03	mTOR inhibitor
Staurosporine	N/A	3,36E-02	1,053	4,54E-03	Broad spectrum protein kinase inhibitor
Napabucasin	N/A	1,95E-02	1,000	5,94E-03	STAT3 inhibitor
Nelfinavir	1,000	6,78E-03	1,000	1,51E-02	Protease inhibitor
Budesonide	2,333	1,94E-03	0,905	8,50E-04	Corticosteroid

4.3 Discussion

Current research into IPF relies heavily upon *in vitro* cell culture of human and rodent cells and *in vivo* mouse models. Though these techniques have yielded significant insight into our understanding of basic disease mechanisms, many candidate drugs derived from these systems often fail to demonstrate sufficient safety or efficacy in human trials [423]. One possible explanation for this phenomenon is the frequent use of reductionist pre-clinical models, in which 2D cell culture, animal models and other non-physiologically relevant cell culture systems are used to bridge the gap from bench to bedside. Indeed, it is widely accepted that current models of IPF fail to recapitulate the intricate and multifaceted pathophysiology of IPF and therefore lack many hallmarks of disease [424-426]. As a result, information surrounding pathophysiological mediators of disease progression in the human lung is extremely limited and warrants further investigation. As research technologies continue to advance, human tissue samples remain invaluable resources for understanding mechanisms of disease and developing targeted therapies. However, at present, most of the research carried out involving human IPF samples has centred on interpatient studies (often small biopsies), comparing healthy and diseased tissue from different patients [205,206,427,428]. Though this approach has undoubtedly aided our understanding of disease it nonetheless fails to consider the incredibly complex spatial and temporal heterogeneity of pathological changes in IPF.

In this chapter, we utilised interpatient and intrapatient approaches to investigate disease progression by comparing macroscopically distinct regions of 'normal', 'intermediate' and 'fibrotic' regions of tissue from within the same IPF lung. We then performed RNA sequencing and proteomic profiling of the differentially affected IPF regions alongside non-diseased, age-matched unused donor lungs to determine gene and protein expression at different stages of disease progression. To begin investigation of these macroscopically distinct regions of IPF tissue, we first sought to identify significantly different genes and proteins in these regions when compared to UD control lungs (interpatient comparisons). Results confirmed that, consistent with previous transcriptomic studies in the literature [429,430], macroscopically normal IPF tissue was considerably different to tissue obtained from non-diseased lungs, with over 1000 genes found to be significantly different to UD controls. We extended these findings further by demonstrating that, alongside changes in gene expression, there were also

significant changes in protein expression in seemingly unaffected regions of IPF tissue with approximately 24% of detected proteins in IPF normal tissue identified as significantly different to 'healthy' controls, suggesting that even at this early stage the lung is primed for injury. Moreover, IPF tissue was shown to become less similar to UD controls, at both the gene and protein level, the further along the disease spectrum the samples were. Further evaluation of IPF tissue alone (intrapatient comparisons) found that normal and intermediate regions of IPF tissue showed few changes in gene expression, likely due to several samples clustering with different macroscopic regions of disease, though was still able to identify differences between early (normal and intermediate) and late (fibrotic) stage disease. However, protein profiling of the same IPF regions demonstrated clear clustering based on disease state, with many significantly different proteins between each region of IPF lungs, including normal and intermediate tissue. Though limited, there is evidence of proteomics studies of human IPF lungs in the literature, comparing healthy tissue to singular IPF tissue samples [431]. For example, Schiller *et al* recently performed proteomic profiling of human ILD samples which revealed, consistent with results in this study, a significant increase of MZB1 positive plasma B cells in fibrotic tissue samples compared to non-diseased samples [432]. However, to the best of our knowledge, this is the first study which has shown that differentially affected regions of IPF tissue have distinct protein profiles depending on the degree of fibrosis.

Consequently, downstream therapeutic target identification focused on analysing protein expression in these different IPF tissue microenvironments. In doing so, we were able to directly interrogate protein expression profiles, which led to the discovery of potentially novel dysregulated proteins/pathways underlying disease progression. For example, we found that several neutrophil-related markers were significantly downregulated in all stages of IPF disease compared to 'healthy' lungs, particularly those relating to neutrophil chemotaxis (*via* IL-8 and CXCL4), degranulation and NET signalling. Neutrophils exert diverse functions in the tissue microenvironment during injury such as phagocytosis, degranulation and release of pro-inflammatory cytokines, ROS and NETs, shaping the ensuing immune response [187]. However, neutrophils also play key roles in the regulation and biosynthesis of collagen ECM, primarily *via* neutrophil elastase (NE) [433]. Downregulation of neutrophil-related proteins such as MM8 (neutrophil collagenase) and NE, which are both involved in cleavage and degradation of ECM

components [434], suggests that altered neutrophil function in IPF results in a reduced ability to fragment ECM. Consistent with these findings, interrogation of ingenuity canonical pathways revealed strong inhibition of several neutrophil-related pathways, including neutrophil degranulation, IL-8 signalling, CXCR4 signalling and neutrophil extracellular trap signalling in all regions of IPF tissue compared to non-diseased lungs, suggesting that altered neutrophil function and/or reduced chemotaxis may play an important role in IPF (Appendix F, Fig 5). These findings were in contradiction to earlier studies within the literature whereby genetic and/or pharmacological ablation of NE *in vivo* was found to have protective effects in several lung injury models of fibrosis [435-437]. Similarly, elevated levels of IL-8 and NE have been reported in the BAL of IPF patients across multiple studies [189,438]. One possible explanation for these contrasting results is the time taken from explantation of IPF donor tissue to snap-freezing for 'omics analysis, with neutrophils known to have a short half-life [439,440]. Additionally, as mass spectrometry-based proteomics often involves complex sample preparation, it is not always be optimised for detection of small and/or transient proteins such as cytokines and chemokines. Consequently, neutrophil markers such as IL-8 and CXCR4 may be challenging to capture and quantify due to their low molecular weight, low abundance due to restrictions in the dynamic range of detection [441].

Interestingly, intrapatient comparisons of IPF tissue provided further insights into the modulation of neutrophil-related markers throughout disease. For instance, initial interpatient analysis found that both MPO (a peroxidase) and cathepsin G (a serine protease) were decreased in all regions of IPF tissue compared to UD lungs. However, intrapatient comparisons provided additional resolution and established that, though these proteins were downregulated in early-stage disease (normal and intermediate IPF tissue), they were significantly upregulated in end-stage fibrotic regions of IPF lungs (compared to normal and intermediate regions). Of these, cathepsin G has been shown to modulate ECM degradation through activation of matrix MMPs (which also increases TNFα and IL-8) [442] and can intracellularly and/or extracellularly regulate tissue remodelling [443]. Reduced expression of cathepsin G in the normal and intermediate IPF regions may therefore limit MMP activation, perpetuating ECM deposition and driving fibrogenesis. Further characterisation of neutrophil phenotypes and signalling pathways during IPF progression may therefore provide further insight into their role in disease pathogenesis.

Other targets of interest identified in this chapter were those which were significantly upregulated in IPF normal and intermediate regions of IPF tissue, and significantly downregulated in terminal fibrotic regions. This approach led to the identification of several proteins which have previously been associated with IPF and/or fibrosis including integrin β6 and various ECM-related proteins such as FBLN4, FBLN5, SPARC, EFEMP2 and COL18A1 [444-446]. For example, SPARC (Secreted Protein, Acidic and Rich in Cysteine), a matricellular protein known to promote collagen assembly in the ECM, has recently been implicated as a potential biomarker of IPF with upregulation of gene and serum protein expression reported across several patient cohorts, often associated with increased disease severity and IPF progression [447-449]. SPARC has also been shown to be highly secreted by IPF fibroblasts *in vitro*, resulting in aberrant epithelial repair responses which impedes effective reestablishment of functional epithelial barriers and integrity [445]. Evaluation of upregulated proteins also revealed a number of potentially novel targets, which have not been extensively studied in the context of IPF. For instance, results showed that MOXD1 (a copper binding protein) was significantly increased in the normal and intermediate regions of IPF tissue compared to end-stage fibrotic regions. These findings were consistent with a recent study by Jia *et al* who utilised single cell RNA sequencing of human IPF tissue to show that early changes in fibroblasts of IPF lung tissue were associated with strong upregulation of copper-binding proteins, including MOXD1. Moreover, velocity analysis revealed that upregulation of MOXD1 occurred prior to known myofibroblast markers, suggesting that MOXD1 expression is a precursor to differentiation to myofibroblasts [450].

Following evaluation of proteins of interest, targets were selected for interrogation *via* inhibitory compounds based on commercial availability and antagonism of upregulated target proteins/pathway. This included several integrin-related proteins such as αv, β3, β5 and β6. Integrins are a group of 24 heterodimeric, transmembrane receptors which are involved in a variety of cellular functions required for regulation of tissue repair and cell-cell and cell-ECM interactions. Of particular note is the αv subunit, which forms heterodimers with β1, β3, β5, β6 or β8 subunits and, if overexpressed or dysregulated, exerts pleiotropic effects in fibrosis and inflammation of multiple organs [451,452]. This subclassification of integrins primarily interacts with the RGD (Arginine-Glycine-Aspartic acid) peptide commonly found in the ECM (e.g., fibronectin, osteopontin and fibrinogen) and TGF-β-associated latency–associated

peptide (LAP) [453]. As a result, αv integrins play a key role in the activation and regulation of TGF-β signalling, making them attractive therapeutic targets [454]. Candidate compounds were also selected to target carbonic anhydrases (CAH) 1 and 2, which were reported to be upregulated in early stage IPF tissue. CAHs are involved in maintaining the acid-base balance in the lungs by catalysing the conversion of carbon dioxide to bicarbonate ions and protons [455]. Overexpression of these enzymes could therefore impact pH levels in IPF lungs, potentially affecting several cellular processes, including ECM remodelling [456]. Argonaute 2 (AGO2) was also selected for target antagonism due to its pivotal role as a core component of the RNA-induced silencing complex (RISC) complex, which is central to microRNA (miRNA)-mediated gene regulation [457]. In the context of IPF, the role of AGO2 loading miRNAs onto the RISC complex is of interest due to the involvement of miRNAs in IPF pathogenesis [458,459], with AGO2 reported to be significantly upregulated in rapidly-progressing cases of IPF compared to normal lung biopsies [460]. The final selected targets were S100-A13 and septin 11, both of which are relatively unstudied in terms of IPF pathogenesis to date. S100A13 is a member of the S100 family of calcium-binding proteins, which are involved in various cellular processes including inflammation, cell proliferation and differentiation and apoptosis [461]. The biological functions of S100-A13 are primarily mediated *via* receptor for advanced glycation end products (RAGE) signalling, which has been extensively linked with IPF [462]. Moreover, S100-A13 has been found to modulate NF-κB activity and SASP expression during cell senescence in an IL1α-dependant manner [463]. Septins are a family of cytoskeletal GTPase proteins also involved in a range of cellular processes such as cytokinesis, cell polarity, vesicle trafficking and receptor signalling [464]. Though research into septin dysfunction has primarily focused on neurodegenerative diseases and cancer, there is some limited evidence, mainly from the liver and kidney, that suggest the septin cytoskeleton is involved in the regulation of aberrant tissue repair during fibrosis [465]. For example, in mouse models of renal fibrosis and human fibrotic kidneys, there is considerable upregulation of various septins which frequently co-localised with αSMA+ cells [466]. In the liver, septins have been suggested to play part of a pro-fibrogenic positive feedback loop involving TGF-β–induced upregulation of septins, which in turn triggers a further increase in TGF-β activation and modulation of HSC activity [465,467]. Alongside these selected targets, a further 18 candidate compounds were identified through upstream regulator analysis *via* IPA, resulting in a total of 30 candidate compounds for investigation.

Though work in this chapter focused primarily on identifying candidate compounds which target proteins/pathways which were significantly upregulated during the actively remodelling regions of tissue, future work should seek to similarly investigate the significantly downregulated proteins/pathways and whether agonism of these targets can ameliorate or blunt fibrogenesis. Similarily, as we exclusively interrogated targets identified through proteomic profiling in this work, exploration of candidate compounds derived from transcriptomic datasets may yield additional insight into potential therapeutic targets, either alone or through integration with proteomic datasets. One of the main caveats of this work was the inability to determine whether the changes in gene and/or protein expression observed within the different IPF regions were due to changes in gene/protein expression in tissue-resident cells or, alternatively, alterations in the cellular composition of the tissue microenvironment. To address this concern, we utilised publicly available single cell datasets of human fibrotic lungs to provide an estimation of cellular expression of targets of interest [83]. However, as current IPF-derived datasets often fail to profile gene expression at different stages of disease and does not provide spatial information of genes, it is possible that results may not be representative of cellular phenotypes in differentially affected regions of IPF tissue. Additionally, while single-cell RNA sequencing provides valuable information about gene expression profiles of individual cell types, this is often insufficient to accurately predict changes in protein abundance due to several factors such as post-transcriptional regulation, mRNA stability, translation efficiency and protein degradation rates [468]**.** Consequently, future work should seek to identify the cellular sources of significantly different proteins directly, potentially through the use of spatial proteomics and/or imaging mass cytometry technologies [469].

Overall, work in this chapter effectively profiled gene and protein heterogeneity in macroscopically distinct regions of IPF tissue in a two-step process. First, comparison of each IPF region to unused donor controls confirmed that all regions of IPF tissue were significantly different to 'healthy' controls. Next, further interrogation of the molecular landscape during progression of IPF samples *via* intrapatient comparisons identified discrete patterns of protein expression that were modulated in line with changes in disease severity. Specifically, interrogation of proteins/pathways which were significantly upregulated in regions of IPF tissue thought to be undergoing active remodelling (normal and intermediate) identified 30

candidate inhibitory compounds for validation in PCLuS to investigate potential roles in disease progression. Taken together, these findings reveal new insights into protein heterogeneity in IPF progression and offer exciting opportunities to explore new therapeutic interventions.

5 Investigation of novel therapeutic targets in IPF using human tissue models

Statement of contribution

- All work in this chapter was performed solely by the author.

5.1 Introduction

Current research into pulmonary fibrosis, including understanding the initiating triggers and the underlying mechanisms, relies heavily upon *in vitro* cell culture of human and rodent cells and *in vivo* mouse models. Though these techniques have undoubtedly contributed to our understanding of disease biology, it has become increasingly clear that more clinically relevant model systems are required to effectively explore disease pathomechanisms and, more importantly, to validate potential therapeutic targets. In the last decade, advances in precision cut slice (PCS) technology have revolutionised the study of human disease, allowing for detailed investigations into the effects of compounds on multiple tissue types. Importantly, unlike traditional 2D monolayer cell culture models, PCS retain the anatomical architecture and structural matrix composition of the native tissue they are derived from, whilst also maintaining cells in their original tissue-matrix configuration [269]. Additionally, other organ-specific features such as metabolic activity, tissue homeostasis and, to an extent, certain immunological functions can also be maintained (or supplemented) throughout culture.

While previous studies involving precision cut lung slices (PCLuS) have predominantly focused on short-term evaluation of toxicology and pharmacology [470-472], recent developments in the generation and culture of PCLuS (particularly from diseased human tissue) have provided an invaluable research tool to enhance our understanding of disease pathobiology and treatment of several chronic lung diseases, including IPF, COPD and lung cancer [294,295]. Despite the clear benefits of PCLuS technology in pulmonary fibrosis research, there are several obstacles which needed to be addressed to improve the suitability and reliability of PCS in future studies. These included establishment of standardised protocols and development of advanced analysis tools (preferably which lend themselves to automation) for routine use as fibrosis assays which, at present, remains challenging [473].

One significant limitation of the current PCLuS methodology is the limited amount of human tissue available for research, which fundamentally restricts the number of compounds and doses that can be tested in a single experiment. This in turn can impede comprehensive screening of potential anti-fibrotic drug candidates or investigative compounds. Consequently, scalability to medium or high-throughput PCLuS culture systems is required to overcome this constraint and improve the efficiency and scope of compound testing in available human tissue. In this context, the implementation of a 96-well slice culture system offers several benefits. Firstly, miniaturisation of the system allows for parallel testing of a larger number of compounds using the same amount of tissue, thereby increasing experimental efficiency. Additionally, by reducing the size of individual PCLuS, more technical repeats from different areas of the same tissue can be used to determine efficacy of individual compounds/doses with more confidence. Finally, scaling to a 96-well format enables exploration of a wider range of compound doses, facilitating more comprehensive screening and enhancing the likelihood of identifying promising candidates for further study.

Here, we developed and validated a highly reproducible 96-well medium-throughput PCLuS methodology which was then used to screen novel targets/compounds identified in Chapter 4 to determine toxicity and efficacy.

5.2 Materials and methods

5.2.1 96-well PCLuS optimisation patient demographics

PCLuS were generated from IPF PCLuS donors 4-6 detailed in Table 20 with ethical approval (outlined in chapter 2).

Table 20: PCLuS donor patient demographics for 96-well methodology optimisation

Donor	Sex	Age	FEV1, L	FVC, L	TLC, L	TLCO, mmol CO/min/kPa	KCO, mmol CO/min/kPa	Smoking history
IPF PCLuS donor 4	M	57	2.34(73%)	2.73(69%)	4.29(60%)	1.84(16%)	0.51(29%)	Ex-smoker (stopped 20 yrs ago), 15pyh
IPF PCLuS donor 5	M	60	1.89(57%)	3.40(81%)	5.78(84%)	1.60(17%)	0.39(28%)	Ex-smoker (stopped 14yrs ago), 25pyh
IPF PCLuS donor 6	M	58	2.31(66%)	2.56(58%)	4.04(57%)	2.14(22%)	2.14(22%)	Never smoked

FEV1= forced expiratory volume in 1 second, FVC= forced vital capacity, TLC= total lung capacity, TLCO= carbon monoxide transfer factor and KCO=carbon monoxide transfer coefficient. Percentages of predicted values are in parentheses.

5.2.2 Generation and treatment of 96-well PCLuS

To optimise the culture of PCLuS in a 96-well cell culture plate, PCLuS were generated as outlined in chapter 2, with the use of 3mm and 4mm biopsy punches (Kai medical) to produce 3mm (n=1 donor; IPF PCLuS donor 4 [Table 20]) and 4mm (n=3 donors; IPF PCLuS donors 4-6 [Table 20]) PCLuS, respectively. To evaluate whether different sized PCLuS could be reproducibly modulated *via* exogenous compounds, both diameter PCLuS were rested for 48hrs post-slicing to allow the stress period to elapse. Following this, PCLuS (n=20 per condition) were challenged with control media, recombinant human TGF-β1 (10ng/ml) alone or in combination with PDGFββ (50ng/ml) to stimulate fibrogenesis or IL1α (1ng/ml) to stimulate inflammation. Additionally, PCLuS were treated with standard of care compounds Pirfenidone (2.5mM) and Nintedanib (2.5µM) or ALK5i (10µM) to blunt fibrosis. Media, including all treatments, was refreshed at 24-hour intervals with conditioned media snap frozen for downstream analysis until the terminal 144hr timepoint.

5.2.3 Generation and treatment of 24-well PCLuS

PCLuS were generated as outlined in chapter 2 (n=1 donor; IPF PCLuS donor 4 [Table 20]) and cultured in a 24-well culture plate, before being rested for 48hrs to allow the post-slicing stress period to elapse. Following this, PCLuS (n=12 per condition) were challenged with control media, recombinant human TGF-β1 (10ng/ml) alone or in combination with (50ng/ml) PDGFββ to stimulate fibrogenesis or IL1α (1ng/ml) to stimulate inflammation. Additionally, PCLuS were treated with standard of care compounds Pirfenidone (2.5mM) and Nintedanib

(2.5µM) or ALK5i (10µM) to blunt fibrosis. Media, including all treatments, was refreshed at 24-hour intervals with conditioned media snap frozen for downstream analysis until the terminal 144hr timepoint.

5.2.4 Primary cell line donor patient demographics

Primary fibroblast cell lines were generated from IPF donors detailed in Table 21 with ethical approval (outlined in chapter 2).

Table 21: Primary cell line donor patient demographics

Donor	Sex	Age	Smoking history
IPF Fib donor 1	M	61	Never smoked
IPF Fib donor 2	M	43	Never smoked
IPF Fib donor 3	M	53	Ex-smoker
IPF Fib donor 4	M	51	Never smoked
IPF Fib donor 5	M	61	Ex-smoker, 15pyh

5.2.5 Isolation and cryopreservation of primary human lung fibroblasts

Areas of parenchyma from IPF explant tissue were disrupted using a tissue mezzaluna to generate 1mm^3 pieces of tissue. 10cm cell culture dishes (664-160, Greiner bio-one) were scored using a scalpel to generate 5 x 5 crosshairs to aid tissue adhesion. Culture medium- Dulbecco's Modified Eagle's Medium – high glucose (DMEM; D5671-500ml, Sigma) supplemented with 1% Penicillin/Streptomycin (Sigma), 1% L-Glutamine and 10% Foetal Bovine Serum (10500-064, Gibco)- was added to each tissue section and incubated at 37^{o}C supplemented with 5% $C0_2$ overnight. Media was replenished bi-weekly with tissue removal occurring after 7 days. Once >4 crosshairs became confluent culture media was removed, cells were detached using trypsin EDTA (PromoCell; C-41010), pelleted by centrifugation at 500*g* for 4mins, resuspended in 15ml culture medium and transferred to a T75 cell culture flask which was incubated at 37°C supplemented with 5% $C0_2$. Media was replenished bi-weekly until the flask was ~90% confluent, at which point fibroblasts were detached *via* trypsinisation and counted using an EVE automatic cell counter (NanoEnTek). Cells were then pelleted at 500*g* for 4mins before being resuspended in Cryo-SFM (PromoCell; C-29912) freezing medium at a density of ~1 million cells/vial and frozen at a rate of -1°C per minute in a Mr Frosty™ for 24 hours, prior to being moved to liquid nitrogen for long-term storage.

5.2.6 Testing of candidate compounds in primary lung fibroblasts

Primary fibroblasts previously isolated and cryopreserved from the parenchyma of IPF explant tissue (outlined above) were reanimated (n=5 donor lines) in culture medium and transferred to a T75 flask which was incubated at 37°c supplemented with 5% $C0_2$. Media was replenished bi-weekly until the flask was deemed confluent, at which point fibroblasts were detached *via* trypsinisation, counted using an EVE automatic cell counter and seeded into a 96-well cell culture plate at a density of 5,000 cells/well. Once cells were approximately 70% confluent, plates were cultured for 24hrs in serum-free culture media before treatment with control media, standard of care compounds Pirfenidone (2.5mM), Nintedanib (2.5µM), ALK5i (10µM) or escalating doses (0.1µM, 1µM or 10µM) of candidate inhibitors (outlined in Table 22) for 24 hours in duplicate (n=2 wells per condition, n=5 donors, n=10 wells total). After 24hrs challenge, conditioned media was snap frozen for further analysis and metabolic activity of cells was assessed by resazurin (as described in chapter 2).

Table 22: Candidate compounds for screening in PCLuS

Selected compounds	Supplier	Code	Vehicle	Reported *in vitro* IC50*
ITD-1	Selleckchem	S6713	DMSO	N/A
EMD 527040	Tocris	7508	DMSO	6nM-1.6µM
SB273005	Selleckchem	S7540	DMSO	1.8nM-3nM (cell-free assay)
Cyclo (-RGDfK)	Selleckchem	S7834	DMSO	41.7nM
GLPG-0187	Tocris	7059	DMSO	1.2nM-7.7nM (cell-free assay)
Cilengitide	Tocris	5870	Water	4.1nM (αvβ3) and 70nM (αvβ5)
Amlexanox	Tocris	4857	DMSO	N/A for S100-A13
BCl-137	Sigma	53155200001	DMSO	342µM
Forchlorfenuron	Abcam	ab143494	Water	N/A
Acetazolamide	Tocris	6742/100	DMSO	N/A
Dorzolamide	Selleckchem	S1375	Water	1.9nM-31nM
Brinzolamide	Selleckchem	S3178	DMSO	3.19nM
IPA compounds				
Tyrphostin AG490	Tocris	414	DMSO	2µM-13.5µM
GW9662	Tocris	1508	DMSO	3.3nM-2µM
T-5224	Selleckchem	S8966	DMSO	4µM-10µM
Gefitinib	Tocris	3000	DMSO	23nM -79nM
Raloxifene	Tocris	2280	DMSO	1nM
Wortmannin	Sigma	W1628	DMSO	3nM
Lactacystin	Tocris	2267	Water	4.8µM
Imatinib	Tocris	5906/100	DMSO	38nM
Bisindolylmalemide I	Selleckchem	S7208	DMSO	~20nM (cell-free assay)
Mifepristone	Tocris	1479/100	DMSO	0.2nM-2.6nM
PLX5622	Selleckchem	S8874	DMSO	16nM (cell-free assay)
Pyrrolidine Dithiocarbamate	Selleckchem	S3633	DMSO	N/A
Entinostat	Tocris	6208	DMSO	0.18nM
Rapamycin	Tocris	1292	DMSO	~0.1nM
Staurosporine	Tocris	1285	DMSO	2.7nM (cell-free assay)
Napabucasin	Selleckchem	S7977	DMSO	291nM-1.19µM
Nelfanivir	Tocris	3766	DMSO	2nM
Budesonide	Tocris	2671/50	DMSO	1-10nM

**Reported IC50 values are generated from 2D cell culture assays (unless otherwise indicated) which can vary depending on cell lines used for validation.*

5.2.7 Candidate compound patient demographics

PCLuS were generated from the donors detailed in Table 23 with ethical approval (outlined in chapter 2).

Table 23: Candidate compound patient demographics

Donor	Sex	Age	FEV1, L	FVC, L	TLC, L	TLCO, mmol CO/min/kPa	KCO, mmol CO/min/kPa	Smoking history
IPF PCLuS donor 6	M	37	1.27(33%)	1.42(32%)	3.10(49%)	N/A	N/A	Never smoked
IPF PCLuS donor 7	M	58	2.31(66%)	2.56(58%)	4.04(57%)	2.14(22%)	2.14(22%)	Never smoked
IPF PCLuS donor 8	F	47	1.20(47%)	1.25(42%)	N/A	N/A	N/A	Never smoked
IPF PCLuS donor 9	F	61	2.23(42%)	2.66(44%)	4.84(51%)	N/A	N/A	Never Smoked

FEV1= forced expiratory volume in 1 second, FVC= forced vital capacity, TLC= total lung capacity, TLCO= carbon monoxide transfer factor, KCO=carbon monoxide transfer coefficient and N/A= not available. Percentages of predicted values are in parentheses.

5.2.8 Generation and treatment of PCLuS

To test candidate compounds at multiple doses, 4mm PCLuS were generated from explant IPF tissue (n=4 donors; IPF PCLuS donors 6-9 [Table 23]) and rested for 48 hours, with media being refreshed after 24 hours, to allow the post-slicing stress period to elapse. Next, PCLuS were challenged with either control media, Pirfenidone (2.5mM), Nintedanib (2.5µM) or ALK5i (10µM) to blunt fibrosis (n=10 PCLuS per condition, n=4 donors, n=40 PCLuS total). Concurrently, PCLuS were challenged with 3 escalating doses (0.1µM, 1µM and 10µM) of each candidate compound (n=6 PCLuS per condition, n=4 donors, n=24 PCLuS total) outlined in Table 3 and 4 to assess the ability to reduce pre-existing fibrosis. Media, including all treatments, was refreshed at 24-hour intervals with conditioned media snap frozen for downstream analysis. At the terminal 144-hour timepoint, PCLuS were harvested for resazurin assay to measure metabolic activity (see chapter 2).

5.2.9 ELISA

ELISA was performed on conditioned media (as described in chapter 2) using the following DuoSet sandwich ELISA kits: Collagen 1α1 (R&D; DY6220), TIMP-1 (R&D; DY970) and IL-8 (R&D; DY208).

5.2.10 Statistical analysis

Statistical analysis was performed using GraphPad Prism 9.5.0. All results are presented as mean ± SEM. Due to the limited number of donor lines (n=5) and homogeny of cell populations, statistical significance of secreted markers from *in vitro* cell culture was

determined using non-parametric Kruskal-Wallis test with post-hoc Dunn's multiple comparisons test where *p<0.05, **p<0.01, ***p<0.001, ****p<0.0001. Statistical significance of secreted markers from PCLuS was determined using ANOVA with post-hoc Dunnett's test where *p<0.05, **p<0.01, ***p<0.001, ****p<0.0001, unless otherwise indicated. Statistical analysis was performed on graphs in this chapter which show secreted marker results as percentage change from baseline (T48 unstimulated PCLuS) after 96hours treatment (T144). Briefly, secretion of pro-fibrotic and pro-inflammatory markers was quantified in PCLuS at T144 for each PCLuS donor, which was then subsequently subtracted from the same PCLuS sample at T48 to provide a % change from baseline value for each individual PCLuS. This normalisation accounts for the differences in the secretion of pro-inflammatory and pro-fibrogenic markers between PCLuS, primarily driven by differences in cellular composition, tissue density and presence/absence/numbers of fibroblastic foci and provides a uniform approach to determine changes in the secretion of markers over the duration of culture. Therefore, the "percentage change from baseline" are the data that should be considered when observing the effects of any given treatment.

Assumption of Normal Distribution in PCLuS for parametric testing: PCLuS data is assumed to follow a normal distribution, where approximately 95% of the data points fall within 2 standard deviations of the mean. Samples that fall outside this range are relatively rare and are considered outliers, potentially distorting the overall data representation.

Minimisation of Outlier Impact: Outliers can significantly skew the mean, consequently impacting the reliability of conclusions drawn from the data in the summary tables included in the report. Consequently, all samples from a particular PCLuS were excluded if values (% change from baseline) were greater than 2 standard deviations from the mean of the other PCLuS in the group.

5.3 Results

5.3.1 Development of 96-well PCLuS methodology

We have previously optimised and validated a PCLuS methodology which can be used to explore disease pathomechanisms and test efficacy of therapeutic targets in human lung tissue. To achieve this, 8mm diameter, 450µm-thick PCLuS are generated from diseased explant lung tissue and cultured in a 24-well format. However, access to large quantities of human tissue remains one of the main limiting factors, often restricting how many compounds and/or doses can be tested in a single experiment. Consequently, work in this chapter aimed to develop a reproducible 96-well PCLuS culture system from IPF-derived human tissue, which could then be used for medium-throughput screening of novel therapeutics in a dose-dependent manner for a larger volume of compounds.

To begin optimising this new methodology, 3mm (450µM-thick) and 4mm (450µM-thick) diameter PCLuS were generated from the same IPF explant donor (IPF PCLuS donor 4; n=20 PCLuS per condition for both diameter PCLuS), placed in a 96-well transwell insert in a 96-well cell culture plate and rested for 48 hours, with media being refreshed after 24 hours. Once the post-slicing stress period elapsed, PCLuS were challenged with control media, recombinant IL1α (1ng/ml), TGF-β1 (10ng/ml) alone or in combination with PDGFββ (50ng/ml) to induce inflammation and fibrogenesis, respectively. Alongside this, PCLuS were challenged with anti-fibrotic compounds including standard of care (SoC) compounds (Pirfenidone and Nintedanib) and ALK5i to assess the ability to blunt pre-existing inflammation and fibrosis. Media, including all treatments, was refreshed at 24-hour intervals with conditioned media snap frozen for downstream analysis. Control PCLuS (n=6 for each size PCLuS) were harvested for resazurin assay at 24-hour intervals to determine metabolic activity, until termination at T144 (Figure 106A).

First, to assess whether IPF-derived PCLuS remained viable in culture, quantification of metabolic activity (Figure 106B) and a soluble marker of cellular death (LDH) (Figure 106C) was performed at each timepoint for both 3mm and 4mm PCLuS. Results showed that both diameter PCLuS remained metabolically active at each time point, maintaining at least 70% of resazurin compared to T0 tissue. Furthermore, after an initial post-slicing spike in LDH in the first 48 hours, the level of cellular damage was reduced and maintained in both diameter PCLuS, suggested there was no significant reduction in cell viability.

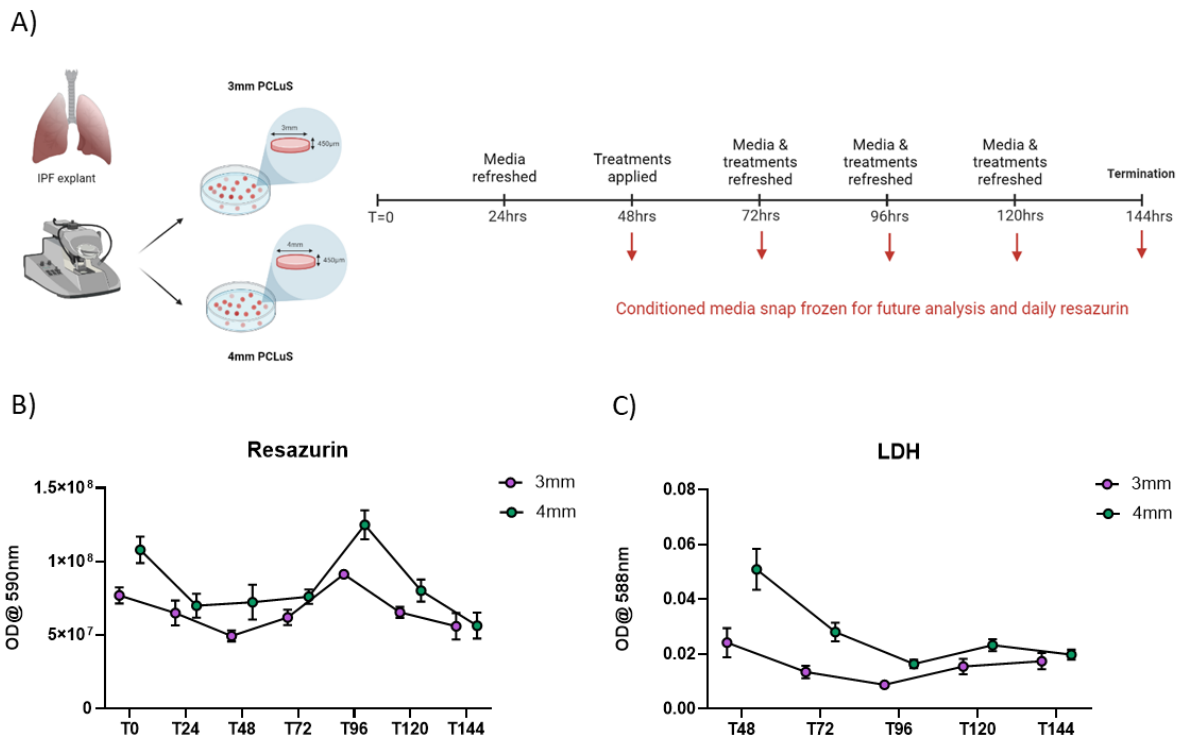

Figure 106: Assessment of 3mm and 4mm PCLuS viability A) 3mm and 4mm (450µM-thick) PCLuS were generated from the same IPF explant donor and cultured in a 96-well cell culture plate. PCLuS (n=20 per condition) were allowed to rest for 48hrs before challenge with either control media, IL1α (1ng/ml), TGF-β1 (10ng/ml) alone or in combination with PDGFββ (50ng/ml), anti-fibrotic compounds including Pirfenidone (2.5mM) and Nintedanib (2.5µM) or ALK5i (10µM). Media, including all treatments, was refreshed at 24-hour intervals with conditioned media snap frozen for downstream analysis. Additionally, control PCLuS (n=6 per day) were harvested at 24-hour intervals for resazurin assay throughout culture. Quantification of metabolic activity *via* B) Resazurin and cell damage *via* C) LDH was used as an indicator of PCLuS viability.

Having confirmed that PCLuS remained viable in 96-well cell culture plates, we next sought to ascertain whether treatment with exogenous stimuli could effectively modulate fibrosis and inflammation. First, quantification of soluble IL-8 was performed *via* ELISA on conditioned culture media of IL1α- challenged PCLuS as a marker of inflammation. Results showed that IL1α stimulation significantly increased secretion of IL-8 ($p<0.0001$) in both 3mm and 4mm PCLuS at each timepoint of culture, confirming effective induction of a pro-inflammatory response (Figure 107). Next, to evaluate response to pro-fibrogenic stimuli, quantification of soluble collagen 1α1 was performed on conditioned media from TGF-β1- and TGF-β1/PDGFββ- challenged PCLuS. Results confirmed that, at the end of culture, TGF-β1/PDGFββ-challenged PCLuS secreted significantly more collagen 1α1 ($p<0.0001$) than unstimulated slices in both 3mm and 4mm PCLuS. Additionally, 4mm PCLuS, but not 3mm PCLuS, challenged with TGF-β1 were also found to significantly increase collagen 1α1 secretion ($p<0.0001$) (Figure 108).

To interrogate this further and normalise for tissue heterogeneity, additional analysis was performed to assess the individual response of each slice by plotting % change in protein from baseline (after 48 hours rest). Results for both pro-inflammatory (Figure 107B, D) and pro-fibrotic (Figure 108B, D) stimuli demonstrated that overall PCLuS responded in a consistent manner to stimulation and was therefore reproducible between slices. For example, once normalised, both 3mm and 4mm PCLuS challenged with TGF-β1/PDGFββ resulted in a significant increase in collagen 1α1 at 120hrs ($p<0.05$) and 144hrs ($p<0.0001$) with no significant increase in response to TGF-β1 alone (Figure 108B, D).

Next, to assess whether anti-fibrotic compounds were able to blunt fibrosis in the 96-well format, quantification of collagen 1α1 secretion was performed on conditioned media from PCLuS treated with SoC compounds and ALK5i at each time point. Once normalised to % change from baseline (T48), results determined a significant reduction in collagen 1α1 secretion in response to ALK5i and Nintedanib ($p<0.0001$), with a smaller reduction in 3mm PCLuS treated with Pirfenidone ($p<0.01$) (Figure 109B, D). Taken together, these data confirmed that both 3mm and 4mm diameter PCLuS remained viable throughout culture and were responsive to modulation *via* exogenous stimuli and anti-fibrotic compounds.

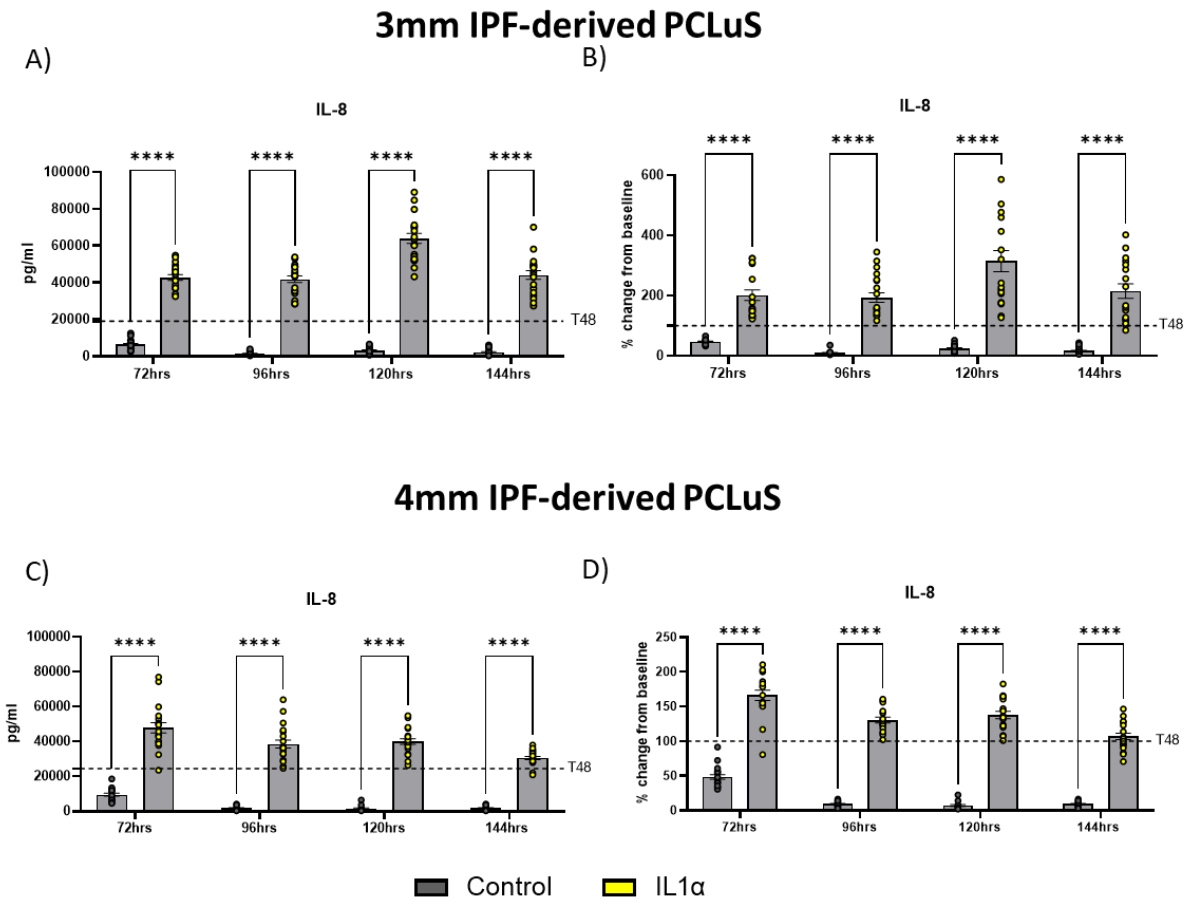

Figure 107: Quantification of soluble IL-8 in IL1α-challenged PCLuS 3mm and 4mm (450µM-thick) PCLuS were generated from the same IPF explant donor and cultured in a 96-well cell culture plate. PCLuS (n=20 per condition) were allowed to rest for 48hrs before challenge with either control media or IL1α (1ng/ml). Media, including all treatments, was refreshed at 24-hour intervals with conditioned media snap frozen for downstream analysis. Quantification of secreted IL-8 was performed *via* ELISA at each time-point and plotted as A, C) absolute pg/ml and normalised to B, D) % change from T48 baseline. All data are mean ± SEM. Statistical significance was determined using multiple unpaired t-tests (*p<0.05, **p<0.01, ***p<0.001 and ****p<0.0001).

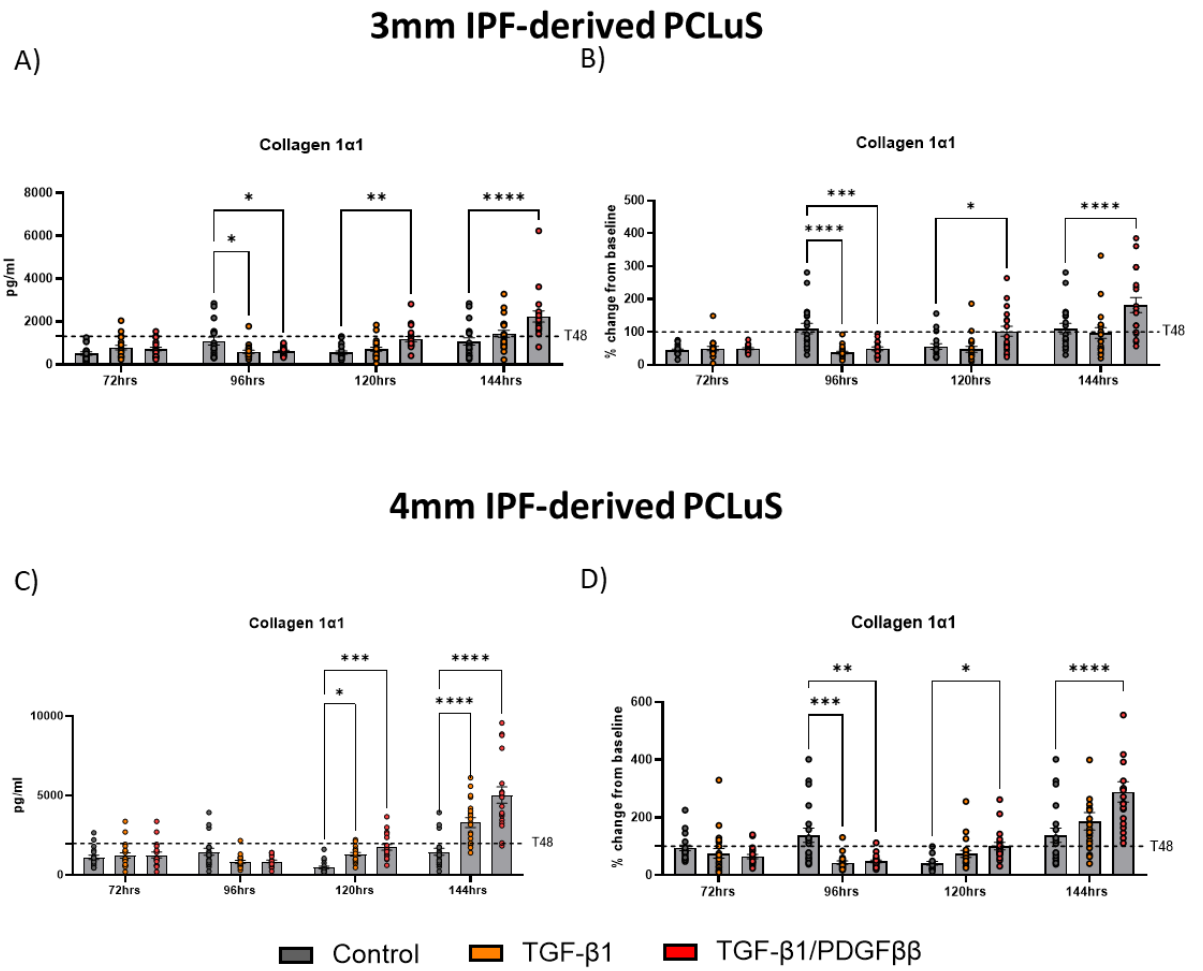

Figure 108: Quantification of soluble collagen 1α1 in fibrotic stimuli-challenged PCLuS 3mm and 4mm (450µM-thick) PCLuS were generated from the same IPF explant donor and cultured in a 96-well cell culture plate. PCLuS (n=20 per condition) were allowed to rest for 48hrs before challenge with either control media, TGF-β1 (10ng/ml) alone or in combination with PDGFββ (50ng/ml). Media, including all treatments, was refreshed at 24-hour intervals with conditioned media snap frozen for downstream analysis. Quantification of secreted collagen 1α1 was performed *via* ELISA at each time-point and plotted as A, C) absolute pg/ml and normalised to B, D) % change from T48 baseline.. All data are mean ± SEM. Statistical significance was determined using two-way ANOVA with multiple comparisons test (*p<0.05, **p<0.01, ***p<0.001 and ****p<0.0001).

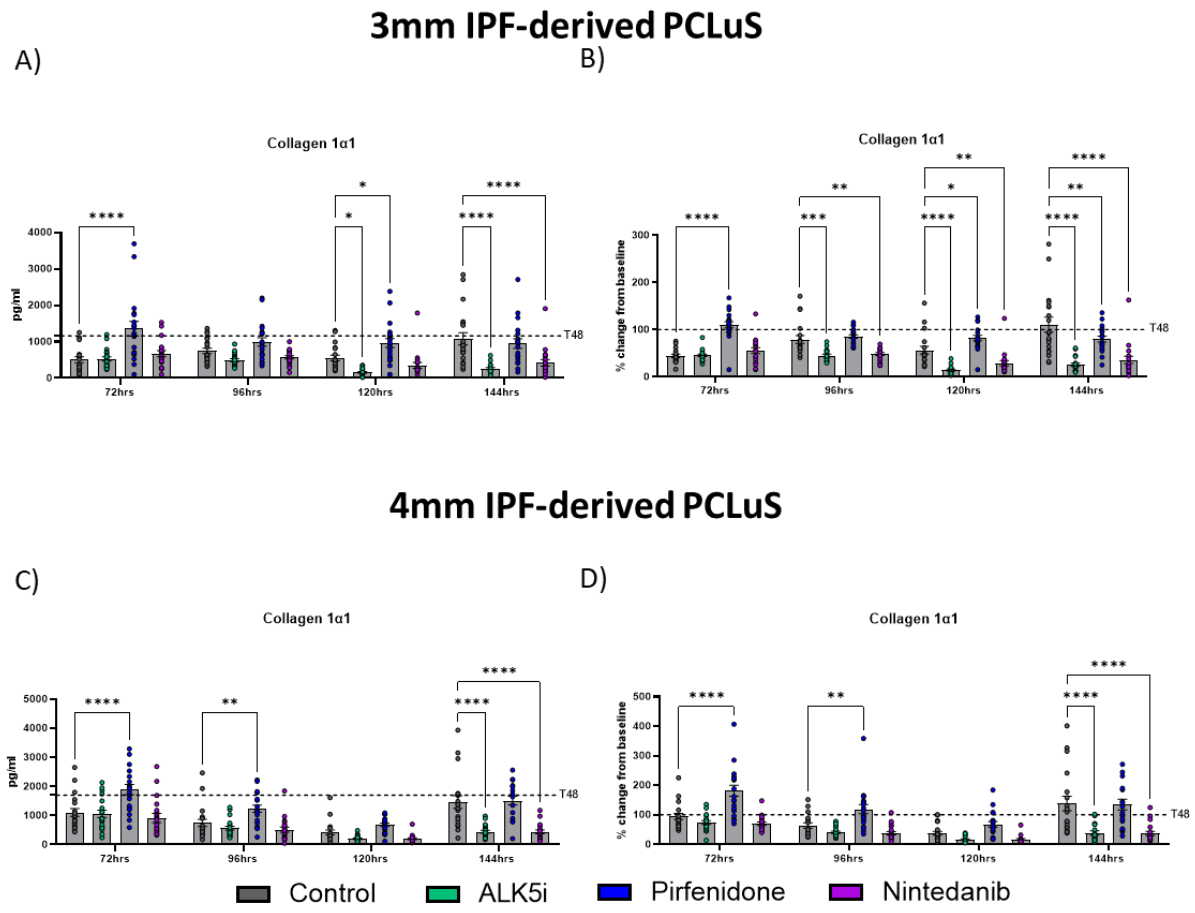

Figure 109: Quantification of soluble collagen 1α1 in anti-fibrotic- challenged PCLuS 3mm and 4mm (450µM-thick) PCLuS were generated from the same IPF explant donor and cultured in a 96-well cell culture plate. PCLuS (n=20 per condition) were allowed to rest for 48hrs before challenge with either control media, anti-fibrotic compounds including Pirfenidone (2.5mM) and Nintedanib (2.5µM) or ALK5i (10µM). Media, including all treatments, was refreshed at 24-hour intervals with conditioned media snap frozen for downstream analysis. Quantification of secreted collagen 1α1 was performed *via* ELISA at each time-point and plotted as A, C) absolute pg/ml and normalised to B, D) % change from T48 baseline. All data are mean ± SEM. Statistical significance was determined using two-way ANOVA with multiple comparisons test (*p<0.05, **p<0.01, ***p<0.001 and ****p<0.0001).

To confirm that results from the 96-well system faithfully recapitulated the previously validated 24-well methodology, 8mm diameter PCLuS were also generated from the same IPF donor tissue, cultured in a 24-well culture plate (n=12 PCLuS per condition) and treated in parallel to the 96-well PCLuS, following the experimental outline detailed above (Figure 106A). Using the same panel of secreted markers, we established that 8mm similarly increased IL-8 secretion in response to IL1α stimulation at each timepoint of culture ($p<0.0001$) (Figure 110A, B). Additionally, PCLuS significantly increased collagen 1α1 secretion in response to pro-fibrogenic stimuli ($p<0.0001$) (Figure 110C, D), whilst treatment with Nintedanib ($p<0.001$) and ALK5i ($p<0.001$), but not Pirfenidone, was able to blunt collagen 1α1 secretion (Figure 110E, F).

Based on these results, 4mm diameter PCLuS were selected for further optimisation and validation was performed in PCLuS generated from additional IPF donor tissue (n=20 PCLuS per condition, n=3 donors, n=60 PCLuS total) as previously described (Figure 106A). Quantification of soluble markers was used to confirm effective modulation of fibrosis at T144, with results normalised to % change from baseline (T48 unstimulated PCLuS) to allow comparison of donors. Results confirmed that PCLuS responded in a consistent manner to stimulation whereby IL1α- challenged PCLuS significantly increased secretion of IL-8 ($p<0.0001$) (Figure 111B) and TGF-β1 and TGF-β1/PDGFββ-challenged PCLuS significantly increased secretion of collagen 1α1 ($p<0.05$ and $p<0.001$) (Figure 111D). Furthermore, we established that Pirfenidone, Nintedanib and ALK5i all demonstrated strong anti-inflammatory and anti-fibrotic effects in all donors as quantified by IL-8 and collagen 1α1, respectively (Figure 112).

These data supported the conclusion that the 4mm PCLuS, 96-well cell culture methodology was a robust, reproducible model and could subsequently be used to test candidate compounds (n=30) previously identified in chapter 4, at multiple doses.

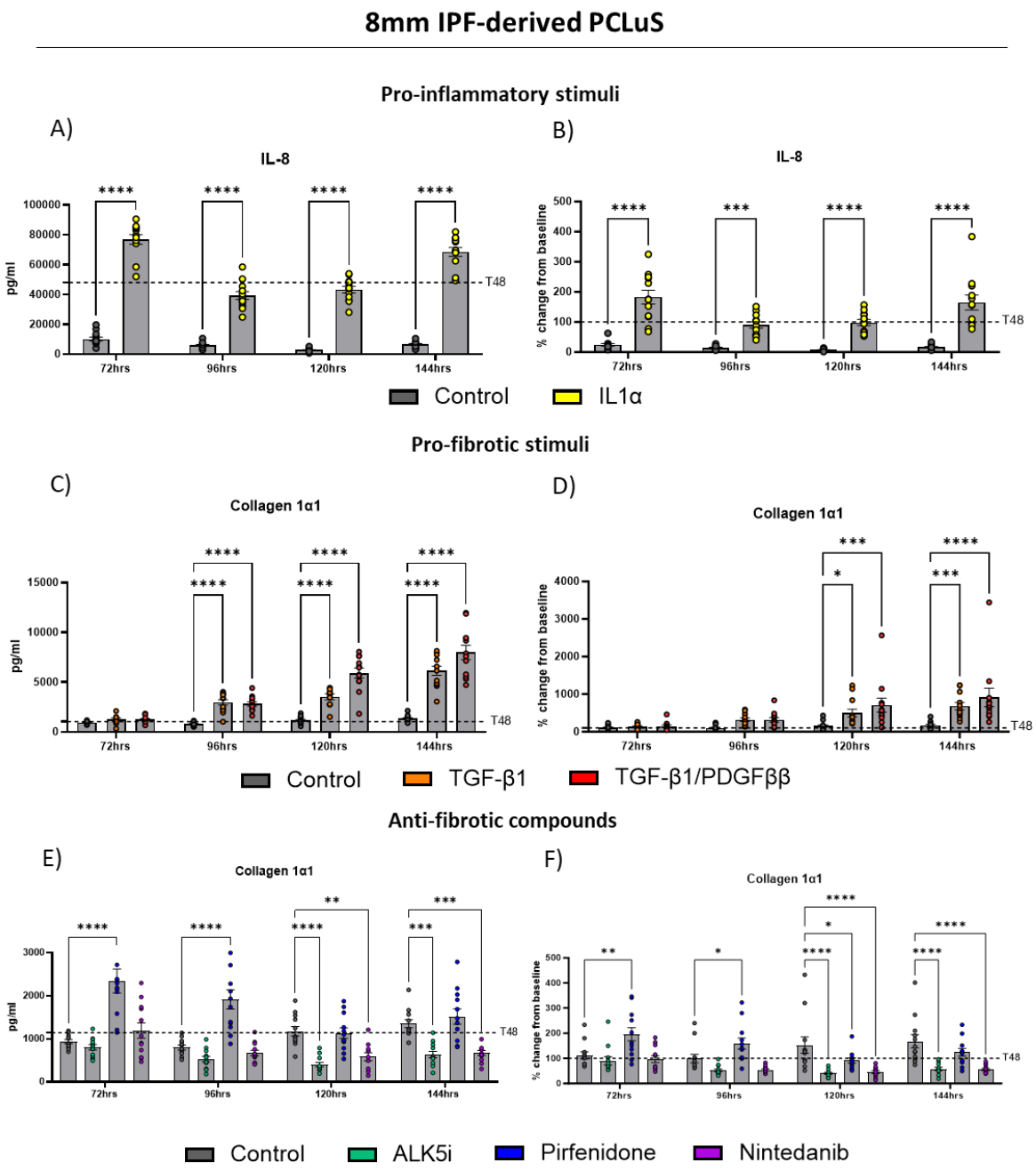

Figure 110: **Modulation of 8mm diameter PCLuS** 8mm PCLuS were generated from the same IPF explant donor and cultured in a 24-well cell culture plate. PCLuS (n=12 per condition) were allowed to rest for 48hrs before challenge with either control media, IL1α (1ng/ml), TGF-β1 (10ng/ml) alone or in combination with PDGFββ (50ng/ml). Concurrently, PCLuS were treated with anti-fibrotic compounds including Pirfenidone (2.5mM) and Nintedanib (2.5μM) or ALK5i (10μM). Media, including all treatments, was refreshed at 24-hour intervals with conditioned media snap frozen for downstream analysis. Quantification of secreted IL-8 was performed *via* ELISA at each time-point and plotted as A) aboslute pg/ml and B) % change from T48 baseline. Collagen 1α1 was quantified in fibrotic stimuli-challenged PCLuS and presented as C) absolute pg/ml and D) % change from T48 baseline and anti-fibrotic- treated PCLuS were presented as E) aboslute pg/ml and F) % change from T48. All data are mean ± SEM. Statistical significance was determined using multiple unpaired t-tests or two-way ANOVA with Dunnett's multiple comparisons test (*p<0.05, **p<0.01, ***p<0.001 and ****p<0.0001).

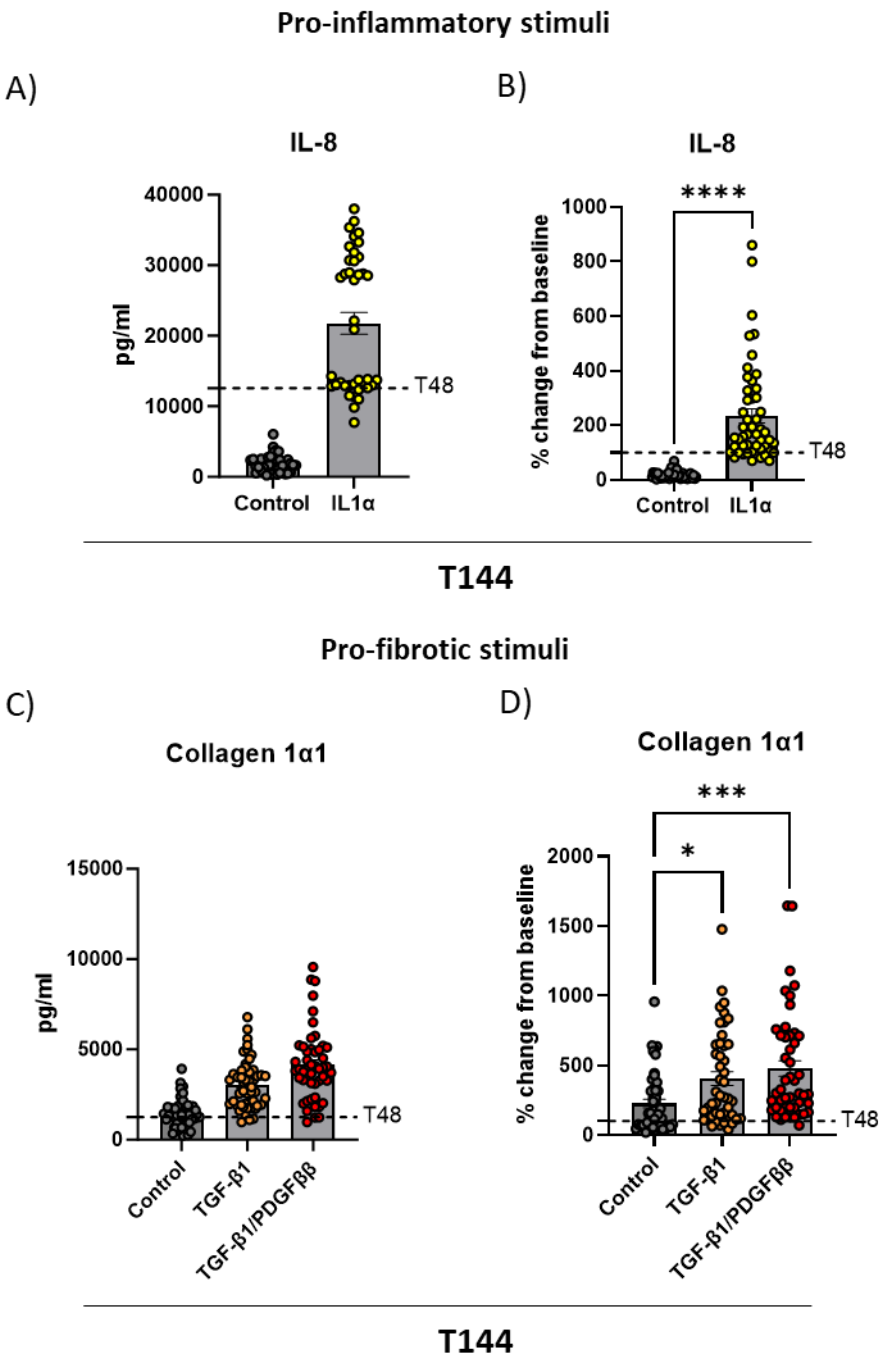

F**igure 111: Validation of 4mm PCLuS response to exogenous stimuli (n=3 donors)** 4mm (450µM-thick) PCLuS were generated from IPF explant donors (n=3 donors) and cultured in a 96-well cell culture plate. PCLuS (n=20 per condition, n=3 donors, n=60 PCLuS total) were allowed to rest for 48hrs before challenge with either control media, IL1α (1ng/ml), TGF-β1 (10ng/ml) alone or in combination with PDGFββ (50ng/ml). Media, including all treatments, was refreshed at 24-hour intervals with conditioned media snap frozen for downstream analysis. Quantification of secreted IL-8 was performed *via* ELISA at T144 and plotted as A) absolute pg/ml and B) % change from T48 baseline for control and IL1α-challenged PCLuS. Quantification of secreted collagen 1α1 was performed *via* ELISA at T144 and plotted as C) absolute pg/ml and D) % change from T48 baseline for control, TGF-β1–challenged and TGF-β1/PDGFββ-challenged PCLuS. All data are mean ± SEM. Statistical significance was determined on graphs B and D using unpaired t-tests or one-way ANOVA with Dunnett's multiple comparisons test (*p<0.05, **p<0.01, ***p<0.001 and ****p<0.0001).

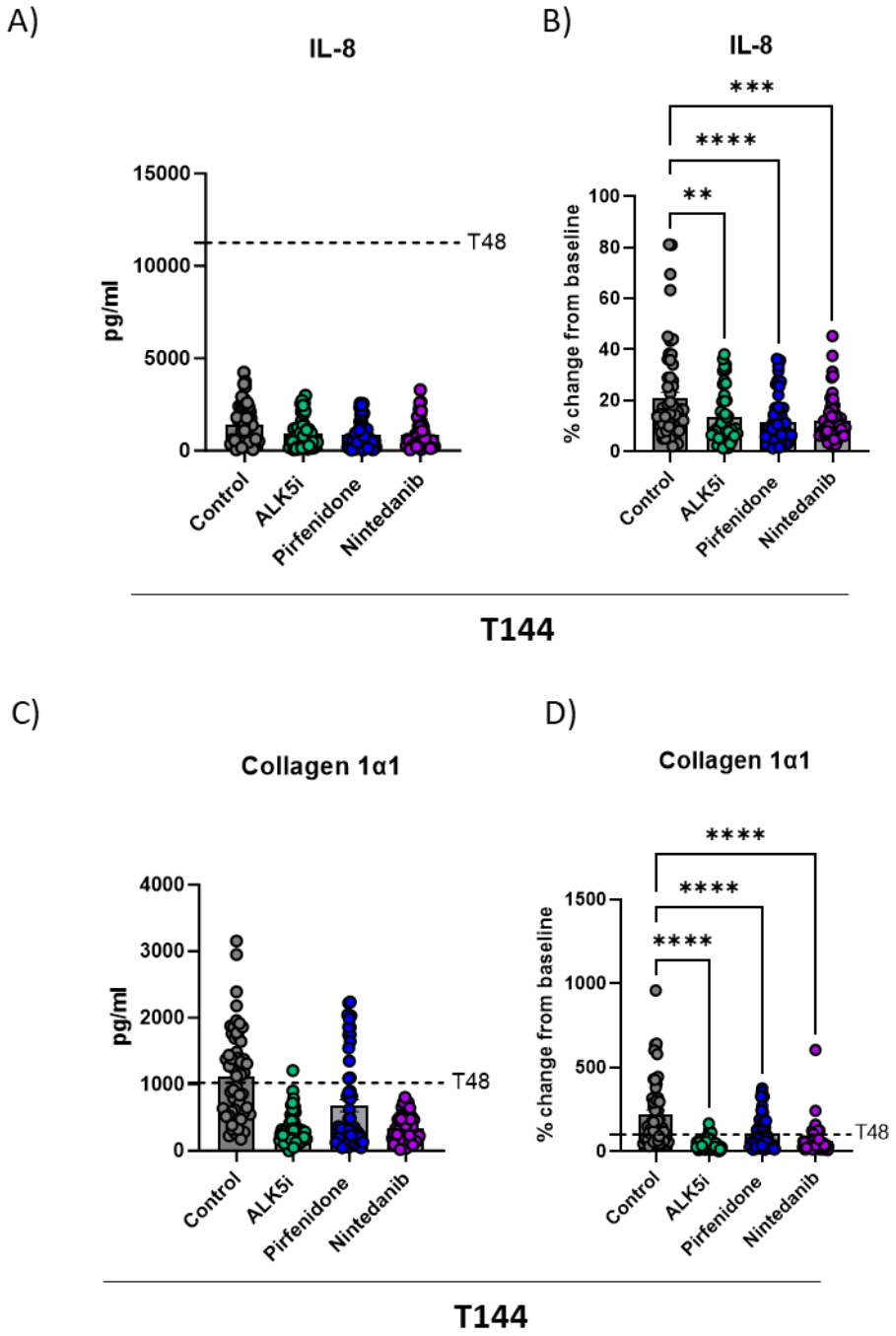

Figure 112: Validation of 4mm PCLuS response to anti-fibrotic compounds (n=3 donors) 4mm (450µM-thick) PCLuS were generated from IPF explant donors (n=3 donors) and cultured in a 96-well cell culture plate. PCLuS (n=20 per condition, n=3 donors, n=60 PCLuS total) were allowed to rest for 48hrs before challenge with either control media, anti-fibrotic compounds including Pirfenidone (2.5mM) and Nintedanib (2.5µM) or ALK5i (10µM). Media, including all treatments, was refreshed at 24-hour intervals with conditioned media snap frozen for downstream analysis. Quantification of secreted IL-8 was performed *via* ELISA at T144 and plotted as A) absolute pg/ml and B) % change from T48 baseline for control and IL1α-challenged PCLuS. Quantification of secreted collagen 1α1 was performed *via* ELISA at T144 and plotted as C) absolute pg/ml and D) % change from T48 baseline for control, TGF-β1–challenged and TGF-β1/PDGFββ-challenged PCLuS. All data are mean ± SEM. Statistical significance was determined on graphs B and D using one-way ANOVA with Dunnett's multiple comparisons test (*p<0.05, **p<0.01, ***p<0.001 and ****p<0.0001).

5.3.2 Investigation of selected candidate compounds

5.3.2.1 Candidate selected compounds in 2D primary cell model

Before progressing to screen compounds of interest in our validated 96-well PCLuS model, we first investigated selected compounds (Table 22) in traditional 2D *in vitro* cell culture models. Here, IPF-derived primary lung fibroblasts (n=5 donors) were seeded into 96-well cell culture plates and, once ~70% confluent, serum-starved for 24hrs prior to treatment with control media, standard of care compounds (Pirfenidone and Nintedanib), ALK5i or escalating doses (0.1µM, 1µM or 10µM) of selected inhibitors for 24 hours (n=2 wells per condition, n=5 donors, n=10 wells total). Media was harvested at T48 and snap frozen for downstream analysis before fibroblasts were incubated with resazurin to determine metabolic activity of cells at the end of culture (Figure 113A). To enable comparison between multiple cell lines, resazurin was then normalised to % change from control fibroblasts for each donor line and an arbitrary 70% threshold was applied where compounds/doses which resulted in <70% metabolic activity compared to unstimulated cells was deemed to have negatively impacted cellular function. Following this, quantification of soluble pro-fibrogenic markers (collagen 1α1 and TIMP-1) was performed *via* ELISA to determine potential anti-fibrotic effects of selected compounds.

First, assessment of fibroblasts treated with SoC compounds was performed in the hope that this would provide a benchmark for candidate compounds. However, results showed that though metabolic activity of ALK5i-challenged fibroblasts was comparable to unstimulated cells, treatment with Pirfenidone and Nintedanib resulted in a considerable reduction of resazurin below the 70% viability threshold, suggesting a negative impact on cellular function (Figure 113B). Interestingly, analysis of soluble pro-fibrogenic markers also found no reduction in collagen 1α1 or TIMP-1 secretion in response to anti-fibrotic compounds, except for Nintedanib-challenged PCLuS which significantly reduced TIMP-1 secretion ($p<0.01$) (Figure 113F). However, as Nintedanib was shown to reduce metabolic activity by more than 50%, this reduction was likely due to decreased cellular viability.

Next, we proceeded to investigate the selected candidate compounds for viability and efficacy. Evaluation of metabolic activity demonstrated that all compounds were generally well tolerated at the lower 0.1µM and 1µm doses and did not affect metabolic activity of cells after 24-hour challenge. However, the higher 10µM dose of SB273005, Cyclo –(RGDfK) and GLPG-0187 all resulted in <70% of resazurin activity compared to control fibroblasts in 3 or

more donor lines (Figure 114). Consequently, doses/compounds which reduced metabolic activity below 70% were excluded from further analysis in relevant donor cell lines, as shown by blank values in summary tables (Figure 115B; Figure 116B). Quantification of soluble collagen 1α1 (Figure 115) and TIMP-1 (Figure 116) was then performed in the conditioned culture media of cells challenged with each inhibitor and normalised to % change from control fibroblasts to allow comparison between donors. Interestingly, results showed no substantial decrease in pro-fibrogenic markers in response to selected inhibitors at any dose, including the highest 10μM dose.

Here, compound screening in 2D cell culture models demonstrated that though selected inhibitors were well tolerated at the lower doses of each inhibitor, treatment with the highest 10μM dose frequently resulted in a reduction in cellular viability. Conversely, lower doses of candidate compounds had no beneficial effect on secretion of pro-fibrotic markers after 24-hours treatment. Similarily, none of the selected compounds resulted in a significant reduction in collagen 1α1 and TIMP-1 at the highest 10μM dose. Overall, these data highlight the limited ability of the selected compounds to inhibit secretion of pro-fibrotic proteins in 2D pulmonary fibroblasts.

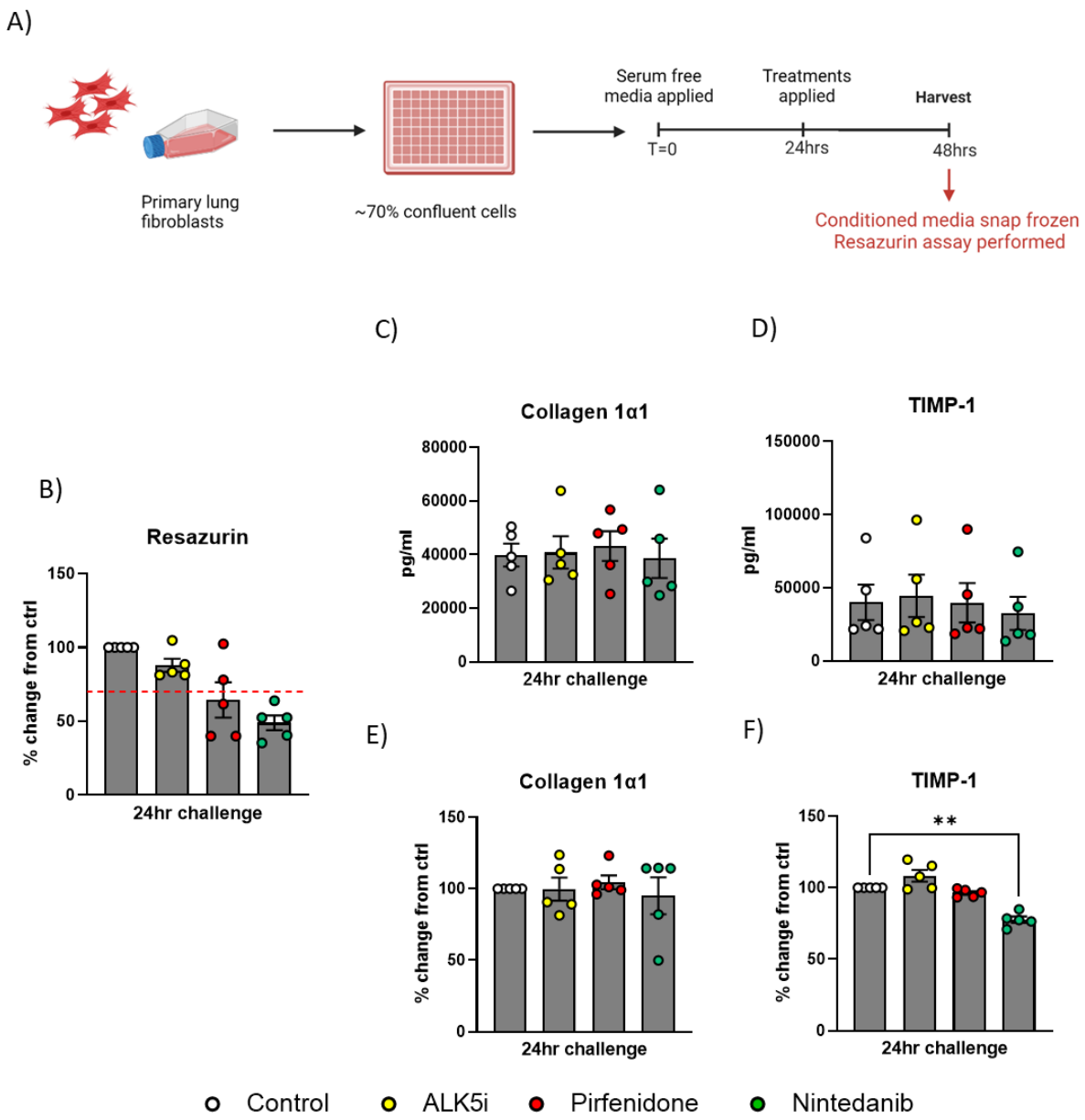

Figure 113: Validation of IPF-derived primary fibroblast viability after selected inhibitor challenge A) IPF-derived primary lung fibroblasts (n=5 donors) were seeded into 96-well cell culture plates and, once ~70% confluent, serum-starved for 24 hours prior to treatment with control media, standard of care compounds Pirfenidone (2.5mM) and Nintedanib (2.5µM), ALK5i (10µM) or escalating doses (0.1µM, 1µM or 10µM) of selected inhibitors for 24 hours (n=2 wells per condition, n=5 donors, n=10 wells total). Media was harvested at T48 and snap frozen for downstream analysis before fibroblasts were incubated with resazurin to determine metabolic activity of cells at the end of culture. B) Resazurin assay performed at T48 presented as the average % of control for each donor (where red dashed line represents arbitrary 70% viability threshold). Quantification of secreted Collagen 1α1 and TIMP-1 was performed on conditioned media *via* ELISA and plotted as C-D) absolute pg/ml per donor and E-F) average % change from control for each donor. All data are mean ± SEM. Statistical significance was determined on graphs E and F using Kruskal-Wallis test with post-hoc Dunn's multiple comparisons test (*p<0.05, **p<0.01, ***p<0.001, ****p<0.0001).

A)

Resazurin- 2D primary fibroblasts

Compound name	0.1µM					1µM					10µM				
	Donor 1	Donor 2	Donor 3	Donor 4	Donor 5	Donor 1	Donor 2	Donor 3	Donor 4	Donor 5	Donor 1	Donor 2	Donor 3	Donor 4	Donor 5
ITD-1	95	159	110	112	89	82	141	98	100	95	56	127	80	89	72
EMD 527040 hydrochloride	103	101	106	71	92	80	92	92	64	97	76	83	96	59	92
SB273005	89	159	83	112	84	61	145	66	102	80	58	95	52	67	61
Cyclo (-RGDfK)	90	106	91	75	85	73	89	79	63	90	63	75	68	53	73
GLPG-0187	75	192	81	135	70	58	132	71	93	58	47	102	50	72	42
Cilengitide	86	167	86	118	90	66	176	80	124	68	63	128	63	90	53
Amlexanox	100	132	92	107	81	92	139	83	110	90	74	157	72	85	66
BCI-137	132	120	98	120	143	125	132	99	132	147	113	98	93	98	131
KT-30	97	106	91	106	125	99	107	98	107	113	81	82	81	82	92
Acetazolamide	84	98	86	98	107	93	98	92	98	110	81	88	86	88	92
Dorzolamide HCl	84	109	87	109	108	86	104	93	104	106	74	88	85	88	89
Brinzolamide	87	99	97	99	113	79	120	98	120	112	74	93	95	93	95

B)

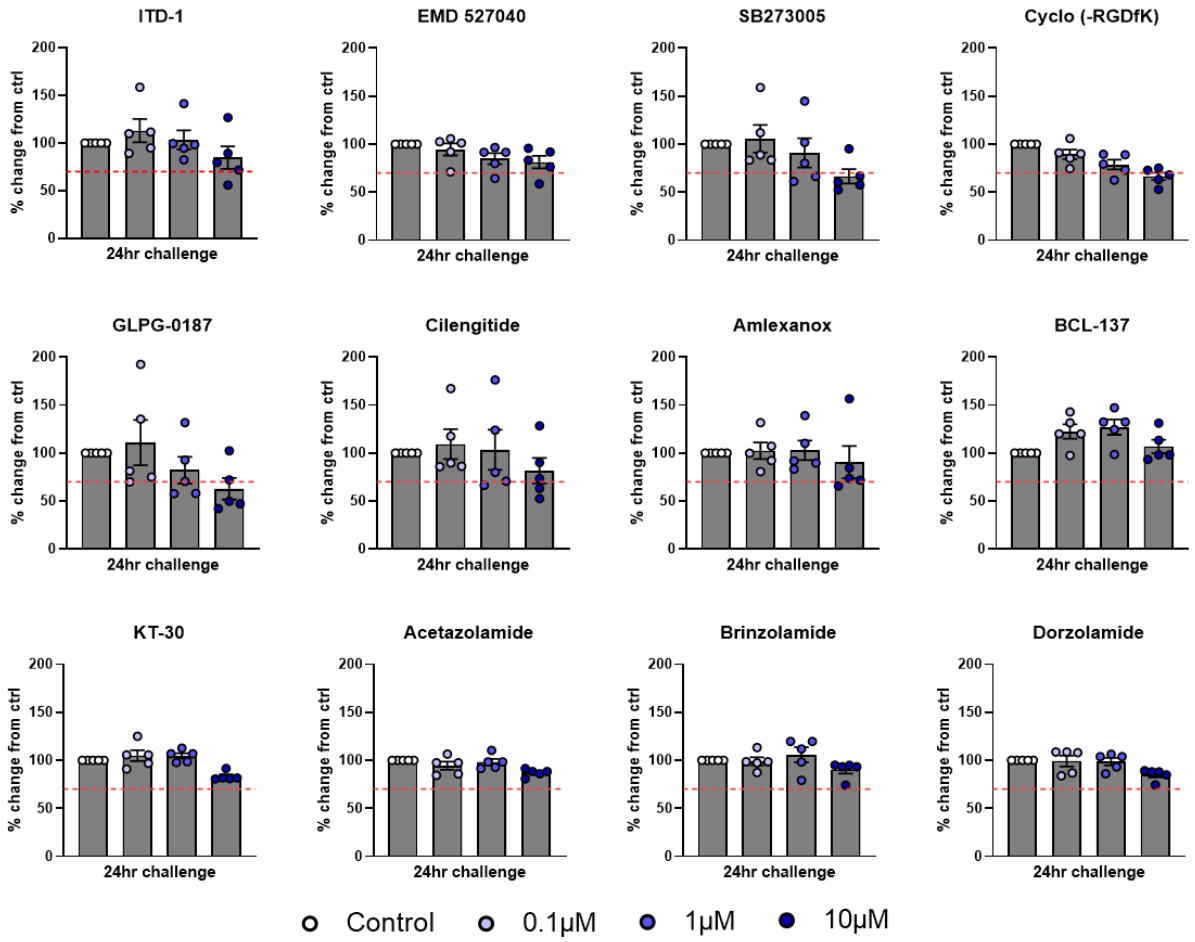

Figure 114: Validation of IPF-derived primary fibroblast viability after selected inhibitor challenge IPF-derived primary lung fibroblasts (n=5 donors) were seeded into 96-well cell culture plates and, once ~70% confluent, serum-starved for 24 hours prior to treatment with control media, standard of care compounds Pirfenidone (2.5mM) and Nintedanib (2.5µM), ALK5i (10µM) or escalating doses (0.1µM, 1µM or 10µM) of selected inhibitors for 24 hours (n=2 wells per condition, n=5 donors, n=10 wells total). Media was harvested at T48 and snap frozen for downstream analysis before fibroblasts were incubated with resazurin to determine metabolic activity of fibroblasts at the end of culture. A) Resazurin was normalised to average % of control for each donor (green values indicate resazurin values ≥70% of control, yellow 50-69% of control and orange/red <50% of control). and B) average % change graphed for each selected inhibitor (where red dashed line represents arbitrary 70% viability threshold) per donor. All data are mean ± SEM.

A)

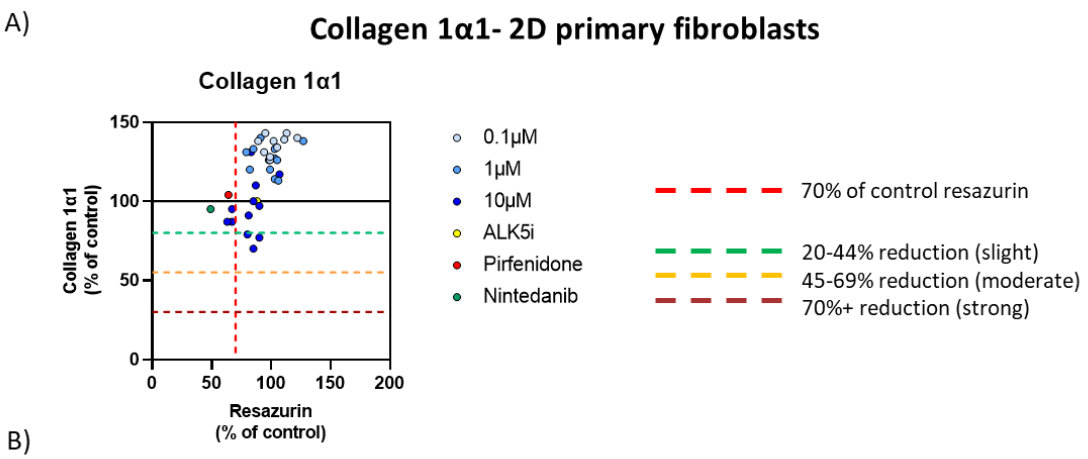

B)

Compound name	0.1μM					1μM					10μM				
	Donor 1	Donor 2	Donor 3	Donor 4	Donor 5	Donor 1	Donor 2	Donor 3	Donor 4	Donor 5	Donor 1	Donor 2	Donor 3	Donor 4	Donor 5
ITD-1	102	124	149	185	153	118	112	125	158	151		46	64	99	94
EMD 527040 hydrochloride	137	125	139	168	148	121	110	130		133	70	88	82		86
SB273005	144	112	166	197	162		119		155	151					
Cyclo (-RGDfK)	123	115	134	150	170	115	105	112		170		96			99
GLPG-0187	128	108	154	143	161		114	122	128			96		85	
Cilengitide	128	110	188	181	164		94	149	143			76		90	
Amlexanox	125	116	167	162	119	118	101	125	112	115		95		79	
BCI-137	151	109	143	143	153	146	103	134	157	147	104	90	131	128	130
KT-30	119	138	173	119	121	125	99	150	142	113	121	105	175	134	119
Acetazolamide	125	117	137	146	130	124	110	150	129	117	114	77	137	138	85
Dorzolamide HCl	131	114	135	131	121	117	102	127	123	131	98	83	114	92	113
Brinzolamide	130	114	148	127	122	123	86	125	119	110	95	83	119	97	90

All inhibitors- 10μM dose only

C)

D)

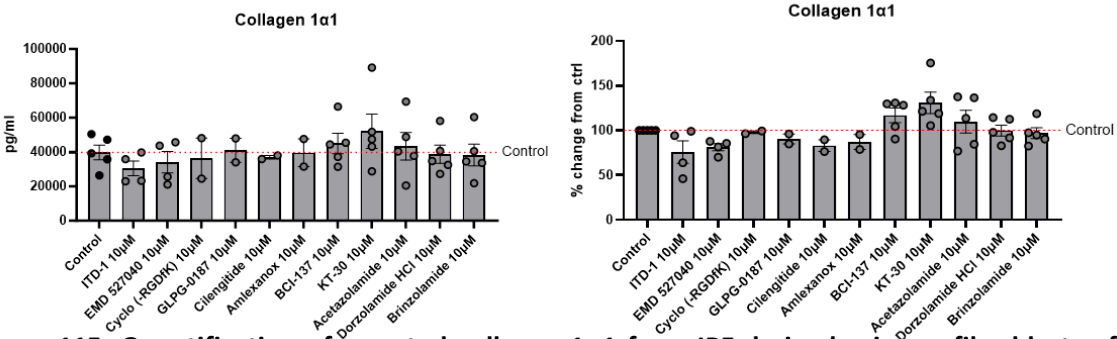

Figure 115: Quantification of secreted collagen 1α1 from IPF-derived primary fibroblasts after selected inhibitor challenge Collagen 1α1 secretion was quantified *via* ELISA after 24-hour inhibitor challenge (n=5 donors, n=2 wells per donor, n=10 samples total) and presented as A) XY graphs depicting resazurin (normalised to control fibroblasts) as a measure of tissue viability vs average % reduction of collagen 1α1 (compared to control fibroblasts) in response to 0.1μM, 1μM or 10μM of each selected inhibitor. Red dashed vertical line at 70% denotes viability threshold (30% reduction compared to control fibroblasts). Dashed lines crossing y-axis mark 20% reduction (green), 45% reduction (orange) and 70% reduction (dark red) compared to collagen 1α1 secretion from control fibroblasts (solid black line). B) Collagen 1α1 values normalised to control fibroblasts for each donor and presented as % of control. Blank values represent results excluded from further analysis due to resazurin falling below viability threshold (<70% of control fibroblasts). The 10μM dose of all candidate compounds were plotted as C) average absolute pg/ml per donor and D) average % change from control fibroblasts where red dashed line denotes unchallenged control fibroblasts. All data are mean ± SEM. Statistical significance was determined using Kruskal-Wallis test with post-hoc Dunn's multiple comparisons test (*p<0.05, **p<0.01, ***p<0.001, ****p<0.0001).

A)

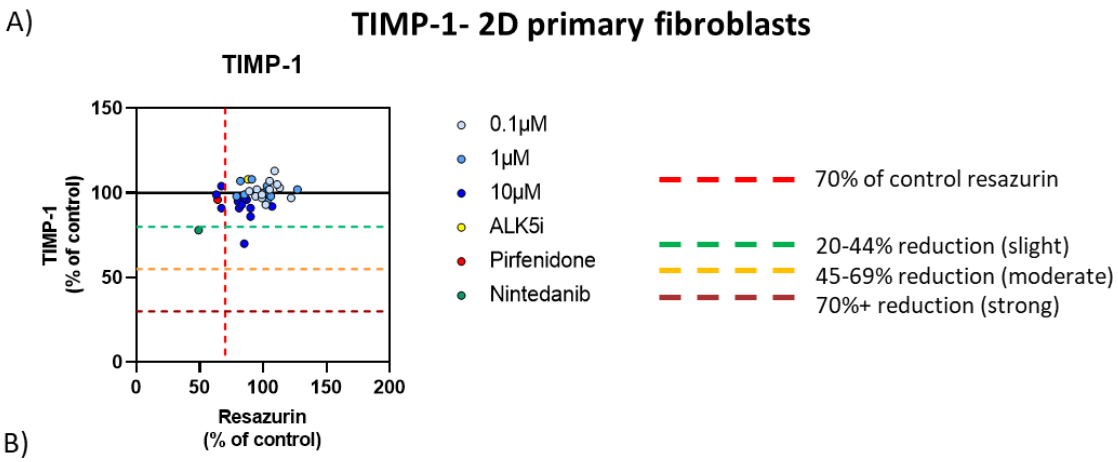

B)

Compound name	0.1µM					1µM					10µM				
	Donor 1	Donor 2	Donor 3	Donor 4	Donor 5	Donor 1	Donor 2	Donor 3	Donor 4	Donor 5	Donor 1	Donor 2	Donor 3	Donor 4	Donor 5
ITD-1	92	111	98	111	100	107	106	103	105	96		64	59	81	76
EMD 527040 hydrochloride	99	111	100	106	96	93	105	104		96	91	91	87		91
SB273005	101	108	110	116	98		106		118	100					
Cyclo (-RGDfK)	102	99	100	108	95	102	88	94		94		81		103	92
GLPG-0187	100	113	107	106	99		117	107	115			105		113	
Cilengitide	143	100	127	100	96		96	103	112			91		104	
Amlexanox	94	78	105	99	88	98	78	100	105	93		70		100	
BCI-137	107	92	72	111	105	101	108	94	107	102	99	84	83	100	96
KT-30	101	108	89	105	107	109	103	87	92	102	98	101	78	90	97
Acetazolamide	101	93	88	109	98	107	93	94	101	97	100	87	86	115	94
Dorzolamide HCL	101	103	88	99	94	107	97	96	104	98	104	91	96	103	91
Brinzolamide	99	96	99	108	93	106	96	90	101	98	99	79	88	95	94

All inhibitors- 10µM dose only

C)

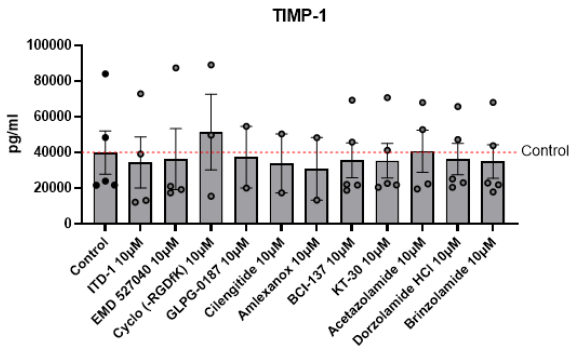

D)

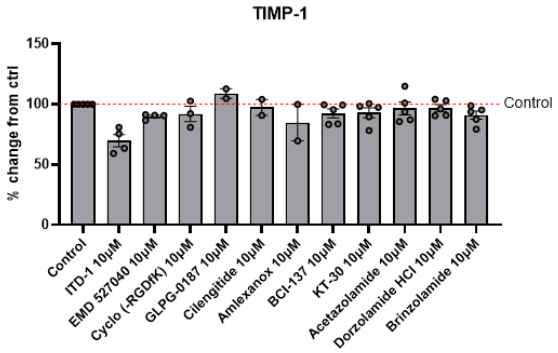

Figure 116: Quantification of secreted TIMP-1 from IPF-derived primary fibroblasts after selected inhibitor challenge TIMP-1 secretion was quantified *via* ELISA after 24-hour inhibitor challenge (n=5 donors, n=2 wells per donor, n=10 samples total) and presented as A) XY graphs depicting resazurin (normalised to control fibroblasts) as a measure of tissue viability vs average % reduction of TIMP-1 (compared to control fibroblasts) in response to 0.1µM, 1µM or 10µM of each selected inhibitor. Red dashed vertical line at 70% denotes viability threshold (30% reduction compared to control fibroblasts). Dashed lines crossing y-axis mark 20% reduction (green), 45% reduction (orange) and 70% reduction (dark red) compared to TIMP-1 secretion from control fibroblasts (solid black line). B) TIMP-1 values normalised to control fibroblasts for each donor and presented as % of control. Blank values represent results excluded from further analysis due to resazurin falling below viability threshold (<70% of control fibroblasts). The 10µM dose of all candidate compounds were plotted as C) average absolute pg/ml per donor and D) average% change from control fibroblasts where red dashed line denotes unchallenged control fibroblasts. All data are mean ± SEM. Statistical significance was determined using Kruskal-Wallis test with post-hoc Dunn's multiple comparisons test(*p<0.05, **p<0.01, ***p<0.001, ****p<0.0001).

5.3.2.2 Candidate selected compounds in PCLuS human tissue model

To interrogate the selected inhibitors in a more clinically relevant model of pulmonary fibrosis, candidate compounds were further assessed in IPF-derived PCLuS (n=4 donors). Once generated, PCLuS (n=10 PCLuS per condition, n=4 donors, n=40 PCLuS total) were rested for 48 hours before challenge with either control media, SoC compounds or ALK5i to blunt fibrosis. Concurrently, PCLuS were challenged with 3 escalating doses (0.1µM, 1µM and 10µM) of each selected compound to assess the ability to reduce pre-existing inflammation and fibrosis (n=6 PCLuS per condition, n=4 donors, n=24 PCLuS total). Media, including all treatments, was refreshed at 24-hour intervals with conditioned media snap frozen for downstream analysis before PCLuS were harvested at T144 for resazurin. Results were normalised to % of control PCLuS for each donor (Figure 117A). Following this, quantification of soluble collagen 1α1, TIMP-1 and IL-8 was performed in the conditioned media of the final timepoint of culture to evaluate individual compound effects on fibrosis and inflammation (absolute pg/ml values available in Appendix G; Figures 1-4).

Using this panel of secreted markers, we first established that Pirfenidone, Nintedanib and ALK5i all demonstrated strong anti-inflammatory and anti-fibrotic effects (Figure 117D-F []), whilst maintaining a level of metabolic activity which was comparable to control PCLuS (Figure 117C). This confirmed that all IPF donor tissue could be effectively modulated via established anti-fibrotic SoC therapeutics without impacting tissue viability, therefore providing a suitable benchmark for candidate compound efficacy.

Subsequent evaluation of PCLuS viability in response to selected compound treatment confirmed that each candidate inhibitor was well tolerated in all donor PCLuS, though IPF donor 3 appeared to be more sensitive to multiple compounds (Figure 117B). Next, quantification of soluble pro-fibrogenic markers in the culture media collected at T144 (normalised to % change from baseline T48 secretion), found that all 12 inhibitors were able to significantly reduce collagen 1α1 secretion at multiple doses, often in a dose dependent manner (Figure 118). To interrogate this in more depth and normalise for donor heterogeneity, further analysis was performed by normalising % change in protein secretion throughout culture to control PCLuS for each IPF donor (Figure 119A). Interestingly, though initial screening identified a strong average reduction in collagen 1α1 secretion in response to inhibitor treatment, assessment of individual donor response to each inhibitor highlighted

varying degrees of compound efficacy across the different IPF donors. For example, after 96 hours treatment with 10µM Amlexanox, PCLuS derived from IPF donor 1 and IPF donor 2 demonstrated ~87% reduction of collagen 1α1 compared to their control PCLuS, whereas PCLuS from IPF donor 3 and 4 reduced collagen 1α1 secretion by 43% and 42%, respectively. One possible explanation for this is differences in patient demographics including ageing, biological sex, lifestyle, ethnicity and genetics.

Average viability and efficacy of all 4 donors was then determined by plotting the average % reduction of collagen 1α1 secretion compared to untreated PCLuS against normalised resazurin values for each inhibitor dose (Figure 119B). Results were then summarised in a table applying the following criteria: one tick represents 20-44% reduction (slight), two ticks show a 45-69% reduction (moderate), whilst three ticks represent the most potent attenuation in each marker, >70% reduction (strong) (Figure 119C). This confirmed that the majority of selected inhibitors were able to reduce collagen 1α1 secretion by 45-69% at varying doses but failed to surpass the efficacy of SoC therapeutics (70%+ reduction).

Further assessment of pro-fibrogenic markers found that 7 of the 12 candidate compounds were able to significantly reduce TIMP-1 secretion at various doses, with GLPG-0187 (Figure 120E), Cilengitide (Figure 120F) and Dorzolamide (Figure 120K) showing the highest attenuation at 0.1µM, 1µM and 10µM doses compared to T48 baseline PCLuS. However, normalisation to % change from control PCLuS revealed that these 3 inhibitors, along with 0.1µM BCL-137, fell into the slight reduction subclassification, failing to surpass the efficacy of Pirfenidone (35% reduction from control PCLuS), Nintedanib (58% reduction from control PCLuS) and ALK5i (50% reduction from control PCLuS) (Figure 121).

Alongside pro-fibrogenic markers, we also sought to identify any potential anti-inflammatory effects of selected inhibitors through quantification of soluble IL-8, a key cytokine widely released during inflammation. After normalisation to baseline secretion, results confirmed that PCLuS significantly reduced IL-8 secretion in response to all inhibitors (except KT-30) at various doses (Figure 122). Of these, GLPG-0187 (a potent αv integrin inhibitor) demonstrated the most significant reduction in soluble IL-8 at 0.1µM ($p<0.001$), 1µM ($p<0.0001$) and 10µM ($p<0.0001$) (Figure 122E). Additional normalisation to % change from control PCLuS further demonstrated varying degrees of drug efficacy across the different IPF donors, with IPF donor 4 showing the highest % reduction of IL-8 in response to several inhibitor compounds,

particularly GLPG-0187, Cilengitide, Amlexanox and Acetazolamide (Figure 123A). Consistent with initial findings, analysis of average efficacy revealed that GLPG-0187- challenged PCLuS had the highest % reduction in IL-8 secretion at 1µM (61% reduction from control PCLuS) and 10µM (56% reduction from control PCLuS) doses, alongside 0.1µM SB273005 (56% reduction from control PCLuS) (Figure 123C). These results were comparable to treatment with Nintedanib (64% reduction from control PCLuS) and ALK5i (64% reduction from control PCLuS). However, Pirfenidone remained the most potent anti-inflammatory compound with a 76% reduction in IL-8 secretion compared to control PCLuS (Figure 123B).

In contrast to findings *in vitro*, compound screening in our PCLuS model demonstrated that candidate inhibitors were well tolerated in whole tissue models of disease (including the highest 10µM dose), whilst exerting considerable anti-fibrotic and anti-inflammatory effects at all doses, including lower 0.1µM and 1µM treatments. Taken together, these data demonstrated that inhibitory compounds targeting significantly upregulated proteins in the normal and intermediate regions of IPF were able to effectively blunt pro-fibrotic and pro-inflammatory markers in our *ex vivo* PCLuS model, supporting a role in disease pathogenesis.

A)

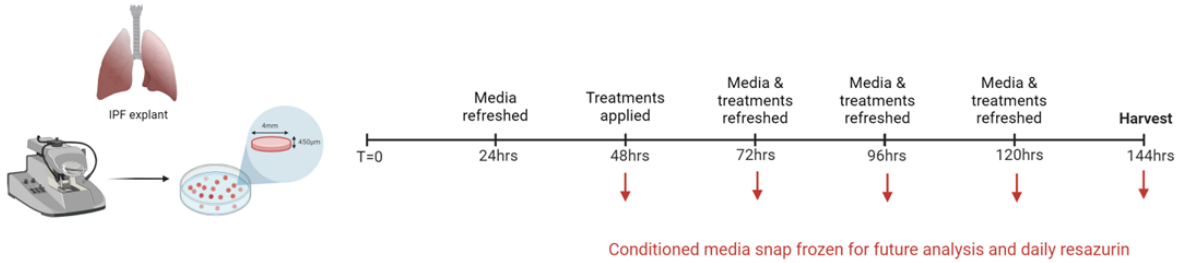

B)

Resazurin- IPF-derived PCLuS

Compound Name	0.1µM				1µM				10µM			
	Donor 1	Donor 2	Donor 3	Donor 4	Donor 1	Donor 2	Donor 3	Donor 4	Donor 1	Donor 2	Donor 3	Donor 4
ITD-1	107	122	72	101	91	115	61	92	125	101	70	86
EMD 527050	102	80	91	90	103	86	74	114	98	100	89	127
SB273005	68	83	72	144	76	87	74	88	106	92	83	92
Cyclo (-RGDfK)	82	104	78	106	96	101	85	117	92	86	97	112
GLPG-0187	79	109	70	113	73	89	61	101	77	106	55	90
Cilengitide	86	95	65	101	100	91	70	89	89	80	70	91
Amlexanox	76	88	70	98	70	90	56	132	65	94	51	92
BCL-137	114	116	83	110	113	103	75	106	111	104	72	129
KT-30	120	94	71	118	112	97	88	127	108	91	62	70
Acetazolamide	100	106	50	119	93	70	57	74	82	71	55	90
Dorzolamide	116	89	70	112	122	104	91	143	123	91	93	127
Brinzolamide	110	81	73	66	122	95	77	91	109	97	75	85

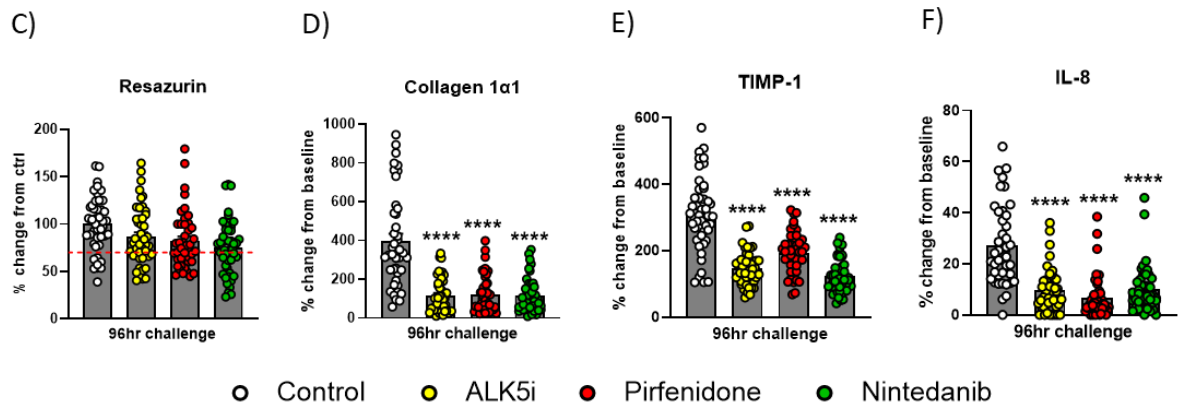

Figure 117: Validation of IPF-derived PCLuS viability for assessment of selected compounds A) PCLuS were generated from explant IPF tissue (n=4 donors) with slices (n=10 per condition) being rested for 48 hours before challenge with either control media, standard of care compounds Pirfenidone (2.5mM) and Nintedanib (2.5µM) or ALK5i (10µM) to blunt fibrosis (n=10 PCLuS per condition, n=4 donors, n=40 PCLuS total). Concurrently, PCLuS were challenged with 3 escalating doses (0.1µM, 1µM and 10µM) of each candidate compound (n=6 per condition) to assess the ability to reduce pre-existing fibrosis (n=6 PCLuS per condition, n=4 donors, n=24 PCLuS total). Media, including all treatments, was refreshed at 24-hour intervals with conditioned media snap frozen for downstream analysis before PCLuS were harvested at T144 for resazurin as an indicator of tissue viability. B) Resazurin assay performed at T144 presented as the average % of control (for n=6 slices) per candidate compound for each donor (green values indicate resazurin values ≥70% of control and yellow 50-69% of control).Quantification of C) Resazurin (where red dashed line represents arbitrary 70% viability threshold) D) Collagen 1α1, E) TIMP-1 and F) IL-8 was performed on T144 media *via* ELISA and plotted as average % change from baseline (T48 unstimulated PCLuS) (n=40 PCLuS per condition) to confirm tissue could be effectively modulated. All data are mean ± SEM. Statistical significance was determined using ANOVA with post-hoc Dunnett's test (*p<0.05, **p<0.01, ***p<0.001, ****p<0.0001).

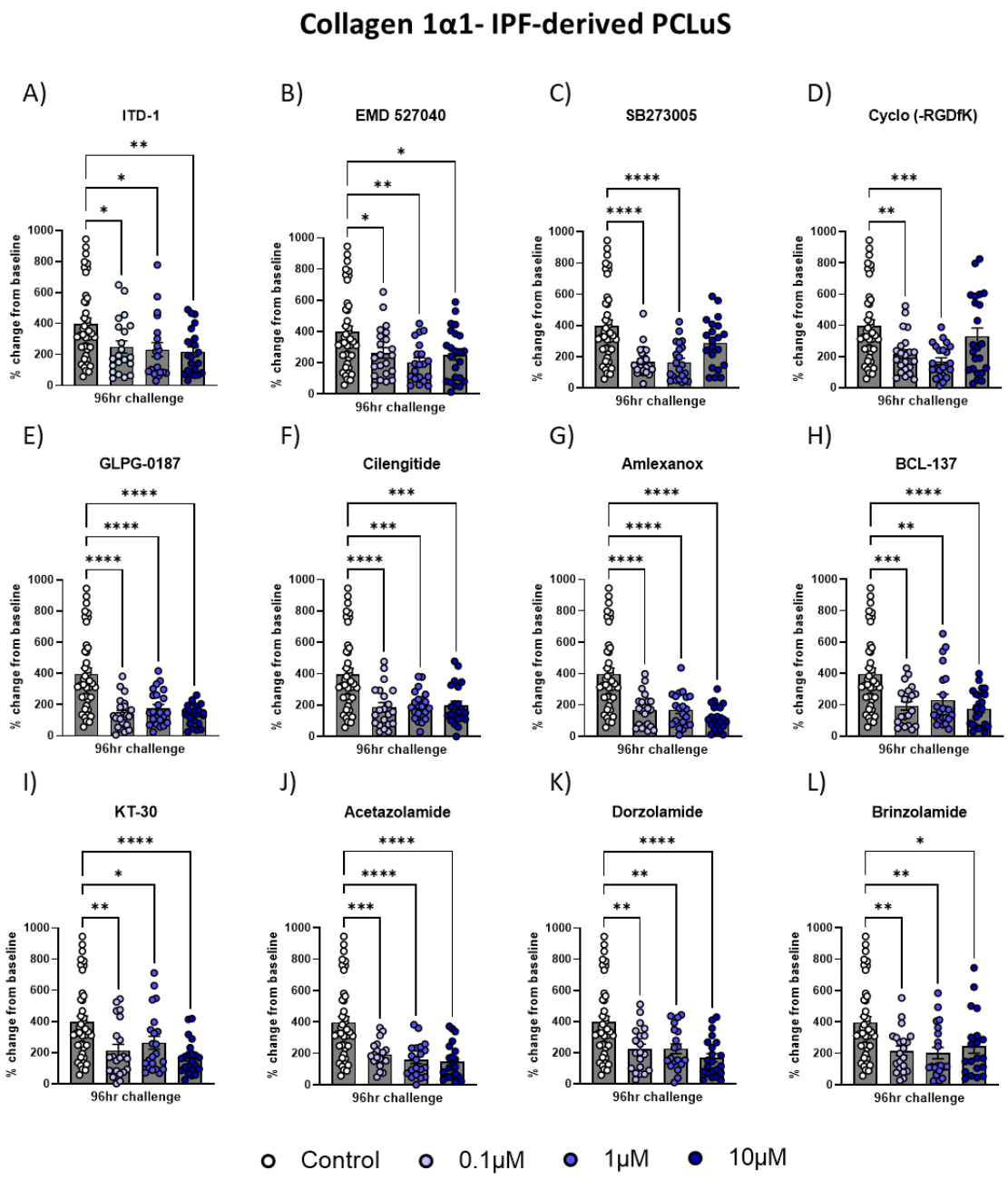

Figure 118: Validation of collagen 1α1 secretion in selected compound- challenged PCLuS PCLuS were generated from explant IPF tissue (n=4 donors) with slices (n=6 per condition) being rested for 48 hours before challenge with either control media or 3 escalating doses (0.1μM, 1μM and 10μM) of each candidate compound to assess the ability to reduce pre-existing fibrosis (n=6 PCLuS per condition, n=4 donors, n=24 PCLuS total). Media, including all treatments, was refreshed at 24-hour intervals with conditioned media snap frozen for downstream analysis before PCLuS were harvested for resazurin at T144 as an indicator of tissue viability. Quantification of Collagen 1α1 was performed *via* ELISA on T144 media and plotted as A-L) average % change from baseline (T48 unstimulated PCLuS) (n=6 conditioned media per donor, n=4 donors, n=24 samples total) to assess potential anti-fibrotic affects. All data are mean ± SEM. Statistical significance was determined using ANOVA with post-hoc Dunnett's test (*p<0.05, **p<0.01, ***p<0.001, ****p<0.0001).

Collagen 1α1- IPF-derived PCLuS

A)

Compound Name	0.1µM				1µM				10µM			
	Donor 1	Donor 2	Donor 3	Donor 4	Donor 1	Donor 2	Donor 3	Donor 4	Donor 1	Donor 2	Donor 3	Donor 4
ITD-1	51	65	91	57	55	27	128	42	33	57	66	68
EMD 527050	61	59	105	37	61	38	81	44	53	51	88	75
SB273005	34	37	60	48	29	39	67	39	61	65	107	70
Cyclo (-RGDfK)	37	56	55	74	30	45	71	33	96	66	119	52
GLPG-0187	13	40	65	41	33	43	64	45	20	29	51	48
Cilengitide	30	55	58	53	40	43	69	57	60	28	67	54
Amlexanox	11	51	67	51	21	41	56	64	13	13	57	58
BCL-137	58	44	53	44	88	54	41	39	29	46	67	41
KT-30	35	50	88	39	62	63	80	43	29	43	44	49
Acetazolamide	29	36	73	84	11	46	59	64	21	34	36	68
Dorzolamide	58	41	80	50	69	60	49	54	39	54	33	36
Brinzolamide	27	65	86	52	42	63	62	35	68	63	55	28

B)

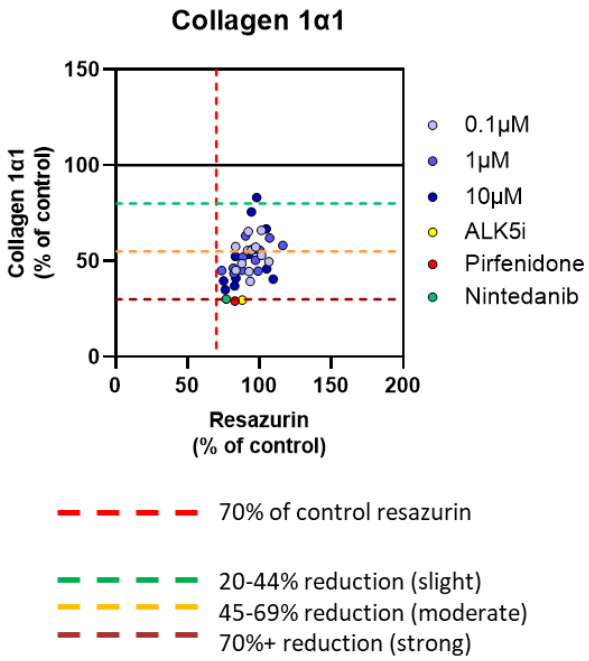

C)

Compound	0.1µM	1µM	10µM
ITD-1	✓	✓	✓
EMD 527040	✓	✓	✓
SB273005	✓✓	✓✓	✓
Cyclo (-RGDfK)	✓	✓✓	
GLPG-0187	✓✓	✓✓	✓✓
Cilengitide	✓✓	✓✓	✓✓
Amlexanox	✓✓	✓✓	✓✓
BCL-137	✓✓	✓	✓✓
KT-30	✓✓	✓	✓✓
Acetazolamide	✓	✓✓	✓✓
Dorzolamide	✓	✓	✓✓
Brinzolamide	✓	✓✓	✓✓

Figure 119: Normalised collagen 1α1 secretion in selected compound- challenged PCLuS Quantification of collagen 1α1, previously normalised to % change from baseline (T48 unstimulated PCLuS) was further normalised to A) % change from control PCLuS at T144 for each explant IPF donor (n=4 donors) to allow assessment of % reduction of collagen 1α1 in response to 96-hour selected compound challenge. B) XY graphs depict resazurin (normalised to control PCLuS) as a measure of tissue viability vs average % reduction of collagen 1α1 (n=4 donors) in response to 0.1µM, 1µM or 10µM of each selected inhibitor. Red dashed vertical line at 70% denotes viability threshold (30% reduction compared to control PCLuS). Dashed lines crossing y-axis mark 20% reduction (green), 45% reduction (orange) and 70% reduction (dark red) compared to collagen 1α1 secretion from control slices (solid black line) C) Average % reduction of collagen 1α1 (n=4 donors) summarised as one green tick for 20% reduction, two orange ticks for 45% reduction and three red ticks for 70% + reduction in Collagen 1α1 vs control PCLuS for compounds deemed not to have significantly impacted tissue viability.

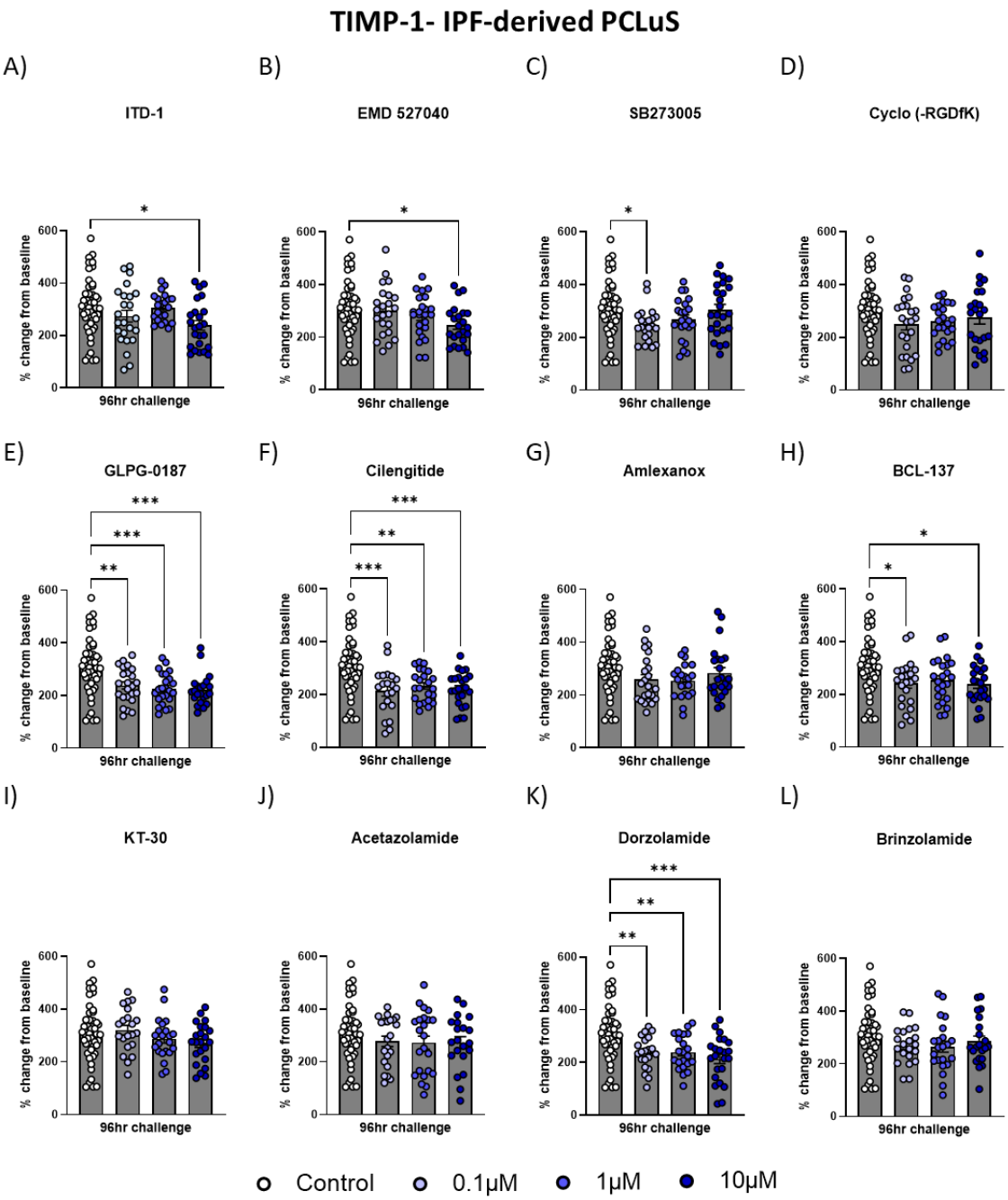

Figure 120: Validation of TIMP-1 secretion in selected compound- challenged PCLuS PCLuS were generated from explant IPF tissue (n=4 donors) with slices (n=6 per condition) being rested for 48 hours before challenge with either control media or 3 escalating doses (0.1µM, 1µM and 10µM) of each candidate compound to assess the ability to reduce pre-existing fibrosis (n=6 PCLuS per condition, n=4 donors, n=24 PCLuS total). Media, including all treatments, was refreshed at 24-hour intervals with conditioned media snap frozen for downstream analysis before PCLuS were harvested for resazurin at T144 as an indicator of tissue viability. Quantification of TIMP-1 was performed *via* ELISA on T144 media and plotted as A-L) average % change from baseline (T48 unstimulated PCLuS) (n=6 conditioned media per donor, n=4 donors, n=24 samples total) to assess potential anti-fibrotic affects. All data are mean ± SEM. Statistical significance was determined using ANOVA with post-hoc Dunnett's test (*p<0.05, **p<0.01, ***p<0.001, ****p<0.0001).

A)

TIMP-1- IPF-derived PCLuS

Compound Name	0.1µM				1µM				10µM			
	Donor 1	Donor 2	Donor 3	Donor 4	Donor 1	Donor 2	Donor 3	Donor 4	Donor 1	Donor 2	Donor 3	Donor 4
ITD-1	61	107	116	80	95	82	153	89	60	80	115	70
EMD 527050	102	107	108	80	83	100	101	83	78	85	91	70
SB273005	75	81	100	71	85	81	107	83	115	104	99	79
Cyclo (-RGDfK)	90	97	82	57	77	90	87	81	110	103	81	65
GLPG-0187	67	88	99	64	82	62	98	61	62	73	95	69
Cilengitide	66	87	52	66	75	71	94	67	72	71	72	71
Amlexanox	76	85	86	88	84	74	108	74	73	97	99	97
BCL-137	84	89	79	66	90	91	73	72	75	85	106	56
KT-30	115	99	123	84	91	102	104	77	72	95	85	88
Acetazolamide	99	92	71	87	85	92	63	95	105	96	53	74
Dorzolamide	71	81	99	62	96	73	77	58	76	73	62	60
Brinzolamide	88	86	100	79	107	86	89	66	102	86	77	80

B)

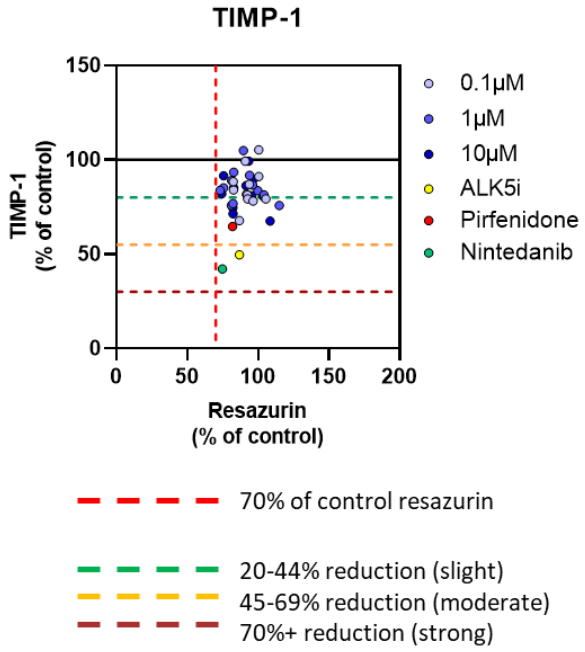

C)

Compound	0.1µM	1µM	10µM
ITD-1			
EMD 527040			
SB273005			
Cyclo (-RGDfK)			
GLPG-0187	✓	✓	✓
Cilengitide	✓	✓	✓
Amlexanox			
BCL-137	✓		
KT-30			
Acetazolamide			
Dorzolamide	✓	✓	✓
Brinzolamide			

Figure 121: Normalised TIMP-1 secretion in selected compound- challenged PCLuS Quantification of TIMP-1, previously normalised to % change from baseline (T48 unstimulated PCLuS) was further normalised to A) % change from control PCLuS at T144 for each explant IPF donor (n=4 donors) to allow assessment of % reduction of TIMP-1 in response to 96-hour selected compound challenge. B) XY graphs depict resazurin (normalised to control PCLuS) as a measure of tissue viability vs average % reduction of TIMP-1 (n=4 donors) in response to 0.1µM, 1µM or 10µM of each selected inhibitor. Red dashed vertical line at 70% denotes viability threshold (30% reduction compared to control PCLuS). Dashed lines crossing y-axis mark 20% reduction (green), 45% reduction (orange) and 70% reduction (dark red) compared to TIMP-1 secretion from control slices (solid black line). C) Average % reduction of TIMP-1 (n=4 donors) summarised as one green tick for 20% reduction, two orange ticks for 45% reduction and three red ticks for 70% + reduction in TIMP-1 vs control PCLuS for compounds deemed not to have significantly impacted tissue viability.

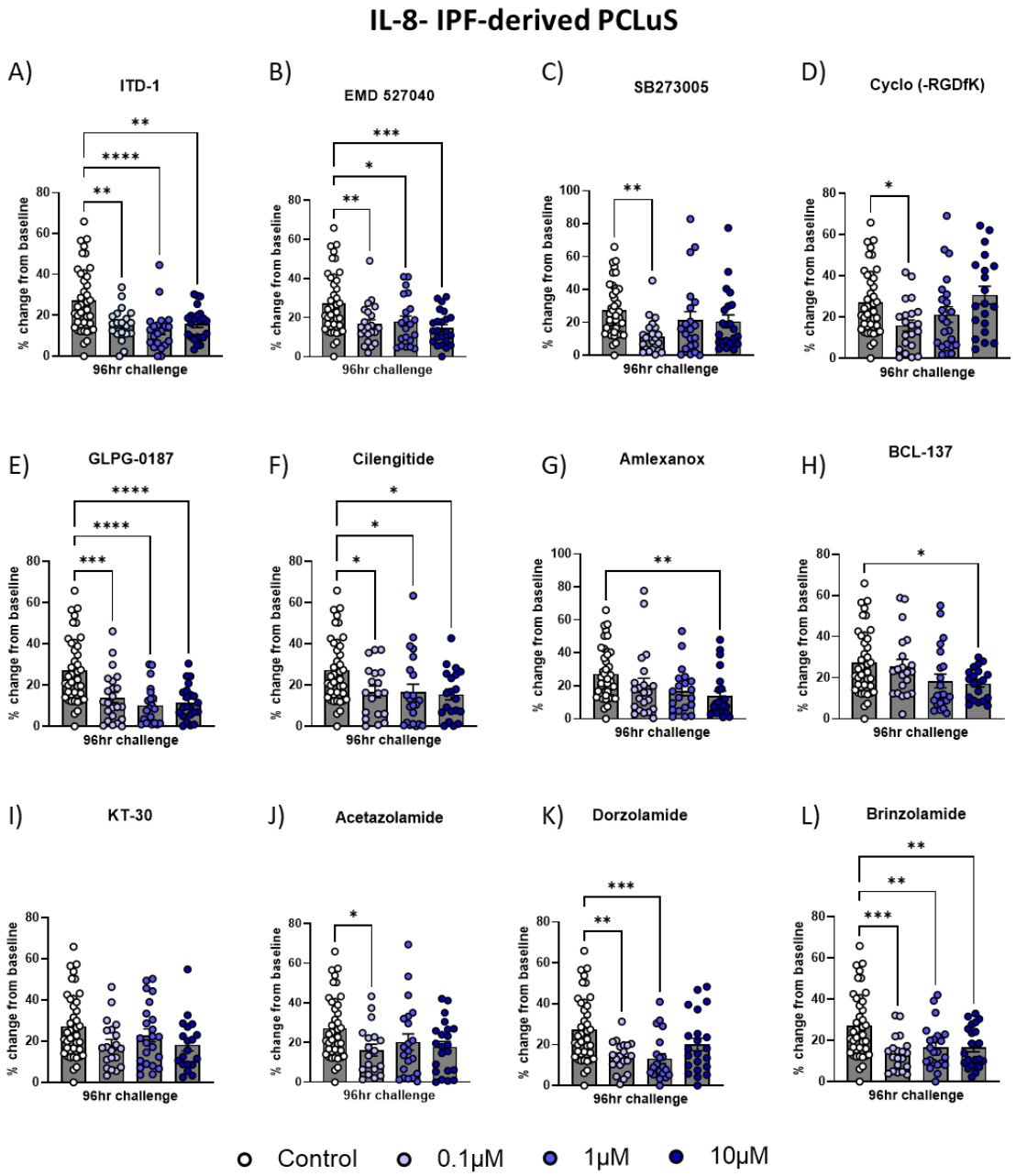

Figure 122: Validation of IL-8 secretion in selected compound- challenged PCLuS PCLuS were generated from explant IPF tissue (n=4 donors) with slices (n=6 per condition) being rested for 48 hours before challenge with either control media or 3 escalating doses (0.1µM, 1µM and 10µM) of each candidate compound to assess the ability to reduce pre-existing inflammation (n=6 PCLuS per condition, n=4 donors, n=24 PCLuS total). Media, including all treatments, was refreshed at 24-hour intervals with conditioned media snap frozen for downstream analysis before PCLuS were harvested for resazurin at T144 as an indicator of tissue viability. Quantification of IL-8 was performed *via* ELISA on T144 media and plotted as A-L) average % change from baseline (T48 unstimulated PCLuS) (n=6 conditioned media per donor, n=4 donors, n=24 samples total) to assess potential anti-inflammatory affects. All data are mean ± SEM. Statistical significance was determined using ANOVA with post-hoc Dunnett's test (*p<0.05, **p<0.01, ***p<0.001, ****p<0.0001).

IL-8- IPF-derived PCLuS

A)

Compound Name	0.1µM				1µM				10µM			
	Donor 1	Donor 2	Donor 3	Donor 4	Donor 1	Donor 2	Donor 3	Donor 4	Donor 1	Donor 2	Donor 3	Donor 4
ITD-1	63	59	78	44	84	59	28	39	65	68	46	53
EMD 527050	48	73	84	46	49	102	101	33	45	83	40	47
SB273005	42	64	38	27	88	89	143	5	92	85	88	51
Cyclo (-RGDfK)	79	78	82	15	45	116	123	35	111	127	102	116
GLPG-0187	64	65	60	24	79	32	39	4	51	45	67	14
Cilengitide	79	68	96	18	84	55	145	3	82	64	74	3
Amlexanox	62	105	116	22	49	85	102	18	65	81	45	15
BCL-137	133	58	58	118	53	44	87	83	51	48	85	64
KT-30	51	76	56	81	69	52	115	108	75	84	50	67
Acetazolamide	97	64	71	9	96	108	102	8	99	87	85	8
Dorzolamide	30	43	65	59	72	32	25	59	74	69	100	63
Brinzolamide	50	47	63	44	70	23	77	79	66	56	65	59

B)

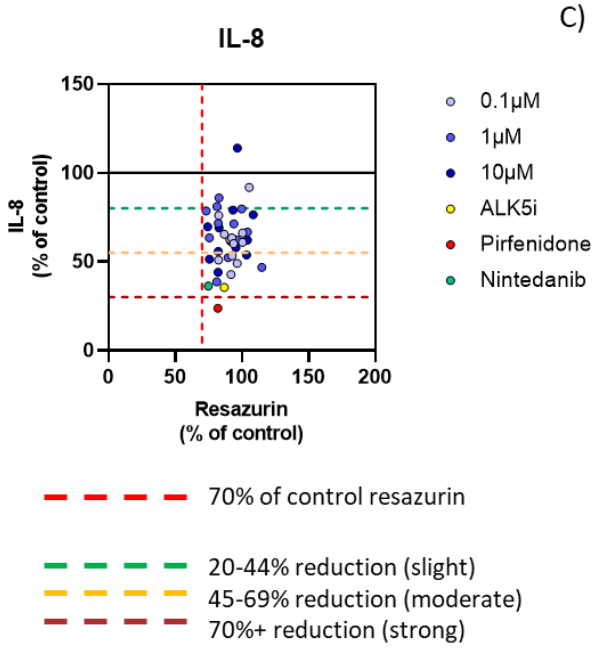

C)

Compound	0.1µM	1µM	10µM
ITD-1	✓	✓✓	✓
EMD 527040	✓	✓	✓✓
SB273005	✓✓		✓
Cyclo (-RGDfK)	✓	✓	
GLPG-0187	✓✓	✓✓	✓✓
Cilengitide	✓	✓	✓
Amlexanox	✓	✓	✓✓
BCL-137		✓	✓
KT-30	✓		✓
Acetazolamide	✓	✓	✓
Dorzolamide	✓✓	✓✓	✓
Brinzolamide	✓✓		✓

Figure 123: Normalised IL-8 secretion in selected compound- challenged PCLuS Quantification of IL-8, previously normalised to % change from baseline (T48 unstimulated PCLuS) was further normalised to A) % change from control PCLuS at T144 for each explant IPF donor (n=4 donors) to allow assessment of % reduction of IL-8 in response to 96-hour selected compound challenge. B) XY graphs depict resazurin (normalised to control PCLuS) as a measure of tissue viability vs average % reduction of IL-8 (n=4 donors) in response to 0.1µM, 1µM or 10µM of each selected inhibitor. Red dashed vertical line at 70% denotes viability threshold (30% reduction compared to control PCLuS). Dashed lines crossing y-axis mark 20% reduction (green), 45% reduction (orange) and 70% reduction (dark red) compared to IL-8 secretion from control slices (solid black line). C) Average % reduction of IL-8 (n=4 donors) summarised as one green tick for 20% reduction, two orange ticks for 45% reduction and three red ticks for 70% + reduction in IL-8 vs control PCLuS for compounds deemed not to have significantly impacted tissue viability.

5.3.2.3 Comparing selected compound efficacy in different pre-clinical models

To gain a robust understanding of compound efficacy in multiple systems, work in this project utilised a comparative analysis approach to discern whether results obtained from 2D cell culture models would translate to more complex, 3D tissue models of disease. Results acquired from *in vitro* and *ex vivo* compound screening of selected inhibitors identified several differences between systems (Figure 124). First, evaluation of SoC compounds revealed that whilst Pirfenidone and Nintedanib appeared to negatively impact cellular function in 2D cell culture models (Figure 125A), SoC compounds had no detrimental effect on PCLuS viability throughout culture (Figure 125B). Moreover, we found that anti-fibrotic compounds had no impact on secretion of pro-fibrogenic markers *in vitro* (Figure 126A, Figure 127A), whilst exerting potent anti-fibrotic effects in IPF-derived PCLuS (Figure 126B, Figure 127B).

Interestingly, quantification of resazurin highlighted numerous inconsistencies in metabolic activity between models in response to candidate compounds. For example, the highest dose of SB273005 (Figure 125C), Cyclo –(RGDfK) (Figure 125E) and GLPG-0187 (Figure 125G) all resulted in >30% reduction of resazurin activity compared to control fibroblasts. However, in PCLuS, all 3 compounds maintained a consistent level of metabolic activity and did not impact overall tissue viability, though we were unable to directly assess potential cell-specific death in PCLuS (Figure 125D, F, H). Similarily, evaluation of soluble collagen 1α1 and TIMP-1 revealed that whilst several candidate compounds had no beneficial effect in 2D cell culture, they could significantly reduce soluble pro-fibrogenic marker secretion in *ex vivo* PCLuS (Figure 126, Figure 127C-F).

These results demonstrate that compounds/doses which may be deemed non-viable or ineffective in conventional 2D systems, can be well tolerated and exert anti-fibrotic effects in more clinically relevant PCLuS models. Consequently, it is important to consider the inherent limitations and advantages of each model when screening compounds as we established that *in vitro* testing alone poses the risk of identifying false negatives, potentially resulting in exclusion of efficacious drugs from further analysis.

A)

2D Primary fibroblasts

Compound	Collagen 1α1			TIMP-1		
	0.1µM	1µM	10µM	0.1µM	1µM	10µM
ITD-1			✓			✓
EMD 527040			✓			
SB273005						
Cyclo (-RGDfK)						
GLPG-0187						
Cilengitide						
Amlexanox						
BCL-137						
KT-30						
Acetazolamide						
Dorzolamide						
Brinzolamide						

B)

IPF-derived PCLuS

Compound	Collagen 1α1			TIMP-1		
	0.1µM	1µM	10µM	0.1µM	1µM	10µM
ITD-1	✓	✓	✓			
EMD 527040	✓	✓	✓			
SB273005	✓✓	✓✓	✓			
Cyclo (-RGDfK)	✓	✓✓				
GLPG-0187	✓✓	✓✓	✓✓	✓	✓	✓
Cilengitide	✓✓	✓✓	✓✓	✓	✓	✓
Amlexanox	✓✓	✓✓	✓✓			
BCL-137	✓✓	✓	✓✓	✓		
KT-30	✓✓	✓	✓✓			
Acetazolamide	✓	✓✓	✓✓			
Dorzolamide	✓	✓	✓✓	✓	✓	✓
Brinzolamide	✓	✓✓	✓✓			

Figure 124: Comparison of selected inhibitor efficacy between 2D primary fibroblasts and IPF-derived PCLuS Summary of average % reduction of Collagen 1α1 and TIMP-1 secretion compared to control for 2D cell culture and PCLuS models after culture. Results summarised as one green tick for 20% reduction, two orange ticks for 45% reduction and three red ticks for 70% + reduction for A) acute 24hour treatment in 2D cell culture model (n=2 wells per donor, n=5 donors, n=10 samples total) and B) 96hour treatment in IPF-derived PCLuS. Blacked out doses represent compounds which were deemed to have significantly impacted viability (<70% resazurin compared to control) and were excluded from downstream analysis.

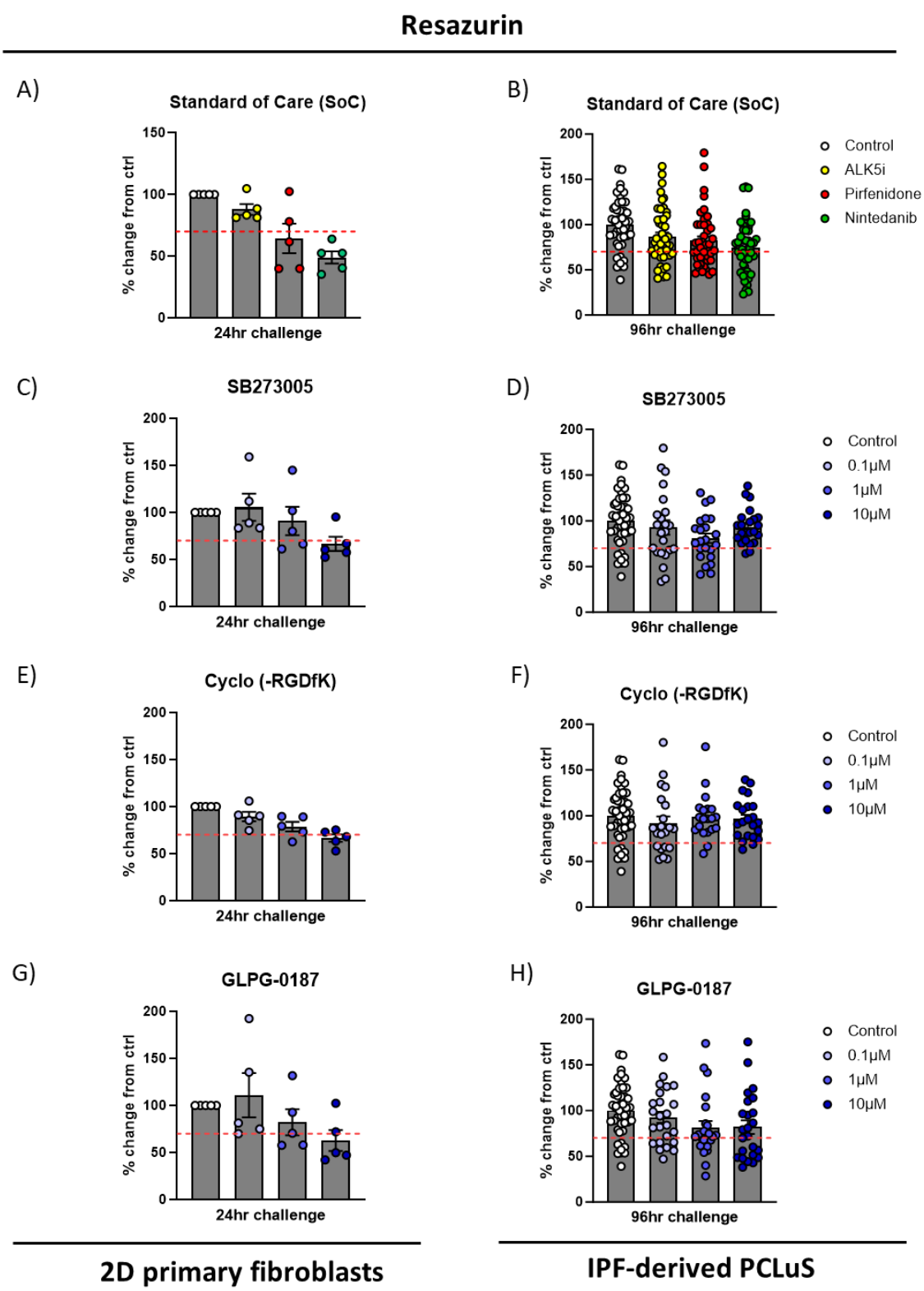

Figure 125: Comparing viability between 2D primary fibroblasts and IPF-derived PCLuS after selected compound challenge After culture of primary fibroblasts and PCLuS with selected inhibitors, resazurin was normalised to average % of control for each donor and presented as % change from control for 2D primary fibroblasts per donor (n=2 wells per donor, n=5 donors, n=10 samples total) and IPF-derived PCLuS (n=6 PCLuS per condition, n=4 donors, n=24 PCLuS total). Results were presented as % change from control (where red dashed line represents arbitrary 70% viability threshold) for A, B) Standard of care (SoC) compounds C, D) SB273005 E, F) Cyclo (-RGDfK) and G, H) GLPG- 0187. All data are mean ± SEM.

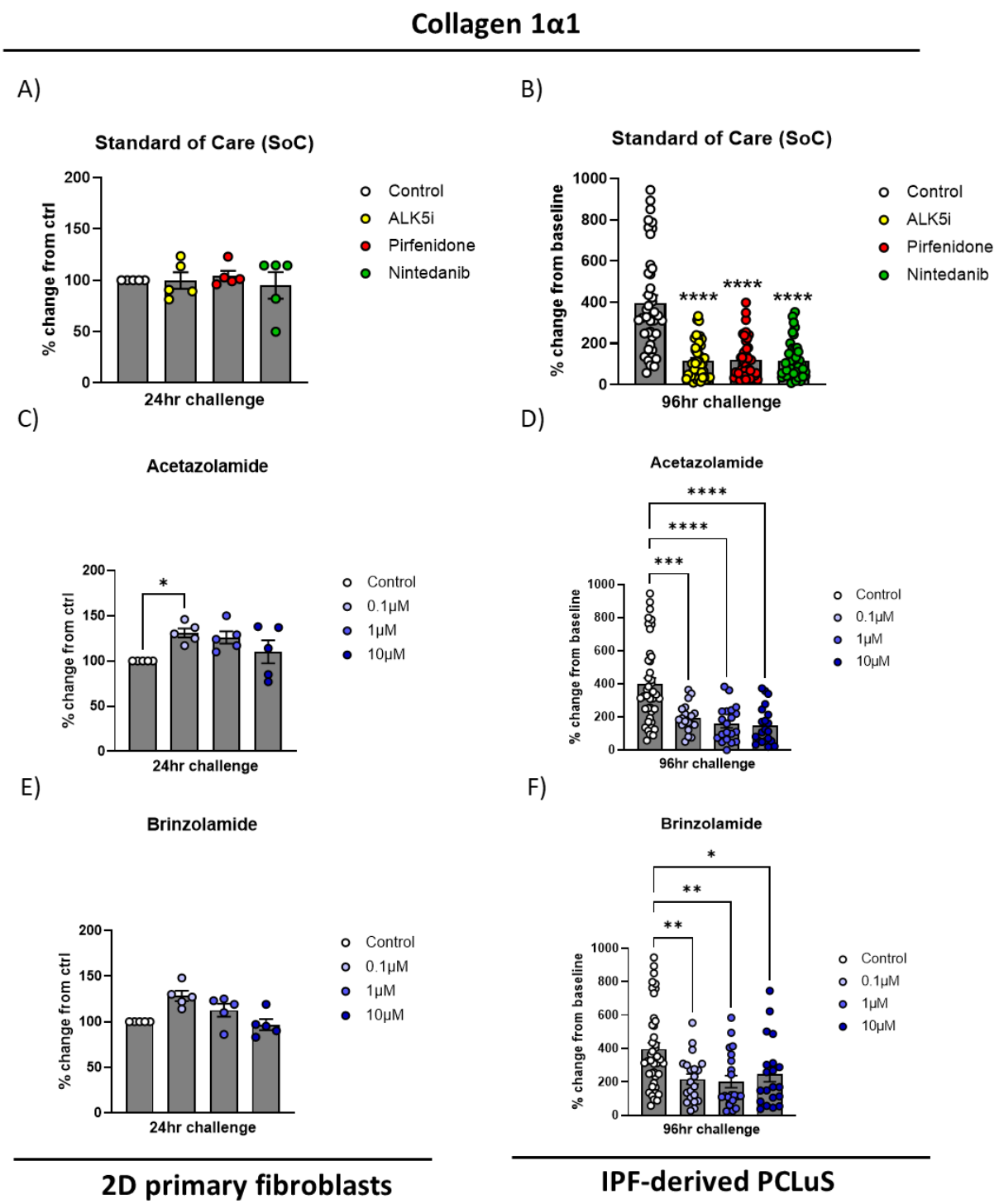

Figure 126: Comparing collagen 1α1 secretion between 2D primary fibroblasts and IPF-derived PCLuS after selected compound challenge After culture of primary fibroblasts and PCLuS with selected inhibitors, collagen 1α1 was normalised to average % of control for each cell line donor for 2D primary fibroblasts per donor (n=2 wells per condition, n=5 donors, n=10 samples total) and to T48 unstimulated PCLuS for IPF-derived PCLuS (n=6 PCLuS per condition, n=4 donors, n=24 PCLuS total). Results were graphed as % change from ctrl for A) SoC compounds, C) Acetazolamide and E) Brinzolamide and as % change from baseline (T48) for PCLuS for B) SoC compounds, D) Acetazolamide and F) Brinzolamide. All data are mean ± SEM. Statistical significance was determined using Kruskal-Wallis with post-hoc Dunn's test for primary fibroblasts and ANOVA with post-hoc Dunnett's test for PCLuS (*p<0.05, **p<0.01, ***p<0.001, ****p<0.0001).

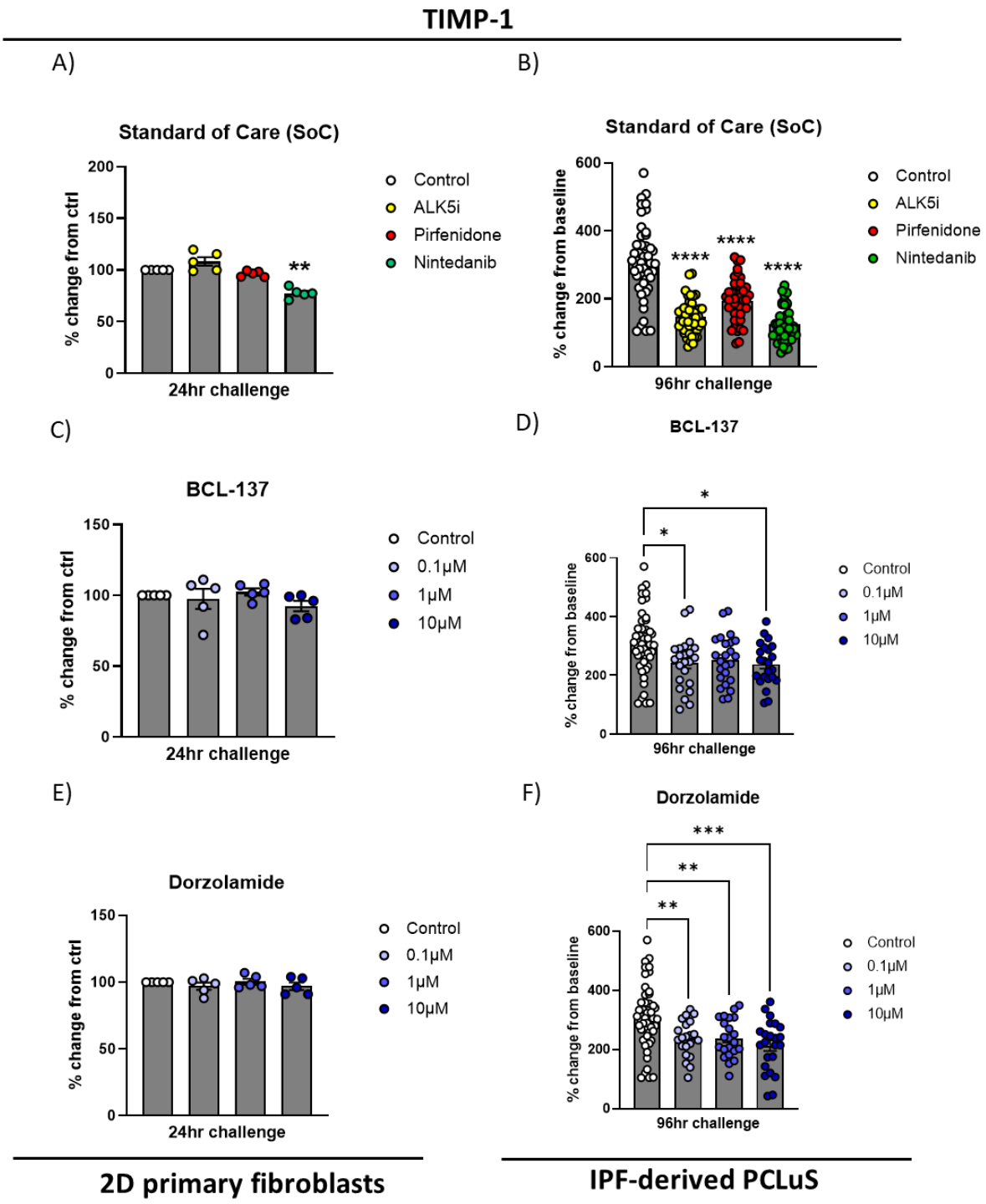

Figure 127: Comparing TIMP-1 secretion between 2D primary fibroblasts and IPF-derived PCLuS after selected compound challenge After culture of primary fibroblasts and PCLuS with selected inhibitors, TIMP-1 was normalised to average % of control for each cell line donor for 2D primary fibroblasts per donor (n=2 wells per condition, n=5 donors, n=10 samples total) and to T48 unstimulated PCLuS for IPF-derived PCLuS (n=6 PCLuS per condition, n=4 donors, n=24 PCLuS total). Results were graphed as % change from ctrl for A) SoC compounds, C) Acetazolamide and E) Brinzolamide and as % change from baseline (T48) for PCLuS for B) SoC compounds, D) Acetazolamide and F) Brinzolamide. All data are mean ± SEM. Statistical significance was determined using Kruskal-Wallis with post-hoc Dunn's test for primary fibroblasts and ANOVA with post-hoc Dunnett's test for PCLuS (*p<0.05, **p<0.01, ***p<0.001, ****p<0.0001).

5.3.3 Investigation of IPA candidate compounds

5.3.3.1 Candidate IPA compounds in 2D primary cell model

Next, to begin investigating novel upstream regulators of fibrosis identified *via* IPA analysis (Table 22), we first sought to replicate the *in vitro* experimental design as previously described (Figure 117A). To achieve this, IPF-derived primary lung fibroblasts (n=5 donors) were seeded into 96-well cell culture plates and, once ~70% confluent, serum-starved for 24hrs prior to treatment with control media, SoC compounds, ALK5i or escalating doses (0.1µM, 1µM or 10µM) of IPA inhibitors for 24 hours (n=2 wells per condition, n=5 donors, n=10 wells total). Media was harvested at T48 and snap frozen for downstream analysis before fibroblasts were incubated with resazurin and results were normalised to % change from control fibroblasts for each donor, as previously described (Figure 128A).

Analysis of metabolic activity revealed that, though candidate IPA compounds were well tolerated at the lower 0.1µM and 1µM doses, several inhibitors resulted in >30% reduction of resazurin activity compared to control fibroblasts (in 3 or more donor lines) at the highest 10µM dose including Raloxifene (Figure 129E), Bisindolylmaleimide I (Figure 129I), Staurosporine (Figure 129O) and Napabucasin (Figure 129P). Consequently, doses/compounds which reduced metabolic activity below 70% were excluded from further analysis in relevant donor cell lines, as shown by blank values in summary tables (Figure 130B, Figure 131B).

Following this, quantification of soluble pro-fibrogenic markers was normalised to % change from control cells for each donor and used to determine potential anti-fibrotic effects of IPA compounds. Consistent with previous *in vitro* findings, there was no observed reduction in soluble collagen 1α1 in response to challenge with lower 0.1µM and 1µM doses of candidate compounds (Figure 130A, B). However, there was a significant reduction with Tyrphostin AG490 ($p<0.05$) and Rapamycin ($p<0.05$) when treated at the highest 10µM dose. (Figure 130D). Similarly, TIMP-1 secretion remained comparable to control fibroblasts in response to the lower doses of each inhibitor but was significantly reduced after 24-hour challenge with the highest dose of Mifepristone ($p<0.05$), Rapamycin ($p<0.001$) and Nelfanivir ($p<0.0001$) (Figure 131D).

Taken together these data show the limited ability of the compounds identified through IPA to inhibit the secretion of pro-fibrotic proteins in 2D fibroblast cultures. Whilst we

demonstrated that a large number of the compounds tested were well tolerated in the 2D culture system, only 4 compounds were able to attenuate secretion of fibrosis markers (Collagen 1α1 and TIMP-1), which needed to be applied at the high dose of 10μM to elicit a beneficial response.

A)

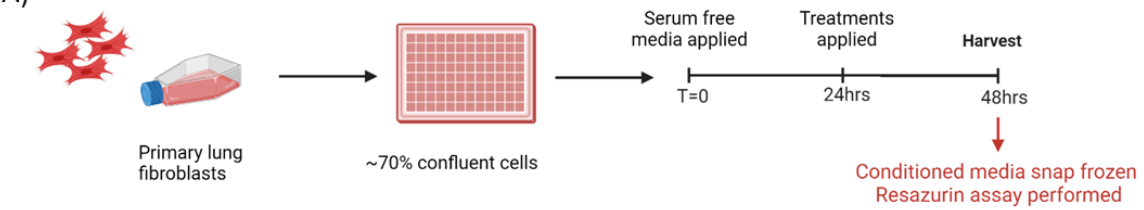

B)

Resazurin- 2D primary fibroblasts

Compound name	0.1µM					1µM					10µM				
	Donor 1	Donor 2	Donor 3	Donor 4	Donor 5	Donor 1	Donor 2	Donor 3	Donor 4	Donor 5	Donor 1	Donor 2	Donor 3	Donor 4	Donor 5
Tyrphostin AG490	98	96	101	96	124	92	107	104	107	104	84	85	81	85	86
GW9662	103	103	99	103	113	95	105	101	105	103	82	91	91	91	94
T-5224	100	136	116	136	137	94	109	99	109	125	87	98	95	98	104
Gefitinib	114	96	119	96	135	94	97	111	97	148	89	71	89	71	89
Raloxifene	100	91	124	91	151	93	86	119	86	140	30	24	28	24	31
Wortmannin	115	98	96	98	110	99	113	138	113	126	110	91	122	91	113
Lactacystin	97	116	121	116	117	92	107	145	107	114	88	83	118	83	96
Imatinib	113	95	93	95	94	92	99	108	99	85	76	72	94	72	63
Bisindolylmaleimide I	96	110	96	110	87	76	75	97	75	68	58	62	76	62	51
Mifepristone	104	100	92	100	110	85	93	96	93	86	72	73	89	73	64
PLX5622	90	102	92	102	101	84	115	111	115	82	77	88	80	88	64
Pyrrolidine Dithiocarbamate	120	102	96	102	158	121	104	96	104	141	116	88	98	88	170
Entinostat	110	112	88	112	116	110	109	90	109	118	102	95	75	95	94
Rapamycin	93	116	81	116	122	129	122	87	122	111	96	83	75	83	85
Staurosporine	90	94	59	94	94	95	82	65	82	77	69	47	45	47	46
Napabucasin	125	120	99	120	142	128	126	103	126	122	26	43	24	43	69
Nelfinavir	105	107	89	107	142	102	107	94	107	128	88	78	74	78	80
Budesonide	76	82	82	82	118	72	77	70	77	100	69	66	74	66	97

Figure 128: Validation of IPF-derived primary fibroblast viability after IPA inhibitor challenge A) IPF-derived primary lung fibroblasts (n=5 donors) were seeded into 96-well cell culture plates and, once ~70% confluent, serum-starved for 24 hours prior to treatment with control media, standard of care compounds Pirfenidone (2.5mM) and Nintedanib (2.5µM), ALK5i (10µM) or escalating doses (0.1µM, 1µM or 10µM) of IPA inhibitors for 24 hours (n=2 wells per condition, n=5 donors, n=10 wells total). Media was harvested at T48 and snap frozen for downstream analysis before fibroblasts were incubated with resazurin as an indicator of metabolic activity. B) Resazurin was normalised to % of control fibroblasts for each donor (green values indicate resazurin values ≥70% of control, yellow 50-69% of control and orange/red <50% of control).

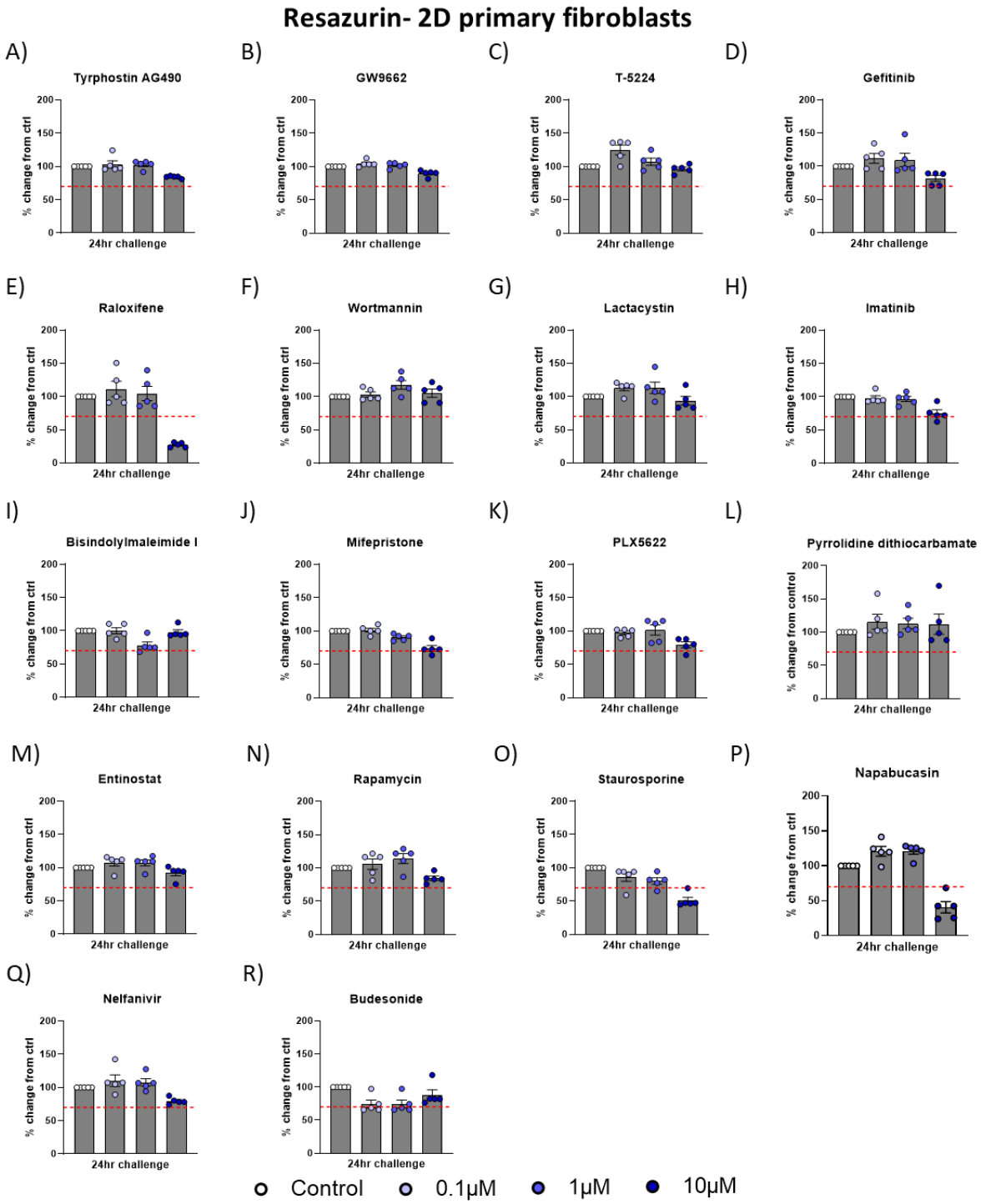

Figure 129: Validation of IPF-derived primary fibroblast viability after IPA inhibitor challenge Graphs of each IPA inhibitor resazurin (n=2 wells per donor, n=5 donors, n=10 samples total) normalised to average % change from control fibroblasts for each donor line (where red dashed line represents arbitrary 70% viability threshold). All data are mean ± SEM.

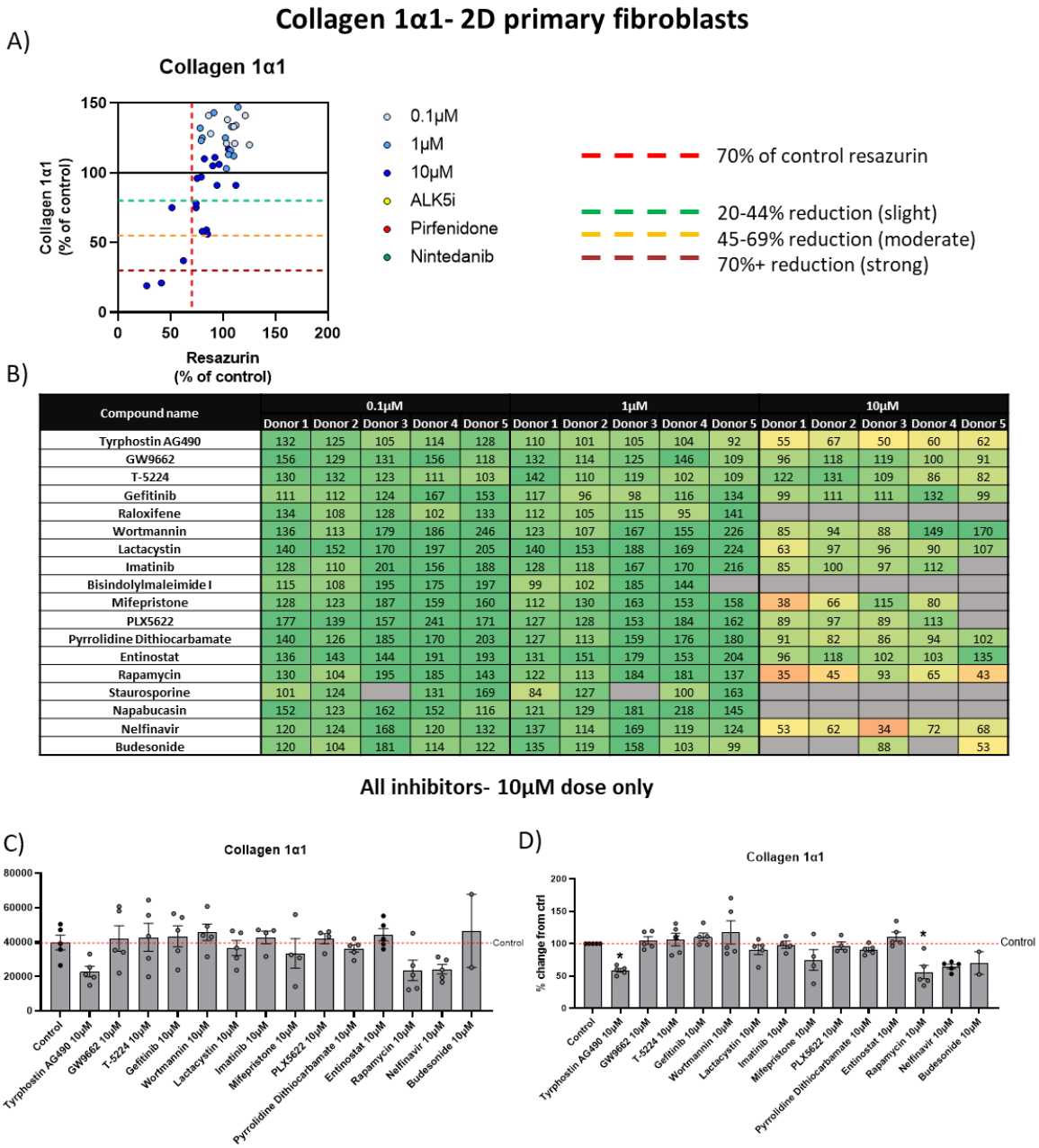

B)

Compound name	0.1μM					1μM					10μM				
	Donor 1	Donor 2	Donor 3	Donor 4	Donor 5	Donor 1	Donor 2	Donor 3	Donor 4	Donor 5	Donor 1	Donor 2	Donor 3	Donor 4	Donor 5
Tyrphostin AG490	132	125	105	114	128	110	101	105	104	92	55	67	50	60	62
GW9662	156	129	131	156	118	132	114	125	146	109	96	118	119	100	91
T-5224	130	132	123	111	103	142	110	119	102	109	122	131	109	86	82
Gefitinib	111	112	124	167	153	117	96	98	116	134	99	111	111	132	99
Raloxifene	134	108	128	102	133	112	105	115	95	141					
Wortmannin	136	113	179	186	246	123	107	167	155	226	85	94	88	149	170
Lactacystin	140	152	170	197	205	140	153	188	169	224	63	97	96	90	107
Imatinib	128	110	201	156	188	128	118	167	170	216	85	100	97	112	
Bisindolylmaleimide I	115	108	195	175	197	99	102	185	144						
Mifepristone	128	123	187	159	160	112	130	163	153	158	38	66	115	80	
PLX5622	177	139	157	241	171	127	128	153	184	162	89	97	89	113	
Pyrrolidine Dithiocarbamate	140	126	185	170	203	127	113	159	176	180	91	82	86	94	102
Entinostat	136	143	144	191	193	131	151	179	153	204	96	118	102	103	135
Rapamycin	130	104	195	185	143	122	113	184	181	137	35	45	93	65	43
Staurosporine	101	124		131	169	84	127		100	163					
Napabucasin	152	123	162	152	116	121	129	181	218	145					
Nelfinavir	120	124	168	120	132	137	114	169	119	124	53	62	34	72	68
Budesonide	120	104	181	114	122	135	119	158	103	99			88		53

Figure 130: Quantification of secreted Collagen 1α1 from IPF-derived primary fibroblasts after IPA inhibitor challenge Collagen 1α1 secretion was quantified *via* ELISA after 24-hour IPA inhibitor challenge (n=5 donors, n=2 wells per donor, n=10 samples total) and presented as A) XY graphs depicting resazurin (normalised to control fibroblasts) as a measure of tissue viability vs average % reduction of collagen 1α1 (compared to control fibroblasts) in response to 0.1μM, 1μM or 10μM of each IPA inhibitor. Red dashed vertical line at 70% denotes viability threshold (30% reduction compared to control fibroblasts). Dashed lines crossing y-axis mark 20% reduction (green), 45% reduction (orange) and 70% reduction (dark red) compared to collagen 1α1 secretion from control fibroblasts (solid black line). B) Collagen 1α1 values normalised to control fibroblasts for each donor and presented as % of control. Blank values represent results excluded from further analysis due to resazurin falling below viability threshold (<70% of control fibroblasts). The 10μM dose of all candidate compounds were plotted as C) average absolute pg/ml per donor and D) average% change from control fibroblasts where red dashed line denotes unchallenged control fibroblasts. All data are mean ± SEM. Statistical significance was determined using Kruskal-Wallis with post-hoc Dunn's multiple comparisons test (*p<0.05, **p<0.01, ***p<0.001, ****p<0.0001).

A)

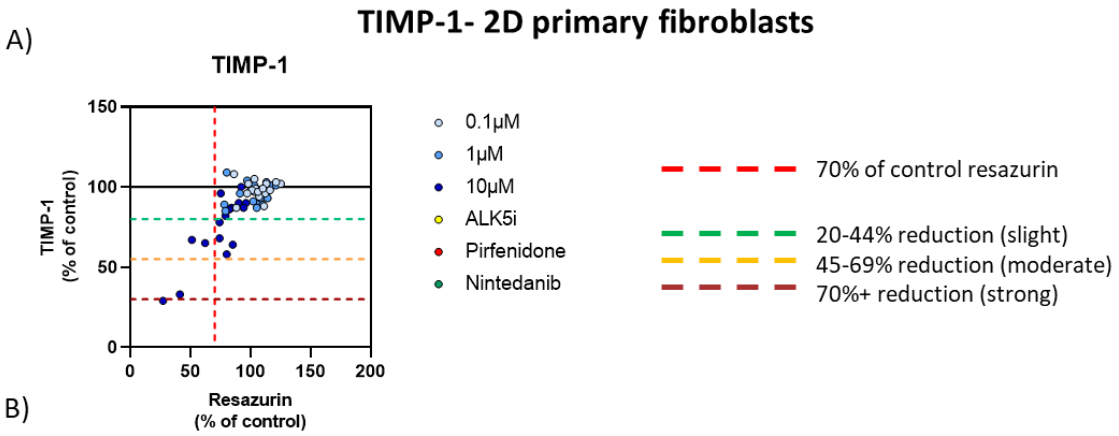

B)

Compound name	0.1µM					1µM					10µM				
	Donor 1	Donor 2	Donor 3	Donor 4	Donor 5	Donor 1	Donor 2	Donor 3	Donor 4	Donor 5	Donor 1	Donor 2	Donor 3	Donor 4	Donor 5
Tyrphostin AG490	94	103	88	102	100	95	109	97	110	92	81	84	76	103	89
GW9662	101	106	82	110	96	98	101	96	103	94	82	90	92	96	90
T-5224	123	105	84	108	92	91	94	86	95	91	86	84	88	98	92
Gefitinib	87	103	93	105	92	86	86	86	97	91	78	82	81	102	84
Raloxifene	65	91	83	108	94	69	80	97	102	88					
Wortmannin	112	92	93	118	109	99	95	98	113	101	100	94	83	114	99
Lactacystin	97	94	95	113	109	94	98	108	110	105	86	89	71	99	90
Imatinib	110	81	103	111	106	109	85	104	114	108	107	98	74	98	
Bisindolylmaleimide I	82	84	106	109	110	75	92	78	94						
Mifepristone	84	89	98	113	105	69	92	106	107	106	55	76	75	91	
PLX5622	96	75	97	107	105	92	78	96	100	90	73	77	78	93	
Pyrrolidine Dithiocarbamate	87	84	108	108	104	70	91	102	109	100	84	105	93	96	99
Entinostat	80	85	92	113	98	81	89	100	102	101	93	98	106	105	96
Rapamycin	75	94	116	105	95	77	91	115	94	89	48	61	82	69	58
Staurosporine	98	99		123	104	101	109		116	106					
Napabucasin	111	117	84	109	97	89	111	97	106	102					
Nelfinavir	88	106	93	108	99	85	107	94	81	96	36	65	63	65	62
Budesonide	79	85	93	82	99	78	89	85	84	89			63		74

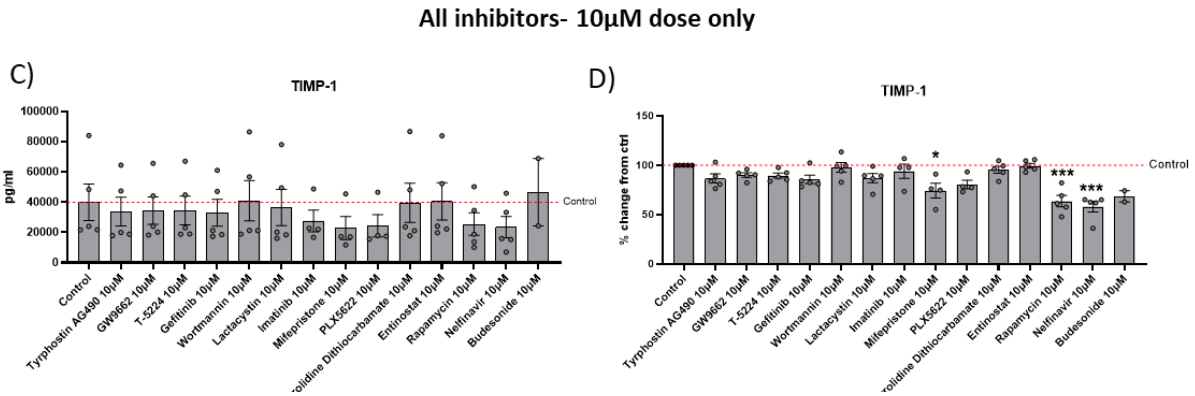

Figure 131: Quantification of secreted TIMP-1 from IPF-derived primary fibroblasts after IPA inhibitor challenge TIMP-1 secretion was quantified *via* ELISA after 24-hour IPA inhibitor challenge (n=5 donors, n=2 wells per donor, n=10 samples total) and presented as A) XY graphs depicting resazurin (normalised to control fibroblasts) as a measure of tissue viability vs average % reduction of TIMP-1 (compared to control fibroblasts) in response to 0.1µM, 1µM or 10µM of each IPA inhibitor. Red dashed vertical line at 70% denotes viability threshold (30% reduction compared to control fibroblasts). Dashed lines crossing y-axis mark 20% reduction (green), 45% reduction (orange) and 70% reduction (dark red) compared to TIMP-1 secretion from control fibroblasts (solid black line). B) TIMP-1 values normalised to control fibroblasts for each donor and presented as % of control. Blank values represent results excluded from further analysis due to resazurin falling below viability threshold (<70% of control fibroblasts). The 10µM dose of all candidate compounds were plotted as C) average absolute pg/ml per donor and D) average% change from control fibroblasts where red dashed line denotes unchallenged control fibroblasts. All data are mean ± SEM. Statistical significance was determined using Kruskal-Wallis with post-hoc Dunn's multiple comparisons test (*p<0.05, **p<0.01, ***p<0.001, ****p<0.0001).

5.3.3.2 Candidate IPA compounds in PCLuS human tissue model

To further investigate IPA candidate compounds in more advanced models of disease, PCLuS were generated from explant IPF tissue (n=4 donors) with slices being rested for 48 hours before challenge with either control media, SoC compounds or ALK5i to blunt fibrosis (n=10 PCLuS per condition, n=4 donors, n=40 PCLuS total). Concurrently, PCLuS were challenged with 3 escalating doses (0.1µM, 1µM and 10µM) of each candidate IPA compound to assess the ability to reduce pre-existing fibrosis (n=6 PCLuS per condition, n=4 donors, n=24 PCLuS total). Media, including all treatments, was refreshed at 24-hour intervals with conditioned media snap frozen for downstream analysis before PCLuS were harvested at 144hrs for resazurin assay and results normalised to % change from control PCLuS (Figure 132A). Next, soluble collagen 1α1, TIMP-1 and IL-8 was quantified in the conditioned media of the final timepoint of culture as previously described (absolute pg/ml values available in Appendix G; Figures 5-8).

Prior to assessment of IPA inhibitors, validation of SoC compounds was performed to confirm effective modulation of IPF donor tissue and suitability for further analysis. Evaluation of resazurin and soluble fibrotic and inflammatory marker secretion established that all donors were responsive to anti-fibrotic compounds (Figure 132B) and could therefore be used to screen candidate IPA compounds. Following this, review of tissue viability at the end of culture identified a number of compounds/doses which were deemed to negatively impact tissue viability (>30% reduction resazurin compared to control PCLuS) and were subsequently excluded from downstream analysis (Figure 133A). These included, 10µM doses of Pyrrolidine dithiocarbamate and Napabucasin (Figure 133B, F), 1µM and 10µM Rapamycin (Figure 133D) and all doses of Entinostat and Staurosporine (Figure 133C, E).

Subsequent interrogation of compound efficacy in viable inhibitors/doses identified several candidate compounds which were able to significantly attenuate collagen 1α1 secretion after 96-hours treatment (normalised to T48 baseline secretion) including 10µM Tyrphostin AG490 ($p<0.0001$), Gefitinib (0.1µM ($p<0.05$), 1µM ($p<0.05$) and 10µM ($p<0.0001$), Wortmannin (0.1µM ($p<0.01$), 1µM ($p<0.0001$) and 10µM ($p<0.0001$), Lactacystin 1µM ($p<0.001$) and 10µM ($p<0.0001$) and 0.1µM Rapamycin ($p<0.0001$) (Figure 134). To investigate this further and account for donor heterogeneity, results were then normalised to % change in protein secretion compared to control PCLuS for each IPF donor (Figure 135A). Average viability and

efficacy of all 4 donors was summarised as previously described and confirmed that 12 of the 18 compounds identified were able to reduce collagen 1α1 secretion by more than 20% at varying doses (Figure 135B, C). Of these, 6 compounds demonstrated strong anti-fibrotic effects with more than 70% reduction in soluble collagen 1α1 compared to unchallenged tissue, including 10µM Tyrphostin A490 (72% reduction from control PCLuS), 10µM Gefitinib (70% reduction from control PCLuS), 1µM and 10µM Wortmannin (70% and 90% reduction from control PCLuS, respectively), 0.1µM Rapamycin (89% reduction from control PCLuS), 10µM Lactacystin (91% reduction from control PCLuS) and 10µM Nelfanivir (71% reduction from control PCLuS). Notably, these results confirmed that several IPA compounds were able to significantly reduce collagen 1α1 secretion more effectively than ALK5i (77% reduction from control PCLuS) and current SoC therapeutics Pirfenidone (68% reduction from control PCLuS), Nintedanib (70% reduction from control PCLuS).

Consistent with these results, quantification of soluble TIMP-1 further confirmed that Tyrphostin AG490 (1µM $p<0.01$ and 10µM $p<0.0001$), Gefitinib 0.1µM ($p<0.01$), 1µM and 10µM ($p<0.0001$), Wortmannin (1µM [$p<0.05$] and 10µM [$p<0.0001$]), Rapamycin (0.1µM [$p<0.0001$]), Lactacystin 10µM ($p<0.0001$), and Nelfanivir (0.1µM [$p<0.05$] and 10µM [$p<0.0001$]) were also able to significantly attenuate TIMP-1 secretion throughout the culture period. Additionally, PCLuS challenged with 10µM Bisindolylmaleimide I, 10µM PLX5622 and all doses of Budesonide were also found to significantly reduce TIMP-1 secretion after 96-hours treatment (Figure 136). Once normalised to % change from control PCLuS, analysis of average efficacy showed that the 10µM doses of Lactacystin (75% reduction from control PCLuS), Gefitinib (66% reduction from control PCLuS) and Nelfanivir (61% reduction from control PCLuS) were all able to reduce TIMP-1 secretion more than Pirfenidone (34% reduction from control PCLuS), Nintedanib (59% reduction from control PCLuS) and ALK5i (50% reduction from control PCLuS), with the remaining efficacious compounds/doses falling into the slight-moderate reduction classification (Figure 137).

Finally, after normalisation to baseline secretion, measurement of soluble IL-8 was used to evaluate potential anti-inflammatory effects of IPA inhibitors. Results found that Gefitinib demonstrated the most significant reduction in IL-8 at 0.1µM ($p=0.053$), 1µM ($p<0.001$) and 10µM ($p<0.0001$) (Figure 138D), followed by 0.1µM Bisindolylmaleimide I ($p<0.001$) and 1µM Raloxifene ($p<0.05$) (Figure 138E, I). Notably, several compounds were also shown to

significantly increase secretion of IL-8, including 10µm Wortmannin ($p<0.0001$), 10µM Lactacystin ($p<0.0001$), 1µM and 10µM Mifepristone ($p<0.0001$) and 1µM Napabucasin ($p<0.05$), suggesting that treatment with these inhibitors stimulated a pro-inflammatory response. Following this, average efficacy of each donor was normalised to % change from control PCLuS (Figure 139A) and results confirmed that Gefitinib was the most potent anti-inflammatory compound (0.1µM (30% reduction from control PCLuS), 1µM (58% reduction from control PCLuS) and 10µM (77% reduction from control PCLuS)). Indeed, 10µM Gefitinib-challenged PCLuS were comparable to treatment with Nintedanib (70% reduction from control PCLuS) and ALK5i (63% reduction from control PCLuS). However, Pirfenidone remained the most potent anti-inflammatory compound with an 83 % reduction in IL-8 secretion compared to control PCLuS (Figure 138B, C).

Overall, we identified n=8 IPA compounds which exhibited promising anti-fibrotic effects and n=7 compounds with anti-inflammatory effects in our PCLuS system. Moreover, we found several inhibitors which were able to reduce secretion of at least one pro-fibrogenic marker more effectively than current SoC compounds.

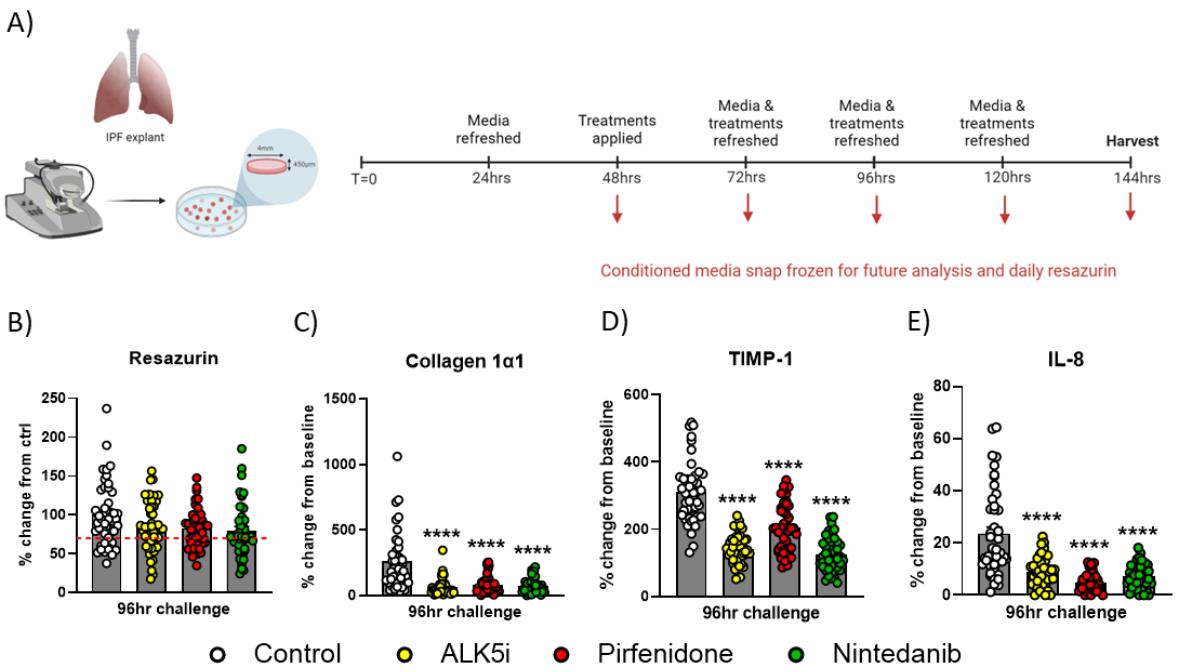

Figure 132: Validation of IPF-derived PCLuS donors for assessment of IPA compounds PCLuS were generated from explant IPF tissue (n=4 donors) with slices (n=6 per condition) being rested for 48 hours before challenge with either control media, standard of care compounds Pirfenidone (2.5mM) and Nintedanib (2.5µM) or ALK5i (10µM) to blunt fibrosis (n=10 PCLuS per condition, n=4 donors, n=40 PCLuS total). Concurrently, PCLuS were challenged with 3 escalating doses (0.1µM, 1µM and 10µM) of each candidate IPA compound to assess the ability to reduce pre-existing fibrosis (n=6 PCLuS per condition, n=4 donors, n=24 PCLuS total). Media, including all treatments, was refreshed at 24-hour intervals with conditioned media snap frozen for downstream analysis before PCLuS were harvested at 144hrs for resazurin assay as an indicator of tissue viability. Quantification of B) Resazurin (where red dashed line represents arbitrary 70% viability threshold) and C) Collagen 1α1, D) TIMP-1 and E) IL-8 was performed on T144 media *via* ELISA and plotted as average % change from baseline (T48 unstimulated PCLuS) (n=6 conditioned media per donor, n=4 donors, n=24 samples total) to confirm tissue could be effectively modulated. All data are mean ± SEM. Statistical significance was determined using ANOVA with post-hoc Dunnett's test (*p<0.05, **p<0.01, ***p<0.001, ****p<0.0001).

A)

Resazurin- IPF-derived PCLuS

Compound Name	0.1µM				1µM				10µM			
	Donor 1	Donor 2	Donor 3	Donor 4	Donor 1	Donor 2	Donor 3	Donor 4	Donor 1	Donor 2	Donor 3	Donor 4
Tyrphostin AG490	78	77	132	114	92	100	120	106	75	72	114	120
GW9662	80	100	89	137	78	92	90	107	94	93	82	115
T-5224	88	100	121	127	69	97	124	116	90	89	113	101
Gefitinib	104	89	139	146	88	73	71	91	72	50	56	80
Raloxifene	86	91	129	105	74	88	116	132	86	63	100	139
Wortmannin	86	63	100	139	78	69	95	79	63	52	79	90
Lactacystin	73	106	115	116	76	81	103	117	79	50	85	114
Imatinib	88	103	112	164	75	84	106	115	89	86	102	137
Bisindolylmaleimide I	80	52	74	92	72	96	104	143	80	74	83	88
Mifepristone	71	113	91	139	79	114	111	136	72	114	90	116
PLX5622	77	85	105	62	74	67	98	139	72	61	82	121
Pyrrolidine Dithiocarbamate	79	79	72	101	82	97	91	98	77	88	15	60
Entinostat	57	21	84	147	48	22	32	39	40	7	13	88
Rapamycin	70	63	80	85	63	58	44	89	57	34	43	72
Staurosporine	62	32	48	76	44	4	23	57	35	6	12	18
Napabucasin	83	81	104	158	65	61	111	110	22	3	4	36
Nelfanivir	71	64	97	185	87	86	124	125	84	62	71	135
Budesonide	59	56	67	104	73	76	78	82	77	72	88	117

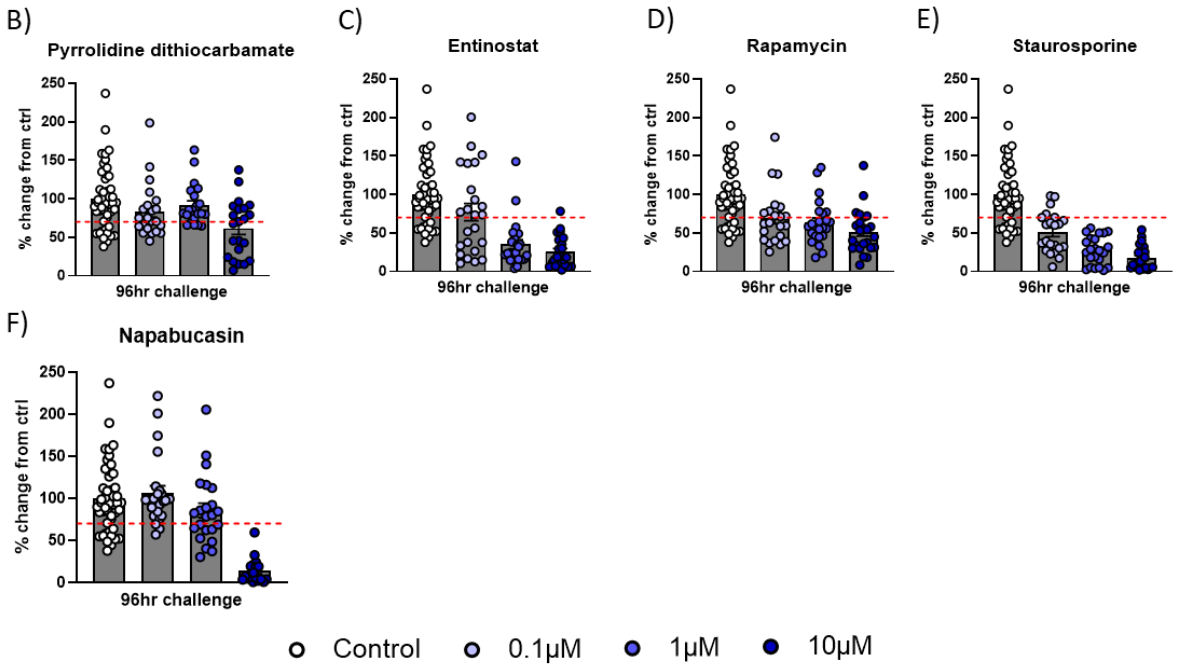

Figure 133: Validation of IPF-derived PCLuS viability in response to IPA compounds A) Resazurin assay performed at T144 presented as the average % of control (n=6 slices) per treatment for each donor. PCLuS were plotted as average % change from baseline (T48 unstimulated PCLuS) (n=6 PCLuS per donor, n=4 donors, n=24 samples total) to confirm metabolic activity of tissue after culture (green values indicate resazurin values ≥70% of control, yellow 50-69% of control and orange/red <50% of control). Quantification of resazurin (where red dashed line represents arbitrary 70% viability threshold) identified several compounds/doses which fell below the 70% viability threshold resulting in exclusion from further analysis including B) Pyrrolidine dithiocarbamate (10µM dose), C) Entinostat, D) Rapamycin (1µM and 10µM dose), E) Staurosporine and F) Napabucasin (10µM dose). All data are mean ± SEM.

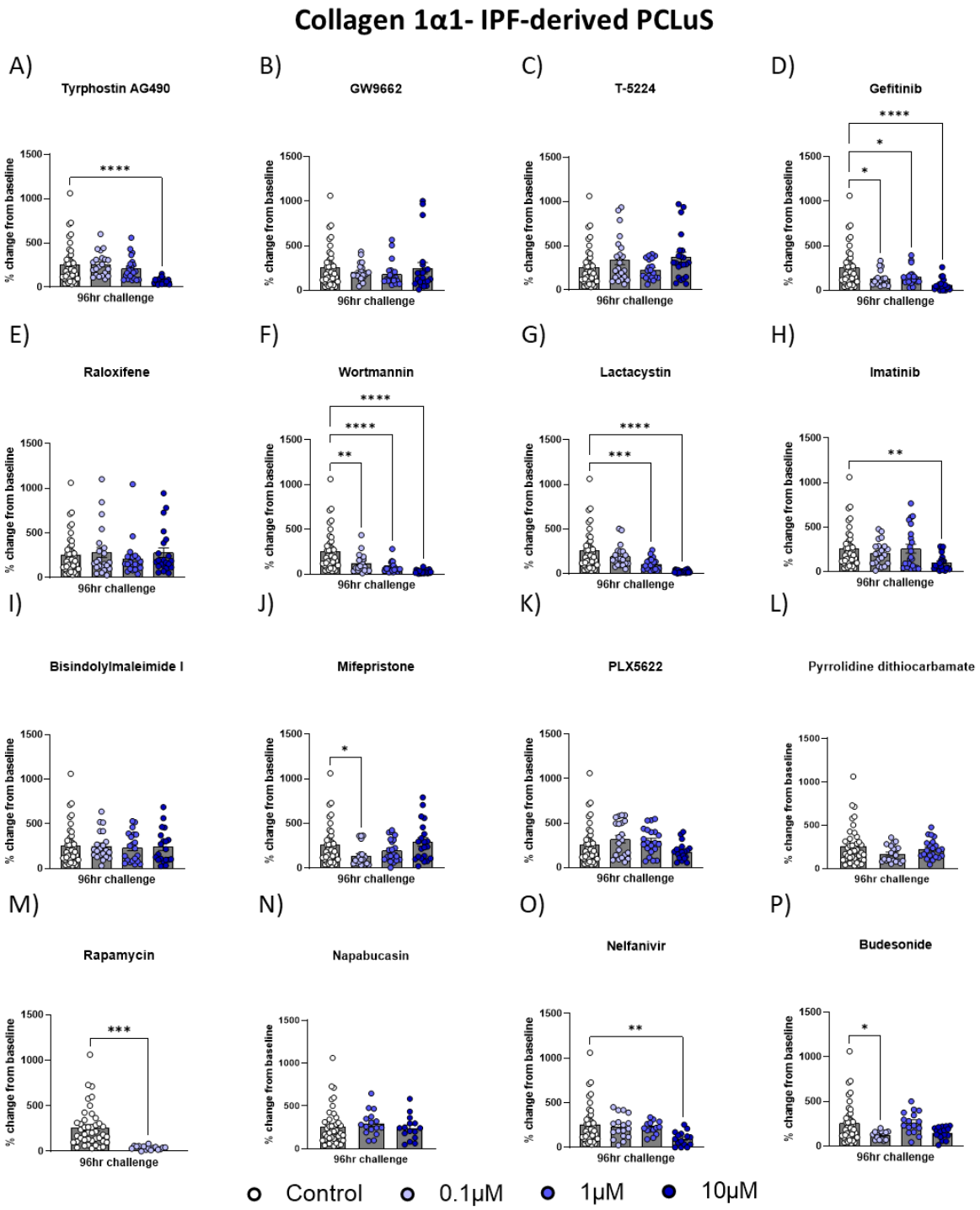

Figure 134: Validation of collagen 1α1 secretion in IPA compound- challenged PCLuS PCLuS were generated from explant IPF tissue (n=4 donors) with slices (n=6 per condition) being rested for 48 hours before challenge with either control media or 3 escalating doses (0.1μM, 1μM and 10μM) of each IPA compound to assess the ability to reduce pre-existing fibrosis (n=6 PCLuS per condition, n=4 donors, n=24 PCLuS total). Media, including all treatments, was refreshed at 24-hour intervals with conditioned media snap frozen for downstream analysis before PCLuS were harvested at 144hrs for resazurin assay. Quantification of secreted collagen 1α1 was performed on T144 media *via* ELISA and plotted as average % change from baseline (T48 unstimulated PCLuS) (n=6 conditioned media per donor, n=4 donors, n=24 samples total) to assess potential anti-fibrotic affects. All data are mean ± SEM. Statistical significance was determined using ANOVA with post-hoc Dunnett's test (*p<0.05, **p<0.01, ***p<0.001, ****p<0.0001).

A)

Collagen 1α1- IPF-derived PCLuS

Compound Name	0.1µM				1µM				10µM			
	Donor 1	Donor 2	Donor 3	Donor 4	Donor 1	Donor 2	Donor 3	Donor 4	Donor 1	Donor 2	Donor 3	Donor 4
Tyrphostin AG490	64	105	100	166	75	67	101	75	20	16	42	34
GW9662	52	63	85	150	82	66	51	80	139	25	101	100
T-5224	142	112	106	142	58	98	96	128	137	111	174	133
Gefitinib	16	68	83	80	28	79	53	94	12	30	21	44
Raloxifene	124	95	108	80	92	86	86	71	136	90	83	72
Wortmannin	34	72	45	42	20	25	37	38	8	11	5	15
Lactacystin	71	63	90	105	23	31	73	65	8	9	10	9
Imatinib	41	110	102	95	65	166	76	67	8	45	73	63
Bisindolylmaleimide I	73	109	105	99	73	100	128	66	96	52	152	79
Mifepristone	12	72	108	71	63	51	116	97	103	124	95	120
PLX5622	108	96	180	103	90	130	155	88	59	65	78	66
Pyrrolidine Dithiocarbamate	41	74	66	95	51	103	110	96				
Entinostat												
Rapamycin	8	13	12									
Staurosporine												
Napabucasin	79	114	81		52	90	111					
Nelfanivir	36	105	94		55	70	79		31	20	36	
Budesonide	21	52	63		72	73	117		29	51	83	

B)

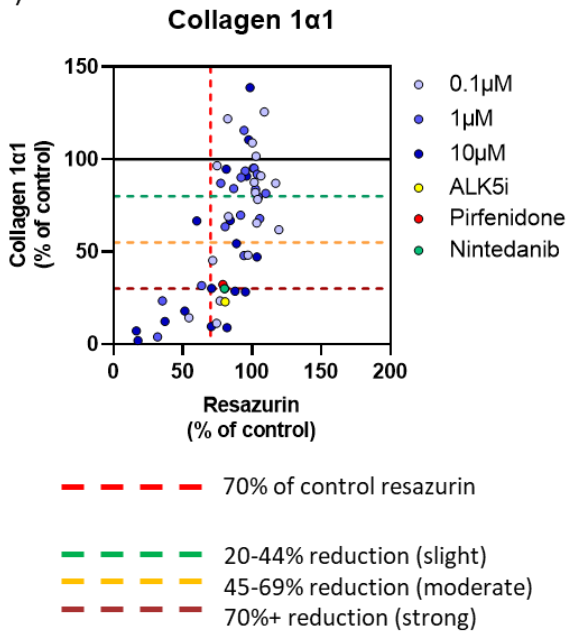

C)

Compound	0.1µM	1µM	10µM
Tryphostin AG90		✓	✓✓✓
GW9662		✓	
T-5224			
Gefitinib	✓	✓	✓✓✓
Raloxifene			
Wortmannin	✓✓	✓✓✓	✓✓✓
Lactacystin		✓✓	✓✓✓
Imatinib			✓✓
Bisindolylmaleimide I			
Mifepristone	✓		
PLX5622			✓
Pyrrolidine dithiocarbamate	✓		
Etinostat			
Rapamycin	✓✓✓		
Staurosporine			
Napabucasin			
Nelfinavir	✓	✓	✓✓✓
Budesonide	✓✓		✓✓

Figure 135: Normalised collagen 1α1 secretion in IPA compound- challenged PCLuS Quantification of collagen 1α1, previously normalised to % change from baseline (T48 unstimulated PCLuS) was further normalised to A) % change from control PCLuS at T144 for each explant IPF donor to allow assessment of % reduction of collagen 1α1 in response to 96-hour IPA compound challenge. B) XY graphs depict resazurin (normalised to control PCLuS) as a measure of tissue viability vs average % reduction of collagen 1α1 (n=4 donors) in response to 0.1µM, 1µM or 10µM of each IPA inhibitor. Red dashed vertical line at 70% denotes viability threshold (30% reduction compared to control PCLuS). Dashed lines crossing y-axis mark 20% reduction (green), 45% reduction (orange) and 70% reduction (dark red) compared to collagen 1α1 secretion from control slices (solid black line) C) Average % reduction of collagen 1α1 (n=4 donors) summarised as one green tick for 20% reduction, two orange ticks for 45% reduction and three red ticks for 70%+ reduction in Collagen 1α1 vs control PCLuS. Blank doses represent compounds deemed to have significantly impacted tissue viability (<70% resazurin compared to control PCLuS) which were excluded from further analysis.

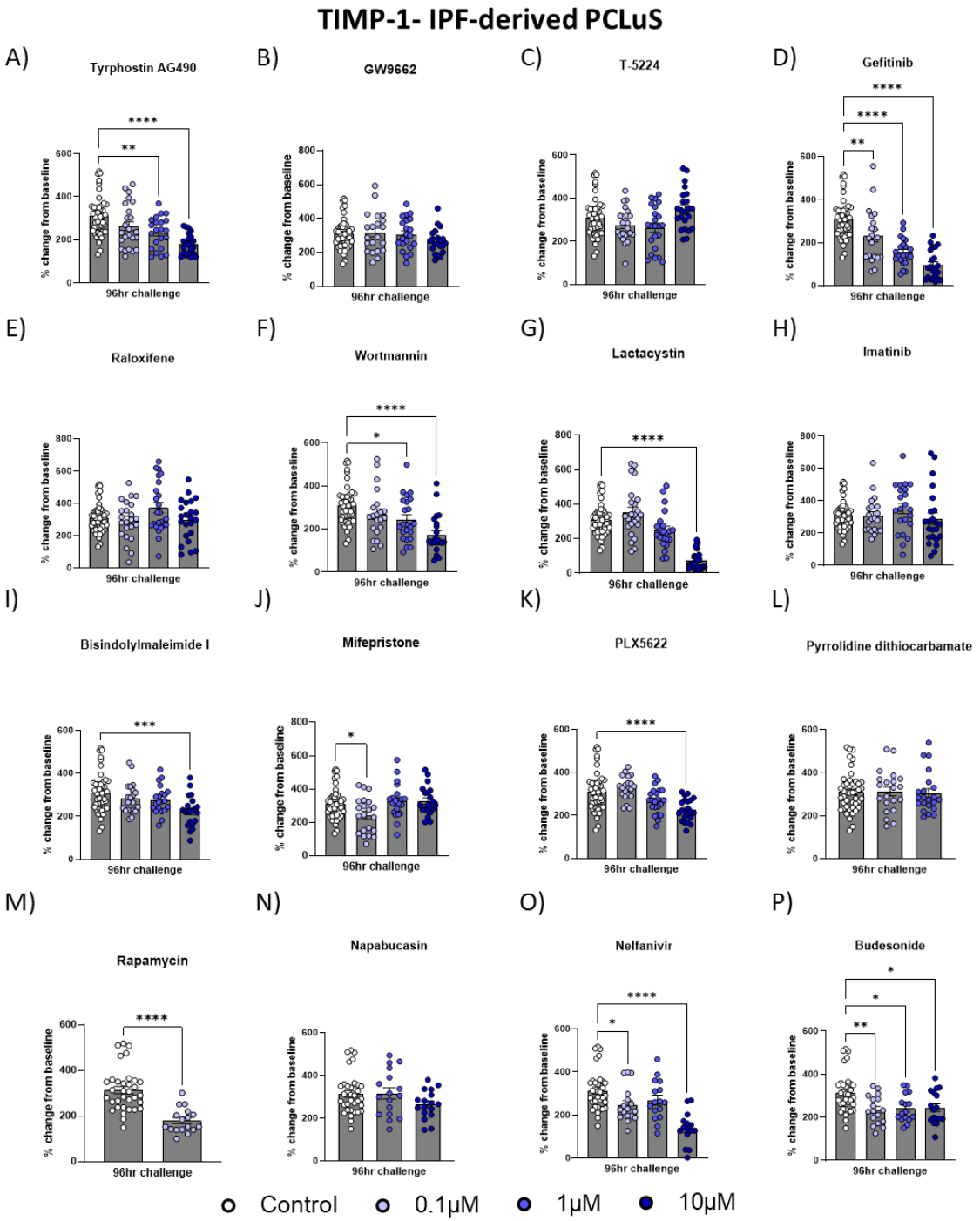

Figure 136: Validation of TIMP-1 secretion in IPA compound- challenged PCLuS PCLuS were generated from explant IPF tissue (n=4 donors) with slices (n=6 per condition) being rested for 48 hours before challenge with either control media or 3 escalating doses (0.1µM, 1µM and 10µM) of each IPA compound to assess the ability to reduce pre-existing fibrosis (n=6 PCLuS per condition, n=4 donors, n=24 PCLuS total). Media, including all treatments, was refreshed at 24-hour intervals with conditioned media snap frozen for downstream analysis before PCLuS were harvested at T144 for resazurin assay. Quantification of TIMP-1 was performed on T144 media *via* ELISA and plotted as average % change from baseline (T48 unstimulated PCLuS) (n=6 conditioned media per donor, n=4 donors, n=24 samples total) to assess potential anti-fibrotic affects. All data are mean ± SEM. Statistical significance was determined using ANOVA with post-hoc Dunnett's test (*p<0.05, **p<0.01, ***p<0.001, ****p<0.0001).

A)

TIMP-1- IPF-derived PCLuS

Compound Name	0.1µM				1µM				10µM			
	Donor 1	Donor 2	Donor 3	Donor 4	Donor 1	Donor 2	Donor 3	Donor 4	Donor 1	Donor 2	Donor 3	Donor 4
Tyrphostin AG490	97	76	54	113	60	88	69	79	48	61	56	72
GW9662	76	103	115	122	109	99	76	99	83	79	79	96
T-5224	96	87	80	93	111	84	43	106	119	112	91	123
Gefitinib	74	33	95	116	52	46	28	73	24	9	45	56
Raloxifene	115	96	80	92	156	89	148	92	126	107	57	96
Wortmannin	88	77	90	94	77	68	70	105	69	36	67	46
Lactacystin	184	97	78	98	137	68	52	69	36	10	27	27
Imatinib	112	84	112	95	128	110	76	138	81	89	113	89
Bisindolylmaleimide I	85	86	102	95	87	93	107	76	91	50	74	76
Mifepristone	40	98	86	90	97	109	109	104	117	88	106	110
PLX5622	102	96	107	119	91	96	84	76	71	75	76	69
Pyrrolidine Dithiocarbamate	111	95	89	110	106	85	90	114				
Entinostat												
Rapamycin	62	50	61	60								
Staurosporine												
Napabucasin	109	98	94		95	77	81					
Nelfanivir	104	65	74		110	78	69		63	15	39	
Budesonide	74	72	80		97	61	72		88	78	65	

B)

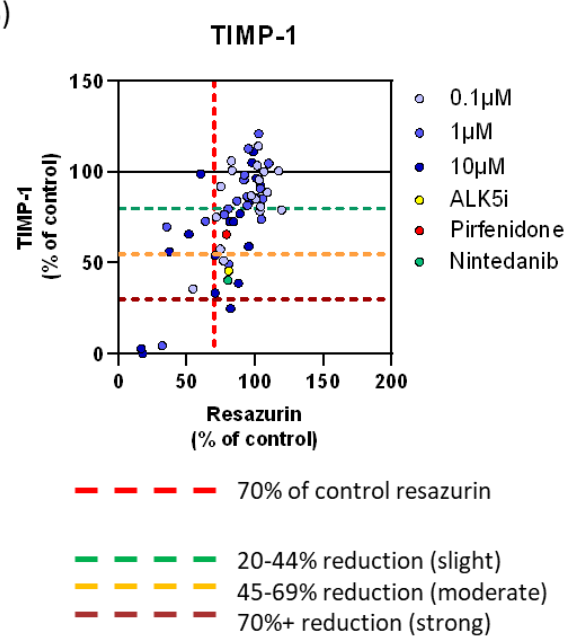

C)

Compound	0.1µM	1µM	10µM
Tyrphostin AG90		✓	✓
GW9662			
T-5224			
Gefitinib	✓	✓✓	✓✓
Raloxifene			
Wortmannin		✓	✓✓
Lactacystin			✓✓✓
Imatinib			
Bisindolylmaleimide I			✓
Mifepristone	✓		
PLX5622			✓
Pyrrolidine dithiocarbamate			
Entinostat			
Rapamycin	✓		
Staurosporine			
Napabucasin			
Nelfinavir			✓✓
Budesonide	✓	✓	✓

Figure 137: Normalised TIMP-1 secretion in IPA compound- challenged PCLuS Quantification of TIMP-1, previously normalised to % change from baseline (T48 unstimulated PCLuS) was further normalised to A) % change from control PCLuS at T144 for each explant IPF donor to allow assessment of % reduction of TIMP-1 in response to 96-hour IPA compound challenge. B) XY graphs depict resazurin (normalised to control PCLuS) as a measure of tissue viability vs average % reduction of TIMP-1 (n=4 donors) in response to 0.1µM, 1µM or 10µM of each IPA inhibitor. Red dashed vertical line at 70% denotes viability threshold (30% reduction compared to control PCLuS). Dashed lines crossing y-axis mark 20% reduction (green), 45% reduction (orange) and 70% reduction (dark red) compared to TIMP-1 secretion from control slices (solid black line) C) Average % reduction of TIMP-1 (n=4 donors) summarised as one green tick for 20% reduction, two orange ticks for 45% reduction and three red ticks for 70%+ reduction in TIMP-1 vs control PCLuS. Blank doses represent compounds deemed to have significantly impacted tissue viability (<70% resazurin compared to control PCLuS) which were excluded from further analysis.

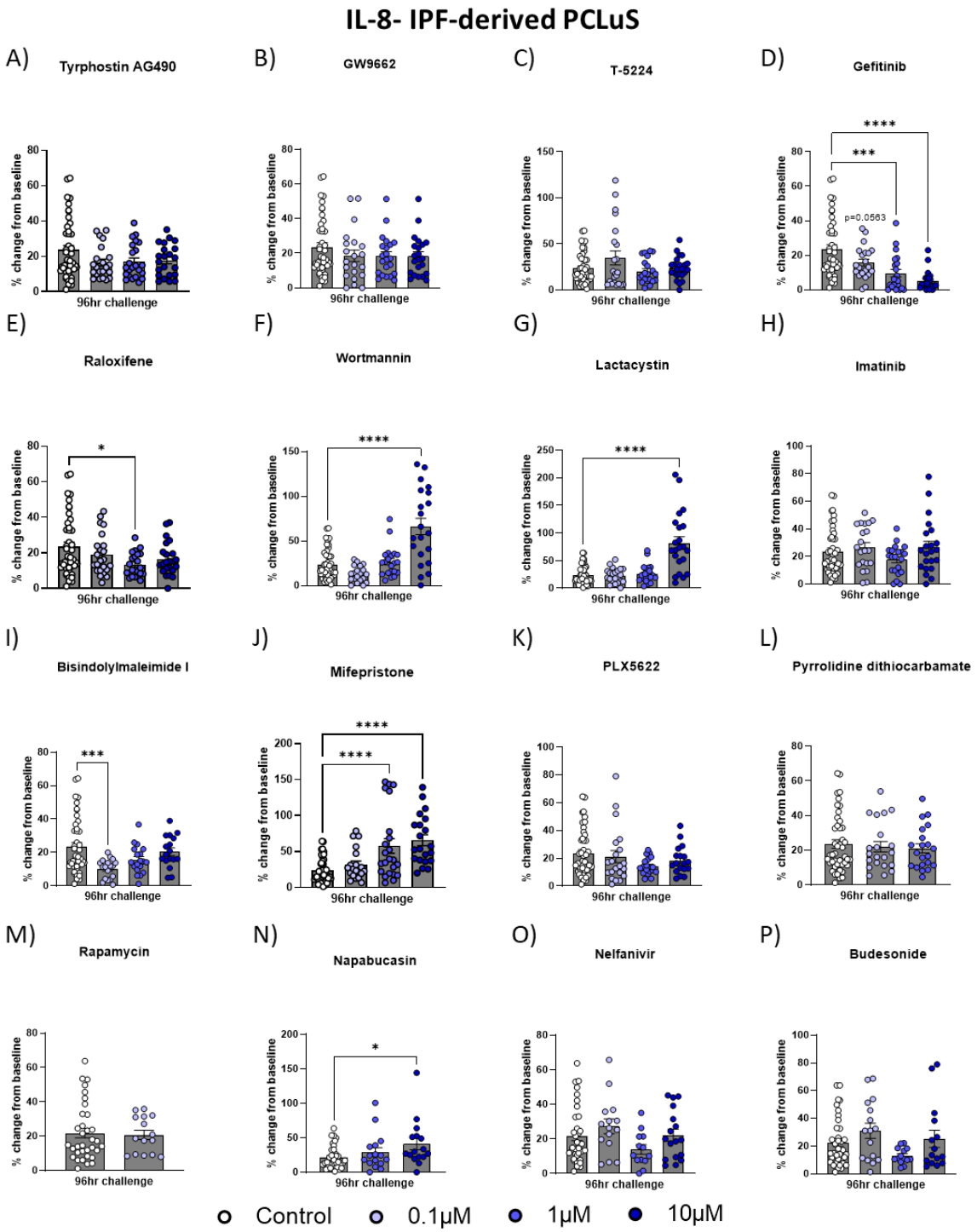

Figure 138: **Validation of IL-8 secretion in IPA compound- challenged PCLuS** PCLuS were generated from explant IPF tissue (n=4 donors) with slices (n=6 per condition) being rested for 48 hours before challenge with either control media or 3 escalating doses (0.1μM, 1μM and 10μM) of each IPA compound to assess the ability to reduce pre-existing inflammation (n=6 PCLuS per condition, n=4 donors, n=24 PCLuS total). Media, including all treatments, was refreshed at 24-hour intervals with conditioned media snap frozen for downstream analysis before PCLuS were harvested at 144hrs for resazurin assay. Quantification of IL-8 was performed on T144 media *via* ELISA and plotted as average % change from baseline (T48 unstimulated PCLuS) (n=6 conditioned media per donor, n=4 donors, n=24 samples total) to assess potential anti-inflammatory affects. All data are mean ± SEM. Statistical significance was determined using ANOVA with post-hoc Dunnett's test (*p<0.05, **p<0.01, ***p<0.001, ****p<0.0001).

A)

IL-8- IPF-derived PCLuS

Compound Name	0.1µM				1µM				10µM			
	Donor 1	Donor 2	Donor 3	Donor 4	Donor 1	Donor 2	Donor 3	Donor 4	Donor 1	Donor 2	Donor 3	Donor 4
Tyrphostin AG490	53	53	111	64	66	68	125	48	62	107	68	71
GW9662	64	83	125	63	67	68	110	73	67	68	110	73
T-5224	150	47	333	114	58	115	104	77	93	131	95	87
Gefitinib	95	31	100	55	27	3	75	63	22	38	19	13
Raloxifene	100	58	91	76	37	48	75	71	47	70	106	64
Wortmannin	70	38	51	61	160	106	140	75	339	440	195	166
Lactacystin	100	80	137	90	160	129	64	80	433	330	304	337
Imatinib	76	102	130	134	90	80	65	61	169	128	83	72
Bisindolylmaleimide I	54	35	49	46	56	61	89	62	120	72	86	71
Mifepristone	175	133	157	69	104	350	392	200	221	145	481	277
PLX5622	165	112	35	56	54	53	67	62	56	69	72	98
Pyrrolidine Dithiocarbamate	67	103	149	76	52	86	73	117				
Entinostat												
Rapamycin	68	133	83									
Staurosporine												
Napabucasin	92	130	208		137	262	150					
Nelfanivir	82	143	154		58	35	108		92	67	168	
Budesonide	62	187	215		54	58	64		108	88	182	

B)

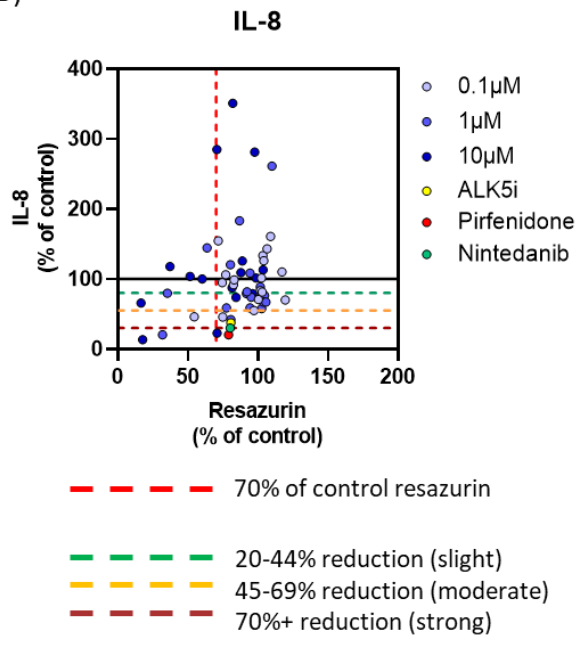

C)

Compound	0.1µM	1µM	10µM
Tyrphostin AG90	✓	✓	✓
GW9662		✓	✓
T-5224			
Gefitinib	✓	✓✓	✓✓✓
Raloxifene		✓	✓
Wortmannin	✓✓		+
Lactacystin			++
Imatinib		✓	
Bisindolylmaleimide I	✓✓	✓	
Mifepristone		+	+
PLX5622		✓	✓
Pyrrolidine dithiocarbamate			
Entinostat			
Rapamycin			
Staurosporine			
Napabucasin			
Nelfinavir		✓	
Budesonide		✓	

Figure 139: Normalised IL-8 secretion in IPA compound- challenged PCLuS Quantification of IL-8, previously normalised to % change from baseline (T48 unstimulated PCLuS) was further normalised to A) % change from control PCLuS at T144 for each explant IPF donor to allow assessment of % reduction of IL-8 in response to 96-hour IPA compound challenge. B) XY graphs depict resazurin (normalised to control PCLuS) as a measure of tissue viability vs average % reduction of IL-8 (n=4 donors) in response to 0.1µM, 1µM or 10µM of each IPA inhibitor. Red dashed vertical line at 70% denotes viability threshold (30% reduction compared to control PCLuS). Dashed lines crossing y-axis mark 20% reduction (green), 45% reduction (orange) and 70% reduction (dark red) compared to IL-8 secretion from control slices (solid black line) C) Average % reduction of IL-8 (n=4 donors) summarised as one green tick for 20% reduction, two orange ticks for 45% reduction and three red ticks for 70%+ reduction in IL-8 vs control PCLuS. + represents >200% increase in IL-8 ++ >300% increase in IL-8 compared to control PCLuS. Blank doses represent compounds deemed to have significantly impacted tissue viability (<70% resazurin compared to control PCLuS) which were excluded from further analysis.

5.3.3.3 Comparing IPA compound efficacy in different pre-clinical models

To investigate the translational potential between 2D cell culture and PCLuS systems further, we next sought to identify any differences or similarities in IPA compound responses between experimental models (Figure 140). As expected, comparison of cell and tissue viability at the end of culture revealed several distinctions between systems. Notably, 2D cell culture models failed to identify several inhibitors which significantly reduced tissue viability in PCLuS. For instance, when examined in 2D cell culture models, Pyrrolidine Dithiocarbamate (Figure 141A), Entinostat (Figure 141C), Rapamycin (Figure 141E) and the lower doses of Staurosporine (Figure 141G) exhibited no effect on metabolic activity. However, in PCLuS, 10µM Pyrrolidine Dithiocarbamate (Figure 141B), 1µM and 10µM doses of Rapamycin (Figure 141F) and all doses of Entinostat and Staurosporine (Figure 141D, H) were all deemed to negatively impact tissue viability, resulting in their exclusion from downstream analysis. Conversely, analysis of results also highlighted instances where compounds which significantly reduced cell viability *in vitro*, were found to have no effect on whole tissue viability in PCLuS models (Figure 141I, J).

Further emphasising the inconsistencies between these models, we also confirmed multiple cases where compounds/doses which significantly attenuated collagen 1α1 secretion in PCLuS, had no discernible beneficial effects in 2D cell cultures. Consistent with these results, quantification of TIMP-1 frequently found that compounds which robustly reduced pro-fibrotic markers in PCLuS, exhibited no effect in 2D cell culture models (Figure 143A-D). In instances where an effect was observed in 2D cultures, a higher dose was often required to achieve a comparable, yet less effective, response than that observed in PCLuS (Figure 143E, F). Collectively, these results indicate that fibroblasts cultured in 2D models exhibit reduced sensitivity to inhibitor treatments compared to more sophisticated human tissue models of the disease such as PCLuS. Furthermore, we showed that while traditional *in vitro* screening offers a convenient and scalable platform for initial evaluations, 2D cell culture models are prone to both false negative and false positive read-outs. Consequently, our study emphasises the importance of incorporating advanced tissue models into the drug discovery process to mitigate the risk of overlooking promising candidates or prematurely advancing compounds with misleading early-stage efficacy.

A)

2D primary fibroblasts

Compound	Collagen 1α1			TIMP-1		
	0.1μM	1μM	10μM	0.1μM	1μM	10μM
Tyrphostin AG90			✓			
GW9662						
T-5224						
Gefitinib						
Raloxifene						
Wortmannin						
Lactacystin						
Imatinib						
Bisindolylmaleimide I						
Mifepristone			✓			✓
PLX5622						
Pyrrolidine dithiocarbamate						
Entinostat						
Rapamycin			✓			✓
Staurosporine						
Napabucasin						
Nelfinavir			✓			✓
Budesonide			✓			✓

B)

IPF-derived PCLuS

Compound	Collagen 1α1			TIMP-1		
	0.1μM	1μM	10μM	0.1μM	1μM	10μM
Tyrphostin AG90		✓	✓✓✓		✓	✓
GW9662		✓				
T-5224						
Gefitinib	✓	✓	✓✓✓	✓	✓✓	✓✓
Raloxifene						
Wortmannin	✓✓	✓✓✓	✓✓✓		✓	✓✓
Lactacystin		✓✓	✓✓✓			✓✓✓
Imatinib			✓✓			
Bisindolylmaleimide I						✓
Mifepristone	✓			✓		
PLX5622			✓			✓
Pyrrolidine dithiocarbamate	✓					
Entinostat						
Rapamycin	✓✓✓			✓		
Staurosporine						
Napabucasin						
Nelfinavir	✓	✓	✓✓✓			✓✓
Budesonide	✓✓		✓✓	✓	✓	✓

Figure 140: Comparison of IPA inhibitor efficacy between 2D primary fibroblasts and IPF-derived PCLuS Summary of average % reduction of collagen 1α1 and TIMP-1 compared to controls. Results summarised as one green tick for 20% reduction, two orange ticks for 45% reduction and three red ticks for 70% + reduction for A) acute 24-hour treatment in 2D cell culture model (n=2 wells per donor, n=5 donors, n=10 samples total) and B) 96-hour treatment in IPF-derived PCLuS (n=6 PCLuS per condition, n=4 donors, n=24 PCLuS total). Blacked out doses represent compounds which were deemed to have significantly impacted viability (<70% resazurin compared to control) and were excluded from downstream analysis.

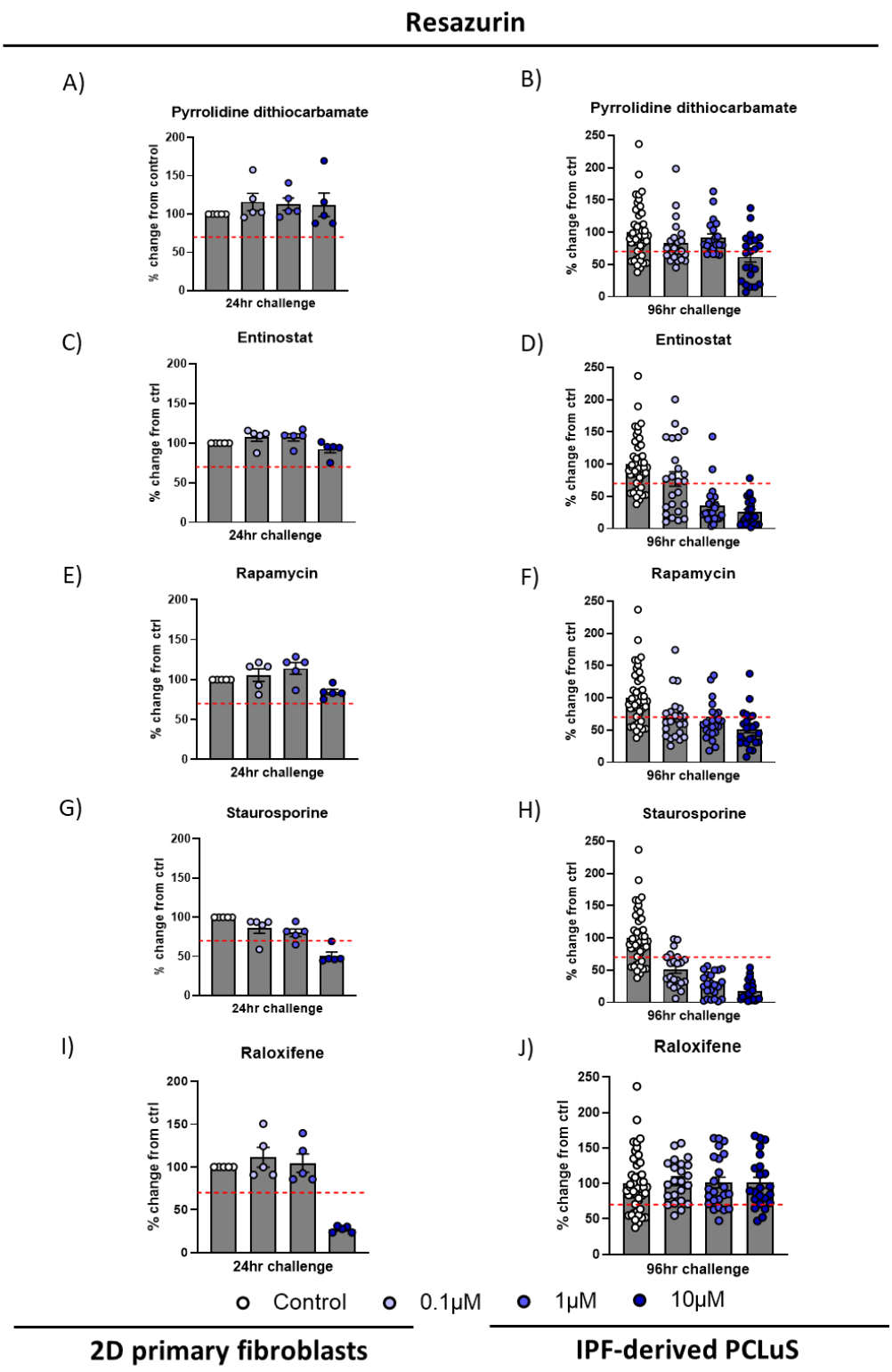

Figure 141: Comparing viability between 2D primary fibroblasts and IPF-derived PCLuS after IPA compound challenge After culture of primary fibroblasts and PCLuS with IPA inhibitors, resazurin was normalised to average % of control for each donor and presented as average % change from control for 2D primary fibroblasts per donor (n=2 wells per donor, n=5 donors, n=10 samples total) and IPF-derived PCLuS (n=6 PCLuS per condition, n=4 donors, n=24 PCLuS total). Results were presented as % change from control (where red dashed line represents arbitrary 70% viability threshold) for A, B) Pyrrolidine dithiocarbamate C, D) Entinostat E, F) Rapamycin G, H) Staurosporine and I, J) Raloxifene. All data are mean ± SEM.

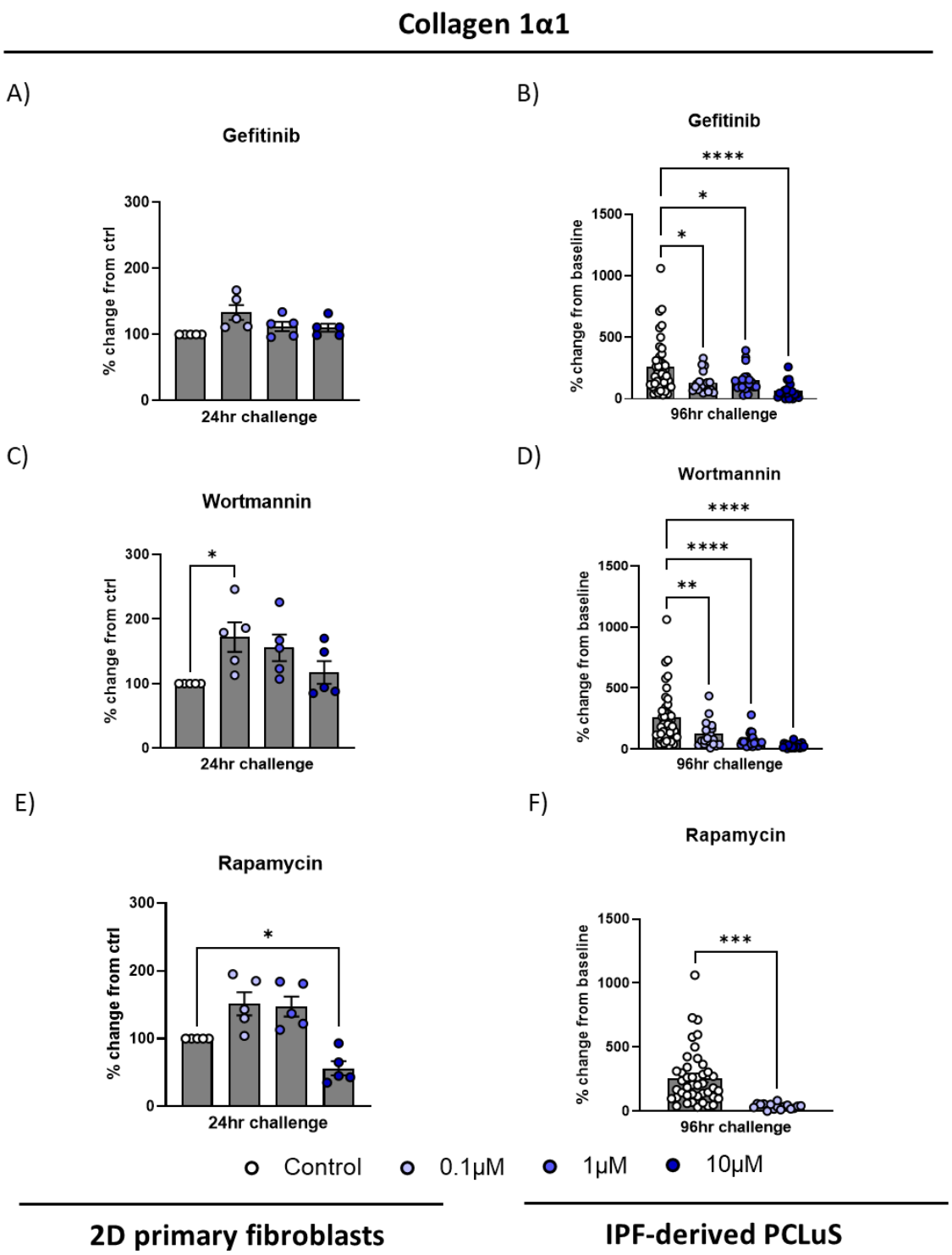

Figure 142: Comparing collagen 1α1 secretion between 2D primary fibroblasts and IPF-derived PCLuS after IPA compound challenge After culture of primary fibroblasts and PCLuS with IPA inhibitors, collagen 1α1 was normalised to average % of control for each cell line donor for 2D primary fibroblasts (n=2 wells per condition, n=5 donors, n=10 samples total) and % change to T48 unstimulated PCLuS for IPF-derived PCLuS (n=6 PCLuS per condition, n=4 donors, n=24 PCLuS total). Results were graphed as % change from ctrl for A-B) Gefitinib, C-D) Wortmannin and E-F) Rapamycin. All data are mean ± SEM. Statistical significance was determined by Kruskal-Wallis with post-hoc Dunn's test for primary fibroblasts and ANOVA with post-hoc Dunnett's test for PCLuS (*p<0.05, **p<0.01, ***p<0.001, ****p<0.0001).

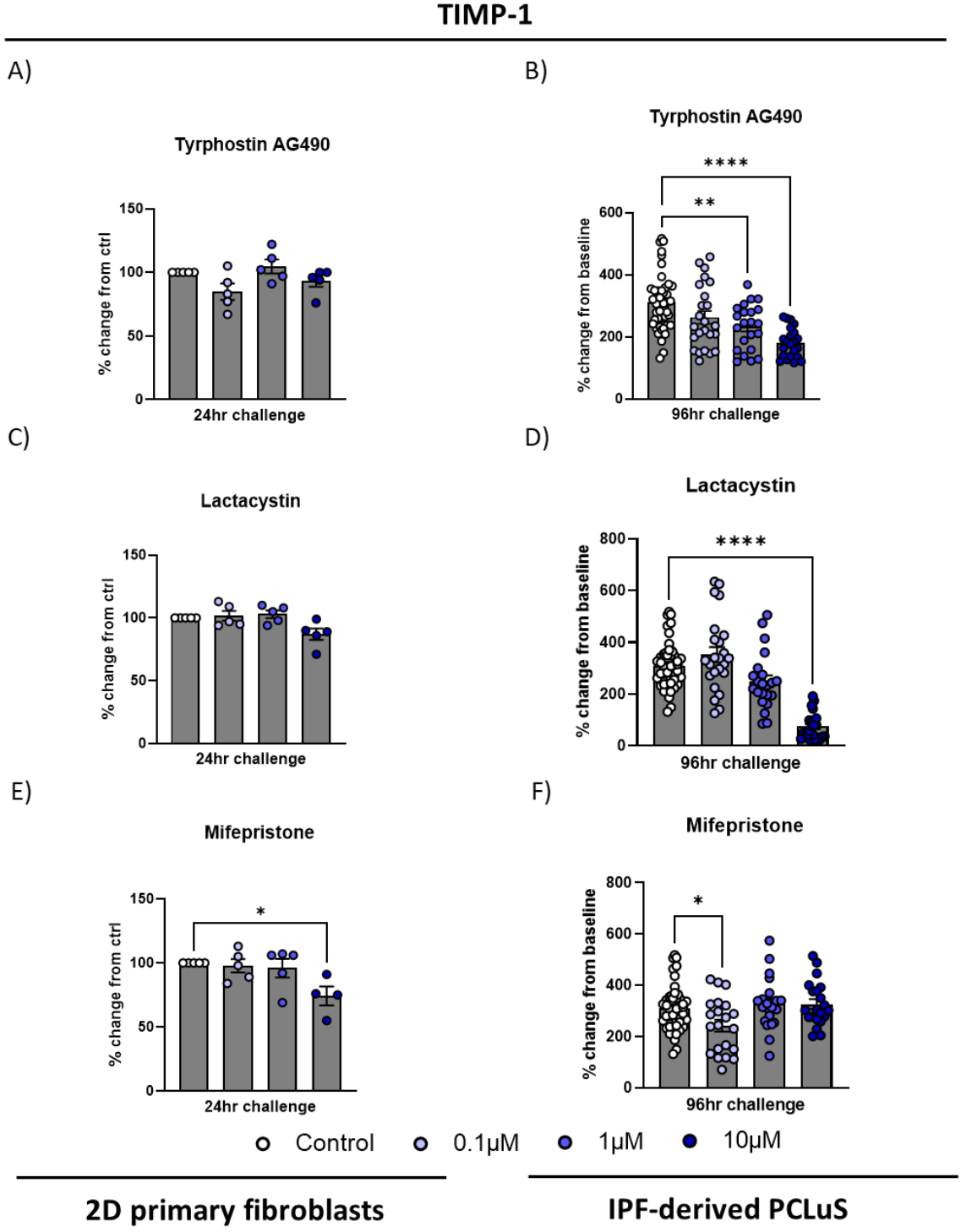

Figure 143: Comparing TIMP-1 secretion between 2D primary fibroblasts and IPF-derived PCLuS after IPA compound challenge After culture of primary fibroblasts and PCLuS with IPA inhibitors, collagen 1α1 was normalised to average % of control for each cell line donor for 2D primary fibroblasts (n=2 wells per condition, n=5 donors, n=10 samples total) and % change to T48 unstimulated PCLuS for IPF-derived PCLuS (n=6 PCLuS per condition, n=4 donors, n=24 PCLuS total). Results were graphed as % change from ctrl for A-B) Tyrphostin AG490, C-D) Lactacystin and E-F) Mifepristone. All data are mean ± SEM. Statistical significance was determined by Kruskal-Wallis with post-hoc Dunn's test for primary fibroblasts and ANOVA with post-hoc Dunnett's test for PCLuS (*p<0.05, **p<0.01, ***p<0.001, ****p<0.0001).

5.4 Discussion

One of the main obstacles hindering development of effective anti-fibrotic and anti-inflammatory therapies is the lack of experimental models that faithfully recapitulate the cellular heterogeneity and complex tissue microenvironment of human disease. Recently, precision cut slices (PCS) have emerged as a cutting-edge platform for disease modelling, preserving the native tissue architecture of human tissue and incorporating patient-specific variables into screening platforms [269]. Consequently, PCS represent a departure from conventional 2D cell culture and *in vivo* animal models of disease, offering a more physiologically relevant *ex vivo* system for investigating targets of interest and testing candidate compounds [474].

To begin investigation of novel therapeutic targets previously identified in Chapter 4, n=30 candidate inhibitory compounds were selected for validation within our PCLuS model. However, due to the amount of explant tissue required, it became apparent that the current 24-well cell culture methodology would limit the number of compounds and/or doses which could be tested in a single donor. To overcome this limitation, we therefore first sought to optimise and validate a 96-well, medium-throughput PCLuS methodology to improve experimental efficiency and facilitate comprehensive compound testing [475,476]. Due to the considerable tissue heterogeneity observed in IPF lungs, one of the primary concerns of reducing PCLuS size was reproducibility between individual slices. However, using established protocols of fibrogenic and inflammatory induction as well as anti-fibrotic SoC compounds (Pirfenidone and Nintedanib) and ALK5i, we confirmed that 4mm diameter slices were able to respond in a consistent matter, comparable to the 24-well cell culture system. These findings were replicated in additional disease explant donors (n=3 donors total), reinforcing that the transition to a 96-well slice culture system represents a reliable platform for the screening of novel therapeutics.

Having validated our 96-well PCLuS methodology, we next proceeded to interrogate selected targets of interest (n=12 compounds) and upstream regulators of fibrosis (n=18 inhibitory compounds) *via* inhibitory compounds in 2D cell culture and 96-well PCLuS models. By utilising a comparative analysis approach, evaluation of candidate compound efficacy identified several key distinctions between systems. For example, while compound screening in 2D tended to yield uniform responses across the different cell lines, PCLuS showed more variation

in drug efficacy and toxicity in different donor tissue. This highlighted an essential advantage of PCLuS, whereby patient variables which can affect drug efficacy and toxicity in clinical settings (e.g., age, gender, genetics and lifestyle) can be accounted for at the pre-clinical stage of drug development. In traditional drug discovery, 2D cell culture models play a crucial role in the initial screening of potential drug candidates, particularly in assessing drug toxicity [477]. Here, we demonstrated that 2D cell culture models may not accurately predict/replicate read-outs in more physiologically-relevant models of disease, reinforcing the need for more advanced 3D systems in the drug discovery pipeline to bridge the gap between *in vitro* simplicity and human disease. However, these discrepancies could also be due, in part, to experimental differences between models. For example, 2D cells only received a single 24-hour treatment of inhibitors, whereas PCLuS received 4 repeated treatments over a 96-hour period. Furthermore, while *in vitro* cells were serum-starved for 24 hours prior to treatment to synchronise cell cycles, this was not possible in PCLuS due to the effect on tissue viability. Additionally, a key caveat of the PCS model is the lack of a circulatory system [478] and inability to replicate the systemic effects of drug administration and pharmacology required to assess drug absorption, distribution, metabolism and excretion which is vital to understand safety and tolerability in humans [423]. Consequently, further assessment of compounds in pre-clinical models which include a circulating immune system and replicate systemic effects (e.g. rodent models) is advised [474].

Evaluation of candidate compounds selected based on the proteins which were significantly upregulated in the normal and intermediate regions of IPF tissue (compared to unused donor controls), but significantly downregulated in end-stage fibrotic IPF tissue identified several inhibitors with anti-fibrotic effects in IPF-derived PCLuS. Of these, the most efficacious compounds were those which targeted integrin proteins. Perhaps the most intensively studied αv integrin in the context of pulmonary fibrosis is the αvβ6 heterodimer. Upon injury, αvβ6 becomes specifically upregulated on epithelial cells, where its primary function is to activate TGF-β [479,480]. Interestingly, the αvβ6 integrin has been found to be upregulated in IPF patients, with high levels of expression associated with a poorer prognosis, suggesting a role in disease pathogenesis [418,419]. These findings are supported by robust pre-clinical studies which demonstrated that inhibition of the αvβ6 integrin protects against the development of pulmonary fibrosis in several models of disease [418,481,482]. For example, previous work

carried out in collaboration with John *et al* found that GSK3008348, a selective small molecule αvβ6 RGD-mimetic, could effectively inhibit pSmad2 in IPF-derived PCLuS, confirming inhibition of TGF-β activation pathways in diseased human tissue. Furthermore, they showed that αvβ6 inhibition also caused a significant reduction in collagen deposition and prolonged inhibition of TGF-β signalling in bleomycin-induced lung fibrosis mouse models [482]. Currently, there are a number of clinical trials underway and/or recently completed investigating the therapeutic potential of targeting αv integrins (particularly αvβ6) in fibrotic lung diseases. Disappointingly, reports published in 2022 from phase 2a (study no: NCT01371305) [483] and 2b (study no: NCT03573505) [484] clinical trials conducted by Raghu *et al* found that BG00011 (a humanised monoclonal antibody targeting the αvβ6 integrin) was associated with a lack of clinical efficacy (as measured by FVC and HRCT), increased adverse effects and exacerbations, resulting in the premature termination of the phase 2b trial [484]. However, more recently, results published by Lancaster *et al* in 2024 from a phase 2a randomised, double-blind, dose-ranging, placebo controlled, multi-centre clinical trial (study no: NCT04396756) found that PLN-74809 (also known as Bexotegrast; an oral small molecule dual inhibitor of the αvβ6 and αvβ1 integrins) was well tolerated in patients with IPF [485]. Furthermore, preliminary analysis of potential anti-fibrotic efficacy found that patients treated with Bexotegrast experienced a reduction in FVC decline over 12 weeks versus placebo-treated patients, with patients receiving the two highest doses of Bexotegrast having 'no or limited progression'. Additionally, there was a dose-dependent anti-fibrotic effect of Bexotegrast treatment as measured by quantitative lung fibrosis HRCT imaging and a reduction of circulating fibrosis-associated biomarkers (ITGB6 and PRO-C3) versus placebo [485].

The discrepancies in the safety, tolerability and potential anti-fibrotic efficacy of these two compounds could be explained by the extent of target inhibition and/or the differences in chemistry of candidate drugs. For example, there were no anti-drug antibodies detected patients treated with BG00011, suggesting that reported adverse results were likely a result of inhibition of αvβ6 integrins directly and not off-target effects [484]. This led Sime *et al* to hypothesise that the adverse effects observed in response to BG00011 treatment in patients could be a result of inhibition of αvβ6 integrin-mediated TGF-β activation pathways which are required for the normal homeostatic function of macrophages. Here, complete TGF-β inhibition is thought to impede TGF-β-mediated regulation of macrophage behaviour causing

enhanced pro-inflammatory responses [486]. This is supported by pre-clinical studies [487,488] and data from the phase 2a study which showed an increased risk of acute exacerbations at the highest dose, resulting in its premature termination during the trial [483]. Additionally, due to their size (approximately 150,000 Daltons) there is reasonable concern that monoclonal antibodies may be unable to effectively penetrate the dense fibrotic matrix in IPF. This in turn may then cause preferential binding to non-fibrotic regions of tissue resulting in enhanced inhibition of homeostatic functions rather than pathological αvβ6 integrins [486]. Conversely, the small molecule inhibitor Bexotegrast (<500 Daltons) is reported to have submaximal αvβ6 receptor occupancy and has been shown to effectively reach and bind to αvβ6 integrins in highly fibrotic regions of IPF lungs as measured by PET/CT and radiotracer distribution (study no: NCT04072315) [489]. Excitingly, a recent press release of clinical data from a phase 2a, 12-week, single-centre, randomised, double-blinded, placebo-controlled trial study (study no: NCT05621252) from Pliant Therapeutics reported that IPF patients who received a single daily dose of Bexotegrast showed a reduction in total lung collagen (as measured by PET imaging and radiotracer methodologies) versus those who received placebo (who displayed an increase in total collagen after 12 weeks). Furthermore, they demonstrated an improvement in FVC and a reduction in cough severity at 4, 8 and 12 weeks compared to placebo, suggesting a potential stabilisation or reversal of fibrosis. Taken together, these studies highlight several important considerations when therapeutically targeting novel proteins/pathways in IPF. As seen in the case of BG00011, complete suppression of a targets physiological function may lead to adverse effects, making a thorough understanding of candidate drug pharmacokinetics essential. Additionally, reliable pharmacodynamic biomarkers are required to confirm target engagement and extent of inhibition. Finally, different targeting strategies (such as monoclonal antibodies *vs* small molecule inhibitors) may result in varying clinical outcomes and, if one is successful, alternative strategies should be considered rather than ruling out the target completely [486].

Consistent with these findings and previous pre-clinical reports, work in this project found that EMD 527040 (a αvβ6 integrin inhibitor) could significantly reduce collagen 1α1, TIMP-1 and IL-8 secretion at various doses in IPF-derived PCLuS. Nevertheless, when normalised to % change from control PCLuS, results showed that EMD 527040 challenge only caused a slight (20-44% reduction) decrease in soluble collagen 1α1 compared to unstimulated PCLuS and

failed to surpass the efficacy of standard of SoC treatments (70%+ reduction). However, as we only tested one commercially available αvβ6 inhibitor, it is possible that this particular compound was less effective at selectively targeting and/or inhibiting αvβ6 than others reported in the literature. As secretion of collagen 1α1 is widely measured in scar-in-a-jar and other *in vitro* models used for anti-fibrotic drug testing [490], work in this project similarly utilised secreted collagen 1α1 as one of the primary readouts to assess anti-fibrotic efficacy of compounds in PCLuS for consistency between models. However, it is possible that potentially significant effects of inhibitors on collagen which is incorporated into the ECM (and not secreted) may be obscured. Consequently, further work is advised to elucidate precise effect on changes in ECM composition, structure and the balance of ECM remodelling. For example, the use of fluorescent probes specific to ECM components or reporters for ECM remodelling activity would allow real-time observation of how a drug affects ECM dynamics [491]. Similarily, advanced imaging techniques such as microCT, multiphoton microscopy, second harmonic generation microscopy and/or confocal microscopy could be considered to help visualise and assess potential changes in collagen organisation and distribution [492,493].

Though the role of αvβ6 integrins has been well described in IPF, the function of αvβ3 and αvβ5 heterodimers in pulmonary fibrosis are less well defined. Instead, previous studies of these integrins have focused primarily on the treatment of various cancers [494]. Here, we report that inhibition of αvβ3 alone (*via* Cyclo- (RGDfK) and Cilengitide), and in combination with αvβ5 (*via* SB273005) using compounds previously developed for the treatment of several cancers [495,496], significantly reduces soluble markers of fibrosis and inflammation in our PCLuS model. Corroborating these results, αvβ3 and αvβ5 have been shown to be upregulated in the dermal epithelium of systemic sclerosis patients, with αvβ5 also upregulated in the fibroblastic foci of human IPF lungs [497]. Moreover, both integrins have been shown to promote myofibroblast differentiation *in vitro* through activation of latent TGF-β1 [498,499]. However, these findings are in contrast to previous *in vivo* studies which found no protective effects of αvβ3/αvβ5 double-knockout in bleomycin-induced lung fibrosis [500]. Similarily, Cilengitide failed to show any anti-fibrotic effects in *in vivo* models of liver fibrosis, instead significantly increasing collagen deposition and pro-fibrotic gene expression [501]. Consequently, further work is required to elucidate the precise roles of αvβ3 and αvβ5 integrins in IPF and confirm anti-fibrotic effects observed *via* inhibitors in PCLuS.

Notably, the most effective selected inhibitor in this work was GLPG-0187, a potent αv integrin inhibitor. Though pan-αv inhibition has not been extensively tested in clinic for fibrotic disease, GLPG-0187 has previously been evaluated for the treatment of solid tumours in phase Ib clinical trials (study no: NCT01313598). Here, results found that despite failing to show signs of monotherapy efficacy, GLPG-0187 was well tolerated in patients [502]. Consistent with these results, GLPG-0187 treatment had no impact on tissue viability in our PCLuS model, suggesting that this compound could potentially be repurposed for treatment of other diseases. Intriguingly, evidence from several pre-clinical studies suggest αv integrin activity is a common, targetable pathway in multi-organ fibrosis [452]. For example, Henderson *et al* demonstrated that selected depletion of αv integrins in myofibroblasts lead to protection against *in vivo* mouse models of fibrosis in several organs, including bleomycin-induced lung fibrosis [452,503]. Similarily, more recent studies performed by Zhang *et al* found that pharmacological inhibition of multiple αv integrins in *in vitro* and *in vivo* models of pulmonary fibrosis resulted in significant anti-fibrotic effects, providing additional validation for therapeutic targeting of αv integrins in IPF [504].

Further assessment of candidate IPA compounds targeting upstream regulators of fibrosis revealed several inhibitors which outperformed current SoC therapeutics in our PCLuS system. Results confirmed that targeted inhibition of mammalian target of rapamycin (mTOR) *via* Rapamycin and phosphatidylinositol 3-kinase (PI3K) *via* Wortmannin both resulted in a significant reduction of pro-fibrotic markers in IPF-derived PCLuS. The PI3K/Akt/mTOR pathway has been widely implicated in IPF pathogenesis, with proven roles in fibroblasts proliferation, TGF-β1-induced myofibroblast differentiation and collagen production [505,506]. Results in our study were comparable to previous work by Mercer *et al* who similarly utilised IPF-derived PCLuS to demonstrate that PI3K/mTOR pathway activation plays a role in disease remodelling and further showed that inhibition of this pathway (*via* GSK2126458) resulted in decreased secretion of pro-fibrogenic markers, suggesting a direct link between PI3K/mTOR signalling and ECM formation in IPF [294]. Interestingly, work in this study provided scientific rationale for progressing GSK2126458 (also known as Omipalisib; a small molecule inhibitor of PI3K/mTOR) to clinical evaluation in a recent proof-of-mechanism trial in IPF patients (study no: NCT01725139) which subsequently demonstrated acceptable safety, tolerability and effective target engagement (both systemically and in IPF lungs) [507]. Taken together, these

data provide a strong proof-of-concept to our experimental approach as targets previously identified in the literature were also present in our IPA targets and found to exert strong anti-fibrotic effects in PCLuS.

In addition to confirming efficacy of previously identified targets, assessment of IPA candidate compounds further demonstrated robust anti-fibrotic effects of epidermal growth factor receptor (EGFR) inhibition *via* Tyrphostin AG490 and Gefitinib in our PCLuS system. EGFR (also known as ErbB1 or HER1) is a tyrosine kinase receptor which, upon ligand binding, activates several downstream signalling pathways involved in regulation of cell growth, proliferation and survival [508]. To date, several EGFR ligands have been identified including EGF, transforming growth factor-α (TGF-α), amphiregulin (AREG), heparin-binding EGF-like growth factor (HB-EGF), betacellulin (BC), epiregulin (EREG) and epigen (EPG) [509]. Overactivation of EGFR signalling has been widely described in several forms of cancer, resulting in the development of multiple EGFR tyrosine kinase inhibitors (TKIs) which are currently approved for clinical use as anti-cancer agents [510]. However, emerging evidence suggests that EGFR signalling and their associated ligands may also be involved in other hyperproliferative diseases including pulmonary fibrosis [509,511,512].

In this study, we found that IPF-derived PCLuS treated with Gefitinib, an EGFR-TKI currently approved for the treatment of non-small cell lung cancer (NSCLC), resulted in potent anti-fibrotic and anti-inflammatory effects [513]. Additionally, Tyrphostin AG490 (a selective EGFR inhibitor) was able to significantly reduce pro-fibrogenic markers throughout the culture period. Consistent with these results, EGFR has been shown to be upregulated in hyperplastic alveolar epithelial cells and fibroblastic foci in IPF lungs, with increasing EGFR mRNA levels negatively correlated to indicators of IPF progression including decreased FVC [512,514]. Similarily, EGFR ligands such as TGF-α and AREG have been reported to be upregulated in IPF lungs, particularly in epithelial cells and fibroblasts [515,516]. Moreover, therapeutic inhibition of EGFR and associated ligands have been repeatedly associated with favourable anti-fibrotic effects *in vitro* and *in vivo* [517,518]. Investigation of EGFR inhibition in other organs suggests that dysregulated EGFR signalling may be a core fibrotic mechanism driving disease progression [519-521]. For instance, work by Cao *et al* reported increased expression of EGFR in interstitial myofibroblasts in human and mouse fibrotic kidneys. Further investigation of EGFR signalling *in vivo* found that selective deletion of EGFR in fibroblast/pericyte cell

populations protected from development of fibrosis in several models of renal injury, highlighting EGFR activation as a key driver of fibroblast migration and proliferation [521].

Notably, administration of Gefitinib has been shown to prevent fibrosis in bleomycin-induced pulmonary fibrosis in multiple studies, significantly inhibiting proliferation of mesenchymal cells and reducing oxidative damage [517,522,523]. However, contrasting studies by Suzuki *et al* have reported negative effects of Gefitinib treatment in bleomycin-induced lung fibrosis. Here, Gefitinib treatment was found to enhance development of fibrosis by reducing the regenerative potential of alveolar epithelial cells [524]. Though the reasons for these contradictory findings are unknown, differences in mouse strains, drug delivery routes and dosages may have played a role. Interestingly, it has also been reported that approximately 1% of NSCLC patients who receive Gefitinib therapy go on to develop interstitial lung disease, suggesting potentially deleterious effects of EGFR inhibition in a minority of cases [525]. Taken together, these data demonstrate a potentially key role of EGFR signalling in fibrotic disease. However, considering the complexity of EGFR-ligand signalling and its role in tissue homeostasis and regeneration, further work is required to evaluate to precise role of EGFR signalling during acute and chronic lung injury and how this may be therapeutically targeted in IPF in the future.

As previously mentioned, when interpreting experimental results in this project it is important to consider the IC50 values of candidate drugs screened (see Table 22). For example, many of the compounds used in this study are reported to have low IC50 values (within the nanomolar range) and could therefore potentially have off-target effects at the higher doses tested when trying to selectively target a protein of interest. Moreover, these higher doses could translate to higher systemic exposure in patients than necessary, if comparable efficacy could be achieved at lower concentrations. Conversely, there were several compounds screened during this project which had reported IC50s within the micromolar range *in vitro* and/or in cell-free assays. For example, Tyrphostin AG490, which showed some anti-fibrotic efficacy at the highest 10µM dose in PCLuS, has the following IC50 values: Jak2 (IC50 = 10µM) and Jak3 (IC50 = 20µM) [526,527], EGFR (IC50 = 2µM) and ErbB2 (IC50 = 13.5µM) [528]. Considering that PCLuS models likely require higher doses than cell-free and 2D monolayer systems, it could therefore be assumed that higher doses of the drugs would need to be screened to ascertain IC50 and anti-fibrotic efficacy in PCLuS more accurately. Similarily, T-224 which displayed no anti-

fibrotic or anti-inflammatory effects in this project, is reported to have an IC50 of ~10µM for the following inflammatory cytokines *in vitro*: MMP-1, MMP-3, IL-6 and TNF-α [529], and may also require higher concentrations in 3D models to effectively inhibit target proteins.

In the case of the compounds identified through IPA analysis, the candidate drugs identified have multiple targets and may affect several pathways simultaneously (see Appendix H; Table 1). As a result, these drugs are more likely to have broader effects on multiple upstream regulators and/or pathways (with target proteins ranging from 4-10 individual proteins), making assessment of on-target inhibition difficult given the broad range of potential interactions. In this regard, IPA compounds are more similar to currently approved anti-fibrotics, such as Pirfenidone, which is thought to affect several pathways including (but not limited to) TGF-β1, NF-κB and other inflammatory cytokines, chemokines and pathways, PI3K/AKT, MAPK and Wnt/β-catenin signalling [530-533]. Therefore, while the *in vitro* IC50 values provide valuable insights into the potency of these compounds, they should not be used in isolation to predict clinical outcomes. Indeed, previous review of the differences in IC50 values between 2D cell culture and 3D spheroid models (as detailed in chapter 3; subsection 3.4) underscores the necessity of integrating multiple experimental approaches to obtain a comprehensive understanding of a drug's efficacy and safety profile. Evaluation in additional physiologically-relevant models, alongside careful consideration of dose-response relationships, is therefore crucial for translating these findings into safe and effective clinical therapies.

To strengthen the validity of these findings, future work should consider further screening candidate compounds in complementary *ex vivo* models of early fibrogenesis utilising a cocktail of pro-fibrogenic and pro-inflammatory stimuli (e.g. TGFβ, TNFα, PDGFAB, and lysophosphatidic acid) in non-diseased human PCLuS [534]. As work in this study exclusively tested compounds in diseased explant tissue, incorporating early disease models would enable a more comprehensive understanding of therapeutic targets and inhibitory compounds at different stages of disease. Additionally, use of gene editing tools in combination with viral vectors, neutralising antibodies or LNP technology should be considered to achieve more targeted inhibition of proteins of interest and reduce off-target effects associated with small molecule inhibitors (previously outlined in chapter 3).

In summary, work in this project effectively optimised the transition of our current PCLuS methodology into a 96-well cell culture format which was then used to validate therapeutic targets and upstream regulator of fibrosis. From this, we identified multiple inhibitory compounds which demonstrated strong anti-fibrotic and/or anti-inflammatory effects in our PCLuS system. Future work will aim to investigate the mode of action of efficacious compounds and interrogate cell-specific effects *via* single RNA sequencing and/or more advanced models of target inhibition, which in turn should improve our understanding of the pathways and proteins involved in disease progression.

6 General discussion

6.1 Final conclusions

Organ fibrosis is a common endpoint for a broad spectrum of chronic diseases and is estimated to contribute to up to 45% of all deaths in the developed world [311]. Within the last few decades, MASH has rapidly become the most common cause of liver transplantation, due to its strong association with obesity and metabolic-associated diseases [535]. Similarily, as the most common and severe ILD, IPF is a prominent fibrotic disease which poses an increasing socioeconomic burden in line with an ageing population. Given that fibrosis progression determines prognosis in MASH and is central to development of IPF, attenuation of fibrosis represents a major therapeutic goal. Despite this, substantial strides in our understanding of MASH and IPF are yet to be made and the underlying aetiology of disease remains to be elucidated. One explanation for this occurrence is the frequent use of reductionist pre-clinical models, which fail to recapitulate the microscopic spatial and temporal heterogeneity of pathological changes within human organs during fibrotic disease [424-426]. As a result, information surrounding pathophysiological mediators of disease progression in human liver and lung tissue is extremely limited and warrants further investigation.

In this project, we aimed to comprehensively profile the molecular landscape of human liver and lung tissue at different stages of disease progression, with the overarching goal of illuminating key cellular phenotypes, proteins and/or molecular pathways underpinning MASH and IPF fibrogenesis. To begin investigating liver fibrosis, single nuclei RNA sequencing was performed by colleagues at Edinburgh University on human liver tissue selected to represent the spectrum of MASH from F1–F4 fibrosis stage and cirrhosis. Following this, computational analysis revealed a disease-associated, collagen type 1 high expressing mesenchymal cell subpopulation with distinct molecular markers. Further analysis of the top 100 differentially expressed genes identified 9 genes of interest, which were almost exclusively upregulated in myofibroblast lineages. Work in this project then systematically evaluated targets of interest in liver-derived PCS. Utilising established protocols of fibrogenic induction (TGF-β1/PDGFββ), we confirmed that 6 of the 9 gene targets became significantly upregulated in response to pro-fibrotic stimuli, whilst protein expression remained unchanged. Furthermore, we confirmed that inhibition of several targets *via* inhibitory small molecule compounds was sufficient to attenuate TGF-β1/PDGFββ-induced fibrogenesis. Of

the efficacious inhibitors, antagonism of HAS2 and components of the Wnt signalling pathway (β-catenin and porcupine) had the most potent anti-fibrotic effects. Notably, further evaluation of inhibitory compounds in PCS generated from non-diseased and IPF lung tissue confirmed multi-organ efficacy, suggesting these may be common fibrogenic regulators.

Simultaneously, we utilised unbiased 'omics approaches to interrogate IPF pathogenesis by profiling gene and protein expression of seemingly unaffected 'normal' regions, actively remodelling 'intermediate' regions and end-stage fibrotic regions from the same IPF lung, in the hope that this would provide an approximation for the molecular changes associated with disease progression. Importantly, evaluation of these macroscopically different regions of tissue identified novel proteins/pathways that are significantly up- and down- regulated in early-stage and actively remodelling tissue (normal and intermediate regions) compared to end-stage fibrotic tissue and non-diseased 'healthy' lungs. To the best of our knowledge, this is the first study to describe, and subsequently interrogate, protein heterogeneity in differentially affected regions of IPF tissue. In doing so, results confirmed various transcriptomic findings previously described in the literature as well as identifying a number of novel targets which have not been widely studied in the context of IPF [414].

Further interrogation of protein heterogeneity within IPF regions resulted in the selection of 30 candidate compounds targeting significantly upregulated proteins/pathways of interest. Previously, targets identified through single-cell or 'omics studies of human tissue have predominantly been validated or further explored in cell culture and/or *in vivo* mouse models [82,430]. However, work in this project utilised *ex vivo* cultures of human lung derived PCS to directly evaluate translational relevance of potential therapeutic targets to human disease. In order to facilitate comprehensive testing of 30 compounds at multiple doses in available human IPF tissue, we optimised and validated a highly reproducible 96-well medium-throughput PCLuS methodology which was then used to screen novel targets/compounds to determine toxicity and anti-fibrotic efficacy. Once optimised, compound screening in the 96-well PCLuS format identified multiple inhibitory compounds which demonstrated strong anti-fibrotic (n=17 compounds) and/or anti-inflammatory (n=14 compounds) effects in our PCLuS system, confirming involvement of the relevant compound targets in IPF pathogenesis.

6.2 Study limitations and future work

Though work in this project provided a number of novel insights into the molecular landscape underpinning fibrosis progression in the liver and lung, there are a number of constraints to consider when interpreting experimental outcomes. For example, though we confirmed that several genes of interest could be modulated in liver tissue *via* exogenous stimuli (TGF-β1/PDGFββ) in our PCS system, as results were representative of whole tissue and not individual cell types, we were unable to directly assess effects on disease-associated myofibroblast subpopulations. To overcome this limitation, future work should consider the use of single-cell sequencing, first to determine the cellular composition of PCS donor tissue and presence of myofibroblast populations prior to culture and, secondly, to evaluate how target gene expression is modulated during fibrogenesis. Furthermore, as results showed no clear changes in target protein expression after 72-hour treatment with pro-fibrotic stimuli, subsequent analysis should seek to determine whether this was due to the limited culture period or whether target upregulation was limited to this small cellular subpopulation (estimated <2% of whole tissue). To achieve this, future experiments should consider extending the culture period as well as employing flow cytometry and/or multi-plex imaging techniques to establish target protein expression in different cell types during fibrogenesis.

In order to evaluate target expression in liver-derived PCS, work in this study utilised exogenous stimuli to induce inflammation and fibrosis within the 96-hour culture period. However, as fibrosis is often seen to develop slowly in humans in response to repeated and sustained damage, it is likely that our model of accelerated disease progression may not fully recapitulate all aspects of disease seen in patients. Similarily, in order to determine anti-fibrotic effects of candidate compounds, inhibitors were co-treated with fibrogenic stimuli to assess the ability to blunt TGF-β1/PDGFββ-induced fibrogenesis. However, as histological assessment of liver donors used to generate PCS confirmed that some targets of interest were already present in liver tissue prior to culture, future work should seek to histologically confirm the presence of all targets of interest and then consider screening candidate compounds in the absence of any stimuli to determine the effects on pre-existing fibrosis. Specifically, assessment of compounds in patient tissue with varying fibrosis grades (ranging from F0-F4) may provide further insight into how these targets are modulated throughout the disease spectrum and their potential role in fibrosis progression and/or regression.

To further investigate results from intrapatient sampling and profiling of IPF tissue, future work should first seek to characterise the tissue microenvironment during macroscopically distinct phases of disease *via* multi-plex imaging and/or flow cytometry. In doing so, results should help clarify whether the changes in gene and protein expression are due to phenotypic changes in tissue-resident cells or changes in the cellular composition of the tissue microenvironment. Additionally, work should aim to identify the cellular source of proteins and map the distribution within tissue *via* spatial proteomics [536]. Further interrogation of existing datasets should also be considered to identify additional proteins/pathways of interest as work in this project focused primarily on proteins which were significantly upregulated during early-stage disease. For example, we found that several important neutrophil-related markers were significantly downregulated in IPF regions compared to 'healthy' controls. However, this was not investigated in this current project due to the lack of infiltrating immune cells in our PCS system and the limited longevity of neutrophils in culture. In this instance, complementary pre-clinical models should be considered such as mouse models, which have the benefit of systemic responses and whole-body physiology. Alternatively, isolation and phenotyping of neutrophils from IPF tissue regions could provide further insights into their seemingly altered function during fibrogenesis. As target identification was based solely on proteomic datasets, interrogation of the transcriptome alone, or through integration of the transcriptome with the proteome, should also be considered. Additionally, single-cell sequencing of regional tissue samples may provide further insights into cellular heterogeneity and target expression.

Importantly, due to the reduction in the availability of donor tissue caused by the Covid-19 pandemic, our first cohort comprised of 8 IPF patient samples. To validate our findings, a second larger cohort of donor tissue should be acquired and sampled to determine whether identified targets are common across multiple cohorts. Additionally, as work in this project stratified regional samples based on macroscopic (gross) and microscopic (histological) assessment, future sampling should consider the use of quantitative measurements of fibrosis to further stratify samples and identify any outliers. For example, in a similar study by McDonough *et al*, samples were clustered based on alveolar surface density measurements computed from microCT imaging and collagen 1 staining [430].

As candidate compounds were exclusively screened in IPF-derived tissue in this project, future studies could also utilise models of early fibrogenesis as previously described [534]. Interestingly, a recent study by Lang *et al* utilised single cell sequencing to evaluate changes in gene expression of non-disease human lung PCLuS treated with this fibrogenic cocktail (FC) alone, and in combination with anti-fibrotic compounds [537]. Results confirmed that FC-treated PCLuS mimicked many aspects of human IPF. Moreover, they demonstrated cell lineage-specific effects of anti-fibrotic compounds, with gene set enrichment analysis revealing that co-treatment of FC with Nintedanib resulted in inhibition of VEGF and PGDF signalling in myofibroblasts [537]. As we did not investigate the mode of action of efficacious drugs in this study, particularly those identified through IPA analysis, a similar approach may yield additional insights into cell-specific effects of candidate compounds.

In this project, potential therapeutic targets were investigated in PCS generated from different disease-states/organs *via* inhibitory compounds and anti-fibrotic efficacy was determined by quantification of secreted fibrogenic markers. However, one of the main limitations of this approach was the inability to selectively inhibit the targets of interest in certain cell types. This is of particular interest in regard to targets identified for the liver, as cell-specific knockdown or overexpression in myofibroblast populations during culture may provide further insights into the precise role in disease progression. Moreover, it is possible that some small molecule inhibitors may exhibit a lack of target specificity resulting in the inhibition of other proteins with structural similarities, potentially leading to off-target effects. Consequently, future work should consider the use of gene editing tools in combination with viral vectors (such as AAVs or lentivirus) or alternative drug delivery methods (e.g., lipid nanoparticles and antibody-drug-conjugates [538,539]) to reduce off-target effects and achieve selective and sustained target inhibition. At present, it is unclear if the compounds which showed little to no anti-fibrotic efficacy was due to downregulated targets having no effect or, alternatively, if compounds were unable to effectively inhibit the protein of interest. As some compounds may have limited tissue/cell penetration and/or incomplete target inhibition, further work is required to confirm target engagement and determine the amount of drug in PCS tissue and its distribution (e.g., imaging mass spectrometry) [540]. Likewise, further investigation is required to determine tolerable patient doses and understand the IC50 within PCS. Notably, a number of compounds appeared to demonstrate strong efficacy at the lowest 0.1µM dose,

highlighting the need for additional dose titration to identify the minimal effective dose in PCS. To obtain an accurate measurement of IC50 values of individual drugs in our PCS model, additional logarithmic dose titration concentrations (at least 5 drug concentrations) would be required, preferably at lower doses to assess reported *in vitro* IC50 concentrations for anti-fibrotic efficacy. To better understand patient tolerability, further work to understand systemic effects of drugs should be considered to identify any potential systemic effects of drugs (e.g. rodent models) due to the lack of circulation in our PCS model. Additionally, further exploration of candidate compounds which have already demonstrated suitable safety and tolerability for the treatment of other drugs should be further investigated for repurposing as an anti-fibrotic therapy. For example, Mercer *et al* utilised available pharmacokinetic data from ongoing clinical trials investigating GSK2128458 in solid tumours and integrated results with *in vitro* mechanistic studies to predict pharmacological engagement for a range of doses *via* stochastic model simulations [294]. Consequently, a similar approach for candidate compounds screened in this study could be utilised in future. Finally, further investigation of target engagement and degree of drug inhibition (rather than drug efficacy alone) with reliable pharmacodynamic biomarkers is recommended to improve our understanding of understand the relationship between target engagement and inhibition of fibrosis in PCLuS. For example, phosphorylation of Smad2 has previously been used as a marker of TGFβ activity in several models, including PCLuS [421]. In doing so, we will be able to better understand potential off-targets effects of candidate compounds. For instance, if target engagement is achieved at relatively low compound concentrations but anti-fibrotic effects are not detected until much higher doses, this could likely be explained by off-target effects of candidate compounds.

Overall, work in this project has shed light on the complex cellular and molecular mechanisms underlying fibrosis progression in the human liver and lung, revealing new insights into cellular and protein heterogeneity during disease progression. We have highlighted several promising targets for further exploration and interrogated translational relevance in the PCS system *via* inhibitors, confirming involvement in disease pathogenesis. Future work should aim to further explore the potential therapeutic targets as outlined above, which in turn should improve our understanding of the proteins/pathways involved in disease progression of MASH and IPF.

Appendix A

SnRNAseq liver donor demographics statistical analysis

Table 1: Liver donor demographics Kruskal-Wallis with post hoc Dunn's multiple comparisons test of donor ages between cohorts

Dunn's multiple comparisons test	Mean rank diff.	Significant?	Summary	Adjusted P Value
Healthy vs. F0	23.18	No	ns	>0.9999
Healthy vs. F1	20.05	No	ns	0.4559
Healthy vs. F2	17.1	No	ns	0.4829
Healthy vs. F3	18.58	No	ns	0.0754
Healthy vs. F4	7.929	No	ns	>0.9999
Healthy vs. Cirrhotic	8.286	No	ns	>0.9999
F0 vs. F1	-3.125	No	ns	>0.9999
F0 vs. F2	-6.083	No	ns	>0.9999
F0 vs. F3	-4.6	No	ns	>0.9999
F0 vs. F4	-15.25	No	ns	>0.9999
F0 vs. Cirrhotic	-14.89	No	ns	>0.9999
F1 vs. F2	-2.958	No	ns	>0.9999
F1 vs. F3	-1.475	No	ns	>0.9999
F1 vs. F4	-12.13	No	ns	>0.9999
F1 vs. Cirrhotic	-11.77	No	ns	>0.9999
F2 vs. F3	1.483	No	ns	>0.9999
F2 vs. F4	-9.167	No	ns	>0.9999
F2 vs. Cirrhotic	-8.81	No	ns	>0.9999
F3 vs. F4	-10.65	No	ns	>0.9999
F3 vs. Cirrhotic	-10.29	No	ns	>0.9999
F4 vs. Cirrhotic	0.3571	No	ns	>0.9999

Enlarged UMAP

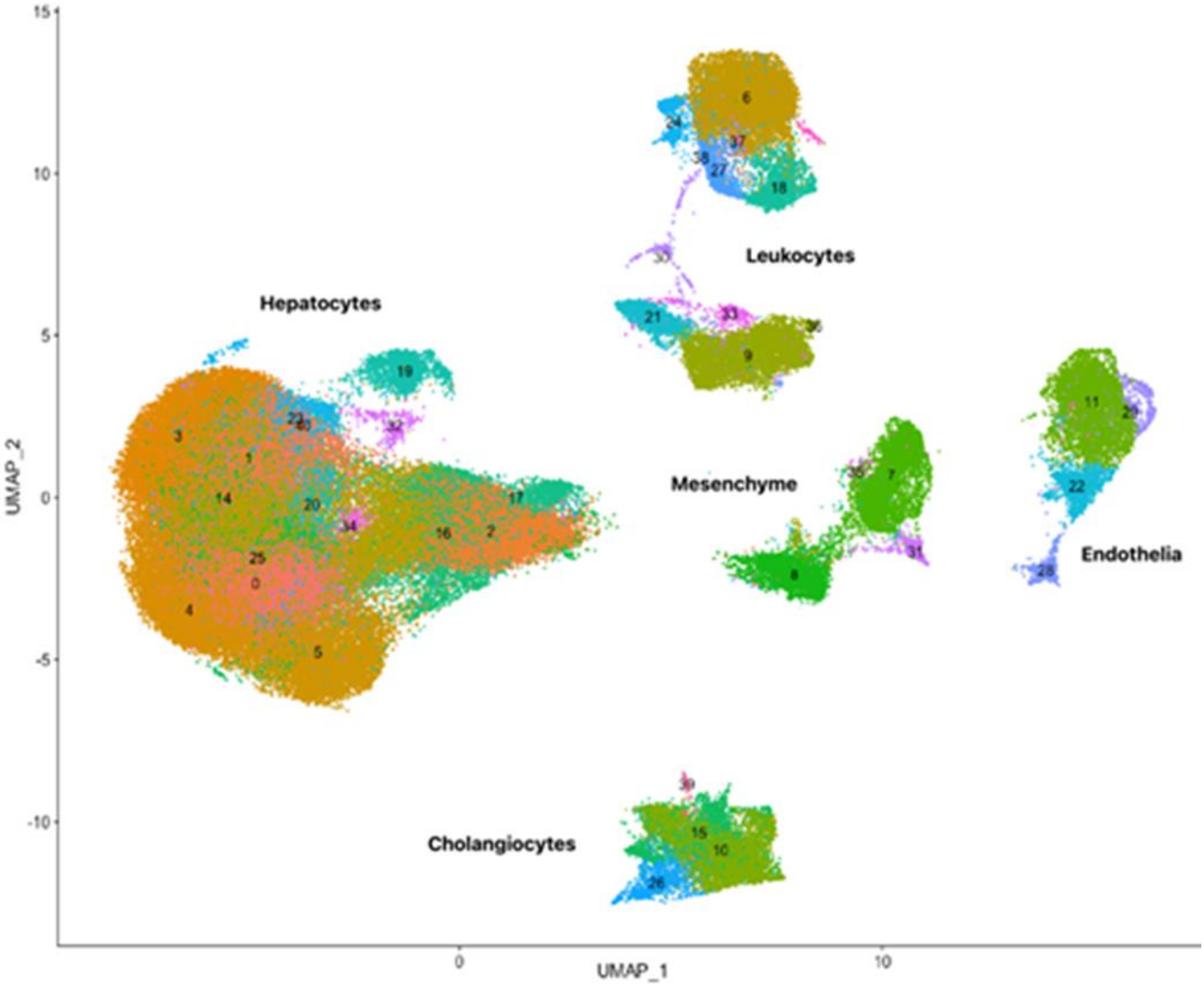

Figure 1: Enlarged UMAP from Figure 12 Clustering datasets (labelled by lineage) featured a large hepatocyte cluster and a smaller mesenchyme compartment, in keeping with the expected liver cell lineage proportions. Enlarged image for better visualisation of numbering.

Negative controls for immunohistochemistry of targets in liver and lung

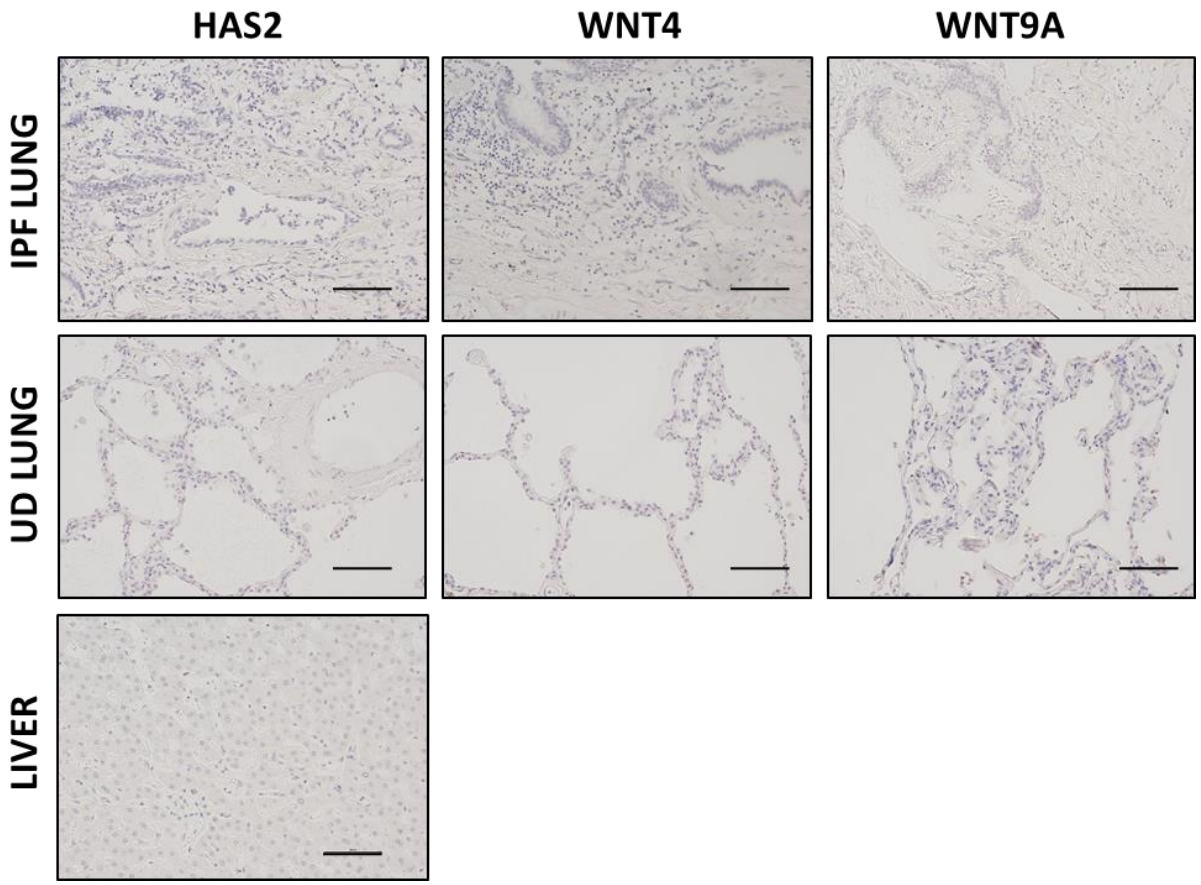

Figure 2: Negative controls of immunohistochemistry in different organs/diseases for targets of interest Representative images of negative controls for selected targets in IPF tissue, unused donor tissue and liver tissue where available (scale bar= 100µm). Immunohistochemistry was performed as previously described (subsection 3.2.8; Table 11), with the exception of incubation with primary antibodies.

Appendix B

Transcriptomic dataset for Figures 15

Experimental outline

Pre-existing transcriptomic datasets were generated from PCLS prepared from resected liver tissue (n=7 donors) detailed in Table 1, with slices (n=6 PCLS per condition) being rested for 24 hours before challenge with either control media, 3ng/ml TGF-β1 to induce fibrogenesis or 1ng/ml IL1α to stimulate an inflammatory response. After 24 hours challenge, PCLS were snap frozen and processed for bulk RNAseq.

Table 1: Donor demographics from pre-existing transcriptomic dataset used in Figure 15

Donor	Sex	Age	Fibrosis	Steatosis
PCLS donor 1	M	84	1	0
PCLS donor 2	F	70	1	0
PCLS donor 3	F	71	0	0
PCLS donor 4	F	63	2	0
PCLS donor 5	F	69	2	0
PCLS donor 6	M	70	4	0
PCLS donor 7	M	69	2	0

RNA isolation, bulk RNA seq and downstream analysis

RNA was isolated from n=2 pooled batched of PCLS per treatment condition for each donor as outlined in Chapter 2 (subsection 2.8.2) before being DNase treated and sent for RNAseq at Genomic Core Facility, Newcastle University. RNAseq and downstream analysis was performed as previously described (see subsection 4.1.3.2) and mRNA values were classified as significantly different when log2 fold change >2 and p-value (adjusted) <0.001.

Appendix C

Transcriptomic dataset for Figures 16

Experimental outline

Pre-existing transcriptomic datasets were generated from PCLS prepared from resected liver tissue, with slices (n=6 PCLS per condition) being rested for 24hrs before challenge with either control media (n=6 donors; PCLS donors 1-6), a combination treatment of pro-fibrotic TGF-β1(3ng/ml)/PDGFββ (50ng/ml) alone (n=6 donors; PCLS donors 1-6) or co-treated with 10μM ALK5i (TGFβ receptor I inhibitor) to blunt the fibrotic response (n=4 donors; PCLS donors 1-4) for 72hrs. Media, including all treatments, was refreshed at 24-hour intervals before PCLS were harvested and snap frozen at 96hrs for RNAseq. Liver donor demographics used to generate this dataset are outlined in Table 1.

Table 1: Donor demographics from pre-existing transcriptomic dataset used in Figure 16

Donor	Sex	Age	Fibrosis	Steatosis
PCLS donor 1	M	37	1	0
PCLS donor 2	F	24	0	0
PCLS donor 3	F	61	0	1
PCLS donor 4	F	67	1	0
PCLS donor 5	F	64	1	0
PCLS donor 6	F	23	2	0
PCLS donor 7	M	60	1	1

RNA isolation, bulk RNA seq and downstream analysis

RNA was isolated from n=2 pooled batched of PCLS per treatment condition for each donor as outlined in Chapter 2 (subsection 2.8.2) before being DNase treated and sent for RNAseq at Genomic Core Facility, Newcastle University. RNAseq and downstream analysis was performed as previously described (see subsection 4.1.3.2) and mRNA values were classified as significantly different when log2 fold change >2 and p-value (adjusted) <0.001.

Appendix D

Transcriptomic dataset for Figures 37 and 38

Experimental outline

Primary fibroblasts previously isolated and cryopreserved from the parenchyma of IPF explant tissue (n=6 donors) and unused donor lungs (n=6 donors) as outlined in subsection 5.2.5. were reanimated (n=5 donor lines) in culture medium and transferred to a T75 flask, incubated at 37°c supplemented with 5% CO_2. Media was replenished bi-weekly until the flask was deemed confluent, at which point fibroblasts were detached *via* trypsinisation, counted using an EVE automatic cell counter and seeded into three T75 flasks at a density of 500,000 cells/flask. Once cells were approximately 70% confluent, flasks were cultured for 24hrs in serum-free culture media before treatment with control media, recombinant human IL-1α (500pg/ml) or recombinant human TGF-β1 (10ng/ml) to induce a pro-inflammatory and pro-fibrotic phenotype, respectively. Following treatment, cells were detached *via* scraping into 4ml of ice-cold PBS, centrifuged for 4 minutes at 500*g* and snap frozen for analysis. Lung donor demographics used to generate these datasets are outlined in Table 1.

Table 1: Donor demographics from pre-existing transcriptomic datasets used in Figures 37-38

Donor	Sex	Age	FEV1, L	FVC, L	TLC, L	TLCO, mmol CO/min/kPa	KCO, mmol CO/min/kPa
IPF Fib 1	M	54	1.97 (52%)	2.38 (50%)	4.02 (54%)	3.08%	Unknown
IPF Fib 2	M	49	1.83 (51%)	2.87 (65%)	5.50 (81%)	1.1 (73%)	Non-smoker
IPF Fib 3	M	57	2.34 (72%)	2.71 (66%)	3.26 (50%)	1.23 (87%)	Non-smoker
IPF Fib 4	M	55	1.9 (51%)	2.27 (49%)	3.80 (51%)	1.0 (70%)	Ex-smoker
IPF Fib 5	M	58	2.25 (70%)	2.60 (63%)	3.97 (61%)	1.68 (116%)	Non-smoker
IPF Fib 6	M	60	2.02 (53%)	2.31 (47%)	3.31 (42%)	0.87 (64%)	Ex-smoker
UD Fib 1	M	36	N/A	N/A	N/A	N/A	No
UD Fib 2	F	52	N/A	N/A	N/A	N/A	Yes
UD Fib 3	M	52	N/A	N/A	N/A	N/A	No
UD Fib 4	F	54	N/A	N/A	N/A	N/A	Yes
UD Fib 5	F	51	N/A	N/A	N/A	N/A	Yes
UD Fib 6	M	60	N/A	N/A	N/A	N/A	Yes

FEV1= forced expiratory volume in 1 second, FVC= forced vital capacity, TLC= total lung capacity, TLCO= carbon monoxide transfer factor, KCO=carbon monoxide transfer coefficient and N/A= not available. Percentages of predicted values are in parentheses.

RNA isolation, bulk RNA seq and downstream analysis

Total RNA was isolated from snap frozen cell pellets using RNeasy mini kits (74104, Qiagen) according to manufacturer's guidelines as outlined in chapter 2 (subsection 2.8.1). Once isolated, RNA was DNase treated and sent for RNAseq at Genomic Core Facility, Newcastle University. RNAseq and downstream analysis was performed as previously described (see subsection 4.1.3.2) and mRNA values were classified as significantly different when log2 fold change >2 and p-value (adjusted) <0.001.

Appendix E

UMAPs of snRNAseq target expression in integrated lung datasets

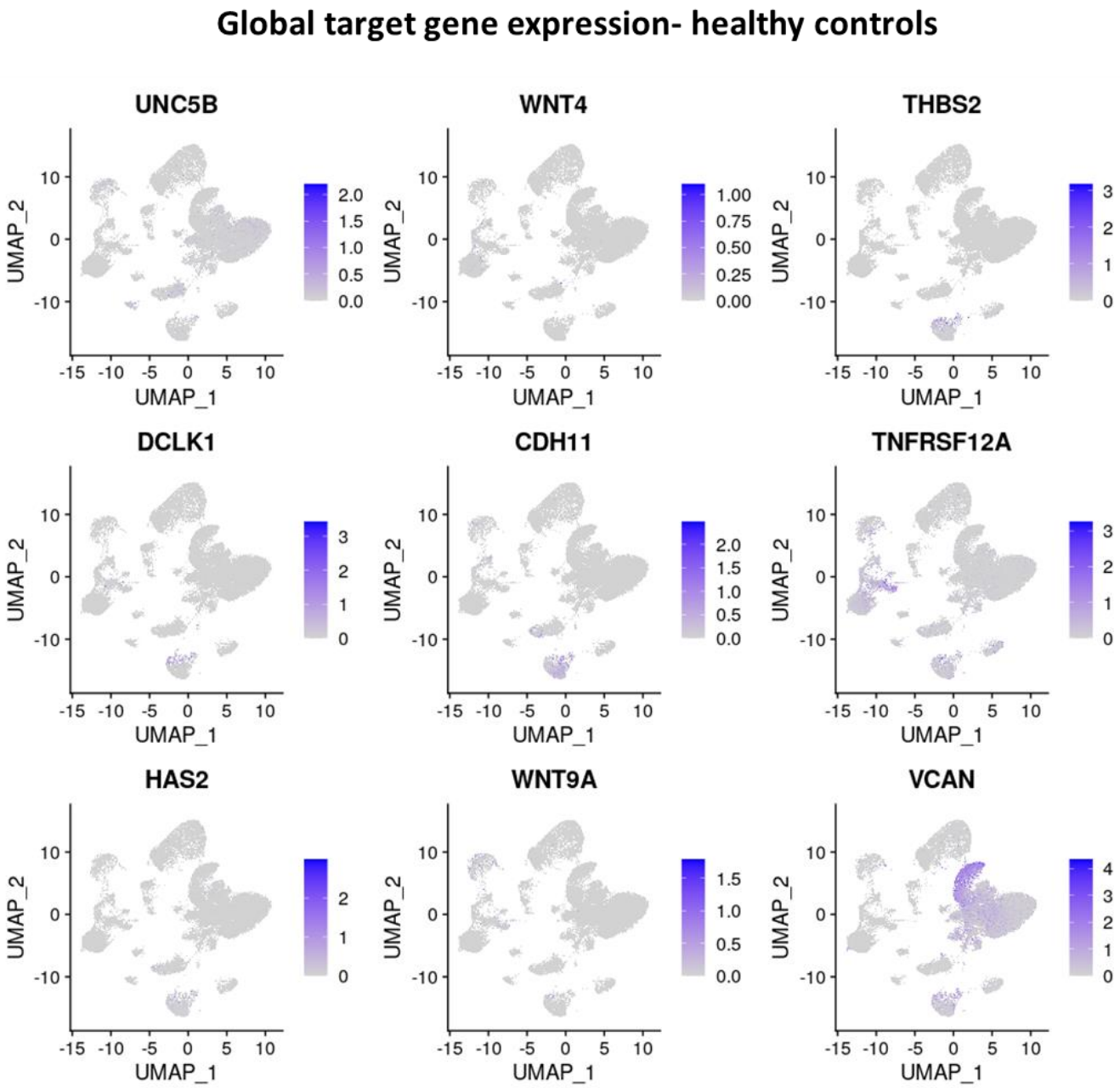

Figure 1: Investigation of global target gene expression in healthy controls of scRNAseq datasets Target gene expression was investigated in scRNA datasets generated from 6 integrated single cell lung atlases (https://singlecell.broadinstitute.org/single_cell/study/SCP2155/) created by Dr Stephen Christensen, Pfizer. A) In total, 716,074 cells were included from multiple different fibrotic lung diseases, comprising 13 different cell lineages. Individual UMAPs of target density are depicted for global target gene expression for healthy control donors only. (Figures provided by Dr Stephen Christensen, Pfizer).

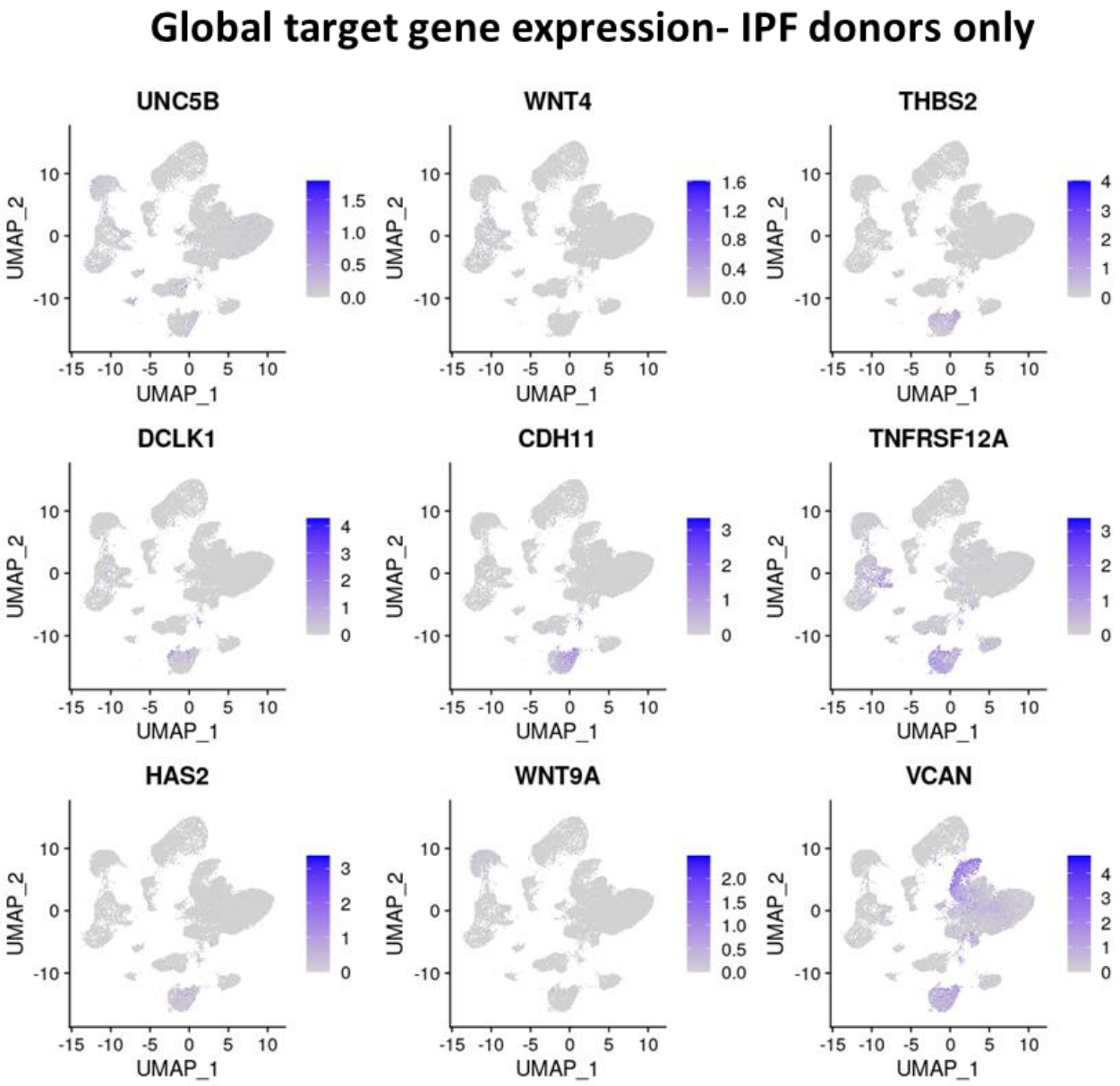

Figure 2: Investigation of global target gene expression in IPF donors of scRNAseq datasets Target gene expression was investigated in scRNA datasets generated from 6 integrated single cell lung atlases (https://singlecell.broadinstitute.org/single_cell/study/SCP2155/) created by Dr Stephen Christensen, Pfizer. A) In total, 716,074 cells were included from multiple different fibrotic lung diseases, comprising 13 different cell lineages. Individual UMAPs of target density are depicted for global target gene expression for IPF donors only. (Figures provided by Dr Stephen Christensen, Pfizer).

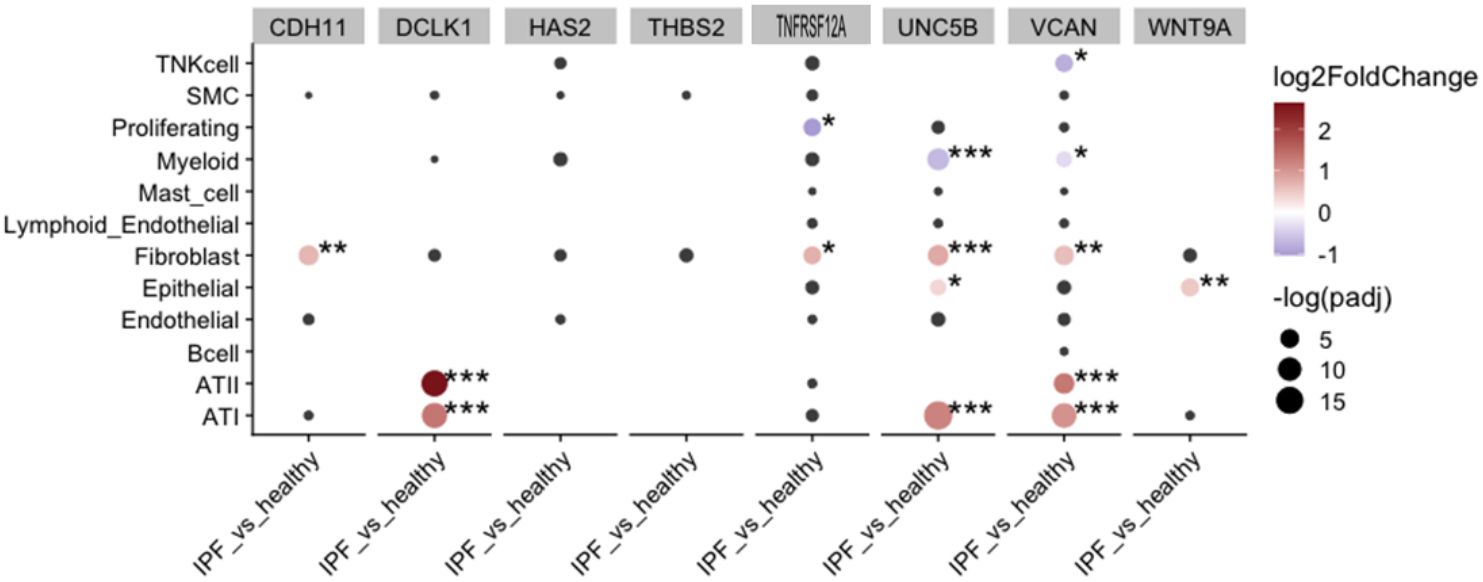

Figure 3: Pseudobulk differential expression of global target genes in scRNAseq datasets Target gene expression was investigated in scRNA datasets generated from 6 integrated single cell lung atlases (https://singlecell.broadinstitute.org/single_cell/study/SCP2155/) created by Dr Stephen Christensen, Pfizer. A) In total, 716,074 cells were included from multiple different fibrotic lung diseases, comprising 13 different cell lineages. Raw counts were aggregated by patient cell type and within each cell DESeq2was ran and statistical significance determined using Benjamini-Hochberg adjusted p values where *p<0.05, **p<0.01, ***p<0.001 and ****p<0.0001). [Figures provided by Dr Stephen Christensen, Pfizer].

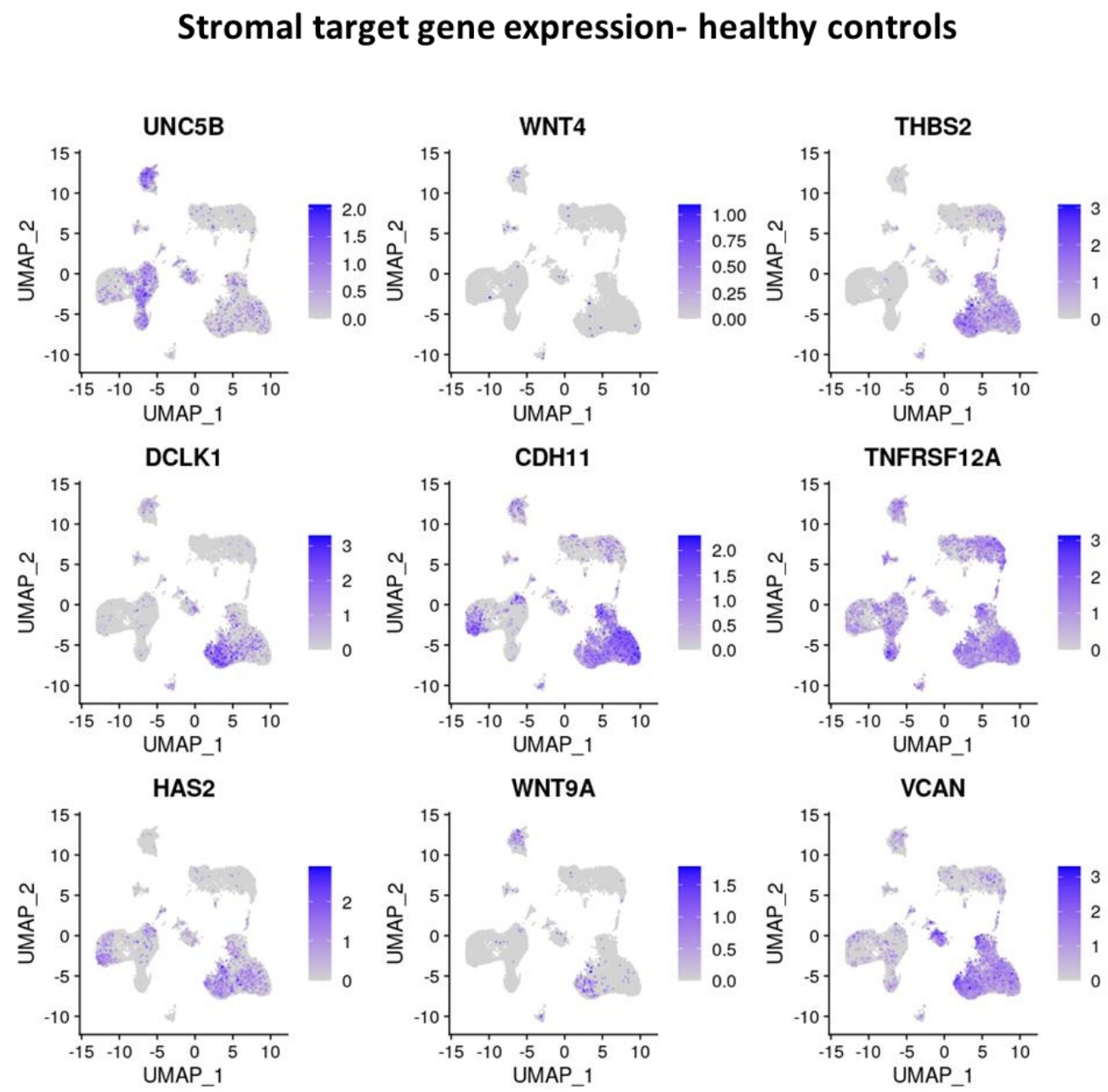

Figure 4: Investigation of stromal target gene expression in healthy controls of scRNAseq datasets Target gene expression was investigated in scRNA datasets generated from 6 integrated single cell lung atlases (https://singlecell.broadinstitute.org/single_cell/study/SCP2155/) created by Dr Stephen Christensen, Pfizer. A) In total, 716,074 cells were included from multiple different fibrotic lung diseases, comprising 13 different cell lineages. Individual UMAPs of target density are depicted for stromal target gene expression for healthy control donors only. (Figures provided by Dr Stephen Christensen, Pfizer).

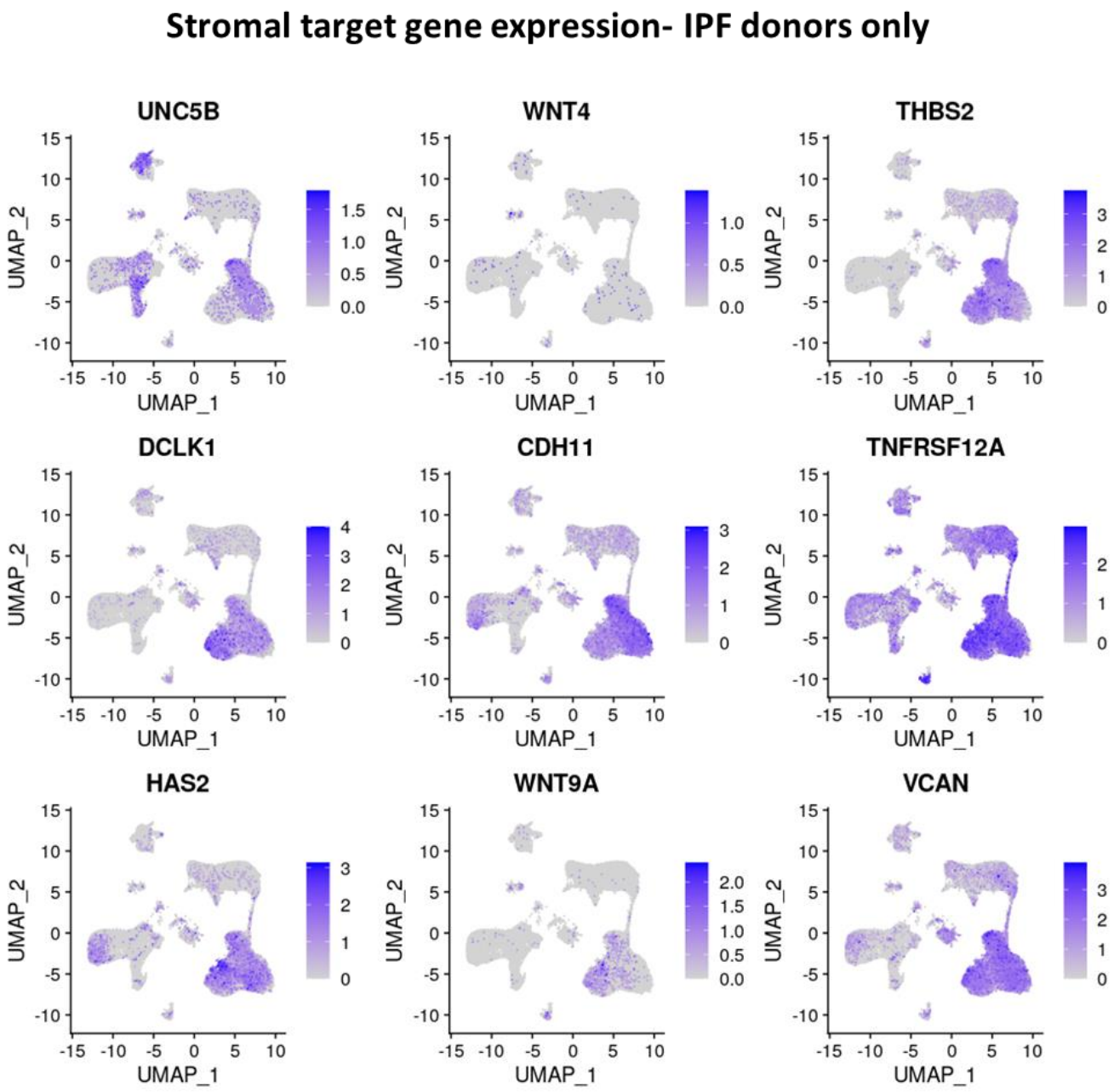

Figure 5: Investigation of stromal target gene expression in IPF donors of scRNAseq datasets Target gene expression was investigated in scRNA datasets generated from 6 integrated single cell lung atlases (https://singlecell.broadinstitute.org/single_cell/study/SCP2155/) created by Dr Stephen Christensen, Pfizer. A) In total, 716,074 cells were included from multiple different fibrotic lung diseases, comprising 13 different cell lineages. Individual UMAPs of target density are depicted for stromal target gene expression for IPF donors only. (Figures provided by Dr Stephen Christensen, Pfizer).

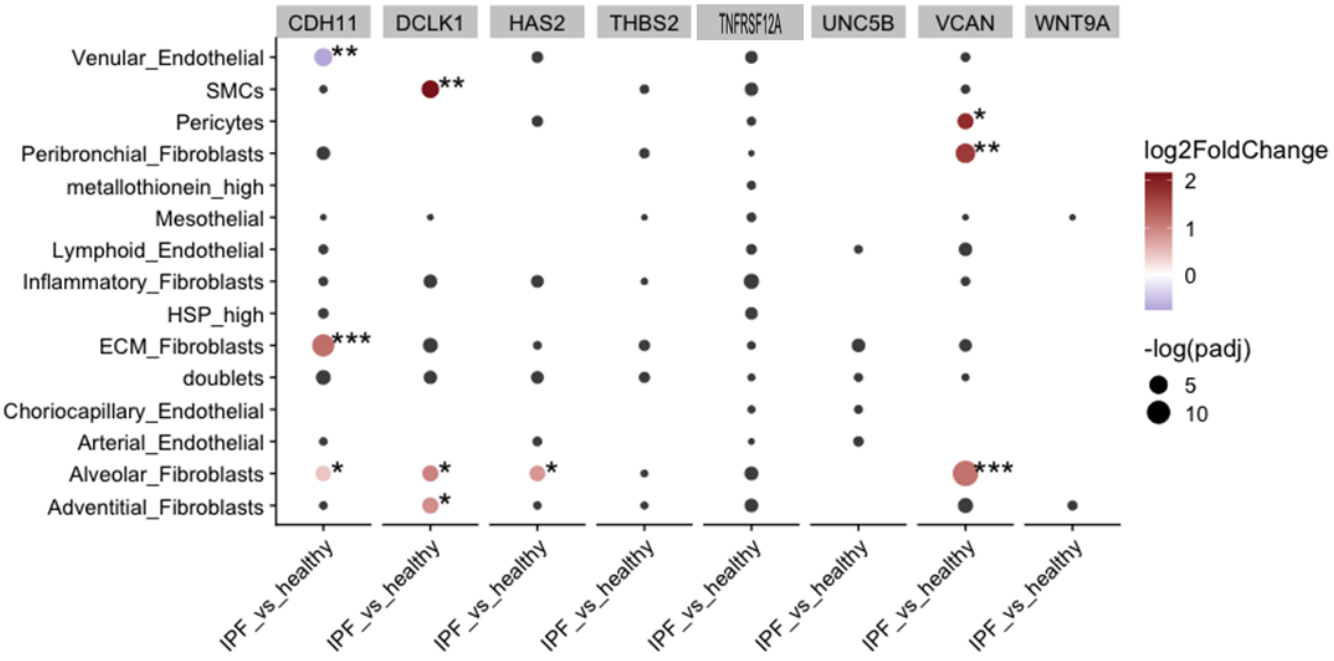

Figure 6: Pseudobulk differential expression of stromal target genes in scRNAseq datasets Target gene expression was investigated in scRNA datasets generated from 6 integrated single cell lung atlases (https://singlecell.broadinstitute.org/single_cell/study/SCP2155/) created by Dr Stephen Christensen, Pfizer. A) In total, 716,074 cells were included from multiple different fibrotic lung diseases, comprising 13 different cell lineages. Raw counts were aggregated by patient cell type and within each cell DESeq2was ran and statistical significance determined using Benjamini-Hochberg adjusted p values where *p<0.05, **p<0.01, ***p<0.001 and ****p<0.0001). [Figures provided by Dr Stephen Christensen, Pfizer].

Appendix F

GO analysis of inter- and intra- patient IPF datasets

GO analysis was performed on all regional IPF comparisons on significantly upregulated and significantly downregulated genes (log2 fold change >2 and p-value (adjusted) <0.05) and presented in the following tables and graphs where gene ratio= the proportion of genes from differentially expressed gene (DEG) list associated with the relevant GO term (no of genes involved in GO term/total no of genes in DEG list), Bg ratio= proportion of genes in the reference list that are associated with the GO term compared to number of genes annotated in the reference list (no of genes involved in GO term from reference gene list/ total no of genes in reference gene list), FE=fold enrichment, Ovalue= (odds ratio) statistical value to account for false discovery rate or how likely a gene in a GO term is to be significant and count= the number of DEGs enriched in each GO term.

Table 1: GO enrichment analysis significantly upregulated genes in IPF normal vs UD

GO ID	Description	GeneRatio	BgRatio	FE	pvalue	p.adjust	Count
GO:0030198	extracellular matrix organization	29/361	332/18888	4.57	1E-11	1.4E-08	29
GO:0043062	extracellular structure organization	29/361	333/18888	4.56	1E-11	1.4E-08	29
GO:0045229	external encapsulating structure organization	29/361	334/18888	4.54	1E-11	1.4E-08	29
GO:0030199	collagen fibril organization	11/361	66/18888	8.72	4E-08	3.8E-05	11
GO:0001503	ossification	26/361	446/18888	3.05	5E-07	0.0004	26
GO:0030574	collagen catabolic process	8/361	45/18888	9.30	2E-06	0.0011	8
GO:0032963	collagen metabolic process	11/361	107/18888	5.38	6E-06	0.0031	11
GO:0042476	odontogenesis	12/361	133/18888	4.72	1E-05	0.0041	12
GO:0031214	biomineral tissue development	13/361	180/18888	3.78	4E-05	0.0170	13
GO:0008217	regulation of blood pressure	13/361	187/18888	3.64	7E-05	0.0206	13
GO:0097553	calcium ion transmembrane import into cytosol	13/361	187/18888	3.64	7E-05	0.0206	13
GO:0045839	negative regulation of mitotic nuclear division	7/361	56/18888	6.54	9E-05	0.0260	7
GO:0010965	regulation of mitotic sister chromatid separation	7/361	59/18888	6.21	0.0001	0.0336	7
GO:0043588	skin development	17/361	318/18888	2.80	0.0001	0.0346	17
GO:0060033	anatomical structure regression	4/361	15/18888	13.95	0.0002	0.0346	4
GO:0051306	mitotic sister chromatid separation	7/361	62/18888	5.91	0.0002	0.0375	7
GO:0051784	negative regulation of nuclear division	7/361	63/18888	5.81	0.0002	0.0384	7
GO:0007094	mitotic spindle assembly checkpoint signaling	6/361	46/18888	6.82	0.0002	0.0384	6
GO:0071173	spindle assembly checkpoint signaling	6/361	46/18888	6.82	0.0002	0.0384	6
GO:0071174	mitotic spindle checkpoint signaling	6/361	46/18888	6.82	0.0002	0.0384	6
GO:0048565	digestive tract development	10/361	133/18888	3.93	0.0002	0.0384	10
GO:0031577	spindle checkpoint signaling	6/361	47/18888	6.68	0.0003	0.0384	6
GO:0033046	negative regulation of sister chromatid segregation	6/361	48/18888	6.54	0.0003	0.0384	6
GO:0033048	negative regulation of mitotic sister chromatid segregation	6/361	48/18888	6.54	0.0003	0.0384	6
GO:0045841	negative regulation of mitotic metaphase/anaphase transition	6/361	48/18888	6.54	0.0003	0.0384	6
GO:2000816	negative regulation of mitotic sister chromatid separation	6/361	48/18888	6.54	0.0003	0.0384	6
GO:0090596	sensory organ morphogenesis	15/361	278/18888	2.82	0.0003	0.0393	15
GO:0034505	tooth mineralization	5/361	32/18888	8.18	0.0003	0.0393	5
GO:0051985	negative regulation of chromosome segregation	6/361	50/18888	6.28	0.0004	0.0393	6
GO:1902100	negative regulation of metaphase/anaphase transition of cell cycle	6/361	50/18888	6.28	0.0004	0.0393	6
GO:1905819	negative regulation of chromosome separation	6/361	50/18888	6.28	0.0004	0.0393	6
GO:0001975	response to amphetamine	5/361	33/18888	7.93	0.0004	0.0393	5
GO:0031069	hair follicle morphogenesis	5/361	33/18888	7.93	0.0004	0.0393	5
GO:2001251	negative regulation of chromosome organization	8/361	93/18888	4.50	0.0004	0.0412	8
GO:0001649	osteoblast differentiation	14/361	257/18888	2.85	0.0005	0.0441	14
GO:0055123	digestive system development	10/361	145/18888	3.61	0.0005	0.0441	10
GO:0097305	response to alcohol	14/361	259/18888	2.83	0.0005	0.0441	14
GO:0002029	desensitization of G protein-coupled receptor signaling pathway	4/361	20/18888	10.46	0.0005	0.0441	4
GO:0008544	epidermis development	18/361	387/18888	2.43	0.0005	0.0441	18
GO:1905818	regulation of chromosome separation	7/361	74/18888	4.95	0.0005	0.0452	7
GO:0033047	regulation of mitotic sister chromatid segregation	6/361	54/18888	5.81	0.0006	0.0466	6
GO:0022401	negative adaptation of signaling pathway	4/361	21/18888	9.97	0.0006	0.0474	4
GO:0051383	kinetochore organization	4/361	21/18888	9.97	0.0006	0.0474	4
GO:0030178	negative regulation of Wnt signaling pathway	11/361	177/18888	3.25	0.0006	0.0474	11
GO:0060349	bone morphogenesis	8/361	99/18888	4.23	0.0006	0.0474	8
GO:0002052	positive regulation of neuroblast proliferation	5/361	37/18888	7.07	0.0007	0.0477	5
GO:0048730	epidermis morphogenesis	5/361	37/18888	7.07	0.0007	0.0477	5
GO:0002429	immune response-activating cell surface receptor signaling pathway	16/361	332/18888	2.52	0.0007	0.0498	16

Table 2: GO enrichment analysis significantly downregulated genes in IPF normal vs UD

GO ID	Description	GeneRatio	BgRatio	FE	pvalue	p.adjust	Count
GO:0032496	response to lipopolysaccharide	31/287	348/18888	5.86	2.3E-15	8.7E-12	31
GO:0071222	cellular response to lipopolysaccharide	25/287	225/18888	7.31	8.4E-15	1.5E-11	25
GO:0002237	response to molecule of bacterial origin	31/287	369/18888	5.53	1.1E-14	1.5E-11	31
GO:0030595	leukocyte chemotaxis	25/287	237/18888	6.94	2.8E-14	2.2E-11	25
GO:0071219	cellular response to molecule of bacterial origin	25/287	238/18888	6.91	3.1E-14	2.2E-11	25
GO:0097529	myeloid leukocyte migration	25/287	239/18888	6.88	3.4E-14	2.2E-11	25
GO:0071216	cellular response to biotic stimulus	25/287	265/18888	6.21	3.6E-13	2.0E-10	25
GO:0060326	cell chemotaxis	27/287	322/18888	5.52	6.8E-13	3.2E-10	27
GO:0071621	granulocyte chemotaxis	18/287	128/18888	9.25	9.3E-13	3.9E-10	18
GO:0097530	granulocyte migration	19/287	154/18888	8.12	2.3E-12	9.0E-10	19
GO:0030593	neutrophil chemotaxis	16/287	107/18888	9.84	6.7E-12	2.3E-09	16
GO:1990266	neutrophil migration	17/287	129/18888	8.67	1.2E-11	3.7E-09	17
GO:0050900	leukocyte migration	28/287	396/18888	4.65	1.5E-11	4.5E-09	28
GO:0071347	cellular response to interleukin-1	15/287	110/18888	8.97	1.2E-10	3.3E-08	15
GO:0006935	chemotaxis	29/287	466/18888	4.10	1.4E-10	3.6E-08	29
GO:0042330	taxis	29/287	468/18888	4.08	1.6E-10	3.7E-08	29
GO:0006959	humoral immune response	21/287	258/18888	5.36	4.7E-10	1.1E-07	21
GO:0070555	response to interleukin-1	15/287	138/18888	7.15	3.0E-09	6.4E-07	15
GO:0009636	response to toxic substance	20/287	260/18888	5.06	3.3E-09	6.6E-07	20
GO:0019730	antimicrobial humoral response	14/287	132/18888	6.98	1.4E-08	2.7E-06	14
GO:0006953	acute-phase response	9/287	47/18888	12.60	3.1E-08	5.7E-06	9
GO:1990868	response to chemokine	12/287	101/18888	7.82	4.3E-08	7.2E-06	12
GO:1990869	cellular response to chemokine	12/287	101/18888	7.82	4.3E-08	7.2E-06	12
GO:0002687	positive regulation of leukocyte migration	14/287	149/18888	6.18	6.6E-08	1.1E-05	14
GO:0010273	detoxification of copper ion	6/287	16/18888	24.68	8.2E-08	1.2E-05	6
GO:1990169	stress response to copper ion	6/287	16/18888	24.68	8.2E-08	1.2E-05	6
GO:0046688	response to copper ion	8/287	38/18888	13.86	8.5E-08	1.2E-05	8
GO:0071280	cellular response to copper ion	7/287	26/18888	17.72	8.9E-08	1.2E-05	7
GO:0044703	multi-organism reproductive process	16/287	204/18888	5.16	9.7E-08	1.3E-05	16
GO:1903524	positive regulation of blood circulation	8/287	39/18888	13.50	1.1E-07	1.3E-05	8
GO:0034612	response to tumor necrosis factor	18/287	263/18888	4.50	1.2E-07	1.5E-05	18
GO:0044706	multi-multicellular organism process	16/287	212/18888	4.97	1.6E-07	1.9E-05	16
GO:0070098	chemokine-mediated signaling pathway	11/287	93/18888	7.78	1.7E-07	1.9E-05	11
GO:0042742	defense response to bacterium	20/287	330/18888	3.99	1.7E-07	1.9E-05	20
GO:0071356	cellular response to tumor necrosis factor	17/287	241/18888	4.64	1.8E-07	1.9E-05	17
GO:0001819	positive regulation of cytokine production	25/287	500/18888	3.29	2.0E-07	2.2E-05	25
GO:0007566	embryo implantation	9/287	59/18888	10.04	2.5E-07	2.5E-05	9
GO:0009266	response to temperature stimulus	14/287	172/18888	5.36	3.9E-07	4.0E-05	14
GO:0097501	stress response to metal ion	6/287	21/18888	18.80	5.2E-07	5.0E-05	6
GO:0009408	response to heat	11/287	104/18888	6.96	5.3E-07	5.0E-05	11
GO:0061687	detoxification of inorganic compound	6/287	22/18888	17.95	7.1E-07	6.6E-05	6
GO:0002526	acute inflammatory response	11/287	109/18888	6.64	8.4E-07	7.7E-05	11
GO:0006882	intracellular zinc ion homeostasis	7/287	36/18888	12.80	9.9E-07	8.9E-05	7
GO:0002548	monocyte chemotaxis	9/287	70/18888	8.46	1.1E-06	9.6E-05	9
GO:0071294	cellular response to zinc ion	6/287	24/18888	16.45	1.2E-06	0.0001	6
GO:0045823	positive regulation of heart contraction	7/287	38/18888	12.12	1.5E-06	0.0001	7
GO:0002822	regulation of adaptive immune response based on somatic recombination of immune receptors	14/287	192/18888	4.80	1.5E-06	0.0001	14
GO:0002690	positive regulation of leukocyte chemotaxis	10/287	93/18888	7.08	1.5E-06	0.0001	10
GO:0048246	macrophage chemotaxis	7/287	40/18888	11.52	2.1E-06	0.0002	7
GO:0002833	positive regulation of response to biotic stimulus	20/287	390/18888	3.37	2.4E-06	0.0002	20

Table 3: GO enrichment analysis significantly regulated genes in IPF intermediate vs UD

GO ID	Description	GeneRatio	BgRatio	FE	pvalue	p.adjust	Count
GO:0002377	immunoglobulin production	58/550	194/18888	10.27	1.8E-42	6.6E-39	58
GO:0016064	immunoglobulin mediated immune response	57/550	208/18888	9.41	2.1E-39	3.8E-36	57
GO:0019724	B cell mediated immunity	57/550	212/18888	9.23	6.5E-39	8.0E-36	57
GO:0002440	production of molecular mediator of immune response	59/550	310/18888	6.54	2.9E-31	2.7E-28	59
GO:0002449	lymphocyte mediated immunity	62/550	372/18888	5.72	2.0E-29	1.2E-26	62
GO:0002460	adaptive immune response based on somatic recombination of immune receptors	63/550	385/18888	5.62	2.0E-29	1.2E-26	63
GO:0002443	leukocyte mediated immunity	63/550	469/18888	4.61	1.5E-24	8.1E-22	63
GO:0050853	B cell receptor signaling pathway	19/550	78/18888	8.37	6.6E-13	3.0E-10	19
GO:0030198	extracellular matrix organization	33/550	332/18888	3.41	8.6E-10	3.4E-07	33
GO:0043062	extracellular structure organization	33/550	333/18888	3.40	9.3E-10	3.4E-07	33
GO:0045229	external encapsulating structure organization	33/550	334/18888	3.39	1.0E-09	3.4E-07	33
GO:0050851	antigen receptor-mediated signaling pathway	23/550	208/18888	3.80	4.5E-08	1.3E-05	23
GO:0030199	collagen fibril organization	13/550	66/18888	6.76	4.7E-08	1.3E-05	13
GO:0019730	antimicrobial humoral response	18/550	132/18888	4.68	5.4E-08	1.4E-05	18
GO:0002429	immune response-activating cell surface receptor signaling pathway	28/550	332/18888	2.90	5.2E-07	0.0001	28
GO:0019731	antibacterial humoral response	12/550	69/18888	5.97	6.4E-07	0.0001	12
GO:0006959	humoral immune response	23/550	258/18888	3.06	2.1E-06	0.0005	23
GO:0002768	immune response-regulating cell surface receptor signaling pathway	28/550	360/18888	2.67	2.6E-06	0.0005	28
GO:0006958	complement activation, classical pathway	9/550	42/18888	7.36	2.7E-06	0.0005	9
GO:0002455	humoral immune response mediated by circulating immunoglobulin	10/550	56/18888	6.13	4.3E-06	0.0008	10
GO:0030574	collagen catabolic process	9/550	45/18888	6.87	4.9E-06	0.0009	9
GO:0006956	complement activation	10/550	67/18888	5.13	2.3E-05	0.0038	10
GO:0032963	collagen metabolic process	12/550	107/18888	3.85	6.6E-05	0.0106	12
GO:0001503	ossification	28/550	446/18888	2.16	0.0001	0.0193	28
GO:1905818	regulation of chromosome separation	9/550	74/18888	4.18	0.0003	0.0418	9
GO:0010965	regulation of mitotic sister chromatid separation	8/550	59/18888	4.66	0.0003	0.0418	8
GO:0007094	mitotic spindle assembly checkpoint signaling	7/550	46/18888	5.23	0.0003	0.0434	7
GO:0071173	spindle assembly checkpoint signaling	7/550	46/18888	5.23	0.0003	0.0434	7
GO:0071174	mitotic spindle checkpoint signaling	7/550	46/18888	5.23	0.0003	0.0434	7
GO:0031577	spindle checkpoint signaling	7/550	47/18888	5.11	0.0004	0.0471	7
GO:0051306	mitotic sister chromatid separation	8/550	62/18888	4.43	0.0004	0.0471	8
GO:0033046	negative regulation of sister chromatid segregation	7/550	48/18888	5.01	0.0004	0.0471	7
GO:0033048	negative regulation of mitotic sister chromatid segregation	7/550	48/18888	5.01	0.0004	0.0471	7
GO:0045841	negative regulation of mitotic metaphase/anaphase transition	7/550	48/18888	5.01	0.0004	0.0471	7
GO:2000816	negative regulation of mitotic sister chromatid separation	7/550	48/18888	5.01	0.0004	0.0471	7

Table 4: GO enrichment analysis significantly downregulated genes in IPF intermediate vs UD

GO ID	Description	GeneRatio	BgRatio	FE	pvalue	p.adjust	Count
GO:0032496	response to lipopolysaccharide	27/271	348/18888	5.41	1.1E-12	4.0E-09	27
GO:0002237	response to molecule of bacterial origin	27/271	369/18888	5.10	4.3E-12	5.3E-09	27
GO:0071347	cellular response to interleukin-1	16/271	110/18888	10.14	4.3E-12	5.3E-09	16
GO:0071222	cellular response to lipopolysaccharide	21/271	225/18888	6.51	1.2E-11	1.1E-08	21
GO:0071219	cellular response to molecule of bacterial origin	21/271	238/18888	6.15	3.6E-11	2.7E-08	21
GO:0070555	response to interleukin-1	16/271	138/18888	8.08	1.5E-10	9.0E-08	16
GO:0030595	leukocyte chemotaxis	20/271	237/18888	5.88	2.4E-10	1.1E-07	20
GO:0071216	cellular response to biotic stimulus	21/271	265/18888	5.52	2.7E-10	1.1E-07	21
GO:0097529	myeloid leukocyte migration	20/271	239/18888	5.83	2.8E-10	1.1E-07	20
GO:0006959	humoral immune response	20/271	258/18888	5.40	1.1E-09	3.9E-07	20
GO:0060326	cell chemotaxis	22/271	322/18888	4.76	1.6E-09	5.5E-07	22
GO:0050900	leukocyte migration	24/271	396/18888	4.22	3.2E-09	9.8E-07	24
GO:0001819	positive regulation of cytokine production	27/271	500/18888	3.76	3.9E-09	1.1E-06	27
GO:0030593	neutrophil chemotaxis	13/271	107/18888	8.47	4.5E-09	1.1E-06	13
GO:0071621	granulocyte chemotaxis	14/271	128/18888	7.62	4.5E-09	1.1E-06	14
GO:1990266	neutrophil migration	14/271	129/18888	7.56	5.0E-09	1.2E-06	14
GO:0097530	granulocyte migration	15/271	154/18888	6.79	6.3E-09	1.4E-06	15
GO:0019730	antimicrobial humoral response	14/271	132/18888	7.39	6.8E-09	1.4E-06	14
GO:0006935	chemotaxis	25/271	466/18888	3.74	1.7E-08	3.3E-06	25
GO:0042330	taxis	25/271	468/18888	3.72	1.9E-08	3.4E-06	25
GO:0034612	response to tumor necrosis factor	18/271	263/18888	4.77	5.1E-08	9.0E-06	18
GO:0031649	heat generation	6/271	16/18888	26.14	5.9E-08	9.9E-06	6
GO:0071356	cellular response to tumor necrosis factor	17/271	241/18888	4.92	7.8E-08	1.3E-05	17
GO:0007566	embryo implantation	9/271	59/18888	10.63	1.5E-07	2.3E-05	9
GO:1990868	response to chemokine	11/271	101/18888	7.59	2.2E-07	3.1E-05	11
GO:1990869	cellular response to chemokine	11/271	101/18888	7.59	2.2E-07	3.1E-05	11
GO:0050727	regulation of inflammatory response	22/271	425/18888	3.61	2.4E-07	3.2E-05	22
GO:0002687	positive regulation of leukocyte migration	13/271	149/18888	6.08	2.4E-07	3.2E-05	13
GO:0001660	fever generation	5/271	11/18888	31.68	2.5E-07	3.2E-05	5
GO:0032757	positive regulation of interleukin-8 production	9/271	63/18888	9.96	2.7E-07	3.4E-05	9
GO:0050729	positive regulation of inflammatory response	13/271	153/18888	5.92	3.3E-07	3.9E-05	13
GO:0030072	peptide hormone secretion	16/271	242/18888	4.61	4.6E-07	5.3E-05	16
GO:0002790	peptide secretion	16/271	247/18888	4.51	6.0E-07	6.7E-05	16
GO:0042886	amide transport	18/271	312/18888	4.02	6.5E-07	7.1E-05	18
GO:0070098	chemokine-mediated signaling pathway	10/271	93/18888	7.49	8.9E-07	9.4E-05	10
GO:0002833	positive regulation of response to biotic stimulus	20/271	390/18888	3.57	9.8E-07	0.0001	20
GO:0009914	hormone transport	18/271	322/18888	3.90	1.0E-06	0.0001	18
GO:0002221	pattern recognition receptor signaling pathway	16/271	259/18888	4.31	1.1E-06	0.0001	16
GO:0009266	response to temperature stimulus	13/271	172/18888	5.27	1.3E-06	0.0001	13
GO:0044703	multi-organism reproductive process	14/271	204/18888	4.78	1.6E-06	0.0001	14
GO:0002819	regulation of adaptive immune response	14/271	207/18888	4.71	1.8E-06	0.0002	14
GO:0015833	peptide transport	16/271	271/18888	4.11	2.0E-06	0.0002	16
GO:0023061	signal release	22/271	487/18888	3.15	2.3E-06	0.0002	22
GO:0002675	positive regulation of acute inflammatory response	6/271	28/18888	14.94	2.4E-06	0.0002	6
GO:0044706	multi-multicellular organism process	14/271	212/18888	4.60	2.4E-06	0.0002	14
GO:0061844	antimicrobial humoral immune response mediated by antimicrobial peptide	9/271	82/18888	7.65	2.7E-06	0.0002	9
GO:0046879	hormone secretion	17/271	311/18888	3.81	2.8E-06	0.0002	17
GO:0002758	innate immune response-activating signaling pathway	16/271	278/18888	4.01	2.8E-06	0.0002	16
GO:2001236	regulation of extrinsic apoptotic signaling pathway	12/271	157/18888	5.33	2.9E-06	0.0002	12
GO:0002822	regulation of adaptive immune response based on somatic recombination of immune receptors	13/271	192/18888	4.72	4.3E-06	0.0003	13

Table 5: GO enrichment analysis significantly upregulated genes in IPF fibrotic vs UD

GO ID	Description	GeneRatio	BgRatio	FE	pvalue	p.adjust	Count
GO:0035082	axoneme assembly	55/1030	97/18888	10.40	4.9E-44	2.2E-40	55
GO:0003341	cilium movement	77/1030	209/18888	6.76	1.2E-43	2.6E-40	77
GO:0001578	microtubule bundle formation	59/1030	126/18888	8.59	8.3E-41	1.2E-37	59
GO:0007018	microtubule-based movement	95/1030	426/18888	4.09	4.7E-33	5.3E-30	95
GO:0001539	cilium or flagellum-dependent cell motility	57/1030	170/18888	6.15	4.8E-30	3.6E-27	57
GO:0060285	cilium-dependent cell motility	57/1030	170/18888	6.15	4.8E-30	3.6E-27	57
GO:0002377	immunoglobulin production	59/1030	194/18888	5.58	1.8E-28	1.2E-25	59
GO:0060294	cilium movement involved in cell motility	54/1030	165/18888	6.00	6.3E-28	3.5E-25	54
GO:0044782	cilium organization	84/1030	412/18888	3.74	2.0E-26	1.0E-23	84
GO:0060271	cilium assembly	76/1030	385/18888	3.62	4.5E-23	2.0E-20	76
GO:0016064	immunoglobulin mediated immune response	54/1030	208/18888	4.76	1.7E-22	6.8E-20	54
GO:0070286	axonemal dynein complex assembly	25/1030	40/18888	11.46	3.6E-22	1.3E-19	25
GO:0019724	B cell mediated immunity	54/1030	212/18888	4.67	4.5E-22	1.5E-19	54
GO:0030317	flagellated sperm motility	41/1030	141/18888	5.33	2.3E-19	7.0E-17	41
GO:0097722	sperm motility	41/1030	141/18888	5.33	2.3E-19	7.0E-17	41
GO:0002440	production of molecular mediator of immune response	61/1030	310/18888	3.61	1.2E-18	3.2E-16	61
GO:0002449	lymphocyte mediated immunity	61/1030	372/18888	3.01	9.3E-15	2.4E-12	61
GO:0003351	epithelial cilium movement involved in extracellular fluid movement	20/1030	43/18888	8.53	1.3E-14	3.3E-12	20
GO:0002460	adaptive immune response based on somatic recombination of immune receptors	61/1030	385/18888	2.91	4.6E-14	1.1E-11	61
GO:0006858	extracellular transport	20/1030	46/18888	7.97	6.5E-14	1.5E-11	20
GO:0044458	motile cilium assembly	24/1030	69/18888	6.38	8.0E-14	1.7E-11	24
GO:0036158	outer dynein arm assembly	14/1030	24/18888	10.70	2.2E-12	4.5E-10	14
GO:0002443	leukocyte mediated immunity	62/1030	469/18888	2.42	8.7E-11	1.7E-08	62
GO:0036159	inner dynein arm assembly	11/1030	17/18888	11.87	1.1E-10	2.1E-08	11
GO:0007288	sperm axoneme assembly	13/1030	29/18888	8.22	1.0E-09	1.9E-07	13
GO:0120316	sperm flagellum assembly	15/1030	45/18888	6.11	7.5E-09	1.3E-06	15
GO:0050853	B cell receptor signaling pathway	19/1030	78/18888	4.47	2.6E-08	4.4E-06	19
GO:0060972	left/right pattern formation	26/1030	143/18888	3.33	5.4E-08	8.7E-06	26
GO:0003352	regulation of cilium movement	13/1030	41/18888	5.81	1.5E-07	2.3E-05	13
GO:0007286	spermatid development	32/1030	214/18888	2.74	2.0E-07	3.0E-05	32
GO:0007368	determination of left/right symmetry	24/1030	137/18888	3.21	3.6E-07	5.0E-05	24
GO:0009799	specification of symmetry	25/1030	147/18888	3.12	3.7E-07	5.0E-05	25
GO:0009855	determination of bilateral symmetry	25/1030	147/18888	3.12	3.7E-07	5.0E-05	25
GO:0048515	spermatid differentiation	32/1030	222/18888	2.64	4.7E-07	6.2E-05	32
GO:0030198	extracellular matrix organization	41/1030	332/18888	2.26	8.7E-07	0.0001	41
GO:0043062	extracellular structure organization	41/1030	333/18888	2.26	9.4E-07	0.0001	41
GO:0045229	external encapsulating structure organization	41/1030	334/18888	2.25	1.0E-06	0.0001	41
GO:0060287	epithelial cilium movement involved in determination of left/right asymmetry	7/1030	13/18888	9.87	1.8E-06	0.0002	7
GO:0019730	antimicrobial humoral response	22/1030	132/18888	3.06	2.6E-06	0.0003	22
GO:0003002	regionalization	47/1030	429/18888	2.01	4.3E-06	0.0005	47
GO:0099111	microtubule-based transport	29/1030	213/18888	2.50	5.1E-06	0.0006	29
GO:0007281	germ cell development	42/1030	371/18888	2.08	6.1E-06	0.0006	42
GO:0060632	regulation of microtubule-based movement	13/1030	57/18888	4.18	9.1E-06	0.0009	13
GO:0007389	pattern specification process	49/1030	474/18888	1.90	1.3E-05	0.0013	49
GO:0003356	regulation of cilium beat frequency	7/1030	17/18888	7.55	1.7E-05	0.0017	7
GO:0022412	cellular process involved in reproduction in multicellular organism	48/1030	482/18888	1.83	4.2E-05	0.0041	48
GO:0006958	complement activation, classical pathway	10/1030	42/18888	4.37	6.6E-05	0.0063	10
GO:0019731	antibacterial humoral response	13/1030	69/18888	3.45	7.8E-05	0.0073	13
GO:0090660	cerebrospinal fluid circulation	6/1030	15/18888	7.34	8.5E-05	0.0077	6
GO:0031424	keratinization	14/1030	83/18888	3.09	0.0001	0.0131	14

Table 6: GO enrichment analysis significantly downregulated genes in IPF fibrotic vs UD

GO ID	Description	GeneRatio	BgRatio	FE	pvalue	p.adjust	Count
GO:0032496	response to lipopolysaccharide	35/367	348/18888	5.18	1.6E-15	6.6E-12	35
GO:0002237	response to molecule of bacterial origin	35/367	369/18888	4.88	9.4E-15	2.0E-11	35
GO:0071222	cellular response to lipopolysaccharide	26/367	225/18888	5.95	3.1E-13	4.3E-10	26
GO:0071219	cellular response to molecule of bacterial origin	26/367	238/18888	5.62	1.2E-12	9.9E-10	26
GO:0006959	humoral immune response	27/367	258/18888	5.39	1.2E-12	9.9E-10	27
GO:0071216	cellular response to biotic stimulus	26/367	265/18888	5.05	1.4E-11	9.5E-09	26
GO:0001819	positive regulation of cytokine production	35/367	500/18888	3.60	6.1E-11	3.7E-08	35
GO:0019730	antimicrobial humoral response	18/367	132/18888	7.02	9.4E-11	4.9E-08	18
GO:1903522	regulation of blood circulation	24/367	262/18888	4.71	3.5E-10	1.6E-07	24
GO:0050727	regulation of inflammatory response	30/367	425/18888	3.63	1.3E-09	5.2E-07	30
GO:0050890	cognition	25/367	322/18888	4.00	4.7E-09	1.8E-06	25
GO:0050729	positive regulation of inflammatory response	17/367	153/18888	5.72	7.7E-09	2.7E-06	17
GO:0031649	heat generation	7/367	16/18888	22.52	9.7E-09	3.1E-06	7
GO:1903532	positive regulation of secretion by cell	23/367	288/18888	4.11	1.2E-08	3.5E-06	23
GO:0044703	multi-organism reproductive process	19/367	204/18888	4.79	1.9E-08	5.1E-06	19
GO:0060047	heart contraction	21/367	249/18888	4.34	2.0E-08	5.1E-06	21
GO:0003018	vascular process in circulatory system	22/367	275/18888	4.12	2.3E-08	5.8E-06	22
GO:0051091	positive regulation of DNA-binding transcription factor activity	20/367	230/18888	4.48	2.6E-08	6.0E-06	20
GO:0071347	cellular response to interleukin-1	14/367	110/18888	6.55	2.9E-08	6.4E-06	14
GO:0044706	multi-multicellular organism process	19/367	212/18888	4.61	3.6E-08	7.5E-06	19
GO:0003015	heart process	21/367	260/18888	4.16	4.2E-08	8.3E-06	21
GO:0035296	regulation of tube diameter	16/367	152/18888	5.42	4.6E-08	8.4E-06	16
GO:0097746	blood vessel diameter maintenance	16/367	152/18888	5.42	4.6E-08	8.4E-06	16
GO:0035150	regulation of tube size	16/367	153/18888	5.38	5.1E-08	8.6E-06	16
GO:0051047	positive regulation of secretion	23/367	312/18888	3.79	5.1E-08	8.6E-06	23
GO:0061844	antimicrobial humoral immune response mediated by antimicrobial peptide	12/367	82/18888	7.53	5.9E-08	9.5E-06	12
GO:0051090	regulation of DNA-binding transcription factor activity	25/367	381/18888	3.38	1.3E-07	1.9E-05	25
GO:0002819	regulation of adaptive immune response	18/367	207/18888	4.48	1.3E-07	1.9E-05	18
GO:0050804	modulation of chemical synaptic transmission	29/367	493/18888	3.03	1.3E-07	1.9E-05	29
GO:0099177	regulation of trans-synaptic signaling	29/367	494/18888	3.02	1.4E-07	1.9E-05	29
GO:0008016	regulation of heart contraction	18/367	208/18888	4.45	1.4E-07	1.9E-05	18
GO:0022407	regulation of cell-cell adhesion	29/367	496/18888	3.01	1.5E-07	2.0E-05	29
GO:0003085	negative regulation of systemic arterial blood pressure	7/367	23/18888	15.66	1.9E-07	2.3E-05	7
GO:0002687	positive regulation of leukocyte migration	15/367	149/18888	5.18	2.2E-07	2.4E-05	15
GO:0032611	interleukin-1 beta production	13/367	110/18888	6.08	2.2E-07	2.4E-05	13
GO:0032651	regulation of interleukin-1 beta production	13/367	110/18888	6.08	2.2E-07	2.4E-05	13
GO:0032612	interleukin-1 production	14/367	129/18888	5.59	2.2E-07	2.4E-05	14
GO:0032652	regulation of interleukin-1 production	14/367	129/18888	5.59	2.2E-07	2.4E-05	14
GO:0034612	response to tumor necrosis factor	20/367	263/18888	3.91	2.3E-07	2.5E-05	20
GO:0097529	myeloid leukocyte migration	19/367	239/18888	4.09	2.4E-07	2.5E-05	19
GO:0050900	leukocyte migration	25/367	396/18888	3.25	2.7E-07	2.7E-05	25
GO:0003073	regulation of systemic arterial blood pressure	12/367	96/18888	6.43	3.5E-07	3.5E-05	12
GO:0050806	positive regulation of synaptic transmission	16/367	177/18888	4.65	3.8E-07	3.7E-05	16
GO:0070555	response to interleukin-1	14/367	138/18888	5.22	5.1E-07	4.8E-05	14
GO:2001237	negative regulation of extrinsic apoptotic signaling pathway	12/367	100/18888	6.18	5.5E-07	5.1E-05	12
GO:0007611	learning or memory	20/367	278/18888	3.70	5.7E-07	5.2E-05	20
GO:0001659	temperature homeostasis	16/367	183/18888	4.50	6.0E-07	5.4E-05	16
GO:0051092	positive regulation of NF-kappaB transcription factor activity	14/367	141/18888	5.11	6.6E-07	5.8E-05	14
GO:0002833	positive regulation of response to biotic stimulus	24/367	390/18888	3.17	7.4E-07	6.3E-05	24
GO:1905952	regulation of lipid localization	16/367	186/18888	4.43	7.5E-07	6.3E-05	16

Table 7: GO enrichment analysis significantly upregulated genes in IPF fibrotic vs IPF normal

GO ID	Description	GeneRatio	BgRatio	FE	pvalue	p.adjust	Count
GO:0035082	axoneme assembly	55/1030	97/18888	10.40	4.9E-44	2.2E-40	55
GO:0003341	cilium movement	77/1030	209/18888	6.76	1.2E-43	2.6E-40	77
GO:0001578	microtubule bundle formation	59/1030	126/18888	8.59	8.3E-41	1.2E-37	59
GO:0007018	microtubule-based movement	95/1030	426/18888	4.09	4.7E-33	5.3E-30	95
GO:0001539	cilium or flagellum-dependent cell motility	57/1030	170/18888	6.15	4.8E-30	3.6E-27	57
GO:0060285	cilium-dependent cell motility	57/1030	170/18888	6.15	4.8E-30	3.6E-27	57
GO:0002377	immunoglobulin production	59/1030	194/18888	5.58	1.8E-28	1.2E-25	59
GO:0060294	cilium movement involved in cell motility	54/1030	165/18888	6.00	6.3E-28	3.5E-25	54
GO:0044782	cilium organization	84/1030	412/18888	3.74	2.0E-26	1.0E-23	84
GO:0060271	cilium assembly	76/1030	385/18888	3.62	4.5E-23	2.0E-20	76
GO:0016064	immunoglobulin mediated immune response	54/1030	208/18888	4.76	1.7E-22	6.8E-20	54
GO:0070286	axonemal dynein complex assembly	25/1030	40/18888	11.46	3.6E-22	1.3E-19	25
GO:0019724	B cell mediated immunity	54/1030	212/18888	4.67	4.5E-22	1.5E-19	54
GO:0030317	flagellated sperm motility	41/1030	141/18888	5.33	2.3E-19	7.0E-17	41
GO:0097722	sperm motility	41/1030	141/18888	5.33	2.3E-19	7.0E-17	41
GO:0002440	production of molecular mediator of immune response	61/1030	310/18888	3.61	1.2E-18	3.2E-16	61
GO:0002449	lymphocyte mediated immunity	61/1030	372/18888	3.01	9.3E-15	2.4E-12	61
GO:0003351	epithelial cilium movement involved in extracellular fluid movement	20/1030	43/18888	8.53	1.3E-14	3.3E-12	20
GO:0002460	adaptive immune response based on somatic recombination of immune receptors	61/1030	385/18888	2.91	4.6E-14	1.1E-11	61
GO:0006858	extracellular transport	20/1030	46/18888	7.97	6.5E-14	1.5E-11	20
GO:0044458	motile cilium assembly	24/1030	69/18888	6.38	8.0E-14	1.7E-11	24
GO:0036158	outer dynein arm assembly	14/1030	24/18888	10.70	2.2E-12	4.5E-10	14
GO:0002443	leukocyte mediated immunity	62/1030	469/18888	2.42	8.7E-11	1.7E-08	62
GO:0036159	inner dynein arm assembly	11/1030	17/18888	11.87	1.1E-10	2.1E-08	11
GO:0007288	sperm axoneme assembly	13/1030	29/18888	8.22	1.0E-09	1.9E-07	13
GO:0120316	sperm flagellum assembly	15/1030	45/18888	6.11	7.5E-09	1.3E-06	15
GO:0050853	B cell receptor signaling pathway	19/1030	78/18888	4.47	2.6E-08	4.4E-06	19
GO:0060972	left/right pattern formation	26/1030	143/18888	3.33	5.4E-08	8.7E-06	26
GO:0003352	regulation of cilium movement	13/1030	41/18888	5.81	1.5E-07	2.3E-05	13
GO:0007286	spermatid development	32/1030	214/18888	2.74	2.0E-07	3.0E-05	32
GO:0007368	determination of left/right symmetry	24/1030	137/18888	3.21	3.6E-07	5.0E-05	24
GO:0009799	specification of symmetry	25/1030	147/18888	3.12	3.7E-07	5.0E-05	25
GO:0009855	determination of bilateral symmetry	25/1030	147/18888	3.12	3.7E-07	5.0E-05	25
GO:0048515	spermatid differentiation	32/1030	222/18888	2.64	4.7E-07	6.2E-05	32
GO:0030198	extracellular matrix organization	41/1030	332/18888	2.26	8.7E-07	0.0001	41
GO:0043062	extracellular structure organization	41/1030	333/18888	2.26	9.4E-07	0.0001	41
GO:0045229	external encapsulating structure organization	41/1030	334/18888	2.25	1.0E-06	0.0001	41
GO:0060287	epithelial cilium movement involved in determination of left/right asymmetry	7/1030	13/18888	9.87	1.8E-06	0.0002	7
GO:0019730	antimicrobial humoral response	22/1030	132/18888	3.06	2.6E-06	0.0003	22
GO:0003002	regionalization	47/1030	429/18888	2.01	4.3E-06	0.0005	47
GO:0099111	microtubule-based transport	29/1030	213/18888	2.50	5.1E-06	0.0006	29
GO:0007281	germ cell development	42/1030	371/18888	2.08	6.1E-06	0.0006	42
GO:0060632	regulation of microtubule-based movement	13/1030	57/18888	4.18	9.1E-06	0.0009	13
GO:0007389	pattern specification process	49/1030	474/18888	1.90	1.3E-05	0.0013	49
GO:0003356	regulation of cilium beat frequency	7/1030	17/18888	7.55	1.7E-05	0.0017	7
GO:0022412	cellular process involved in reproduction in multicellular organism	48/1030	482/18888	1.83	4.2E-05	0.0041	48
GO:0006958	complement activation, classical pathway	10/1030	42/18888	4.37	6.6E-05	0.0063	10
GO:0019731	antibacterial humoral response	13/1030	69/18888	3.45	7.8E-05	0.0073	13
GO:0090660	cerebrospinal fluid circulation	6/1030	15/18888	7.34	8.5E-05	0.0077	6
GO:0031424	keratinization	14/1030	83/18888	3.09	0.0001	0.0131	14

Table 8: GO enrichment analysis significantly upregulated genes in IPF fibrotic vs IPF intermediate

GO ID	Description	GeneRatio	BgRatio	FE	pvalue	p.adjust	Count
GO:0003341	cilium movement	18/112	209/18888	14.52	3.4E-16	4.6E-13	18
GO:0001539	cilium or flagellum-dependent cell motility	15/112	170/18888	14.88	8.1E-14	3.7E-11	15
GO:0060285	cilium-dependent cell motility	15/112	170/18888	14.88	8.1E-14	3.7E-11	15
GO:0060294	cilium movement involved in cell motility	14/112	165/18888	14.31	9.9E-13	3.4E-10	14
GO:0007018	microtubule-based movement	19/112	426/18888	7.52	7.1E-12	1.9E-09	19
GO:0035082	axoneme assembly	11/112	97/18888	19.12	1.3E-11	2.9E-09	11
GO:0030317	flagellated sperm motility	12/112	141/18888	14.35	4.4E-11	7.4E-09	12
GO:0097722	sperm motility	12/112	141/18888	14.35	4.4E-11	7.4E-09	12
GO:0001578	microtubule bundle formation	11/112	126/18888	14.72	2.2E-10	3.4E-08	11
GO:0044782	cilium organization	17/112	412/18888	6.96	3.3E-10	4.6E-08	17
GO:0060271	cilium assembly	16/112	385/18888	7.01	1.0E-09	1.3E-07	16
GO:0070286	axonemal dynein complex assembly	6/112	40/18888	25.30	1.2E-07	1.4E-05	6
GO:0044458	motile cilium assembly	7/112	69/18888	17.11	1.7E-07	1.8E-05	7
GO:0007286	spermatid development	10/112	214/18888	7.88	5.8E-07	5.7E-05	10
GO:0048515	spermatid differentiation	10/112	222/18888	7.60	8.2E-07	7.5E-05	10
GO:0007368	determination of left/right symmetry	8/112	137/18888	9.85	1.6E-06	0.0001	8
GO:0060972	left/right pattern formation	8/112	143/18888	9.43	2.2E-06	0.0002	8
GO:0009799	specification of symmetry	8/112	147/18888	9.18	2.7E-06	0.0002	8
GO:0009855	determination of bilateral symmetry	8/112	147/18888	9.18	2.7E-06	0.0002	8
GO:0003351	epithelial cilium movement involved in extracellular fluid movement	5/112	43/18888	19.61	5.4E-06	0.0004	5
GO:0120316	sperm flagellum assembly	5/112	45/18888	18.74	6.8E-06	0.0004	5
GO:0006858	extracellular transport	5/112	46/18888	18.33	7.6E-06	0.0005	5
GO:0003002	regionalization	12/112	429/18888	4.72	9.2E-06	0.0005	12
GO:0007281	germ cell development	11/112	371/18888	5.00	1.3E-05	0.0007	11
GO:0007389	pattern specification process	12/112	474/18888	4.27	2.5E-05	0.0013	12
GO:0007288	sperm axoneme assembly	4/112	29/18888	23.26	2.5E-05	0.0013	4
GO:0022412	cellular process involved in reproduction in multicellular organism	12/112	482/18888	4.20	2.9E-05	0.0015	12
GO:0036159	inner dynein arm assembly	3/112	17/18888	29.76	0.0001	0.0063	3
GO:0036158	outer dynein arm assembly	3/112	24/18888	21.08	0.0004	0.0177	3
GO:0018149	peptide cross-linking	3/112	27/18888	18.74	0.0005	0.0244	3
GO:0090183	regulation of kidney development	3/112	34/18888	14.88	0.0011	0.0468	3

Top 10 enriched GO pathways- upregulated genes UD vs IPF normal

A)

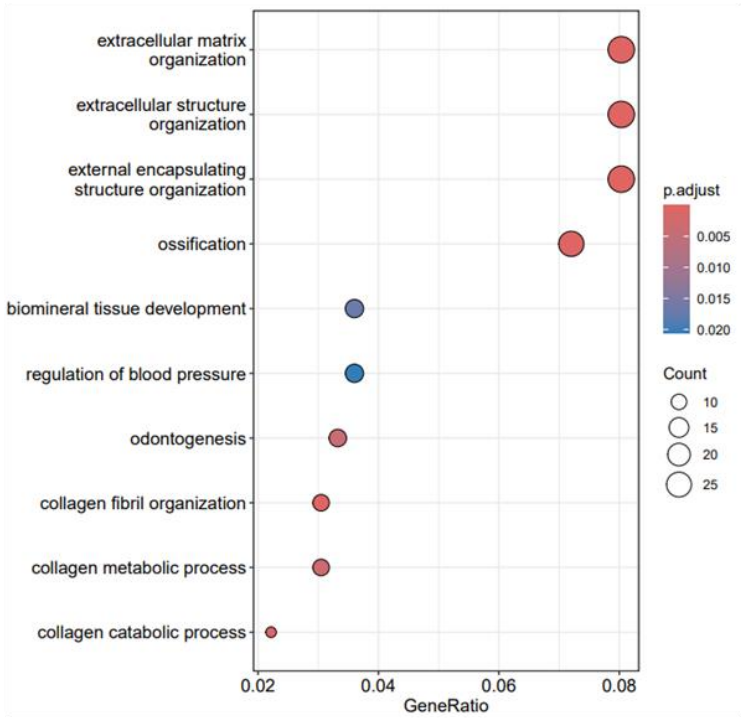

Top 10 enriched GO pathways- downregulated genes UD vs IPF normal

B)

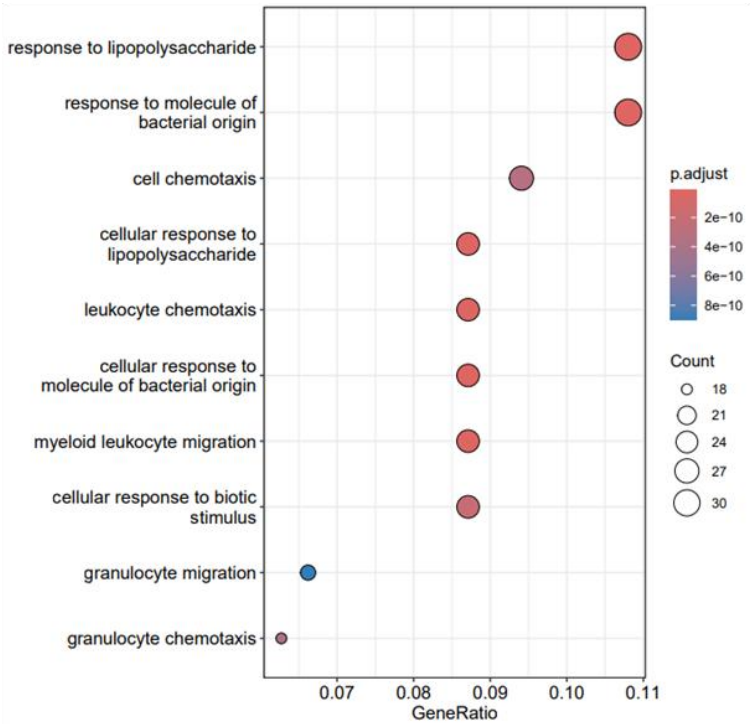

Figure 1: Top 10 enriched GO pathways in significant upregulated and significantly downregulated DEGs in UD vs IPF normal Dot plots of A) the top 10 enriched GO terms in significantly upregulated DEGs in IPF normal vs UD and B) the top 10 enriched GO terms in significantly downregulated DEGs in IPF normal vs UD.

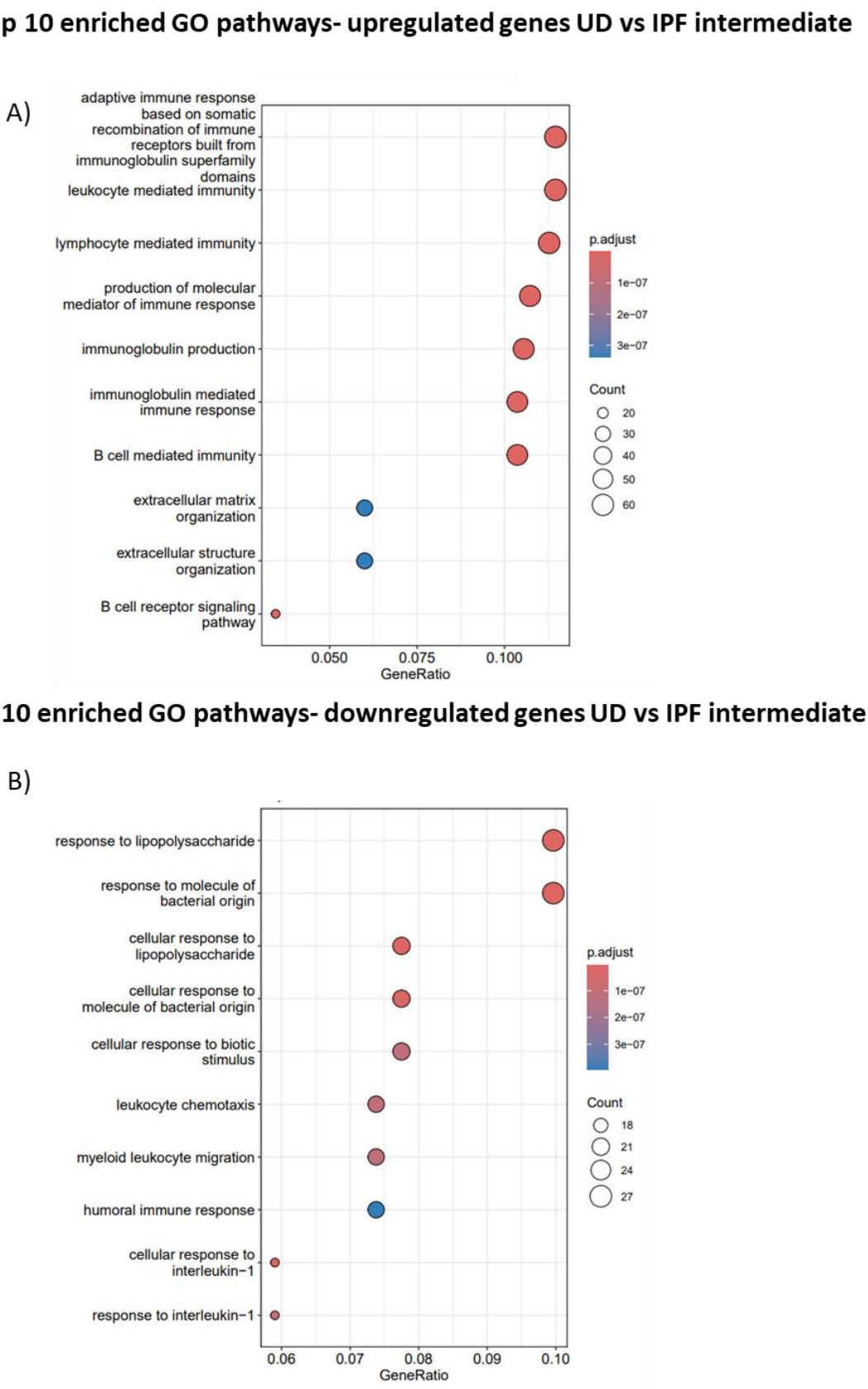

Figure 2: Top 10 enriched GO pathways in significant upregulated and significantly downregulated DEGs in UD vs IPF intermediate Dot plots of A) the top 10 enriched GO terms in significantly upregulated DEGs in IPF intermediate vs UD and B) the top 10 enriched GO terms in significantly downregulated DEGs in IPF intermediate vs UD.

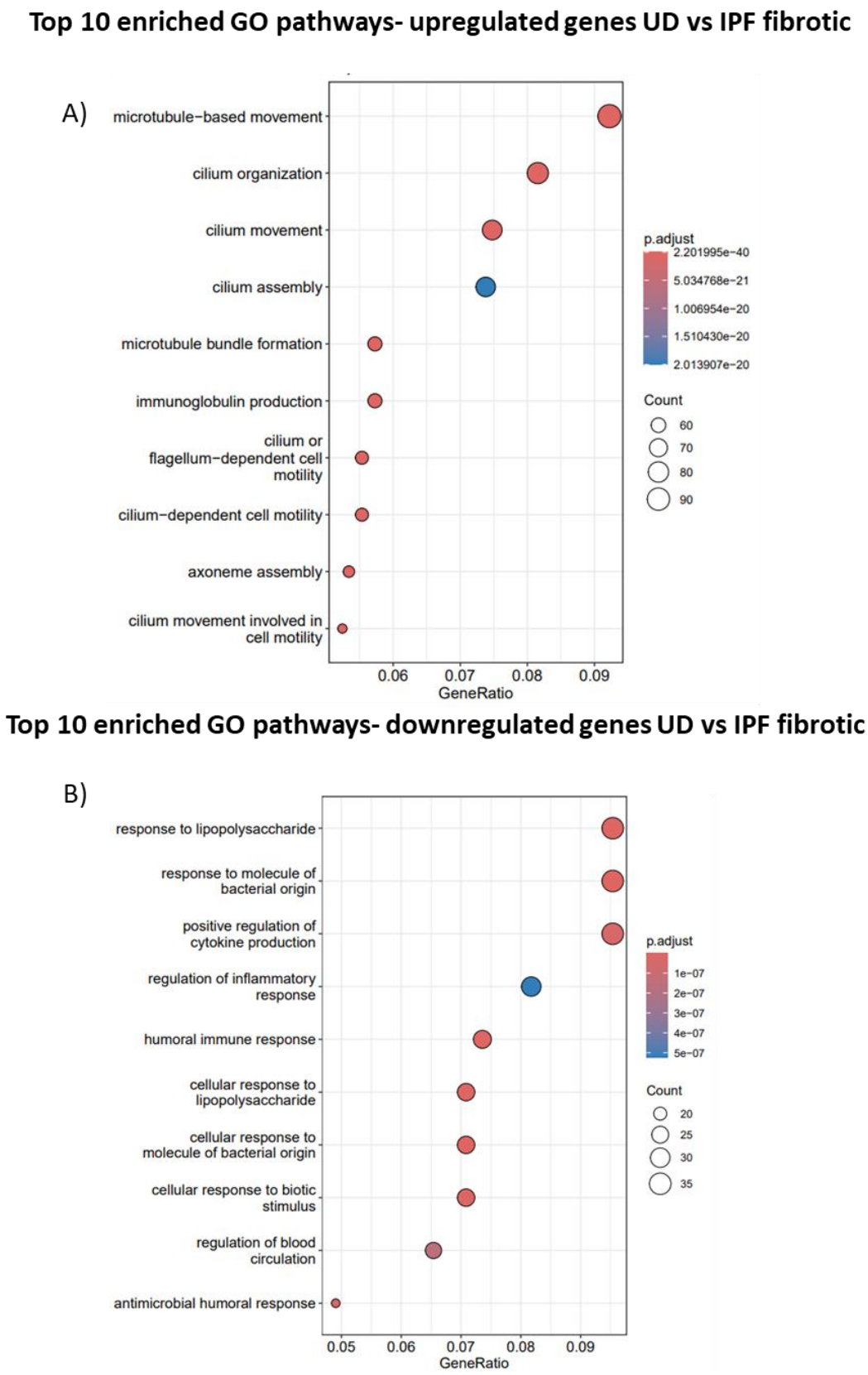

Figure 3: Top 10 enriched GO pathways in significant upregulated and significantly downregulated DEGs in UD vs IPF fibrotic Dot plots of A) the top 10 enriched GO terms in significantly upregulated DEGs in IPF fibrotic vs UD and B) the top 10 enriched GO terms in significantly downregulated DEGs in IPF fibrotic vs UD.

Top 10 enriched GO pathways- upregulated genes IPF fibrotic vs IPF normal

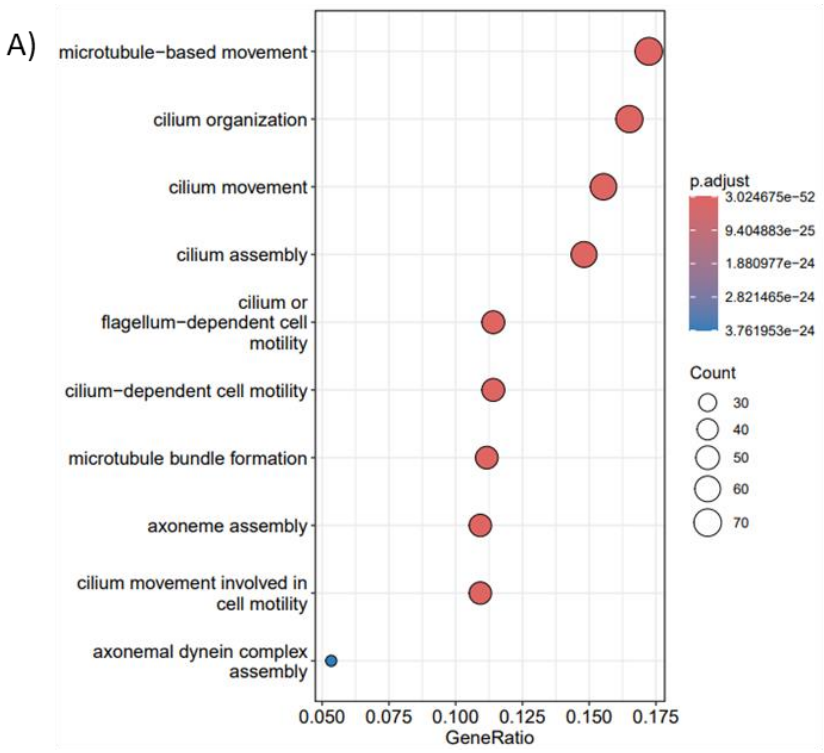

Top 10 enriched GO pathways- upregulated genes IPF fibrotic vs IPF intermediate

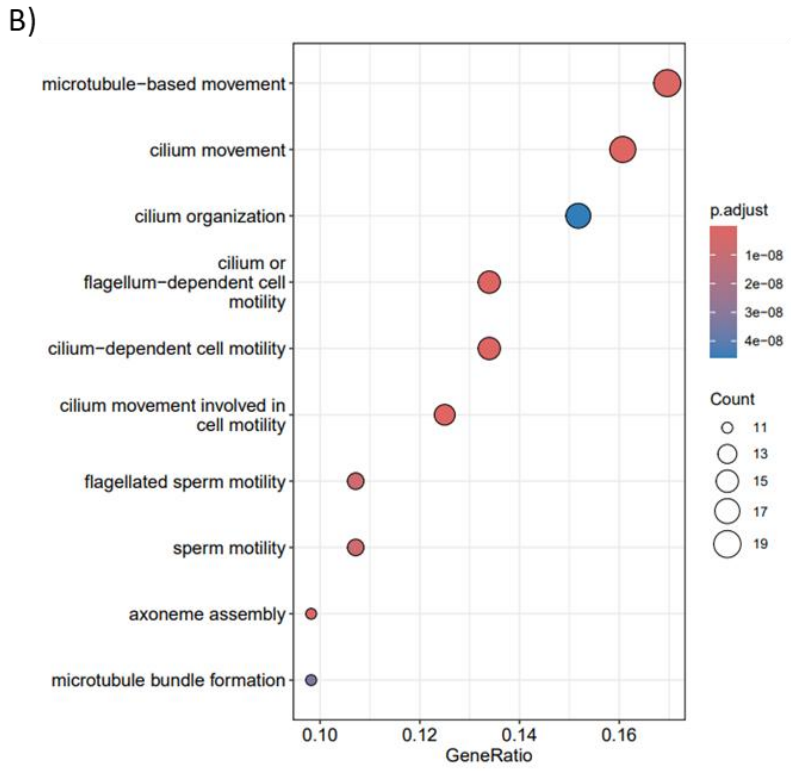

Figure 4: Top 10 enriched GO pathways in significant upregulated and significantly DEGs in IPF fibrotic vs IPF normal and IPF fibrotic vs IPF intermediate Dot plots of A) the top 10 enriched GO terms in significantly upregulated DEGs in IPF fibrotic vs IPF normal and B) the top 10 enriched GO terms in significantly upregulated DEGs in IPF fibrotic vs IPF intermediate.

A)

Ingenuity Canonical Pathways	UD vs IPF normal			UD vs IPF intermediate			UD vs IPF fibrotic		
	-log(p-value)	Ratio	z-score	-log(p-value)	Ratio	z-score	-log(p-value)	Ratio	z-score
Neutrophil degranulation	3,21E01	1,09E-01	-5,547	30	1,13E-01	-6,260	3,61E01	1,43E-01	-6,063
IL-8 Signaling	1,33E01	1,05E-01	-2,524	1,45E01	1,19E-01	-3,710	1,34E01	1,29E-01	-4,082
CXCR4 Signaling	1,11E01	1,07E-01	-1,604	9,84E00	1,07E-01	-3,051	1,3E01	1,43E-01	-3,441
Neutrophil Extracellular Trap Signaling Pathway	9,26E00	0.06	-0,816	7,71E00	0.06	-0,816	8,17E00	7,25E-02	-0,928
fMLP Signaling in Neutrophils	1,08E01	1,22E-01	-2,496	1,07E01	1,3E-01	-3,606	1,14E01	1,53E-01	-4,000
Leukocyte Extravasation Signaling	9,2E00	8,81E-02	-2,668	1,06E01	1,04E-01	-2,683	1,08E01	1,19E-01	-2,711

B)

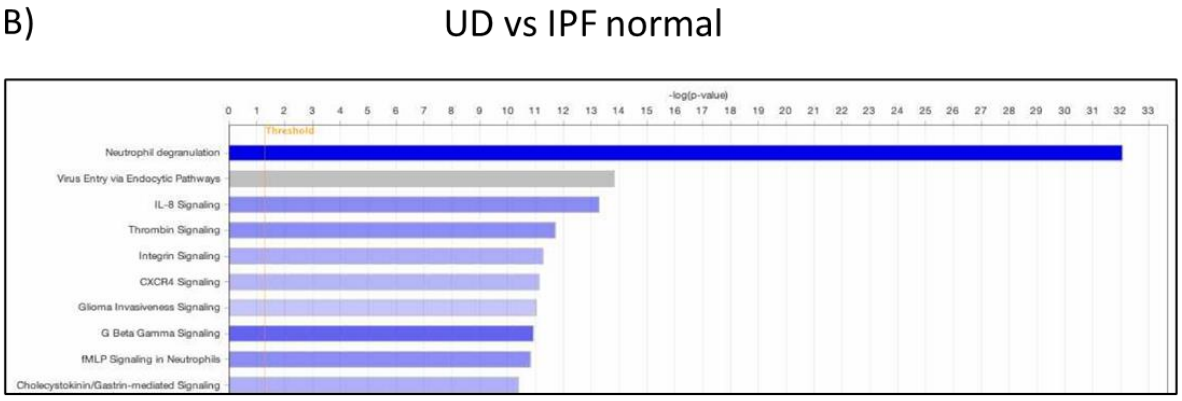

C)

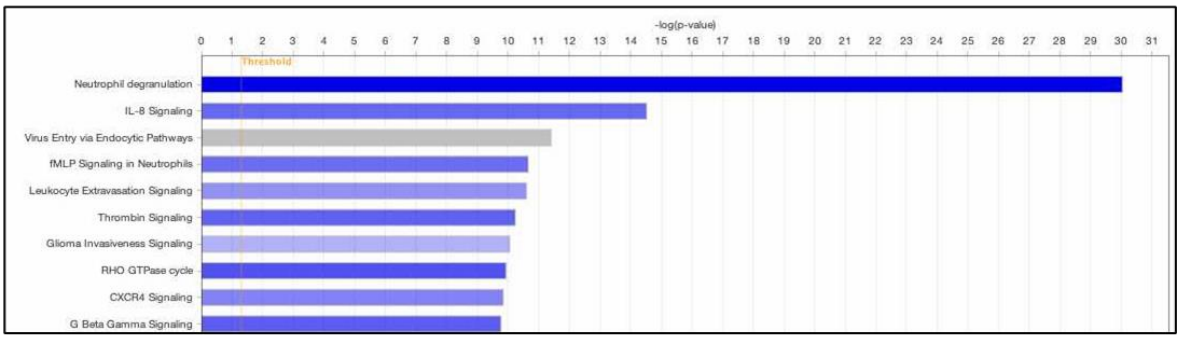

D)

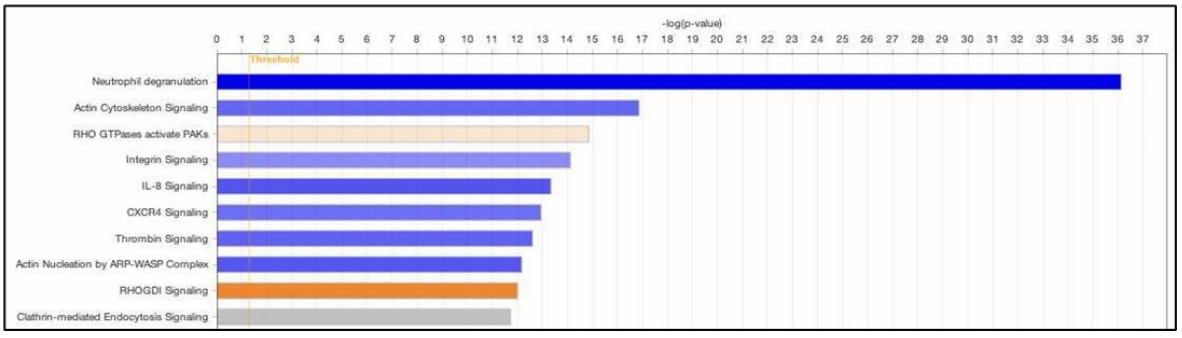

Figure 5: Ingenuity canonical pathways A) Table of top significantly affected pathways In IPF regions vs UD. B) Top affected pathways in IPF normal vs UD C) Top affected pathways in IPF intermediate vs UD and D) Top affected pathways in IPF fibrotic vs UD.

Appendix G

Absolute pg/ml graphs for compound screening in PCLuS

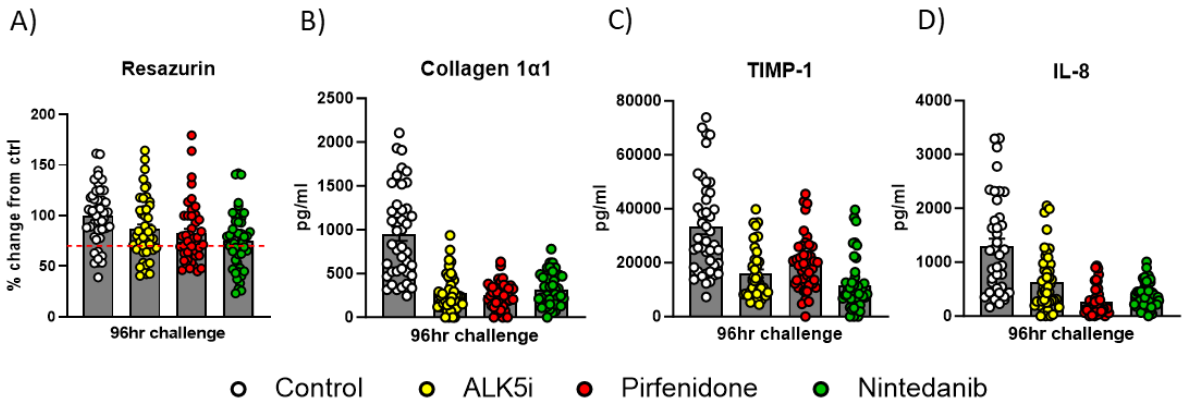

Figure 1: Validation of IPF-derived PCLuS viability for assessment of selected compounds PCLuS were generated from explant IPF tissue (n=4 donors) with slices (n=10 per condition) being rested for 48 hours before challenge with either control media, standard of care compounds Pirfenidone (2.5mM) and Nintedanib (2.5µM) or ALK5i (10µM) to blunt fibrosis (n=10 PCLuS per condition, n=4 donors, n=40 PCLuS total). Concurrently, PCLuS were challenged with 3 escalating doses (0.1µM, 1µM and 10µM) of each candidate compound (n=6 per condition) to assess the ability to reduce pre-existing fibrosis (n=6 PCLuS per condition, n=4 donors, n=24 PCLuS total). Media, including all treatments, was refreshed at 24-hour intervals with conditioned media snap frozen for downstream analysis before PCLuS were harvested at T144 for resazurin as an indicator of tissue viability. Resazurin assay performed at T144 presented as the average % of control (for n=6 slices) per candidate compound for each donor. Quantification of A) Resazurin (where red dashed line represents arbitrary 70% viability threshold) B) Collagen 1α1, C) TIMP-1 and D) IL-8 was performed on T144 media *via* ELISA and plotted as absolute pg/ml values to confirm tissue could be effectively modulated. All data are mean ± SEM.

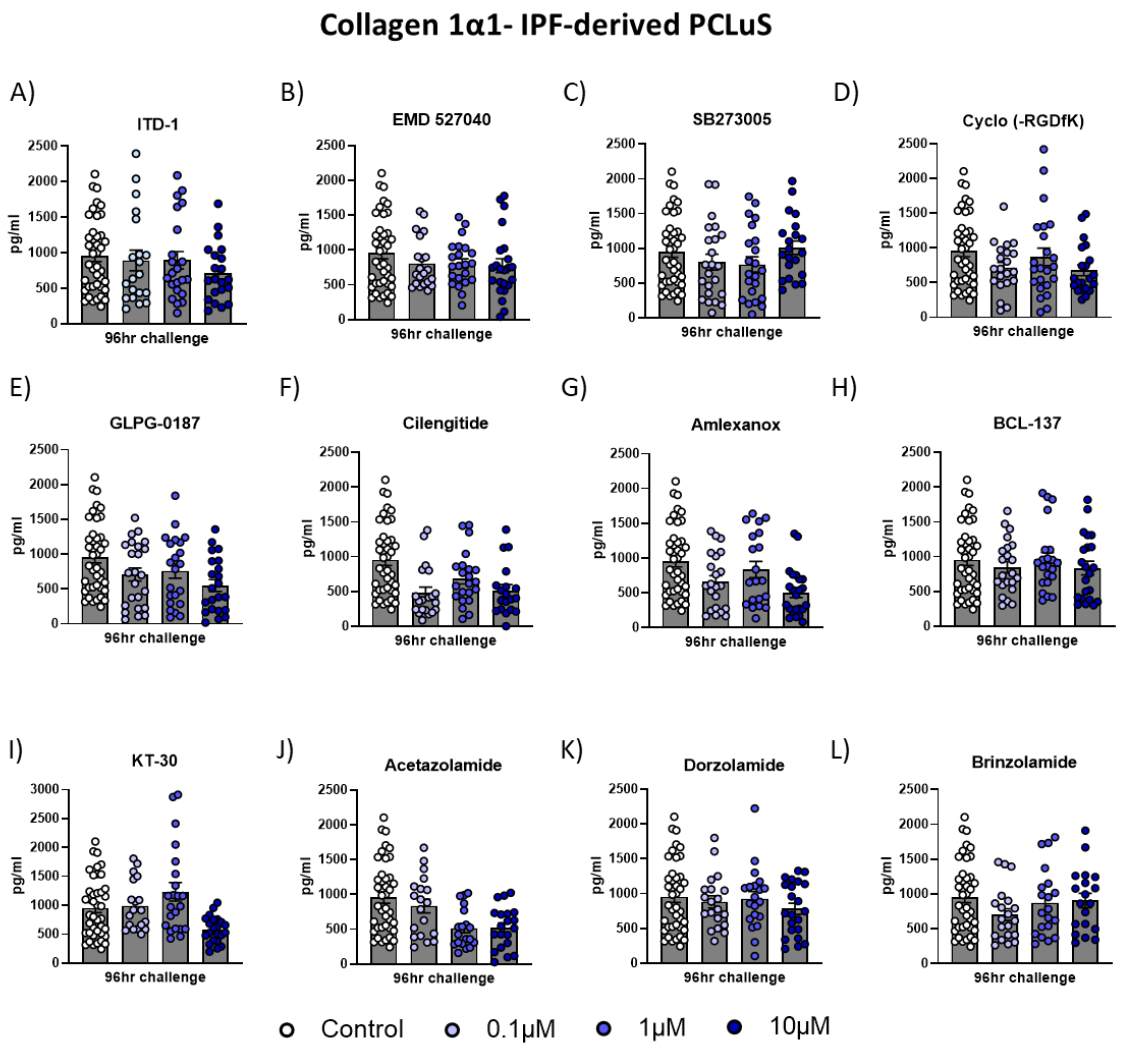

Figure 2: Quantification of secreted collagen 1α1 from IPF-derived PCLuS after selected inhibitor challenge PCLuS were generated from explant IPF tissue (n=4 donors) with slices (n=6 per condition) being rested for 48 hours before challenge with either control media or 3 escalating doses (0.1μM, 1μM and 10μM) of each candidate compound to assess the ability to reduce pre-existing fibrosis. Media, including all treatments, was refreshed at 24-hour intervals with conditioned media snap frozen for downstream analysis before PCLuS were harvested for resazurin at T144 as an indicator of tissue viability. Quantification of collagen 1α1 was performed *via* ELISA on T144 media and plotted as A-L) absolute pg/ml values (n=6 conditioned media per donor, n=4 donors, n=24 samples total) to assess potential anti-fibrotic affects. All data are mean ± SEM.

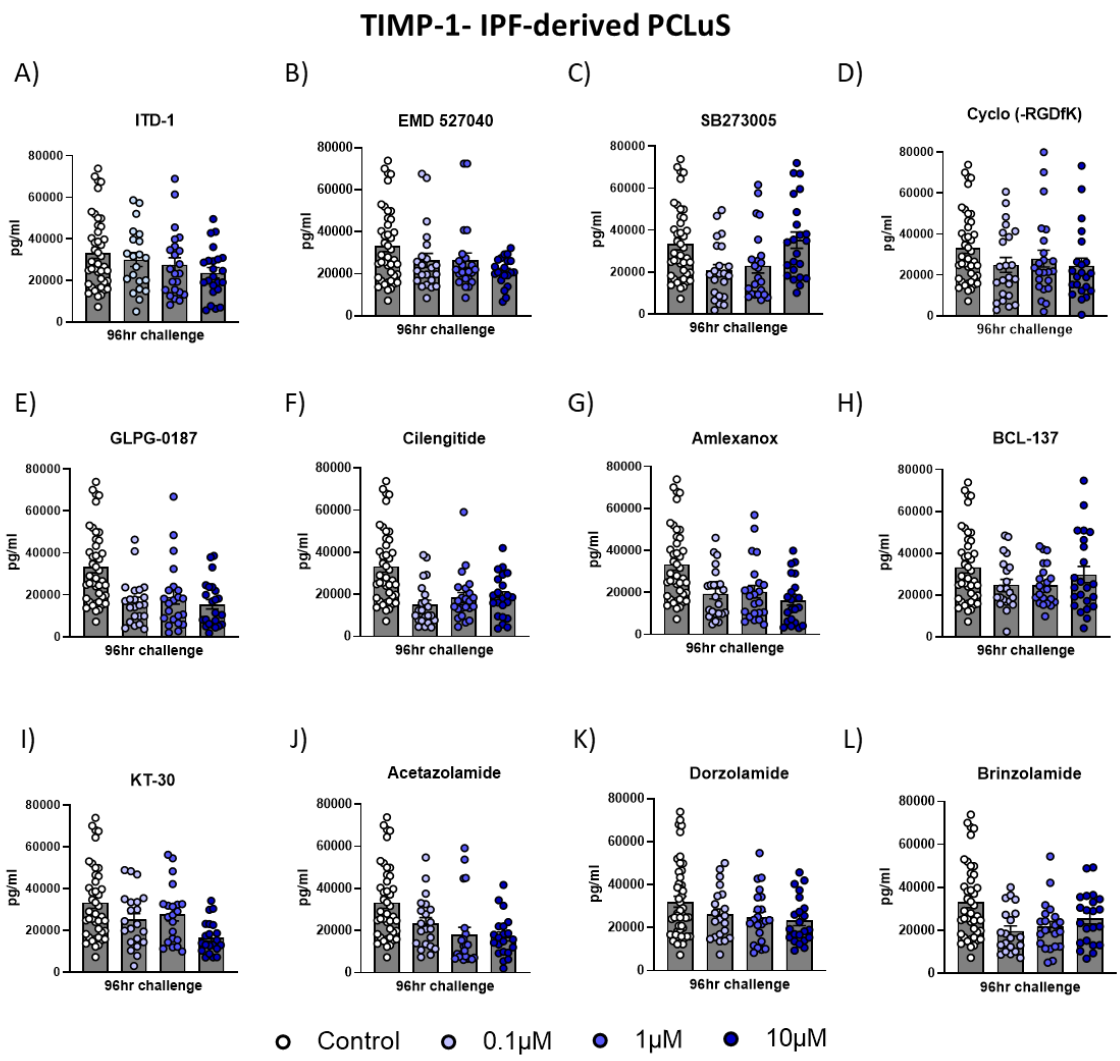

Figure 3: Quantification of secreted TIMP-1 from IPF-derived PCLuS after selected inhibitor challenge PCLuS were generated from explant IPF tissue (n=4 donors) with slices (n=6 per condition) being rested for 48 hours before challenge with either control media or 3 escalating doses (0.1µM, 1µM and 10µM) of each candidate compound to assess the ability to reduce pre-existing fibrosis. Media, including all treatments, was refreshed at 24-hour intervals with conditioned media snap frozen for downstream analysis before PCLuS were harvested for resazurin at T144 as an indicator of tissue viability. Quantification of TIMP-1 was performed *via* ELISA on T144 media and plotted as A-L) absolute pg/ml values (n=6 conditioned media per donor, n=4 donors, n=24 samples total) to assess potential anti-fibrotic affects. All data are mean ± SEM.

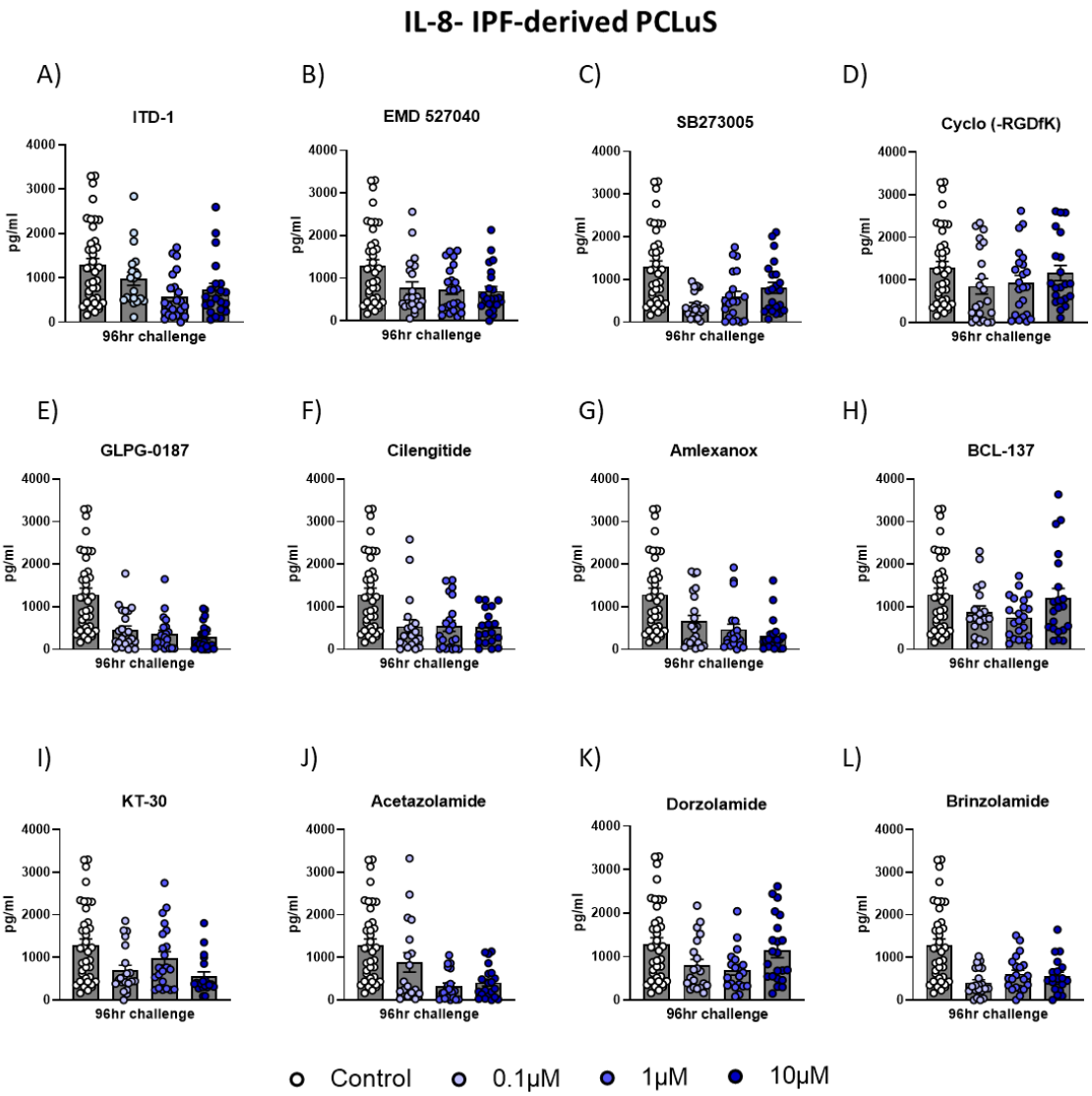

Figure 4: Quantification of secreted IL-8 from IPF-derived PCLuS after selected inhibitor challenge PCLuS were generated from explant IPF tissue (n=4 donors) with slices (n=6 per condition) being rested for 48 hours before challenge with either control media or 3 escalating doses (0.1µM, 1µM and 10µM) of each candidate compound to assess the ability to reduce pre-existing fibrosis. Media, including all treatments, was refreshed at 24-hour intervals with conditioned media snap frozen for downstream analysis before PCLuS were harvested for resazurin at T144 as an indicator of tissue viability. Quantification of IL-8 was performed *via* ELISA on T144 media and plotted as A-L) absolute pg/ml values (n=6 conditioned media per donor, n=4 donors, n=24 samples total) to assess potential anti-fibrotic affects. All data are mean ± SEM.

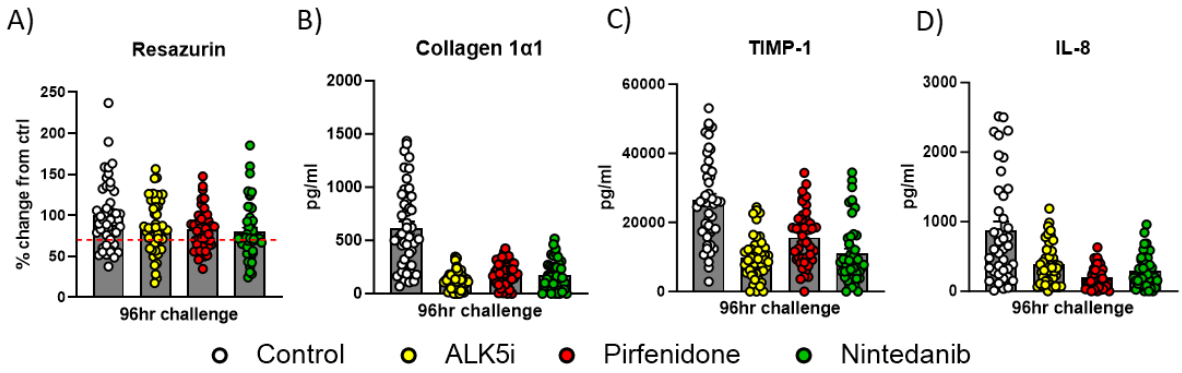

Figure 5: Validation of IPF-derived PCLuS viability for assessment of IPA compounds PCLuS were generated from explant IPF tissue (n=4 donors) with slices (n=10 per condition) being rested for 48 hours before challenge with either control media, standard of care compounds Pirfenidone (2.5mM) and Nintedanib (2.5µM) or ALK5i (10µM) to blunt fibrosis (n=10 PCLuS per condition, n=4 donors, n=40 PCLuS total). Concurrently, PCLuS were challenged with 3 escalating doses (0.1µM, 1µM and 10µM) of each candidate compound (n=6 per condition) to assess the ability to reduce pre-existing fibrosis (n=6 PCLuS per condition, n=4 donors, n=24 PCLuS total). Media, including all treatments, was refreshed at 24-hour intervals with conditioned media snap frozen for downstream analysis before PCLuS were harvested at T144 for resazurin as an indicator of tissue viability. Resazurin assay performed at T144 presented as the average % of control (for n=6 slices) per candidate compound for each donor. Quantification of A) Resazurin (where red dashed line represents arbitrary 70% viability threshold) B) Collagen 1α1, C) TIMP-1 and D) IL-8 was performed on T144 media *via* ELISA and plotted as absolute pg/ml values to confirm tissue could be effectively modulated. All data are mean ± SEM.

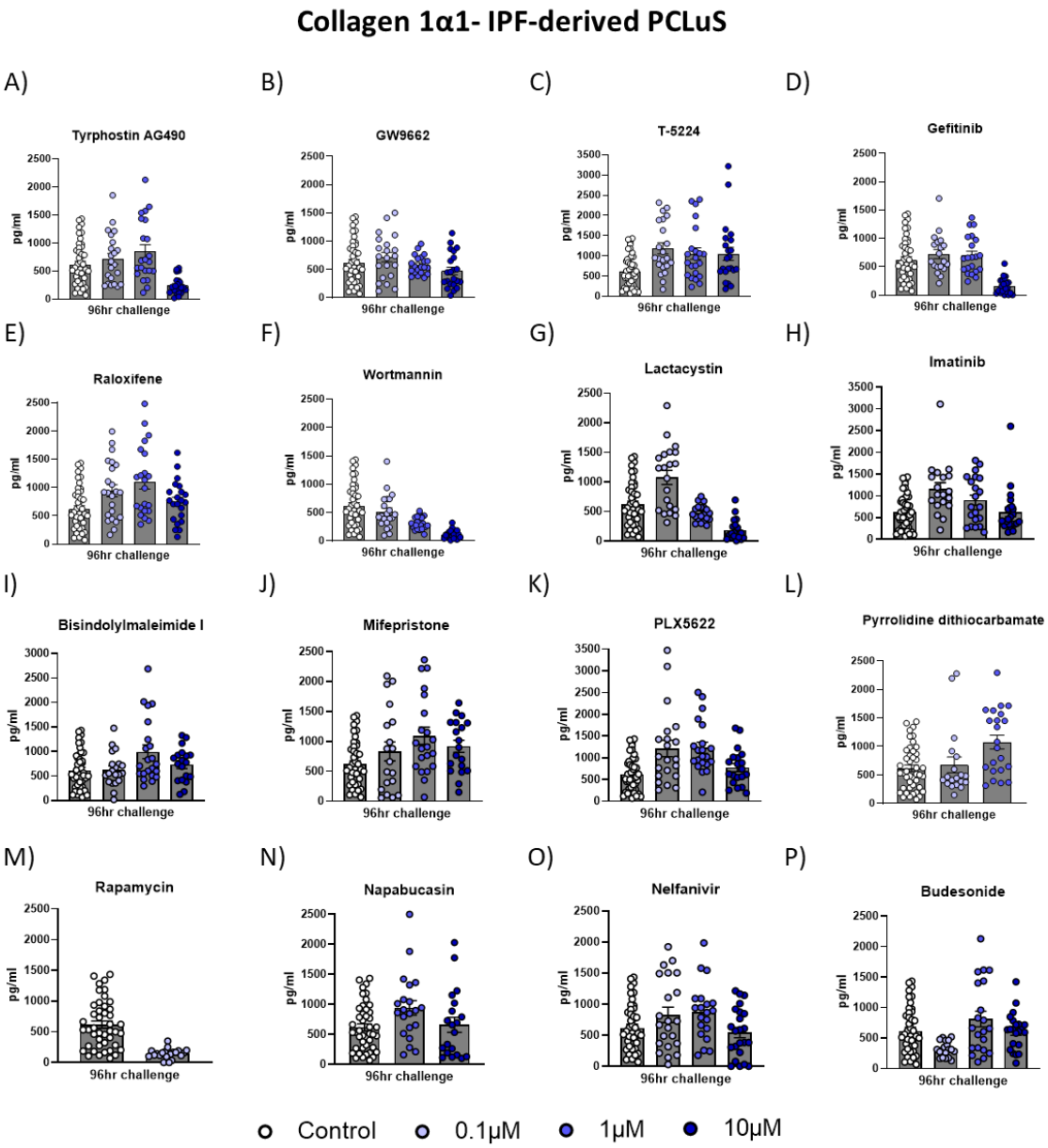

Figure 6: Quantification of secreted collagen 1α1 from IPF-derived PCLuS after selected inhibitor challenge PCLuS were generated from explant IPF tissue (n=4 donors) with slices (n=6 per condition) being rested for 48 hours before challenge with either control media or 3 escalating doses (0.1μM, 1μM and 10μM) of each candidate compound to assess the ability to reduce pre-existing fibrosis. Media, including all treatments, was refreshed at 24-hour intervals with conditioned media snap frozen for downstream analysis before PCLuS were harvested for resazurin at T144 as an indicator of tissue viability. Quantification of collagen 1α1 was performed *via* ELISA on T144 media and plotted as A-L) absolute pg/ml values (n=6 conditioned media per donor, n=4 donors, n=24 samples total) to assess potential anti-fibrotic affects. All data are mean ± SEM.

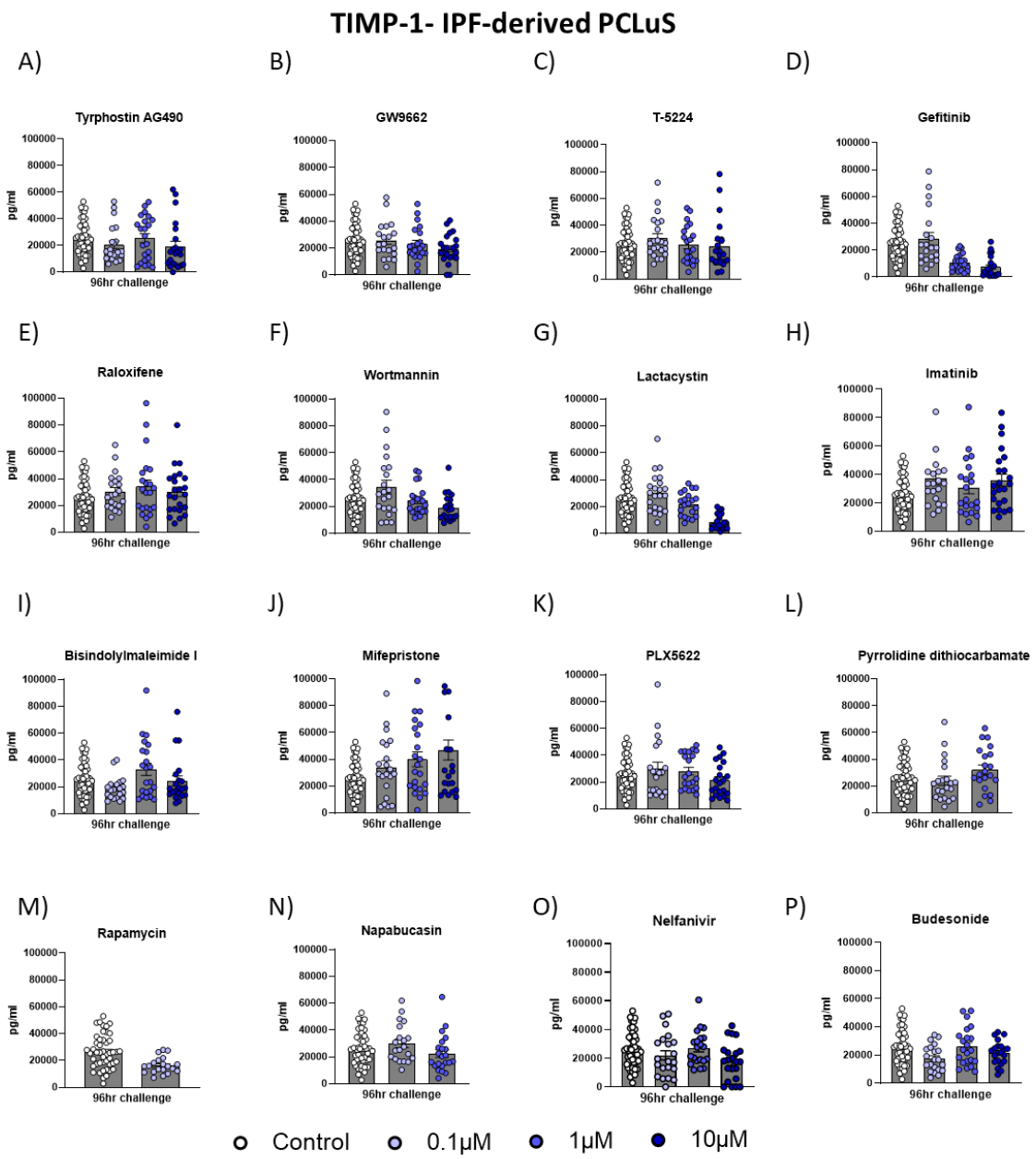

Figure 7: Quantification of secreted TIMP-1 from IPF-derived PCLuS after selected inhibitor challenge PCLuS were generated from explant IPF tissue (n=4 donors) with slices (n=6 per condition) being rested for 48 hours before challenge with either control media or 3 escalating doses (0.1μM, 1μM and 10μM) of each candidate compound to assess the ability to reduce pre-existing fibrosis. Media, including all treatments, was refreshed at 24-hour intervals with conditioned media snap frozen for downstream analysis before PCLuS were harvested for resazurin at T144 as an indicator of tissue viability. Quantification of TIMP-1 was performed *via* ELISA on T144 media and plotted as A-L) absolute pg/ml values (n=6 conditioned media per donor, n=4 donors, n=24 samples total) to assess potential anti-fibrotic affects. All data are mean ± SEM.

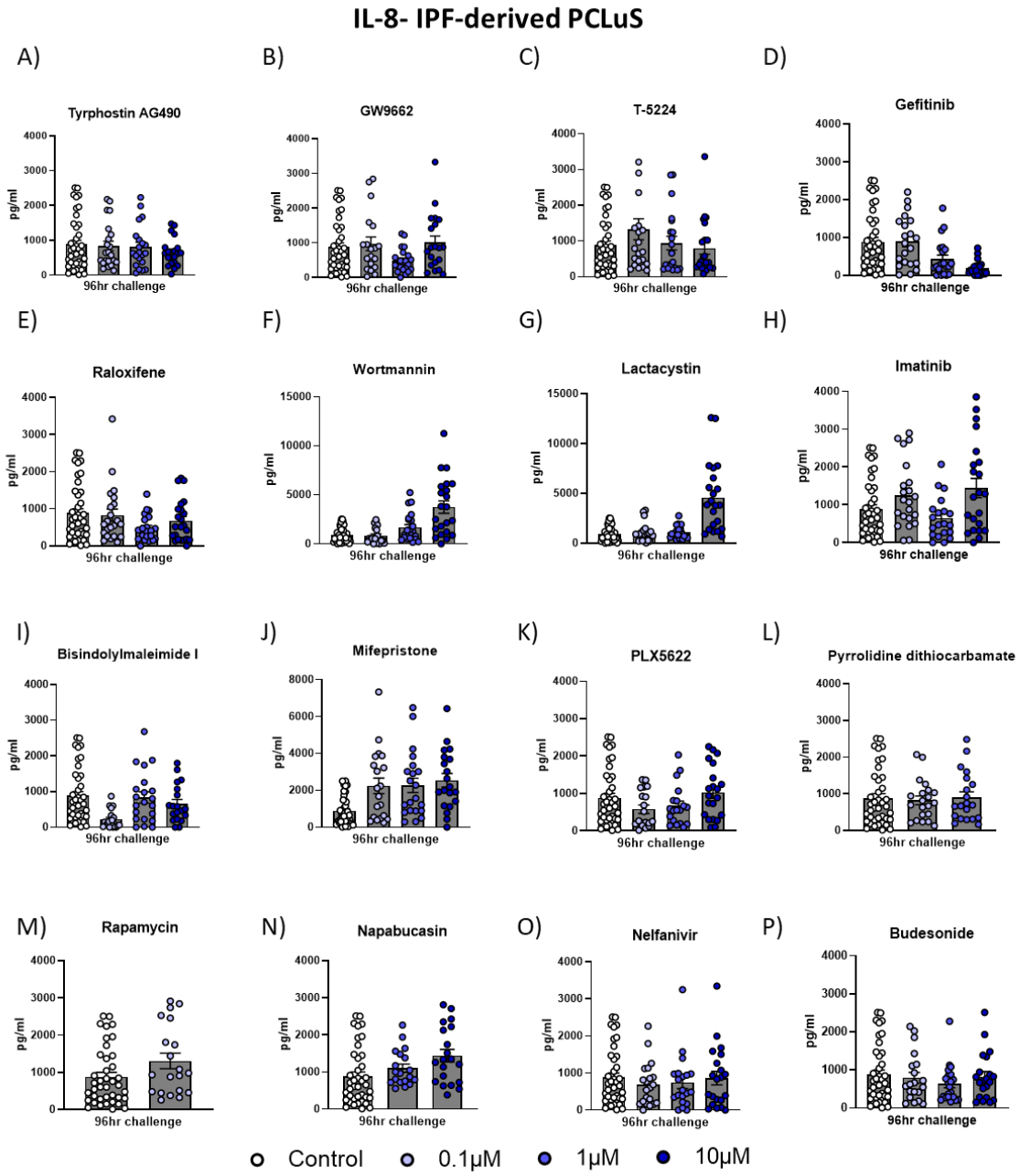

Figure 8: Quantification of secreted IL-8 from IPF-derived PCLuS after selected inhibitor challenge PCLuS were generated from explant IPF tissue (n=4 donors) with slices (n=6 per condition) being rested for 48 hours before challenge with either control media or 3 escalating doses (0.1μM, 1μM and 10μM) of each candidate compound to assess the ability to reduce pre-existing fibrosis. Media, including all treatments, was refreshed at 24-hour intervals with conditioned media snap frozen for downstream analysis before PCLuS were harvested for resazurin at T144 as an indicator of tissue viability. Quantification of IL-8 was performed *via* ELISA on T144 media and plotted as A-L) absolute pg/ml values (n=6 conditioned media per donor, n=4 donors, n=24 samples total) to assess potential anti-fibrotic affects. All data are mean ± SEM.

Appendix H

Target molecules for IPA inhibitors datasets

Table 1: Target molecules for IPA inhibitors in IPF normal and intermediate regions

Upstream Regulator	Target Molecules in IPF normal regions	Target Molecules in IPF intermediate regions
Tyrphostin AG490	ACE,BAX,CD68,HMGB1,MMP9,MYH11,PTX3,RETN,STAT1	ACE,BAX,HMGB1,MMP9,MYH11,RETN
GW9662		BAX,CAV1,CD36,FABP4,G6PD
T-5224	ACSL1,FKBP5,LSS,PTX3,WDR44	ACSL1,FKBP5,GYS1,LSS
Gefitinib	EHD1,HSPB1,MMP9,STAT1,TGM2,TIMP3	EGFR,EHD1,HSPB1,MMP9,TGM2,TIMP3
Raloxifene	ANXA3,GPRC5A,MMP2,NDRG1,TIMP3	ANXA3,GNS,GPRC5A,MIF,MMP2,NDRG1,RAC1,TIMP3
Wortmannin	BAX,CD36,MMP2,MMP9,MYH11,RAP1A,RETN	BAX,CD36,MMP2,MMP9,MYH11,RAP1A,RETN,TPM1
Lactacystin	ACTB,APOB,FAS,HBB,HMGB2,HSPB1,MAP1B,MMP2,MMP9	ACTB,APOB,FAS,GNAI2,HBB,HMGB2,HSPB1,MAP1B,MMP2,MMP9
Imatinib		BAX,CDC42,HMGB1,IGKC,PDIA4,PDIA6,RAB31,RAP1A,RPN1
Bisindolylmaleimide I	ACE,CD55,MMP2,MMP9	ACE,CD55,EGFR,MMP2,MMP9
Mifepristone	ACE,ANXA1,BAX,CSN2,FAS,FKBP5,MMP9,NDRG1,PTX3,RHOC	ACE,ANXA1,BAX,CAV1,EPCAM,FAS,FBLN2,FKBP5,MMP9,NDRG1
PLX5622	ACTB,BAX,CD68,GRN,MMP2,SERPINF1,STAT1	ACTB,BAX,MIF,MMP2,SERPINF1
Pyrrolidine dithiocarbamate	ANXA1,FABP4,MMP2,MMP9	ANXA1,FABP4,GNAI2,MMP2,MMP9
Entinostat	BAX,MMP2,MMP9	BAX,EGFR,MMP2,MMP9
Rapamycin	ACTB,BAX,CALD1,CD36,CD68,CSN2,FAS,HMGB1,LMNA,MMP2	ACTB,BAX,CALD1,CD36,CREG1,FAS,G6PD,HMGB1,LDHB,LMNA
Staurosporine	CPNE3,FAS,MMP2,MMP9	CPNE3,CREG1,EGFR,FAS,MMP2,MMP9
Napabucasin	ACTB,DDR1,FLOT2	ACTB,CD34,EPCAM,FLOT2
Nelfinavir	APOBR,FABP4,MMP9,NNMT	APOBR,FABP4,MMP9,NNMT
Budesonide	CAB39,CD68,DOCK9,GNA11,GNAQ,ITPR1,LGMN,RAB5B,RHOC	

Appendix I

Conferences and travel awards

- **British Thoracic Society-** Winter Meeting (London, UK) **November 2023**
  - Selected for oral presentation (presented by Dr Lee Borthwick)

- **Keystone Symposia-** Fibrosis Pathogenesis and Resolution (Alberta, Canada) **March 2023**
  - Selected for oral and poster presentation

- **Aegean conference**- Tissue Repair, Regeneration and Fibrosis (Crete, Greece) **October 2022**
  - Selected for oral and poster presentation
  - Travel award for excellent research contribution

- **Newcastle/Edinburgh/Cambridge/Sheffield (NECS) Collaborative Meeting** (Sheffield, UK) **November 2022**
  - Selected for oral presentation

- **Northeast Postgraduate Conference-** (Newcastle, UK) **November 2022**
  - Selected for oral presentation

Appendix J

Publications during PhD

- **Burgoyne RA**, Fisher AJ, Borthwick LA. The Role of Epithelial Damage in the Pulmonary Immune Response. Cells. 2021;10(10):2763.

- Reilly WJ, **Burgoyne RA,** Borthwick LA. The Role of the Interleukin 1 Family in Lung Disease. In: Janes SM, editor. Encyclopedia of Respiratory Medicine (Second Edition). Oxford: Academic Press; 2022. p. 275-89
  .

- Younes R, **Burgoyne R**, Tiniakos D, Govaere O. Clinical implications of hepatic progenitor cell activation in non-alcoholic fatty liver disease. Hepatoma Res 2021; 7:15**.**

- Weeratunga, P.; Hunter, B.; Sergeant, M.; Bull, J.; Clelland, C.; Denney, L.; Vuppusetty, C.; **Burgoyne, R**.; Woo, J.; Hu, T.; et al. Temporo-spatial cellular atlas of the regenerating alveolar niche in idiopathic pulmonary fibrosis. *medRxiv* 2024, 2024.2004.2010.24305440, doi:10.1101/2024.04.10.24305440.

- Wilkinson AL, John AE, Barrett JW, Gower E, Morrison VS, Man Y, Pun KT, Roper JA, Luckett JC, Borthwick LA, Barksby BS, **Burgoyne RA**, Barnes R, Fisher AJ, Procopiou PA, Hatley RJD, Barrett TN, Marshall RP, Macdonald SJF, Jenkins RG, Slack RJ. Pharmacological characterisation of GSK3335103, an oral αvβ6 integrin small molecule RGD-mimetic inhibitor for the treatment of fibrotic disease. European Journal of Pharmacology. 2021;913:174618.

- John AE, Graves RH, Pun KT, Vitulli G, Forty EJ, Mercer PF, Morrell JL, Barrett JW, Rogers RF, Hafeji M, Bibby LI, Gower E, Morrison VS, Man Y, Roper JA, Luckett JC, Borthwick LA, Barksby BS, **Burgoyne RA**, Barnes R, Le J, Flint DJ, Pyne S, Habgood A, Organ LA, Joseph C, Edwards-Pritchard RC, Maher TM, Fisher AJ, Gudmann NS, Leeming DJ, Chambers RC, Lukey PT, Marshall RP, Macdonald SJF, Jenkins RG, Slack RJ. Translational pharmacology of an inhaled small molecule αvβ6 integrin inhibitor for idiopathic pulmonary fibrosis. Nat Commun. 2020 Sep 16;11(1):4659.

- Garcia-Macia M, Santos-Ledo A, Leslie J, Paish HL, Collins AL, Scott RS, Watson A, **Burgoyne RA,** White S, French J, Hammond J, Borthwick LA, Mann J, Bolaños JP, Korolchuk VI, Oakley F, Mann DA. A Mammalian Target of Rapamycin-Perilipin 3 (mTORC1-Plin3) Pathway is essential to Activate Lipophagy and Protects Against Hepatosteatosis. Hepatology. 2021 Dec;74(6):3441-3459.

- Leslie J, Macia MG, Luli S, Worrell JC, Reilly WJ, Paish HL, Knox A, Barksby BS, Gee LM, Zaki MYW, Collins AL, **Burgoyne RA,** Cameron R, Bragg C, Xu X, Chung GW, Brown CDA, Blanchard AD, Nanthakumar CB, Karsdal M, Robinson SM, Manas DM, Sen G, French J, White SA, Murphy S, Trost M, Zakrzewski JL, Klein U, Schwabe RF, Mederacke I, Nixon C, Bird T, Teuwen LA, Schoonjans L, Carmeliet P, Mann J, Fisher AJ, Sheerin NS, Borthwick LA, Mann DA, Oakley F. c-Rel orchestrates energy-dependent epithelial and macrophage reprogramming in fibrosis. Nat Metab. 2020 Nov;2(11):1350-1367.

- Gee, L.M.V.; Barron-Millar, B.; Leslie, J.; Richardson, C.; Zaki, M.Y.W.; Luli, S.; **Burgoyne, R.A.;** Cameron, R.I.T.; Smith, G.R.; Brain, J.G.; et al. Anti–Cholestatic Therapy with Obeticholic Acid Improves Short-Term Memory in Bile Duct–Ligated Mice. *The American Journal of Pathology* 2023, *193*, 11-26

- Lagan, A.; Patel, J.; Barksby, B.; **Burgoyne, R.A.;** MacIssac, J.L.; Lin, D.T.S.; May, S.T.; Castellanos-Uribe, M.; Kobor, M.S.; Hackett, T.-L.; et al. Distinct Idiopathic Pulmonary Fibrosis Associated Transcriptome and Methylome Changes in Airway and Parenchymal Fibroblasts. In *D29. TRANSLATIONAL RESEARCH IN IPF*; pp. A6477-A6477. [CONFERENCE ABSTRACT]

- Lagan AL, Patel J, Barksby B, **Burgoyne RA**, MacIsaac J, Lin DTS, et al. Differential IPF Associated Gene Expression and DNA Methylation Changes in Human Airway and Parenchymal Fibroblasts. C109 PULMONARY FIBROSIS: MOVING FORWARD WITH GENETICS AND SEQUENCING. p. A4977-A. [CONFERENCE ABSTRACT] .

- **Burgoyne R,** Barksby B, Murphy S*, et al* S101 Identification and validation of novel therapeutic targets in IPF using human tissue models *Thorax* 2023;**78:**A73. [CONFERENCE ABSTRACT]

Bibliography

1. Gurtner, G.C.; Werner, S.; Barrandon, Y.; Longaker, M.T. Wound repair and regeneration. *Nature* **2008**, *453*, 314-321, doi:10.1038/nature07039.
2. Borthwick, L.A.; Wynn, T.A.; Fisher, A.J. Cytokine mediated tissue fibrosis. *Biochim Biophys Acta* **2013**, *1832*, 1049-1060, doi:10.1016/j.bbadis.2012.09.014.
3. Kim, S.Y.; Nair, M.G. Macrophages in wound healing: activation and plasticity. *Immunology and cell biology* **2019**, *97*, 258-267, doi:10.1111/imcb.12236.
4. Li, B.; Wang, J.H. Fibroblasts and myofibroblasts in wound healing: force generation and measurement. *J Tissue Viability* **2011**, *20*, 108-120, doi:10.1016/j.jtv.2009.11.004.
5. Wynn, T.A. Cellular and molecular mechanisms of fibrosis. *J Pathol* **2008**, *214*, 199-210, doi:10.1002/path.2277.
6. Wynn, T.A.; Ramalingam, T.R. Mechanisms of fibrosis: therapeutic translation for fibrotic disease. *Nat Med* **2012**, *18*, 1028-1040, doi:10.1038/nm.2807.
7. Dulai, P.S.; Singh, S.; Patel, J.; Soni, M.; Prokop, L.J.; Younossi, Z.; Sebastiani, G.; Ekstedt, M.; Hagstrom, H.; Nasr, P.; et al. Increased risk of mortality by fibrosis stage in nonalcoholic fatty liver disease: Systematic review and meta-analysis. *Hepatology* **2017**, *65*, 1557-1565, doi:10.1002/hep.29085.
8. Distler, J.H.W.; Györfi, A.-H.; Ramanujam, M.; Whitfield, M.L.; Königshoff, M.; Lafyatis, R. Shared and distinct mechanisms of fibrosis. *Nature Reviews Rheumatology* **2019**, *15*, 705-730, doi:10.1038/s41584-019-0322-7.
9. Moon, A.M.; Singal, A.G.; Tapper, E.B. Contemporary Epidemiology of Chronic Liver Disease and Cirrhosis. *Clin Gastroenterol Hepatol* **2020**, *18*, 2650-2666, doi:10.1016/j.cgh.2019.07.060.
10. Asrani, S.K.; Devarbhavi, H.; Eaton, J.; Kamath, P.S. Burden of liver diseases in the world. *J Hepatol* **2019**, *70*, 151-171, doi:10.1016/j.jhep.2018.09.014.
11. Cheemerla, S.; Balakrishnan, M. Global Epidemiology of Chronic Liver Disease. *Clinical Liver Disease* **2021**, *17*, 365-370, doi:https://doi.org/10.1002/cld.1061.
12. Anstee, Q.M.; Targher, G.; Day, C.P. Progression of NAFLD to diabetes mellitus, cardiovascular disease or cirrhosis. *Nat Rev Gastroenterol Hepatol* **2013**, *10*, 330-344, doi:10.1038/nrgastro.2013.41.
13. Angulo, P.; Kleiner, D.E.; Dam-Larsen, S.; Adams, L.A.; Bjornsson, E.S.; Charatcharoenwitthaya, P.; Mills, P.R.; Keach, J.C.; Lafferty, H.D.; Stahler, A.; et al. Liver Fibrosis, but No Other Histologic Features, Is Associated With Long-term Outcomes of Patients With Nonalcoholic Fatty Liver Disease. *Gastroenterology* **2015**, *149*, 389-397.e310, doi:10.1053/j.gastro.2015.04.043.
14. Younossi, Z.M.; Koenig, A.B.; Abdelatif, D.; Fazel, Y.; Henry, L.; Wymer, M. Global epidemiology of nonalcoholic fatty liver disease-Meta-analytic assessment of prevalence, incidence, and outcomes. *Hepatology* **2016**, *64*, 73-84, doi:10.1002/hep.28431.
15. Riazi, K.; Azhari, H.; Charette, J.H.; Underwood, F.E.; King, J.A.; Afshar, E.E.; Swain, M.G.; Congly, S.E.; Kaplan, G.G.; Shaheen, A.A. The prevalence and incidence of NAFLD worldwide: a systematic review and meta-analysis. *Lancet Gastroenterol Hepatol* **2022**, *7*, 851-861, doi:10.1016/s2468-1253(22)00165-0.
16. Gastaldelli, A. Fatty liver disease: the hepatic manifestation of metabolic syndrome. *Hypertens Res* **2010**, *33*, 546-547, doi:10.1038/hr.2010.60.
17. Bedogni, G.; Miglioli, L.; Masutti, F.; Tiribelli, C.; Marchesini, G.; Bellentani, S. Prevalence of and risk factors for nonalcoholic fatty liver disease: the Dionysos nutrition and liver study. *Hepatology* **2005**, *42*, 44-52, doi:10.1002/hep.20734.
18. De Vincentis, A.; Tavaglione, F.; Jamialahmadi, O.; Picardi, A.; Antonelli Incalzi, R.; Valenti, L.; Romeo, S.; Vespasiani-Gentilucci, U. A Polygenic Risk Score to Refine Risk Stratification and Prediction for Severe Liver Disease by Clinical Fibrosis Scores. *Clin Gastroenterol Hepatol* **2022**, *20*, 658-673, doi:10.1016/j.cgh.2021.05.056.

19. Eslam, M.; George, J. Genetic contributions to NAFLD: leveraging shared genetics to uncover systems biology. *Nat Rev Gastroenterol Hepatol* **2020**, *17*, 40-52, doi:10.1038/s41575-019-0212-0.
20. Eslam, M.; Valenti, L.; Romeo, S. Genetics and epigenetics of NAFLD and NASH: Clinical impact. *J Hepatol* **2018**, *68*, 268-279, doi:10.1016/j.jhep.2017.09.003.
21. Basu Ray, S. PNPLA3-I148M: a problem of plenty in non-alcoholic fatty liver disease. *Adipocyte* **2019**, *8*, 201-208, doi:10.1080/21623945.2019.1607423.
22. Samarasinghe, S.M.; Hewage, A.S.; Siriwardana, R.C.; Tennekoon, K.H.; Niriella, M.A.; De Silva, S. Genetic and metabolic aspects of non-alcoholic fatty liver disease (NAFLD) pathogenicity. *Egyptian Journal of Medical Human Genetics* **2023**, *24*, 53, doi:10.1186/s43042-023-00433-x.
23. Romeo, S.; Kozlitina, J.; Xing, C.; Pertsemlidis, A.; Cox, D.; Pennacchio, L.A.; Boerwinkle, E.; Cohen, J.C.; Hobbs, H.H. Genetic variation in PNPLA3 confers susceptibility to nonalcoholic fatty liver disease. *Nat Genet* **2008**, *40*, 1461-1465, doi:10.1038/ng.257.
24. Kozlitina, J.; Smagris, E.; Stender, S.; Nordestgaard, B.G.; Zhou, H.H.; Tybjærg-Hansen, A.; Vogt, T.F.; Hobbs, H.H.; Cohen, J.C. Exome-wide association study identifies a TM6SF2 variant that confers susceptibility to nonalcoholic fatty liver disease. *Nat Genet* **2014**, *46*, 352-356, doi:10.1038/ng.2901.
25. Liu, Y.-L.; Reeves, H.L.; Burt, A.D.; Tiniakos, D.; McPherson, S.; Leathart, J.B.S.; Allison, M.E.D.; Alexander, G.J.; Piguet, A.-C.; Anty, R.; et al. TM6SF2 rs58542926 influences hepatic fibrosis progression in patients with non-alcoholic fatty liver disease. *Nature Communications* **2014**, *5*, 4309, doi:10.1038/ncomms5309.
26. Tong, X.-f.; Wang, Q.-y.; Zhao, X.-y.; Sun, Y.-m.; Wu, X.-n.; Yang, L.-l.; Lu, Z.-z.; Ou, X.-j.; Jia, J.-d.; You, H. Histological assessment based on liver biopsy: the value and challenges in NASH drug development. *Acta Pharmacologica Sinica* **2022**, *43*, 1200-1209, doi:10.1038/s41401-022-00874-x.
27. Li, G.; Zhang, X.; Lin, H.; Liang, L.Y.; Wong, G.L.; Wong, V.W. Non-invasive tests of non-alcoholic fatty liver disease. *Chin Med J (Engl)* **2022**, *135*, 532-546, doi:10.1097/cm9.0000000000002027.
28. Sanyal, A.J.; Shankar, S.S.; Yates, K.P.; Bolognese, J.; Daly, E.; Dehn, C.A.; Neuschwander-Tetri, B.; Kowdley, K.; Vuppalanchi, R.; Behling, C.; et al. Diagnostic performance of circulating biomarkers for non-alcoholic steatohepatitis. *Nat Med* **2023**, *29*, 2656-2664, doi:10.1038/s41591-023-02539-6.
29. Di Mauro, S.; Scamporrino, A.; Filippello, A.; Di Pino, A.; Scicali, R.; Malaguarnera, R.; Purrello, F.; Piro, S. Clinical and Molecular Biomarkers for Diagnosis and Staging of NAFLD. *Int J Mol Sci* **2021**, *22*, doi:10.3390/ijms222111905.
30. Vali, Y.; Lee, J.; Boursier, J.; Petta, S.; Wonders, K.; Tiniakos, D.; Bedossa, P.; Geier, A.; Francque, S.; Allison, M.; et al. Biomarkers for staging fibrosis and non-alcoholic steatohepatitis in non-alcoholic fatty liver disease (the LITMUS project): a comparative diagnostic accuracy study. *The Lancet Gastroenterology & Hepatology* **2023**, *8*, 714-725, doi:10.1016/S2468-1253(23)00017-1.
31. Takahashi, Y.; Fukusato, T. Histopathology of nonalcoholic fatty liver disease/nonalcoholic steatohepatitis. *World J Gastroenterol* **2014**, *20*, 15539-15548, doi:10.3748/wjg.v20.i42.15539.
32. Burt, A.D.; Lackner, C.; Tiniakos, D.G. Diagnosis and Assessment of NAFLD: Definitions and Histopathological Classification. *Semin Liver Dis* **2015**, *35*, 207-220, doi:10.1055/s-0035-1562942.
33. Bellentani, S. The epidemiology of non-alcoholic fatty liver disease. *Liver Int* **2017**, *37 Suppl 1*, 81-84, doi:10.1111/liv.13299.
34. Chalasani, N.; Younossi, Z.; Lavine, J.E.; Charlton, M.; Cusi, K.; Rinella, M.; Harrison, S.A.; Brunt, E.M.; Sanyal, A.J. The diagnosis and management of nonalcoholic fatty liver disease: Practice

guidance from the American Association for the Study of Liver Diseases. *Hepatology* **2018**, *67*, 328-357, doi:10.1002/hep.29367.
35. Caldwell, S.; Ikura, Y.; Dias, D.; Isomoto, K.; Yabu, A.; Moskaluk, C.; Pramoonjago, P.; Simmons, W.; Scruggs, H.; Rosenbaum, N.; et al. Hepatocellular ballooning in NASH. *J Hepatol* **2010**, *53*, 719-723, doi:10.1016/j.jhep.2010.04.031.
36. Brown, G.T.; Kleiner, D.E. Histopathology of nonalcoholic fatty liver disease and nonalcoholic steatohepatitis. *Metabolism* **2016**, *65*, 1080-1086, doi:10.1016/j.metabol.2015.11.008.
37. Loomba, R.; Adams, L.A. The 20% Rule of NASH Progression: The Natural History of Advanced Fibrosis and Cirrhosis Caused by NASH. *Hepatology* **2019**, *70*, 1885-1888, doi:10.1002/hep.30946.
38. Kabarra, K.; Golabi, P.; Younossi, Z.M. Nonalcoholic steatohepatitis: global impact and clinical consequences. *Endocr Connect* **2021**, *10*, R240-r247, doi:10.1530/ec-21-0048.
39. Dyson, J.K.; Anstee, Q.M.; McPherson, S. Non-alcoholic fatty liver disease: a practical approach to diagnosis and staging. *Frontline Gastroenterol* **2014**, *5*, 211-218, doi:10.1136/flgastro-2013-100403.
40. Younossi, Z.M.; Stepanova, M.; Rafiq, N.; Makhlouf, H.; Younoszai, Z.; Agrawal, R.; Goodman, Z. Pathologic criteria for nonalcoholic steatohepatitis: interprotocol agreement and ability to predict liver-related mortality. *Hepatology* **2011**, *53*, 1874-1882, doi:10.1002/hep.24268.
41. Younossi, Z.M.; Loomba, R.; Anstee, Q.M.; Rinella, M.E.; Bugianesi, E.; Marchesini, G.; Neuschwander-Tetri, B.A.; Serfaty, L.; Negro, F.; Caldwell, S.H.; et al. Diagnostic modalities for nonalcoholic fatty liver disease, nonalcoholic steatohepatitis, and associated fibrosis. *Hepatology* **2018**, *68*, 349-360, doi:10.1002/hep.29721.
42. Diehl, A.M.; Day, C. Cause, Pathogenesis, and Treatment of Nonalcoholic Steatohepatitis. *N Engl J Med* **2017**, *377*, 2063-2072.
43. Huang, D.Q.; El-Serag, H.B.; Loomba, R. Global epidemiology of NAFLD-related HCC: trends, predictions, risk factors and prevention. *Nat Rev Gastroenterol Hepatol* **2021**, *18*, 223-238.
44. Sanyal, A.J.; Van Natta, M.L.; Clark, J.; Neuschwander-Tetri, B.A.; Diehl, A.; Dasarathy, S.; Loomba, R.; Chalasani, N.; Kowdley, K.; Hameed, B.; et al. Prospective Study of Outcomes in Adults with Nonalcoholic Fatty Liver Disease. *N Engl J Med* **2021**, *385*, 1559-1569, doi:10.1056/NEJMoa2029349.
45. Vilar-Gomez, E.; Calzadilla-Bertot, L.; Wai-Sun Wong, V.; Castellanos, M.; Aller-de la Fuente, R.; Metwally, M.; Eslam, M.; Gonzalez-Fabian, L.; Alvarez-Quiñones Sanz, M.; Conde-Martin, A.F.; et al. Fibrosis Severity as a Determinant of Cause-Specific Mortality in Patients With Advanced Nonalcoholic Fatty Liver Disease: A Multi-National Cohort Study. *Gastroenterology* **2018**, *155*, 443-457.e417, doi:10.1053/j.gastro.2018.04.034.
46. Taylor, R.S.; Taylor, R.J.; Bayliss, S.; Hagström, H.; Nasr, P.; Schattenberg, J.M.; Ishigami, M.; Toyoda, H.; Wai-Sun Wong, V.; Peleg, N.; et al. Association Between Fibrosis Stage and Outcomes of Patients With Nonalcoholic Fatty Liver Disease: A Systematic Review and Meta-Analysis. *Gastroenterology* **2020**, *158*, 1611-1625.e1612, doi:10.1053/j.gastro.2020.01.043.
47. Sanyal, A.J.; Anstee, Q.M.; Trauner, M.; Lawitz, E.J.; Abdelmalek, M.F.; Ding, D.; Han, L.; Jia, C.; Huss, R.S.; Chung, C.; et al. Cirrhosis regression is associated with improved clinical outcomes in patients with nonalcoholic steatohepatitis. *Hepatology* **2022**, *75*, 1235-1246, doi:10.1002/hep.32204.
48. Tanaka, M.; Miyajima, A. Liver regeneration and fibrosis after inflammation. *Inflammation and Regeneration* **2016**, *36*, 19, doi:10.1186/s41232-016-0025-2.
49. Hernandez-Gea, V.; Friedman, S.L. Pathogenesis of Liver Fibrosis. *Annual Review of Pathology: Mechanisms of Disease* **2011**, *6*, 425-456, doi:10.1146/annurev-pathol-011110-130246.
50. Bataller, R.; Brenner, D.A. Liver fibrosis. *J Clin Invest* **2005**, *115*, 209-218.
51. Campana, L.; Esser, H.; Huch, M.; Forbes, S. Liver regeneration and inflammation: from fundamental science to clinical applications. *Nature Reviews Molecular Cell Biology* **2021**, *22*, 608-624, doi:10.1038/s41580-021-00373-7.

52. Klaas, M.; Kangur, T.; Viil, J.; Mäemets-Allas, K.; Minajeva, A.; Vadi, K.; Antsov, M.; Lapidus, N.; Järvekülg, M.; Jaks, V. The alterations in the extracellular matrix composition guide the repair of damaged liver tissue. *Sci Rep* **2016**, *6*, 27398, doi:10.1038/srep27398.
53. Tsuchida, T.; Friedman, S.L. Mechanisms of hepatic stellate cell activation. *Nature Reviews Gastroenterology & Hepatology* **2017**, *14*, 397-411, doi:10.1038/nrgastro.2017.38.
54. Ortiz, C.; Schierwagen, R.; Schaefer, L.; Klein, S.; Trepat, X.; Trebicka, J. Extracellular Matrix Remodeling in Chronic Liver Disease. *Current Tissue Microenvironment Reports* **2021**, *2*, 41-52, doi:10.1007/s43152-021-00030-3.
55. Schulze, R.J.; Schott, M.B.; Casey, C.A.; Tuma, P.L.; McNiven, M.A. The cell biology of the hepatocyte: A membrane trafficking machine. *J Cell Biol* **2019**, *218*, 2096-2112, doi:10.1083/jcb.201903090.
56. Treyer, A.; Müsch, A. Hepatocyte polarity. *Compr Physiol* **2013**, *3*, 243-287, doi:10.1002/cphy.c120009.
57. Schwabe, R.F.; Tabas, I.; Pajvani, U.B. Mechanisms of Fibrosis Development in Nonalcoholic Steatohepatitis. *Gastroenterology* **2020**, *158*, 1913-1928, doi:10.1053/j.gastro.2019.11.311.
58. Han, H.; Desert, R.; Das, S.; Song, Z.; Athavale, D.; Ge, X.; Nieto, N. Danger signals in liver injury and restoration of homeostasis. *Journal of Hepatology* **2020**, *73*, 933-951, doi:https://doi.org/10.1016/j.jhep.2020.04.033.
59. Kovach, M.A.; Standiford, T.J. The function of neutrophils in sepsis. *Curr Opin Infect Dis* **2012**, *25*, 321-327, doi:10.1097/QCO.0b013e3283528c9b.
60. McHedlidze, T.; Waldner, M.; Zopf, S.; Walker, J.; Rankin, A.L.; Schuchmann, M.; Voehringer, D.; McKenzie, A.N.; Neurath, M.F.; Pflanz, S.; et al. Interleukin-33-dependent innate lymphoid cells mediate hepatic fibrosis. *Immunity* **2013**, *39*, 357-371, doi:10.1016/j.immuni.2013.07.018.
61. Mederacke, I.; Filliol, A.; Affo, S.; Nair, A.; Hernandez, C.; Sun, Q.; Hamberger, F.; Brundu, F.; Chen, Y.; Ravichandra, A.; et al. The purinergic P2Y14 receptor links hepatocyte death to hepatic stellate cell activation and fibrogenesis in the liver. *Sci Transl Med* **2022**, *14*, eabe5795, doi:10.1126/scitranslmed.abe5795.
62. Kao, Y.-H.; Jawan, B.; Goto, S.; Hung, C.-T.; Lin, Y.-C.; Nakano, T.; Hsu, L.-W.; Lai, C.-Y.; Tai, M.-H.; Chen, C.-L. High-mobility group box 1 protein activates hepatic stellate cells in vitro. In Proceedings of the Transplantation proceedings, 2008; pp. 2704-2705.
63. Ge, X.; Arriazu, E.; Magdaleno, F.; Antoine, D.J.; Dela Cruz, R.; Theise, N.; Nieto, N. High Mobility Group Box-1 Drives Fibrosis Progression Signaling via the Receptor for Advanced Glycation End Products in Mice. *Hepatology* **2018**, *68*, 2380-2404, doi:10.1002/hep.30093.
64. Mridha, A.R.; Wree, A.; Robertson, A.A.B.; Yeh, M.M.; Johnson, C.D.; Van Rooyen, D.M.; Haczeyni, F.; Teoh, N.C.; Savard, C.; Ioannou, G.N.; et al. NLRP3 inflammasome blockade reduces liver inflammation and fibrosis in experimental NASH in mice. *J Hepatol* **2017**, *66*, 1037-1046, doi:10.1016/j.jhep.2017.01.022.
65. Fabre, T.; Kared, H.; Friedman, S.L.; Shoukry, N.H. IL-17A enhances the expression of profibrotic genes through upregulation of the TGF-β receptor on hepatic stellate cells in a JNK-dependent manner. *J Immunol* **2014**, *193*, 3925-3933, doi:10.4049/jimmunol.1400861.
66. Fabre, T.; Molina, M.F.; Soucy, G.; Goulet, J.P.; Willems, B.; Villeneuve, J.P.; Bilodeau, M.; Shoukry, N.H. Type 3 cytokines IL-17A and IL-22 drive TGF-β-dependent liver fibrosis. *Sci Immunol* **2018**, *3*, doi:10.1126/sciimmunol.aar7754.
67. Meng, F.; Wang, K.; Aoyama, T.; Grivennikov, S.I.; Paik, Y.; Scholten, D.; Cong, M.; Iwaisako, K.; Liu, X.; Zhang, M.; et al. Interleukin-17 signaling in inflammatory, Kupffer cells, and hepatic stellate cells exacerbates liver fibrosis in mice. *Gastroenterology* **2012**, *143*, 765-776.e763, doi:10.1053/j.gastro.2012.05.049.
68. Moles, A.; Murphy, L.; Wilson, C.L.; Chakraborty, J.B.; Fox, C.; Park, E.J.; Mann, J.; Oakley, F.; Howarth, R.; Brain, J.; et al. A TLR2/S100A9/CXCL-2 signaling network is necessary for

neutrophil recruitment in acute and chronic liver injury in the mouse. *J Hepatol* **2014**, *60*, 782-791, doi:10.1016/j.jhep.2013.12.005.
69. Gehrke, N.; Nagel, M.; Straub, B.K.; Wörns, M.A.; Schuchmann, M.; Galle, P.R.; Schattenberg, J.M. Loss of cellular FLICE-inhibitory protein promotes acute cholestatic liver injury and inflammation from bile duct ligation. *Am J Physiol Gastrointest Liver Physiol* **2018**, *314*, G319-g333, doi:10.1152/ajpgi.00097.2017.
70. Pulli, B.; Ali, M.; Iwamoto, Y.; Zeller, M.W.; Schob, S.; Linnoila, J.J.; Chen, J.W. Myeloperoxidase-Hepatocyte-Stellate Cell Cross Talk Promotes Hepatocyte Injury and Fibrosis in Experimental Nonalcoholic Steatohepatitis. *Antioxid Redox Signal* **2015**, *23*, 1255-1269, doi:10.1089/ars.2014.6108.
71. Zhou, Z.; Xu, M.J.; Cai, Y.; Wang, W.; Jiang, J.X.; Varga, Z.V.; Feng, D.; Pacher, P.; Kunos, G.; Torok, N.J.; et al. Neutrophil-Hepatic Stellate Cell Interactions Promote Fibrosis in Experimental Steatohepatitis. *Cell Mol Gastroenterol Hepatol* **2018**, *5*, 399-413.
72. Calvente, C.J.; Tameda, M.; Johnson, C.D.; Del Pilar, H.; Lin, Y.C.; Adronikou, N.; De Mollerat Du Jeu, X.; Llorente, C.; Boyer, J.; Feldstein, A.E. Neutrophils contribute to spontaneous resolution of liver inflammation and fibrosis via microRNA-223. *J Clin Invest* **2019**, *129*, 4091-4109, doi:10.1172/jci122258.
73. Harty, M.W.; Muratore, C.S.; Papa, E.F.; Gart, M.S.; Ramm, G.A.; Gregory, S.H.; Tracy, T.F., Jr. Neutrophil depletion blocks early collagen degradation in repairing cholestatic rat livers. *Am J Pathol* **2010**, *176*, 1271-1281, doi:10.2353/ajpath.2010.090527.
74. Krenkel, O.; Puengel, T.; Govaere, O.; Abdallah, A.T.; Mossanen, J.C.; Kohlhepp, M.; Liepelt, A.; Lefebvre, E.; Luedde, T.; Hellerbrand, C.; et al. Therapeutic inhibition of inflammatory monocyte recruitment reduces steatohepatitis and liver fibrosis. *Hepatology* **2018**, *67*, 1270-1283, doi:10.1002/hep.29544.
75. Krenkel, O.; Hundertmark, J.; Abdallah, A.T.; Kohlhepp, M.; Puengel, T.; Roth, T.; Branco, D.P.P.; Mossanen, J.C.; Luedde, T.; Trautwein, C.; et al. Myeloid cells in liver and bone marrow acquire a functionally distinct inflammatory phenotype during obesity-related steatohepatitis. *Gut* **2020**, *69*, 551-563, doi:10.1136/gutjnl-2019-318382.
76. Krenkel, O.; Tacke, F. Liver macrophages in tissue homeostasis and disease. *Nature Reviews Immunology* **2017**, *17*, 306-321, doi:10.1038/nri.2017.11.
77. Wen, Y.; Lambrecht, J.; Ju, C.; Tacke, F. Hepatic macrophages in liver homeostasis and diseases-diversity, plasticity and therapeutic opportunities. *Cellular & Molecular Immunology* **2021**, *18*, 45-56, doi:10.1038/s41423-020-00558-8.
78. Bonnardel, J.; T'Jonck, W.; Gaublomme, D.; Browaeys, R.; Scott, C.L.; Martens, L.; Vanneste, B.; De Prijck, S.; Nedospasov, S.A.; Kremer, A.; et al. Stellate Cells, Hepatocytes, and Endothelial Cells Imprint the Kupffer Cell Identity on Monocytes Colonizing the Liver Macrophage Niche. *Immunity* **2019**, *51*, 638-654.e639, doi:10.1016/j.immuni.2019.08.017.
79. Scott, C.L.; Zheng, F.; De Baetselier, P.; Martens, L.; Saeys, Y.; De Prijck, S.; Lippens, S.; Abels, C.; Schoonooghe, S.; Raes, G.; et al. Bone marrow-derived monocytes give rise to self-renewing and fully differentiated Kupffer cells. *Nat Commun* **2016**, *7*, 10321, doi:10.1038/ncomms10321.
80. Karlmark, K.R.; Weiskirchen, R.; Zimmermann, H.W.; Gassler, N.; Ginhoux, F.; Weber, C.; Merad, M.; Luedde, T.; Trautwein, C.; Tacke, F. Hepatic recruitment of the inflammatory Gr1+ monocyte subset upon liver injury promotes hepatic fibrosis. *Hepatology* **2009**, *50*, 261-274.
81. Baeck, C.; Wehr, A.; Karlmark, K.R.; Heymann, F.; Vucur, M.; Gassler, N.; Huss, S.; Klussmann, S.; Eulberg, D.; Luedde, T.; et al. Pharmacological inhibition of the chemokine CCL2 (MCP-1) diminishes liver macrophage infiltration and steatohepatitis in chronic hepatic injury. *Gut* **2012**, *61*, 416-426, doi:10.1136/gutjnl-2011-300304.
82. Ramachandran, P.; Dobie, R.; Wilson-Kanamori, J.R.; Dora, E.F.; Henderson, B.E.P.; Luu, N.T.; Portman, J.R.; Matchett, K.P.; Brice, M.; Marwick, J.A.; et al. Resolving the fibrotic niche of

human liver cirrhosis at single-cell level. *Nature* **2019**, *575*, 512-518, doi:10.1038/s41586-019-1631-3.
83. Fabre, T.; Barron, A.M.S.; Christensen, S.M.; Asano, S.; Bound, K.; Lech, M.P.; Wadsworth, M.H., 2nd; Chen, X.; Wang, C.; Wang, J.; et al. Identification of a broadly fibrogenic macrophage subset induced by type 3 inflammation. *Sci Immunol* **2023**, *8*, eadd8945, doi:10.1126/sciimmunol.add8945.
84. Seidman, J.S.; Troutman, T.D.; Sakai, M.; Gola, A.; Spann, N.J.; Bennett, H.; Bruni, C.M.; Ouyang, Z.; Li, R.Z.; Sun, X.; et al. Niche-Specific Reprogramming of Epigenetic Landscapes Drives Myeloid Cell Diversity in Nonalcoholic Steatohepatitis. *Immunity* **2020**, *52*, 1057-1074.e1057.
85. Hou, J.; Zhang, J.; Cui, P.; Zhou, Y.; Liu, C.; Wu, X.; Ji, Y.; Wang, S.; Cheng, B.; Ye, H.; et al. TREM2 sustains macrophage-hepatocyte metabolic coordination in nonalcoholic fatty liver disease and sepsis. *J Clin Invest* **2021**, *131*, doi:10.1172/jci135197.
86. Ouyang, J.F.; Mishra, K.; Xie, Y.; Park, H.; Huang, K.Y.; Petretto, E.; Behmoaras, J. Systems level identification of a matrisome-associated macrophage polarisation state in multi-organ fibrosis. *eLife* **2023**, *12*, e85530, doi:10.7554/eLife.85530.
87. Kisseleva, T. The origin of fibrogenic myofibroblasts in fibrotic liver. *Hepatology* **2017**, *65*, 1039-1043, doi:https://doi.org/10.1002/hep.28948.
88. Xu, J.; Liu, X.; Brenner, D.A.; Kisseleva, T. Novel perspectives on the origins of the hepatic myofibroblasts. *Cell Health and Cytoskeleton* **2015**, *7*, 111-119, doi:10.2147/CHC.S57679.
89. Kim, H.Y.; Sakane, S.; Eguileor, A.; Carvalho Gontijo Weber, R.; Lee, W.; Liu, X.; Lam, K.; Ishizuka, K.; Rosenthal, S.B.; Diggle, K.; et al. The Origin and Fate of Liver Myofibroblasts. *Cellular and Molecular Gastroenterology and Hepatology* **2024**, *17*, 93-106, doi:https://doi.org/10.1016/j.jcmgh.2023.09.008.
90. Iwaisako, K.; Jiang, C.; Zhang, M.; Cong, M.; Moore-Morris, T.J.; Park, T.J.; Liu, X.; Xu, J.; Wang, P.; Paik, Y.H.; et al. Origin of myofibroblasts in the fibrotic liver in mice. *Proc Natl Acad Sci U S A* **2014**, *111*, E3297-3305, doi:10.1073/pnas.1400062111.
91. Friedman, S.L. Hepatic stellate cells: protean, multifunctional, and enigmatic cells of the liver. *Physiol Rev* **2008**, *88*, 125-172, doi:10.1152/physrev.00013.2007.
92. Xu, F.; Liu, C.; Zhou, D.; Zhang, L. TGF-β/SMAD Pathway and Its Regulation in Hepatic Fibrosis. *J Histochem Cytochem* **2016**, *64*, 157-167, doi:10.1369/0022155415627681.
93. Mederacke, I.; Hsu, C.C.; Troeger, J.S.; Huebener, P.; Mu, X.; Dapito, D.H.; Pradere, J.P.; Schwabe, R.F. Fate tracing reveals hepatic stellate cells as dominant contributors to liver fibrosis independent of its aetiology. *Nat Commun* **2013**, *4*, 2823, doi:10.1038/ncomms3823.
94. Krizhanovsky, V.; Yon, M.; Dickins, R.A.; Hearn, S.; Simon, J.; Miething, C.; Yee, H.; Zender, L.; Lowe, S.W. Senescence of activated stellate cells limits liver fibrosis. *Cell* **2008**, *134*, 657-667, doi:10.1016/j.cell.2008.06.049.
95. Gonzalez, S.A.; Fiel, M.I.; Sauk, J.; Canchis, P.W.; Liu, R.C.; Chiriboga, L.; Yee, H.T.; Jacobson, I.M.; Talal, A.H. Inverse association between hepatic stellate cell apoptosis and fibrosis in chronic hepatitis C virus infection. *J Viral Hepat* **2009**, *16*, 141-148, doi:10.1111/j.1365-2893.2008.01052.x.
96. Krenkel, O.; Hundertmark, J.; Ritz, T.P.; Weiskirchen, R.; Tacke, F. Single Cell RNA Sequencing Identifies Subsets of Hepatic Stellate Cells and Myofibroblasts in Liver Fibrosis. *Cells* **2019**, *8*, doi:10.3390/cells8050503.
97. Rosenthal, S.B.; Liu, X.; Ganguly, S.; Dhar, D.; Pasillas, M.P.; Ricciardelli, E.; Li, R.Z.; Troutman, T.D.; Kisseleva, T.; Glass, C.K.; et al. Heterogeneity of HSCs in a Mouse Model of NASH. *Hepatology* **2021**, *74*, 667-685, doi:10.1002/hep.31743.
98. Kisseleva, T.; Brenner, D. Molecular and cellular mechanisms of liver fibrosis and its regression. *Nature Reviews Gastroenterology & Hepatology* **2021**, *18*, 151-166, doi:10.1038/s41575-020-00372-7.
99. Nishio, T.; Hu, R.; Koyama, Y.; Liang, S.; Rosenthal, S.B.; Yamamoto, G.; Karin, D.; Baglieri, J.; Ma, H.-Y.; Xu, J.; et al. Activated hepatic stellate cells and portal fibroblasts contribute to

cholestatic liver fibrosis in MDR2 knockout mice. *Journal of Hepatology* **2019**, *71*, 573-585, doi:10.1016/j.jhep.2019.04.012.
100. Marcellin, P.; Gane, E.; Buti, M.; Afdhal, N.; Sievert, W.; Jacobson, I.M.; Washington, M.K.; Germanidis, G.; Flaherty, J.F.; Aguilar Schall, R.; et al. Regression of cirrhosis during treatment with tenofovir disoproxil fumarate for chronic hepatitis B: a 5-year open-label follow-up study. *Lancet* **2013**, *381*, 468-475, doi:10.1016/s0140-6736(12)61425-1.
101. Hardy, T.; Anstee, Q.M.; Day, C.P. Nonalcoholic fatty liver disease: new treatments. *Curr Opin Gastroenterol* **2015**, *31*, 175-183, doi:10.1097/mog.0000000000000175.
102. Friedman, S.L.; Neuschwander-Tetri, B.A.; Rinella, M.; Sanyal, A.J. Mechanisms of NAFLD development and therapeutic strategies. *Nat Med* **2018**, *24*, 908-922, doi:10.1038/s41591-018-0104-9.
103. Antoniou, K.M.; Margaritopoulos, G.A.; Tomassetti, S.; Bonella, F.; Costabel, U.; Poletti, V. Interstitial lung disease. *Eur Respir Rev* **2014**, *23*, 40-54, doi:10.1183/09059180.00009113.
104. Wijsenbeek, M.; Cottin, V. Spectrum of Fibrotic Lung Diseases. *N Engl J Med* **2020**, *383*, 958-968, doi:10.1056/NEJMra2005230.
105. Miller, E.R.; Putman, R.K.; Diaz, A.A.; Xu, H.; San José Estépar, R.; Araki, T.; Nishino, M.; Poli de Frías, S.; Hida, T.; Ross, J.; et al. Increased Airway Wall Thickness in Interstitial Lung Abnormalities and Idiopathic Pulmonary Fibrosis. *Ann Am Thorac Soc* **2019**, *16*, 447-454, doi:10.1513/AnnalsATS.201806-424OC.
106. Wijsenbeek, M.; Suzuki, A.; Maher, T.M. Interstitial lung diseases. *The Lancet* **2022**, *400*, 769-786.
107. Cottin, V.; Hirani, N.A.; Hotchkin, D.L.; Nambiar, A.M.; Ogura, T.; Otaola, M.; Skowasch, D.; Park, J.S.; Poonyagariyagorn, H.K.; Wuyts, W.; et al. Presentation, diagnosis and clinical course of the spectrum of progressive-fibrosing interstitial lung diseases. *Eur Respir Rev* **2018**, *27*, doi:10.1183/16000617.0076-2018.
108. Spagnolo, P.; Bonniaud, P.; Rossi, G.; Sverzellati, N.; Cottin, V. Drug-induced interstitial lung disease. *European Respiratory Journal* **2022**, 2102776, doi:10.1183/13993003.02776-2021.
109. Baughman, R.P.; Valeyre, D.; Korsten, P.; Mathioudakis, A.G.; Wuyts, W.A.; Wells, A.; Rottoli, P.; Nunes, H.; Lower, E.E.; Judson, M.A.; et al. ERS clinical practice guidelines on treatment of sarcoidosis. *Eur Respir J* **2021**, *58*, doi:10.1183/13993003.04079-2020.
110. Raghu, G.; Remy-Jardin, M.; Ryerson, C.J.; Myers, J.L.; Kreuter, M.; Vasakova, M.; Bargagli, E.; Chung, J.H.; Collins, B.F.; Bendstrup, E.; et al. Diagnosis of Hypersensitivity Pneumonitis in Adults: An Official ATS/JRS/ALAT Clinical Practice Guideline. *American Journal of Respiratory and Critical Care Medicine* **2020**, *202*, e36-e69, doi:10.1164/rccm.202005-2032ST.
111. Grunewald, J.; Eklund, A. State of the Art. Role of CD4+ T Cells in Sarcoidosis. *Proceedings of the American Thoracic Society* **2007**, *4*, 461-464, doi:10.1513/pats.200606-130MS.
112. Costabel, U.; Miyazaki, Y.; Pardo, A.; Koschel, D.; Bonella, F.; Spagnolo, P.; Guzman, J.; Ryerson, C.J.; Selman, M. Hypersensitivity pneumonitis. *Nature Reviews Disease Primers* **2020**, *6*, 65, doi:10.1038/s41572-020-0191-z.
113. Nathan, S.D.; Shlobin, O.A.; Weir, N.; Ahmad, S.; Kaldjob, J.M.; Battle, E.; Sheridan, M.J.; du Bois, R.M. Long-term Course and Prognosis of Idiopathic Pulmonary Fibrosis in the New Millennium. *Chest* **2011**, *140*, 221-229, doi:https://doi.org/10.1378/chest.10-2572.
114. Wolters, P.J.; Collard, H.R.; Jones, K.D. Pathogenesis of idiopathic pulmonary fibrosis. *Annu Rev Pathol* **2014**, *9*, 157-179.
115. Hutchinson, J.; Fogarty, A.; Hubbard, R.; McKeever, T. Global incidence and mortality of idiopathic pulmonary fibrosis: a systematic review. *European Respiratory Journal* **2015**, *46*, 795-806, doi:10.1183/09031936.00185114.
116. Maher, T.M.; Bendstrup, E.; Dron, L.; Langley, J.; Smith, G.; Khalid, J.M.; Patel, H.; Kreuter, M. Global incidence and prevalence of idiopathic pulmonary fibrosis. *Respiratory Research* **2021**, *22*, 197, doi:10.1186/s12931-021-01791-z.

117. Taskar, V.S.; Coultas, D.B. Is idiopathic pulmonary fibrosis an environmental disease? *Proc Am Thorac Soc* **2006**, *3*, 293-298, doi:10.1513/pats.200512-131TK.
118. Kreuter, M.; Ehlers-Tenenbaum, S.; Palmowski, K.; Bruhwyler, J.; Oltmanns, U.; Muley, T.; Heussel, C.P.; Warth, A.; Kolb, M.; Herth, F.J. Impact of Comorbidities on Mortality in Patients with Idiopathic Pulmonary Fibrosis. *PLoS One* **2016**, *11*, e0151425, doi:10.1371/journal.pone.0151425.
119. Raghu, G.; Amatto, V.C.; Behr, J.; Stowasser, S. Comorbidities in idiopathic pulmonary fibrosis patients: a systematic literature review. *European Respiratory Journal* **2015**, *46*, 1113-1130, doi:10.1183/13993003.02316-2014.
120. Pardo, A.; Selman, M. The Interplay of the Genetic Architecture, Aging, and Environmental Factors in the Pathogenesis of Idiopathic Pulmonary Fibrosis. *American Journal of Respiratory Cell and Molecular Biology* **2021**, *64*, 163-172, doi:10.1165/rcmb.2020-0373PS.
121. Seibold, M.A.; Wise, A.L.; Speer, M.C.; Steele, M.P.; Brown, K.K.; Loyd, J.E.; Fingerlin, T.E.; Zhang, W.; Gudmundsson, G.; Groshong, S.D.; et al. A common MUC5B promoter polymorphism and pulmonary fibrosis. *N Engl J Med* **2011**, *364*, 1503-1512, doi:10.1056/NEJMoa1013660.
122. Borie, R.; Crestani, B.; Dieude, P.; Nunes, H.; Allanore, Y.; Kannengiesser, C.; Airo, P.; Matucci-Cerinic, M.; Wallaert, B.; Israel-Biet, D.; et al. The MUC5B variant is associated with idiopathic pulmonary fibrosis but not with systemic sclerosis interstitial lung disease in the European Caucasian population. *PLoS One* **2013**, *8*, e70621, doi:10.1371/journal.pone.0070621.
123. Kaur, A.; Mathai, S.K.; Schwartz, D.A. Genetics in idiopathic pulmonary fibrosis pathogenesis, prognosis, and treatment. *Frontiers in medicine* **2017**, *4*, 154.
124. Kropski, J.A.; Blackwell, T.S.; Loyd, J.E. The genetic basis of idiopathic pulmonary fibrosis. *European Respiratory Journal* **2015**, *45*, 1717-1727, doi:10.1183/09031936.00163814.
125. Gupta, R.; Morgan, A.D.; George, P.M.; Quint, J.K. Incidence, prevalence and mortality of idiopathic pulmonary fibrosis in England from 2008 to 2018: a cohort study. *Thorax* **2024**, *79*, 624-631, doi:10.1136/thorax-2023-220887.
126. Luppi, F.; Kalluri, M.; Faverio, P.; Kreuter, M.; Ferrara, G. Idiopathic pulmonary fibrosis beyond the lung: understanding disease mechanisms to improve diagnosis and management. *Respir Res* **2021**, *22*, 109, doi:10.1186/s12931-021-01711-1.
127. Meiners, S.; Eickelberg, O.; Königshoff, M. Hallmarks of the ageing lung. *European Respiratory Journal* **2015**, *45*, 807-827, doi:10.1183/09031936.00186914.
128. López-Otín, C.; Blasco, M.A.; Partridge, L.; Serrano, M.; Kroemer, G. The hallmarks of aging. *Cell* **2013**, *153*, 1194-1217, doi:10.1016/j.cell.2013.05.039.
129. Selman, M.; Pardo, A. Revealing the pathogenic and aging-related mechanisms of the enigmatic idiopathic pulmonary fibrosis. an integral model. *Am J Respir Crit Care Med* **2014**, *189*, 1161-1172, doi:10.1164/rccm.201312-2221PP.
130. Li, X.; Li, C.; Zhang, W.; Wang, Y.; Qian, P.; Huang, H. Inflammation and aging: signaling pathways and intervention therapies. *Signal Transduction and Targeted Therapy* **2023**, *8*, 239, doi:10.1038/s41392-023-01502-8.
131. Raghu, G.; Remy-Jardin, M.; Richeldi, L.; Thomson, C.C.; Inoue, Y.; Johkoh, T.; Kreuter, M.; Lynch, D.A.; Maher, T.M.; Martinez, F.J.; et al. Idiopathic Pulmonary Fibrosis (an Update) and Progressive Pulmonary Fibrosis in Adults: An Official ATS/ERS/JRS/ALAT Clinical Practice Guideline. *American Journal of Respiratory and Critical Care Medicine* **2022**, *205*, e18-e47, doi:10.1164/rccm.202202-0399ST.
132. Smith, M.L. The histologic diagnosis of usual interstitial pneumonia of idiopathic pulmonary fibrosis. Where we are and where we need to go. *Modern Pathology* **2022**, *35*, 8-14, doi:10.1038/s41379-021-00889-5.
133. Herrera, J.A.; Dingle, L.; Montero, M.A.; Venkateswaran, R.V.; Blaikley, J.F.; Lawless, C.; Schwartz, M.A. The UIP/IPF fibroblastic focus is a collagen biosynthesis factory embedded in a distinct extracellular matrix. *JCI Insight* **2022**, *7*, doi:10.1172/jci.insight.156115.

134. Mäkelä, K.; Mäyränpää, M.I.; Sihvo, H.-K.; Bergman, P.; Sutinen, E.; Ollila, H.; Kaarteenaho, R.; Myllärniemi, M. Artificial intelligence identifies inflammation and confirms fibroblast foci as prognostic tissue biomarkers in idiopathic pulmonary fibrosis. *Human Pathology* **2021**, *107*, 58-68.
135. Parimon, T.; Yao, C.; Stripp, B.R.; Noble, P.W.; Chen, P. Alveolar Epithelial Type II Cells as Drivers of Lung Fibrosis in Idiopathic Pulmonary Fibrosis. *Int J Mol Sci* **2020**, *21*, doi:10.3390/ijms21072269.
136. Noble, P.W. Epithelial fibroblast triggering and interactions in pulmonary fibrosis. *European Respiratory Review* **2008**, *17*, 123-129, doi:10.1183/09059180.00010904.
137. Barkauskas, C.E.; Cronce, M.J.; Rackley, C.R.; Bowie, E.J.; Keene, D.R.; Stripp, B.R.; Randell, S.H.; Noble, P.W.; Hogan, B.L. Type 2 alveolar cells are stem cells in adult lung. *J Clin Invest* **2013**, *123*, 3025-3036, doi:10.1172/jci68782.
138. Wang, Z.N.; Tang, X.X. New Perspectives on the Aberrant Alveolar Repair of Idiopathic Pulmonary Fibrosis. *Front Cell Dev Biol* **2020**, *8*, 580026, doi:10.3389/fcell.2020.580026.
139. Jacob, A.; Morley, M.; Hawkins, F.; McCauley, K.B.; Jean, J.C.; Heins, H.; Na, C.L.; Weaver, T.E.; Vedaie, M.; Hurley, K.; et al. Differentiation of Human Pluripotent Stem Cells into Functional Lung Alveolar Epithelial Cells. *Cell Stem Cell* **2017**, *21*, 472-488.e410, doi:10.1016/j.stem.2017.08.014.
140. Suwara, M.I.; Green, N.J.; Borthwick, L.A.; Mann, J.; Mayer-Barber, K.D.; Barron, L.; Corris, P.A.; Farrow, S.N.; Wynn, T.A.; Fisher, A.J.; et al. IL-1alpha released from damaged epithelial cells is sufficient and essential to trigger inflammatory responses in human lung fibroblasts. *Mucosal immunology* **2014**, *7*, 684-693, doi:10.1038/mi.2013.87.
141. Morimoto, K.; Janssen, W.J.; Terada, M. Defective efferocytosis by alveolar macrophages in IPF patients. *Respir Med* **2012**, *106*, 1800-1803, doi:10.1016/j.rmed.2012.08.020.
142. Wu, H.; Yu, Y.; Huang, H.; Hu, Y.; Fu, S.; Wang, Z.; Shi, M.; Zhao, X.; Yuan, J.; Li, J.; et al. Progressive Pulmonary Fibrosis Is Caused by Elevated Mechanical Tension on Alveolar Stem Cells. *Cell* **2020**, *180*, 107-121.e117, doi:10.1016/j.cell.2019.11.027.
143. Haschek, W.M.; Witschi, H.R.; Nikula, K.J. 28 - Respiratory System. In *Handbook of Toxicologic Pathology (Second Edition)*, Haschek, W.M., Rousseaux, C.G., Wallig, M.A., Eds.; Academic Press: San Diego, 2002; pp. 3-83.
144. Whitsett, J.A.; Alenghat, T. Respiratory epithelial cells orchestrate pulmonary innate immunity. *Nature Immunology* **2015**, *16*, 27-35, doi:10.1038/ni.3045.
145. Little, D.R.; Gerner-Mauro, K.N.; Flodby, P.; Crandall, E.D.; Borok, Z.; Akiyama, H.; Kimura, S.; Ostrin, E.J.; Chen, J. Transcriptional control of lung alveolar type 1 cell development and maintenance by NK homeobox 2-1. *Proceedings of the National Academy of Sciences* **2019**, *116*, 20545-20555, doi:10.1073/pnas.1906663116.
146. Dietl, P.; Haller, T.; Frick, M. Spatio-temporal aspects, pathways and actions of Ca(2+) in surfactant secreting pulmonary alveolar type II pneumocytes. *Cell Calcium* **2012**, *52*, 296-302, doi:10.1016/j.ceca.2012.04.010.
147. Günther, J.; Seyfert, H.M. The first line of defence: insights into mechanisms and relevance of phagocytosis in epithelial cells. *Semin Immunopathol* **2018**, *40*, 555-565, doi:10.1007/s00281-018-0701-1.
148. Suwara, M.I.; Green, N.J.; Borthwick, L.A.; Mann, J.; Mayer-Barber, K.D.; Barron, L.; Corris, P.A.; Farrow, S.N.; Wynn, T.A.; Fisher, A.J.; et al. IL-1α released from damaged epithelial cells is sufficient and essential to trigger inflammatory responses in human lung fibroblasts. *Mucosal immunology* **2014**, *7*, 684-693, doi:https://doi.org/10.1038/mi.2013.87.
149. Burgoyne, R.A.; Fisher, A.J.; Borthwick, L.A. The Role of Epithelial Damage in the Pulmonary Immune Response. *Cells* **2021**, *10*, 2763.
150. Herbig, U.; Jobling, W.A.; Chen, B.P.; Chen, D.J.; Sedivy, J.M. Telomere shortening triggers senescence of human cells through a pathway involving ATM, p53, and p21(CIP1), but not p16(INK4a). *Molecular cell* **2004**, *14*, 501-513, doi:10.1016/s1097-2765(04)00256-4.

151. Munoz-Espin, D.; Serrano, M. Cellular senescence: from physiology to pathology. *Nat Rev Mol Cell Biol* **2014**, *15*, 482-496, doi:10.1038/nrm3823.
152. Birch, J.; Gil, J. Senescence and the SASP: many therapeutic avenues. *Genes & development* **2020**, *34*, 1565-1576, doi:10.1101/gad.343129.120.
153. Angelidis, I.; Simon, L.M.; Fernandez, I.E.; Strunz, M.; Mayr, C.H.; Greiffo, F.R.; Tsitsiridis, G.; Ansari, M.; Graf, E.; Strom, T.-M. An atlas of the aging lung mapped by single cell transcriptomics and deep tissue proteomics. *Nature communications* **2019**, *10*, 963.
154. Hansel, C.; Jendrossek, V.; Klein, D. Cellular Senescence in the Lung: The Central Role of Senescent Epithelial Cells. *Int J Mol Sci* **2020**, *21*, doi:10.3390/ijms21093279.
155. Lomas, N.J.; Watts, K.L.; Akram, K.M.; Forsyth, N.R.; Spiteri, M.A. Idiopathic pulmonary fibrosis: immunohistochemical analysis provides fresh insights into lung tissue remodelling with implications for novel prognostic markers. *International journal of clinical and experimental pathology* **2012**, *5*, 58-71.
156. Kuwano, K.; Kunitake, R.; Kawasaki, M.; Nomoto, Y.; Hagimoto, N.; Nakanishi, Y.; Hara, N. P21Waf1/Cip1/Sdi1 and p53 expression in association with DNA strand breaks in idiopathic pulmonary fibrosis. *Am J Respir Crit Care Med* **1996**, *154*, 477-483, doi:10.1164/ajrccm.154.2.8756825.
157. Minagawa, S.; Araya, J.; Numata, T.; Nojiri, S.; Hara, H.; Yumino, Y.; Kawaishi, M.; Odaka, M.; Morikawa, T.; Nishimura, S.L.; et al. Accelerated epithelial cell senescence in IPF and the inhibitory role of SIRT6 in TGF-β-induced senescence of human bronchial epithelial cells. *American journal of physiology. Lung cellular and molecular physiology* **2011**, *300*, L391-401, doi:10.1152/ajplung.00097.2010.
158. DePianto, D.J.; Heiden, J.A.V.; Morshead, K.B.; Sun, K.H.; Modrusan, Z.; Teng, G.; Wolters, P.J.; Arron, J.R. Molecular mapping of interstitial lung disease reveals a phenotypically distinct senescent basal epithelial cell population. *JCI Insight* **2021**, *6*, doi:10.1172/jci.insight.143626.
159. Chen, X.; Xu, H.; Hou, J.; Wang, H.; Zheng, Y.; Li, H.; Cai, H.; Han, X.; Dai, J. Epithelial cell senescence induces pulmonary fibrosis through Nanog-mediated fibroblast activation. *Aging* **2019**, *12*, 242-259, doi:10.18632/aging.102613.
160. Yao, C.; Guan, X.; Carraro, G.; Parimon, T.; Liu, X.; Huang, G.; Mulay, A.; Soukiasian, H.J.; David, G.; Weigt, S.S.; et al. Senescence of Alveolar Type 2 Cells Drives Progressive Pulmonary Fibrosis. *Am J Respir Crit Care Med* **2021**, *203*, 707-717, doi:10.1164/rccm.202004-1274OC.
161. Justice, J.N.; Nambiar, A.M.; Tchkonia, T.; LeBrasseur, N.K.; Pascual, R.; Hashmi, S.K.; Prata, L.; Masternak, M.M.; Kritchevsky, S.B.; Musi, N.; et al. Senolytics in idiopathic pulmonary fibrosis: Results from a first-in-human, open-label, pilot study. *EBioMedicine* **2019**, *40*, 554-563, doi:10.1016/j.ebiom.2018.12.052.
162. Lehmann, M.; Korfei, M.; Mutze, K.; Klee, S.; Skronska-Wasek, W.; Alsafadi, H.N.; Ota, C.; Costa, R.; Schiller, H.B.; Lindner, M.; et al. Senolytic drugs target alveolar epithelial cell function and attenuate experimental lung fibrosis ex vivo. *Eur Respir J* **2017**, *50*, doi:10.1183/13993003.02367-2016.
163. Calhoun, C.; Shivshankar, P.; Saker, M.; Sloane, L.B.; Livi, C.B.; Sharp, Z.D.; Orihuela, C.J.; Adnot, S.; White, E.S.; Richardson, A.; et al. Senescent Cells Contribute to the Physiological Remodeling of Aged Lungs. *The journals of gerontology. Series A, Biological sciences and medical sciences* **2016**, *71*, 153-160, doi:10.1093/gerona/glu241.
164. Xu, Y.; Mizuno, T.; Sridharan, A.; Du, Y.; Guo, M.; Tang, J.; Wikenheiser-Brokamp, K.A.; Perl, A.T.; Funari, V.A.; Gokey, J.J.; et al. Single-cell RNA sequencing identifies diverse roles of epithelial cells in idiopathic pulmonary fibrosis. *JCI Insight* **2016**, *1*, e90558.
165. Lehmann, M.; Hu, Q.; Hu, Y.; Hafner, K.; Costa, R.; van den Berg, A.; Königshoff, M. Chronic WNT/β-catenin signaling induces cellular senescence in lung epithelial cells. *Cell Signal* **2020**, *70*, 109588, doi:10.1016/j.cellsig.2020.109588.

166. Plataki, M.; Koutsopoulos, A.V.; Darivianaki, K.; Delides, G.; Siafakas, N.M.; Bouros, D. Expression of apoptotic and antiapoptotic markers in epithelial cells in idiopathic pulmonary fibrosis. *Chest* **2005**, *127*, 266-274, doi:10.1378/chest.127.1.266.
167. Anathy, V.; Roberson, E.; Cunniff, B.; Nolin, J.D.; Hoffman, S.; Spiess, P.; Guala, A.S.; Lahue, K.G.; Goldman, D.; Flemer, S.; et al. Oxidative processing of latent Fas in the endoplasmic reticulum controls the strength of apoptosis. *Mol Cell Biol* **2012**, *32*, 3464-3478, doi:10.1128/mcb.00125-12.
168. McMillan, D.H.; van der Velden, J.L.; Lahue, K.G.; Qian, X.; Schneider, R.W.; Iberg, M.S.; Nolin, J.D.; Abdalla, S.; Casey, D.T.; Tew, K.D.; et al. Attenuation of lung fibrosis in mice with a clinically relevant inhibitor of glutathione-S-transferase π. *JCI Insight* **2016**, *1*, doi:10.1172/jci.insight.85717.
169. Kuwano, K.; Hagimoto, N.; Kawasaki, M.; Yatomi, T.; Nakamura, N.; Nagata, S.; Suda, T.; Kunitake, R.; Maeyama, T.; Miyazaki, H.; et al. Essential roles of the Fas-Fas ligand pathway in the development of pulmonary fibrosis. *J Clin Invest* **1999**, *104*, 13-19, doi:10.1172/jci5628.
170. Zhang, M.; Guo, Y.; Fu, H.; Hu, S.; Pan, J.; Wang, Y.; Cheng, J.; Song, J.; Yu, Q.; Zhang, S. Chop deficiency prevents UUO-induced renal fibrosis by attenuating fibrotic signals originated from Hmgb1/TLR4/NFκB/IL-1β signaling. *Cell death & disease* **2015**, *6*, e1847-e1847.
171. Zhang, W.; Lavine, K.J.; Epelman, S.; Evans, S.A.; Weinheimer, C.J.; Barger, P.M.; Mann, D.L. Necrotic myocardial cells release damage-associated molecular patterns that provoke fibroblast activation in vitro and trigger myocardial inflammation and fibrosis in vivo. *Journal of the American Heart Association* **2015**, *4*, e001993.
172. Shimizu, H.; Sakamoto, S.; Isshiki, T.; Furuya, K.; Kurosaki, A.; Homma, S. Association of serum high-mobility group box protein 1 level with outcomes of acute exacerbation of idiopathic pulmonary fibrosis and fibrosing nonspecific interstitial pneumonia. *PLoS One* **2018**, *13*, e0196558.
173. Yamaguchi, K.; Iwamoto, H.; Sakamoto, S.; Horimasu, Y.; Masuda, T.; Miyamoto, S.; Nakashima, T.; Ohshimo, S.; Fujitaka, K.; Hamada, H. Serum high-mobility group box 1 is associated with the onset and severity of acute exacerbation of idiopathic pulmonary fibrosis. *Respirology* **2020**, *25*, 275-280.
174. Ebina, M.; Taniguchi, H.; Miyasho, T.; Yamada, S.; Shibata, N.; Ohta, H.; Hisata, S.; Ohkouchi, S.; Tamada, T.; Nishimura, H. Gradual increase of high mobility group protein b1 in the lungs after the onset of acute exacerbation of idiopathic pulmonary fibrosis. *Pulmonary medicine* **2011**, *2011*.
175. Müller, T.; Fay, S.; Vieira, R.P.; Karmouty-Quintana, H.; Cicko, S.; Ayata, K.; Zissel, G.; Goldmann, T.; Lungarella, G.; Ferrari, D. The purinergic receptor subtype P2Y2 mediates chemotaxis of neutrophils and fibroblasts in fibrotic lung disease. *Oncotarget* **2017**, *8*, 35962.
176. Akiyama, N.; Hozumi, H.; Isayama, T.; Okada, J.; Sugiura, K.; Yasui, H.; Suzuki, Y.; Kono, M.; Karayama, M.; Furuhashi, K. Clinical significance of serum S100 calcium-binding protein A4 in idiopathic pulmonary fibrosis. *Respirology* **2020**, *25*, 743-749.
177. Hamada, N.; Maeyama, T.; Kawaguchi, T.; Yoshimi, M.; Fukumoto, J.; Yamada, M.; Yamada, S.; Kuwano, K.; Nakanishi, Y. The role of high mobility group box1 in pulmonary fibrosis. *American journal of respiratory cell and molecular biology* **2008**, *39*, 440-447.
178. Janssen, L.J.; Farkas, L.; Rahman, T.; Kolb, M.R. ATP stimulates Ca2+-waves and gene expression in cultured human pulmonary fibroblasts. *The international journal of biochemistry & cell biology* **2009**, *41*, 2477-2484.
179. Hodono, S.; Shimokawa, A.; Stewart, N.J.; Yamauchi, Y.; Nishimori, R.; Yamane, M.; Imai, H.; Fujiwara, H.; Kimura, A. Ethyl pyruvate improves pulmonary function in mice with bleomycin-induced lung injury as monitored with hyperpolarized 129Xe MR imaging. *Magnetic Resonance in Medical Sciences* **2018**, *17*, 331.

180. Pittet, J.-F.; Koh, H.; Fang, X.; Iles, K.; Christiaans, S.; Anjun, N.; Wagener, B.M.; Park, D.W.; Zmijewski, J.W.; Matthay, M.A. HMGB1 accelerates alveolar epithelial repair via an IL-1β-and αvβ6 integrin-dependent activation of TGF-β1. *PloS one* **2013**, *8*, e63907.
181. Li, L.-C.; Li, D.-L.; Xu, L.; Mo, X.-T.; Cui, W.-H.; Zhao, P.; Zhou, W.-C.; Gao, J.; Li, J. High-mobility group box 1 mediates epithelial-to-mesenchymal transition in pulmonary fibrosis involving transforming growth factor-β1/Smad2/3 signaling. *Journal of Pharmacology and Experimental Therapeutics* **2015**, *354*, 302-309.
182. Wang, P.; Luo, R.; Zhang, M.; Wang, Y.; Song, T.; Tao, T.; Li, Z.; Jin, L.; Zheng, H.; Chen, W. A cross-talk between epithelium and endothelium mediates human alveolar–capillary injury during SARS-CoV-2 infection. *Cell death & disease* **2020**, *11*, 1042.
183. Koh, T.J.; DiPietro, L.A. Inflammation and wound healing: the role of the macrophage. *Expert reviews in molecular medicine* **2011**, *13*, e23, doi:10.1017/s1462399411001943.
184. Ardain, A.; Marakalala, M.J.; Leslie, A. Tissue-resident innate immunity in the lung. *Immunology* **2020**, *159*, 245-256, doi:10.1111/imm.13143.
185. Hartl, D.; Tirouvanziam, R.; Laval, J.; Greene, C.M.; Habiel, D.; Sharma, L.; Yildirim, A.; Dela Cruz, C.S.; Hogaboam, C.M. Innate Immunity of the Lung: From Basic Mechanisms to Translational Medicine. *Journal of innate immunity* **2018**, *10*, 487-501, doi:10.1159/000487057.
186. Croasdell Lucchini, A.; Gachanja, N.N.; Rossi, A.G.; Dorward, D.A.; Lucas, C.D. Epithelial Cells and Inflammation in Pulmonary Wound Repair. *Cells* **2021**, *10*, doi:10.3390/cells10020339.
187. Yan, S.; Li, M.; Liu, B.; Ma, Z.; Yang, Q. Neutrophil extracellular traps and pulmonary fibrosis: an update. *Journal of Inflammation* **2023**, *20*, 2, doi:10.1186/s12950-023-00329-y.
188. Mitsuhashi, H.; Asano, S.; Nonaka, T.; Hamamura, I.; Masuda, K.; Kiyoki, M. Administration of truncated secretory leukoprotease inhibitor ameliorates bleomycin-induced pulmonary fibrosis in hamsters. *Am J Respir Crit Care Med* **1996**, *153*, 369-374, doi:10.1164/ajrccm.153.1.8542145.
189. Tasaka, S.; Mizoguchi, K.; Funatsu, Y.; Namkoong, H.; Yamasawa, W.; Ishii, M.; Hasegawa, N.; Betsuyaku, T. Cytokine profile of bronchoalveolar lavage fluid in patients with combined pulmonary fibrosis and emphysema. *Respirology* **2012**, *17*, 814-820, doi:10.1111/j.1440-1843.2012.02182.x.
190. Tabuena, R.P.; Nagai, S.; Tsutsumi, T.; Handa, T.; Minoru, T.; Mikuniya, T.; Shigematsu, M.; Hamada, K.; Izumi, T.; Mishima, M. Cell profiles of bronchoalveolar lavage fluid as prognosticators of idiopathic pulmonary fibrosis/usual interstitial pneumonia among Japanese patients. *Respiration* **2005**, *72*, 490-498.
191. Achaiah, A.; Rathnapala, A.; Pereira, A.; Bothwell, H.; Dwivedi, K.; Barker, R.; Iotchkova, V.; Benamore, R.; Hoyles, R.K.; Ho, L.P. Neutrophil lymphocyte ratio as an indicator for disease progression in Idiopathic Pulmonary Fibrosis. *BMJ Open Respir Res* **2022**, *9*, doi:10.1136/bmjresp-2022-001202.
192. Kinder, B.W.; Brown, K.K.; Schwarz, M.I.; Ix, J.H.; Kervitsky, A.; King, T.E., Jr. Baseline BAL neutrophilia predicts early mortality in idiopathic pulmonary fibrosis. *Chest* **2008**, *133*, 226-232, doi:10.1378/chest.07-1948.
193. Wynn, T.A.; Vannella, K.M. Macrophages in Tissue Repair, Regeneration, and Fibrosis. *Immunity* **2016**, *44*, 450-462, doi:10.1016/j.immuni.2016.02.015.
194. Lech, M.; Anders, H.J. Macrophages and fibrosis: How resident and infiltrating mononuclear phagocytes orchestrate all phases of tissue injury and repair. *Biochim Biophys Acta* **2013**, *1832*, 989-997, doi:10.1016/j.bbadis.2012.12.001.
195. Murray, P.J.; Wynn, T.A. Protective and pathogenic functions of macrophage subsets. *Nat Rev Immunol* **2011**, *11*, 723-737, doi:10.1038/nri3073.
196. Sica, A.; Mantovani, A. Macrophage plasticity and polarization: in vivo veritas. *J Clin Invest* **2012**, *122*, 787-795, doi:10.1172/jci59643.
197. Lv, J.; Gao, H.; Ma, J.; Liu, J.; Tian, Y.; Yang, C.; Li, M.; Zhao, Y.; Li, Z.; Zhang, X.; et al. Dynamic atlas of immune cells reveals multiple functional features of macrophages associated with

progression of pulmonary fibrosis. *Front Immunol* **2023**, *14*, 1230266, doi:10.3389/fimmu.2023.1230266.
198. Misharin, A.V.; Morales-Nebreda, L.; Reyfman, P.A.; Cuda, C.M.; Walter, J.M.; McQuattie-Pimentel, A.C.; Chen, C.-I.; Anekalla, K.R.; Joshi, N.; Williams, K.J. Monocyte-derived alveolar macrophages drive lung fibrosis and persist in the lung over the life span. *Journal of Experimental Medicine* **2017**, *214*, 2387-2404.
199. McCubbrey, A.L.; Barthel, L.; Mohning, M.P.; Redente, E.F.; Mould, K.J.; Thomas, S.M.; Leach, S.M.; Danhorn, T.; Gibbings, S.L.; Jakubzick, C.V. Deletion of c-FLIP from CD11bhi macrophages prevents development of bleomycin-induced lung fibrosis. *American journal of respiratory cell and molecular biology* **2018**, *58*, 66-78.
200. Joshi, N.; Watanabe, S.; Verma, R.; Jablonski, R.P.; Chen, C.-I.; Cheresh, P.; Markov, N.S.; Reyfman, P.A.; McQuattie-Pimentel, A.C.; Sichizya, L. A spatially restricted fibrotic niche in pulmonary fibrosis is sustained by M-CSF/M-CSFR signalling in monocyte-derived alveolar macrophages. *European Respiratory Journal* **2020**, *55*.
201. Kreuter, M.; Lee, J.S.; Tzouvelekis, A.; Oldham, J.M.; Molyneaux, P.L.; Weycker, D.; Atwood, M.; Kirchgaessler, K.-U.; Maher, T.M. Monocyte count as a prognostic biomarker in patients with idiopathic pulmonary fibrosis. *American journal of respiratory and critical care medicine* **2021**, *204*, 74-81.
202. Isshiki, T.; Vierhout, M.; Naiel, S.; Ali, P.; Yazdanshenas, P.; Kumaran, V.; Yang, Z.; Dvorkin-Gheva, A.; Rullo, A.F.; Kolb, M.R.J.; et al. Therapeutic strategies targeting pro-fibrotic macrophages in interstitial lung disease. *Biochemical Pharmacology* **2023**, *211*, 115501, doi:https://doi.org/10.1016/j.bcp.2023.115501.
203. Cai, M.; Bonella, F.; He, X.; Sixt, S.U.; Sarria, R.; Guzman, J.; Costabel, U. CCL18 in serum, BAL fluid and alveolar macrophage culture supernatant in interstitial lung diseases. *Respiratory medicine* **2013**, *107*, 1444-1452.
204. Prasse, A.; Probst, C.; Bargagli, E.; Zissel, G.; Toews, G.B.; Flaherty, K.R.; Olschewski, M.; Rottoli, P.; Müller-Quernheim, J. Serum CC-chemokine ligand 18 concentration predicts outcome in idiopathic pulmonary fibrosis. *American journal of respiratory and critical care medicine* **2009**, *179*, 717-723.
205. Adams, T.S.; Schupp, J.C.; Poli, S.; Ayaub, E.A.; Neumark, N.; Ahangari, F.; Chu, S.G.; Raby, B.A.; DeIuliis, G.; Januszyk, M.; et al. Single-cell RNA-seq reveals ectopic and aberrant lung-resident cell populations in idiopathic pulmonary fibrosis. *Sci Adv* **2020**, *6*, eaba1983, doi:10.1126/sciadv.aba1983.
206. Reyfman, P.A.; Walter, J.M.; Joshi, N.; Anekalla, K.R.; McQuattie-Pimentel, A.C.; Chiu, S.; Fernandez, R.; Akbarpour, M.; Chen, C.I.; Ren, Z.; et al. Single-Cell Transcriptomic Analysis of Human Lung Provides Insights into the Pathobiology of Pulmonary Fibrosis. *Am J Respir Crit Care Med* **2019**, *199*, 1517-1536, doi:10.1164/rccm.201712-2410OC.
207. Morse, C.; Tabib, T.; Sembrat, J.; Buschur, K.L.; Bittar, H.T.; Valenzi, E.; Jiang, Y.; Kass, D.J.; Gibson, K.; Chen, W. Proliferating SPP1/MERTK-expressing macrophages in idiopathic pulmonary fibrosis. *European Respiratory Journal* **2019**, *54*.
208. Wang, J.; Jiang, M.; Xiong, A.; Zhang, L.; Luo, L.; Liu, Y.; Liu, S.; Ran, Q.; Wu, D.; Xiong, Y.; et al. Integrated analysis of single-cell and bulk RNA sequencing reveals pro-fibrotic PLA2G7high macrophages in pulmonary fibrosis. *Pharmacological Research* **2022**, *182*, 106286, doi:https://doi.org/10.1016/j.phrs.2022.106286.
209. Kendall, R.T.; Feghali-Bostwick, C.A. Fibroblasts in fibrosis: novel roles and mediators. *Frontiers in pharmacology* **2014**, *5*, 123, doi:10.3389/fphar.2014.00123.
210. Abdelaziz, M.M.; Devalia, J.L.; Khair, O.A.; Calderon, M.; Sapsford, R.J.; Davies, R.J. The effect of conditioned medium from cultured human bronchial epithelial cells on eosinophil and neutrophil chemotaxis and adherence in vitro. *Am J Respir Cell Mol Biol* **1995**, *13*, 728-737, doi:10.1165/ajrcmb.13.6.7576711.

211. Li, B.; Wang, J.H.-C. Fibroblasts and myofibroblasts in wound healing: force generation and measurement. *Journal of tissue viability* **2011**, *20*, 108-120.
212. Hung, C.F. Origin of Myofibroblasts in Lung Fibrosis. *Current Tissue Microenvironment Reports* **2020**, *1*, 155-162, doi:10.1007/s43152-020-00022-9.
213. Biernacka, A.; Dobaczewski, M.; Frangogiannis, N.G. TGF-β signaling in fibrosis. *Growth Factors* **2011**, *29*, 196-202, doi:10.3109/08977194.2011.595714.
214. Scotton, C.J.; Chambers, R.C. Molecular Targets in Pulmonary Fibrosis: The Myofibroblast in Focus. *Chest* **2007**, *132*, 1311-1321, doi:https://doi.org/10.1378/chest.06-2568.
215. Phillips, R.J.; Burdick, M.D.; Hong, K.; Lutz, M.A.; Murray, L.A.; Xue, Y.Y.; Belperio, J.A.; Keane, M.P.; Strieter, R.M. Circulating fibrocytes traffic to the lungs in response to CXCL12 and mediate fibrosis. *J Clin Invest* **2004**, *114*, 438-446, doi:10.1172/jci20997.
216. Rowley, J.E.; Johnson, J.R. Pericytes in Chronic Lung Disease. *International Archives of Allergy and Immunology* **2014**, *164*, 178-188, doi:10.1159/000365051.
217. Kramann, R.; Humphreys, B.D. Kidney pericytes: roles in regeneration and fibrosis. *Seminars in nephrology* **2014**, *34*, 374-383, doi:10.1016/j.semnephrol.2014.06.004.
218. Chang, F.-C.; Chou, Y.-H.; Chen, Y.-T.; Lin, S.-L. Novel insights into pericyte–myofibroblast transition and therapeutic targets in renal fibrosis. *Journal of the Formosan Medical Association* **2012**, *111*, 589-598, doi:https://doi.org/10.1016/j.jfma.2012.09.008.
219. Greenhalgh, S.N.; Iredale, J.P.; Henderson, N.C. Origins of fibrosis: pericytes take centre stage. *F1000Prime Rep* **2013**, *5*, 37, doi:10.12703/p5-37.
220. Mori, L.; Bellini, A.; Stacey, M.A.; Schmidt, M.; Mattoli, S. Fibrocytes contribute to the myofibroblast population in wounded skin and originate from the bone marrow. *Experimental cell research* **2005**, *304*, 81-90, doi:10.1016/j.yexcr.2004.11.011.
221. Brenner, D.A.; Kisseleva, T.; Scholten, D.; Paik, Y.H.; Iwaisako, K.; Inokuchi, S.; Schnabl, B.; Seki, E.; De Minicis, S.; Oesterreicher, C.; et al. Origin of myofibroblasts in liver fibrosis. *Fibrogenesis & Tissue Repair* **2012**, *5*, S17, doi:10.1186/1755-1536-5-S1-S17.
222. Bellini, A.; Mattoli, S. The role of the fibrocyte, a bone marrow-derived mesenchymal progenitor, in reactive and reparative fibroses. *Lab Invest* **2007**, *87*, 858-870, doi:10.1038/labinvest.3700654.
223. Bianchetti, L.; Barczyk, M.; Cardoso, J.; Schmidt, M.; Bellini, A.; Mattoli, S. Extracellular matrix remodelling properties of human fibrocytes. *J Cell Mol Med* **2012**, *16*, 483-495, doi:10.1111/j.1582-4934.2011.01344.x.
224. Rowley, J.E.; Johnson, J.R. Pericytes in chronic lung disease. *International archives of allergy and immunology* **2014**, *164*, 178-188, doi:10.1159/000365051.
225. Jolly, M.K.; Ward, C.; Eapen, M.S.; Myers, S.; Hallgren, O.; Levine, H.; Sohal, S.S. Epithelial-mesenchymal transition, a spectrum of states: Role in lung development, homeostasis, and disease. *Dev Dyn* **2018**, *247*, 346-358, doi:10.1002/dvdy.24541.
226. Milara, J.; Peiró, T.; Serrano, A.; Cortijo, J. Epithelial to mesenchymal transition is increased in patients with COPD and induced by cigarette smoke. *Thorax* **2013**, *68*, 410-420, doi:10.1136/thoraxjnl-2012-201761.
227. Renaud-Picard, B.; Vallière, K.; Toussaint, J.; Kreutter, G.; El-Habhab, A.; Kassem, M.; El-Ghazouani, F.; Olland, A.; Hirschi, S.; Porzio, M.; et al. Epithelial-mesenchymal transition and membrane microparticles: Potential implications for bronchiolitis obliterans syndrome after lung transplantation. *Transplant Immunology* **2020**, *59*, 101273, doi:https://doi.org/10.1016/j.trim.2020.101273.
228. Salton, F.; Volpe, M.C.; Confalonieri, M. Epithelial¯Mesenchymal Transition in the Pathogenesis of Idiopathic Pulmonary Fibrosis. *Medicina (Kaunas)* **2019**, *55*, doi:10.3390/medicina55040083.
229. Piera-Velazquez, S.; Li, Z.; Jimenez, S.A. Role of endothelial-mesenchymal transition (EndoMT) in the pathogenesis of fibrotic disorders. *Am J Pathol* **2011**, *179*, 1074-1080, doi:10.1016/j.ajpath.2011.06.001.

230. Nataraj, D.; Ernst, A.; Kalluri, R. Idiopathic Pulmonary Fibrosis Is Associated With Endothelial To Mesenchymal Transition. *American Journal of Respiratory Cell and Molecular Biology* **2010**, *43*, 129-130, doi:10.1165/rcmb.2010-0044ED.
231. Lovisa, S.; Fletcher-Sananikone, E.; Sugimoto, H.; Hensel, J.; Lahiri, S.; Hertig, A.; Taduri, G.; Lawson, E.; Dewar, R.; Revuelta, I.; et al. Endothelial-to-mesenchymal transition compromises vascular integrity to induce Myc-mediated metabolic reprogramming in kidney fibrosis. *Science Signaling* **2020**, *13*, eaaz2597, doi:10.1126/scisignal.aaz2597.
232. Darby, I.A.; Laverdet, B.; Bonté, F.; Desmoulière, A. Fibroblasts and myofibroblasts in wound healing. *Clinical, cosmetic and investigational dermatology* **2014**, *7*, 301-311, doi:10.2147/ccid.s50046.
233. Wallach-Dayan, S.B.; Golan-Gerstl, R.; Breuer, R. Evasion of myofibroblasts from immune surveillance: a mechanism for tissue fibrosis. *Proc Natl Acad Sci U S A* **2007**, *104*, 20460-20465, doi:10.1073/pnas.0705582104.
234. Hanson, K.M.; Hernady, E.B.; Reed, C.K.; Johnston, C.J.; Groves, A.M.; Finkelstein, J.N. Apoptosis Resistance in Fibroblasts Precedes Progressive Scarring in Pulmonary Fibrosis and Is Partially Mediated by Toll-Like Receptor 4 Activation. *Toxicological Sciences* **2019**, *170*, 489-498, doi:10.1093/toxsci/kfz103.
235. Waters, D.W.; Blokland, K.E.C.; Pathinayake, P.S.; Burgess, J.K.; Mutsaers, S.E.; Prele, C.M.; Schuliga, M.; Grainge, C.L.; Knight, D.A. Fibroblast senescence in the pathology of idiopathic pulmonary fibrosis. *American Journal of Physiology-Lung Cellular and Molecular Physiology* **2018**, *315*, L162-L172, doi:10.1152/ajplung.00037.2018.
236. Alvarez, D.; Cardenes, N.; Sellares, J.; Bueno, M.; Corey, C.; Hanumanthu, V.S.; Peng, Y.; D'Cunha, H.; Sembrat, J.; Nouraie, M.; et al. IPF lung fibroblasts have a senescent phenotype. *American journal of physiology. Lung cellular and molecular physiology* **2017**, *313*, L1164-l1173, doi:10.1152/ajplung.00220.2017.
237. Blokland, K.; Waters, D.; Schuliga, M.; Pouwels, S.; Grainge, C.; Mutsaers, S.; Prêle, C.; Westall, G.; Jaffar, J.; Knight, D.; et al. Alveolar epithelial wound repair is delayed by scenescent lung fibroblasts in IPF. *European Respiratory Journal* **2019**, *54*, PA596, doi:10.1183/13993003.congress-2019.PA596.
238. Orjalo, A.V.; Bhaumik, D.; Gengler, B.K.; Scott, G.K.; Campisi, J. Cell surface-bound IL-1α is an upstream regulator of the senescence-associated IL-6/IL-8 cytokine network. *Proceedings of the National Academy of Sciences* **2009**, *106*, 17031-17036, doi:10.1073/pnas.0905299106.
239. Wu, B.; Tang, L.; Kapoor, M. Fibroblasts and their responses to chronic injury in pulmonary fibrosis. *Semin Arthritis Rheum* **2021**, *51*, 310-317, doi:10.1016/j.semarthrit.2020.12.003.
240. Flavell, S.J.; Hou, T.Z.; Lax, S.; Filer, A.D.; Salmon, M.; Buckley, C.D. Fibroblasts as novel therapeutic targets in chronic inflammation. *British Journal of Pharmacology* **2008**, *153*, S241-S246, doi:https://doi.org/10.1038/sj.bjp.0707487.
241. Tsukui, T.; Sun, K.-H.; Wetter, J.B.; Wilson-Kanamori, J.R.; Hazelwood, L.A.; Henderson, N.C.; Adams, T.S.; Schupp, J.C.; Poli, S.D.; Rosas, I.O.; et al. Collagen-producing lung cell atlas identifies multiple subsets with distinct localization and relevance to fibrosis. *Nature Communications* **2020**, *11*, 1920, doi:10.1038/s41467-020-15647-5.
242. Kapnadak, S.G.; Raghu, G. Lung transplantation for interstitial lung disease. *Eur Respir Rev* **2021**, *30*, doi:10.1183/16000617.0017-2021.
243. Cameli, P.; Refini, R.M.; Bergantini, L.; d'Alessandro, M.; Alonzi, V.; Magnoni, C.; Rottoli, P.; Sestini, P.; Bargagli, E. Long-Term Follow-Up of Patients With Idiopathic Pulmonary Fibrosis Treated With Pirfenidone or Nintedanib: A Real-Life Comparison Study. *Front Mol Biosci* **2020**, *7*, 581828, doi:10.3389/fmolb.2020.581828.
244. Barkauskas, C.E.; Noble, P.W. Cellular mechanisms of tissue fibrosis. 7. New insights into the cellular mechanisms of pulmonary fibrosis. *Am J Physiol Cell Physiol* **2014**, *306*, C987-996, doi:10.1152/ajpcell.00321.2013.

245. Noble, P.W.; Albera, C.; Bradford, W.Z.; Costabel, U.; du Bois, R.M.; Fagan, E.A.; Fishman, R.S.; Glaspole, I.; Glassberg, M.K.; Lancaster, L.; et al. Pirfenidone for idiopathic pulmonary fibrosis: analysis of pooled data from three multinational phase 3 trials. *Eur Respir J* **2016**, *47*, 243-253, doi:10.1183/13993003.00026-2015.
246. Noble, P.W.; Albera, C.; Bradford, W.Z.; Costabel, U.; Glassberg, M.K.; Kardatzke, D.; King, T.E., Jr.; Lancaster, L.; Sahn, S.A.; Szwarcberg, J.; et al. Pirfenidone in patients with idiopathic pulmonary fibrosis (CAPACITY): two randomised trials. *Lancet* **2011**, *377*, 1760-1769, doi:10.1016/s0140-6736(11)60405-4.
247. King, T.E., Jr.; Bradford, W.Z.; Castro-Bernardini, S.; Fagan, E.A.; Glaspole, I.; Glassberg, M.K.; Gorina, E.; Hopkins, P.M.; Kardatzke, D.; Lancaster, L.; et al. A phase 3 trial of pirfenidone in patients with idiopathic pulmonary fibrosis. *N Engl J Med* **2014**, *370*, 2083-2092, doi:10.1056/NEJMoa1402582.
248. Cho, M.E.; Kopp, J.B. Pirfenidone: an anti-fibrotic therapy for progressive kidney disease. *Expert Opin Investig Drugs* **2010**, *19*, 275-283, doi:10.1517/13543780903501539.
249. Glassberg, M.K. Overview of idiopathic pulmonary fibrosis, evidence-based guidelines, and recent developments in the treatment landscape. *Am J Manag Care* **2019**, *25*, S195-s203.
250. Saito, S.; Alkhatib, A.; Kolls, J.K.; Kondoh, Y.; Lasky, J.A. Pharmacotherapy and adjunctive treatment for idiopathic pulmonary fibrosis (IPF). *J Thorac Dis* **2019**, *11*, S1740-s1754, doi:10.21037/jtd.2019.04.62.
251. Collins, B.F.; Raghu, G. Antifibrotic therapy for fibrotic lung disease beyond idiopathic pulmonary fibrosis. *Eur Respir Rev* **2019**, *28*, doi:10.1183/16000617.0022-2019.
252. Richeldi, L.; du Bois, R.M.; Raghu, G.; Azuma, A.; Brown, K.K.; Costabel, U.; Cottin, V.; Flaherty, K.R.; Hansell, D.M.; Inoue, Y.; et al. Efficacy and safety of nintedanib in idiopathic pulmonary fibrosis. *N Engl J Med* **2014**, *370*, 2071-2082, doi:10.1056/NEJMoa1402584.
253. Richeldi, L.; Kreuter, M.; Selman, M.; Crestani, B.; Kirsten, A.M.; Wuyts, W.A.; Xu, Z.; Bernois, K.; Stowasser, S.; Quaresma, M.; et al. Long-term treatment of patients with idiopathic pulmonary fibrosis with nintedanib: results from the TOMORROW trial and its open-label extension. *Thorax* **2018**, *73*, 581-583, doi:10.1136/thoraxjnl-2016-209701.
254. Lamb, Y.N. Nintedanib: A Review in Fibrotic Interstitial Lung Diseases. *Drugs* **2021**, *81*, 575-586, doi:10.1007/s40265-021-01487-0.
255. Wollin, L.; Wex, E.; Pautsch, A.; Schnapp, G.; Hostettler, K.E.; Stowasser, S.; Kolb, M. Mode of action of nintedanib in the treatment of idiopathic pulmonary fibrosis. *Eur Respir J* **2015**, *45*, 1434-1445, doi:10.1183/09031936.00174914.
256. Knüppel, L.; Ishikawa, Y.; Aichler, M.; Heinzelmann, K.; Hatz, R.; Behr, J.; Walch, A.; Bächinger, H.P.; Eickelberg, O.; Staab-Weijnitz, C.A. A Novel Antifibrotic Mechanism of Nintedanib and Pirfenidone. Inhibition of Collagen Fibril Assembly. *Am J Respir Cell Mol Biol* **2017**, *57*, 77-90, doi:10.1165/rcmb.2016-0217OC.
257. Bargagli, E.; Piccioli, C.; Rosi, E.; Torricelli, E.; Turi, L.; Piccioli, E.; Pistolesi, M.; Ferrari, K.; Voltolini, L. Pirfenidone and Nintedanib in idiopathic pulmonary fibrosis: Real-life experience in an Italian referral centre. *Pulmonology* **2019**, *25*, 149-153, doi:10.1016/j.pulmoe.2018.06.003.
258. Rochwerg, B.; Neupane, B.; Zhang, Y.; Garcia, C.C.; Raghu, G.; Richeldi, L.; Brozek, J.; Beyene, J.; Schünemann, H. Treatment of idiopathic pulmonary fibrosis: a network meta-analysis. *BMC Med* **2016**, *14*, 18, doi:10.1186/s12916-016-0558-x.
259. Wright, W.A.; Crowley, L.E.; Parekh, D.; Crawshaw, A.; Dosanjh, D.P.; Nightingale, P.; Thickett, D.R. Real-world retrospective observational study exploring the effectiveness and safety of antifibrotics in idiopathic pulmonary fibrosis. *BMJ Open Respir Res* **2021**, *8*, doi:10.1136/bmjresp-2020-000782.
260. Justet, A.; Klay, D.; Porcher, R.; Cottin, V.; Ahmad, K.; Molina Molina, M.; Nunes, H.; Reynaud-Gaubert, M.; Naccache, J.M.; Manali, E.; et al. Safety and efficacy of pirfenidone and nintedanib

in patients with idiopathic pulmonary fibrosis and carrying a telomere-related gene mutation. *Eur Respir J* **2021**, *57*, doi:10.1183/13993003.03198-2020.
261. Ogura, T.; Taniguchi, H.; Azuma, A.; Inoue, Y.; Kondoh, Y.; Hasegawa, Y.; Bando, M.; Abe, S.; Mochizuki, Y.; Chida, K.; et al. Safety and pharmacokinetics of nintedanib and pirfenidone in idiopathic pulmonary fibrosis. *Eur Respir J* **2015**, *45*, 1382-1392, doi:10.1183/09031936.00198013.
262. Feng, H.; Zhao, Y.; Li, Z.; Kang, J. Real-life experiences in a single center: efficacy of pirfenidone in idiopathic pulmonary fibrosis and fibrotic idiopathic non-specific interstitial pneumonia patients. *Ther Adv Respir Dis* **2020**, *14*, 1753466620963015, doi:10.1177/1753466620963015.
263. Verma, N.; Kumar, P.; Mitra, S.; Taneja, S.; Dhooria, S.; Das, A.; Duseja, A.; Dhiman, R.K.; Chawla, Y. Drug idiosyncrasy due to pirfenidone presenting as acute liver failure: Case report and mini-review of the literature. *Hepatol Commun* **2018**, *2*, 142-147, doi:10.1002/hep4.1133.
264. Librero Jiménez, M.; Heredia Carrasco, C.; Fernández Cano, M.D.C. Severe hepatotoxicity secondary to nintedanib. *Rev Esp Enferm Dig* **2022**, *114*, 244-245, doi:10.17235/reed.2020.7585/2020.
265. Hughes, G.; Toellner, H.; Morris, H.; Leonard, C.; Chaudhuri, N. Real World Experiences: Pirfenidone and Nintedanib are Effective and Well Tolerated Treatments for Idiopathic Pulmonary Fibrosis. *J Clin Med* **2016**, *5*, doi:10.3390/jcm5090078.
266. Maher, T.M.; Molina-Molina, M.; Russell, A.M.; Bonella, F.; Jouneau, S.; Ripamonti, E.; Axmann, J.; Vancheri, C. Unmet needs in the treatment of idiopathic pulmonary fibrosis-insights from patient chart review in five European countries. *BMC Pulm Med* **2017**, *17*, 124.
267. Booth, A.J.; Hadley, R.; Cornett, A.M.; Dreffs, A.A.; Matthes, S.A.; Tsui, J.L.; Weiss, K.; Horowitz, J.C.; Fiore, V.F.; Barker, T.H.; et al. Acellular normal and fibrotic human lung matrices as a culture system for in vitro investigation. *Am J Respir Crit Care Med* **2012**, *186*, 866-876, doi:10.1164/rccm.201204-0754OC.
268. Hay, M.; Thomas, D.W.; Craighead, J.L.; Economides, C.; Rosenthal, J. Clinical development success rates for investigational drugs. *Nat Biotechnol* **2014**, *32*, 40-51, doi:10.1038/nbt.2786.
269. Oakley, F.; Gee, L.M.; Sheerin, N.S.; Borthwick, L.A. Implementation of pre-clinical methodologies to study fibrosis and test anti-fibrotic therapy. *Current opinion in pharmacology* **2019**, *49*, 95-101.
270. Seyhan, A.A. Lost in translation: the valley of death across preclinical and clinical divide – identification of problems and overcoming obstacles. *Translational Medicine Communications* **2019**, *4*, 18, doi:10.1186/s41231-019-0050-7.
271. Jaroch, K.; Jaroch, A.; Bojko, B. Cell cultures in drug discovery and development: The need of reliable in vitro-in vivo extrapolation for pharmacodynamics and pharmacokinetics assessment. *J Pharm Biomed Anal* **2018**, *147*, 297-312, doi:10.1016/j.jpba.2017.07.023.
272. Costa, E.C.; Moreira, A.F.; de Melo-Diogo, D.; Gaspar, V.M.; Carvalho, M.P.; Correia, I.J. 3D tumor spheroids: an overview on the tools and techniques used for their analysis. *Biotechnology Advances* **2016**, *34*, 1427-1441, doi:https://doi.org/10.1016/j.biotechadv.2016.11.002.
273. Kapałczyńska, M.; Kolenda, T.; Przybyła, W.; Zajączkowska, M.; Teresiak, A.; Filas, V.; Ibbs, M.; Bliźniak, R.; Łuczewski, Ł.; Lamperska, K. 2D and 3D cell cultures - a comparison of different types of cancer cell cultures. *Arch Med Sci* **2018**, *14*, 910-919, doi:10.5114/aoms.2016.63743.
274. Marinković, A.; Liu, F.; Tschumperlin, D.J. Matrices of physiologic stiffness potently inactivate idiopathic pulmonary fibrosis fibroblasts. *Am J Respir Cell Mol Biol* **2013**, *48*, 422-430, doi:10.1165/rcmb.2012-0335OC.
275. Liu, F.; Mih, J.D.; Shea, B.S.; Kho, A.T.; Sharif, A.S.; Tager, A.M.; Tschumperlin, D.J. Feedback amplification of fibrosis through matrix stiffening and COX-2 suppression. *Journal of Cell Biology* **2010**, *190*, 693-706, doi:10.1083/jcb.201004082.

276. Gould, S.T.; Anseth, K.S. Role of cell–matrix interactions on VIC phenotype and tissue deposition in 3D PEG hydrogels. *Journal of Tissue Engineering and Regenerative Medicine* **2016**, *10*, E443-E453, doi:https://doi.org/10.1002/term.1836.
277. Kim, W.; Gwon, Y.; Park, S.; Kim, H.; Kim, J. Therapeutic strategies of three-dimensional stem cell spheroids and organoids for tissue repair and regeneration. *Bioactive Materials* **2023**, *19*, 50-74, doi:https://doi.org/10.1016/j.bioactmat.2022.03.039.
278. Mannaerts, I.; Leite, S.B.; Verhulst, S.; Claerhout, S.; Eysackers, N.; Thoen, L.F.; Hoorens, A.; Reynaert, H.; Halder, G.; van Grunsven, L.A. The Hippo pathway effector YAP controls mouse hepatic stellate cell activation. *J Hepatol* **2015**, *63*, 679-688, doi:10.1016/j.jhep.2015.04.011.
279. Verjans, E.T.; Doijen, J.; Luyten, W.; Landuyt, B.; Schoofs, L. Three-dimensional cell culture models for anticancer drug screening: Worth the effort? *J Cell Physiol* **2018**, *233*, 2993-3003, doi:10.1002/jcp.26052.
280. Vazquez-Armendariz, A.I.; Barroso, M.M.; El Agha, E.; Herold, S. 3D In Vitro Models: Novel Insights into Idiopathic Pulmonary Fibrosis Pathophysiology and Drug Screening. *Cells* **2022**, *11*, 1526.
281. Scalise, M.; Marino, F.; Salerno, L.; Cianflone, E.; Molinaro, C.; Salerno, N.; De Angelis, A.; Viglietto, G.; Urbanek, K.; Torella, D. From Spheroids to Organoids: The Next Generation of Model Systems of Human Cardiac Regeneration in a Dish. *Int J Mol Sci* **2021**, *22*, doi:10.3390/ijms222413180.
282. Li, F.; He, J.; Wei, J.; Cho, W.C.; Liu, X. Diversity of Epithelial Stem Cell Types in Adult Lung. *Stem Cells International* **2015**, *2015*, 11.
283. Bao, Y.L.; Wang, L.; Pan, H.T.; Zhang, T.R.; Chen, Y.H.; Xu, S.J.; Mao, X.L.; Li, S.W. Animal and Organoid Models of Liver Fibrosis. *Front Physiol* **2021**, *12*, 666138, doi:10.3389/fphys.2021.666138.
284. B, B.M.; Lawson, W.E.; Oury, T.D.; Sisson, T.H.; Raghavendran, K.; Hogaboam, C.M. Animal models of fibrotic lung disease. *Am J Respir Cell Mol Biol* **2013**, *49*, 167-179, doi:10.1165/rcmb.2013-0094TR.
285. Sisson, T.H.; Mendez, M.; Choi, K.; Subbotina, N.; Courey, A.; Cunningham, A.; Dave, A.; Engelhardt, J.F.; Liu, X.; White, E.S.; et al. Targeted injury of type II alveolar epithelial cells induces pulmonary fibrosis. *Am J Respir Crit Care Med* **2010**, *181*, 254-263, doi:10.1164/rccm.200810-1615OC.
286. Shay, T.; Lederer, J.A.; Benoist, C. Genomic responses to inflammation in mouse models mimic humans: we concur, apples to oranges comparisons won't do. *Proc Natl Acad Sci U S A* **2015**, *112*, E346, doi:10.1073/pnas.1416629111.
287. Paish, H.L.; Reed, L.H.; Brown, H.; Bryan, M.C.; Govaere, O.; Leslie, J.; Barksby, B.S.; Garcia Macia, M.; Watson, A.; Xu, X.; et al. A Bioreactor Technology for Modeling Fibrosis in Human and Rodent Precision-Cut Liver Slices. *Hepatology* **2019**, *70*, 1377-1391, doi:10.1002/hep.30651.
288. Stribos, E.G.D.; Luangmonkong, T.; Leliveld, A.M.; de Jong, I.J.; van Son, W.J.; Hillebrands, J.-L.; Seelen, M.A.; van Goor, H.; Olinga, P.; Mutsaers, H.A.M. Precision-cut human kidney slices as a model to elucidate the process of renal fibrosis. *Translational Research* **2016**, *170*, 8-16.e11, doi:https://doi.org/10.1016/j.trsl.2015.11.007.
289. Liu, G.; Betts, C.; Cunoosamy, D.M.; Åberg, P.M.; Hornberg, J.J.; Sivars, K.B.; Cohen, T.S. Use of precision cut lung slices as a translational model for the study of lung biology. *Respiratory Research* **2019**, *20*, 162, doi:10.1186/s12931-019-1131-x.
290. Graaf, I.A.; Groothuis, G.M.; Olinga, P. Precision-cut tissue slices as a tool to predict metabolism of novel drugs. *Expert Opin Drug Metab Toxicol* **2007**, *3*, 879-898, doi:10.1517/17425255.3.6.879.
291. Stegmayr, J.; Alsafadi, H.N.; Lindstedt, S.; Wagner, D.E. Human precision-cut lung slices generated from excess donor lungs as a model for IPF and drug screening. *ERJ Open Research* **2021**, *7*, 106, doi:10.1183/23120541.Lsc-2021.106.

292. Paish, H.L.; Reed, L.H.; Brown, H.; Bryan, M.C.; Govaere, O.; Leslie, J.; Barksby, B.S.; Garcia Macia, M.; Watson, A.; Xu, X. A bioreactor technology for modeling fibrosis in human and rodent precision-cut liver slices. *Hepatology* **2019**, *70*, 1377-1391.
293. Zimmermann, M.; Lampe, J.; Lange, S.; Smirnow, I.; Königsrainer, A.; Hann-von-Weyhern, C.; Fend, F.; Gregor, M.; Bitzer, M.; Lauer, U.M. Improved reproducibility in preparing precision-cut liver tissue slices. *Cytotechnology* **2009**, *61*, 145-152, doi:10.1007/s10616-009-9246-4.
294. Mercer, P.F.; Woodcock, H.V.; Eley, J.D.; Platé, M.; Sulikowski, M.G.; Durrenberger, P.F.; Franklin, L.; Nanthakumar, C.B.; Man, Y.; Genovese, F.; et al. Exploration of a potent PI3 kinase/mTOR inhibitor as a novel anti-fibrotic agent in IPF. *Thorax* **2016**, *71*, 701-711, doi:10.1136/thoraxjnl-2015-207429.
295. Uhl, F.E.; Vierkotten, S.; Wagner, D.E.; Burgstaller, G.; Costa, R.; Koch, I.; Lindner, M.; Meiners, S.; Eickelberg, O.; Königshoff, M. Preclinical validation and imaging of Wnt-induced repair in human 3D lung tissue cultures. *Eur Respir J* **2015**, *46*, 1150-1166, doi:10.1183/09031936.00183214.
296. Guyot, C.; Lepreux, S.; Combe, C.; Sarrazy, V.; Billet, F.; Balabaud, C.; Bioulac-Sage, P.; Desmoulière, A. Fibrogenic cell phenotype modifications during remodelling of normal and pathological human liver in cultured slices. *Liver Int* **2010**, *30*, 1529-1540, doi:10.1111/j.1478-3231.2010.02342.x.
297. Yu, G.; Ibarra, G.H.; Kaminski, N. Fibrosis: Lessons from OMICS analyses of the human lung. *Matrix Biology* **2018**, *68-69*, 422-434, doi:https://doi.org/10.1016/j.matbio.2018.03.014.
298. Selman, M.; Ruiz, V.; Cabrera, S.; Segura, L.; Ramírez, R.; Barrios, R.; Pardo, A. TIMP-1, -2, -3, and -4 in idiopathic pulmonary fibrosis. A prevailing nondegradative lung microenvironment? *American journal of physiology. Lung cellular and molecular physiology* **2000**, *279*, L562-574, doi:10.1152/ajplung.2000.279.3.L562.
299. Zuo, F.; Kaminski, N.; Eugui, E.; Allard, J.; Yakhini, Z.; Ben-Dor, A.; Lollini, L.; Morris, D.; Kim, Y.; DeLustro, B.; et al. Gene expression analysis reveals matrilysin as a key regulator of pulmonary fibrosis in mice and humans. *Proc Natl Acad Sci U S A* **2002**, *99*, 6292-6297, doi:10.1073/pnas.092134099.
300. Jaffar, J.; Wong, M.; Fishbein, G.A.; Alhamdoosh, M.; McMillan, L.; Gamell-Fulla, C.; Ng, M.; Wilson, N.; Symons, K.; Glaspole, I.; et al. Matrix metalloproteinase-7 is increased in lung bases but not apices in idiopathic pulmonary fibrosis. *ERJ Open Res* **2022**, *8*, doi:10.1183/23120541.00191-2022.
301. Vukmirovic, M.; Herazo-Maya, J.D.; Blackmon, J.; Skodric-Trifunovic, V.; Jovanovic, D.; Pavlovic, S.; Stojsic, J.; Zeljkovic, V.; Yan, X.; Homer, R.; et al. Identification and validation of differentially expressed transcripts by RNA-sequencing of formalin-fixed, paraffin-embedded (FFPE) lung tissue from patients with Idiopathic Pulmonary Fibrosis. *BMC Pulm Med* **2017**, *17*, 15, doi:10.1186/s12890-016-0356-4.
302. Herazo-Maya, J.D.; Noth, I.; Duncan, S.R.; Kim, S.; Ma, S.F.; Tseng, G.C.; Feingold, E.; Juan-Guardela, B.M.; Richards, T.J.; Lussier, Y.; et al. Peripheral blood mononuclear cell gene expression profiles predict poor outcome in idiopathic pulmonary fibrosis. *Sci Transl Med* **2013**, *5*, 205ra136, doi:10.1126/scitranslmed.3005964.
303. Herazo-Maya, J.D.; Sun, J.; Molyneaux, P.L.; Li, Q.; Villalba, J.A.; Tzouvelekis, A.; Lynn, H.; Juan-Guardela, B.M.; Risquez, C.; Osorio, J.C.; et al. Validation of a 52-gene risk profile for outcome prediction in patients with idiopathic pulmonary fibrosis: an international, multicentre, cohort study. *Lancet Respir Med* **2017**, *5*, 857-868, doi:10.1016/s2213-2600(17)30349-1.
304. Manzoni, C.; Kia, D.A.; Vandrovcova, J.; Hardy, J.; Wood, N.W.; Lewis, P.A.; Ferrari, R. Genome, transcriptome and proteome: the rise of omics data and their integration in biomedical sciences. *Brief Bioinform* **2018**, *19*, 286-302, doi:10.1093/bib/bbw114.
305. Landi, C.; Bergantini, L.; Cameli, P.; d'Alessandro, M.; Carleo, A.; Shaba, E.; Rottoli, P.; Bini, L.; Bargagli, E. Idiopathic Pulmonary Fibrosis Serum proteomic analysis before and after nintedanib therapy. *Scientific Reports* **2020**, *10*, 9378, doi:10.1038/s41598-020-66296-z.

306. Wang, L.; Zhu, M.; Li, Y.; Yan, P.; Li, Z.; Chen, X.; Yang, J.; Pan, X.; Zhao, H.; Wang, S.; et al. Serum Proteomics Identifies Biomarkers Associated With the Pathogenesis of Idiopathic Pulmonary Fibrosis. *Mol Cell Proteomics* **2023**, *22*, 100524, doi:10.1016/j.mcpro.2023.100524.
307. Ruan, P.; Todd, J.L.; Zhao, H.; Liu, Y.; Vinisko, R.; Soellner, J.F.; Schmid, R.; Kaner, R.J.; Luckhardt, T.R.; Neely, M.L.; et al. Integrative multi-omics analysis reveals novel idiopathic pulmonary fibrosis endotypes associated with disease progression. *Respiratory Research* **2023**, *24*, 141, doi:10.1186/s12931-023-02435-0.
308. Jabeen, A.; Mohamedali, A.; Ranganathan, S. Looking for Missing Proteins. In *Reference Module in Life Sciences*; Elsevier: 2019.
309. Emrich, S.J.; Barbazuk, W.B.; Li, L.; Schnable, P.S. Gene discovery and annotation using LCM-454 transcriptome sequencing. *Genome Res* **2007**, *17*, 69-73, doi:10.1101/gr.5145806.
310. Li, X.; Wang, C.-Y. From bulk, single-cell to spatial RNA sequencing. *International Journal of Oral Science* **2021**, *13*, 36, doi:10.1038/s41368-021-00146-0.
311. Henderson, N.C.; Rieder, F.; Wynn, T.A. Fibrosis: from mechanisms to medicines. *Nature* **2020**, *587*, 555-566, doi:10.1038/s41586-020-2938-9.
312. Olsen, T.K.; Baryawno, N. Introduction to Single-Cell RNA Sequencing. *Curr Protoc Mol Biol* **2018**, *122*, e57, doi:10.1002/cpmb.57.
313. Chung, B.K.; Øgaard, J.; Reims, H.M.; Karlsen, T.H.; Melum, E. Spatial transcriptomics identifies enriched gene expression and cell types in human liver fibrosis. *Hepatol Commun* **2022**, *6*, 2538-2550, doi:10.1002/hep4.2001.
314. Mehal, W.Z.; Iredale, J.; Friedman, S.L. Scraping fibrosis: expressway to the core of fibrosis. *Nat Med* **2011**, *17*, 552-553, doi:10.1038/nm0511-552.
315. Martinez, F.J.; Collard, H.R.; Pardo, A.; Raghu, G.; Richeldi, L.; Selman, M.; Swigris, J.J.; Taniguchi, H.; Wells, A.U. Idiopathic pulmonary fibrosis. *Nat Rev Dis Primers* **2017**, *3*, 17074, doi:10.1038/nrdp.2017.74.
316. Maher, T.M.; Bendstrup, E.; Dron, L.; Langley, J.; Smith, G.; Khalid, J.M.; Patel, H.; Kreuter, M. Global incidence and prevalence of idiopathic pulmonary fibrosis. *Respir Res* **2021**, *22*, 197, doi:10.1186/s12931-021-01791-z.
317. Wouters, O.J.; McKee, M.; Luyten, J. Estimated Research and Development Investment Needed to Bring a New Medicine to Market, 2009-2018. *Jama* **2020**, *323*, 844-853, doi:10.1001/jama.2020.1166.
318. Nelson, M.R.; Tipney, H.; Painter, J.L.; Shen, J.; Nicoletti, P.; Shen, Y.; Floratos, A.; Sham, P.C.; Li, M.J.; Wang, J.; et al. The support of human genetic evidence for approved drug indications. *Nat Genet* **2015**, *47*, 856-860.
319. Sun, Z.; Lou, Y.; Hu, X.; Song, F.; Zheng, X.; Hu, Y.; Ding, H.; Zhang, Y.; Huang, P. Single-cell sequencing analysis fibrosis provides insights into the pathobiological cell types and cytokines of radiation-induced pulmonary fibrosis. *BMC Pulmonary Medicine* **2023**, *23*, 149, doi:10.1186/s12890-023-02424-5.
320. Deng, C.-C.; Hu, Y.-F.; Zhu, D.-H.; Cheng, Q.; Gu, J.-J.; Feng, Q.-L.; Zhang, L.-X.; Xu, Y.-P.; Wang, D.; Rong, Z.; et al. Single-cell RNA-seq reveals fibroblast heterogeneity and increased mesenchymal fibroblasts in human fibrotic skin diseases. *Nature Communications* **2021**, *12*, 3709, doi:10.1038/s41467-021-24110-y.
321. Slyper, M.; Porter, C.B.M.; Ashenberg, O.; Waldman, J.; Drokhlyansky, E.; Wakiro, I.; Smillie, C.; Smith-Rosario, G.; Wu, J.; Dionne, D.; et al. A single-cell and single-nucleus RNA-Seq toolbox for fresh and frozen human tumors. *Nat Med* **2020**, *26*, 792-802, doi:10.1038/s41591-020-0844-1.
322. Wolock, S.L.; Lopez, R.; Klein, A.M. Scrublet: computational identification of cell doublets in single-cell transcriptomic data. *Cell systems* **2019**, *8*, 281-291. e289.
323. Young, M.D.; Behjati, S. SoupX removes ambient RNA contamination from droplet-based single-cell RNA sequencing data. *Gigascience* **2020**, *9*, giaa151.

324. Hafemeister, C.; Satija, R. Normalization and variance stabilization of single-cell RNA-seq data using regularized negative binomial regression. *Genome Biol* **2019**, *20*, 296.
325. Row, S.; Liu, Y.; Alimperti, S.; Agarwal, S.K.; Andreadis, S.T. Cadherin-11 is a novel regulator of extracellular matrix synthesis and tissue mechanics. *J Cell Sci* **2016**, *129*, 2950-2961.
326. Langhe, R.P.; Gudzenko, T.; Bachmann, M.; Becker, S.F.; Gonnermann, C.; Winter, C.; Abbruzzese, G.; Alfandari, D.; Kratzer, M.-C.; Franz, C.M.; et al. Cadherin-11 localizes to focal adhesions and promotes cell–substrate adhesion. *Nature Communications* **2016**, *7*, 10909.
327. Kalantari, E.; Razmi, M.; Tajik, F.; Asadi-Lari, M.; Ghods, R.; Madjd, Z. Oncogenic functions and clinical significances of DCLK1 isoforms in colorectal cancer: a systematic review and meta-analysis. *Cancer Cell International* **2022**, *22*, 217, doi:10.1186/s12935-022-02632-9.
328. Vijai, M.; Baba, M.; Ramalingam, S.; Thiyagaraj, A. DCLK1 and its interaction partners: An effective therapeutic target for colorectal cancer. *Oncol Lett* **2021**, *22*, 850, doi:10.3892/ol.2021.13111.
329. Kobayashi, T.; Chanmee, T.; Itano, N. Hyaluronan: Metabolism and Function. *Biomolecules* **2020**, *10*, 1525.
330. Garantziotis, S.; Savani, R.C. Hyaluronan biology: A complex balancing act of structure, function, location and context. *Matrix Biol* **2019**, *78-79*, 1-10, doi:10.1016/j.matbio.2019.02.002.
331. Calabro, N.E.; Kristofik, N.J.; Kyriakides, T.R. Thrombospondin-2 and extracellular matrix assembly. *Biochim Biophys Acta* **2014**, *1840*, 2396-2402, doi:10.1016/j.bbagen.2014.01.013.
332. Iwadare, T.; Kimura, T.; Tanaka, N.; Yamazaki, T.; Wakabayashi, S.-i.; Okumura, T.; Kobayashi, H.; Yamashita, Y.; Pydi, S.P.; Nakajima, T.; et al. Circulating thrombospondin 2 levels reflect fibrosis severity and disease activity in HCV-infected patients. *Scientific Reports* **2022**, *12*, 18900, doi:10.1038/s41598-022-23357-9.
333. Winkles, J.A. The TWEAK-Fn14 cytokine-receptor axis: discovery, biology and therapeutic targeting. *Nat Rev Drug Discov* **2008**, *7*, 411-425, doi:10.1038/nrd2488.
334. Lu, X.; Le Noble, F.; Yuan, L.; Jiang, Q.; De Lafarge, B.; Sugiyama, D.; Bréant, C.; Claes, F.; De Smet, F.; Thomas, J.L.; et al. The netrin receptor UNC5B mediates guidance events controlling morphogenesis of the vascular system. *Nature* **2004**, *432*, 179-186, doi:10.1038/nature03080.
335. Islam, S.; Watanabe, H. Versican: A Dynamic Regulator of the Extracellular Matrix. *J Histochem Cytochem* **2020**, *68*, 763-775, doi:10.1369/0022155420953922.
336. Wight, T.N.; Kang, I.; Evanko, S.P.; Harten, I.A.; Chang, M.Y.; Pearce, O.M.T.; Allen, C.E.; Frevert, C.W. Versican-A Critical Extracellular Matrix Regulator of Immunity and Inflammation. *Front Immunol* **2020**, *11*, 512, doi:10.3389/fimmu.2020.00512.
337. Zhang, Q.; Pan, Y.; Ji, J.; Xu, Y.; Zhang, Q.; Qin, L. Roles and action mechanisms of WNT4 in cell differentiation and human diseases: a review. *Cell Death Discovery* **2021**, *7*, 287, doi:10.1038/s41420-021-00668-w.
338. Hu, H.-H.; Cao, G.; Wu, X.-Q.; Vaziri, N.D.; Zhao, Y.-Y. Wnt signaling pathway in aging-related tissue fibrosis and therapies. *Ageing Research Reviews* **2020**, *60*, 101063, doi:https://doi.org/10.1016/j.arr.2020.101063.
339. Duspara, K.; Bojanic, K.; Pejic, J.I.; Kuna, L.; Kolaric, T.O.; Nincevic, V.; Smolic, R.; Vcev, A.; Glasnovic, M.; Curcic, I.B.; et al. Targeting the Wnt Signaling Pathway in Liver Fibrosis for Drug Options: An Update. *Journal of Clinical and Translational Hepatology* **2021**, *9*, 960-971, doi:10.14218/JCTH.2021.00065.
340. Miao, L.; Targher, G.; Byrne, C.D.; Cao, Y.-Y.; Zheng, M.-H. Current status and future trends of the global burden of MASLD. *Trends in Endocrinology & Metabolism* **2024**, *35*, 697-707, doi:https://doi.org/10.1016/j.tem.2024.02.007.
341. Pergolizzi, J.V., Jr.; LeQuang, J.A.; Varrassi, M.; Breve, F.; Magnusson, P.; Varrassi, G. What Do We Need to Know About Rising Rates of Idiopathic Pulmonary Fibrosis? A Narrative Review and Update. *Adv Ther* **2023**, *40*, 1334-1346, doi:10.1007/s12325-022-02395-9.

342. Yang, X.; Li, Q.; Liu, W.; Zong, C.; Wei, L.; Shi, Y.; Han, Z. Mesenchymal stromal cells in hepatic fibrosis/cirrhosis: from pathogenesis to treatment. *Cellular & Molecular Immunology* **2023**, doi:10.1038/s41423-023-00983-5.
343. Westra, I.M.; Mutsaers, H.A.; Luangmonkong, T.; Hadi, M.; Oosterhuis, D.; de Jong, K.P.; Groothuis, G.M.; Olinga, P. Human precision-cut liver slices as a model to test antifibrotic drugs in the early onset of liver fibrosis. *Toxicol In Vitro* **2016**, *35*, 77-85, doi:10.1016/j.tiv.2016.05.012.
344. Liu, J.; Xiao, Q.; Xiao, J.; Niu, C.; Li, Y.; Zhang, X.; Zhou, Z.; Shu, G.; Yin, G. Wnt/β-catenin signalling: function, biological mechanisms, and therapeutic opportunities. *Signal Transduction and Targeted Therapy* **2022**, *7*, 3, doi:10.1038/s41392-021-00762-6.
345. Qin, K.; Yu, M.; Fan, J.; Wang, H.; Zhao, P.; Zhao, G.; Zeng, W.; Chen, C.; Wang, Y.; Wang, A.; et al. Canonical and noncanonical Wnt signaling: Multilayered mediators, signaling mechanisms and major signaling crosstalk. *Genes Dis* **2024**, *11*, 103-134, doi:10.1016/j.gendis.2023.01.030.
346. Mehta, S.; Hingole, S.; Chaudhary, V. The Emerging Mechanisms of Wnt Secretion and Signaling in Development. *Front Cell Dev Biol* **2021**, *9*, 714746, doi:10.3389/fcell.2021.714746.
347. Liu, Y.; Qi, X.; Donnelly, L.; Elghobashi-Meinhardt, N.; Long, T.; Zhou, R.W.; Sun, Y.; Wang, B.; Li, X. Mechanisms and inhibition of Porcupine-mediated Wnt acylation. *Nature* **2022**, *607*, 816-822.
348. Torres, V.I.; Godoy, J.A.; Inestrosa, N.C. Modulating Wnt signaling at the root: Porcupine and Wnt acylation. *Pharmacology & Therapeutics* **2019**, *198*, 34-45.
349. Li, S.-S.; Sun, Q.; Hua, M.-R.; Suo, P.; Chen, J.-R.; Yu, X.-Y.; Zhao, Y.-Y. Targeting the Wnt/β-Catenin Signaling Pathway as a Potential Therapeutic Strategy in Renal Tubulointerstitial Fibrosis. *Frontiers in pharmacology* **2021**, *12*, doi:10.3389/fphar.2021.719880.
350. Lam, A.P.; Gottardi, C.J. β-catenin signaling: a novel mediator of fibrosis and potential therapeutic target. *Curr Opin Rheumatol* **2011**, *23*, 562-567, doi:10.1097/BOR.0b013e32834b3309.
351. Yousefi, F.; Shabaninejad, Z.; Vakili, S.; Derakhshan, M.; Movahedpour, A.; Dabiri, H.; Ghasemi, Y.; Mahjoubin-Tehran, M.; Nikoozadeh, A.; Savardashtaki, A.; et al. TGF-β and WNT signaling pathways in cardiac fibrosis: non-coding RNAs come into focus. *Cell Commun Signal* **2020**, *18*, 87.
352. Chilosi, M.; Poletti, V.; Zamò, A.; Lestani, M.; Montagna, L.; Piccoli, P.; Pedron, S.; Bertaso, M.; Scarpa, A.; Murer, B.; et al. Aberrant Wnt/β-Catenin Pathway Activation in Idiopathic Pulmonary Fibrosis. *The American Journal of Pathology* **2003**, *162*, 1495-1502, doi:https://doi.org/10.1016/S0002-9440(10)64282-4.
353. Beyer, C.; Schramm, A.; Akhmetshina, A.; Dees, C.; Kireva, T.; Gelse, K.; Sonnylal, S.; Crombrugghe, B.d.; Taketo, M.M.; Distler, O.; et al. β-catenin is a central mediator of pro-fibrotic Wnt signaling in systemic sclerosis. *Annals of the Rheumatic Diseases* **2012**, *71*, 761-767, doi:10.1136/annrheumdis-2011-200568.
354. Nishikawa, K.; Osawa, Y.; Kimura, K. Wnt/β-Catenin Signaling as a Potential Target for the Treatment of Liver Cirrhosis Using Antifibrotic Drugs. *Int J Mol Sci* **2018**, *19*, doi:10.3390/ijms19103103.
355. Cao, H.; Wang, C.; Chen, X.; Hou, J.; Xiang, Z.; Shen, Y.; Han, X. Inhibition of Wnt/β-catenin signaling suppresses myofibroblast differentiation of lung resident mesenchymal stem cells and pulmonary fibrosis. *Scientific Reports* **2018**, *8*, 13644, doi:10.1038/s41598-018-28968-9.
356. Akcora, B.; Storm, G.; Bansal, R. Inhibition of canonical WNT signaling pathway by β-catenin/CBP inhibitor ICG-001 ameliorates liver fibrosis in vivo through suppression of stromal CXCL12. *Biochim Biophys Acta Mol Basis Dis* **2018**, *1864*, 804-818, doi:10.1016/j.bbadis.2017.12.001.
357. Emami, K.H.; Nguyen, C.; Ma, H.; Kim, D.H.; Jeong, K.W.; Eguchi, M.; Moon, R.T.; Teo, J.L.; Kim, H.Y.; Moon, S.H.; et al. A small molecule inhibitor of beta-catenin/CREB-binding protein

transcription [corrected]. *Proc Natl Acad Sci U S A* **2004**, *101*, 12682-12687, doi:10.1073/pnas.0404875101.
358. Henderson, W.R., Jr.; Chi, E.Y.; Ye, X.; Nguyen, C.; Tien, Y.T.; Zhou, B.; Borok, Z.; Knight, D.A.; Kahn, M. Inhibition of Wnt/beta-catenin/CREB binding protein (CBP) signaling reverses pulmonary fibrosis. *Proc Natl Acad Sci U S A* **2010**, *107*, 14309-14314.
359. Burgy, O.; Königshoff, M. The WNT signaling pathways in wound healing and fibrosis. *Matrix Biology* **2018**, *68-69*, 67-80.
360. Yin, C.; Ye, Z.; Wu, J.; Huang, C.; Pan, L.; Ding, H.; Zhong, L.; Guo, L.; Zou, Y.; Wang, X.; et al. Elevated Wnt2 and Wnt4 activate NF-κB signaling to promote cardiac fibrosis by cooperation of Fzd4/2 and LRP6 following myocardial infarction. *EBioMedicine* **2021**, *74*, 103745, doi:10.1016/j.ebiom.2021.103745.
361. Surendran, K.; McCaul, S.P.; Simon, T.C. A role for Wnt-4 in renal fibrosis. *American Journal of Physiology-Renal Physiology* **2002**, *282*, F431-F441.
362. Ishak, K.; Baptista, A.; Bianchi, L.; Callea, F.; De Groote, J.; Gudat, F.; Denk, H.; Desmet, V.; Korb, G.; MacSween, R.N.; et al. Histological grading and staging of chronic hepatitis. *J Hepatol* **1995**, *22*, 696-699, doi:10.1016/0168-8278(95)80226-6.
363. Kimura, K.; Kanto, T.; Shimoda, S.; Harada, K.; Kimura, M.; Nishikawa, K.; Imamura, J.; Ogawa, E.; Saio, M.; Ikura, Y.; et al. Safety, tolerability, and anti-fibrotic efficacy of the CBP/β-catenin inhibitor PRI-724 in patients with hepatitis C and B virus-induced liver cirrhosis: An investigator-initiated, open-label, non-randomised, multicentre, phase 1/2a study. *EBioMedicine* **2022**, *80*, doi:10.1016/j.ebiom.2022.104069.
364. Yu, F.; Yu, C.; Li, F.; Zuo, Y.; Wang, Y.; Yao, L.; Wu, C.; Wang, C.; Ye, L. Wnt/β-catenin signaling in cancers and targeted therapies. *Signal Transduction and Targeted Therapy* **2021**, *6*, 307, doi:10.1038/s41392-021-00701-5.
365. Kondo, S.; Kawazoe, A.; Iwasa, S.; Yamamoto, N.; Ueda, Y.; Nagao, S.; Kimura, T.; Suzuki, I.; Hayata, N.; Tamai, T.; et al. A phase 1 study of E7386, a CREB-binding protein (CBP)/β-catenin interaction inhibitor, in patients (pts) with advanced solid tumors including colorectal cancer: Updated dose-escalation part. *Journal of Clinical Oncology* **2023**, *41*, 106-106, doi:10.1200/JCO.2023.41.4_suppl.106.
366. Rodon, J.; Argilés, G.; Connolly, R.M.; Vaishampayan, U.; de Jonge, M.; Garralda, E.; Giannakis, M.; Smith, D.C.; Dobson, J.R.; McLaughlin, M.E.; et al. Phase 1 study of single-agent WNT974, a first-in-class Porcupine inhibitor, in patients with advanced solid tumours. *Br J Cancer* **2021**, *125*, 28-37, doi:10.1038/s41416-021-01389-8.
367. Jang, J.; Jung, Y.; Kim, Y.; Jho, E.H.; Yoon, Y. LPS-induced inflammatory response is suppressed by Wnt inhibitors, Dickkopf-1 and LGK974. *Sci Rep* **2017**, *7*, 41612, doi:10.1038/srep41612.
368. Jang, J.; Song, J.; Lee, H.; Sim, I.; Kwon, Y.V.; Jho, E.-h.; Yoon, Y. LGK974 suppresses lipopolysaccharide-induced endotoxemia in mice by modulating the crosstalk between the Wnt/β-catenin and NF-κB pathways. *Experimental & Molecular Medicine* **2021**, *53*, 407-421, doi:10.1038/s12276-021-00577-z.
369. Ray, K. HAstening the development of liver fibrosis. *Nature Reviews Gastroenterology & Hepatology* **2019**, *16*, 455-455.
370. Kim, S.M.; Song, G.Y.; Shim, A.; Lee, J.H.; Eom, C.B.; Liu, C.; Yang, Y.M.; Seki, E. Hyaluronan synthase 2, a target of miR-200c, promotes carbon tetrachloride-induced acute and chronic liver inflammation via regulation of CCL3 and CCL4. *Experimental & Molecular Medicine* **2022**, *54*, 739-752, doi:10.1038/s12276-022-00781-5.
371. Kim, Y.H.; Lee, S.B.; Shim, S.; Kim, A.; Park, J.H.; Jang, W.S.; Lee, S.J.; Myung, J.K.; Park, S.; Lee, S.J.; et al. Hyaluronic acid synthase 2 promotes malignant phenotypes of colorectal cancer cells through transforming growth factor beta signaling. *Cancer Sci* **2019**, *110*, 2226-2236, doi:10.1111/cas.14070.
372. Karalis, T. Targeting Hyaluronan Synthesis in Cancer: A Road Less Travelled. *Biologics* **2023**, *3*, 402-414.

373. Kim, J.; Seki, E. Hyaluronan in liver fibrosis: basic mechanisms, clinical implications, and therapeutic targets. *Hepatol Commun* **2023**, *7*, doi:10.1097/hc9.0000000000000083.
374. Halimani, N.; Nesterchuk, M.; Tsitrina, A.A.; Sabirov, M.; Andreichenko, I.N.; Dashenkova, N.O.; Petrova, E.; Kulikov, A.M.; Zatsepin, T.S.; Romanov, R.A.; et al. Knockdown of Hyaluronan synthase 2 suppresses liver fibrosis in mice via induction of transcriptomic changes similar to 4MU treatment. *Scientific Reports* **2024**, *14*, 2797, doi:10.1038/s41598-024-53089-x.
375. Yang, Y.M.; Noureddin, M.; Liu, C.; Ohashi, K.; Kim, S.Y.; Ramnath, D.; Powell, E.E.; Sweet, M.J.; Roh, Y.S.; Hsin, I.-F.; et al. Hyaluronan synthase 2–mediated hyaluronan production mediates Notch1 activation and liver fibrosis. *Science Translational Medicine* **2019**, *11*, eaat9284, doi:doi:10.1126/scitranslmed.aat9284.
376. Vollmann, E.H.; Cao, L.; Amatucci, A.; Reynolds, T.; Hamann, S.; Dalkilic-Liddle, I.; Cameron, T.O.; Hossbach, M.; Kauffman, K.J.; Mir, F.F. Identification of novel fibrosis modifiers by in vivo siRNA silencing. *Molecular Therapy-Nucleic Acids* **2017**, *7*, 314-323.
377. Li, Y.; Liang, J.; Yang, T.; Monterrosa Mena, J.; Huan, C.; Xie, T.; Kurkciyan, A.; Liu, N.; Jiang, D.; Noble, P.W. Hyaluronan synthase 2 regulates fibroblast senescence in pulmonary fibrosis. *Matrix Biol* **2016**, *55*, 35-48.
378. Nagy, N.; Kuipers, H.F.; Frymoyer, A.R.; Ishak, H.D.; Bollyky, J.B.; Wight, T.N.; Bollyky, P.L. 4-methylumbelliferone treatment and hyaluronan inhibition as a therapeutic strategy in inflammation, autoimmunity, and cancer. *Front Immunol* **2015**, *6*, 123, doi:10.3389/fimmu.2015.00123.
379. Rosser, J.I.; Nagy, N.; Goel, R.; Kaber, G.; Demirdjian, S.; Saxena, J.; Bollyky, J.B.; Frymoyer, A.R.; Pacheco-Navarro, A.E.; Burgener, E.B.; et al. Oral hymecromone decreases hyaluronan in human study participants. *J Clin Invest* **2022**, *132*, doi:10.1172/jci157983.
380. Hallgren, R.; Samuelsson, T.; Laurent, T.C.; Modig, J. Accumulation of hyaluronan (hyaluronic acid) in the lung in adult respiratory distress syndrome. *Am Rev Respir Dis* **1989**, *139*, 682-687.
381. Ding, M.; Zhang, Q.; Li, Q.; Wu, T.; Huang, Y.-z. Correlation analysis of the severity and clinical prognosis of 32 cases of patients with COVID-19. *Respiratory medicine* **2020**, *167*.
382. Hellman, U.; Karlsson, M.G.; Engström-Laurent, A.; Cajander, S.; Dorofte, L.; Ahlm, C.; Laurent, C.; Blomberg, A. Presence of hyaluronan in lung alveoli in severe Covid-19: An opening for new treatment options? *Journal of Biological Chemistry* **2020**, *295*, 15418-15422.
383. Yang, S.; Ling, Y.; Zhao, F.; Li, W.; Song, Z.; Wang, L.; Li, Q.; Liu, M.; Tong, Y.; Chen, L.; et al. Hymecromone: a clinical prescription hyaluronan inhibitor for efficiently blocking COVID-19 progression. *Signal Transduction and Targeted Therapy* **2022**, *7*, 91, doi:10.1038/s41392-022-00952-w.
384. Carre, A.L.; James, A.W.; MacLeod, L.; Kong, W.; Kawai, K.; Longaker, M.T.; Lorenz, H.P. Interaction of Wingless Protein (Wnt), Transforming Growth Factor-β1, and Hyaluronan Production in Fetal and Postnatal Fibroblasts. *Plastic and Reconstructive Surgery* **2010**, *125*, 74-88, doi:10.1097/PRS.0b013e3181c495d1.
385. Sun, Y.; Ying, X.; Li, R.; Weng, M.; Shi, J.; Chen, Z. FGF9 Promotes Expression of HAS2 in Palatal Elevation via the Wnt/β-Catenin/TCF7L2 Pathway. *Biomolecules* **2022**, *12*, doi:10.3390/biom12111639.
386. Akhmetshina, A.; Palumbo, K.; Dees, C.; Bergmann, C.; Venalis, P.; Zerr, P.; Horn, A.; Kireva, T.; Beyer, C.; Zwerina, J.; et al. Activation of canonical Wnt signalling is required for TGF-β-mediated fibrosis. *Nature Communications* **2012**, *3*, 735, doi:10.1038/ncomms1734.
387. Martín-Acosta, P.; Xiao, X. PROTACs to address the challenges facing small molecule inhibitors. *Eur J Med Chem* **2021**, *210*, 112993, doi:10.1016/j.ejmech.2020.112993.
388. Imai, K.; Takaoka, A. Comparing antibody and small-molecule therapies for cancer. *Nat Rev Cancer* **2006**, *6*, 714-727, doi:10.1038/nrc1913.
389. Berrouet, C.; Dorilas, N.; Rejniak, K.A.; Tuncer, N. Comparison of Drug Inhibitory Effects (IC50) in Monolayer and Spheroid Cultures. *Bull Math Biol* **2020**, *82*, 68, doi:10.1007/s11538-020-00746-7.

390. Yamada, K.; Hori, Y.; Inoue, S.; Yamamoto, Y.; Iso, K.; Kamiyama, H.; Yamaguchi, A.; Kimura, T.; Uesugi, M.; Ito, J.; et al. E7386, a Selective Inhibitor of the Interaction between β-Catenin and CBP, Exerts Antitumor Activity in Tumor Models with Activated Canonical Wnt Signaling. *Cancer Res* **2021**, *81*, 1052-1062, doi:10.1158/0008-5472.Can-20-0782.
391. Ferguson, F.M.; Nabet, B.; Raghavan, S.; Liu, Y.; Leggett, A.L.; Kuljanin, M.; Kalekar, R.L.; Yang, A.; He, S.; Wang, J.; et al. Discovery of a selective inhibitor of doublecortin like kinase 1. *Nat Chem Biol* **2020**, *16*, 635-643, doi:10.1038/s41589-020-0506-0.
392. Liu, J.; Pan, S.; Hsieh, M.H.; Ng, N.; Sun, F.; Wang, T.; Kasibhatla, S.; Schuller, A.G.; Li, A.G.; Cheng, D.; et al. Targeting Wnt-driven cancer through the inhibition of Porcupine by LGK974. *Proc Natl Acad Sci U S A* **2013**, *110*, 20224-20229, doi:10.1073/pnas.1314239110.
393. Shultz, M.D.; Cheung, A.K.; Kirby, C.A.; Firestone, B.; Fan, J.; Chen, C.H.; Chen, Z.; Chin, D.N.; Dipietro, L.; Fazal, A.; et al. Identification of NVP-TNKS656: the use of structure-efficiency relationships to generate a highly potent, selective, and orally active tankyrase inhibitor. *J Med Chem* **2013**, *56*, 6495-6511, doi:10.1021/jm400807n.
394. Volpe, D.A.; Hamed, S.S.; Zhang, L.K. Use of different parameters and equations for calculation of IC_{50} values in efflux assays: potential sources of variability in IC_{50} determination. *Aaps j* **2014**, *16*, 172-180, doi:10.1208/s12248-013-9554-7.
395. Grygielko, E.T.; Martin, W.M.; Tweed, C.; Thornton, P.; Harling, J.; Brooks, D.P.; Laping, N.J. Inhibition of Gene Markers of Fibrosis with a Novel Inhibitor of Transforming Growth Factor-β Type I Receptor Kinase in Puromycin-Induced Nephritis. *Journal of Pharmacology and Experimental Therapeutics* **2005**, *313*, 943-951, doi:10.1124/jpet.104.082099.
396. Gong, X.; Lin, C.; Cheng, J.; Su, J.; Zhao, H.; Liu, T.; Wen, X.; Zhao, P. Generation of Multicellular Tumor Spheroids with Microwell-Based Agarose Scaffolds for Drug Testing. *PLoS One* **2015**, *10*, e0130348, doi:10.1371/journal.pone.0130348.
397. Farhat, J.; Pandey, I.; AlWahsh, M. Transcending toward Advanced 3D-Cell Culture Modalities: A Review about an Emerging Paradigm in Translational Oncology. *Cells* **2021**, *10*, doi:10.3390/cells10071657.
398. Langhans, S.A. Three-Dimensional in Vitro Cell Culture Models in Drug Discovery and Drug Repositioning. *Frontiers in pharmacology* **2018**, *9*, 6, doi:10.3389/fphar.2018.00006.
399. Nowacka, M.; Sterzynska, K.; Andrzejewska, M.; Nowicki, M.; Januchowski, R. Drug resistance evaluation in novel 3D in vitro model. *Biomedicine & Pharmacotherapy* **2021**, *138*, 111536, doi:https://doi.org/10.1016/j.biopha.2021.111536.
400. Firuzi, O.; Che, P.P.; El Hassouni, B.; Buijs, M.; Coppola, S.; Löhr, M.; Funel, N.; Heuchel, R.; Carnevale, I.; Schmidt, T.; et al. Role of c-MET Inhibitors in Overcoming Drug Resistance in Spheroid Models of Primary Human Pancreatic Cancer and Stellate Cells. *Cancers (Basel)* **2019**, *11*, doi:10.3390/cancers11050638.
401. Perocheau, D.; Gurung, S.; Touramanidou, L.; Duff, C.; Sharma, G.; Sebire, N.; Finn, P.F.; Cavedon, A.; Siddiqui, S.; Rice, L.; et al. Ex vivo precision-cut liver slices model disease phenotype and monitor therapeutic response for liver monogenic diseases. *F1000Research* **2024**, *12*, doi:https://doi.org/10.12688/f1000research.142014.2.
402. Lederer, D.J.; Martinez, F.J. Idiopathic Pulmonary Fibrosis. *New England Journal of Medicine* **2018**, *378*, 1811-1823, doi:10.1056/NEJMra1705751.
403. Raghu, G.; Remy-Jardin, M.; Myers, J.L.; Richeldi, L.; Ryerson, C.J.; Lederer, D.J.; Behr, J.; Cottin, V.; Danoff, S.K.; Morell, F.; et al. Diagnosis of Idiopathic Pulmonary Fibrosis. An Official ATS/ERS/JRS/ALAT Clinical Practice Guideline. *American Journal of Respiratory and Critical Care Medicine* **2018**, *198*, e44-e68, doi:10.1164/rccm.201807-1255ST.
404. Kapnadak, S.G.; Raghu, G. Lung transplantation for interstitial lung disease. *European Respiratory Review* **2021**, *30*, 210017, doi:10.1183/16000617.0017-2021.
405. Richeldi, L.; du Bois, R.M.; Raghu, G.; Azuma, A.; Brown, K.K.; Costabel, U.; Cottin, V.; Flaherty, K.R.; Hansell, D.M.; Inoue, Y.; et al. Efficacy and Safety of Nintedanib in Idiopathic Pulmonary

Fibrosis. *New England Journal of Medicine* **2014**, *370*, 2071-2082, doi:10.1056/NEJMoa1402584.
406. King, T.E.; Bradford, W.Z.; Castro-Bernardini, S.; Fagan, E.A.; Glaspole, I.; Glassberg, M.K.; Gorina, E.; Hopkins, P.M.; Kardatzke, D.; Lancaster, L.; et al. A Phase 3 Trial of Pirfenidone in Patients with Idiopathic Pulmonary Fibrosis. *New England Journal of Medicine* **2014**, *370*, 2083-2092, doi:10.1056/NEJMoa1402582.
407. Maher, T.M.; Strek, M.E. Antifibrotic therapy for idiopathic pulmonary fibrosis: time to treat. *Respir Res* **2019**, *20*, 205, doi:10.1186/s12931-019-1161-4.
408. Moor, C.C.; Mostard, R.L.M.; Grutters, J.C.; Bresser, P.; Aerts, J.G.J.V.; Dirksen, C.D.; Kimman, M.L.; Wijsenbeek, M.S. Patient expectations, experiences and satisfaction with nintedanib and pirfenidone in idiopathic pulmonary fibrosis: a quantitative study. *Respiratory Research* **2020**, *21*, 196, doi:10.1186/s12931-020-01458-1.
409. Marijic, P.; Schwarzkopf, L.; Schwettmann, L.; Ruhnke, T.; Trudzinski, F.; Kreuter, M. Pirfenidone vs. nintedanib in patients with idiopathic pulmonary fibrosis: a retrospective cohort study. *Respiratory Research* **2021**, *22*, 268, doi:10.1186/s12931-021-01857-y.
410. Kim, E.; Mathai, S.K.; Stancil, I.T.; Ma, X.; Hernandez-Gutierrez, A.; Becerra, J.N.; Marrero-Torres, E.; Hennessy, C.E.; Hatakka, K.; Wartchow, E.P.; et al. Aberrant Multiciliogenesis in Idiopathic Pulmonary Fibrosis. *American Journal of Respiratory Cell and Molecular Biology* **2022**, *67*, 188-200, doi:10.1165/rcmb.2021-0554OC.
411. Yang, I.V.; Coldren, C.D.; Leach, S.M.; Seibold, M.A.; Murphy, E.; Lin, J.; Rosen, R.; Neidermyer, A.J.; McKean, D.F.; Groshong, S.D.; et al. Expression of cilium-associated genes defines novel molecular subtypes of idiopathic pulmonary fibrosis. *Thorax* **2013**, *68*, 1114-1121, doi:10.1136/thoraxjnl-2012-202943.
412. Gharib, S.A.; Altemeier, W.A.; Van Winkle, L.S.; Plopper, C.G.; Schlesinger, S.Y.; Buell, C.A.; Brauer, R.; Lee, V.; Parks, W.C.; Chen, P. Matrix metalloproteinase-7 coordinates airway epithelial injury response and differentiation of ciliated cells. *Am J Respir Cell Mol Biol* **2013**, *48*, 390-396, doi:10.1165/rcmb.2012-0083OC.
413. Englert, J.M.; Hanford, L.E.; Kaminski, N.; Tobolewski, J.M.; Tan, R.J.; Fattman, C.L.; Ramsgaard, L.; Richards, T.J.; Loutaev, I.; Nawroth, P.P.; et al. A role for the receptor for advanced glycation end products in idiopathic pulmonary fibrosis. *Am J Pathol* **2008**, *172*, 583-591.
414. Vukmirovic, M.; Kaminski, N. Impact of Transcriptomics on Our Understanding of Pulmonary Fibrosis. *Front Med (Lausanne)* **2018**, *5*, 87.
415. Nakano, Y.; Yang, I.V.; Walts, A.D.; Watson, A.M.; Helling, B.A.; Fletcher, A.A.; Lara, A.R.; Schwarz, M.I.; Evans, C.M.; Schwartz, D.A. MUC5B Promoter Variant rs35705950 Affects MUC5B Expression in the Distal Airways in Idiopathic Pulmonary Fibrosis. *Am J Respir Crit Care Med* **2016**, *193*, 464-466, doi:10.1164/rccm.201509-1872LE.
416. Yang, I.V.; Fingerlin, T.E.; Evans, C.M.; Schwarz, M.I.; Schwartz, D.A. MUC5B and Idiopathic Pulmonary Fibrosis. *Ann Am Thorac Soc* **2015**, *12 Suppl 2*, S193-199.
417. Hancock, L.A.; Hennessy, C.E.; Solomon, G.M.; Dobrinskikh, E.; Estrella, A.; Hara, N.; Hill, D.B.; Kissner, W.J.; Markovetz, M.R.; Grove Villalon, D.E.; et al. Muc5b overexpression causes mucociliary dysfunction and enhances lung fibrosis in mice. *Nature Communications* **2018**, *9*, 5363, doi:10.1038/s41467-018-07768-9.
418. Horan, G.S.; Wood, S.; Ona, V.; Li, D.J.; Lukashev, M.E.; Weinreb, P.H.; Simon, K.J.; Hahm, K.; Allaire, N.E.; Rinaldi, N.J.; et al. Partial inhibition of integrin alpha(v)beta6 prevents pulmonary fibrosis without exacerbating inflammation. *Am J Respir Crit Care Med* **2008**, *177*, 56-65, doi:10.1164/rccm.200706-805OC.
419. Saini, G.; Porte, J.; Weinreb, P.H.; Violette, S.M.; Wallace, W.A.; McKeever, T.M.; Jenkins, G. αvβ6 integrin may be a potential prognostic biomarker in interstitial lung disease. *Eur Respir J* **2015**, *46*, 486-494, doi:10.1183/09031936.00210414.
420. Sheppard, D. The role of integrins in pulmonary fibrosis. *European Respiratory Review* **2008**, *17*, 157-162, doi:10.1183/09059180.00010909.

421. John, A.E.; Graves, R.H.; Pun, K.T.; Vitulli, G.; Forty, E.J.; Mercer, P.F.; Morrell, J.L.; Barrett, J.W.; Rogers, R.F.; Hafeji, M.; et al. Translational pharmacology of an inhaled small molecule αvβ6 integrin inhibitor for idiopathic pulmonary fibrosis. *Nature Communications* **2020**, *11*, 4659.
422. Wilkinson, A.L.; John, A.E.; Barrett, J.W.; Gower, E.; Morrison, V.S.; Man, Y.; Pun, K.T.; Roper, J.A.; Luckett, J.C.; Borthwick, L.A.; et al. Pharmacological characterisation of GSK3335103, an oral αvβ6 integrin small molecule RGD-mimetic inhibitor for the treatment of fibrotic disease. *European Journal of Pharmacology* **2021**, *913*, 174618, doi:https://doi.org/10.1016/j.ejphar.2021.174618.
423. Sun, D.; Gao, W.; Hu, H.; Zhou, S. Why 90% of clinical drug development fails and how to improve it? *Acta Pharmaceutica Sinica B* **2022**, *12*, 3049-3062, doi:https://doi.org/10.1016/j.apsb.2022.02.002.
424. Tashiro, J.; Rubio, G.A.; Limper, A.H.; Williams, K.; Elliot, S.J.; Ninou, I.; Aidinis, V.; Tzouvelekis, A.; Glassberg, M.K. Exploring Animal Models That Resemble Idiopathic Pulmonary Fibrosis. *Front Med (Lausanne)* **2017**, *4*, 118, doi:10.3389/fmed.2017.00118.
425. Degryse, A.L.; Lawson, W.E. Progress toward improving animal models for idiopathic pulmonary fibrosis. *Am J Med Sci* **2011**, *341*, 444-449, doi:10.1097/MAJ.0b013e31821aa000.
426. Sundarakrishnan, A.; Chen, Y.; Black, L.D.; Aldridge, B.B.; Kaplan, D.L. Engineered cell and tissue models of pulmonary fibrosis. *Advanced Drug Delivery Reviews* **2018**, *129*, 78-94, doi:https://doi.org/10.1016/j.addr.2017.12.013.
427. Zheng, P.; Sun, S.; Wang, J.; Cheng, Z.J.; Lei, K.C.; Xue, M.; Zhang, T.; Huang, H.; Zhang, X.D.; Sun, B. Integrative omics analysis identifies biomarkers of idiopathic pulmonary fibrosis. *Cell Mol Life Sci* **2022**, *79*, 66, doi:10.1007/s00018-021-04094-0.
428. Habermann, A.C.; Gutierrez, A.J.; Bui, L.T.; Yahn, S.L.; Winters, N.I.; Calvi, C.L.; Peter, L.; Chung, M.I.; Taylor, C.J.; Jetter, C.; et al. Single-cell RNA sequencing reveals profibrotic roles of distinct epithelial and mesenchymal lineages in pulmonary fibrosis. *Sci Adv* **2020**, *6*, eaba1972, doi:10.1126/sciadv.aba1972.
429. Luzina, I.G.; Salcedo, M.V.; Rojas-Peña, M.L.; Wyman, A.E.; Galvin, J.R.; Sachdeva, A.; Clerman, A.; Kim, J.; Franks, T.J.; Britt, E.J.; et al. Transcriptomic evidence of immune activation in macroscopically normal-appearing and scarred lung tissues in idiopathic pulmonary fibrosis. *Cell Immunol* **2018**, *325*, 1-13.
430. McDonough, J.E.; Ahangari, F.; Li, Q.; Jain, S.; Verleden, S.E.; Herazo-Maya, J.; Vukmirovic, M.; DeIuliis, G.; Tzouvelekis, A.; Tanabe, N.; et al. Transcriptional regulatory model of fibrosis progression in the human lung. *JCI Insight* **2019**, *4*.
431. Tian, Y.; Li, H.; Gao, Y.; Liu, C.; Qiu, T.; Wu, H.; Cao, M.; Zhang, Y.; Ding, H.; Chen, J.; et al. Quantitative proteomic characterization of lung tissue in idiopathic pulmonary fibrosis. *Clinical Proteomics* **2019**, *16*, 6.
432. Schiller, H.B.; Mayr, C.H.; Leuschner, G.; Strunz, M.; Staab-Weijnitz, C.; Preisendörfer, S.; Eckes, B.; Moinzadeh, P.; Krieg, T.; Schwartz, D.A.; et al. Deep Proteome Profiling Reveals Common Prevalence of MZB1-Positive Plasma B Cells in Human Lung and Skin Fibrosis. *American Journal of Respiratory and Critical Care Medicine* **2017**, *196*, 1298-1310, doi:10.1164/rccm.201611-2263OC.
433. DeNichilo, M.O.; Panagopoulos, V.; Rayner, T.E.; Borowicz, R.A.; Greenwood, J.E.; Evdokiou, A. Peroxidase Enzymes Regulate Collagen Extracellular Matrix Biosynthesis. *The American Journal of Pathology* **2015**, *185*, 1372-1384, doi:https://doi.org/10.1016/j.ajpath.2015.01.013.
434. Zhu, Y.; Huang, Y.; Ji, Q.; Fu, S.; Gu, J.; Tai, N.; Wang, X. Interplay between Extracellular Matrix and Neutrophils in Diseases. *J Immunol Res* **2021**, *2021*, 8243378.
435. Chua, F.; Dunsmore, S.E.; Clingen, P.H.; Mutsaers, S.E.; Shapiro, S.D.; Segal, A.W.; Roes, J.; Laurent, G.J. Mice lacking neutrophil elastase are resistant to bleomycin-induced pulmonary fibrosis. *Am J Pathol* **2007**, *170*, 65-74.

436. Gregory, A.D.; Kliment, C.R.; Metz, H.E.; Kim, K.H.; Kargl, J.; Agostini, B.A.; Crum, L.T.; Oczypok, E.A.; Oury, T.A.; Houghton, A.M. Neutrophil elastase promotes myofibroblast differentiation in lung fibrosis. *J Leukoc Biol* **2015**, *98*, 143-152.
437. Takemasa, A.; Ishii, Y.; Fukuda, T. A neutrophil elastase inhibitor prevents bleomycin-induced pulmonary fibrosis in mice. *Eur Respir J* **2012**, *40*, 1475-1482.
438. Ziegenhagen, M.W.; Zabel, P.; Zissel, G.; Schlaak, M.; Müller-Quernheim, J. Serum level of interleukin 8 is elevated in idiopathic pulmonary fibrosis and indicates disease activity. *Am J Respir Crit Care Med* **1998**, *157*, 762-768.
439. Lahoz-Beneytez, J.; Elemans, M.; Zhang, Y.; Ahmed, R.; Salam, A.; Block, M.; Niederalt, C.; Asquith, B.; Macallan, D. Human neutrophil kinetics: modeling of stable isotope labeling data supports short blood neutrophil half-lives. *Blood* **2016**, *127*, 3431-3438, doi:10.1182/blood-2016-03-700336.
440. Summers, C.; Rankin, S.M.; Condliffe, A.M.; Singh, N.; Peters, A.M.; Chilvers, E.R. Neutrophil kinetics in health and disease. *Trends Immunol* **2010**, *31*, 318-324, doi:10.1016/j.it.2010.05.006.
441. Kupcova Skalnikova, H.; Cizkova, J.; Cervenka, J.; Vodicka, P. Advances in Proteomic Techniques for Cytokine Analysis: Focus on Melanoma Research. *Int J Mol Sci* **2017**, *18*, doi:10.3390/ijms18122697.
442. Son, E.D.; Kim, H.; Choi, H.; Lee, S.H.; Lee, J.Y.; Kim, S.; Closs, B.; Lee, S.; Chung, J.H.; Hwang, J.S. Cathepsin G increases MMP expression in normal human fibroblasts through fibronectin fragmentation, and induces the conversion of proMMP-1 to active MMP-1. *J Dermatol Sci* **2009**, *53*, 150-152, doi:10.1016/j.jdermsci.2008.08.006.
443. Taggart, C.; Mall, M.A.; Lalmanach, G.; Cataldo, D.; Ludwig, A.; Janciauskiene, S.; Heath, N.; Meiners, S.; Overall, C.M.; Schultz, C.; et al. Protean proteases: at the cutting edge of lung diseases. *European Respiratory Journal* **2017**, *49*, 1501200, doi:10.1183/13993003.01200-2015.
444. Wong, S.L.; Sukkar, M.B. The SPARC protein: an overview of its role in lung cancer and pulmonary fibrosis and its potential role in chronic airways disease. *Br J Pharmacol* **2017**, *174*, 3-14.
445. Conforti, F.; Ridley, R.; Brereton, C.; Alzetani, A.; Johnson, B.; Marshall, B.G.; Fletcher, S.V.; Ottensmeier, C.H.; Richeldi, L.; Skipp, P.; et al. Paracrine SPARC signaling dysregulates alveolar epithelial barrier integrity and function in lung fibrosis. *Cell Death Discovery* **2020**, *6*, 54.
446. Nakasaki, M.; Hwang, Y.; Xie, Y.; Kataria, S.; Gund, R.; Hajam, E.Y.; Samuel, R.; George, R.; Danda, D.; M.J, P.; et al. The matrix protein Fibulin-5 is at the interface of tissue stiffness and inflammation in fibrosis. *Nature Communications* **2015**, *6*, 8574.
447. Sivakumar, P.; Ammar, R.; Thompson, J.R.; Luo, Y.; Streltsov, D.; Porteous, M.; McCoubrey, C.; Cantu, E.; Beers, M.F.; Jarai, G.; et al. Integrated plasma proteomics and lung transcriptomics reveal novel biomarkers in idiopathic pulmonary fibrosis. *Respiratory Research* **2021**, *22*, 273.
448. Todd, J.L.; Neely, M.L.; Overton, R.; Durham, K.; Gulati, M.; Huang, H.; Roman, J.; Newby, L.K.; Flaherty, K.R.; Vinisko, R.; et al. Peripheral blood proteomic profiling of idiopathic pulmonary fibrosis biomarkers in the multicentre IPF-PRO Registry. *Respir Res* **2019**, *20*, 227.
449. Kehlet, S.N.; Manon-Jensen, T.; Sun, S.; Brix, S.; Leeming, D.J.; Karsdal, M.A.; Willumsen, N. A fragment of SPARC reflecting increased collagen affinity shows pathological relevance in lung cancer – implications of a new collagen chaperone function of SPARC. *Cancer Biology & Therapy* **2018**, *19*, 904-912.
450. Jia, M.; Rosas, L.; Kapetanaki, M.G.; Tabib, T.; Sebrat, J.; Cruz, T.; Bondonese, A.; Mora, A.L.; Lafyatis, R.; Rojas, M.; et al. Early events marking lung fibroblast transition to profibrotic state in idiopathic pulmonary fibrosis. *Respiratory Research* **2023**, *24*, 116.
451. Akhurst, R.J.; Hata, A. Targeting the TGFβ signalling pathway in disease. *Nat Rev Drug Discov* **2012**, *11*, 790-811, doi:10.1038/nrd3810.

452. Conroy, K.P.; Kitto, L.J.; Henderson, N.C. αv integrins: key regulators of tissue fibrosis. *Cell Tissue Res* **2016**, *365*, 511-519, doi:10.1007/s00441-016-2407-9.
453. Mamuya, F.A.; Duncan, M.K. aV integrins and TGF-β-induced EMT: a circle of regulation. *J Cell Mol Med* **2012**, *16*, 445-455, doi:10.1111/j.1582-4934.2011.01419.x.
454. Xiao, T.; Takagi, J.; Coller, B.S.; Wang, J.-H.; Springer, T.A. Structural basis for allostery in integrins and binding to fibrinogen-mimetic therapeutics. *Nature* **2004**, *432*, 59-67.
455. Henry, R.P.; Swenson, E.R. The distribution and physiological significance of carbonic anhydrase in vertebrate gas exchange organs. *Respiration Physiology* **2000**, *121*, 1-12.
456. Nava, V.E.; Khosla, R.; Shin, S.; Mordini, F.E.; Bandyopadhyay, B.C. Enhanced carbonic anhydrase expression with calcification and fibrosis in bronchial cartilage during COPD. *Acta Histochem* **2022**, *124*, 151834.
457. Iwakawa, H.O.; Tomari, Y. Life of RISC: Formation, action, and degradation of RNA-induced silencing complex. *Molecular cell* **2022**, *82*, 30-43.
458. Cadena-Suárez, A.R.; Hernández-Hernández, H.A.; Alvarado-Vásquez, N.; Rangel-Escareño, C.; Sommer, B.; Negrete-García, M.C. Role of MicroRNAs in Signaling Pathways Associated with the Pathogenesis of Idiopathic Pulmonary Fibrosis: A Focus on Epithelial-Mesenchymal Transition. *Int J Mol Sci* **2022**, *23*.
459. Pandit, K.V.; Milosevic, J.; Kaminski, N. MicroRNAs in idiopathic pulmonary fibrosis. *Transl Res* **2011**, *157*, 191-199.
460. Oak, S.R.; Murray, L.; Herath, A.; Sleeman, M.; Anderson, I.; Joshi, A.D.; Coelho, A.L.; Flaherty, K.R.; Toews, G.B.; Knight, D.; et al. A micro RNA processing defect in rapidly progressing idiopathic pulmonary fibrosis. *PLoS One* **2011**, *6*, e21253.
461. Donato, R.; Cannon, B.R.; Sorci, G.; Riuzzi, F.; Hsu, K.; Weber, D.J.; Geczy, C.L. Functions of S100 proteins. *Curr Mol Med* **2013**, *13*, 24-57.
462. Perkins, T.N.; Oury, T.D. The perplexing role of RAGE in pulmonary fibrosis: causality or casualty? *Ther Adv Respir Dis* **2021**, *15*, 17534666211016071.
463. Su, Y.; Xu, C.; Sun, Z.; Liang, Y.; Li, G.; Tong, T.; Chen, J. S100A13 promotes senescence-associated secretory phenotype and cellular senescence via modulation of non-classical secretion of IL-1α. *Aging* **2019**, *11*, 549-572.
464. Bridges, A.A.; Gladfelter, A.S. Septin Form and Function at the Cell Cortex. *J Biol Chem* **2015**, *290*, 17173-17180, doi:10.1074/jbc.R114.634444.
465. Ivanov, A.I.; Le, H.T.; Naydenov, N.G.; Rieder, F. Novel Functions of the Septin Cytoskeleton: Shaping Up Tissue Inflammation and Fibrosis. *The American Journal of Pathology* **2021**, *191*, 40-51.
466. Neubauer, K.; Neubauer, B.; Seidl, M.; Zieger, B. Characterization of septin expression in normal and fibrotic kidneys. *Cytoskeleton* **2019**, *76*, 143-153.
467. Fan, Y.; Du, Z.; Steib, C.J.; Ding, Q.; Lu, P.; Tian, D.; Liu, M. Effect of SEPT6 on the biological behavior of hepatic stellate cells and liver fibrosis in rats and its mechanism. *Laboratory Investigation* **2019**, *99*, 17-36.
468. Liu, Y.; Beyer, A.; Aebersold, R. On the Dependency of Cellular Protein Levels on mRNA Abundance. *Cell* **2016**, *165*, 535-550.
469. Lundberg, E.; Borner, G.H.H. Spatial proteomics: a powerful discovery tool for cell biology. *Nature Reviews Molecular Cell Biology* **2019**, *20*, 285-302.
470. de Jong, M.; Essers, J.; van Weerden, W.M. Imaging preclinical tumour models: improving translational power. *Nat Rev Cancer* **2014**, *14*, 481-493, doi:10.1038/nrc3751.
471. Liberati, T.A.; Randle, M.R.; Toth, L.A. In vitro lung slices: a powerful approach for assessment of lung pathophysiology. *Expert Rev Mol Diagn* **2010**, *10*, 501-508, doi:10.1586/erm.10.21.
472. Sewald, K.; Braun, A. Assessment of immunotoxicity using precision-cut tissue slices. *Xenobiotica* **2013**, *43*, 84-97, doi:10.3109/00498254.2012.731543.
473. Uhl, F.E.; Vierkotten, S.; Wagner, D.E.; Burgstaller, G.; Costa, R.; Koch, I.; Lindner, M.; Meiners, S.; Eickelberg, O.; Königshoff, M. Preclinical validation and imaging of Wnt-induced repair in

human 3D lung tissue cultures. *European Respiratory Journal* **2015**, *46*, 1150-1166, doi:10.1183/09031936.00183214.
474. Koziol-White, C.; Gebski, E.; Cao, G.; Panettieri, R.A. Precision cut lung slices: an integrated ex vivo model for studying lung physiology, pharmacology, disease pathogenesis and drug discovery. *Respiratory Research* **2024**, *25*, 231, doi:10.1186/s12931-024-02855-6.
475. Catania, J.M.; Pershing, A.M.; Gandolfi, A.J. Precision-cut tissue chips as an in vitro toxicology system. *Toxicology in Vitro* **2007**, *21*, 956-961, doi:https://doi.org/10.1016/j.tiv.2007.02.001.
476. Brennan, P.N.; Elsharkawy, A.M.; Kendall, T.J.; Loomba, R.; Mann, D.A.; Fallowfield, J.A. Antifibrotic therapy in nonalcoholic steatohepatitis: time for a human-centric approach. *Nature Reviews Gastroenterology & Hepatology* **2023**, *20*, 679-688, doi:10.1038/s41575-023-00796-x.
477. Cardoso, B.D.; Castanheira, E.M.S.; Lanceros-Méndez, S.; Cardoso, V.F. Recent Advances on Cell Culture Platforms for In Vitro Drug Screening and Cell Therapies: From Conventional to Microfluidic Strategies. *Advanced Healthcare Materials* **2023**, *12*, 2202936, doi:https://doi.org/10.1002/adhm.202202936.
478. Lam, M.; Lamanna, E.; Organ, L.; Donovan, C.; Bourke, J.E. Perspectives on precision cut lung slices—powerful tools for investigation of mechanisms and therapeutic targets in lung diseases. *Frontiers in pharmacology* **2023**, *14*, doi:10.3389/fphar.2023.1162889.
479. Koivisto, L.; Bi, J.; Häkkinen, L.; Larjava, H. Integrin αvβ6: Structure, function and role in health and disease. *Int J Biochem Cell Biol* **2018**, *99*, 186-196, doi:10.1016/j.biocel.2018.04.013.
480. Brzozowska, E.; Deshmukh, S. Integrin Alpha v Beta 6 (αvβ6) and Its Implications in Cancer Treatment. *Int J Mol Sci* **2022**, *23*, doi:10.3390/ijms232012346.
481. Munger, J.S.; Huang, X.; Kawakatsu, H.; Griffiths, M.J.; Dalton, S.L.; Wu, J.; Pittet, J.F.; Kaminski, N.; Garat, C.; Matthay, M.A.; et al. The integrin alpha v beta 6 binds and activates latent TGF beta 1: a mechanism for regulating pulmonary inflammation and fibrosis. *Cell* **1999**, *96*, 319-328.
482. John, A.E.; Graves, R.H.; Pun, K.T.; Vitulli, G.; Forty, E.J.; Mercer, P.F.; Morrell, J.L.; Barrett, J.W.; Rogers, R.F.; Hafeji, M.; et al. Translational pharmacology of an inhaled small molecule αvβ6 integrin inhibitor for idiopathic pulmonary fibrosis. *Nat Commun* **2020**, *11*, 4659, doi:10.1038/s41467-020-18397-6.
483. Raghu, G.; Mouded, M.; Prasse, A.; Stebbins, C.; Zhao, G.; Song, G.; Arefayene, M.; Violette, S.M.; Gallagher, D.; Gibson, K.F. Randomized Phase IIa Clinical Study of an Anti-α(v)β(6) Monoclonal Antibody in Idiopathic Pulmonary Fibrosis. *Am J Respir Crit Care Med* **2022**, *206*, 1166-1168, doi:10.1164/rccm.202205-0868LE.
484. Raghu, G.; Mouded, M.; Chambers, D.C.; Martinez, F.J.; Richeldi, L.; Lancaster, L.H.; Hamblin, M.J.; Gibson, K.F.; Rosas, I.O.; Prasse, A.; et al. A Phase IIb Randomized Clinical Study of an Anti-α(v)β(6) Monoclonal Antibody in Idiopathic Pulmonary Fibrosis. *Am J Respir Crit Care Med* **2022**, *206*, 1128-1139, doi:10.1164/rccm.202112-2824OC.
485. Lancaster, L.; Cottin, V.; Ramaswamy, M.; Wuyts, W.A.; Jenkins, R.G.; Scholand, M.B.; Kreuter, M.; Valenzuela, C.; Ryerson, C.J.; Goldin, J.; et al. Bexotegrast in Patients with Idiopathic Pulmonary Fibrosis: The INTEGRIS-IPF Clinical Trial. *American Journal of Respiratory and Critical Care Medicine* **2024**, *210*, 424-434, doi:10.1164/rccm.202403-0636OC.
486. Sime, P.; Jenkins, G. Goldilocks and the Three Trials: Clinical Trials Targeting the α(v)β(6) Integrin in Idiopathic Pulmonary Fibrosis. *Am J Respir Crit Care Med* **2022**, *206*, 1062-1063, doi:10.1164/rccm.202208-1579ED.
487. Koth, L.L.; Alex, B.; Hawgood, S.; Nead, M.A.; Sheppard, D.; Erle, D.J.; Morris, D.G. Integrin beta6 mediates phospholipid and collectin homeostasis by activation of latent TGF-beta1. *Am J Respir Cell Mol Biol* **2007**, *37*, 651-659, doi:10.1165/rcmb.2006-0428OC.
488. Morris, D.G.; Huang, X.; Kaminski, N.; Wang, Y.; Shapiro, S.D.; Dolganov, G.; Glick, A.; Sheppard, D. Loss of integrin alpha(v)beta6-mediated TGF-beta activation causes Mmp12-dependent emphysema. *Nature* **2003**, *422*, 169-173, doi:10.1038/nature01413.

489. Wardak, M.; Turner, S.; Mooney, J.; Rizzo, G.; Morris, K.; Jacobs, s.; Duan, H.; Lefebvre, E.; Cosgrove, G.; Wong, S.; et al. Phase 2 drug target engagement study of PLN-74809 in patients with idiopathic pulmonary fibrosis using a novel αvβ6 cystine knot PET imaging tracer. *Journal of Nuclear Medicine* **2022**, *63*, 2236-2236.
490. Stebler, S.; Raghunath, M. The Scar-in-a-JarScar-in-a-Jar: In Vitro Fibrosis Model for Anti-Fibrotic Drug Testing. In *Myofibroblasts: Methods and Protocols*, Hinz, B., Lagares, D., Eds.; Springer US: New York, NY, 2021; pp. 147-156.
491. Poole, J.J.A.; Mostaço-Guidolin, L.B. Optical Microscopy and the Extracellular Matrix Structure: A Review. *Cells* **2021**, *10*, doi:10.3390/cells10071760.
492. Wijsman, P.C.; van Smoorenburg, L.H.; de Bruin, D.M.; Annema, J.T.; Kerstjens, H.A.M.; Mets, O.M.; van den Berge, M.; Bonta, P.I.; Burgess, J.K. Imaging the pulmonary extracellular matrix. *Current Opinion in Physiology* **2021**, *22*, 100444, doi:https://doi.org/10.1016/j.cophys.2021.05.007.
493. Ochoa, L.F.; Kholodnykh, A.; Villarreal, P.; Tian, B.; Pal, R.; Freiberg, A.N.; Brasier, A.R.; Motamedi, M.; Vargas, G. Imaging of Murine Whole Lung Fibrosis by Large Scale 3D Microscopy aided by Tissue Optical Clearing. *Scientific Reports* **2018**, *8*, 13348, doi:10.1038/s41598-018-31182-2.
494. Slack, R.J.; Macdonald, S.J.F.; Roper, J.A.; Jenkins, R.G.; Hatley, R.J.D. Emerging therapeutic opportunities for integrin inhibitors. *Nat Rev Drug Discov* **2022**, *21*, 60-78, doi:10.1038/s41573-021-00284-4.
495. Reardon, D.A.; Cheresh, D. Cilengitide: a prototypic integrin inhibitor for the treatment of glioblastoma and other malignancies. *Genes Cancer* **2011**, *2*, 1159-1165, doi:10.1177/1947601912450586.
496. Dai, X.; Su, Z.; Liu, J.O. An improved synthesis of a selective αvβ3-integrin antagonist cyclo(-RGDfK-). *Tetrahedron Letters* **2000**, *41*, 6295-6298, doi:https://doi.org/10.1016/S0040-4039(00)01060-1.
497. Scotton, C.J.; Krupiczojc, M.A.; Königshoff, M.; Mercer, P.F.; Lee, Y.C.; Kaminski, N.; Morser, J.; Post, J.M.; Maher, T.M.; Nicholson, A.G.; et al. Increased local expression of coagulation factor X contributes to the fibrotic response in human and murine lung injury. *J Clin Invest* **2009**, *119*, 2550-2563.
498. Asano, Y.; Ihn, H.; Jinnin, M.; Mimura, Y.; Tamaki, K. Involvement of alphavbeta5 integrin in the establishment of autocrine TGF-beta signaling in dermal fibroblasts derived from localized scleroderma. *J Invest Dermatol* **2006**, *126*, 1761-1769, doi:10.1038/sj.jid.5700331.
499. Asano, Y.; Ihn, H.; Yamane, K.; Jinnin, M.; Mimura, Y.; Tamaki, K. Increased expression of integrin alpha(v)beta3 contributes to the establishment of autocrine TGF-beta signaling in scleroderma fibroblasts. *J Immunol* **2005**, *175*, 7708-7718, doi:10.4049/jimmunol.175.11.7708.
500. Atabai, K.; Jame, S.; Azhar, N.; Kuo, A.; Lam, M.; McKleroy, W.; Dehart, G.; Rahman, S.; Xia, D.D.; Melton, A.C.; et al. Mfge8 diminishes the severity of tissue fibrosis in mice by binding and targeting collagen for uptake by macrophages. *J Clin Invest* **2009**, *119*, 3713-3722, doi:10.1172/jci40053.
501. Patsenker, E.; Popov, Y.; Stickel, F.; Schneider, V.; Ledermann, M.; Sägesser, H.; Niedobitek, G.; Goodman, S.L.; Schuppan, D. Pharmacological inhibition of integrin alphavbeta3 aggravates experimental liver fibrosis and suppresses hepatic angiogenesis. *Hepatology* **2009**, *50*, 1501-1511, doi:10.1002/hep.23144.
502. Cirkel, G.A.; Kerklaan, B.M.; Vanhoutte, F.; Van der Aa, A.; Lorenzon, G.; Namour, F.; Pujuguet, P.; Darquenne, S.; de Vos, F.Y.; Snijders, T.J.; et al. A dose escalating phase I study of GLPG0187, a broad spectrum integrin receptor antagonist, in adult patients with progressive high-grade glioma and other advanced solid malignancies. *Invest New Drugs* **2016**, *34*, 184-192.
503. Henderson, N.C.; Arnold, T.D.; Katamura, Y.; Giacomini, M.M.; Rodriguez, J.D.; McCarty, J.H.; Pellicoro, A.; Raschperger, E.; Betsholtz, C.; Ruminski, P.G.; et al. Targeting of αv integrin

identifies a core molecular pathway that regulates fibrosis in several organs. *Nat Med* **2013**, *19*, 1617-1624.
504. Zhang, J.; Wang, T.; Saigal, A.; Johnson, J.; Morrisson, J.; Tabrizifard, S.; Hollingsworth, S.A.; Eddins, M.J.; Mao, W.; O'Neill, K.; et al. Discovery of a new class of integrin antibodies for fibrosis. *Scientific Reports* **2021**, *11*, 2118, doi:10.1038/s41598-021-81253-0.
505. White, E.S.; Atrasz, R.G.; Hu, B.; Phan, S.H.; Stambolic, V.; Mak, T.W.; Hogaboam, C.M.; Flaherty, K.R.; Martinez, F.J.; Kontos, C.D.; et al. Negative regulation of myofibroblast differentiation by PTEN (Phosphatase and Tensin Homolog Deleted on chromosome 10). *Am J Respir Crit Care Med* **2006**, *173*, 112-121, doi:10.1164/rccm.200507-1058OC.
506. Xia, H.; Diebold, D.; Nho, R.; Perlman, D.; Kleidon, J.; Kahm, J.; Avdulov, S.; Peterson, M.; Nerva, J.; Bitterman, P.; et al. Pathological integrin signaling enhances proliferation of primary lung fibroblasts from patients with idiopathic pulmonary fibrosis. *J Exp Med* **2008**, *205*, 1659-1672, doi:10.1084/jem.20080001.
507. Lukey, P.T.; Harrison, S.A.; Yang, S.; Man, Y.; Holman, B.F.; Rashidnasab, A.; Azzopardi, G.; Grayer, M.; Simpson, J.K.; Bareille, P.; et al. A randomised, placebo-controlled study of omipalisib (PI3K/mTOR) in idiopathic pulmonary fibrosis. *Eur Respir J* **2019**, *53*.
508. Schlessinger, J. Receptor tyrosine kinases: legacy of the first two decades. *Cold Spring Harb Perspect Biol* **2014**, *6*.
509. Schramm, F.; Schaefer, L.; Wygrecka, M. EGFR Signaling in Lung Fibrosis. *Cells* **2022**, *11*, doi:10.3390/cells11060986.
510. Abourehab, M.A.S.; Alqahtani, A.M.; Youssif, B.G.M.; Gouda, A.M. Globally Approved EGFR Inhibitors: Insights into Their Syntheses, Target Kinases, Biological Activities, Receptor Interactions, and Metabolism. *Molecules* **2021**, *26*.
511. Venkataraman, T.; Frieman, M.B. The role of epidermal growth factor receptor (EGFR) signaling in SARS coronavirus-induced pulmonary fibrosis. *Antiviral Research* **2017**, *143*, 142-150, doi:https://doi.org/10.1016/j.antiviral.2017.03.022.
512. Epstein Shochet, G.; Brook, E.; Eyal, O.; Edelstein, E.; Shitrit, D. Epidermal growth factor receptor paracrine upregulation in idiopathic pulmonary fibrosis fibroblasts is blocked by nintedanib. *American journal of physiology. Lung cellular and molecular physiology* **2019**, *316*, L1025-l1034, doi:10.1152/ajplung.00526.2018.
513. Maemondo, M.; Inoue, A.; Kobayashi, K.; Sugawara, S.; Oizumi, S.; Isobe, H.; Gemma, A.; Harada, M.; Yoshizawa, H.; Kinoshita, I.; et al. Gefitinib or chemotherapy for non-small-cell lung cancer with mutated EGFR. *N Engl J Med* **2010**, *362*, 2380-2388, doi:10.1056/NEJMoa0909530.
514. Tzouvelekis, A.; Ntolios, P.; Karameris, A.; Vilaras, G.; Boglou, P.; Koulelidis, A.; Archontogeorgis, K.; Kaltsas, K.; Zacharis, G.; Sarikloglou, E.; et al. Increased expression of epidermal growth factor receptor (EGF-R) in patients with different forms of lung fibrosis. *Biomed Res Int* **2013**, *2013*, 654354.
515. Baughman, R.P.; Lower, E.E.; Miller, M.A.; Bejarano, P.A.; Heffelfinger, S.C. Overexpression of transforming growth factor-alpha and epidermal growth factor-receptor in idiopathic pulmonary fibrosis. *Sarcoidosis Vasc Diffuse Lung Dis* **1999**, *16*, 57-61.
516. Stancil, I.T.; Michalski, J.E.; Davis-Hall, D.; Chu, H.W.; Park, J.A.; Magin, C.M.; Yang, I.V.; Smith, B.J.; Dobrinskikh, E.; Schwartz, D.A. Pulmonary fibrosis distal airway epithelia are dynamically and structurally dysfunctional. *Nat Commun* **2021**, *12*, 4566, doi:10.1038/s41467-021-24853-8.
517. Wang, P.; Tian, Q.; Liang, Z.X.; Yang, Z.; Xu, S.F.; Sun, J.P.; Chen, L.A. Gefitinib attenuates murine pulmonary fibrosis induced by bleomycin. *Chin Med J (Engl)* **2010**, *123*, 2259-2264.
518. Zhou, Y.; Lee, J.-Y.; Lee, C.-M.; Cho, W.-K.; Kang, M.-J.; Koff, J.L.; Yoon, P.-O.; Chae, J.; Park, H.-O.; Elias, J.A.; et al. Amphiregulin, an Epidermal Growth Factor Receptor Ligand, Plays an Essential Role in the Pathogenesis of Transforming Growth Factor-β-induced Pulmonary Fibrosis. *Journal of Biological Chemistry* **2012**, *287*, 41991-42000, doi:https://doi.org/10.1074/jbc.M112.356824.

519. Liang, D.; Chen, H.; Zhao, L.; Zhang, W.; Hu, J.; Liu, Z.; Zhong, P.; Wang, W.; Wang, J.; Liang, G. Inhibition of EGFR attenuates fibrosis and stellate cell activation in diet-induced model of nonalcoholic fatty liver disease. *Biochimica et Biophysica Acta (BBA) - Molecular Basis of Disease* **2018**, *1864*, 133-142, doi:https://doi.org/10.1016/j.bbadis.2017.10.016.
520. Wang, L.; Liu, N.; Xiong, C.; Xu, L.; Shi, Y.; Qiu, A.; Zang, X.; Mao, H.; Zhuang, S. Inhibition of EGF Receptor Blocks the Development and Progression of Peritoneal Fibrosis. *J Am Soc Nephrol* **2016**, *27*, 2631-2644, doi:10.1681/asn.2015030299.
521. Cao, S.; Pan, Y.; Terker, A.S.; Arroyo Ornelas, J.P.; Wang, Y.; Tang, J.; Niu, A.; Kar, S.A.; Jiang, M.; Luo, W.; et al. Epidermal growth factor receptor activation is essential for kidney fibrosis development. *Nature Communications* **2023**, *14*, 7357, doi:10.1038/s41467-023-43226-x.
522. Ishii, Y.; Fujimoto, S.; Fukuda, T. Gefitinib prevents bleomycin-induced lung fibrosis in mice. *Am J Respir Crit Care Med* **2006**, *174*, 550-556, doi:10.1164/rccm.200509-1534OC.
523. Li, L.; Cai, L.; Zheng, L.; Hu, Y.; Yuan, W.; Guo, Z.; Li, W. Gefitinib Inhibits Bleomycin-Induced Pulmonary Fibrosis via Alleviating the Oxidative Damage in Mice. *Oxid Med Cell Longev* **2018**, *2018*, 8249693, doi:10.1155/2018/8249693.
524. Suzuki, H.; Aoshiba, K.; Yokohori, N.; Nagai, A. Epidermal growth factor receptor tyrosine kinase inhibition augments a murine model of pulmonary fibrosis. *Cancer Res* **2003**, *63*, 5054-5059.
525. Inomata, S.; Takahashi, H.; Nagata, M.; Yamada, G.; Shiratori, M.; Tanaka, H.; Satoh, M.; Saitoh, T.; Sato, T.; Abe, S. Acute lung injury as an adverse event of gefitinib. *Anticancer Drugs* **2004**, *15*, 461-467, doi:10.1097/01.cad.0000127666.12215.7b.
526. Meydan, N.; Grunberger, T.; Dadi, H.; Shahar, M.; Arpaia, E.; Lapidot, Z.; Leeder, J.S.; Freedman, M.; Cohen, A.; Gazit, A.; et al. Inhibition of acute lymphoblastic leukaemia by a Jak-2 inhibitor. *Nature* **1996**, *379*, 645-648, doi:10.1038/379645a0.
527. Murakami, K.; Takagi, T. Clustering and detection of 5' splice sites of mRNA by k weight-matrices model. *Pac Symp Biocomput* **1999**, 171-181, doi:10.1142/9789814447300_0017.
528. Gazit, A.; Osherov, N.; Posner, I.; Yaish, P.; Poradosu, E.; Gilon, C.; Levitzki, A. Tyrphostins. 2. Heterocyclic and alpha-substituted benzylidenemalononitrile tyrphostins as potent inhibitors of EGF receptor and ErbB2/neu tyrosine kinases. *J Med Chem* **1991**, *34*, 1896-1907, doi:10.1021/jm00110a022.
529. Aikawa, Y.; Morimoto, K.; Yamamoto, T.; Chaki, H.; Hashiramoto, A.; Narita, H.; Hirono, S.; Shiozawa, S. Treatment of arthritis with a selective inhibitor of c-Fos/activator protein-1. *Nature Biotechnology* **2008**, *26*, 817-823, doi:10.1038/nbt1412.
530. Ruwanpura, S.M.; Thomas, B.J.; Bardin, P.G. Pirfenidone: Molecular Mechanisms and Potential Clinical Applications in Lung Disease. *American Journal of Respiratory Cell and Molecular Biology* **2020**, *62*, 413-422, doi:10.1165/rcmb.2019-0328TR.
531. Lv, Q.; Wang, J.; Xu, C.; Huang, X.; Ruan, Z.; Dai, Y. Pirfenidone alleviates pulmonary fibrosis in vitro and in vivo through regulating Wnt/GSK-3β/β-catenin and TGF-β1/Smad2/3 signaling pathways. *Mol Med* **2020**, *26*, 49, doi:10.1186/s10020-020-00173-3.
532. Conte, E.; Gili, E.; Fagone, E.; Fruciano, M.; Iemmolo, M.; Vancheri, C. Effect of pirfenidone on proliferation, TGF-β-induced myofibroblast differentiation and fibrogenic activity of primary human lung fibroblasts. *European Journal of Pharmaceutical Sciences* **2014**, *58*, 13-19, doi:https://doi.org/10.1016/j.ejps.2014.02.014.
533. Li, Z.; Liu, X.; Wang, B.; Nie, Y.; Wen, J.; Wang, Q.; Gu, C. Pirfenidone suppresses MAPK signalling pathway to reverse epithelial-mesenchymal transition and renal fibrosis. *Nephrology (Carlton)* **2017**, *22*, 589-597, doi:10.1111/nep.12831.
534. Alsafadi, H.N.; Staab-Weijnitz, C.A.; Lehmann, M.; Lindner, M.; Peschel, B.; Königshoff, M.; Wagner, D.E. An ex vivo model to induce early fibrosis-like changes in human precision-cut lung slices. *American Journal of Physiology-Lung Cellular and Molecular Physiology* **2017**, *312*, L896-L902, doi:10.1152/ajplung.00084.2017.

535. Khalil, A.; Quaglia, A.; Gélat, P.; Saffari, N.; Rashidi, H.; Davidson, B. New Developments and Challenges in Liver Transplantation. *Journal of Clinical Medicine* **2023**, *12*, 5586.
536. Goodwin, R.J.A.; Platz, S.J.; Reis-Filho, J.S.; Barry, S.T. Accelerating Drug Development Using Spatial Multi-omics. *Cancer Discovery* **2024**, *14*, 620-624.
537. Lang, N.J.; Gote-Schniering, J.; Porras-Gonzalez, D.; Yang, L.; De Sadeleer, L.J.; Jentzsch, R.C.; Shitov, V.A.; Zhou, S.; Ansari, M.; Agami, A.; et al. Ex vivo tissue perturbations coupled to single-cell RNA-seq reveal multilineage cell circuit dynamics in human lung fibrogenesis. *Science Translational Medicine* **2023**, *15*, eadh0908.
538. Mehta, M.; Bui, T.A.; Yang, X.; Aksoy, Y.; Goldys, E.M.; Deng, W. Lipid-Based Nanoparticles for Drug/Gene Delivery: An Overview of the Production Techniques and Difficulties Encountered in Their Industrial Development. *ACS Materials Au* **2023**, *3*, 600-619.
539. Pettinato, M.C. Introduction to Antibody-Drug Conjugates. *Antibodies (Basel)* **2021**, *10*.
540. Takai, N.; Tanaka, Y.; Saji, H. Quantification of small molecule drugs in biological tissue sections by imaging mass spectrometry using surrogate tissue-based calibration standards. *Mass Spectrom (Tokyo)* **2014**, *3*, A0025.